Journal of Healthcare Engineering

Computer Vision for Human Health and Medical Application

Lead Guest Editor: Kaijian Xia
Guest Editors: Joon Huang Chuah and Gu Xiaoqing

Computer Vision for Human Health and Medical Application

Journal of Healthcare Engineering

Computer Vision for Human Health and Medical Application

Lead Guest Editor: Kaijian Xia
Guest Editors: Joon Huang Chuah and Gu Xiaoqing

Copyright © 2023 Hindawi Limited. All rights reserved.

This is a special issue published in "Journal of Healthcare Engineering." All articles are open access articles distributed under the Creative Commons Attribution License, which permits unrestricted use, distribution, and reproduction in any medium, provided the original work is properly cited.

Associate Editors

Xiao-Jun Chen, China
Feng-Huei Lin, Taiwan
Maria Lindén, Sweden

Academic Editors

Cherif Adnen, Tunisia
Saverio Affatato, Italy
Óscar Belmonte Fernández, Spain
Sweta Bhattacharya, India
Prabadevi Boopathy, India
Weiwei Cai, USA
Gin-Shin Chen, Taiwan
Hongwei Chen, USA
Daniel H.K. Chow, Hong Kong
Gianluca Ciardelli, Italy
Olawande Daramola, South Africa
Elena De Momi, Italy
Costantino Del Gaudio, Italy
Ayush Dogra, India
Luobing Dong, China
Daniel Espino, United Kingdom
Sadiq Fareed, China
Mostafa Fatemi, USA
Jesus Favela, Mexico
Jesus Fontecha, Spain
Agostino Forestiero, Italy
Jean-Luc Gennisson, France
Badicu Georgian, Romania
Mehdi Gheisari, China
Luca Giancardo, USA
Antonio Gloria, Italy
Kheng Lim Goh, Singapore
Carlos Gómez, Spain
Philippe Gorce, France
Vincenzo Guarino, Italy
Muhammet Gul, Turkey
Valentina Hartwig, Italy
David Hewson, United Kingdom
Yan Chai Hum, Malaysia
Ernesto Iadanza, Italy
Cosimo Ieracitano, Italy
Giovanni Improta, Italy
Norio Iriguchi, Japan
Mihajlo Jakovljevic, Japan
Rutvij Jhaveri, India
Yizhang Jiang, China
Zhongwei Jiang, Japan
Rajesh Kaluri, India
Venkatachalam Kandasamy, Czech Republic
Pushpendu Kar, India
Rashed Karim, United Kingdom
Pasi A. Karjalainen, Finland
John S. Katsanis, Greece
Smith Khare, United Kingdom
Terry K.K. Koo, USA
Srinivas Koppu, India
Jui-Yang Lai, Taiwan
Kuruva Lakshmanna, India
Xiang Li, USA
Lun-De Liao, Singapore
Qiu-Hua Lin, China
Aiping Liu, China
Zufu Lu, Australia
Basem M. ElHalawany, Egypt
Praveen Kumar Reddy Maddikunta, India
Ilias Maglogiannis, Greece
Saverio Maietta, Italy
M.Sabarimalai Manikandan, India
Mehran Moazen, United Kingdom
Senthilkumar Mohan, India
Sanjay Mohapatra, India
Rafael Morales, Spain
Mehrbakhsh Nilashi, Malaysia
Sharnil Pandya, India
Jialin Peng, China
Vincenzo Positano, Italy
Saeed Mian Qaisar, Saudi Arabia
Alessandro Ramalli, Italy
Alessandro Reali, Italy
Vito Ricotta, Italy
Jose Joaquin Rieta, Spain
Emanuele Rizzuto, Italy

Dinesh Rokaya, Thailand
Sébastien Roth, France
Simo Saarakkala, Finland
Mangal Sain, Republic of Korea
Nadeem Sarwar, Pakistan
Emiliano Schena, Italy
Prof. Asadullah Shaikh, Saudi Arabia
Jiann-Shing Shieh, Taiwan
Tiago H. Silva, Portugal
Sharan Srinivas, USA
Kathiravan Srinivasan, India
Neelakandan Subramani, India
Le Sun, China
Fabrizio Taffoni, Italy
Jinshan Tang, USA
Ioannis G. Tollis, Greece
Ikram Ud Din, Pakistan
Sathishkumar V E, Republic of Korea
Cesare F. Valenti, Italy
Qiang Wang, China
Uche Wejinya, USA
Yuxiang Wu, China
Ying Yang, United Kingdom
Elisabetta Zanetti, Italy
Haihong Zhang, Singapore
Ping Zhou, USA

Contents

Contents

Contents

Hindawi
Journal of Healthcare Engineering
Volume 2023, Article ID 9891612, 1 page
https://doi.org/10.1155/2023/9891612

Retraction

Retracted: Analysis of the Diagnostic Effect of EUS-RTE on Giant Cystic Tumours of the Oesophagus Based on Cluster Analysis

Journal of Healthcare Engineering

Received 5 December 2023; Accepted 5 December 2023; Published 6 December 2023

Copyright © 2023 Journal of Healthcare Engineering. This is an open access article distributed under the Creative Commons Attribution License, which permits unrestricted use, distribution, and reproduction in any medium, provided the original work is properly cited.

This article has been retracted by Hindawi, as publisher, following an investigation undertaken by the publisher [1]. This investigation has uncovered evidence of systematic manipulation of the publication and peer-review process. We cannot, therefore, vouch for the reliability or integrity of this article.

Please note that this notice is intended solely to alert readers that the peer-review process of this article has been compromised.

Wiley and Hindawi regret that the usual quality checks did not identify these issues before publication and have since put additional measures in place to safeguard research integrity.

We wish to credit our Research Integrity and Research Publishing teams and anonymous and named external researchers and research integrity experts for contributing to this investigation.

The corresponding author, as the representative of all authors, has been given the opportunity to register their agreement or disagreement to this retraction. We have kept a record of any response received.

References

[1] H. Yang, Z. Zhang, Y. He et al., "Analysis of the Diagnostic Effect of EUS-RTE on Giant Cystic Tumours of the Oesophagus Based on Cluster Analysis," *Journal of Healthcare Engineering*, vol. 2021, Article ID 1395826, 11 pages, 2021.

Hindawi
Journal of Healthcare Engineering
Volume 2023, Article ID 9849703, 1 page
https://doi.org/10.1155/2023/9849703

Retraction

Retracted: Analysis of the Mechanism of Breast Metastasis Based on Image Recognition and Ultrasound Diagnosis

Journal of Healthcare Engineering

Received 5 December 2023; Accepted 5 December 2023; Published 6 December 2023

Copyright © 2023 Journal of Healthcare Engineering. This is an open access article distributed under the Creative Commons Attribution License, which permits unrestricted use, distribution, and reproduction in any medium, provided the original work is properly cited.

This article has been retracted by Hindawi, as publisher, following an investigation undertaken by the publisher [1]. This investigation has uncovered evidence of systematic manipulation of the publication and peer-review process. We cannot, therefore, vouch for the reliability or integrity of this article.

Please note that this notice is intended solely to alert readers that the peer-review process of this article has been compromised.

Wiley and Hindawi regret that the usual quality checks did not identify these issues before publication and have since put additional measures in place to safeguard research integrity.

We wish to credit our Research Integrity and Research Publishing teams and anonymous and named external researchers and research integrity experts for contributing to this investigation.

The corresponding author, as the representative of all authors, has been given the opportunity to register their agreement or disagreement to this retraction. We have kept a record of any response received.

References

[1] Y. Huang, S. Zheng, and B. Lai, "Analysis of the Mechanism of Breast Metastasis Based on Image Recognition and Ultrasound Diagnosis," *Journal of Healthcare Engineering*, vol. 2021, Article ID 4452500, 11 pages, 2021.

Hindawi
Journal of Healthcare Engineering
Volume 2023, Article ID 9836495, 1 page
https://doi.org/10.1155/2023/9836495

Retraction

Retracted: Intracavitary Electrocardiogram Guidance Aids Excavation of Rhythm Abnormalities in Patients with Occult Heart Disease

Journal of Healthcare Engineering

Received 5 December 2023; Accepted 5 December 2023; Published 6 December 2023

Copyright © 2023 Journal of Healthcare Engineering. This is an open access article distributed under the Creative Commons Attribution License, which permits unrestricted use, distribution, and reproduction in any medium, provided the original work is properly cited.

This article has been retracted by Hindawi, as publisher, following an investigation undertaken by the publisher [1]. This investigation has uncovered evidence of systematic manipulation of the publication and peer-review process. We cannot, therefore, vouch for the reliability or integrity of this article.

Please note that this notice is intended solely to alert readers that the peer-review process of this article has been compromised.

Wiley and Hindawi regret that the usual quality checks did not identify these issues before publication and have since put additional measures in place to safeguard research integrity.

We wish to credit our Research Integrity and Research Publishing teams and anonymous and named external researchers and research integrity experts for contributing to this investigation.

The corresponding author, as the representative of all authors, has been given the opportunity to register their agreement or disagreement to this retraction. We have kept a record of any response received.

References

[1] Y. Wei, Y. Zhu, X. Wen, Q. Rui, and W. Hu, "Intracavitary Electrocardiogram Guidance Aids Excavation of Rhythm Abnormalities in Patients with Occult Heart Disease," *Journal of Healthcare Engineering*, vol. 2021, Article ID 2230383, 11 pages, 2021.

Hindawi
Journal of Healthcare Engineering
Volume 2023, Article ID 9817063, 1 page
https://doi.org/10.1155/2023/9817063

Retraction

Retracted: Interventional Treatment of Bronchiectasis Macrosomia Based on Multirow CT Tomography Monitoring

Journal of Healthcare Engineering

Received 5 December 2023; Accepted 5 December 2023; Published 6 December 2023

Copyright © 2023 Journal of Healthcare Engineering. This is an open access article distributed under the Creative Commons Attribution License, which permits unrestricted use, distribution, and reproduction in any medium, provided the original work is properly cited.

This article has been retracted by Hindawi, as publisher, following an investigation undertaken by the publisher [1]. This investigation has uncovered evidence of systematic manipulation of the publication and peer-review process. We cannot, therefore, vouch for the reliability or integrity of this article.

Please note that this notice is intended solely to alert readers that the peer-review process of this article has been compromised.

Wiley and Hindawi regret that the usual quality checks did not identify these issues before publication and have since put additional measures in place to safeguard research integrity.

We wish to credit our Research Integrity and Research Publishing teams and anonymous and named external researchers and research integrity experts for contributing to this investigation.

The corresponding author, as the representative of all authors, has been given the opportunity to register their agreement or disagreement to this retraction. We have kept a record of any response received.

References

[1] D. Lu, W. Chai, X. Gao, and X. Yan, “Interventional Treatment of Bronchiectasis Macrosomia Based on Multirow CT Tomography Monitoring,” *Journal of Healthcare Engineering*, vol. 2021, Article ID 9116765, 12 pages, 2021.

Hindawi
Journal of Healthcare Engineering
Volume 2023, Article ID 9873656, 1 page
https://doi.org/10.1155/2023/9873656

Retraction

Retracted: Online Automatic Diagnosis System of Cardiac Arrhythmias Based on MIT-BIH ECG Database

Journal of Healthcare Engineering

Received 10 October 2023; Accepted 10 October 2023; Published 11 October 2023

Copyright © 2023 Journal of Healthcare Engineering. This is an open access article distributed under the Creative Commons Attribution License, which permits unrestricted use, distribution, and reproduction in any medium, provided the original work is properly cited.

This article has been retracted by Hindawi following an investigation undertaken by the publisher [1]. This investigation has uncovered evidence of one or more of the following indicators of systematic manipulation of the publication process:

(1) Discrepancies in scope
(2) Discrepancies in the description of the research reported
(3) Discrepancies between the availability of data and the research described
(4) Inappropriate citations
(5) Incoherent, meaningless and/or irrelevant content included in the article
(6) Peer-review manipulation

The presence of these indicators undermines our confidence in the integrity of the article's content and we cannot, therefore, vouch for its reliability. Please note that this notice is intended solely to alert readers that the content of this article is unreliable. We have not investigated whether authors were aware of or involved in the systematic manipulation of the publication process.

Wiley and Hindawi regrets that the usual quality checks did not identify these issues before publication and have since put additional measures in place to safeguard research integrity.

We wish to credit our own Research Integrity and Research Publishing teams and anonymous and named external researchers and research integrity experts for contributing to this investigation.

The corresponding author, as the representative of all authors, has been given the opportunity to register their agreement or disagreement to this retraction. We have kept a record of any response received.

References

[1] W. Yan and Z. Zhang, "Online Automatic Diagnosis System of Cardiac Arrhythmias Based on MIT-BIH ECG Database," *Journal of Healthcare Engineering*, vol. 2021, Article ID 1819112, 9 pages, 2021.

Hindawi
Journal of Healthcare Engineering
Volume 2023, Article ID 9870814, 1 page
https://doi.org/10.1155/2023/9870814

Retraction

Retracted: Spinal Biomechanical Modelling in the Process of Lumbar Intervertebral Disc Herniation in Middle-Aged and Elderly

Journal of Healthcare Engineering

Received 10 October 2023; Accepted 10 October 2023; Published 11 October 2023

Copyright © 2023 Journal of Healthcare Engineering. This is an open access article distributed under the Creative Commons Attribution License, which permits unrestricted use, distribution, and reproduction in any medium, provided the original work is properly cited.

This article has been retracted by Hindawi following an investigation undertaken by the publisher [1]. This investigation has uncovered evidence of one or more of the following indicators of systematic manipulation of the publication process:

(1) Discrepancies in scope
(2) Discrepancies in the description of the research reported
(3) Discrepancies between the availability of data and the research described
(4) Inappropriate citations
(5) Incoherent, meaningless and/or irrelevant content included in the article
(6) Peer-review manipulation

The presence of these indicators undermines our confidence in the integrity of the article's content and we cannot, therefore, vouch for its reliability. Please note that this notice is intended solely to alert readers that the content of this article is unreliable. We have not investigated whether authors were aware of or involved in the systematic manipulation of the publication process.

In addition, our investigation has also shown that one or more of the following human-subject reporting requirements has not been met in this article: ethical approval by an Institutional Review Board (IRB) committee or equivalent, patient/participant consent to participate, and/or agreement to publish patient/participant details (where relevant).

Wiley and Hindawi regrets that the usual quality checks did not identify these issues before publication and have since put additional measures in place to safeguard research integrity.

We wish to credit our own Research Integrity and Research Publishing teams and anonymous and named external researchers and research integrity experts for contributing to this investigation.

The corresponding author, as the representative of all authors, has been given the opportunity to register their agreement or disagreement to this retraction. We have kept a record of any response received.

References

[1] X. Zhang, Z. Zhao, C. Niu et al., "Spinal Biomechanical Modelling in the Process of Lumbar Intervertebral Disc Herniation in Middle-Aged and Elderly," *Journal of Healthcare Engineering*, vol. 2021, Article ID 2869488, 12 pages, 2021.

Hindawi
Journal of Healthcare Engineering
Volume 2023, Article ID 9864805, 1 page
https://doi.org/10.1155/2023/9864805

Retraction

Retracted: Regression Analysis of Factors Based on Cluster Analysis of Acute Radiation Pneumonia due to Radiation Therapy for Lung Cancer

Journal of Healthcare Engineering

Received 10 October 2023; Accepted 10 October 2023; Published 11 October 2023

Copyright © 2023 Journal of Healthcare Engineering. This is an open access article distributed under the Creative Commons Attribution License, which permits unrestricted use, distribution, and reproduction in any medium, provided the original work is properly cited.

This article has been retracted by Hindawi following an investigation undertaken by the publisher [1]. This investigation has uncovered evidence of one or more of the following indicators of systematic manipulation of the publication process:

(1) Discrepancies in scope
(2) Discrepancies in the description of the research reported
(3) Discrepancies between the availability of data and the research described
(4) Inappropriate citations
(5) Incoherent, meaningless and/or irrelevant content included in the article
(6) Peer-review manipulation

The presence of these indicators undermines our confidence in the integrity of the article's content and we cannot, therefore, vouch for its reliability. Please note that this notice is intended solely to alert readers that the content of this article is unreliable. We have not investigated whether authors were aware of or involved in the systematic manipulation of the publication process.

In addition, our investigation has also shown that one or more of the following human-subject reporting requirements has not been met in this article: ethical approval by an Institutional Review Board (IRB) committee or equivalent, patient/participant consent to participate, and/or agreement to publish patient/participant details (where relevant).

Wiley and Hindawi regrets that the usual quality checks did not identify these issues before publication and have since put additional measures in place to safeguard research integrity.

We wish to credit our own Research Integrity and Research Publishing teams and anonymous and named external researchers and research integrity experts for contributing to this investigation.

The corresponding author, as the representative of all authors, has been given the opportunity to register their agreement or disagreement to this retraction. We have kept a record of any response received.

References

[1] X. Zhang, B. Lv, L. Rui, L. Cai, and F. Liu, "Regression Analysis of Factors Based on Cluster Analysis of Acute Radiation Pneumonia due to Radiation Therapy for Lung Cancer," *Journal of Healthcare Engineering*, vol. 2021, Article ID 3727794, 12 pages, 2021.

Hindawi
Journal of Healthcare Engineering
Volume 2023, Article ID 9852487, 1 page
https://doi.org/10.1155/2023/9852487

Retraction

Retracted: Spiral Computed Tomography in the Quantitative Measurement of the Adjacent Structure of the Left Atrial Appendage in Patients with Atrial Fibrillation

Journal of Healthcare Engineering

Received 10 October 2023; Accepted 10 October 2023; Published 11 October 2023

Copyright © 2023 Journal of Healthcare Engineering. This is an open access article distributed under the Creative Commons Attribution License, which permits unrestricted use, distribution, and reproduction in any medium, provided the original work is properly cited.

This article has been retracted by Hindawi following an investigation undertaken by the publisher [1]. This investigation has uncovered evidence of one or more of the following indicators of systematic manipulation of the publication process:

(1) Discrepancies in scope
(2) Discrepancies in the description of the research reported
(3) Discrepancies between the availability of data and the research described
(4) Inappropriate citations
(5) Incoherent, meaningless and/or irrelevant content included in the article
(6) Peer-review manipulation

The presence of these indicators undermines our confidence in the integrity of the article's content and we cannot, therefore, vouch for its reliability. Please note that this notice is intended solely to alert readers that the content of this article is unreliable. We have not investigated whether authors were aware of or involved in the systematic manipulation of the publication process.

In addition, our investigation has also shown that one or more of the following human-subject reporting requirements has not been met in this article: ethical approval by an Institutional Review Board (IRB) committee or equivalent, patient/participant consent to participate, and/or agreement to publish patient/participant details (where relevant).

Wiley and Hindawi regrets that the usual quality checks did not identify these issues before publication and have since put additional measures in place to safeguard research integrity.

We wish to credit our own Research Integrity and Research Publishing teams and anonymous and named external researchers and research integrity experts for contributing to this investigation.

The corresponding author, as the representative of all authors, has been given the opportunity to register their agreement or disagreement to this retraction. We have kept a record of any response received.

References

[1] Z. Zhang and W. Yan, "Spiral Computed Tomography in the Quantitative Measurement of the Adjacent Structure of the Left Atrial Appendage in Patients with Atrial Fibrillation," *Journal of Healthcare Engineering*, vol. 2021, Article ID 9893358, 10 pages, 2021.

Hindawi
Journal of Healthcare Engineering
Volume 2023, Article ID 9827370, 1 page
https://doi.org/10.1155/2023/9827370

Retraction

Retracted: Artificial Intelligence-Based Echocardiographic Left Atrial Volume Measurement with Pulmonary Vein Comparison

Journal of Healthcare Engineering

Received 10 October 2023; Accepted 10 October 2023; Published 11 October 2023

Copyright © 2023 Journal of Healthcare Engineering. This is an open access article distributed under the Creative Commons Attribution License, which permits unrestricted use, distribution, and reproduction in any medium, provided the original work is properly cited.

This article has been retracted by Hindawi following an investigation undertaken by the publisher [1]. This investigation has uncovered evidence of one or more of the following indicators of systematic manipulation of the publication process:

(1) Discrepancies in scope
(2) Discrepancies in the description of the research reported
(3) Discrepancies between the availability of data and the research described
(4) Inappropriate citations
(5) Incoherent, meaningless and/or irrelevant content included in the article
(6) Peer-review manipulation

The presence of these indicators undermines our confidence in the integrity of the article's content and we cannot, therefore, vouch for its reliability. Please note that this notice is intended solely to alert readers that the content of this article is unreliable. We have not investigated whether authors were aware of or involved in the systematic manipulation of the publication process.

In addition, our investigation has also shown that one or more of the following human-subject reporting requirements has not been met in this article: ethical approval by an Institutional Review Board (IRB) committee or equivalent, patient/participant consent to participate, and/or agreement to publish patient/participant details (where relevant).

Wiley and Hindawi regrets that the usual quality checks did not identify these issues before publication and have since put additional measures in place to safeguard research integrity.

We wish to credit our own Research Integrity and Research Publishing teams and anonymous and named external researchers and research integrity experts for contributing to this investigation.

The corresponding author, as the representative of all authors, has been given the opportunity to register their agreement or disagreement to this retraction. We have kept a record of any response received.

References

[1] M. Zhu, X. Fan, W. Liu et al., "Artificial Intelligence-Based Echocardiographic Left Atrial Volume Measurement with Pulmonary Vein Comparison," *Journal of Healthcare Engineering*, vol. 2021, Article ID 1336762, 11 pages, 2021.

Hindawi
Journal of Healthcare Engineering
Volume 2023, Article ID 9817018, 1 page
https://doi.org/10.1155/2023/9817018

Retraction

Retracted: Prediction and Analysis of Length of Stay Based on Nonlinear Weighted XGBoost Algorithm in Hospital

Journal of Healthcare Engineering

Received 10 October 2023; Accepted 10 October 2023; Published 11 October 2023

Copyright © 2023 Journal of Healthcare Engineering. This is an open access article distributed under the Creative Commons Attribution License, which permits unrestricted use, distribution, and reproduction in any medium, provided the original work is properly cited.

This article has been retracted by Hindawi following an investigation undertaken by the publisher [1]. This investigation has uncovered evidence of one or more of the following indicators of systematic manipulation of the publication process:

(1) Discrepancies in scope
(2) Discrepancies in the description of the research reported
(3) Discrepancies between the availability of data and the research described
(4) Inappropriate citations
(5) Incoherent, meaningless and/or irrelevant content included in the article
(6) Peer-review manipulation

The presence of these indicators undermines our confidence in the integrity of the article's content and we cannot, therefore, vouch for its reliability. Please note that this notice is intended solely to alert readers that the content of this article is unreliable. We have not investigated whether authors were aware of or involved in the systematic manipulation of the publication process.

Wiley and Hindawi regrets that the usual quality checks did not identify these issues before publication and have since put additional measures in place to safeguard research integrity.

We wish to credit our own Research Integrity and Research Publishing teams and anonymous and named external researchers and research integrity experts for contributing to this investigation.

The corresponding author, as the representative of all authors, has been given the opportunity to register their agreement or disagreement to this retraction. We have kept a record of any response received.

References

[1] Y. Chen, "Prediction and Analysis of Length of Stay Based on Nonlinear Weighted XGBoost Algorithm in Hospital," *Journal of Healthcare Engineering*, vol. 2021, Article ID 4714898, 9 pages, 2021.

Hindawi
Journal of Healthcare Engineering
Volume 2023, Article ID 9805274, 1 page
https://doi.org/10.1155/2023/9805274

Retraction

Retracted: Application of Dynamic Enhanced Magnetic Resonance Imaging in the Diagnosis of Hematological Malignancies

Journal of Healthcare Engineering

Received 10 October 2023; Accepted 10 October 2023; Published 11 October 2023

Copyright © 2023 Journal of Healthcare Engineering. This is an open access article distributed under the Creative Commons Attribution License, which permits unrestricted use, distribution, and reproduction in any medium, provided the original work is properly cited.

This article has been retracted by Hindawi following an investigation undertaken by the publisher [1]. This investigation has uncovered evidence of one or more of the following indicators of systematic manipulation of the publication process:

(1) Discrepancies in scope
(2) Discrepancies in the description of the research reported
(3) Discrepancies between the availability of data and the research described
(4) Inappropriate citations
(5) Incoherent, meaningless and/or irrelevant content included in the article
(6) Peer-review manipulation

The presence of these indicators undermines our confidence in the integrity of the article's content and we cannot, therefore, vouch for its reliability. Please note that this notice is intended solely to alert readers that the content of this article is unreliable. We have not investigated whether authors were aware of or involved in the systematic manipulation of the publication process.

In addition, our investigation has also shown that one or more of the following human-subject reporting requirements has not been met in this article: ethical approval by an Institutional Review Board (IRB) committee or equivalent, patient/participant consent to participate, and/or agreement to publish patient/participant details (where relevant).

Wiley and Hindawi regrets that the usual quality checks did not identify these issues before publication and have since put additional measures in place to safeguard research integrity.

We wish to credit our own Research Integrity and Research Publishing teams and anonymous and named external researchers and research integrity experts for contributing to this investigation.

The corresponding author, as the representative of all authors, has been given the opportunity to register their agreement or disagreement to this retraction. We have kept a record of any response received.

References

[1] Y. Shao, X. Bao, C. Song, and D. Cui, "Application of Dynamic Enhanced Magnetic Resonance Imaging in the Diagnosis of Hematological Malignancies," *Journal of Healthcare Engineering*, vol. 2021, Article ID 4623850, 12 pages, 2021.

Hindawi
Journal of Healthcare Engineering
Volume 2023, Article ID 9781637, 1 page
https://doi.org/10.1155/2023/9781637

Retraction

Retracted: Diagnosis and Etiological Analysis of Gastroesophageal Reflux Disease by Gastric Filling Ultrasound and GerdQ Scale

Journal of Healthcare Engineering

Received 10 October 2023; Accepted 10 October 2023; Published 11 October 2023

Copyright © 2023 Journal of Healthcare Engineering. This is an open access article distributed under the Creative Commons Attribution License, which permits unrestricted use, distribution, and reproduction in any medium, provided the original work is properly cited.

This article has been retracted by Hindawi following an investigation undertaken by the publisher [1]. This investigation has uncovered evidence of one or more of the following indicators of systematic manipulation of the publication process:

(1) Discrepancies in scope
(2) Discrepancies in the description of the research reported
(3) Discrepancies between the availability of data and the research described
(4) Inappropriate citations
(5) Incoherent, meaningless and/or irrelevant content included in the article
(6) Peer-review manipulation

The presence of these indicators undermines our confidence in the integrity of the article's content and we cannot, therefore, vouch for its reliability. Please note that this notice is intended solely to alert readers that the content of this article is unreliable. We have not investigated whether authors were aware of or involved in the systematic manipulation of the publication process.

In addition, our investigation has also shown that one or more of the following human-subject reporting requirements has not been met in this article: ethical approval by an Institutional Review Board (IRB) committee or equivalent, patient/participant consent to participate, and/or agreement to publish patient/participant details (where relevant).

Wiley and Hindawi regrets that the usual quality checks did not identify these issues before publication and have since put additional measures in place to safeguard research integrity.

We wish to credit our own Research Integrity and Research Publishing teams and anonymous and named external researchers and research integrity experts for contributing to this investigation.

The corresponding author, as the representative of all authors, has been given the opportunity to register their agreement or disagreement to this retraction. We have kept a record of any response received.

References

[1] B. Wang, Q. Sun, Y. Du, K. Mu, and J. Jiao, "Diagnosis and Etiological Analysis of Gastroesophageal Reflux Disease by Gastric Filling Ultrasound and GerdQ Scale," *Journal of Healthcare Engineering*, vol. 2021, Article ID 5629067, 6 pages, 2021.

Hindawi
Journal of Healthcare Engineering
Volume 2023, Article ID 9760590, 1 page
https://doi.org/10.1155/2023/9760590

Retraction

Retracted: Detection of 3D Arterial Centerline Extraction in Spiral CT Coronary Angiography

Journal of Healthcare Engineering

Received 10 October 2023; Accepted 10 October 2023; Published 11 October 2023

Copyright © 2023 Journal of Healthcare Engineering. This is an open access article distributed under the Creative Commons Attribution License, which permits unrestricted use, distribution, and reproduction in any medium, provided the original work is properly cited.

This article has been retracted by Hindawi following an investigation undertaken by the publisher [1]. This investigation has uncovered evidence of one or more of the following indicators of systematic manipulation of the publication process:

(1) Discrepancies in scope
(2) Discrepancies in the description of the research reported
(3) Discrepancies between the availability of data and the research described
(4) Inappropriate citations
(5) Incoherent, meaningless and/or irrelevant content included in the article
(6) Peer-review manipulation

The presence of these indicators undermines our confidence in the integrity of the article's content and we cannot, therefore, vouch for its reliability. Please note that this notice is intended solely to alert readers that the content of this article is unreliable. We have not investigated whether authors were aware of or involved in the systematic manipulation of the publication process.

In addition, our investigation has also shown that one or more of the following human-subject reporting requirements has not been met in this article: ethical approval by an Institutional Review Board (IRB) committee or equivalent, patient/participant consent to participate, and/or agreement to publish patient/participant details (where relevant).

Wiley and Hindawi regrets that the usual quality checks did not identify these issues before publication and have since put additional measures in place to safeguard research integrity.

We wish to credit our own Research Integrity and Research Publishing teams and anonymous and named external researchers and research integrity experts for contributing to this investigation.

The corresponding author, as the representative of all authors, has been given the opportunity to register their agreement or disagreement to this retraction. We have kept a record of any response received.

References

[1] W. Cai, Y. Wang, L. Gu, X. Ji, Q. Shen, and X. Ren, "Detection of 3D Arterial Centerline Extraction in Spiral CT Coronary Angiography," *Journal of Healthcare Engineering*, vol. 2021, Article ID 2670793, 16 pages, 2021.

Hindawi
Journal of Healthcare Engineering
Volume 2023, Article ID 9897527, 1 page
https://doi.org/10.1155/2023/9897527

Retraction

Retracted: Modified Look-Locker Inverse-Recovery (MOLLI) Sequence of Quantitative Imaging in Dirty Magnetic Resonance Longitudinal Relaxation Time Diagnostic Value of GE Combined with Longitudinal Relaxation Time Quantitative Imaging for Myocardial Amyloidosis

Journal of Healthcare Engineering

Received 10 October 2023; Accepted 10 October 2023; Published 11 October 2023

Copyright © 2023 Journal of Healthcare Engineering. This is an open access article distributed under the Creative Commons Attribution License, which permits unrestricted use, distribution, and reproduction in any medium, provided the original work is properly cited.

This article has been retracted by Hindawi following an investigation undertaken by the publisher [1]. This investigation has uncovered evidence of one or more of the following indicators of systematic manipulation of the publication process:

(1) Discrepancies in scope
(2) Discrepancies in the description of the research reported
(3) Discrepancies between the availability of data and the research described
(4) Inappropriate citations
(5) Incoherent, meaningless and/or irrelevant content included in the article
(6) Peer-review manipulation

The presence of these indicators undermines our confidence in the integrity of the article's content and we cannot, therefore, vouch for its reliability. Please note that this notice is intended solely to alert readers that the content of this article is unreliable. We have not investigated whether authors were aware of or involved in the systematic manipulation of the publication process.

In addition, our investigation has also shown that one or more of the following human-subject reporting requirements has not been met in this article: ethical approval by an Institutional Review Board (IRB) committee or equivalent, patient/participant consent to participate, and/or agreement to publish patient/participant details (where relevant).

Wiley and Hindawi regrets that the usual quality checks did not identify these issues before publication and have since put additional measures in place to safeguard research integrity.

We wish to credit our own Research Integrity and Research Publishing teams and anonymous and named external researchers and research integrity experts for contributing to this investigation.

The corresponding author, as the representative of all authors, has been given the opportunity to register their agreement or disagreement to this retraction. We have kept a record of any response received.

References

[1] Q. Lao, W. Xia, J. Jin, Y. Jia, and J. Feng, "Modified Look-Locker Inverse-Recovery (MOLLI) Sequence of Quantitative Imaging in Dirty Magnetic Resonance Longitudinal Relaxation Time Diagnostic Value of GE Combined with Longitudinal Relaxation Time Quantitative Imaging for Myocardial Amyloidosis," *Journal of Healthcare Engineering*, vol. 2021, Article ID 2800891, 12 pages, 2021.

Hindawi
Journal of Healthcare Engineering
Volume 2023, Article ID 9769563, 1 page
https://doi.org/10.1155/2023/9769563

Retraction

Retracted: Study on the Impact of Online Courses for Pregnant and Lying-In Women on Maternal and Infant Health during the Epidemic

Journal of Healthcare Engineering

Received 3 October 2023; Accepted 3 October 2023; Published 4 October 2023

Copyright © 2023 Journal of Healthcare Engineering. This is an open access article distributed under the Creative Commons Attribution License, which permits unrestricted use, distribution, and reproduction in any medium, provided the original work is properly cited.

This article has been retracted by Hindawi following an investigation undertaken by the publisher [1]. This investigation has uncovered evidence of one or more of the following indicators of systematic manipulation of the publication process:

(1) Discrepancies in scope
(2) Discrepancies in the description of the research reported
(3) Discrepancies between the availability of data and the research described
(4) Inappropriate citations
(5) Incoherent, meaningless and/or irrelevant content included in the article
(6) Peer-review manipulation

The presence of these indicators undermines our confidence in the integrity of the article's content and we cannot, therefore, vouch for its reliability. Please note that this notice is intended solely to alert readers that the content of this article is unreliable. We have not investigated whether authors were aware of or involved in the systematic manipulation of the publication process.

Wiley and Hindawi regrets that the usual quality checks did not identify these issues before publication and have since put additional measures in place to safeguard research integrity.

We wish to credit our own Research Integrity and Research Publishing teams and anonymous and named external researchers and research integrity experts for contributing to this investigation.

The corresponding author, as the representative of all authors, has been given the opportunity to register their agreement or disagreement to this retraction. We have kept a record of any response received.

References

[1] L. Shi, L. Yuan, L. Zhou, S. Zhang, and X. Lei, "Study on the Impact of Online Courses for Pregnant and Lying-In Women on Maternal and Infant Health during the Epidemic," *Journal of Healthcare Engineering*, vol. 2021, Article ID 4019210, 11 pages, 2021.

Hindawi
Journal of Healthcare Engineering
Volume 2023, Article ID 9798509, 1 page
https://doi.org/10.1155/2023/9798509

Retraction

Retracted: Multicentre Study Using Machine Learning Methods in Clinical Diagnosis of Knee Osteoarthritis

Journal of Healthcare Engineering

Received 13 September 2023; Accepted 13 September 2023; Published 14 September 2023

Copyright © 2023 Journal of Healthcare Engineering. This is an open access article distributed under the Creative Commons Attribution License, which permits unrestricted use, distribution, and reproduction in any medium, provided the original work is properly cited.

This article has been retracted by Hindawi following an investigation undertaken by the publisher [1]. This investigation has uncovered evidence of one or more of the following indicators of systematic manipulation of the publication process:

(1) Discrepancies in scope
(2) Discrepancies in the description of the research reported
(3) Discrepancies between the availability of data and the research described
(4) Inappropriate citations
(5) Incoherent, meaningless and/or irrelevant content included in the article
(6) Peer-review manipulation

The presence of these indicators undermines our confidence in the integrity of the article's content and we cannot, therefore, vouch for its reliability. Please note that this notice is intended solely to alert readers that the content of this article is unreliable. We have not investigated whether authors were aware of or involved in the systematic manipulation of the publication process.

In addition, our investigation has also shown that one or more of the following human-subject reporting requirements has not been met in this article: ethical approval by an Institutional Review Board (IRB) committee or equivalent, patient/participant consent to participate, and/or agreement to publish patient/participant details (where relevant).

Wiley and Hindawi regrets that the usual quality checks did not identify these issues before publication and have since put additional measures in place to safeguard research integrity.

We wish to credit our own Research Integrity and Research Publishing teams and anonymous and named external researchers and research integrity experts for contributing to this investigation.

The corresponding author, as the representative of all authors, has been given the opportunity to register their agreement or disagreement to this retraction. We have kept a record of any response received.

References

[1] K. Zeng, Y. Hua, J. Xu et al., "Multicentre Study Using Machine Learning Methods in Clinical Diagnosis of Knee Osteoarthritis," *Journal of Healthcare Engineering*, vol. 2021, Article ID 1765404, 12 pages, 2021.

Hindawi
Journal of Healthcare Engineering
Volume 2023, Article ID 9871531, 1 page
https://doi.org/10.1155/2023/9871531

Retraction

Retracted: Intervention of WeChat Group Guidance in Rapid Rehabilitation after Gynecological Laparoscopic Surgery

Journal of Healthcare Engineering

Received 27 June 2023; Accepted 27 June 2023; Published 28 June 2023

Copyright © 2023 Journal of Healthcare Engineering. This is an open access article distributed under the Creative Commons Attribution License, which permits unrestricted use, distribution, and reproduction in any medium, provided the original work is properly cited.

This article has been retracted by Hindawi following an investigation undertaken by the publisher [1]. This investigation has uncovered evidence of one or more of the following indicators of systematic manipulation of the publication process:

(1) Discrepancies in scope
(2) Discrepancies in the description of the research reported
(3) Discrepancies between the availability of data and the research described
(4) Inappropriate citations
(5) Incoherent, meaningless and/or irrelevant content included in the article
(6) Peer-review manipulation

The presence of these indicators undermines our confidence in the integrity of the article's content and we cannot, therefore, vouch for its reliability. Please note that this notice is intended solely to alert readers that the content of this article is unreliable. We have not investigated whether authors were aware of or involved in the systematic manipulation of the publication process.

In addition, our investigation has also shown that one or more of the following human-subject reporting requirements has not been met in this article: ethical approval by an Institutional Review Board (IRB) committee or equivalent, patient/participant consent to participate, and/or agreement to publish patient/participant details (where relevant).

Wiley and Hindawi regrets that the usual quality checks did not identify these issues before publication and have since put additional measures in place to safeguard research integrity.

We wish to credit our own Research Integrity and Research Publishing teams and anonymous and named external researchers and research integrity experts for contributing to this investigation.

The corresponding author, as the representative of all authors, has been given the opportunity to register their agreement or disagreement to this retraction. We have kept a record of any response received.

References

[1] J. Wang, Y. Lin, Y. Wei et al., "Intervention of WeChat Group Guidance in Rapid Rehabilitation after Gynecological Laparoscopic Surgery," *Journal of Healthcare Engineering*, vol. 2021, Article ID 8914997, 11 pages, 2021.

Hindawi
Journal of Healthcare Engineering
Volume 2023, Article ID 9865097, 1 page
https://doi.org/10.1155/2023/9865097

Retraction

Retracted: Analysis of Influencing Factors on Hospitalization Expenses of Patients with Breast Malignant Tumor Undergoing Surgery: Based on the Neural Network and Support Vector Machine

Journal of Healthcare Engineering

Received 27 June 2023; Accepted 27 June 2023; Published 28 June 2023

Copyright © 2023 Journal of Healthcare Engineering. This is an open access article distributed under the Creative Commons Attribution License, which permits unrestricted use, distribution, and reproduction in any medium, provided the original work is properly cited.

This article has been retracted by Hindawi following an investigation undertaken by the publisher [1]. This investigation has uncovered evidence of one or more of the following indicators of systematic manipulation of the publication process:

(1) Discrepancies in scope
(2) Discrepancies in the description of the research reported
(3) Discrepancies between the availability of data and the research described
(4) Inappropriate citations
(5) Incoherent, meaningless and/or irrelevant content included in the article
(6) Peer-review manipulation

The presence of these indicators undermines our confidence in the integrity of the article's content and we cannot, therefore, vouch for its reliability. Please note that this notice is intended solely to alert readers that the content of this article is unreliable. We have not investigated whether authors were aware of or involved in the systematic manipulation of the publication process.

In addition, our investigation has also shown that one or more of the following human-subject reporting requirements has not been met in this article: ethical approval by an Institutional Review Board (IRB) committee or equivalent, patient/participant consent to participate, and/or agreement to publish patient/participant details (where relevant).

Wiley and Hindawi regrets that the usual quality checks did not identify these issues before publication and have since put additional measures in place to safeguard research integrity.

We wish to credit our own Research Integrity and Research Publishing teams and anonymous and named external researchers and research integrity experts for contributing to this investigation.

The corresponding author, as the representative of all authors, has been given the opportunity to register their agreement or disagreement to this retraction. We have kept a record of any response received.

References

[1] J. Zhang and L. Sun, "Analysis of Influencing Factors on Hospitalization Expenses of Patients with Breast Malignant Tumor Undergoing Surgery: Based on the Neural Network and Support Vector Machine," *Journal of Healthcare Engineering*, vol. 2021, Article ID 9268660, 7 pages, 2021.

Hindawi
Journal of Healthcare Engineering
Volume 2023, Article ID 9851032, 1 page
https://doi.org/10.1155/2023/9851032

Retraction

Retracted: The Promise for Reducing Healthcare Cost with Predictive Model: An Analysis with Quantized Evaluation Metric on Readmission

Journal of Healthcare Engineering

Received 27 June 2023; Accepted 27 June 2023; Published 28 June 2023

Copyright © 2023 Journal of Healthcare Engineering. This is an open access article distributed under the Creative Commons Attribution License, which permits unrestricted use, distribution, and reproduction in any medium, provided the original work is properly cited.

This article has been retracted by Hindawi following an investigation undertaken by the publisher [1]. This investigation has uncovered evidence of one or more of the following indicators of systematic manipulation of the publication process:

(1) Discrepancies in scope
(2) Discrepancies in the description of the research reported
(3) Discrepancies between the availability of data and the research described
(4) Inappropriate citations
(5) Incoherent, meaningless and/or irrelevant content included in the article
(6) Peer-review manipulation

The presence of these indicators undermines our confidence in the integrity of the article's content and we cannot, therefore, vouch for its reliability. Please note that this notice is intended solely to alert readers that the content of this article is unreliable. We have not investigated whether authors were aware of or involved in the systematic manipulation of the publication process.

In addition, our investigation has also shown that one or more of the following human-subject reporting requirements has not been met in this article: ethical approval by an Institutional Review Board (IRB) committee or equivalent, patient/participant consent to participate, and/or agreement to publish patient/participant details (where relevant).

Wiley and Hindawi regrets that the usual quality checks did not identify these issues before publication and have since put additional measures in place to safeguard research integrity.

We wish to credit our own Research Integrity and Research Publishing teams and anonymous and named external researchers and research integrity experts for contributing to this investigation.

The corresponding author, as the representative of all authors, has been given the opportunity to register their agreement or disagreement to this retraction. We have kept a record of any response received.

References

[1] K. Teo, C. W. Yong, F. Muhamad et al., "The Promise for Reducing Healthcare Cost with Predictive Model: An Analysis with Quantized Evaluation Metric on Readmission," *Journal of Healthcare Engineering*, vol. 2021, Article ID 9208138, 10 pages, 2021.

Hindawi
Journal of Healthcare Engineering
Volume 2023, Article ID 9849317, 1 page
https://doi.org/10.1155/2023/9849317

Retraction

Retracted: The Factors Affecting Orthodontic Pain with Periodontitis

Journal of Healthcare Engineering

Received 27 June 2023; Accepted 27 June 2023; Published 28 June 2023

Copyright © 2023 Journal of Healthcare Engineering. This is an open access article distributed under the Creative Commons Attribution License, which permits unrestricted use, distribution, and reproduction in any medium, provided the original work is properly cited.

This article has been retracted by Hindawi following an investigation undertaken by the publisher [1]. This investigation has uncovered evidence of one or more of the following indicators of systematic manipulation of the publication process:

(1) Discrepancies in scope
(2) Discrepancies in the description of the research reported
(3) Discrepancies between the availability of data and the research described
(4) Inappropriate citations
(5) Incoherent, meaningless and/or irrelevant content included in the article
(6) Peer-review manipulation

The presence of these indicators undermines our confidence in the integrity of the article's content and we cannot, therefore, vouch for its reliability. Please note that this notice is intended solely to alert readers that the content of this article is unreliable. We have not investigated whether authors were aware of or involved in the systematic manipulation of the publication process.

In addition, our investigation has also shown that one or more of the following human-subject reporting requirements has not been met in this article: ethical approval by an Institutional Review Board (IRB) committee or equivalent, patient/participant consent to participate, and/or agreement to publish patient/participant details (where relevant).

Wiley and Hindawi regrets that the usual quality checks did not identify these issues before publication and have since put additional measures in place to safeguard research integrity.

We wish to credit our own Research Integrity and Research Publishing teams and anonymous and named external researchers and research integrity experts for contributing to this investigation.

The corresponding author, as the representative of all authors, has been given the opportunity to register their agreement or disagreement to this retraction. We have kept a record of any response received.

References

[1] Y. Peng and S. Tang, "The Factors Affecting Orthodontic Pain with Periodontitis," *Journal of Healthcare Engineering*, vol. 2021, Article ID 8942979, 11 pages, 2021.

Hindawi
Journal of Healthcare Engineering
Volume 2023, Article ID 9831620, 1 page
https://doi.org/10.1155/2023/9831620

Retraction

Retracted: Study on the Correlation Factors of Tumour Prognosis after Intravascular Interventional Therapy

Journal of Healthcare Engineering

Received 27 June 2023; Accepted 27 June 2023; Published 28 June 2023

Copyright © 2023 Journal of Healthcare Engineering. This is an open access article distributed under the Creative Commons Attribution License, which permits unrestricted use, distribution, and reproduction in any medium, provided the original work is properly cited.

This article has been retracted by Hindawi following an investigation undertaken by the publisher [1]. This investigation has uncovered evidence of one or more of the following indicators of systematic manipulation of the publication process:

(1) Discrepancies in scope
(2) Discrepancies in the description of the research reported
(3) Discrepancies between the availability of data and the research described
(4) Inappropriate citations
(5) Incoherent, meaningless and/or irrelevant content included in the article
(6) Peer-review manipulation

The presence of these indicators undermines our confidence in the integrity of the article's content and we cannot, therefore, vouch for its reliability. Please note that this notice is intended solely to alert readers that the content of this article is unreliable. We have not investigated whether authors were aware of or involved in the systematic manipulation of the publication process.

In addition, our investigation has also shown that one or more of the following human-subject reporting requirements has not been met in this article: ethical approval by an Institutional Review Board (IRB) committee or equivalent, patient/participant consent to participate, and/or agreement to publish patient/participant details (where relevant).

Wiley and Hindawi regrets that the usual quality checks did not identify these issues before publication and have since put additional measures in place to safeguard research integrity.

We wish to credit our own Research Integrity and Research Publishing teams and anonymous and named external researchers and research integrity experts for contributing to this investigation.

The corresponding author, as the representative of all authors, has been given the opportunity to register their agreement or disagreement to this retraction. We have kept a record of any response received.

References

[1] L. Zheng, H. Feng, L. Yin et al., "Study on the Correlation Factors of Tumour Prognosis after Intravascular Interventional Therapy," *Journal of Healthcare Engineering*, vol. 2021, Article ID 6940056, 11 pages, 2021.

Hindawi
Journal of Healthcare Engineering
Volume 2023, Article ID 9781915, 1 page
https://doi.org/10.1155/2023/9781915

Retraction

Retracted: Cardiac Rehabilitation Improves Long-Term Prognosis for People with Chronic Kidney Disease Undergoing Percutaneous Coronary Intervention: A Propensity Matching Analysis

Journal of Healthcare Engineering

Received 17 November 2022; Accepted 17 November 2022; Published 20 January 2023

Copyright © 2023 Journal of Healthcare Engineering. This is an open access article distributed under the Creative Commons Attribution License, which permits unrestricted use, distribution, and reproduction in any medium, provided the original work is properly cited.

Journal of Healthcare Engineering has retracted the article titled "Cardiac Rehabilitation Improves Long-Term Prognosis for People with Chronic Kidney Disease Undergoing Percutaneous Coronary Intervention: A Propensity Matching Analysis" [1] due to concerns that the peer review process has been compromised.

Following an investigation conducted by the Hindawi Research Integrity team [2], significant concerns were identified with the peer reviewers assigned to this article; the investigation has concluded that the peer review process was compromised. We therefore can no longer trust the peer review process, and the article is being retracted with the agreement of the Chief Editor.

References

[1] H. M. Qin, D. Zheng, and J. Wu, "Cardiac Rehabilitation Improves Long-Term Prognosis for People with Chronic Kidney Disease Undergoing Percutaneous Coronary Intervention: A Propensity Matching Analysis," *Journal of Healthcare Engineering*, vol. 2022, Article ID 1196682, 6 pages, 2022.

[2] L. Ferguson, "Advancing Research Integrity Collaboratively and with Vigour," 2022, https://www.hindawi.com/post/advancing-research-integrity-collaboratively-and-vigour/.

Hindawi
Journal of Healthcare Engineering
Volume 2023, Article ID 9781915, 1 page
https://doi.org/10.1155/2023/9781915

Retraction

Retracted: Cardiac Rehabilitation Improves Long-Term Prognosis for People with Chronic Kidney Disease Undergoing Percutaneous Coronary Intervention: A Propensity Matching Analysis

Journal of Healthcare Engineering

Received 17 November 2022; Accepted 17 November 2022; Published 20 January 2023

Copyright © 2023 Journal of Healthcare Engineering. This is an open access article distributed under the Creative Commons Attribution License, which permits unrestricted use, distribution, and reproduction in any medium, provided the original work is properly cited.

Journal of Healthcare Engineering has retracted the article titled "Cardiac Rehabilitation Improves Long-Term Prognosis for People with Chronic Kidney Disease Undergoing Percutaneous Coronary Intervention: A Propensity Matching Analysis" [1] due to concerns that the peer review process has been compromised.

Following an investigation conducted by the Hindawi Research Integrity team [2], significant concerns were identified with the peer reviewers assigned to this article; the investigation has concluded that the peer review process was compromised. We therefore can no longer trust the peer review process, and the article is being retracted with the agreement of the Chief Editor.

References

[1] H. M. Qin, D. Zheng, and J. Wu, "Cardiac Rehabilitation Improves Long-Term Prognosis for People with Chronic Kidney Disease Undergoing Percutaneous Coronary Intervention: A Propensity Matching Analysis," *Journal of Healthcare Engineering*, vol. 2022, Article ID 1196682, 6 pages, 2022.

[2] L. Ferguson, "Advancing Research Integrity Collaboratively and with Vigour," 2022, https://www.hindawi.com/post/advancing-research-integrity-collaboratively-and-vigour/.

Hindawi
Journal of Healthcare Engineering
Volume 2022, Article ID 1196682, 6 pages
https://doi.org/10.1155/2022/1196682

Research Article

Cardiac Rehabilitation Improves Long-Term Prognosis for People with Chronic Kidney Disease Undergoing Percutaneous Coronary Intervention: A Propensity Matching Analysis

Hong Mei Qin,[1] Dan Zheng,[1] and Jie Wu[2]

[1]*Department of Physical Examination Department, First People's Hospital of Chongqing Liangjiang New Area, Chongqing, China*
[2]*Department of Emergency Department, First People's Hospital of Chongqing Liangjiang New Area, Chongqing, China*

Correspondence should be addressed to Jie Wu; wujie801231@sg.edu.vn

Received 15 November 2021; Accepted 31 December 2021; Published 9 February 2022

Academic Editor: Gu Xiaoqing

Copyright © 2022 Hong Mei Qin et al. This is an open access article distributed under the Creative Commons Attribution License, which permits unrestricted use, distribution, and reproduction in any medium, provided the original work is properly cited.

Objectives. According to researches, many people with chronic kidney disease (CKD) had the higher incidence rate and mortality rate of coronary artery disease (CAD) after percutaneous coronary intervention than those who did not receive percutaneous coronary intervention, while coronary rehabilitation was beneficial for patients who received percutaneous coronary intervention I. This study aims to analyze whether coronary rehabilitation was beneficial to patients with CKD after percutaneous coronary intervention. *Patients and Methods*. A retrospective survey was used to collect clinical data of patients undergoing percutaneous coronary intervention due to CAD, and CKD patients were screened for further analysis. According to whether patients had received coronary rehabilitation treatment, research subjects were divided into two groups, the coronary rehabilitation group and the noncoronary rehabilitation group. The baseline characteristics of the propensity score matching between the two groups were compared. Survival analysis used the Cox hazard ratio (HR) model as regression method to compare the relative risk of the endpoints in the coronary rehabilitation group and the noncoronary rehabilitation group. *Results*. From January 2007 to January 2012, a total of 246 CKD patients treated with percutaneous coronary intervention were included in this study, and 106 of them obtained coronary rehabilitation after surgery. After propensity score matching, there were 89 pairs of patients in the two groups who had no significant difference in demographic and clinical characteristics (all $P > 0.05$). CKD patients receiving coronary rehabilitation had a significant reduction in all-cause mortality (HR 0.465, 95% CI 0.233–0.926, $P = 0.029$) and cardiac complications (HR 0.532, 95% CI 0.287–0.984, $P = 0.044$). Survival analysis showed that the survival rate of the coronary rehabilitation group was significantly higher than that of the noncoronary rehabilitation group ($P = 0.024$). *Conclusions*. For CKD patients undergoing percutaneous coronary intervention, receiving cardiac rehabilitation can significantly improve long-term survival and reduce cardiac events.

RETRACTED

1. Introduction

Although the mortality rate of people suffering from coronary artery disease (CAD) has been on a downward trend due to the successful development of more and more effective interventional technologies and cardiovascular drugs [1–3], serious cardiogenic death and recurrence risks still pose a serious threat to CAD patients. CAD patients are necessary for comprehensive treatment. Cardiac rehabilitation including health education level, recommendations for reducing cardiovascular accidents, physical exercise, and stress management are some of the comprehensive measures for patients with heart disease [4]. And well-designed coronary rehabilitation includes the following factors: medical assessment, prescribed exercise, correction of cardiac risk factors, education and counseling, and long-term continuous implementation [5–7]. The survey shows that although the cost of coronary rehabilitation is low and the curative effect is good, the participation rate of CAD patients is only 20% to 40% [8]. In China, the participation rate of CAD patients for coronary rehabilitation becomes worse due to the relatively undeveloped socio-economic conditions, which requires more clinical practice to promote the efficacy of coronary rehabilitation for CAD patients [9].

Chronic kidney disease (CKD) complication of CAD has attracted social attention for the increasing incidence of CAD and the long-term risks of cardiac events [10, 11]. More and more studies strongly recommend that people with acute coronary syndrome (ACS) (including ST segment elevation myocardial infarction and non-ST segment elevation myocardial infarction), with unstable angina pectoris and with undergoing reperfusion, receive coronary rehabilitation treatment [12]. In view of the current lack of relevant research data on whether coronary rehabilitation has a significant effect on ACS patients with CKD, in this study, we used a retrospective propensity matching study to analyze the prognostic intervention of long-term standardized coronary rehabilitation in people who have undergone percutaneous coronary intervention. This study provided more evidence for the benefits and indications of coronary rehabilitation.

2. Patients and Methods

2.1. Study Population. We retrospectively compiled the clinical data of patients who meet the following criteria: (1) the patient diagnosed with ACS and receiving percutaneous coronary intervention treatment according to the 2011 ACCF/AHA/SCAI guideline [13]; (2) the patient who had a history of CKD or eGFR lower than 60 mL/min/1.73 m^2; (3) the patient who had no contraindications of coronary rehabilitation including unstable angina, severe heart failure (with LVEF < 30%), and uncontrolled ventricular arrhythmia [14]; (4) the patient who completed routine follow-up; (5) the patient who signed an informed consent of admission.

The study compared demographical characteristics, examination results during hospitalization, and long-term subsequent prognosis outcomes. The study was also approved by the hospital Medical Ethics Committee.

Accorded to the abovementioned criteria, there were 246 eligible CKD patients receiving percutaneous coronary intervention in the hospital between January 2007 and January 2012. Accorded to whether the patients had received coronary rehabilitation treatment, the research subjects were divided into two groups, the coronary rehabilitation group and the noncoronary rehabilitation group.

2.2. Cardiac Rehabilitation. According to the BACPR Standard 2[15], the coronary rehabilitation program was launched in the Department of Cardiology Hospital, since February 2010, when a group of coronary rehabilitation was founded including cardiologists, nurse specialists, physiotherapists, dietitians, psychologists, exercise specialists, occupational therapists, and clerical administrators. A well-designed coronary rehabilitation plan was made for each patient who was willing to receive treatment. The coronary rehabilitation plan included the following steps: first of all, health education and habit correction; secondly, lifestyle analysis and risk factor control (outdoor activities, exercise, diet correction, and smoking cessation); third, psychological counseling and evaluation; fourth, medical evaluation and risk factor control; fifth, cardioprotective therapies; sixth, long-term follow-up on time; and seventh, regularly evaluate the coronary rehabilitation program. The patients who received coronary rehabilitation plan needed to attend the coronary rehabilitation sessions within 3 months after percutaneous coronary intervention and the multidisciplinary program must last more than 1 year (more than 3 sessions of coronary rehabilitation).

2.3. Follow-Up and Endpoints. The follow-up lasts from January 2010 to January 2017 by telephone or out-patient clinics; each patient was given an annual inquiry of their conditions. The data were regarded as meaningless if the patient's clinical data were incomplete or the contact was interrupted during long-term follow-up. Primary and secondary endpoint studies were as follows: the primary endpoint was defined as all-cause mortality during long-term follow-up; the secondary endpoints were defined as composite adverse outcomes, including adverse outcomes such as myocardial infarction and unexpected revascularization and so on.

2.4. Statistical Analysis. In this study, IBM SPSS Statistics version 19.0 (SPSS, Inc, Armonk, NY) was used for statistical analysis. Firstly, the normal distribution test of variables was carried out to check the distribution of variables. Continuous variables conforming to normal distribution were expressed as mean ± standard deviation, and classified variables were expressed as proportion.

The comparison of continuous variables between the two groups used the independent sample *t*-test. The chi-square test was performed in different evaluations of categorical variables. Multiple logistic regression was performed to calculate propensity scores by considering demographic and clinical variables. Use the "greedy matching" method to match patients with the closest propensity score. After propensity score matching, Student's *t*-test and McNemar paired sample were used for analysis.

Survival analysis used Cox hazard ratio (HR) model as a regression method to compare the relative risk of the endpoints in the coronary rehabilitation group and the noncoronary rehabilitation group. We performed univariate analysis between covariates and endpoints. The Kaplan–Meier survival curve and log rank test were used to compare the survival status of the coronary rehabilitation group and the noncoronary rehabilitation group. *P* value less than 0.05 was considered as statistically significance.

3. Results

3.1. Patient Characteristics. There were 246 eligible research subjects that were included in this study. 106 patients were enrolled in the coronary rehabilitation group and 140 patients in the noncoronary rehabilitation group. The demographical characteristics and clinical data of the two groups are shown in Table 1. In the demographical part, it showed that the patients in the coronary rehabilitation group were younger than those in the noncoronary rehabilitation group,

RETRACTED

Table 1: Demographical characteristics and clinical data of the coronary rehabilitation group and the noncoronary rehabilitation group before propensity score match.

Variables	The coronary rehabilitation group ($n = 106$)	The noncoronary rehabilitation group ($n = 140$)	P value
Demographics			
Age (y, mean ± SD)	58.4 ± 17.5	65.7 ± 17.2	0.001
Gender (male %)	65 (61.3%)	76 (54.3%)	0.299
BMI (kg/m^{-2})	22.8 ± 3.1	24.0 ± 3.2	0.003
Smoking (%)	37 (34.9%)	48 (34.3%)	1.000
Most recent MI			0.011
<24 h	24 (22.6%)	54 (38.6%)	
1–7 d	17 (16.0%)	19 (13.6%)	
>7 d	25 (23.6%)	15 (10.7%)	
Never	40 (37.7%)	52 (37.1%)	
Unstable angina	76 (71.7%)	92 (65.7%)	0.336
Prior percutaneous coronary intervention	16 (15.1%)	32 (22.9%)	0.145
Prior CABG	13 (12.3%)	25 (17.9%)	0.286
Contemporary percutaneous coronary intervention			0.001
Emergency percutaneous coronary intervention	23 (21.7%)	51 (36.4%)	
Urgent percutaneous coronary intervention	43 (40.6%)	65 (46.4%)	
Elective percutaneous coronary intervention	40 (37.7%)	24 (17.1%)	
Drug-eluting stent	48 (45.3%)	39 (27.9%)	0.007
GP IIb/IIIa use	66 (62.3%)	76 (54.3%)	0.241
LVEF	49.1 ± 12.2	53.3 ± 11.4	0.006
Comorbidities			
Heart failure	31 (29.2%)	19 (13.6%)	0.004
Hypertension	66(62.3%)	65 (46.4%)	0.015
Diabetes mellitus	22 (20.8%)	27 (19.3%)	0.872
Chronic lung disease	26 (24.5%)	31 (22.1%)	0.760
Cerebrovascular disease	1 (0.9%)	6 (4.3%)	0.244
Tumor	8 (7.5%)	5 (3.6%)	0.249

BMI, body mass index; MI, myocardial infarction; CABG, coronary artery bypass graft; LVEF, left ventricular ejection fraction.

and the results were statistically significant ($P = 0.001$), and the BMI of the coronary rehabilitation group was lower than that of the noncoronary rehabilitation group ($P = 0.003$). There were also significant differences in the time between the most recent MI ($P = 0.011$) and the percutaneous coronary intervention type in the same period ($P = 0.001$). As for follow-up treatment, more patients in the coronary rehabilitation group received drug-eluting stent treatment ($P = 0.007$). In terms of comorbidities, the coronary rehabilitation group had a higher proportion of heart failure ($P = 0.004$) and hypertension ($P = 0.015$). There were no significant differences on gender and smoking status ($P > 0.05$). There were no statistical differences in the proportion of diabetes, chronic lung disease, cerebrovascular disease, and tumor ($P > 0.05$). After the propensity match, there were no statistical differences in the variables listed in Table 2 (all $P > 0.05$).

3.2. Primary Endpoint. During the average (38.9 ± 22.5) months of follow-up, there were 37 primary endpoint events (all-cause deaths), including 28 cardiovascular deaths and 9 noncardiovascular deaths. As shown in Table 3, the hazard ratio (HR) of coronary rehabilitation for primary endpoint was 0.465 95% CI (0.233–0.926) ($P = 0.029$). Survival analysis also showed that the survival rate of the coronary rehabilitation group was higher than that of the noncoronary rehabilitation group ($P = 0.024$).

3.3. Secondary Endpoint. During the follow-up period, 44 secondary endpoint events occurred, including 18 cases of myocardial infarction and 26 cases of emergency revascularization. Compared with the noncoronary rehabilitation group, the risk of cardiac events in the coronary rehabilitation group was significantly lower, with HR of 0.532 95% CI (0.287–0.984) ($P = 0.044$). There were no statistical significance in subgroup analysis of myocardial infarction and emergency revascularization ($P > 0.05$). The Kaplan–Meier survival curve showed that the coronary rehabilitation group had fewer cardiovascular events than the noncoronary rehabilitation group ($O = 0.039$).

4. Discussion

As far as we know, this study retrospectively compared patients treated with coronary rehabilitation and patients who did not receive coronary rehabilitation. It was the first

RETRACTED

RETRACTED

Table 2: Demographical characteristics and clinical data of the coronary rehabilitation group and the noncoronary rehabilitation group after propensity score match.

Variables	The coronary rehabilitation group ($n = 89$)	The noncoronary rehabilitation group ($n = 89$)	*P* value
Demographics			
Age (y, mean ± SD)	59.9 ± 17.7	61.3 ± 17.8	0.517
Gender (male %)	59 (66.3%)	64 (71.9%)	0.219
BMI (kg/m^{-2})	23.1 ± 3.0	23.5 ± 3.1	0.406
Smoking(%)	29 (32.6%)	27 (30.3%)	0.872
Most recent MI			0.503
<24 h	24 (27.0%)	30 (33.7%)	
1–7 d	17 (19.1%)	15 (16.9%)	
>7 d	15 (16.9%)	9 (10.1%)	
Never	33 (37.1%)	35 (39.3%)	
Unstable angina	61 (68.5%)	56 (62.9%)	0.528
Prior percutaneous coronary intervention	12 (13.5%)	14 (15.7%)	0.832
Prior CABG	11(6.7%)	19 (21.3%)	0.160
Contemporary percutaneous coronary intervention			0.301
Emergency percutaneous coronary intervention	23 (25.6%)	30(33.7%)	
Urgent percutaneous coronary intervention	33 (37.1%)	35 (39.3%)	
Elective percutaneous coronary intervention	33 (37.1%)	24 (27.0%)	
Drug-eluting stent	34 (38.2%)	28 (31.5%)	0.432
GP IIb/IIIa use	51 (57.3%)	52 (58.4%)	1.000
LVEF	49.8 ± 12.3	51.9 ± 12.4	0.243
Comorbidities			
Heart failure	24 (27.0%)	19 (21.3%)	0.484
Hypertension	50(56.2%)	42 (47.2%)	0.294
Diabetes mellitus	19 (21.3%)	18 (20.2%)	1.000
Chronic lung disease	15 (16.9%)	10 (11.2%)	0.389
Cerebrovascular disease	1 (1.1%)	5 (5.6%)	0.211
Tumor	1 (1.1%)	2 (2.2%)	1.000

BMI, body mass index; MI, myocardial infarction; CABG, coronary artery bypass graft; GP, glycoprotein; LVEF, left ventricular ejection fraction.

Table 3: Hazard ratio (HR) of endpoint for patients treated with coronary rehabilitation compared with patients without coronary rehabilitation.

	HR	95% CI	*P* value
Primary endpoint	0.465	0.233–0.926	0.029
Secondary endpoint			
Myocardial infarction	0.465	0.174–1.239	0.125
Emergent revascularization	0.482	0.264–1.285	0.180
Overall	0.532	0.287–0.984	0.044

time that coronary rehabilitation can effectively reduce all-cause mortality and cardiac events in patients with CKD after percutaneous coronary intervention. It is worth mentioning that, in this study, the conclusions were more convincing as baseline bias was eliminated by propensity score matching.

Previous studies had provided a close link between coronary rehabilitation training and the reduction of all-cause mortality [15]. A systematic review and meta-analysis of 148 randomized controlled trials with a total of 97,486 participants strengthened the reduction of mortality in people with coronary heart disease through coronary rehabilitation [16]. However, there are still some controversies regarding the indications and risks of coronary rehabilitation, especially for high-risk patients. Some studies had found that coronary rehabilitation was less effective in diabetic patients [17, 18], and one study found that coronary rehabilitation had the same effect in DM patients as in non-DM patients [19]. Those controversies required more researches to focus on specific patients, especially patients with some complications.

CKD is an independent risk factor for CAD. CAD is the main cause of incidence rate and mortality of CKD patients [20–22]. For patients undergoing percutaneous coronary intervention, even in the era of drug-eluting stents, CKD complications can lead to higher surgical complications, restenosis, and future cardiac events [23]. Compared with patients of simple CKD or CAD, patients with both CKD and CAD have a higher risk of death and cardiac events. Some studies have investigated the effectiveness of coronary rehabilitation for CAD patients, which suggested that coronary rehabilitation can significantly improve renal function and reduce the coronary artery risk in CKD patients [24–27]. However, no previous studies have observed the long-term effects of coronary rehabilitation on CKD patients. Propensity score matching eliminates baseline features that may affect survival, including age, BMI, the percutaneous coronary intervention emergency, most recent mitral insufficiency (MI) history, cardiac function, and other complications. After the propensity match, there was no statistical significance.

Univariate Cox regression analysis was performed between the two groups to compare the all-cause and mortality and cardiac events in the coronary rehabilitation group and the noncoronary rehabilitation group. The result was positive which was caused by two main mechanisms. On the one hand, coronary rehabilitation complexes including exercise, smoking cessation, and weight loss have been shown to be beneficial to endothelial function, which may play a role in improving renal function and revascularization of coronary arteries [28]. On the other hand, some studies have showed that coronary rehabilitation can reduce the level of oxidized low-density lipoprotein (ox-LDL), which is essential for the development and deterioration of CAD [29].

No matter how great the benefits of coronary rehabilitation are, without people participation and compliance, the result is nonsense. Despite years of promotion, the participation rate of coronary rehabilitation is still very low, especially in countries with undeveloped medical conditions. According to the Canadian Institutes of Health Research, only 38.8% of countries have heart rehabilitation programs, of which 68.0% are in high income countries and 23% are in low and middle income countries [12]. In China, a survey showed that only 30 out of 124 people (24%) said they had initiated the coronary rehabilitation program [30]. The main obstacles hindering the coronary rehabilitation program are low referral rate, poor patient compliance, lack of doctor approval, obesity, multiple diseases, poor or no exercise habits, smoking, mental health, traffic problems, lack of social support, and lack of rest time [31]. In this study, approximately 46% (106 out of 246) CKD patients participated in the coronary rehabilitation program, which is above average, which could be attributed to the complete coronary rehabilitation team.

It should also be noted that there are several limitations of this study. Firstly, retrospective design has effect on the strength of evidence. Secondly, the follow-up data are not as good as the cohort study, the proportion of censored data is relatively high, and there may be a certain deviation in the final result. Finally, because the clinical data of CKD are incomplete, this study lacked CKD staging information.

5. Conclusions

In conclusion, this study demonstrated that long-term coronary rehabilitation program would effectively reduce the risk of death and the incidence of cardiac events in patients with CKD. More efforts are needed to promote coronary rehabilitation in patients with CAD, especially for those with CKD.

Data Availability

The data that support the findings of this study are available from the corresponding author upon reasonable request.

Disclosure

The authors received no financial support for the research, authorship, and/or publication of this article.

Conflicts of Interest

The authors declare no potential conflicts of interest with respect to the research, authorship, and/or publication of this article.

Authors' Contributions

Hong Mei Qin and Dan Zheng contributed equally to this work.

References

[1] G. J. Balady, P. A. Ades, V. A. Bittner et al., "Referral, Enrollment, and Delivery of cardiac rehabilitation/secondary prevention programs at clinical Centers and beyond," *Circulation*, vol. 124, no. 25, pp. 2951–2960, 2011.
[2] M. Golino, F. R. Spera, L. Manfredonia et al., "Microvascular ischemia in patients with successful percutaneous coronary intervention: effects of ranolazine and isosorbide-5-mononitrate," *European Review for Medical and Pharmacological Sciences*, vol. 22, pp. 6545–6550, 2018.
[3] K. Liu, B. T. Hua, T. Guo, and L. J. Pu, "The assessment of the long-term effects of elective CRT-D of coronary heart disease after PCI," *European Review for Medical and Pharmacological Sciences*, vol. 21, pp. 1313–1317, 2017.
[4] H. M. Dalal, P. Doherty, and R. S. Taylor, "Cardiac rehabilitation," *BMJ*, vol. 351, Article ID h5000, 2015.
[5] K. Goel, R. J. Lennon, R. T. Tilbury, R. W. Squires, and R. J. Thomas, "Impact of cardiac rehabilitation on mortality and cardiovascular events after percutaneous coronary intervention in the community," *Circulation*, vol. 123, no. 21, pp. 2344–2352, 2011.
[6] Q. R. Pack, K. Goel, B. D. Lahr et al., "Participation in cardiac rehabilitation and survival after coronary artery bypass graft Surgery," *Circulation*, vol. 128, no. 6, pp. 590–597, 2013.
[7] N. V. Pogosova, O. Y. Sokolova, Y. M. Yufereva, I. V. Osipova, and I. N. Ryamzina, "First results of analysis of the Russian part of the European register on cardiac rehabilitation EuroCaReD (European cardiac rehabilitation Database)," *Kardiologiia*, vol. 55, pp. 49–56, 2015.
[8] L. Ingle and S. Carroll, "Cardiac rehabilitation and exercise training," *Heart*, vol. 99, p. 1298, 2013.
[9] D. Hu, "[Bright beginning of Chinese cardiac rehabilitation post a rough road]," *Zhonghua Xinxueguanbing Zazhi*, vol. 43, p. 118, 2015.
[10] O. Kurihara, K. Okamatsu, K. Mizuno et al., "Coronary atherosclerosis and risk of acute coronary syndromes in chronic kidney disease using angioscopy and the kidney disease: improving global outcomes (KDIGO) classification," *Atherosclerosis*, vol. 243, no. 2, pp. 567–572, 2015.
[11] C. Melloni, J. H. Cornel, G. Hafley et al., "Impact of chronic kidney disease on long-term ischemic and bleeding outcomes in medically managed patients with acute coronary syndromes: Insights from the TRILOGY ACS Trial," *European Heart Journal: Acute Cardiovascular Care*, vol. 5, no. 6, pp. 443–454, 2016.

RETRACTED

Hindawi
Journal of Healthcare Engineering
Volume 2022, Article ID 5499354, 10 pages
https://doi.org/10.1155/2022/5499354

Research Article

Shear Wave Elastography-Assisted Ultrasound Breast Image Analysis and Identification of Abnormal Data

Caoxin Yan ,[1] Zhiyan Luo ,[2] Zimei Lin ,[2] Huilin He ,[1] Yunkai Luo ,[1] and Jian Chen [1]

[1]*Department of Ultrasound in Medicine, The Fourth Affiliated Hospital of Zhejiang University School of Medicine, Yiwu, Zhejiang 322000, China*
[2]*Department of Ultrasound in Medicine, The Second Affiliated Hospital Zhejiang University School of Medicine, Hangzhou, Zhejiang 310009, China*

Correspondence should be addressed to Caoxin Yan; yancaoxin@zju.edu.cn

Received 21 October 2021; Revised 22 November 2021; Accepted 2 December 2021; Published 7 January 2022

Academic Editor: Kaijian Xia

Copyright © 2022 Caoxin Yan et al. This is an open access article distributed under the Creative Commons Attribution License, which permits unrestricted use, distribution, and reproduction in any medium, provided the original work is properly cited.

In this paper, shear wave elastography was used to study and analyze the images of the breast in-depth and identify the abnormal image data. Sixty breast lesions were evaluated, and quantitative metrics were reproducible in the static and dynamic modes of shear wave elastography with a higher interobserver agreement in dynamic qualitative metrics than in the static mode. There were no statistically significant differences between the two modes of imaging in quantitative metrics, and quantitative metrics were more effective than qualitative metrics. Postoperative immunohistochemical expression of ER, PR, HER-2, Ki-67, molecular typing, pathological type, histological grading, and axillary lymph node status of breast cancer was obtained based on pathological results. The correlation between mass size, patient age, and WiMAX values of breast cancer masses was analyzed using Pearson correlation, and the differences in SWVmax values of breast cancer masses between different expressions of immunohistochemical parameters ER, PR, HER-2, Ki-67, and axillary lymph node status were compared using tests. The variables with correlations and differences were included in the multiple linear regression analysis to assess the factors influencing the SWVmax values. The performance of TDPM, SPM, and TSPM was compared using PVA body models with different freeze-thaw cycles. The results showed that TSPM performed better than SPM in general, and TDPM showed excellent performance because of high temporal resolution and low random error, especially when the number of freeze-thaw cycles increased and the hardness of the PVA body mold increased. Measurements at different depths of inhomogeneous body models also showed that the TDPM method was less affected by depth, and the results were more stable. Finally, the reliability of the shear wave velocity (SWS) measured by the TDPM and SPM methods was investigated using porcine ligament tissue, and the results showed that the mean values of SWS goodness of fit for TDPM and SPM were 0.94 and 0.87, respectively, and the estimated elastic modulus of TDPM was very close to the mechanical test results.

1. Introduction

The mammary glands are located on the surface of the chest wall at the level of the second to sixth ribs between the subcutaneous fascia and the fascia of the pectoralis muscle, and they are symmetrical from left to right. The mammary glands consist of 15–20 lobes arranged in a radial pattern with the nipple as the center, and the lobes are composed of lobules, which, in turn, are composed of each branch of the milk duct and its associated alveoli. The milk duct branches begin in the peripheral ducts and merge in a "two-and-one" fashion from the lower ducts to the higher ducts, ending in the milk-transmitting sinus. Most peripheral ducts, terminal ducts, and the surrounding alveolar tissue form the basic unit of the breast tissue, the terminal ductal lobule, which is the site of most breast diseases [1]. Intramammary lumps are a common clinical manifestation of breast disease mostly because of benign conditions such as fibroadenomas and cysts. However, in recent years, the incidence of breast cancer (BC) has been increasing year by year, ranking first among female malignant tumors. Although the prevalence of breast cancer in China is lower than that in Europe and the United States, the statistics are still not optimistic as Chinese women account for 12.2% of the newly diagnosed breast cancer patients worldwide each year. The trend is younger, which is an important cause of premature death in women and brings a heavy burden to families and society, making it a major public health problem [2]. Define the labeled breast tumor image data set in the source domain, and define the unlabeled target breast tumor image data set to be classified as the target domain, which, respectively, represent the number of samples in the source domain and the target domain. However, the mortality rate of breast cancer is decreasing compared to the increasing trend of breast cancer prevalence. At this time, the advantages of conventional ultrasonography (US), which is inexpensive, convenient, and safe without radiation, come to the fore. Conventional 2D ultrasound provides a unique anatomical cross-sectional image of the mass of the surrounding tissues, providing information including mass size, morphology, margins, echogenic pattern, posterior attenuation, and internal calcification, which provides a basis for the detection of breast cancer. The application of Doppler ultrasound is valuable in observing the characteristics of blood flow distribution and hemodynamic features within and around the mass and aids the conventional two-dimensional ultrasound to complete the diagnosis and differential diagnosis. However, it is influenced to some extent by the subjective judgment of the examiner with fair sensitivity and poor specificity [3].

However, as the sonograms of benign breast lesions and breast cancer overlap to a certain extent and the sonograms of breast cancer lesions are complex and variable because of the diversity of their clinicopathological features, conventional color Doppler ultrasonography has some limitations to some extent. Although ultrasound elastography, which generates strain by applying pressure, helps assist diagnosis, it is susceptible to physician subjectivity and manipulation during operation [4]. In contrast, real-time shear wave elastography (SWE), also known as E imaging, is a new quantitative ultrasound elastography technique that obtains elastic modulus values by quantitatively detecting the actual stiffness of the breast masses, thus providing a more objective and quantitative evaluation of breast lesions. It can overcome interference from the tissues outside the region of interest with high reproducibility. It has advantages in unique diagnostic and differential diagnosis in breast diseases, and thus it can overcome the subjective influence and inherent defects of stress elastography.

However, morphological criteria alone are not sufficient to measure the nature of breast masses. In clinical applications, the same lesions show different hardness values on different machines, probably because different manufacturers apply different imaging principles. The Mindray Reson 7 machine offers both shear wave static and dynamic elastography, where a higher quality image can be obtained on static mode elastography. However, in dynamic mode elastography, three levels of frame rate can be selected (0.4, 0.7, and 1.0 frames/sec) to choose the best quality one among multiple consecutive images. It may be more advantageous for areas affected by cardiac motion advantage. Little research has been done on the superiority of these two modes of elastography for the diagnosis of breast lesions. The purpose of this section is to evaluate the interobserver agreement between the qualitative and quantitative indices of static and dynamic imaging modalities and the diagnostic efficacy of the same for breast lesions and to compare them.

2. Current Status of Research

Currently, high-frequency ultrasound and color Doppler ultrasonography have become important screening tools in breast cancer screening and clinical management. The sonographic presentation of breast cancer is based on pathological morphological changes. The diversity of pathological histology, gross staging, and immunohistochemical features of the breast cancer causes the sonographic presentation of breast cancer lesions to be complex and variable as well [5]. Especially, the early biological features and ultrasound manifestations of small breast masses are extremely atypical, or when early breast cancer masses do not show typical sonographic manifestations, they bring confusion to ultrasound diagnosis. In addition, traditional ultrasound elastography is a semiquantitative method to determine the hardness of lesions, and it is easily affected by physician subjectivity and manipulation during the operation. STE, compared with traditional elastography, obtains quantitative elastic modulus values, and it can quantitatively analyze the elasticity of soft tissues in real-time, which can effectively avoid the subjectivity of scoring methods and assess the elastic changes of the tissues by the changes of elastic modulus values [6]. It can effectively avoid the subjectivity of scoring methods and assess the elasticity changes of tissues by the changes of elastic modulus values and realize the study of tissue characterization. The quantitative display of tissue elasticity is obtained by the probe without applying pressure to the tissue, avoiding the influence of strain by the operator and/or the tissue, and under the same pressure, the soft tissue can produce different deformations according to its position and the position of the adjacent hard tissue. Shear waves are generated fully automatically by the probe, and the sweep technique is nondependent with repeatable image patterns and good repeatability of elastic modulus values [7].

Most of the studies on the differential diagnostic value of STE for benign and malignant breast lesions have been reported by scholars, and the methods are mostly based on surgical pathology as the gold standard for diagnosis [8]. The sensitivity of using the maximum elasticity reference value as the diagnostic threshold for benign and malignant lesions was higher than that of the average elasticity reference value, while the specificity of the former was lower than that of the latte. The application of the area under the ROC curve to compare the maximum and average elasticity values for the diagnosis of benign and malignant breast lesions showed that the accuracy of using the maximum elasticity value for the diagnosis of benign and malignant breast lesions was higher [9]. When the lesion is accompanied by hemorrhagic necrosis, calcification, or collagen fibrosis, elasticity measurement is performed [10].

Elastography, as a novel imaging technique that can reflect and measure tissue stiffness noninvasively, has gained widespread attention and rapid development among clinicians and sonographers not only to identify benign and malignant breast lesions but also to assess histological information by describing the distribution of internal tissue stiffness [11]. Eliminate cross-domain feature distribution differences in the feature space. After the source domain samples are migrated, the feature learning category prototype is obtained, and the training process of the feature classification model of the breast tumor pathological image in the target domain is guided based on this. Early elastography, such as strain force elastography, which requires external manual pressure to show elastic deformation based on tissue displacement, is highly operator-dependent, susceptible to external pressure, and poorly reproducible. In recent years, the current newer shear wave elastography technique acquires transverse wave signals in the tissues by ultrasound machines equipped with ultrafast imaging capture systems and calculates the shear wave velocity from the time difference between the adjacent peaks of the shear wave and the wavelength. Tissue stiffness can be quantitatively evaluated by the shear wave velocity, and this operation does not require operator pressure, overcoming the limitations of result variability and operator dependence.

3. Identification of Abnormal Ultrasound Breast Image Data Analysis Assisted by Shear Wave Elastography

3.1. Shear Wave Elastography-Assisted Ultrasound Breast Imaging Experiments. The ultrasonic radiation force comes from the change of linear momentum when the ultrasonic wave propagates in the medium, i.e., the ultrasonic wave in the medium will produce energy density difference because of absorption or scattering. Only in a viscoelastic liquid or solid with a certain attenuation coefficient can the sound radiation force be produced [12]. The action of acoustic radiation force by the emission of a series of detection pulses can get the corresponding position of the tissue vibration. The obtained vibration information for the relevant algorithm processing can get the displacement curve of the tissue. When the tissue is deformed because of the excitation, the echo signal of the same mass is detected with a certain time shift. The time-to-peak method is one of the most widely used methods to estimate the shear wave velocity using linear regression, which, firstly, determines the time of shear wave propagation to each detection point. Then, it makes a linear regression of each arrival time against the distance of the passage passed in the corresponding time and estimates the shear wave velocity from the slope of the linear regression. The shear wave velocity is estimated from the slope of the regression [13]. The variation of the vibration displacement with time for each of the n channels to the right of the acoustic radiation force excitation point can be represented. The slope of the mass point vibration displacement versus propagation time is fitted linearly by calculating the distance between the corresponding feature points and the time between wave propagation to the crest of the corresponding feature points to obtain the corresponding shear wave velocity value.

A total of 70 patients with 64 lumps suspected to be solid masses of BI-RADS grade 4 and above were collected from two hospitals, namely The Second Affiliated Hospital of Medical College of Zhejiang University and The Fourth Affiliated Hospital of Zhejiang University School of Medicine, without any treatment, and they were detected by routine ultrasonography and/or mammography of the breast. The above patients underwent multimodal ultrasound including 2D gray-scale, color Doppler with elastography for the masses suspected of BI-RADS grade 4 and above before undergoing pathological examination (hollow-core needle aspiration biopsy, minimally invasive episiotomy, mass excision, or radical surgery). The images were stored, and the data was recorded [14]. To improve diagnostic quality, the operating physician was trained in image acquisition and image quality control before the operation, and routine ultrasound and STE examinations were performed by a physician with 7 years of experience in breast ultrasound diagnosis using a high-quality line array probe from a fixed ultrasound instrument. The patient was placed in a supine position with arms raised to fully expose the breast, axilla, and upper and lower clavicle, and a routine radiographic scan was performed centered on the nipple. After finding the mass, the largest diameter section of the mass was selected, the probe was adjusted to clearly show the relationship between the mass and the surrounding tissues, and machine parameters such as depth, dynamic range, and depth gain compensation were adjusted to maintain the stability of the probe. To reduce the distribution difference between the domains at the category level, the feature distribution difference between the domains is often optimized and reduced by the MMD constraint on the average feature value of the entire domain. 2D gray-scale ultrasound images of the largest diameter section of the mass were acquired, and the mass size, margin, morphology, presence of lobulation and angulation, internal echogenicity, posterior echogenicity, and the presence of microcalcifications were recorded. The color flow signal within and around the mass was determined, and the PW mode was switched to obtain the spectral pattern and record the resistance index as shown in Table 1.

The study was performed by two physicians, one sonographer with 6 years of experience operating shear wave elastography and 20 years of experience operating conventional ultrasound practice, and the other with 6 years of experience operating conventional ultrasound practice and was trained to operate 30 cases of shear wave elastography on the ultrasound machine used in this study before the study began. The 30 cases of simulated training were not included in the data for this study. All ultrasound data were obtained using a Mindray ultrasound machine with a 14 L5 high-frequency line array probe (range 5–14 MHz). Each patient underwent a routine ultrasound examination before SWE. Before the examination, the patient was instructed to lie in a flat position with hands raised, and if the lateral breast was to be examined, the patient was turned slightly on his or

Table 1: Types of pathology studied by shear wave.

Malignant mass	Number of cases	Benign mass	Number of cases
Invasive ductal carcinoma	2	Fibroadenoma	3
Ductal carcinoma in situ	4	Adenopathy	4
Papillary carcinoma	10	Papilloma	11
Mucinous carcinoma	20	Benign phyllodes tumor	24
Invasive lobular carcinoma	10	Adenopathy with papilloma	10
Invasive adenocarcinoma	18	Interstitial sclerosis	18
Total	64	Total	70

her side to fully expose both breasts, and parameter settings such as gain and depth were adjusted according to the location and size of the breast mass. Then, the operator recorded basic information such as quadrant location, size, echogenicity, boundary, shape, and posterior echogenic attenuation of the breast lesion. Color Doppler flow imaging (CDFI) showed the peripheral and internal blood flow of the mass as shown in Figure 1.

The quantitative metrics for static-mode elastography and dynamic-mode elastography have an excellent interobserver agreement. The intragroup correlation coefficient ICC of dEmax in the dynamic mode is 0.962. The intragroup correlation coefficient ICC of dEmean in the dynamic mode is 0.915. The intragroup correlation coefficient ICC of DSD in the dynamic mode is 0.962. The interobserver agreement in the dynamic mode is slightly higher than that in the static mode.

Then, the Shear Wave real-time shear wave elastic ultrasound diagnostic instrument was used in two-dimensional gray-scale ultrasound mode to lightly place the probe on the skin. Determine the location of the breast lesion, add a sufficient amount of coupling agent, and fix the probe without applying pressure. Then, switch to SWE mode, place the elastic sampling frame in the area of interest, adjust the size of the real-time elastic imaging area, ask the patient to hold his breath if necessary, and rest for about 3 s [15]. If necessary, the patient was instructed to hold his breath, and the image was stored in a fixed frame after standing for approximately 3 s to 5 s to stabilize. Then, the same area of interest was positioned three times, the maximum elastic modulus value (E_{max}) and the average elastic modulus value (Eman) of the shear wave were measured, and the average value of Emax and Eman of the three groups was taken as the final data. The dynamic changes of the elastic modulus value of the area of interest were continuously observed, and the maximum and minimum changes of Emax were taken to obtain the extreme difference of the change of E_{max}. There is a 90° phase difference between stress, and hence, the ideal viscous body is represented by a viscous pot, which means that the container contains a liquid that obeys Newton's law of fluid. Compare the elastic modulus values of each group as shown in Figure 2.

A review of the relevant literature and the results of the early STE pretest in this study suggest that compared with benign lesions, malignant solid lesions have a "multivariable sign" with variable and unstable elastic signals, a "hard ring sign" with high surrounding elastic modulus values, and a "black hole sign" with the absence of internal shear wave

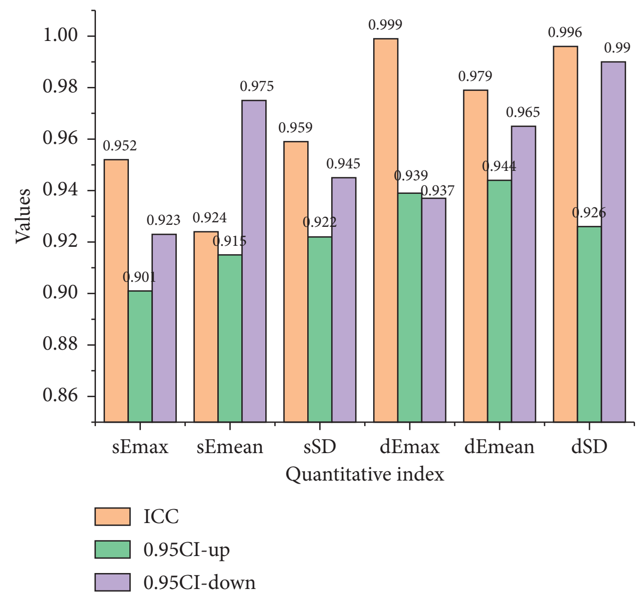

Figure 1: Interobserver agreement of quantitative metrics for shear fluctuation/static mode elastography.

elastic signals. Therefore, in this study, we prospectively performed a comprehensive analysis of lesions based on the presence or absence of these three features, readjusted the first BI-RADS classification, and compared the diagnostic efficacy of the two examination methods using pathological findings as to the gold standard [16]. This section covers standard heterogeneous mimic elasticity measurements based on an ultrasound data acquisition platform to compare focused versus unfocused comb pulse excitation modalities at different parameters. Hypotheses are formulated from the results of the first set of standard heterogeneous mimic body pre-experiments. Hypothesis one is verified by observing the acoustic field energy distribution under focused and unfocused comb pulse excitation methods by linear and convex arrays comb excitation pulse simulation. The proposed hypotheses one and two are verified by the second set of standard mimic experiments, and finally, the excitation algorithm used in this study is selected.

The midpoint of the probe was aligned with the marker point. The long axis of the probe was parallel to the muscle fibers. No pressure was applied. The muscle echogenicity and muscle fiber direction were carefully observed on the grayscale image. After displaying more than 3 continuous muscle fiberss, the shear wave elastography mode under the elastography menu was selected, the left and right borders of

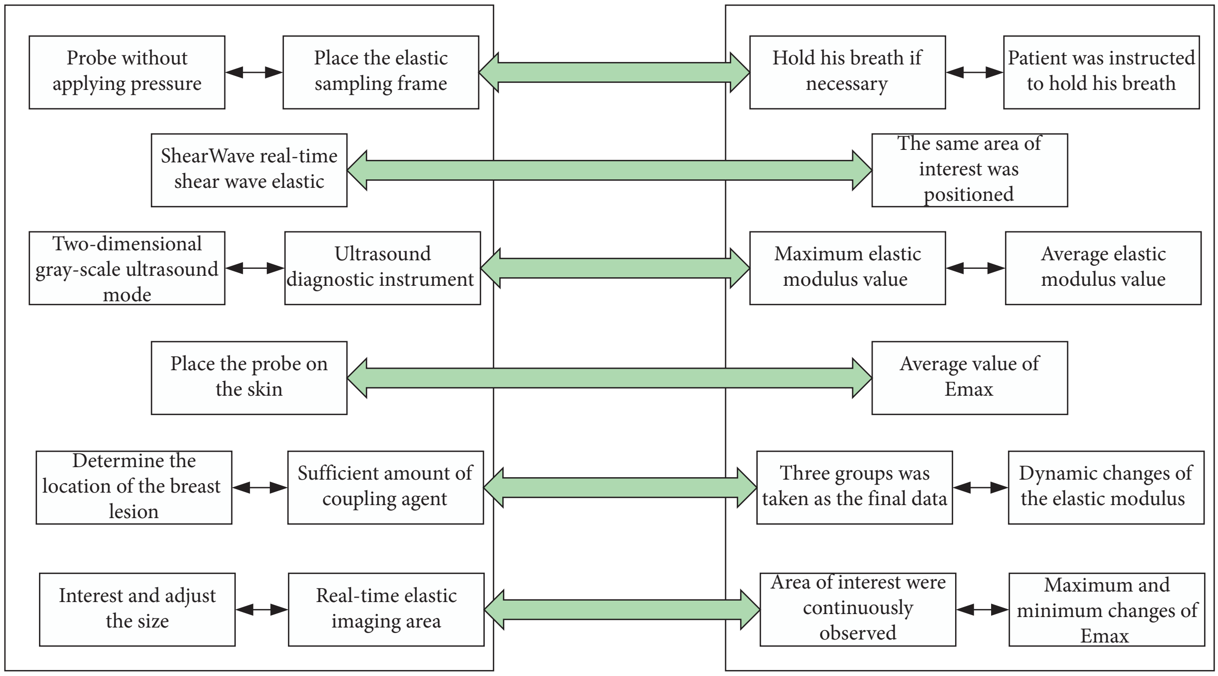

Figure 2: Experimental steps.

the region of interest (ROI) were adjusted to the maximum, and the upper and lower boundaries of the ROI are extracted. The patient was asked to hold his breath, the elastography image was acquired. For the upper right corner, the corner motion stability index (M-STB index) of the image was five green stars. Ten subjects were randomly selected, and the control group measured the trapezius muscle from the spinous process of the seventh cervical vertebra to the midpoint of the left acromion line. The case group measured the trapezius trigger point area from the spinous process of the seventh cervical vertebra to the midpoint of the acromion line on the painful side, and the mean values of SWVmax, swVmean, and SWVmin were recorded three times. The labeling of skin lesion images often requires experienced doctors or experts in the field to complete, and the labeling cost is much more expensive than natural visual images. The subjects were tested by 2 physicians separately (without knowledge of each other's findings and knowledge of the patient's pain level) according to the above measurements, and the reproducibility of the measurements between the different tests was compared. Physician A measured the same subject again half an hour later to compare the reproducibility of measurements between the times for the same examiner.

3.2. Discriminatory Analysis of Abnormal Data from Glandular Images. The prototype network model introduces the idea of a statistical generative model that learns a generative model about a dataset by extending the variational self-encoder rather than using independent sample points as the learning object. The main module of the model, namely the statistical network, summarizes a series of data sample points into a statistical vector [17].

$$\mu_c = \frac{1}{|\varsigma_c|} \sum_{x_i \in S_c} f\left(x_i^2, \theta^2\right). \tag{1}$$

In this case, the direct migration of trained classification models to new datasets inevitably results in a large degree of loss of effectiveness. Also, the new dataset faces the problem of labeling difficulties. From the above, PTGAN aims to achieve the migration of the model trained in the source domain data to the unlabeled target domain without labeling the new data to improve the classification of breast tumor pathology images. Firstly, a dataset of the breast tumor images with existing labels in the source domain is defined, and a dataset of unlabeled target breast tumor images to be classified is defined as the target domain. It represents the number of samples in the source and target domains, respectively, representing the class labels of the samples in the source domain.

$$\begin{aligned} h_i^s &= f\left(x_i^s, \theta_f^2\right), \\ h_j^t &= f\left(x_j^t, \theta_f^2\right). \end{aligned} \tag{2}$$

After the target-biased generation of adversarial networks, the migration effect of the samples in the source and target domains at the image style level is guaranteed. However, the migration problem at the feature level in the classification task has not been solved. Therefore, this subsection designs a prototype migration module to further migrate the features extracted from the network by cross-domain feature migration loss to eliminate the differences in cross-domain feature distribution in the feature space. It is the site where most breast diseases occur. Masses in the breast are common clinical manifestations of breast diseases, most of which are caused by benign diseases, such as fibroadenoma, cysts, etc. The source domain samples are migrated to obtain the feature learning category prototype, and this is used to guide the training process of the feature classification model for breast tumor pathology images in the target domain as shown in Figure 3.

MMD is the maximized mean deviation used to measure the difference in data distribution between the source and target domains. After the MMD loss constraint, the difference between the distribution of the source domain features and the target domain features after style transformation is reduced, and domain adaptation is achieved at the feature level.

$$L_{MMN} = \left\| \frac{1}{N_s} \sum_{i=1}^{N_s} h_i^s + \frac{1}{N_s} \sum_{j=1}^{N_t} h_j^s \right\|,$$
$$D_{KL}(p \,\|\, q) = \sum_{c=1}^{c} \ln \frac{p_i^c}{q_j^c}. \tag{3}$$

As shown in Figure 4, often in viscoelastic studies of biological tissues, some biological models are used to fit the mechanical properties of the tissues [18]. For purely viscous materials, there is a 90° phase difference between stress. Hence, the ideal viscous body is represented by a vicious pot, representing a container containing a liquid obeying Newton's law of fluids. However, for purely elastic materials, there is no phase difference between stress. Hence, the ideal elastomer is represented by a spring [19]. The Voigt model for the study of bio-viscoelasticity can be obtained by connecting the spring in parallel with the viscous pot. To improve the performance of deep neural networks during medical image classification, it is common to consider scaling up the model training by increasing the amount of labeled medical image data.

However, in real scenarios, these medical data differ to some extent in terms of light intensity, viewpoint, background, etc. Meanwhile, the quality of medical image annotation relies on the degree of expertise of the annotators, which requires years of accumulated expertise and experience [20]. Provide information, including tumor size, shape, edge, echo pattern, whether there is attenuation behind, and whether there is calcification inside, etc., to provide a basis for finding breast cancer. With the increasing standard of intelligent-assisted classification and diagnosis of skin lesion images in clinical practice, the annotation of skin lesion images often requires experienced doctors or experts in the field to complete, and its annotation cost is much more expensive compared with natural visual images. Thus, the task of automatic classification of skin lesion images faces difficulties and limitations, such as complex sample data, uneven distribution, and expensive annotation of labeled samples.

Existing research works mainly focused on the fields of machine learning and data mining, which can be summarized into two categories: clustering and domain adaptive methods. These research works assume that the number of classes of the target medical image is known in advance and then applied to the image classification problem lacking labeled information to achieve unsupervised medical image classification results. However, this assumption premise is usually difficult to hold in practical scenarios because, in medical images, there will be additional unexpectedly generated symptom classes in addition to the already known symptom classes, a situation that existing clustering and domain adaptive algorithms cannot cope with. In other words, the existing machine learning clustering algorithms cannot automatically construct information about the categories of the data and cannot interpret conceptual information about the categories of objects, etc., without external supervision.

4. Analysis of Results

4.1. Experimental Results. Benign masses such as breast adenopathy and fibroadenoma have loosely arranged tumor cells with a high content of interstitial mucopolysaccharides, and therefore, lower hardness values. In contrast, malignant tumors contain abundant connective tissues, blood vessels, and lymphatic vessels inside, and the tumor cells are tightly wrapped by proliferative fibrous tissues. In addition, malignant tumors have the ability of distant invasion, and during the process of tumor growth, they continuously adhere to and invade the surrounding tissues, resulting in adhesions between the masses and the surrounding tissues, thus reducing the elasticity of the tissues leading to an increase in the hardness value. Class 4A masses were corrected to class 3, of which 2 cases were missed. 1 case was ductal carcinoma in situ and the other case was ductal carcinoma in situ with acne-like necrosis 4 masses were upgraded from category 4A to category 4B, 1 of which was correctly upgraded, and the pathology was intraductal papillary carcinoma, while the remaining 3 masses were benign, namely, lobular granulomatous mastitis, adenopathy with fibroadenoma formation, and focal chronic inflammatory cell infiltration, all of which were large. Six masses were downgraded from category 4B to 4A, three of which were intraductal papilloma's and were correctly downgraded, while the other three were incorrectly downgraded, with the diameters of 11 mm, 5 mm, and 11 mm, respectively, and the pathological types of intraductal carcinoma, ductal carcinoma in situ, and ductal carcinoma in situ with local infiltration, respectively. It also has important clinical value in the differential diagnosis of benign and malignant breast lesions. However, the ultrasound charts of benign breast lesions and breast cancer now overlap to a certain extent. It is also complicated and changeable because of the diversity of its clinicopathological characteristics. The ratio, SD, and Emax of all three masses were below the diagnostic threshold, as shown in Figure 5.

Breast cancer is usually insidious, with no clinical symptoms in the early stage and is usually detected by chance. Routine ultrasound screening for breast cancer has the advantages of noninvasiveness, nonradiation, low price,

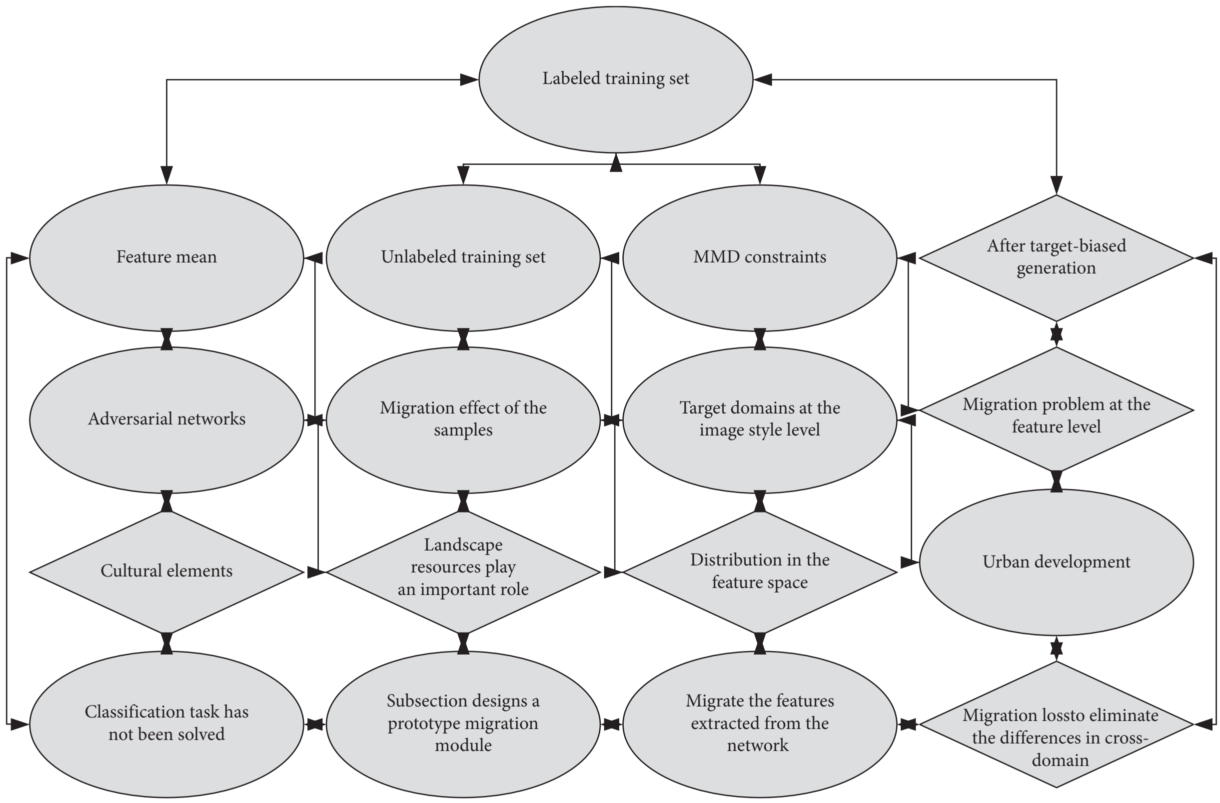

Figure 3: Migration metric learning framework diagram.

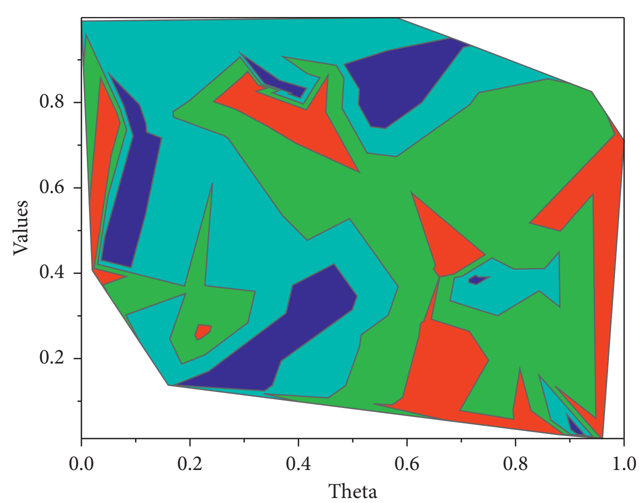

Figure 4: Radon transformation method for shear wave group velocity.

and good reproducibility. Together with mammography and magnetic resonance imaging, it has become the three major imaging methods for noninvasive diagnosis of breast diseases.

To standardize the description of breast masses, the US-BI-RADS classification criteria are gradually applied in clinical practice. Although the sensitivity of US-BI-RADS was fair, the specificity, accuracy, and NPV were low, and the benign rate was as high as 51% in grade 4 and above masses enrolled in this study. It can overcome the interference of tissues outside the region of interest, has high repeatability, and has unique advantages in the diagnosis and differential diagnosis of breast diseases. Therefore, it can overcome the subjective influence and inherent defects of stress elastography technology. If such patients were blindly selected for puncture biopsy or surgical management, it would not only cause trauma to the patients but also result in a waste of valuable medical resources. In addition, the mid- and long-term follow-up of conservative treatment of benign masses confirmed by puncture biopsy faces the challenge of whether

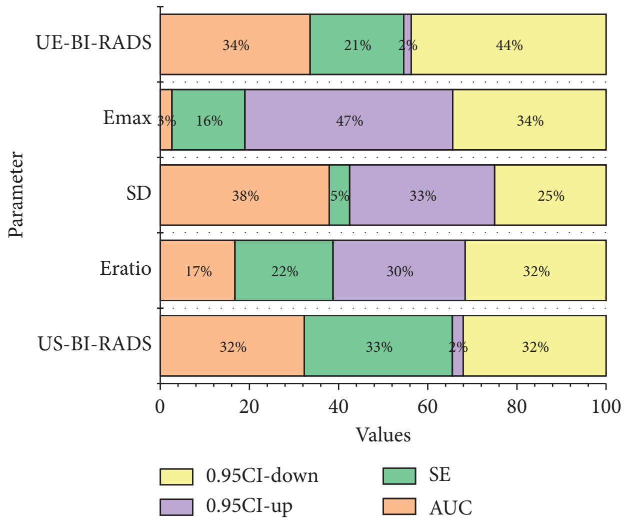

Figure 5: ROC curves for the diagnosis of breast masses.

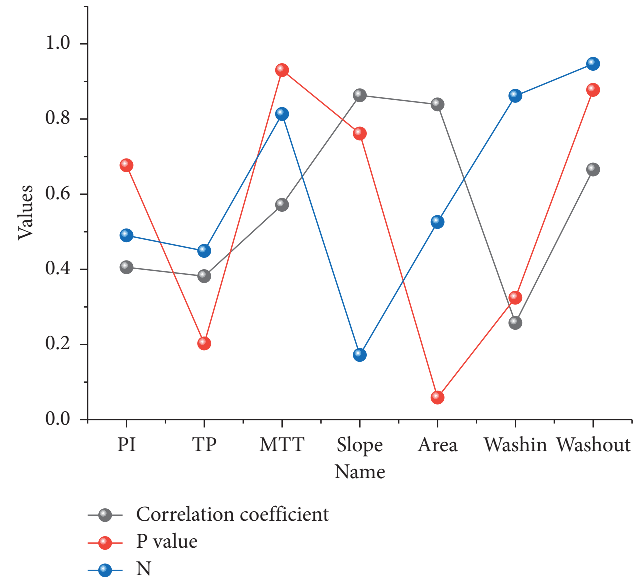

Figure 6: Relationship between quantitative indicators of shear wave static mode elastography and quantitative indicators of ultrasonography in benign masses.

to rashly downgrade the mass to benign based on the previous pathological findings or to determine whether the mass has undergone minor suspicious changes based on the morphological features of the mass, which poses a certain challenge to ultrasonographers at each follow-up visit. In addition, it is difficult to use puncture biopsy as a routine follow-up in clinical practice. Therefore, there is an urgent need for a safe, reliable, and simple noninvasive method as a supplement to US-BI-RADS to improve the specificity and accuracy of diagnosis to reduce unnecessary puncture biopsies and surgical management as shown in Figure 6.

Neovascularization is an important stage in the growth of malignant masses over 2–3 mm, and tumor growth and metastasis are associated with angiogenesis, which is a hot topic for research into new anticancer approaches. Many antineovascularization therapies use this principle to destroy or limit tumor angiogenesis. The current study demonstrates the relationship between breast malignant mass stiffness and blood flow, while shear wave elastography is easy and less time-consuming to perform compared to ultrasonography. Without the need for intravenous injection and background software analysis, it allows for a rapid understanding of the approximate fibrous tissue and blood flow within the mass and assessment of the sensitivity of ant neovascular therapy. A higher-quality image can be obtained on static mode elastography, three levels of frame rate can be selected in dynamic mode elastography, and multiple images can be selected in succession. Firstly, the sample size of this study was not large enough. A total of 70 breast masses were included in this study, including 64 malignant masses. The sample size should be expanded for further study in future studies. Secondly, in the quantitative analysis of breast lumps, the ROI should be sampled several times to determine the quantitative indicators and averaged to make it more objective. Thirdly, the choice of ROI location also affects the perfusion of the time-intensity curve. Angiogenesis is more active in the peripheral region of a malignant mass than in the central region. The central region is filled with bridging and fibrous tissue. Hence, the parenchyma is stiffer, and vascular growth is difficult in it. Hence, the interior is not as vascular, and again, there is central calcified necrosis formation.

4.2. Results of Anomalous Data Identification. To improve the automatic classification performance of breast tumor histopathology images with insufficient labeled samples, semisupervised learning has been gradually introduced in the field of medical image classification research. Compared with unsupervised learning, the semisupervised learning approach can apply the inherent characteristics and patterns of the unlabeled sample data and can improve the status quo of unsupervised learning classification methods with unsatisfactory results accuracy. Therefore, this chapter introduces a semisupervised framework for classifying histopathological images of breast tumors. It utilizes a small number of labeled samples and many unlabeled samples to constitute the training data, effectively overcoming the overfitting problem of unsupervised classification methods and improving the classification accuracy without the need for a large-scale data annotation effort. The PTGAN model was used to test the classification performance on the breast tumor pathology image dataset while reporting the performance of multiple breast tumor pathology image classification methods used on the BreaKHis dataset. The experimental results of this method on image samples with different magnifications are shown in Table 2.

The source domain image samples do not have any overlapping data with the target domain image samples. In addition, considering the different relevance of sample data in different source domains for migration to the target domain, a fuzzy attention mechanism is designed in this chapter to calculate their weights for migration to the target domain. This method, firstly, determines the time for the shear wave to

Table 2: Image classification results of PTGAN model on BreakHis dataset.

Multiple	Accuracy 1	Accuracy 2	Recall rate	F1-score
40x	84.9	94.6	89.3	88.5
100x	88.9	93.4	88.7	97.5
200x	90.5	96.9	80.6	95.1
400x	84.3	86.3	95.5	80.8
Average value	83.4	89.5	87.8	95.5

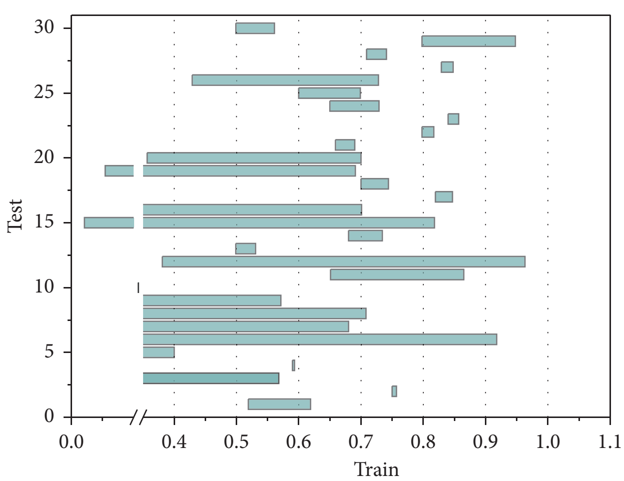

Figure 7: Accuracy and loss variation on the test and training sets.

propagate to each detection point. Then, it performs a linear regression on the distance between each arrival time and the passage through the corresponding time and estimates the speed of the shear wave from the slope of the linear regression. With the learned weights of different source domains, MFAN can learn a shared robust feature space for breast tumor histopathology images and train the fine-tuned classification models adapted to the target domain by label inference.

Most of the available research works report classification results in two categories, benign and malignant. This chapter focuses on the problem of dichotomizing PTGAN in breast tumor pathology images, and therefore, it only considers the experimental results of existing work under the dichotomization task at the image level for control. The experiments of the existing work are performed at 40x, 100x, 200x, and 400x magnifications for binary classification and multiclassification problems. Based on the BreaKHis dataset, an 85% accuracy at the patient level was obtained by applying different features. AlexNet is used to conduct a two-classification study on pathological images of breast tumors. The average accuracy rate of the image level is 89.0%, and the average accuracy rate of the patient level is 90.0%. To demonstrate the variation of loss versus accuracy on the training and test sets during PTGAN training, this subsection shows the accuracy and the curve dynamics of network loss during the model training iterations in Figure 7 using 100x magnification breast tumor pathology image data as an example.

The style migration across domains is achieved by the target domain bias-generative adversarial network to reduce the style differences between source and target domains. The extracted sample features are mapped into a cross-domain feature space by cross-domain loss constraints, thus training the classification in the cross-domain feature space using source and target domain features. To improve the quality of diagnosis, the operating doctor conducts image acquisition training and image quality control before the operation. Routine ultrasound and SWE examinations are completed by a doctor with 7 years of breast ultrasound diagnosis experience using a high-quality linear array probe with a fixed ultrasound instrument. Validation tests are conducted on the BreaKHis dataset, and the core module of PTGAN is discussed in this chapter, showing that it has excellent feature extraction capabilities. Also, it achieves an accuracy level closer to that of supervised learning methods without the advantage of large-scale data annotation efforts, and it scales well.

5. Conclusion

Shear wave elastography may provide a certain reference basis for the selection of breast cancer treatment strategy and prognosis judgment. To determine the accuracy of TDPM measurement, a total of four gelatin body molds with different agar contents were made as validation objects in this experiment, and the body molds were soaked in glycerol to increase their toughness. SWE and mechanical tensile experiments were performed. The conventional SPM was introduced to compare the results of the two ultrasonic measurements, and the results of the mechanical tests were used as the gold standard to verify the results of the ultrasonic experiments. The results show that the displacement data measured by SPM are not well-fitted linearly in the process of fitting the group velocity. However, TDPM is more accurate in detecting the feature points because of the improved sampling resolution. The linear fit is better, and the fitted shear wave group velocity is more accurate. The measurement results of TDPM have less variance, less random error, better precision, and are closer to MT results. Because of the complex pathological process of adenopathy and the lack of specific sonographic features, there is some overlap with the sonogram of breast malignancy, and the misdiagnosis rate is high. In clinical practice, we should fully understand the ultrasound image features and pathological characteristics of adenopathy, combine clinical data, image features, and elastography parameters to make a comprehensive analysis. When suspicious signs are found, puncture biopsy under ultrasound guidance promptly to improve the diagnostic compliance rate and reduce the misdiagnosis rate.

Data Availability

The data used to support the findings of this study are available from the corresponding author upon request.

Conflicts of Interest

There are no conflicts of interest in this article.

Acknowledgments

This study was supported by the Excellent Youth Talents Foundation of Traditional Chinese Medicine of Zhejiang

Province (2021ZQ054), Key Science and Technology Program Of Jinhua Science and Technology Bureau (2021-3-006), and General Research Project of Zhejiang Provincial Department of Education (Y202146078).

References

[1] S. H. S. Chou, M. Baikpour, W. Zhang, S. F. Mercaldo, C. D. Lehman, and A. E. Samir, “Shear-wave elastography of the breast: impact of technical image quality parameters on diagnostic accuracy,” *American Journal of Roentgenology*, vol. 216, no. 5, pp. 1205–1215, 2021.

[2] T. Fujioka, L. Katsuta, K. Kubota et al., “Classification of breast masses on ultrasound shear wave elastography using convolutional neural networks,” *Ultrasonic Imaging*, vol. 42, no. 4-5, pp. 213–220, 2020.

[3] J. H. Youk, J. Y. Kwak, E. Lee, E. J. Son, and J. A. Kim, “Grayscale ultrasound radiomic features and shear-wave elastography radiomic features in benign and malignant breast masses,” *Ultraschall in der Medizin - European Journal of Ultrasound*, vol. 41, no. 4, pp. 390–396, 2020.

[4] C. Hangard, J. L. Gennisson, C. Reinhold, and L. S. Fournier, “Diagnostic accuracy of four levels of manual compression applied in supersonic shear wave elastography of the breast,” *Academic Radiology*, vol. 28, no. 4, pp. 481–486, 2021.

[5] A. Peker, P. Balci, I. Basara Akin, H. A. Özgül, S. Ö. Aksoy, and D. Gürel, “Shear-wave elastography-guided core needle biopsy for the determination of breast cancer molecular subtype,” *Journal of Ultrasound in Medicine*, vol. 40, no. 6, pp. 1183–1192, 2021.

[6] G. B. Makal and İ. Güvenç, “The role of shear wave elastography in differentiating idiopathic granulomatous mastitis from breast cancer,” *Academic Radiology*, vol. 28, no. 3, pp. 339–344, 2021.

[7] X. Zheng, Y. Huang, Y. Liu et al., “Shear-wave elastography of the breast: added value of a quality map in diagnosis and prediction of the biological characteristics of breast cancer,” *Korean Journal of Radiology*, vol. 21, no. 2, pp. 172–180, 2020.

[8] W. Jia, T. Luo, Y. Dong, X. Zhang, W. Zhan, and J. Zhou, “Breast elasticity imaging techniques: comparison of strain elastography and shear-wave elastography in the same population,” *Ultrasound in Medicine and Biology*, vol. 47, no. 1, pp. 104–113, 2021.

[9] T. Luo, J. W. Zhang, Y. Zhu, Y. J. Dong, W. W. Zhan, and J. Q. Zhou, “Virtual touch imaging quantification shear-wave elastography for breast lesions: the diagnostic value of qualitative and quantitative features,” *Clinical Radiology*, vol. 76, no. 4, pp. 316. e1–316. e8, 2021.

[10] L. Zhang, Y.-J. Dong, J.-Q. Zhou, X.-H. Jia, S. Li, and W. W. Zhan, “Similar reproducibility for strain and shear wave elastography in breast mass evaluation: a prospective study using the same ultrasound system,” *Ultrasound in Medicine and Biology*, vol. 46, no. 4, pp. 981–991, 2020.

[11] K. Pesce, F. Binder, M. J. Chico, M. P. Swiecicki, D. H. Galindo, and S. Terrasa, “Diagnostic performance of shear wave elastography in discriminating malignant and benign breast lesions,” *Journal of Ultrasound*, vol. 23, no. 4, pp. 575–583, 2020.

[12] A. V. Polat, M. Ozturk, A. K. Polat, U. Karabacak, T. Bekci, and N. Murat, “Efficacy of ultrasound and shear wave elastography for the diagnosis of breast cancer-related lymphedema,” *Journal of Ultrasound in Medicine*, vol. 39, no. 4, pp. 795–803, 2020.

[13] A. Chiorean, R. M. Pintican, M. M. Duma et al., “Visualization of the shear wave on gray-scale ultrasound: experience with a complex breast cyst,” *Medical ultrasonography*, vol. 22, no. 4, pp. 492–494, 2020.

[14] R. G. Barr, “Breast elastography: how to perform and integrate into a “Best-Practice” patient treatment algorithm,” *Journal of Ultrasound in Medicine*, vol. 39, no. 1, pp. 7–17, 2020.

[15] D. Yildirim, Ö Akıncı, and D. E. Tekcan, “Quantitative ultrasound elastography of breast: a review and update with emphasis on shear wave imaging (ARFI),” *Open Journal of Medical Imaging*, vol. 11, no. 2, pp. 58–72, 2021.

[16] E. Uysal, M. Öztürk, A. Kilinçer, and M. Koplay, “Comparison of the effectiveness of shear wave elastography and superb microvascular imaging in the evaluation of breast masses,” *Ultrasound Quarterly*, vol. 37, no. 2, pp. 191–197, 2021.

[17] H. Jiang, X. Yu, L. Zhang, L. Song, and X. Gao, “Diagnostic values of shear wave elastography and strain elastography for breast lesions,” *Revista Medica de Chile*, vol. 148, no. 9, pp. 1239–1245, 2020.

[18] M. H. Lee, E. K. Kim, E. J. Lee, H. Y. Kim, and J. H. Yoon, “Application of point shearwave elastography to breast ultrasonography: initial experience using “S-shearwave” in differential diagnosis,” *Journal of the Korean Society of Radiology*, vol. 81, no. 1, pp. 157–165, 2020.

[19] S. J. Bae, J. H. Youk, C. I. Yoon et al., “A nomogram constructed using intraoperative ex vivo shear-wave elastography precisely predicts metastasis of sentinel lymph nodes in breast cancer,” *European Radiology*, vol. 30, no. 2, pp. 789–797, 2020.

[20] A. A. Gemici, S. T. Ozal, E. Hocaoglu, and E. Inci, “Relationship between shear wave elastography findings and histologic prognostic factors of invasive breast cancer,” *Ultrasound Quarterly*, vol. 36, no. 1, pp. 79–83, 2020.

Hindawi
Journal of Healthcare Engineering
Volume 2023, Article ID 9805274, 1 page
https://doi.org/10.1155/2023/9805274

Retraction

Retracted: Application of Dynamic Enhanced Magnetic Resonance Imaging in the Diagnosis of Hematological Malignancies

Journal of Healthcare Engineering

Received 10 October 2023; Accepted 10 October 2023; Published 11 October 2023

Copyright © 2023 Journal of Healthcare Engineering. This is an open access article distributed under the Creative Commons Attribution License, which permits unrestricted use, distribution, and reproduction in any medium, provided the original work is properly cited.

This article has been retracted by Hindawi following an investigation undertaken by the publisher [1]. This investigation has uncovered evidence of one or more of the following indicators of systematic manipulation of the publication process:

(1) Discrepancies in scope
(2) Discrepancies in the description of the research reported
(3) Discrepancies between the availability of data and the research described
(4) Inappropriate citations
(5) Incoherent, meaningless and/or irrelevant content included in the article
(6) Peer-review manipulation

The presence of these indicators undermines our confidence in the integrity of the article's content and we cannot, therefore, vouch for its reliability. Please note that this notice is intended solely to alert readers that the content of this article is unreliable. We have not investigated whether authors were aware of or involved in the systematic manipulation of the publication process.

In addition, our investigation has also shown that one or more of the following human-subject reporting requirements has not been met in this article: ethical approval by an Institutional Review Board (IRB) committee or equivalent, patient/participant consent to participate, and/or agreement to publish patient/participant details (where relevant).

Wiley and Hindawi regrets that the usual quality checks did not identify these issues before publication and have since put additional measures in place to safeguard research integrity.

We wish to credit our own Research Integrity and Research Publishing teams and anonymous and named external researchers and research integrity experts for contributing to this investigation.

The corresponding author, as the representative of all authors, has been given the opportunity to register their agreement or disagreement to this retraction. We have kept a record of any response received.

References

[1] Y. Shao, X. Bao, C. Song, and D. Cui, "Application of Dynamic Enhanced Magnetic Resonance Imaging in the Diagnosis of Hematological Malignancies," *Journal of Healthcare Engineering*, vol. 2021, Article ID 4623850, 12 pages, 2021.

Hindawi
Journal of Healthcare Engineering
Volume 2021, Article ID 4623850, 12 pages
https://doi.org/10.1155/2021/4623850

Research Article

Application of Dynamic Enhanced Magnetic Resonance Imaging in the Diagnosis of Hematological Malignancies

Yanping Shao [1] **Xueping Bao** [2] **Caifang Song** [3] **and Danping Cui** [4]

[1]*Department of Hematology, Taizhou Hospital of Zhejiang Province Affiliated to Wenzhou Medical University, Taizhou, Zhejiang 317000, China*
[2]*Taizhou Hospital of Zhejiang Province Affiliated to Wenzhou Medical University, Taizhou, Zhejiang 317000, China*
[3]*Department of Gastroenterology, Taizhou Hospital of Zhejiang Province Affiliated to Wenzhou Medical University, Taizhou, Zhejiang 317000, China*
[4]*Department of Geriatrics, Taizhou Hospital of Zhejiang Province Affiliated to Wenzhou Medical University, Taizhou, Zhejiang 317000, China*

Correspondence should be addressed to Danping Cui; cdp@enzemed.com

Received 19 August 2021; Revised 26 September 2021; Accepted 9 October 2021; Published 23 December 2021

Academic Editor: Gu Xiaoqing

Copyright © 2021 Yanping Shao et al. This is an open access article distributed under the Creative Commons Attribution License, which permits unrestricted use, distribution, and reproduction in any medium, provided the original work is properly cited.

The use of dynamic enhanced magnetic resonance imaging technology can effectively explore the diagnosis and clinical application of hematological malignancies. This paper selected 60 patients with hematological malignancies from 2015 to 2019; all of whom were diagnosed with hematological malignancies, including 40 men and 20 women, aged between 40 and 77 years. The main clinical manifestations of the patient are hematological malignancies, fever, and other symptoms. We used Siemens 3.0T to perform MRI and dynamic enhanced MRI examinations on 30 patients with hematological tumors. The PACS system was used to collect and organize clinical data. All patients were pathologically confirmed and clinically diagnosed with hematological malignancies. Based on the clinical data of the patients, retrospective analysis and summary were conducted and the clinical manifestations of hematological malignancies were discussed. The results showed that the diagnostic accuracy of 30 cases of dynamic enhanced MRI was 100%, while the diagnostic accuracy of ordinary MRI was lower than that of dynamic enhanced MRI, $P < 0.05$, and the difference was statistically significant. In addition, compared with dynamic enhanced MRI and MRI, $P > 0.05$, the difference was not statistically significant. Therefore, the application of dynamic enhanced MRI in the diagnosis of hematological malignancies is valuable.

RETRACTED

1. Introduction

With the development of urbanization, industrialization, and the advent of population aging, the incidence rate is on the rise. Malignant tumors have brought serious harm to human health. Researching malignant tumors to design more effective treatment plans is an important direction of modern medicine development. With the invention and application of new technologies, the overall diagnosis level has significantly improved, and with the clinical application of new drugs, the treatment level has improved significantly [1]. The scientific and effective application of various diagnostic indicators to make them play the best guiding role in the treatment is a challenge facing the field of hematological malignancies. Diagnosis is the prerequisite for achieving accurate treatment. Only accurate diagnosis can play its clinical guiding role, and the implementation of magnetic resonance imaging is the basis for accurate diagnosis [2]. The prospect of new technology is very bright, but the current application is not very satisfactory.

Dynamic enhanced magnetic resonance imaging (DE-MRI) is a functional imaging method that noninvasively evaluates the characteristics of tissues and tumor blood vessels through intravenous injection of contrast medium. The current MRI-enhanced contrast agents include small molecule contrast agents that can quickly diffuse into the extracellular space (relative molecular mass <1000). The small molecule contrast agent DCE-MRI technology has successfully entered the clinical application stage and has played an important role. The DCE-MRI technology is in the early stage of clinical trials and clinical applications. In the process of research on malignant tumors by researchers and doctors, dynamic contrast-enhanced magnetic resonance imaging as an imaging technique that reflects the characteristics of tissue hemodynamics has received more and more clinical applications [3, 4]. In DE-MRI imaging, a paramagnetic substance has usually been injected into the patient's body through an intravenous injection, which results in a shortened T1 time during tissue imaging. Repeated imaging is used to track the diffusion of the contrast agent into the tissue over time. This can reflect hemodynamic information such as microangiogenesis and permeability of living tumors and plays an important role in the diagnosis and research of malignant tumors. The DE-MRI image analysis is mainly carried out in two aspects: (1) analysis pixel by pixel in the spatial domain and (2) time domain analysis in the image sequence, by analyzing the changes in the concentration of the local spatial contrast agent, calculating the relevant hemodynamic parameters.

Today, the level of informatization is getting higher, and the massive growth in medical imaging data makes it more necessary to use computers for automatic processing or to extract key information for doctors, thereby promoting the development of computer-aided diagnosis. Dynamically enhanced MRI uses imaging, medical image processing technology, and other possible physiological and biochemical methods, which improves the accuracy of lesion location [5]. The use of dynamic enhancement of MRI can speed up the diagnosis process, reduce the rate of misdiagnosis, improve the quantitative evaluation results, and help correct the doctor's subjective diagnosis error [6]. Nevertheless, the application of dynamic enhancement MRI technology in the field of DE-MRI imaging is only relatively mature in multiple myeloma research, and the clinical application of other diseases needs further development [7]. Therefore, how to improve and strengthen the MRI technology so that the DE-MRI image processing and analysis field has better clinical promotion is the key to promoting the development of related technologies.

We transfer all the collected original images to the Extended MR Workspace (EWS) workstation provided by Philips, which contains the Functool toolkit for postprocessing all images. The film was read by two experienced MRI diagnostic doctors, and the pathological results were not known before the film. When there is a disagreement, it will be decided by the two doctors after mutual consultation. If the lesion is multiple, the largest lesion diameter is included when analyzing the MRI image. The data was sorted and summarized, a database was established with Excel 2010, SPSS 24.0 was used for statistical analysis of all the data, the measurement data was tested for normal distribution by the Kolmogorov–Smirnov method, and the homogeneity of variance test was performed by the Leneve method. If the data conform to the normal distribution and the variance is homogeneous, then the paired-sample t-test or the two-independent-sample t-test will be used. If the data does not conform to the normal distribution and the homogeneity of variance, the nonparametric rank-sum test is used. The comparison of count data, morphology, and TIC curve type was analyzed by X^2 test and Fisher exact probability method. $P < 0.05$ is considered the difference to be statistically significant; $P > 0.05$ is considered the difference not to be statistically significant. We draw receiver operating characteristic curves for statistically significant indicators. Specifically, the technical contributions of this paper can be summarized as follows:

First, this paper innovatively uses dynamic enhanced magnetic resonance imaging technology to explore the diagnosis and clinical application of hematological malignancies.

Second, through Siemens 3.0T, we performed MRI and dynamic enhanced MRI on 30 patients with hematological tumors and used the PACS system to collect and organize clinical data.

Third, this paper conducts a retrospective analysis and summary to discuss the clinical manifestations of hematological malignancies. The results prove that the application of dynamic enhanced MRI in the diagnosis of hematological malignancies is very effective.

2. Materials and Methods

2.1. General Information. Sixty patients with hematological malignancies who came to our hospital from January 2015 to December 2019 were selected as the research subjects. All of them had fever, bone pain, weight loss, and symptoms such as low fever; all were diagnosed as hematological malignancies. Patients who had low compliance and had mental disorders were excluded. According to the order of visits, they were divided into the control group and experimental group, each with 30 cases. In the control group, there were 20 males and 10 females; they were 46–68 years old, with an average of 48.5 ± 1.5 years old. In the experimental group, there were 20 males and 10 females. They were 46–68 years old, with an average of 48.7 ± 1.4 years old. There was no statistically significant difference between the two groups of patients in terms of condition, age, and other pieces of information ($P > 0.05$), and they were comparable.

2.2. Method. Patients in the control group were given MRI examinations. First, the vertebral bodies of the patients were scanned, and the thickness was controlled at 5 mm. Secondly, the imaging staff carefully observe the soft tissue window and bone window of the patient's image. Finally, a small number of patients with hematological malignancies were given meglumine by intravenous injection, then enhanced scanning was performed, and images were acquired to diagnose their condition [8]. The experimental group was diagnosed with MR, and the patients were scanned with Siemens 3.0T MR instrument, combined with the patient's condition, including T2W1, axial FSE, and SE sequence T1W1. All subjects underwent a full spine scan and moved the bed according to the needs of the scan. The relevant parameters of the scan include the following: the sagittal

RETRACTED

scan layer thickness is 3 to 4 mm, and the separation distance is 0.35 mm. Then, 10~12 ml of diethylenepentamine gadolinium acetate is used to give the patient, and then the enhanced scan is performed, $b = 700$ mm/s, and the number of excitations is 2 to 3 times [9].

2.3. Statistical Methods. The software SPSS 19.8 was used to process the data, the measurement data was expressed as $x \pm s$, and the t-test was used; the count data was expressed in 97%, and the χ^2 test was used; $P < 0.05$ indicates that the difference is statistically significant.

3. Modeling and Simulation Results

3.1. DE-MRI

3.1.1. MRI. DE-MRI uses a fast T1WI sequence to scan the lesions in multiple phases and measures the changes of T1 signal intensity before and after intravenous bolus injection of contrast medium, which obtains tissue perfusion, capillary surface area, vascular permeability, and dynamic enhancement curves through postprocessing techniques in Figure 1. Such as a series of semiquantitative and quantitative parameters can more objectively reflect the pathophysiological characteristics of the disease. T1WI sequence usually uses gradient-echo sequence and saturation recovery/reversal recovery rapid imaging sequence, such as rapid three-dimensional volumetric interpolated breath-hold examination (VIBE), multiple myeloma, and liver acquisition with volume acceleration (LAVA) sequence, and tries to avoid the influence of T2 and T2∗ signals.

The basic principle of magnetic resonance imaging is to place the object under inspection in a strong magnetic field, and the magnetic moments of certain protons are arranged along the magnetic field and move around the direction of the magnetic field at a certain frequency [10]. On this basis, a radio frequency pulse with the same frequency as the motion of the proton is used to excite the proton magnetic moment to cause energy level conversion, release energy, and generate a signal during the relaxation of the proton. The receiving coil of MRI acquires the above-mentioned signals, then amplifies them through an amplifier, and inputs them to a computer for image reconstruction, thereby obtaining the magnetic resonance images we need. In addition to the charge and mass of the nucleus, about half of the nuclei of the elements can spin. Since the nucleus is a positively charged particle, its spin will generate a small magnetic field. The total magnetic moment $\vec{\mu}_j$ and the total angular momentum $\vec{P}_k$ have the following relationship:

$$\vec{\mu}_k = -g\frac{E}{2m_e}\vec{P}_k = g\frac{2\pi\mu_B}{h}\vec{P}_k = \gamma\vec{P}_k, \tag{1}$$

where E is the Delang factor, e and m_e are the electronic charge and mass, μ_B is called the Bohr magneton, and R represents the gyromagnetic ratio of the atom. For nuclei with nonzero spin, the nuclear magnetic moment $\vec{\mu}_j$ and spin angular momentum $\vec{P}_k$ also have the following relationship:

$$\vec{\mu}_I = -g_N\frac{E}{2m_p}\vec{P}_k = g_N\frac{2\pi\mu_N}{h}\vec{P}_k = \gamma\vec{P}_k. \tag{2}$$

According to quantum theory, there is a quantum mechanical system of nuclear spin and nuclear magnetic moment. In an external magnetic field B_0, the energy level will undergo Zeeman splitting. There is an energy difference ΔE among adjacent energy levels. When external conditions provide the same magnetic energy ΔE, it will cause a phase. The magnetic dipole transition between adjacent Zeeman energy levels, for example, the energy difference $\Delta E = (RD_0 h/2\pi)$ of the Zeeman energy level, is that the hydrogen nucleus emits a photon of energy $h\nu$. At that time, the hydrogen nucleus will absorb this photon and transition from a low Zeeman energy level to a high Zeeman energy level [11]. It can be seen from Figure 1 that nuclear magnetic resonance occurs and the condition is that the circular frequency of electromagnetic waves is as follows:

$$\omega_0 = RD_0. \tag{3}$$

When nuclei with spins are in a uniform fixed magnetic field, they will interact. As a result, the spin axis of the nuclei will move along the circular orbit in the magnetic field. This movement is called precession. The precession frequency ω_0 of the spin nucleus is proportional to the applied magnetic field strength H_0, where R is the gyromagnetic ratio, which is a constant characterized by different nuclei; that is, different nuclei have their own inherent gyromagnetic ratio γ, which is the basis for qualitative analysis using nuclear magnetic resonance spectrometer. It can be seen from the above formula that if the spin nucleus is in a fixed magnetic field with a magnetic field strength of H_0 and tries to measure its precession frequency ω_0, the gyromagnetic ratio γ can be obtained, thereby achieving the purpose of qualitative analysis. At the same time, you can keep ω_0 unchanged, measure H_0, find γ, and realize qualitative analysis.

In recent years, with the development of magnetic resonance imaging equipment software and hardware, especially the development of gradient magnetic field technology, MR scanning speed is getting faster and faster. A new dynamic enhancement MRI method—contrast-enhanced dynamic enhancement MRI (DE-MRI)—came into being [12]. Dynamic enhanced MRI has a wide range of applications and strong practicability, especially for the chest blood vessels (including heart and large blood vessels and pulmonary blood vessels), abdominal blood vessels, and pulsating limb blood vessels in the physiological movement area. For example, in limb vascular imaging, dynamic enhanced MRI can overcome the shortcomings of ordinary TOF and PCA techniques such as long imaging time, overevaluation of vascular stenosis, and obvious pulsation artifacts, which has high spatial resolution.

3.1.2. Structure and Composition of the 400 MHz MRI Spectrometer. Figure 2 shows the structure and composition of 400 MHz MRI spectrometer. The whole system is composed of the machine body, main cabinet, and console. The electromagnetic signal from the console is converted into an

RETRACTED

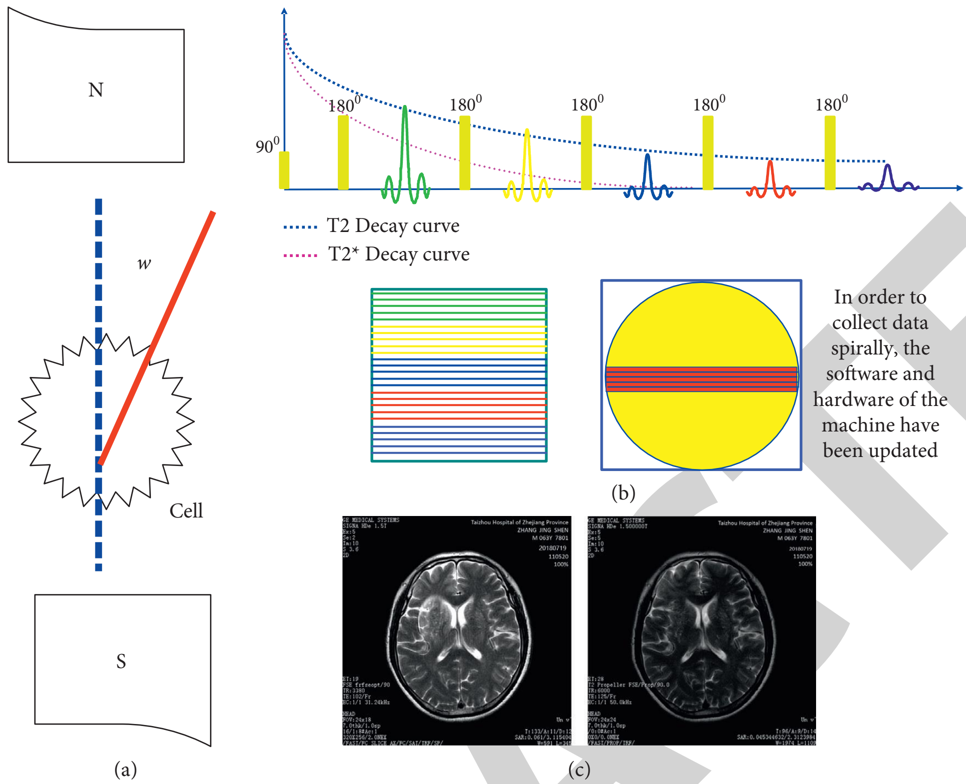

Figure 1: MRI equipment: (a) principle of magnetic field spin; (b) MRI decay curve; (c) MRI strip.

RETRACTED

analog signal by the main cabinet to control the process of the body to complete the experiment. The analog signal collected by the body detector is converted into an electrical signal by the main cabinet, and the range is to the console and saved as a nuclear magnetic spectrogram. The body is composed of a superconducting magnet, sampler, detector, and so on [13]. The superconducting magnet is the core component of a nuclear magnetic spectrometer, which is used to generate the magnetic field required for the operation of the instrument. There are 72 sets of coils around the superconducting magnet. The superconducting magnet is surrounded by a cooling pool of liquid nitrogen and liquid helium to maintain the low-temperature environment required by the superconducting magnet. The instrument is equipped with a 60-position autosampler, which can arrange sequential experiments. The detector consists of a transmitter coil and a receiver coil to detect the nuclear magnetic signal of the sample.

Dynamic enhanced MRI uses a fast gradient-echo sequence of very short TR and very short TE. In the case of such short TR and TE, the longitudinal magnetization of various tissues is very small, and the signal strength is also very small. If a paramagnetic contrast agent is injected into the blood vessel, the T1 relaxation time of the blood will be extremely shortened. The T1 relaxation time of the blood vessel is much shorter than the T1 relaxation time of the background tissue. The blood has a high signal, forming a strong contrast between the blood vessel and the background [14].

In dynamic enhanced MRI, digital subtraction technology can also be used to subtract the corresponding pixel signal intensity between the two sets of images obtained before and during the injection of gadolinium contrast agent. Subtractive dynamic enhanced MRI is compared with nonsubtractive dynamic enhanced MRI which improves the contrast/noise ratio and improves the display of blood vessels. Figure 3 shows the signal recognition of DE-MRI. The advantages of magnetic resonance imaging are nonradiation and noninvasive and multidirectional and arbitrary-angle imaging. Many imaging parameters have strong diagnostic significance for the location and nature of the lesion; the high resolution of soft tissues is increasingly receiving clinical attention and welcome.

Due to the increase in scanning speed, patients can perform multiple volume acquisitions of organs of interest in one breath-hold, which improves the time resolution of lesion detection. Alternatively, high scanning speed can be exchanged for high-resolution scanning to improve spatial resolution.

3.2. Clinical Trials and Results Analysis. Research progress of dynamic enhancement MRI is based on DE-MRI images of malignant tumors. The application of dynamic enhancement MRI in the field of DE-MRI imaging can mainly include the following steps: ① image preprocessing; ② segmentation of interesting areas; ③ feature extraction; ④ classification and tumor region recognition. As shown in Figure 4, the process of the entire dynamic enhancement MRI system is shown.

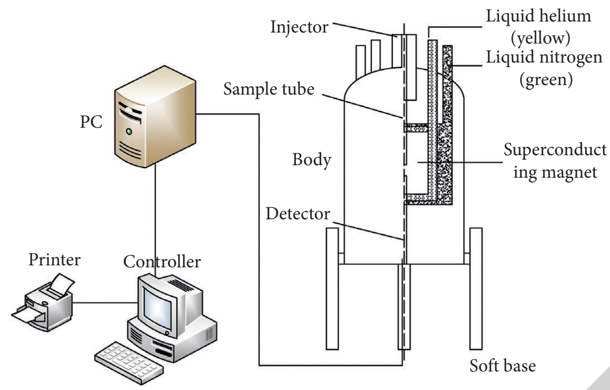

Figure 2: Structure and composition of the 400 MHz MRI spectrometer.

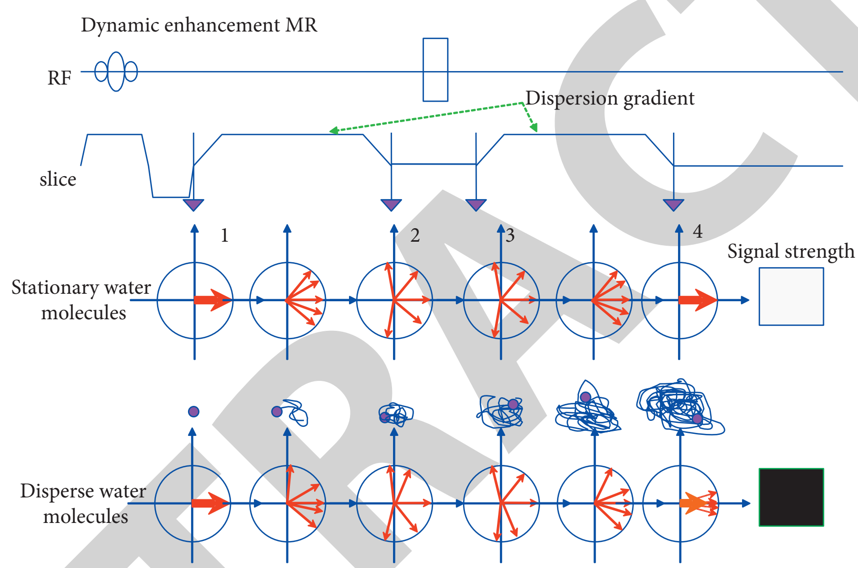

Figure 3: Signal recognition of DE-MRI.

RETRACTED

3.2.1. Image Preprocessing. Image preprocessing mainly includes noise reduction and image sequence registration. Its main purposes are as follows: (1) DE-MRI imaging time is short, and the image signal-to-noise ratio is low, so the image noise reduction is extra important. (2) The patient is undergoing DCE. The movement of the body due to breathing or other reasons during the MRI imaging process will cause coordinate deviations between DE-MRI images, which must be corrected. Most researchers mainly use a Gaussian low-pass filter to reduce noise [14], but the Gaussian low-pass filter will smooth the image, causing the resolution of the image to decrease, so a more ideal filtering method is required. As shown in Figure 4, a summary of several commonly used image noise reduction is given, and the advantages and disadvantages of each algorithm are briefly summarized. For the research on motion compensation of DE-MRI image sequence, the classification of commonly used image registration methods is given, and the advantages and disadvantages of each method are summarized.

Image preprocessing can reduce image noise, correct errors generated in the imaging process, improve image quality, and provide more accurate information. It can be seen from Table 1 that the main problem of the existing methods is that the noise reduction process may reduce the spatial resolution of the image and cause the loss of image information. Therefore, future research should focus on how to minimize the loss of image information while ensuring the noise reduction effect, and it can be seen that, in the existing registration algorithms, the registration accuracy is affected by various factors. In the future, when studying the new DE-MRI image sequence registration, it is necessary to distinguish whether the algorithm used is actually suitable for rigid body registration or nonrigid body registration, and at the same time, the factors that affect the registration accuracy should be identified.

3.2.2. Tumor Area Division. After denoising the image and correcting the motion error of the image sequence, preliminary segmentation of the tumor region is needed to reduce the computational cost. The main methods are manual segmentation and automatic segmentation. The manual division has performed by a doctor, so the accuracy is limited by the doctor's clinical experience, which is time-consuming. In recent years, the application of dynamic

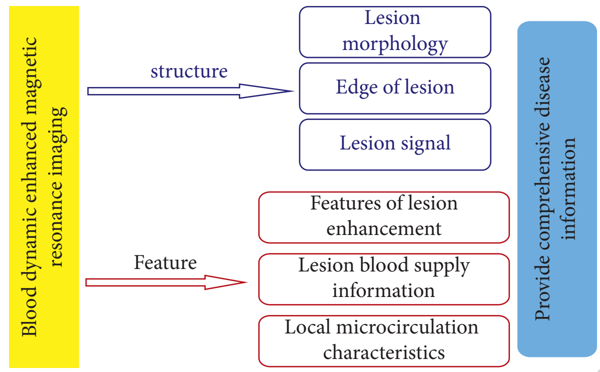

Figure 4: MRI hematological malignant tumor imaging process.

Table 1: Comparison of MRI and DE-MRI.

Common image noise reduction methods	Algorithm advantages	Algorithm disadvantages
MRI	The algorithm is simple, the convolution speed is fast, and it has a good removal effect for Gaussian noise, and so on	Unable to retain complete image information, it is easy to confirm the disease and cause misdiagnosis
DE-MRI	Under the condition that the complete image information is retained to the greatest extent, noise removal is performed to avoid misdiagnosis	The equipment is complex and the running speed is slow

enhanced MRI for automatic segmentation has gradually attracted people's attention. Among them, the more common methods are clustering and the hybrid algorithm that combines the aforementioned methods. As shown in Figure 5, the advantages and disadvantages of these algorithms are summarized.

Tumor area segmentation can increase the speed of image processing and eliminate unnecessary backgrounds. Currently, the commonly used tumor region segmentation for DE-MRI images is shown in Table 2. Among them, the clustering method is well-researched and the process is simple, but the results of the image segmentation obtained are often not ideal. Compared with the traditional clustering algorithm, the image segmentation accuracy of the horizontal set, Markov random field, artificial neural network, and other algorithms has been significantly improved, but due to the higher number of algorithm iterations, the calculation time has also increased significantly [15]. Therefore, in the future, when selecting the tumor region segmentation for DE-MRI images, it is necessary to weigh the pros and cons of each method and find the optimal algorithm with shorter time-consuming and higher segmentation accuracy.

3.2.3. Feature Extraction. In order to analyze the tumor area, such as judging whether the area is a diseased area, it is often necessary to estimate certain features or characteristics of the ROI area, which is also the extraction of the characteristics of the tumor area. Dynamically enhanced MRI uses a computer to replace or assist the human brain to identify tumor areas, and the ability of features to express data determines the ultimate effect that dynamic enhanced MRI can achieve to a certain extent [16]. Features with strong expression ability should well characterize the differences between different tissues (tumor area and nontumor area), and at the same time, the dimension should not be too high, to ensure the efficiency of calculation. The common features of DE-MRI images mainly include morphological characteristics, texture characteristics, hemodynamic curve characteristics, and pharmacokinetic characteristics. As shown in Table 2, the related literature is given, and the advantages and disadvantages of these features are briefly summarized.

As shown in Table 2, among the common features of DE-MRI images listed, morphological features and texture features are commonly used in image processing, while hemodynamic and pharmacokinetic features are DE-MRI images' unique characteristics [17]. Compared with morphological and texture characteristics, hemodynamic characteristics and pharmacokinetic characteristics can reflect the change characteristics of the DE-MRI image sequence. Therefore, the classifier trained as a feature has a better classification and recognition effect. It should be pointed out that the features listed in Table 2 are only part of the feature information contained in DE-MRI images. Therefore, the focus of future research is to find more and better features to characterize the characteristics of DE-MRI images.

3.3. Results

3.3.1. Flat Sweep. Of the 30 patients, 20 had a single lesion and 10 had multiple lesions. A total of 67 lesions were found, of which 54 were located in the right lobe of the liver and 13 were located in the left lobe of the liver.

19 lesions were round and 48 were round or irregular. The size of the lesion is 7~85 mm, average 25–11 mm; 15 lesions > 30 mm. Seven cases were complicated by liver cysts.

Dynamic enhanced scanning adopts 3D-FLASH plus fat suppression sequence TR/TE = 4.42/1.46 ms in Table 3;

RETRACTED

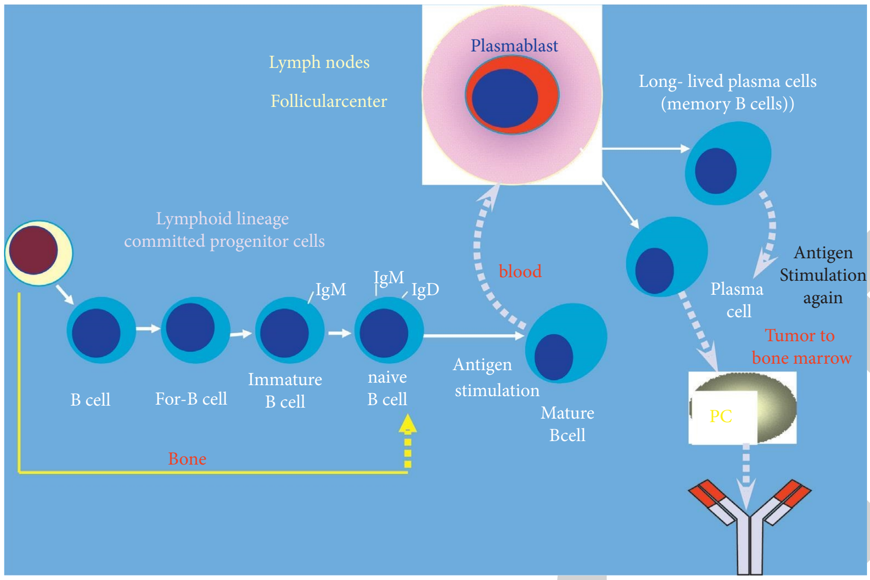

Figure 5: The development process of malignant hematological tumor cells.

Table 2: DE-MRI image features.

Common features	Description	Evaluation
Morphological characteristics	Roundness: the roundness of the lesion Area: the area of the lesion Edge sharpness: average signal gradient at the edge of the lesion Border irregularity: the shape deviation of the edge of the lesion	Important guiding role in the judgment of benign and malignant tumors, and the calculation is relatively simple. Classification effect is not as good as other features.
Texture feature	Contrast: it reflects the sharpness of the image Autocorrelation: it reflects the texture consistency of the image ASM energy: it reflects the uniformity of image grayscale Inverse moment of difference: it reflects the homogeneity of image texture Entropy: it reflects the nonuniformity of image texture	Reflect the texture characteristics of the image. Classifiers trained as features are better than morphological features.
Hemodynamic characteristics	Maximum absorption: the peak of the kinetic curve Peak time: the time required to reach the peak Absorption rate: the absorption rate of the contrast agent Attenuation rate: the rate of attenuation of the contrast agent Enhancement ratio: the ratio of signal strength before enhancement to average signal strength enhancement	The classifier trained as a feature works best.

FOV = 320 mm. The matrix is 320 × 512. Layer thickness is 0.8 mm, and interval is 0.18 mm. The inversion angle is 12°. The scanning range includes the whole cavity which is repeatedly scanned 6–8 times continuously, with an interval of 20 seconds after the first scan, for the injection of contrast agent, and the scanning time is 7–9 minutes as in Table 3.

3.3.2. Dynamic Enhancement. In 30 patients, 46 lesions showed discontinuous marginal nodular enhancement, which filled the center of the lesion with time, and 21 lesions showed irregular or rapid peripheral enhancement. Early dynamic enhancement of 3 lesions (equivalent to arterial phase) showed the blood supply artery, 5 lesions showed early visualization and drainage vein (Figure 6), and 14 tumors around the enhancement (4 showed irregular edge enhancement, and 10 showed liver pack wedge strengthening under the membrane) [18]. During the dynamic scanning period, 27 lesions were completely filled and enhanced (Figure 6(d)), and 40 lesions were not completely filled and enhanced.

RETRACTED

Table 3: Flat sweep.

	T1WI	T2WI	T2-Tirm	DWI (SE-EPI)
TR (ms)	580	4420	8690	3680
TE (ms)	12	96	71	60
FOV (mm)	310	340	420	300
Matrix	310 × 512	330 × 512	360 × 512	128 × 128
Layer thickness (mm)	4	4	4	5
Interval (mm)	1	1	1	2

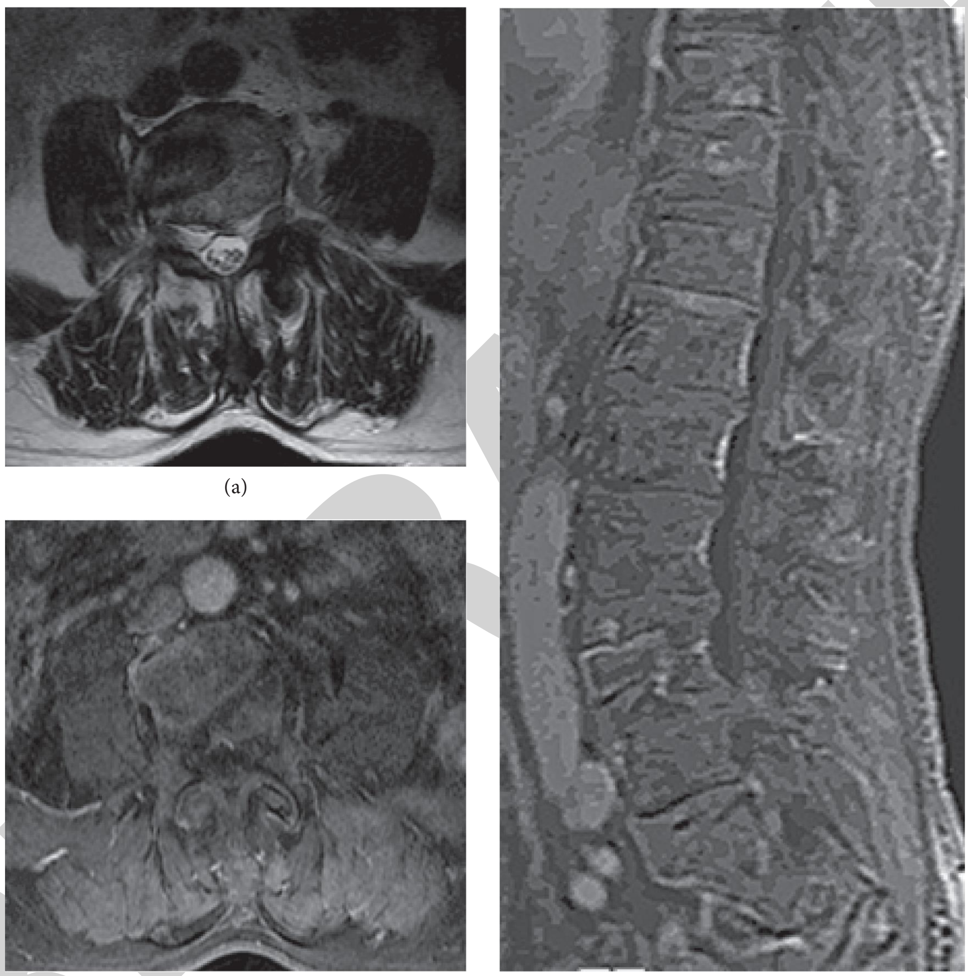

(a) (b) (c)

Figure 6: MRI image of hemangioma. (a, b) DE-MRI showing angiography of hemangioma; (c) nodule changes in lesions; (d) filler angiography of advanced hemangioma.

3.3.3. Delayed Enhanced Scanning. The delay time is 6–9 min, average (7.3 ± 0.8) min. 53 lesions were completely filled and enhanced, of which 37 lesions were relatively high signals, and 16 lesions had equal signals. The filling area of 14 lesions showed high signal or isointensity, and the unfilled area showed patchy or crack-like low signal (Figure 7).

After the examination of 30 multiple myeloma patients, the results of the dynamic time-signal intensity curve were 3 cases with type I curve, 17 cases with type II curve, and 20 cases with type III curve. See Table 1 for details. Hematological malignancies can occur at any age, and most of them occur in adults, most commonly between 46 and 68 years old. There are more males than females. The multiple myeloma varies in size, and those over 40mm are rare.

3.3.4. Comparison of Results. Pathologically, the cut surface of multiple myeloma is filled with blood. The microscopic examination of of Multiple Myeloma shows that it is composed of cystic blood sinusoids or blood pools of varying sizes. There is a fibrous tissue septum between the blood sinusoids. The blood flows slowly in it, mostly from the edge of the tumor to the center [19]. The nodules around the lesion are enhanced at an early stage and filled to the center

RETRACTED

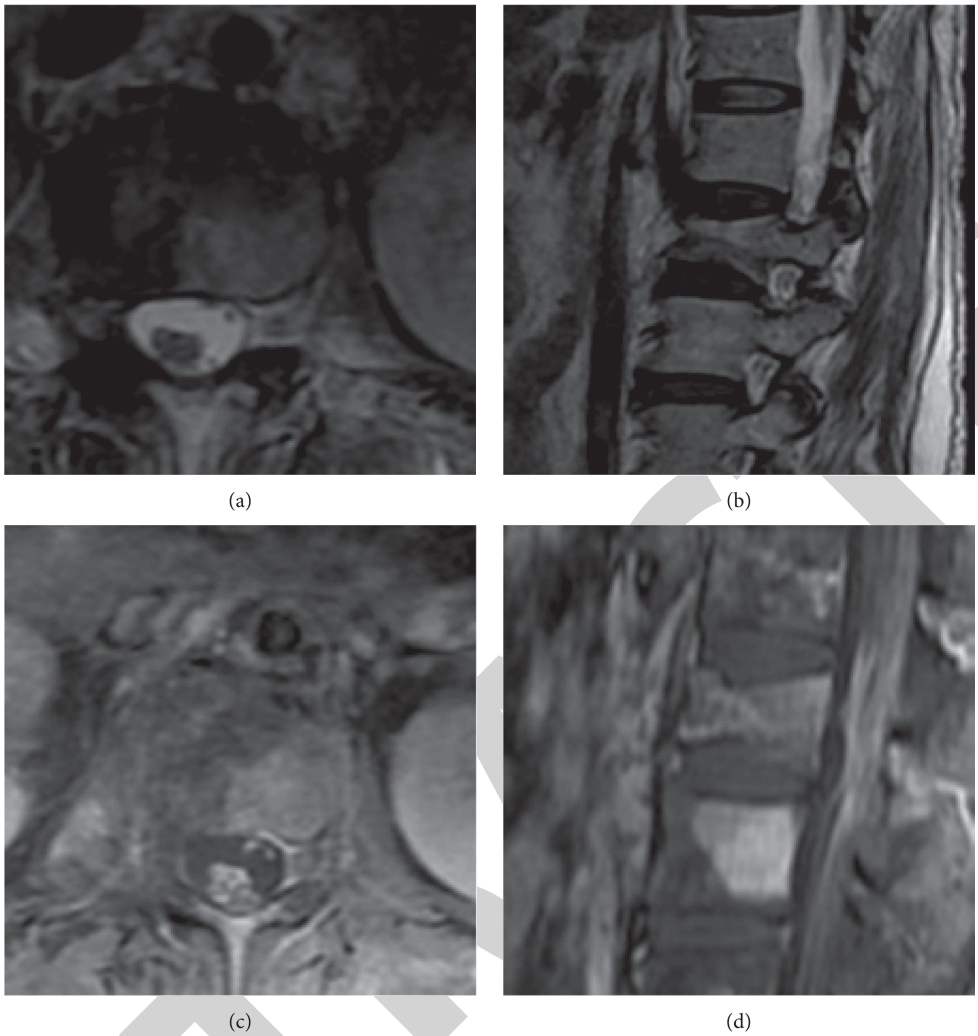

FIGURE 7: MRI image of liver hemangioma. (a) DE-MRI showing angiography of hemangioma; (b) filling angiography of advanced liver hemangioma.

of the lesion despite the prolonged time. The rapid filling after enhancement seems to relate to the size of multiple myeloma. The proportion of multiple myeloma is about 16%, but it accounts for 42% of the enhancement mode of small hemangioma. During the dynamic enhancement period, 41% (25/60) of multiple myeloma were seen to be fully filled and enhanced. Compared with the surrounding normal multiple myeloma, it was a high signal or iso-signal. 19% (11/60) of the lesions showed low signal shadow with an incomplete filling of flaky or fissure-like enhancement, which may be related to liquefaction, hemorrhage, thrombosis, and extensive hyaline degeneration and fibrosis in the multiple myeloma in Figure 8. Hepatic hemangioma has often accompanied by an arteriovenous short circuit, which was to be seen in malignant liver tumors in the past. Figure 8 shows the comparing results of MRI and DE-MRI.

In the early stage of dynamic enhanced MRI scan, 25% (15/60 lesions) of multiple myeloma showed temporary substantial enhancement. 67% (40/60) of which were related to the existence of increased erythrocyte sedimentation rate [20]. Dynamic enhanced MRI in the early stage of MRI found that 50.1% (31/60 lesions) of multiple myeloma showed temporary substantial enhancement in the adjacent area, and it was more common in rapidly enhancing lesions [3]. In this group, 8% (5/60) of the lesions showed enhancement of early venous visualization, and 23% (14/60) multiple myeloma parenchyma enhanced. Dynamic enhanced MRI scan found that 49% (28/60) of multiple myeloma showed temporary enhancement around the tumor, which has mainly manifested as enhanced early subcapsular wedge enhancement and increased erythrocyte sedimentation rate. This change is more seen in small lesions that rapidly strengthen. It is inferred that small multiple myelomas with rapid strengthening are usually in a hyperhemodynamic state, which contains large and rapid drainage that causes the tumor to rapidly strengthen the larger arterial blood flow and causes early increased erythrocyte sedimentation rate and enhancement of the surrounding parenchyma. Figure 9 shows the different segments of multiple myeloma MRI.

In most cases, it is not difficult to make a differential diagnosis of multiple myeloma on imaging examination. The T2WI imaging of the MRI of a typical multiple

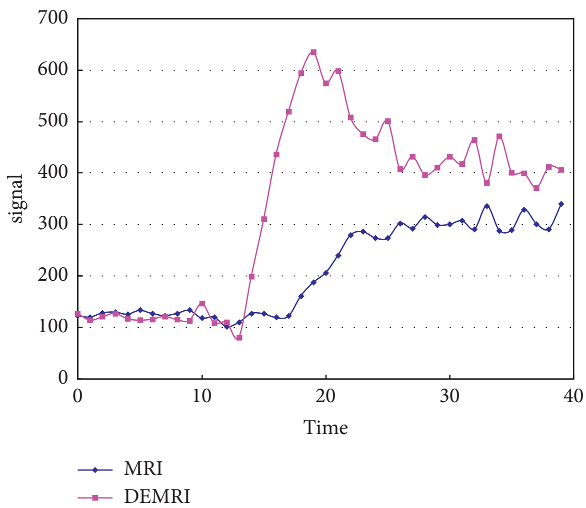

FIGURE 8: Comparing results of MRI and DE-MRI.

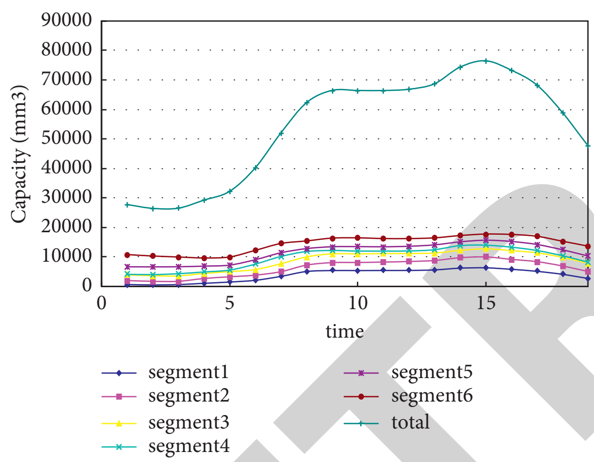

FIGURE 9: Different segments of liver hemangioma MRI.

myeloma is characteristic. With the extension of TE, the signal increases, with a typical/bulb sign 0. The enhancement is manifested as uniform enhancement in the arterial phase or enhancement of the marginal nodules, which is consistent with the enhancement of adjacent arteries, which is delayed. At the time, the enhancement of the lesion is obvious, while for liver cancer, it is the enhancement performance of/fast forward and fast out 0. Neuroendocrine tumors and metastases of breast and colon cancers show strong T2 signals [5]. Delayed enhancement of MRI in some malignant tumors with rich blood supply is similar to a few atypical multiple myeloma. Once the hepatic hemangioma shows that the enhanced area will not disappear, the combined consideration of multiple imaging signs will help the differential diagnosis. Multiple Myeloma is manifested as increased erythrocyte sedimentation rate and wedge-shaped or irregular enhancement around the tumor, which is more common in small rapidly enhancing multiple myeloma and unevenly enhancing lesions. The appearance of this sign is conducive to the differential diagnosis of multiple myeloma.

3.4. Discussion. DE-MRI has evolved from simple qualitative analysis to multiparameter quantitative analysis, and clinical research has expanded from the nervous system to the whole body. Among the most widely used tumor imaging, the research of DE-MRI covers various aspects such as the differential diagnosis of benign and malignant lesions, clear tumor grading, evaluation of efficacy and prognosis, and detection of tumor recurrence. In recent years, clinical research on tumor antivascular therapy has been widely carried out. Traditional biomarker technology is difficult to evaluate the efficacy of antitumor vascular drugs early. The application of quantitative parameters related to DE-MRI which can help in terms of tumor morphology, vascular function, and cell metabolism dynamic observation of the treatment effect is convenient for timely adjustment of drug dosage and optimization of the treatment plan.

3.4.1. Tumor Diagnosis and Differential Diagnosis. DE-MRI is widely used in the differential diagnosis of benign and malignant tumors in various systems. Among them, the diagnosis of multiple myeloma, prostate cancer, glioma, and other solid tumors has been a research hotspot in recent years in Figure 10. The microenvironment such as hypoxia and weak acidity in malignant tumors and the activation of oncogenes can induce the expression of vascular endothelial growth factor (vascular endothelial growth, VEGF) and other vascular endothelial genes to increase, thereby stimulating the massive formation of abnormal blood vessels in the tumor. New tumors have tortuous and irregular microvessels, incomplete basement membranes, and widened endothelial cell gaps, leading to increased tumor vascular resistance and microvascular permeability. Therefore, the quantitative parameter values reflecting tumor area tissue perfusion and vascular endothelial cell integrity have abnormal changes. A series of studies have shown that there are significant differences in the Ktrans value, initial enhancement time, maximum enhancement level, and enhancement curve of prostate cancer and prostate hyperplasia tissue. In recent years, there have been many studies on gliomas. The results showed that Vp (plasma volume fraction) is the quantitative parameter with the highest sensitivity and specificity in the differential diagnosis of the two. The accuracy of the differential diagnosis between the two when the Ktrans value and the Vp value are combined can reach 96%.

3.4.2. Tumor Pathological Type and Grade. Tumor tissues differentiated from different tissues have different biological characteristics. Because the pharmacokinetics of contrast agents in different pathological tissues is different, DE-MRI can reflect the essential differences of different pathological types of tumors. DCEMRI quantitative analysis method is to retrospectively study squamous cell carcinoma, undifferentiated carcinoma, and lymphoma that occurred in the head and neck, and the results showed that the Ktrans value of undifferentiated carcinoma was significantly higher than that of the other two malignancies. Tumors and the Ktrans

RETRACTED

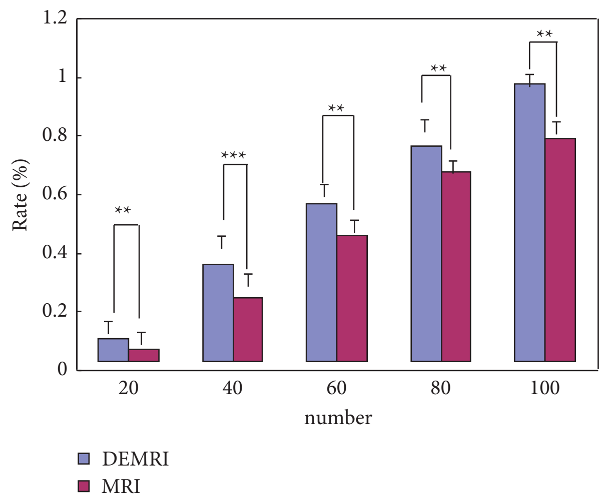

Figure 10: Tumor diagnosis by MRI and DE-MRI.

values of the three tumors are consistent with VEGF expression levels. The higher the grade and the poorer the level of differentiation of the same pathological type of tumor, the higher the permeability of the blood vessel wall and the ratio of extracellular extravascular space and the faster the contrast medium exchange rate (Ktrans).

3.4.3. Efficacy Evaluation and Prognosis Judgment. Radiotherapy and chemotherapy are indispensable links in tumor treatment, but the therapeutic effect has directly related to the sensitivity of tumor tissue. Therefore, predicting the sensitivity of tumors to radiotherapy and chemotherapy plays an important role in the choice of treatment options. The sensitivity of tumor radiotherapy is determined by the level of hypoxia. The DE-MRI study of rectal cancer patients undergoing neoadjuvant chemotherapy showed that the Ktrans value of the treatment response group (judged by tumor staging and tumor regression) before treatment was higher than the nonresponse group chemotherapy. The mechanism and high permeability blood vessels have better oxygenation ability, and chemotherapeutic drugs are easier to enter to play a therapeutic effect.

3.4.4. Application in the Development of Antiangiogenic Drugs. Antitumor angiogenesis-targeted drugs can inhibit the vascular endothelial growth factor receptor (vascular endothelial growth, VEGFR) signal transduction pathway, acting on the angiogenic factors released by endothelial cells or surrounding stromal cells, thereby promoting the normalization of tumor blood vessels. It is a hot spot for targeted tumor therapy in recent years. The quantitative indicators of DE-MRI can accurately assess the inhibition of tumor microvascular permeability and the improvement of tumor vascular normalization by antitumor angiogenesis-targeted drugs. More than 100 items use DE-MRI to evaluate the early clinical stage of antivascular therapy showing that DE-MRI has broad clinical application prospects in evaluating the dynamic changes of tumor blood vessels, exploring the "effective time window" of antiangiogenesis, and monitoring antiangiogenesis efficacy.

4. Conclusion

In this paper, dynamic enhanced magnetic resonance imaging technology can be used to effectively explore the diagnosis and clinical application of hematological malignancies. We used Siemens 3.0T to perform MRI and dynamic enhanced MRI on 30 patients with multiple myeloma. The MRI of MM that occurs in the spine is mainly manifested as multiple osteolytic destruction of the spine and extensive osteoporosis. Osteolytic destruction is mainly manifested as trough-like changes or worm-eaten changes, which are diffusely distributed in the vertebral body and appendages. Compared with normal bone marrow, MM's T1WI is mainly low signal, T2WI is high signal, SIRT and T2 fat saturation suppression sequence have fat high signal suppression, and the contrast between the lesion signal and normal bone marrow is more obvious. The enhanced scan is based on its blood supply and different degrees of reinforcement. Most of the selected cases in this group showed this signal's characteristic, and compared with other diseases, the signal characteristic was not specific. The results showed that the diagnostic accuracy of 30 cases of dynamic enhanced MRI was 100%, while the diagnostic accuracy of ordinary MRI was lower than that of dynamic enhanced MRI, $p<0.05$, and the difference was significant. To sum up, the clinical use of MRI can detect and diagnose MM early, combined with clinical data for comprehensive analysis and diagnosis, which is helpful to formulate effective treatment plans, prolong their survival time, and improve their quality of life.

The imaging features of the 60 patients with hematological malignancies in this study are mainly as follows: ① The blood density of the patients with hematological malignancies during MRI examination is lower than that of normal patients, but there is no obvious soft tissue damage. ② If the patient's blood vessels are swelling and damaged, the MRI performance is mainly that the edges are relatively clear, and there are many bright areas of different sizes. These bright areas are formed by the destruction of hematological tumor lesions. ③ If there is a soft tissue mass, it will appear on MRI that the signal is generally low, and some are in the state of "salt and pepper sign." This study showed that the diagnostic sensitivity of MRI in diagnosing hematological malignancies was 65.3%, while the diagnostic accuracy rate was 68.1%, indicating that MRI can still be used as an early detection method for hematological malignancies. However, for some relatively few lesions and special lesions, the diagnosis rate of MRI is not very high. Therefore, dynamic enhanced MRI is needed for another diagnosis, which has higher tissue density and resolution than MRI.

As a noninvasive and dynamic imaging technique for evaluating tumor microcirculation function, the research and clinical application prospects of DE-MRI are very broad. With the development of multicenter research and the cooperation of various interdisciplinary, DE-MRI will be

RETRACTED

Hindawi
Journal of Healthcare Engineering
Volume 2023, Article ID 9769563, 1 page
https://doi.org/10.1155/2023/9769563

Retraction

Retracted: Study on the Impact of Online Courses for Pregnant and Lying-In Women on Maternal and Infant Health during the Epidemic

Journal of Healthcare Engineering

Received 3 October 2023; Accepted 3 October 2023; Published 4 October 2023

Copyright © 2023 Journal of Healthcare Engineering. This is an open access article distributed under the Creative Commons Attribution License, which permits unrestricted use, distribution, and reproduction in any medium, provided the original work is properly cited.

This article has been retracted by Hindawi following an investigation undertaken by the publisher [1]. This investigation has uncovered evidence of one or more of the following indicators of systematic manipulation of the publication process:

(1) Discrepancies in scope
(2) Discrepancies in the description of the research reported
(3) Discrepancies between the availability of data and the research described
(4) Inappropriate citations
(5) Incoherent, meaningless and/or irrelevant content included in the article
(6) Peer-review manipulation

The presence of these indicators undermines our confidence in the integrity of the article's content and we cannot, therefore, vouch for its reliability. Please note that this notice is intended solely to alert readers that the content of this article is unreliable. We have not investigated whether authors were aware of or involved in the systematic manipulation of the publication process.

Wiley and Hindawi regrets that the usual quality checks did not identify these issues before publication and have since put additional measures in place to safeguard research integrity.

We wish to credit our own Research Integrity and Research Publishing teams and anonymous and named external researchers and research integrity experts for contributing to this investigation.

The corresponding author, as the representative of all authors, has been given the opportunity to register their agreement or disagreement to this retraction. We have kept a record of any response received.

References

[1] L. Shi, L. Yuan, L. Zhou, S. Zhang, and X. Lei, "Study on the Impact of Online Courses for Pregnant and Lying-In Women on Maternal and Infant Health during the Epidemic," *Journal of Healthcare Engineering*, vol. 2021, Article ID 4019210, 11 pages, 2021.

Hindawi
Journal of Healthcare Engineering
Volume 2021, Article ID 4019210, 11 pages
https://doi.org/10.1155/2021/4019210

RETRACTED

Research Article

Study on the Impact of Online Courses for Pregnant and Lying-In Women on Maternal and Infant Health during the Epidemic

Liangfang Shi, Ling Yuan, Lin Zhou, Shuixian Zhang, and Xia Lei

Department of Obstetrics, Affiliated Hangzhou First People's Hospital, Zhejiang University School of Medicine, Zhejiang, Hangzhou 310006, China

Correspondence should be addressed to Ling Yuan; 2017a600@zcmu.edu.cn

Received 18 October 2021; Revised 3 November 2021; Accepted 5 November 2021; Published 20 December 2021

Academic Editor: Gu Xiaoqing

Copyright © 2021 Liangfang Shi et al. This is an open access article distributed under the Creative Commons Attribution License, which permits unrestricted use, distribution, and reproduction in any medium, provided the original work is properly cited.

The sudden outbreak of the new crown pneumonia has brought online learning from a supporting role to the center of the teaching stage in an instant. On the basis of the feasibility analysis and demand analysis of the microcourse learning system, this paper uses Sina cloud server to build the WeChat public platform learning online course and designs and implements the microcourse learning system function based on the microcourse public platform. We completed the recording, editing, publishing, and testing of microclass courses and provided services for teachers and pregnant women's microclass learning in order to achieve better learning results. A total of 151 people regularly participate in maternity school courses, accounting for 30.4%. There are 190 people who have never attended the maternity school course, accounting for 38.2%. There are 156 people who occasionally participate in maternity school courses, accounting for 31.4%. The top five sources of health information during pregnancy are books, maternity schools, experience of elders, the Internet, and television. The results of one-way analysis of variance showed that pregnant women of different ages had statistically different scores in the dimensions of knowledge and ideas ($P < 0.05$). There are statistical differences in the scores of pregnant women with different economic incomes in this dimension ($P < 0.05$). The women with economic income ≥5000 yuan/month have the highest scores, and those with economic income ≥5000 yuan/month have the lowest scores. The scores of pregnant women who participated in the maternity school were significantly higher than those who did not participate in the maternity school ($P < 0.05$). There are statistical differences in the scores of maternal and child health basic skills among pregnant women of different age groups ($P < 0.05$). The women aged ≥35 years old have the highest scores, and those aged 20–24 years old have the lowest scores. The differences in the scores of pregnant women with different economic incomes in this dimension are statistically significant ($P < 0.05$). The women with economic income ≥5000 yuan/month have the highest score, and those with economic income<2000 yuan/month have the lowest score. Participation in maternity schools has an impact on the scores of this dimension. Pregnant women who regularly participate in maternity schools have the highest average scores, and those who do not participate in maternity schools have the lowest average scores.

1. Introduction

Since December, 2019, a new type of coronavirus infection pneumonia has broken out in our country [1]. The online teaching setoff under the background of "stopping classes and not stopping school" has brought "rare" development opportunities for the promotion of teaching reform in the era of "Internet + education", renewing teaching concepts and innovative teaching methods, as well as many severe challenges [2]. In order to ensure that pregnant women can carry out online learning at home, some teachers use online course platforms for asynchronous course teaching, some teachers use live broadcast tools or video conference tools for live synchronous teaching, and some teachers use WeChat groups for instant interactive teaching. It is undeniable that diversified media tools provide many feasible solutions to the problem of time-space separation between teachers and students in online teaching. However, on the one hand, because the online teaching programs formulated by some local education administrative departments have not been widely used, many teachers mistakenly believe that online teaching is "traditional classroom online moving", resulting in a simplification of online teaching methods. Fully online teaching is prone to low learning input and low satisfaction among pregnant women, which arouses reflections from managers and teachers. How to help teachers recognize and understand online teaching and how to organize and carry out online teaching efficiently has become a problem we must face [3].

Due to the continuous updating of the concept of childbirth and the lack of childbirth experience of primiparas, primiparas have an urgent need for health education knowledge before, during, and after delivery [4]. Pregnant women's school is a fixed place for prenatal health education. Routine prenatal health education is conducted in groups of pregnant women's schools, issuing health education manuals, taught by full-time teachers, and recorded by the mothers, and the teaching time is mostly carried out on working days. Because each primipara has a different understanding of perinatal knowledge, in the traditional health education model of maternity school group teaching, there is a real problem that full-time teachers give lectures in class, and primiparas cannot keep up with the rhythm [5]. As time goes by, primiparas will have more and more doubts about prenatal health education knowledge. The traditional mode of teaching in groups for pregnant women is at a fixed time, and most of them are taught on weekdays. Primiparous women cannot attend classes in time due to work and other reasons, which will affect the learning effect, fail to achieve the expected goal of prenatal health education, and affect the treatment effect and patient satisfaction. The traditional prenatal health education model can no longer fully meet the needs of primiparous women for prenatal health education knowledge [6, 7]. Therefore, it is particularly important to explore the prenatal health education model combined with Internet technology.

This article has completed the feasibility analysis and demand analysis of the microcourse learning system and analyzed and designed the microcourse curriculum. The main content of this article is the design and implementation of a microcourse learning system based on the WeChat official account, which mainly includes the design and implementation of the WeChat terminal and background management system. We record and edit the microclass curriculum and publish the microclass curriculum to the microclass learning system after the microclass production is completed. Combining the relevant functions and modules of the WeChat official account design, it is convenient for teachers and pregnant women to better use the microclass courses for learning. The results of multivariate analysis showed that age and attendance of pregnant women's school were the influencing factors of maternal and child health literacy qualifications of pregnant and lying-in women. Pregnant and lying-in women have a better grasp of basic skills and have a poorer understanding of lifestyle and behavior. Age, economic income, and attendance of maternal school may be the influencing factors of the scores of maternal knowledge and ideas.

2. Related Work

In recent years, with the vigorous development of microvideo, research on the background, development and prospects, current situation and problems, design and application of microvideo has become a hot spot for domestic scholars [8]. Specifically, microvideos are used for network communication. Scholars believe that microvideo can be used as a way of spreading news and events on the Internet and has an important position in the era of mobile Internet [9]. The advantages of video resources can satisfy users who are not limited by time and space and can watch the resources they need. Through the research and analysis of the current situation, problems and solutions of the microvideo development, the content construction, operation mode, resource integration, and other aspects of the microvideo website are discussed.

Regarding the application of microvideo to education and teaching, most scholars study the application of microvideo in specific disciplines, as well as the application in distance education and training. In addition, the application research of microvideo in informal learning is also a hot issue. With the theoretical support of mobile learning, microlearning, ubiquitous learning, fragmented learning, informal learning, etc. and the background of the times, microvideo has been widely used in many fields due to its short, precise, and fast characteristics. Research on the application of microvideos in different fields has also been showing an upward trend. The fields and research related to this research include microvideo design research in family counseling for children, research on the production and application of nursing videos for pregnant women and newborn babies, and research on pediatric nursing training and teaching based on microvideo technology. However, there are relatively few researches on the design and development of mobile learning resources for microvideos for mothers and babies.

In terms of education and teaching, Youku has a very close cooperation with the Massachusetts Institute of Technology in the United States. The school unconditionally uploads excellent teaching courses and resources to the Youku network to facilitate independent learning by pregnant women. The foreign education field has brought a huge impact and has brought a good start to the equalization of educational resources relying on the Internet [10]. With the open sharing of Internet resources, microvideo learning resources have been used by more and more people from all walks of life, so that learners can enjoy without the restrictions of the network, education level, regional differences, time, space, etc. These excellent microvideo course resources promote the change and development of people's learning and life and play an important role in education fairness, social harmony, and improving people's happiness [11].

The study found that the proportion of pregnant women with various health literacy is less than 50%, but the correct answer rate for some common infectious diseases to be checked and prevented for the first prenatal check-up is higher, which is more in line with the promotion of the

RETRACTED

RETRACTED

prevention and control of infectious diseases [12]. However, other maternal and child health care knowledge is not relevant enough. Related scholars' research on the current status of maternal health in Wuhan found that the cesarean section rate in Wuhan rose from 46.26% in 2003 to 65.28% in 2008, and it has shown an upward trend in recent years [13]. There are many reasons for the increase in the cesarean section rate, and the subjective wishes of pregnant women play a big role, which may be related to their level of health literacy. Relevant scholars conducted a survey on the health literacy status of mothers and infants among 1,800 participants who participated in health education activities in Haidian District, Beijing [14]. The results found that the survey participants had the highest awareness of mothers' basic knowledge, which shows that pregnant women pay more attention to their own health care. Research shows that prenatal health education for primiparas based on flipped classrooms can improve the self-efficacy of childbirth, breastfeeding self-efficacy, and maternal and infant health literacy of primiparas and is an effective way to carry out prenatal health education for pregnant women [15]. However, its research only implemented prenatal health education in the flipped classroom model at 36 to 39 weeks of gestation and did not systematically design the prenatal health education program, so its results cannot fully reflect the effect of the implementation of prenatal health education for primiparas.

Studies have found that the level of health literacy of women in New York is related to whether they can correctly understand prescriptions and drug instructions and use them correctly [16]. Studies have shown that pregnant women of different races have different levels of knowledge about health literacy [17]. 8% of black women still smoke during pregnancy, while the proportion of whites is as high as 34%. Many people do not know enough about the extent to which smoking harms the fetus. Relevant scholars found in a study that 16% of women have a low level of education, 61% of women start antenatal care three months after pregnancy, and 50% of the survey subjects underutilize antenatal care [18]. Researchers' cross-sectional study of pregnant women in rural India showed that the utilization rate of health care services among survey respondents was low, and there was no difference in utilization rates among survey respondents of different social status [19]. A current status study conducted by related scholars on pregnant women found that more than 40% of the 2257 study subjects did not supplement iron intake as required. The study showed that there is a need to increase iron supplement coverage for pregnant women, especially those who are considered high-risk pregnancy [20]. The longevity of Japanese people is supported by data, which has a non-negligible relationship with their good health status. In the field of maternal and child public health, Japan has implemented a folic acid supplement program to reduce neural tube defects in newborns.

3. Social Support Analysis of WeChat Parenting Group Users

3.1. Obtain Information to Support Self-Empowerment. Information support refers to providing suggestions and guidance to the other party that help solve problems. The traditional offline social support system can provide pregnant women with sufficient emotional support and substantial support, but they cannot provide them with sufficient parenting information support.

Due to advances in technology, the information obtained from the online parenting community is often updated faster than the information provided by offline professional health care workers and relatives of pregnant women. Compared with family members, there is a weak relationship between pregnant women and members of the online parenting community. As the main offline information support source, the female relatives of pregnant women have many similarities with their own backgrounds and experiences. They can provide parenting support, but they tend to be homogeneous, and the amount of useful information is not large. However, due to the greater differences in knowledge structure, experience, background, etc. among members in the online parenting community, the information exchange between each other is more diversified. Figure 1 shows the changes in social support received by WeChat parenting group users.

In the new era, young women use the Internet to obtain information support in various ways. They can obtain existing information from traditional Internet search engines to forums, and they can also obtain online information support through social network media. The role of social networks in supporting information after women give birth is particularly important. It is worth noting that these pregnant and lying-in women are wary of the fact that the unevenness of parenting information on the Internet will also confuse searchers. At the same time, there are differences in the level of Internet use by users. Therefore, there are individual differences in the level of cognition and discrimination of information on the Internet, and users need to improve their own efficiency to distinguish, learn, and respond to this information.

In the process of pregnant women using WeChat groups to improve self-empowerment, practical information is often the fastest and most effective. In online parenting groups, what is most needed every day is often this kind of information. Even some group members will provide a lot of parenting knowledge without anyone asking. During the outbreak of vaccine issues, members of the group will share new developments in vaccine reports every day. In addition, information on discounts at major online and offline shopping malls is also useful and frequently discussed information regarding future employment.

The strong interactivity in the WeChat group is also a necessary reason for pregnant women to complete their self-

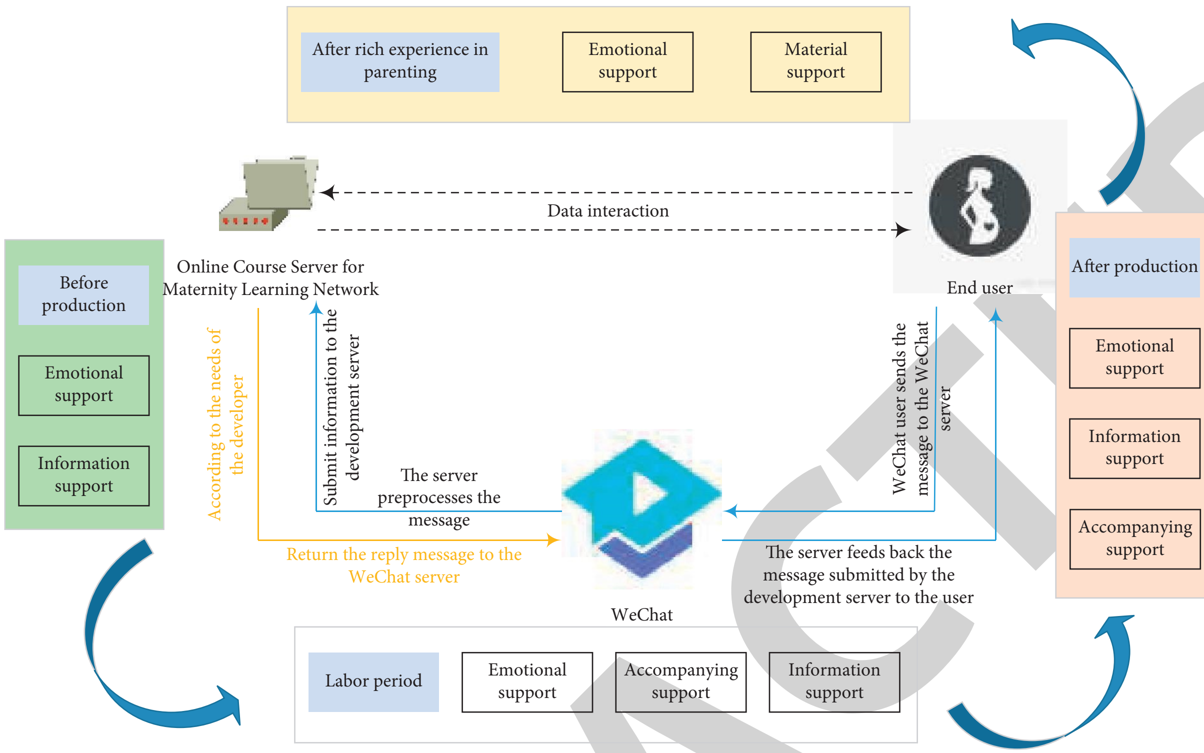

FIGURE 1: Social support received by users of WeChat parenting group.

empowerment. The online parenting group observed this time has more than 100 members, who speak a lot every day, and often chat messages in one day reach 999+. Whether it is consultation or answer, the speech of group members will drive the next wave of interaction within the group. For example, when a group member indicated that they wanted to go to a newly opened mall, several group members immediately asked them to share the new store and new discount information of the mall. The members of the group also used multimedia to give detailed explanations of the mall from pictures to videos, to voices, to texts, and even attached specific locations and transportation methods. Then the group members continued to ask questions, and the group members continued to answer.

3.2. Obtaining Companion Support and Conversion of Online and Offline Relationships. Companionship support refers to the support when an individual spends time with others to provide personal relaxation or entertainment and help others reduce stress. Although the WeChat parenting group is a weakly connected group, group members often accompany each other during pregnancy. Many mothers will tell everyone in this group before giving birth, and people in the group will also accompany them online. Although they cannot accompany them like offline relationships, they can accompany them regardless of time and place online, and they will not be unable to accompany them because of geographic distance.

Although this group does not discuss much about the content of work at work, and a certain percentage of mothers are recuperating at this time, there are still enthusiastic group members who make suggestions. When group members encounter the embarrassing situation of breastfeeding and cannot communicate with colleagues, group members can also achieve online "cloud accompany" to comfort and provide support to the parties in time and sometimes even enlighten the parties with their previous experiences and ease them.

In addition, there are not a few people who transform online relationships into offline relationships. Sometimes it was for the purpose of trading second-hand items and sometimes because the place of residence was close, and online group members met offline. After getting acquainted with each other, the members of the group will also meet to go shopping together, gather together, play mahjong together, and go to beautify together. Group members who are acquainted with each other even talk about baby kisses with a smile after seeing each other's babies.

4. Design of the Online Microcourse Learning System for Pregnant and Lying-In Women

4.1. WeChat Official Account Learning Network Online Course Development Model. Considering the needs of microcourse courses, this study uses the subscription number in the WeChat official account. In terms of microcourse teaching, the subscription number has some advantages compared with the service account and the enterprise account. To meet the needs of microcourse courses, it is convenient for teachers to share teaching resources with learners through WeChat public accounts.

RETRACTED

RETRACTED

The WeChat official platform provides an editing mode and a development mode. The two modes are mutually exclusive and cannot be opened at the same time, but they can be switched at any time. The development mode of the micro official account is not open to all users. The official account cannot be used for the development of high-end interfaces. The development of high-end interfaces can only be carried out after passing WeChat authentication. There are three authentication methods: legal representative authentication, payment authentication, and WeChat authentication. After the WeChat subscription account authentication is completed, we can enter the development mode of WeChat. The developer mode of WeChat includes four modules, namely basic configuration, developer tools, operation and maintenance center, and interface permissions. After entering the development mode, open the developer password and fill in the server configuration information.

4.1.1. Server URL Access. WeChat public platform needs to do some preparatory work between development, mainly about the configuration of the server address (URL) and the verification of the token because we must first ensure that the server is in the public network environment to ensure that the WeChat server can be accessed. Common public network servers include Sina Cloud and Baidu Cloud. The public network server selected in this study is Sina Cloud Server.

4.1.2. Data Exchange Method. After the WeChat public platform successfully connects to the website, the developer can obtain the authority of the message interface, and the message interface provides developers with the function of communicating with users. When a WeChat user sends a message to the WeChat official account via WeChat, the WeChat server will send the message to the developer's URL. When the URL receives the message, after parsing and classifying the message, the content that needs to be replied is returned to the WeChat server, and the WeChat server replies the returned message to the WeChat user.

4.2. The Overall Architecture Design of the System. Figure 2 shows the overall architecture diagram and specific system functions and characteristics of the microcourse learning system based on WeChat public.

4.2.1. Basic Layer. The construction of the basic layer of the system is the basis for the construction of the system. The basic layer of this research includes two parts: physical facilities and IaaS. The physical facility layer includes servers, storage, and network parts. IaaS mainly refers to virtual servers. The server mainly relies on Sina Cloud to support the application requirements of the learning system to meet the needs of WeChat users.

4.2.2. Data Layer. The data layer of the microcourse learning system mainly manages the information of WeChat users, including the storage, processing, and exchange of user information in order to better manage user information.

4.2.3. Service Layer. It mainly includes system management services, data analysis services, and task handling services. This article mainly connects the WeChat official platform through the WeChat platform server to provide services for learners who are concerned about the WeChat official account.

4.2.4. Exchange Layer. The exchange layer of the microcourse learning system mainly connects the service layer and the application layer. It mainly includes two parts: a message bus and an interface service. The message bus transmits asynchronous messages to the application layer.

4.2.5. Application Layer. The system application layer is the presentation layer of the system construction. The microcourse learning system mainly provides various application modules provided by the system to teachers and learners. These modules provide course information and related services to learners and teachers.

4.2.6. User Layer. The user layer of the system is the experience layer constructed by the system. The user layer of the microcourse learning system mainly provides services for the users of the WeChat official account.

4.3. System Function Module Design. The front-end WeChat front-end is convenient for managers of WeChat official accounts to manage teaching resources and users' personal information.

4.3.1. Front-End Module Design. Figure 3 shows the functional schematic diagram of the microcourse learning system based on the WeChat official account. The three modules of the microcourse learning system can basically meet the curriculum needs of learners and teachers. In addition, the microcourse learning system has designed relevant submodules according to the needs of users to enable learners to achieve better learning results.

4.3.2. Back-End Module Design. With the help of the WeChat public platform, teachers can easily complete the management operations of the microcourse learning content without the help of administrators and send relevant information and course content by themselves. The back-end management based on the microcourse learning system is the guarantee for the front-end operation of WeChat, which mainly includes two parts: user management and resource management.

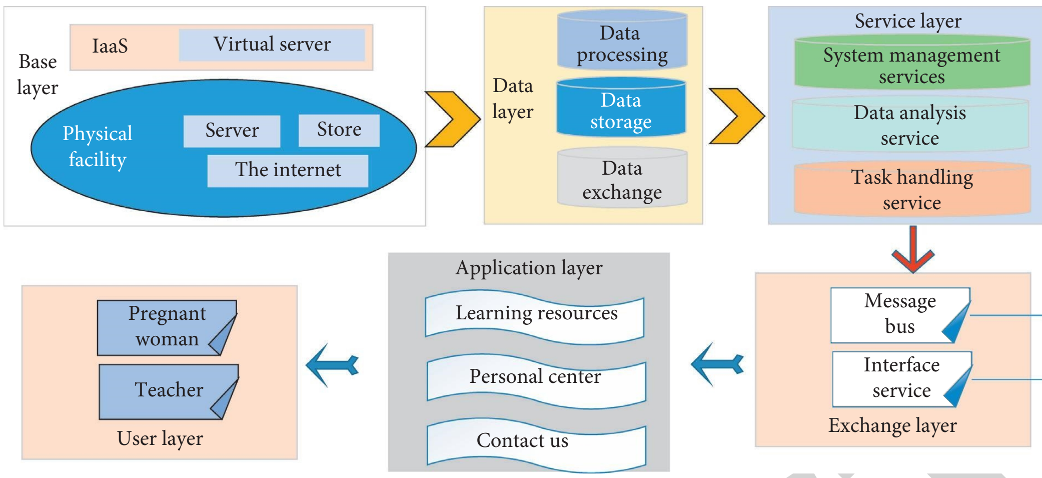

Figure 2: System overall architecture diagram.

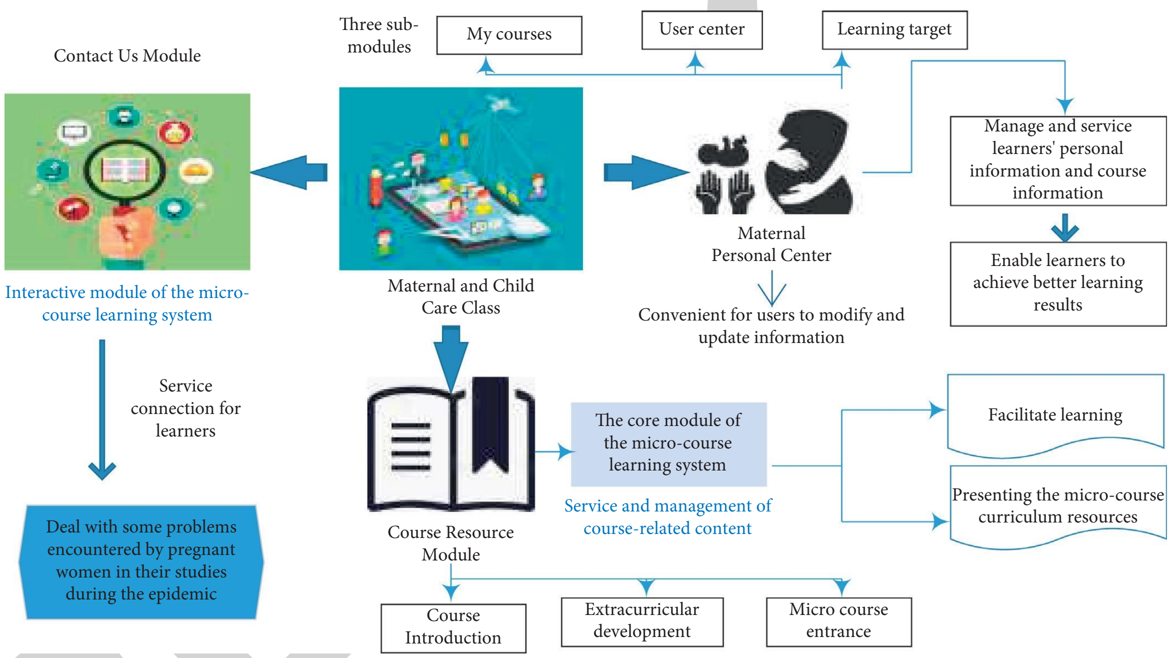

Figure 3: Schematic diagram of system front-end functions.

The user management module mainly includes two submodules, user information and user authority. User information includes teachers and maternal users. Users who follow the WeChat official account can use this module to improve and modify their information. The user authority module mainly sets different authority for teachers and learners through the WeChat public platform. The authority of the teacher user is higher than that of the learner user, which is convenient for better management of microcourse teaching to achieve better teaching effect.

The resource management module mainly includes two submodules: message management and course management. Message management means that teachers use the WeChat public platform to group and send messages to users who follow the WeChat official account according to the learner's different learning conditions, and learners use this module to feed back the problems encountered in learning to teachers in a timely manner. The course management module is for teachers to manage course information through the WeChat public platform, which mainly includes the classification, uploading, and replacement of course resources, so as to better serve the microcourse learning system.

4.4. Evaluation of the Impact of Online Courses on Maternal and Infant Health. It is generally measured from three aspects: consistency, monotonicity, and accuracy. Among them, consistency means that the error of the designed evaluation algorithm under different test samples is as small as possible, that is to say, the evaluation algorithm should be widely used; monotonicity refers to the change rule of the

RETRACTED

evaluation value of the designed evaluation algorithm and the subjective evaluation value. Accuracy means that the error between the evaluation value of the designed evaluation algorithm and the subjective evaluation value should be as small as possible. Here are a few more commonly used mathematical evaluation indicators:

(1) The formula of Spearman rank ordered correlation Coefficient (SROCC) is as follows:

$$\text{SROOC} = 1 - \frac{\prod_{i=0}^{n-1}\left(r_{xi} - r_{yi}\right)^2}{(n-1)(n-2)}. \quad (1)$$

Among them, r_{xi} and r_{yi} are the sorting positions of the corresponding sequence of x and y, respectively, and n is the number of samples tested.

(2) Linear Pearson Correlation Coefficient (LPCC) formula is as follows:

$$\text{LPCC} = \frac{\prod_i\left(s_i - \widehat{s}\right) \bullet \left(s_{pi} - \widehat{s}_p\right)}{\sqrt{\prod_i\left(s_i - \widehat{s}\right)^2} \bullet \sqrt{\prod_i\left(s_{pi} - \widehat{s}_p\right)^2}}. \quad (2)$$

Among them, s_i represents the subjective score, and s_p represents the image quality prediction score based on the regression function.

(3) Kullback-Leibler divergence (KLD), also known as KL distance and relative entropy, is used to measure the difference in the distribution of two probability density functions. The algorithm formula is as follows:

$$\text{KLD}\left(\frac{p}{q}\right) = \prod_i p(i)\log\left[\frac{q(i)}{p(i+1)}\right]. \quad (3)$$

Among them, p represents the true histogram mapping generated by the probability density function, and q represents the predicted histogram mapping generated by the probability density function.

(4) The formula of Outlier Ratio (OR) is as follows:

$$\text{OR} = \frac{\gamma}{\Gamma}. \quad (4)$$

Among them, γ represents the number that exceeds the subjective score by 2 standard deviations, and Γ represents the total number of participants in the predictive evaluation.

(5) The formula of Outlier Distance (OD) is as follows:

$$\text{OD} = \prod_{i \longrightarrow I_f} \min\left[s(i) - f(i) - 2\delta_s s(i) + 2f(i) - 2\delta_s\right]. \quad (5)$$

Among them, I_f represents the set of outliers, $s(i)$ represents the DMOS or MOS value of image i, and $f(i)$ is the predicted value after logical transformation. The logical transformation formula is as follows:

$$f(x) = \frac{\theta_1 - \theta_2}{1 - \exp\left(x - \theta_3/\theta_4\right)} - \theta_2. \quad (6)$$

Among them, θ_1, θ_2, θ_3, and θ_4 are model parameters selected from the minimum mean square error between the predicted value and the subjective value.

5. Results and Analysis

5.1. Prenatal Education Received by Pregnant Women. Pregnant women who have participated in all courses of the maternity school are defined as regular attendance, and women who have participated but have not participated in all courses are defined as occasional attendance. Among the 800 pregnant women surveyed, the number of women who were able to regularly participate in maternity school courses was the least, with a total of 100 women, accounting for 12.5%. The number of people who have never participated in maternity school courses is the largest, with a total of 500 people, accounting for 62.5%. There are 200 people who occasionally attend the maternity school courses, accounting for 25%. This shows that the proportion of pregnant women receiving formal prenatal education is relatively low, and the penetration rate of pregnant women's schools needs to be increased. See Table 1 for the participation of pregnant women in school education for pregnant women.

A survey of the sources of health information received by pregnant women during pregnancy found that, in descending order of the number of people, they were online courses, books, pregnant women's schools, elders' experience, Internet, television, and medical staff. Figure 4 shows the sources of health information for pregnant women during pregnancy.

5.2. Awareness of Maternal Knowledge and Concepts and Analysis of Influencing Factors. A survey on the awareness of pregnant women's knowledge and concept dimensions found that the highest awareness rate is "understanding the dangers of diet, nutritional requirements and smoking, drug abuse and alcohol abuse in the third trimester of pregnancy" to the fetus. 474 of the 497 pregnant women said they were aware of it. The awareness rate was 95.37%. Followed by "knowing the benefits of breastfeeding", 466 pregnant women said they were aware; the awareness rate was 93.76%. The item with the third awareness rate is "normal fetal heart sounds are 110–160 beats/min." There are 434 pregnant and lying-in women expressing awareness, and the awareness rate is 87.32%. The item with the lowest awareness rate is "knowing the time of the first antenatal check-up". Only 241 pregnant women said they knew it, and the awareness rate was 48.49%. The knowledge and concept awareness of 800 pregnant women are shown in Figure 5.

A one-way analysis of variance was performed on the factors that may affect the scores of maternal knowledge and concept dimensions. As the age increases, the scores of knowledge and concept dimensions are higher. The average score of pregnant women aged 20 to 24 is 10.06 points. While the average score of pregnant women aged 35 and

Table 1: Participation of pregnant women in school education for pregnant women ($n = 800$).

Attend a maternity school	Number of people	Composition ratio (%)
Participate regularly	100	12.5
Participate occasionally	200	25
Never participated	500	62.5
Total	800	100

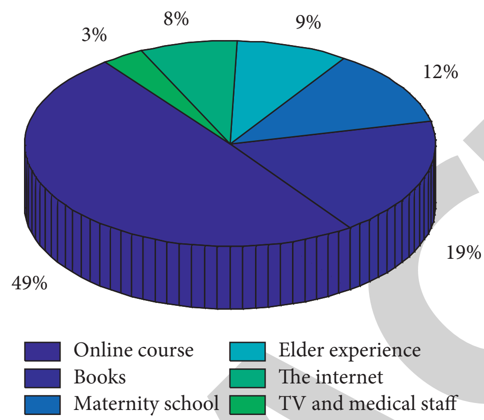

Figure 4: Sources of information on pregnant women's health during pregnancy.

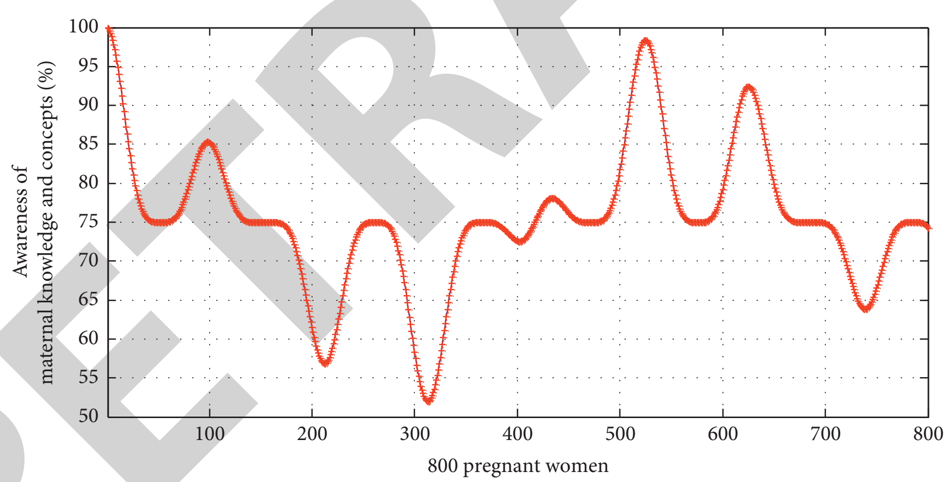

Figure 5: Awareness of maternal knowledge and concepts.

above was 11.08 points, and the scores of pregnant women of different age groups were statistically different (P $P < 0.05$). Economic income has a significant impact on the scores of the knowledge and ideal dimensions. With the increase of economic income, the scores of pregnant women in this dimension increase ($P < 0.05$). The scores of pregnant women who participated in the maternity school were significantly higher than those who did not participate in the maternity school ($P < 0.05$). There were no statistically significant differences in the scores of maternal knowledge and concepts of different education levels and different pregnancies ($P > 0.05$). The effect of online courses on maternal and child health is shown in Figure 6.

Multivariate linear regression analysis is performed on the factors that may be meaningful ($P < 0.1$) in the single factor analysis. Multicategorical variables enter the regression equation in the form of dummy variables. The results showed that three variables, age, income, and participation in maternity school, entered the regression equation. The scores of pregnant women aged 35 and above were significantly higher than those of 20–24 years old ($P < 0.05$). The scores of pregnant women with economic income between 2000 yuan/month and 4999 yuan/month were significantly higher than those with economic income<2000/month ($P < 0.05$). The scores of pregnant women who did not attend maternity school were significantly lower than those of

RETRACTED

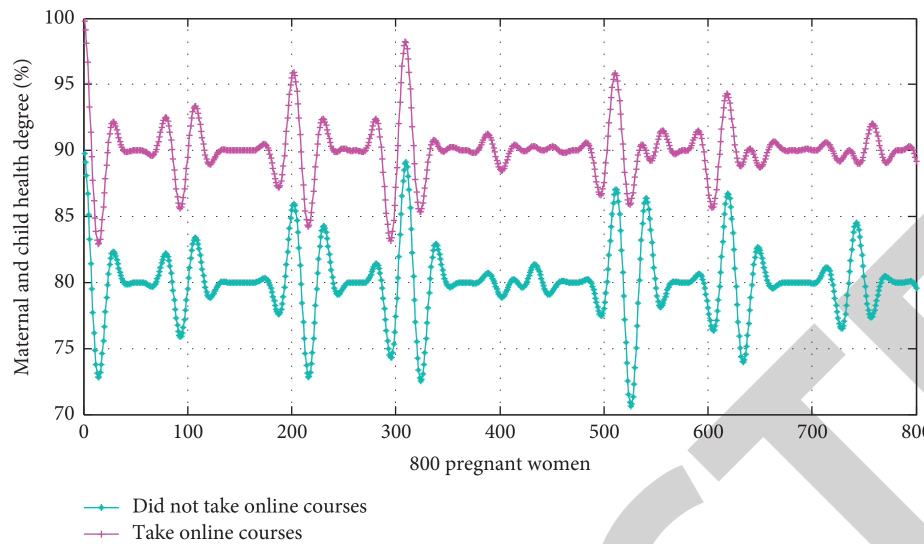

FIGURE 6: The impact of online courses on maternal and infant health.

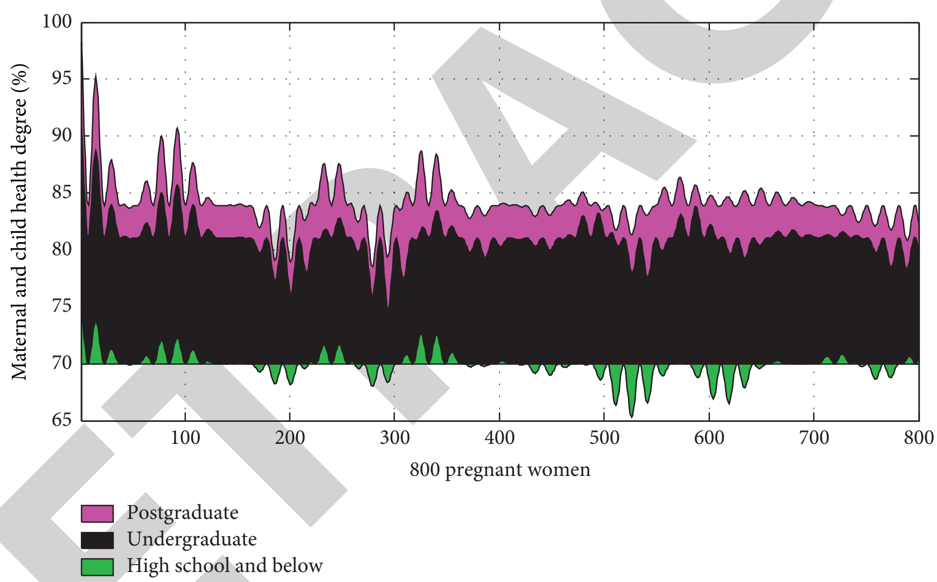

FIGURE 7: The impact of maternal education on maternal and infant health.

RETRACTED

women who regularly attended maternity school ($P < 0.05$). There was no significant difference between the scores of women who occasionally attended maternity school and those who regularly participated in maternity school ($P > 0.05$). The influence of maternal education on maternal and infant health is shown in Figure 7.

5.3. The Mastery of Basic Maternal and Infant Health Skills of Pregnant Women and Analysis of Influencing Factors. A survey on the mastery of the basic skills dimension of maternal and child health of pregnant and lying-in women found that the overall mastery of this dimension is relatively good, and only the mastery rate of "the treatment of abnormal nipples" is below 80%. The highest mastery rate is "breastfeeding skills", with 457 pregnant women expressing mastery, with a mastery rate of 91.95. The second is "the content and methods of family guardianship". 427 pregnant women said they had mastered it, and the mastery rate was 85.92%.

A one-way analysis of variance was performed on the factors that may affect the scores of the basic skills of maternal and child health of pregnant and lying-in women. The results showed that there were statistical differences in the scores of pregnant women of different age groups ($P < 0.05$). The women aged ≥35 years old had the highest scores, and those aged 20–24 years old had the lowest scores. The differences in the scores of pregnant women with different economic incomes in this dimension are statistically significant ($P < 0.05$). The women with economic income ≥5000 yuan/month have the highest score, and those with economic income<2000 yuan/month have the lowest score.

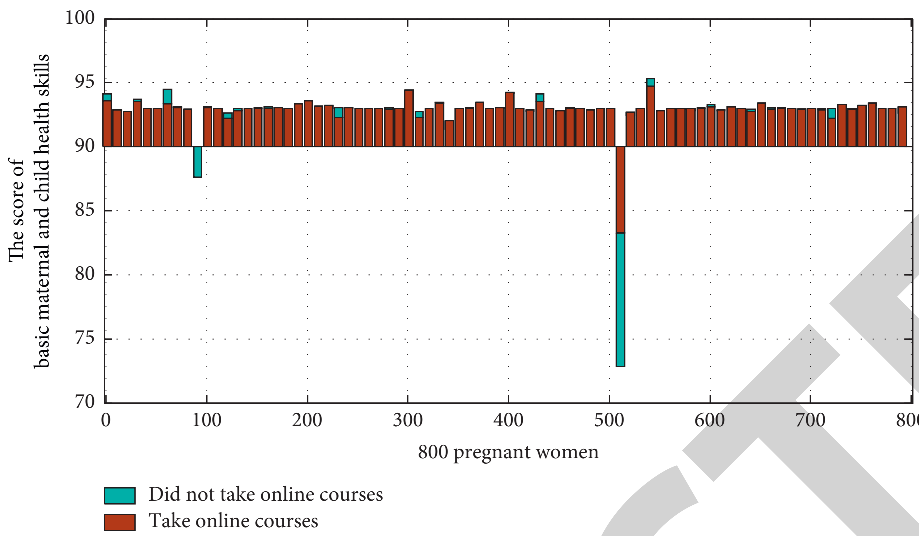

Figure 8: Maternal and child health basic skills scores.

RETRACTED

Participation in the maternity school has an impact on the score of this dimension. Figure 8 shows the scores of maternal basic skills dimensions.

The factors that may be meaningful ($P < 0.1$) in the univariate analysis were subjected to multiple linear regression analysis. Four variables, age, education level, economic income, and participation in maternity school, were entered into the regression equation. The scores of pregnant women aged 25–29 years in this dimension were significantly lower than those of women aged 20–24 years ($P < 0.05$), and women aged 35 and above scored significantly higher than those aged 20–24 years ($P < 0.05$). The scores of pregnant women with college education and above were significantly higher than those with junior high school education and below ($P < 0.05$). The scores of pregnant women with economic income of 2000–4999 yuan/month ($P < 0.05$) and more than 5000 yuan/month were significantly higher than those with economic income of less than 2000 yuan/month ($P < 0.05$).

6. Conclusion

The results of the one-way analysis of variance showed that as the age increased, the scores of the knowledge and concept dimensions were higher. Economic income has a significant impact on the scores of the knowledge and ideal dimensions. With the increase of economic income, the scores of pregnant women in this dimension increase ($P < 0.05$). The scores of pregnant women who participated in the maternity school were significantly higher than those who did not participate in the maternity school ($P < 0.05$). There were no statistically significant differences in the scores of maternal knowledge and concepts of different education levels and different pregnancies ($P > 0.05$). There are statistical differences in the scores of pregnant women of different age groups in this dimension ($P < 0.05$). The women aged ≥35 years old have the highest scores, and those aged 20–24 years old have the lowest scores. The differences in the scores of pregnant women with different economic incomes in this dimension are statistically significant ($P < 0.05$). The women with economic income ≥5000 yuan/month have the highest score, and those with economic income<2000 yuan/month have the lowest score. Participation in the maternity school has an impact on the score of this dimension. The average score of pregnant women who regularly attend the maternity school is 95 points, the average score of pregnant women who occasionally participates in the maternity school is 90 points, and the average score of pregnant women who do not participate in the maternity school is 80 points; the difference is statistically significant. Multiple linear regression analysis found that age, education level, economic income, and participation in maternal school are the influencing factors of maternal basic skills dimension scores.

Data Availability

The data used to support the findings of this study are available from the corresponding author upon request.

Conflicts of Interest

The authors declare that there are no conflicts of interest in this article.

Acknowledgments

This work was supported by the project of Medical Health Science and Technology Project of Zhejiang Province (clinical applied research of early neonatal basic health care in family group pregnancy care model, no. 2019KY128) and the project of Medical and Health Science and Technology of Zhejiang Province (study on the design and application of special midwifery equipment for free position delivery, no. 2020PY018) Medical Key Discipline of Hangzhou.

Hindawi
Journal of Healthcare Engineering
Volume 2023, Article ID 9873656, 1 page
https://doi.org/10.1155/2023/9873656

Retraction

Retracted: Online Automatic Diagnosis System of Cardiac Arrhythmias Based on MIT-BIH ECG Database

Journal of Healthcare Engineering

Received 10 October 2023; Accepted 10 October 2023; Published 11 October 2023

Copyright © 2023 Journal of Healthcare Engineering. This is an open access article distributed under the Creative Commons Attribution License, which permits unrestricted use, distribution, and reproduction in any medium, provided the original work is properly cited.

This article has been retracted by Hindawi following an investigation undertaken by the publisher [1]. This investigation has uncovered evidence of one or more of the following indicators of systematic manipulation of the publication process:

(1) Discrepancies in scope
(2) Discrepancies in the description of the research reported
(3) Discrepancies between the availability of data and the research described
(4) Inappropriate citations
(5) Incoherent, meaningless and/or irrelevant content included in the article
(6) Peer-review manipulation

The presence of these indicators undermines our confidence in the integrity of the article's content and we cannot, therefore, vouch for its reliability. Please note that this notice is intended solely to alert readers that the content of this article is unreliable. We have not investigated whether authors were aware of or involved in the systematic manipulation of the publication process.

Wiley and Hindawi regrets that the usual quality checks did not identify these issues before publication and have since put additional measures in place to safeguard research integrity.

We wish to credit our own Research Integrity and Research Publishing teams and anonymous and named external researchers and research integrity experts for contributing to this investigation.

The corresponding author, as the representative of all authors, has been given the opportunity to register their agreement or disagreement to this retraction. We have kept a record of any response received.

References

[1] W. Yan and Z. Zhang, "Online Automatic Diagnosis System of Cardiac Arrhythmias Based on MIT-BIH ECG Database," *Journal of Healthcare Engineering*, vol. 2021, Article ID 1819112, 9 pages, 2021.

Hindawi
Journal of Healthcare Engineering
Volume 2021, Article ID 1819112, 9 pages
https://doi.org/10.1155/2021/1819112

Research Article

Online Automatic Diagnosis System of Cardiac Arrhythmias Based on MIT-BIH ECG Database

Wei Yan and Zhen Zhang

Department of Cardiovascular Medicine, Affiliated Hospital of Youjiang Medical College for Nationalities, Guangxi, Baise, China

Correspondence should be addressed to Zhen Zhang; 2197@ymun.edu.cn

Received 18 October 2021; Revised 19 November 2021; Accepted 22 November 2021; Published 16 December 2021

Academic Editor: Kaijian Xia

Copyright © 2021 Wei Yan and Zhen Zhang. This is an open access article distributed under the Creative Commons Attribution License, which permits unrestricted use, distribution, and reproduction in any medium, provided the original work is properly cited.

Arrhythmias are a relatively common type of cardiovascular disease. Most cardiovascular diseases are often accompanied by arrhythmias. In clinical practice, an electrocardiogram (ECG) can be used as a primary diagnostic tool for cardiac activity and is commonly used to detect arrhythmias. Based on the hidden and sudden nature of the MIT-BIH ECG database signal and the small-signal amplitude, this paper constructs a hybrid model for the temporal correlation characteristics of the MIT-BIH ECG database data, to learn the deep-seated essential features of the target data, combine the characteristics of the information processing mechanism of the arrhythmia online automatic diagnosis system, and automatically extract the spatial features and temporal characteristics of the diagnostic data. First, a combination of median filter and bandstop filter is used to preprocess the data in the ECG database with individual differences in ECG waveforms, and there are problems of feature inaccuracy and useful feature omission which cannot effectively extract the features implied behind the massive ECG signals. Its diagnostic algorithm integrates feature extraction and classification into one, which avoids some bias in the feature extraction process and provides a new idea for the automatic diagnosis of cardiovascular diseases. To address the problem of feature importance variability in the temporal data of the MIT-BIH ECG database, a hybrid model is constructed by introducing algorithms in deep neural networks, which can enhance its diagnostic efficiency.

RETRACTED

1. Introduction

Cardiac diseases are the deadliest chronic diseases and are characterized by high morbidity, disability, and mortality. Nowadays, the prevalence and mortality of cardiovascular diseases are still on the rise worldwide [1]. Electrocardiogram (ECG) is the main diagnostic tool for CVD in clinical practice and is commonly used to detect cardiac arrhythmias. Arrhythmias are a common and complex cardiovascular disease that usually precedes the onset of arrhythmias. Early detection allows for appropriate intervention and thus can reduce unnecessary disability and death in the early stages of cardiovascular disease. ECG signals are insidious and abrupt, making it difficult to provide a comprehensive and accurate picture of a patient's cardiac status. Holter generates a large amount of ECG data, but the current manual ECG signal analysis is limited in real-time and accuracy [2]. Currently, physicians mainly use post hoc analysis to determine whether a patient is ill and the possible type of disease through waveform analysis, which is time-consuming, inefficient, and not highly reliable due to factors such as physician expertise and experience level. Physicians are unable to complete real-time online analysis of large-scale ECG data. Computer-aided analysis based on ECG can effectively improve medical diagnosis efficiency and shorten diagnosis time and has reliable clinical application value. The basis of automatic analysis technology of ECG data is to effectively extract features and then use a priori knowledge or machine learning methods to classify and diagnose. A priori knowledge comes from doctors' clinical experience, and ECG algorithms have limitations in P wave and T-wave recognition and cannot analyze their bands as a complete wave group [3]. Traditional automatic analysis methods of machine learning often use shallow neural networks to classify and identify ECG data waveform features, which can automatically adjust parameters and cover multiple features, with limited nonlinear fitting and approximation capabilities in the face of complex classified ECG data. In the context of big data-driven training, the recognition efficiency of shallow neural network classifiers is not high for big data training; in addition, the nonlinear fitting ability and accuracy are limited. Deep learning fuses feature extraction and classification, which is beneficial to improve recognition rates. However, deep neural networks deepen the difficulty of training optimization as the number of layers deepens, and the models lack strong interpretability. Under the condition of massive ECG data, traditional feature extraction cannot effectively extract the deep essential features of the target data, and how to automatically analyze and explore the potential value becomes an important opportunity and challenge in the field of ECG. Aiming at remote ECG monitoring, the core key issues in waveform features that distinguish it from the traditional ones are addressed by designing and implementing a remote ECG monitoring system. Conducting research on data-driven and deep learning-based intelligent classification and identification of cardiac arrhythmias and proposing convenient and feasible methods for self-diagnosis of cardiovascular diseases are of great practical significance for economic and social development and people's health [4].

ECG diagnosis is currently done mainly by manual analysis, but in today's world where cardiovascular diseases are generally high, an extremely large amount of ECG data is generated every day and every hour, and the types of heartbeats are very diverse, so manual management and analysis of ECG on a beat-by-beat basis is a task that is difficult to accomplish effectively. Especially in a clinical monitoring or wearable health monitoring environment, real-time diagnosis is even more of an unachievable task for healthcare staff due to the lack of expert resources for ECG diagnosis and high labor intensity. In addition, the suddenness and infrequency of the appearance of some abnormal heartbeats make it difficult for cardiologists to capture some important changes in an emergency condition promptly, which will directly threaten the life safety of patients. How to automatically and timely identify abnormal heartbeats from a large amount of ECG data and improve the accuracy and timeliness of ECG diagnosis is an important and necessary task. ECG automatic diagnosis technology can reduce the labor intensity of ECG specialists, eliminate misdiagnosis and misdiagnosis caused by subjective factors of medical personnel, and thus improve monitoring and diagnosis. The ECG automatic diagnosis system can be embedded into wearable devices (bracelets, medical vests, etc.) to provide long-term real-time monitoring of cardiac conditions, enhance prevention and thus timely detect heartbeat abnormalities, buy valuable time for further treatment of patients, provide favorable conditions, reduce medical costs, and ease the burden on patients, thus increasing the cure rate of cardiovascular diseases. Therefore, the research of ECG automatic diagnosis technology has an important role in promoting the progress of medicine and is of great significance in solving the current problems in ECG diagnosis.

2. Related Work

Automatic diagnosis of ECG is one of the hot spots in the field of ECG research, especially in the field of real-time diagnosis of ECG signals [5]. The variability of heartbeat waveforms in various heart disease patients and the fact that the recording devices of heartbeat signals are often influenced by the working environment and introduce a large number of different types of noise information make the effective diagnosis of ECG very difficult, and it is still a challenging research problem. Various methods have emerged in the area of heartbeat recognition, which is broadly classified into supervised and unsupervised methods. Supervised recognition methods are recognition algorithms that are constructed based on data with labels. The representative methods are convolutional neural networks [6], radial basis neural networks, least squares support vector machines, and so on. Unsupervised recognition methods refer to recognition algorithms constructed based on data with labels, and representative methods are self-coding neural networks [7], K-means clustering algorithms, and so on. Among them, the literature uses a convolutional neural network model to identify the heartbeat of a specific patient for the specificity between different patients. The method takes into account the blind spots in the diagnosis of new patients and provides a new idea for the automatic diagnosis of ECG. After this feature learning phase [8], the algorithm adds a softmax classification layer on top of the generated hidden representation layer to generate a deep neural network (DNN). The DNN model is then used to identify the heartbeat. This method can reduce the expert interaction to some extent. A deep learning-based method for single-lead ECG signal classification was proposed by literature. The method is an application of finite Boltzmann machine (RBM) and deep confidence network (DBN) for ECG classification after detection of ventricular and supraventricular heartbeats in single-lead ECG. The algorithm is validated using the MIT-BIH ECG database at a low sampling rate of 114 HZ. The RBM and DBN are selected with appropriate parameters, and higher performance can be obtained for heartbeat recognition, and it achieves better recognition results at a lower sampling rate compared to conventional methods [9].

The literature uses a five-level discrete wavelet transform to decompose the signal into six subband signals with different frequency distributions. Three RR interval correlation features were added to construct a feature vector of 30 features, and finally [10] the features were fed into a feedforward backpropagation neural network to achieve the classification of seven signals. Transformation extracted wavelet coefficients of ECG signals as the first features and optimized the wavelet extracted features using a combination of principal component analysis and independent component analysis and then fused intervals as the final features. Finally, the classification of six classes of ECG signals was achieved in the classifier and achieved 96.31% accuracy [11]. The literature uses geometric positions on the phase curve to extract ECG signal features from the detected R-peaks. Finally, the extracted features were fed

RETRACTED

into a support vector machine and K-neighborhood to achieve normal and abnormal signal classification [12]. The literature used the first-order derivative of Gaussian function as wavelet basis function and ECG feature extraction by examining the position of the modal maximal pair in the corresponding level of wavelet transform as a range for searching R-wave vertices in QRS waves, thus achieving 93% accuracy of abnormal heart rate in MIT-BIH database. The literature et al. used discrete wavelet transform combined with three-dimensionality reduction methods, principal component analysis, linear discriminant analysis, and ICA [13] and sent the reduced features to SVM, neural network, and probabilistic neural network classifier to achieve the automatic classification of a total of five ECG signals, namely, nonheterodyne beats, supraventricular heterodyne beats, ventricular heterodyne beats, fused heartbeats, and paced heartbeats. The contribution uses Harr wavelet transform to extract features from ECG signals. Feedforward neural network was used for preprocessing and classification of ECG signals. Classification of left bundle branch block, right bundle branch block, premature ventricular beats, premature atrial beats, premature lymph node beats, and normal beats was implemented in the MIT-BIH database [14].

3. MIT-BIH Cardiac Database for Online Automatic Diagnosis of Cardiac Arrhythmias

3.1. MIT-BIH ECG Database. The ECG signal is an electrical signal generated by the movement of the heart measured from the surface of the human body by an instrument. In the process of obtaining the ECG signal, there are inevitably many interfering factors, such as the instrument and the environment. These interferences will alter the true ECG signal. These interferences will alter the real human ECG signal, which is the basis for doctors to diagnose heart diseases, and any interference will cause misdiagnosis [15], thus causing irreparable harm to the patient. For the researcher, the noise generated by the interference will affect the results of the study. The MIT-BIH ECG data collected under different devices and different environmental conditions can interfere with the real signal to different degrees due to various interference factors, and we call the data in the MIT-BIH database heterogeneous data. To reduce or even avoid the harm caused by noise, the main work in this section is the study of MIT-BIH ECG databases, by perfecting the preprocessing methods so that MIT-BIH data can be cross-used [16], each MIT-BIH ECG database has its characteristics, such as the number of leads, storage format, and sampling frequency, but the common purpose is to conduct research or perform disease diagnosis. The principle of the formula lies in

$$A = \sum_{i=1}^{n} X_i Y_i + \sum_{i=1}^{n} X_i Y_i. \tag{1}$$

Formula (1) plays an important role in the construction of the database in the article. It can ensure the normal operation of the database and ensure that there is enough storage space. This is its role and can help the normal operation of the entire system. Currently, there are many ECG databases, but there is no single standard, and researchers can only analyze one ECG database for their research and cannot use others, which is a great waste of resources. For research analysis in cardiac diseases, adequate data is an important guarantee for the sustainability of the research. In addition to the number of leads and storage formats, the different sampling frequencies and signal quality of the MIT-BIH ECG databases are also obstacles to cross-use between the MIT-BIH ECG databases. The concept of big data is now known and valued by more and more researchers, entrepreneurs, companies, etc., and can be used to fully exploit the correlations and useful information in huge data sets using advanced algorithms, which can then be applied in practice to bring greater value to people, with data algorithms as

$$T = \frac{\Delta y}{\Delta x} \cdot \frac{\delta y}{\delta x} \cdot \frac{\partial^2 \Omega}{\partial u \, \partial v}. \tag{2}$$

The function of formula (2) has a connecting effect on the paper. For the structure of the paper, formula (1) can be further described, or a series of introductions can be made to the following content to optimize the structure of this chapter. It is also true for ECG database, data is money, how to make full use of the existing database, how to remove the barriers between MIT-BIH ECG databases and facilitate the cross-use between MIT-BIH databases, these studies are very valuable. The ECG database is the first database for the Chinese population, containing 11 major categories of ECG abnormalities and 100+ categories of subdivided ECG symptoms, with data types including conventional ECG, single-lead, 3-5-lead, and 12-lead ECG. In the form of data presentation, each ECG data contains data source, recording time, length, ECG plot, analysis of various indexes, and expert labeling. At the same time, each ECG data records patient age, gender, disease information, and so on. The database covers a wider range of ECG abnormality types and richer data types, which can provide shared services and technical support for related institutions and significantly reduce the R&D cost. The traditional encoder is shown in Figure 1.

To verify the effectiveness of the above combination of denoising methods on heterogeneous data, preprocessing was performed, followed by a detailed similarity comparison. PTB is a German diagnostic ECG database. PTB is a German diagnostic ECG database containing 549 records from 290 individuals with 15 lead signal records per individual in the conventional 12 leads (i, ii, iii v1, v2, v3, v4, v5, and v6) and 3 Frank leads (vx, vy, and vz) with a sampling frequency of 1000 Hz, containing a wide range of disease samples and healthy comparison samples; VGHTC is an ECG database from Taichung Veterans General Hospital, containing tens of thousands of cases, each with a conventional 12-lead ECG signal with a sampling frequency of MIT-BIH being a self-collected ECG database containing 30 individual samples with a two-lead approach and a sampling frequency of 250 Hz, and due to the limitations, the samples

RETRACTED

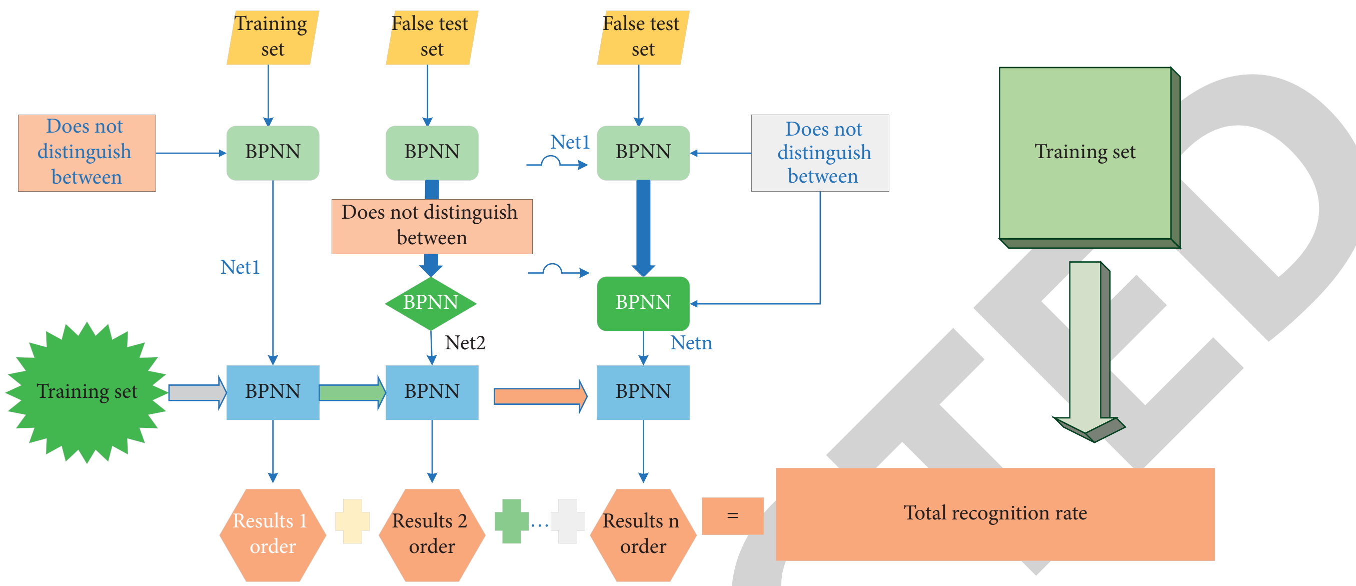

Figure 1: Conventional self-encoder structure.

in this database are all healthy samples. Since the samples in each heterogeneous ECG database have different types of diseases but all contain healthy samples, the healthy samples from the three databases were chosen for this experiment to ensure the consistency of the experimental data [17]. Left bundle branch conduction block, also known as left bundle branch block, results from delayed conduction of electrical excitation in the left bundle branch of the heart or interrupted; the excitation can only be transmitted from the right to the left ventricle of the heart, resulting in some delay in the excitation of the left ventricle. Right bundle branch conduction block is caused by a block in the right bundle branch of the heart, which in turn causes electrical excitation to fail via the pathway into the right ventricle and must be signaled by signals from the left ventricle [18]. However, the electrical signals from the left ventricle must pass through myocardial afferents, and this pathway is transmitted more slowly than the original Hitchcock–Purkinje fiber pathway, so on the ECG, the patient will have a wider complex wave. Also, because the left ventricle depolarizes faster than the right ventricles and therefore in the wave will produce a condition where the heart axis is offset, atrial preterm contraction is also known as atrial premature beat. It is a single or paired ectopic atrial excitation that originates anywhere in the atria other than the sinus node. In the presence of atrial premature beats, the P wave is distinctly different from the normal sinus P wave, and the time frame of the P-R interval is generally outside the normal range. Ventricular contractions, or premature ventricular contractions, are a premature excitation of the ventricles due to various causes. The arrhythmia can occur in patients of any age with cardiovascular disease and the general population. In the ECG signal, abnormally wide wave clusters are observable, and there is an inversion of the T-wave following the QRS wave cluster. Pacemaker rhythm is the rhythm produced by controlling the heartbeat with external electrical stimulation when sinus bradycardia, sinus arrest, and simultaneous block of the right and left bundle branches of the AV node result in severe ventricular rate slowing that is unable to maintain the body's physiological needs. Due to different clinical needs, the pacemaker program control mode is set differently, and the human autonomic rhythm often coordinates with the pacing rhythm to control the heartbeat, making the pacing ECG variable and a difficult clinical diagnosis. The types of pacing are divided into atrial pacing, ventricular pacing, three-chamber pacing, and four-chamber pacing, depending on the location. In most cases, arrhythmias are unconditioned, and they occasionally occur in normal individuals. However, frequent arrhythmias are usually caused by cardiovascular disease, and therefore the diagnosis of arrhythmias is important for the prevention of cardiovascular disease.

3.2. MIT-BIH Arrhythmia Online Automatic Diagnosis System. The MIT-BIH Arrhythmia Database is MIT's international standard-based, expertly diagnosed, and annotated ECG database, and the standard ECG database is widely recognized and used in academia. The database in this paper is an important source of data for the research work on automatic arrhythmia diagnosis algorithm. The MIT-BIH arrhythmia database has more than a dozen types of arrhythmias, totaling more than 100,000 heartbeats, excluding most of the normal beats, among which are atrial premature beats, ventricular premature beats, bundle branch block, atrial fibrillation, and many other types of abnormal heartbeats. The database provides a uniform naming of the various arrhythmias. For ease of annotation, each beat is marked with a special symbol. Arrhythmias are abnormalities in the frequency, rhythm, origin, conduction velocity, and sequence of excitation of the electrical impulses of the heart, with the direct consequence of sudden cardiac death and heart failure [19]. It is estimated that there are hundreds of millions of cardiovascular patients worldwide, of whom 26.8% suffer from arrhythmias, and the prevalence and mortality rates are still on the rise. Currently, various imaging techniques, electrocardiograms, and electrocardiogram imaging are available for the diagnosis of arrhythmias, and treatments include antiarrhythmic drugs, artificial pacemakers, heart transplants, cardiac stents, heart bypasses, radiofrequency ablation, and so on. Although advanced treatment techniques and drugs have reduced the death rate of arrhythmias, some treatment modalities (such as antiarrhythmic drugs and radiofrequency ablation) have not only failed to cure arrhythmias but also become the key factors leading to arrhythmias, making the death rate of arrhythmias remain high. Despite the rapid development of modern medical technology, the incidence of arrhythmias remains high. Taking atrial fibrillation as an example, ECG is still the core method of arrhythmia diagnosis. Traditional arrhythmia diagnosis relies on ambulatory electrocardiography (Holter) to provide 24 h ECG monitoring. Patients carry continuous ECG information with them. The need for patients to carry instruments, leads, and spacers with them to use the Holter is extremely uncomfortable and disruptive, and the subsequent data processing is cumbersome, limiting its use on a large scale, while short-duration 12-lead ECGs often lead to missed arrhythmias. ECG signals are low-frequency and weak electrical signals collected from the human body surface by ECG monitoring equipment through multiple electrodes. The amplitude of ECG signals is usually in the millivolt range, which is very low, and the signal frequency is usually in the range of 0.05–100 Hz, which is in the low-frequency band. Moreover, the ECG signal may fluctuate due to the difference between the human body and monitoring equipment. Due to the weak characteristics and instability of ECG signals, ECG signals are extremely vulnerable to the influence of external noise. As can be seen from the noise sources, ECG interference is mainly divided into three main categories: one is the industrial frequency interference brought by the circuit equipment; the second is the electromyographic interference brought by the human skin and muscles at the electrode acquisition position; the third is the baseline drift caused by the human body movement or electrode movement and other large changes in position. Industrial frequency interference is the signal acquisition process. The interference signal is generated by the influence of the circuit system. Currently, the domestic frequency of industrial frequency interference is 50 Hz. Industrial frequency interference is the most common and unavoidable interference in the ECG signal, and the maximum amplitude of interference can reach about 50% of the normal ECG signal amplitude. Because the frequency of the IDF interference does not change much, it is usually evident in the ECG. Baseline drift occurs when the ECG signal fluctuates up and down frequently, resulting in a baseline that cannot be maintained at the same level. The main cause of baseline drift is movement during signal acquisition, including the movement of the body and movement of the equipment. Baseline drift is extremely common in 24-hour ECGs. Baseline drift can severely affect the amplitude of the ECG signal, making it impossible to calculate the exact amplitude of individual waveforms from a baseline position, which in turn can affect the diagnosis of disease. Figure 2 shows the neural network structure.

Wavelet transform (WT) is a mathematical transformation method proposed and popularized at the end of the last century. Wavelet transform can maximize the local characteristics of the signal through mathematical transformation and realize time-frequency localization analysis. The mathematical transform is used to decompose the signal data on multiple scales, to process the high and low frequencies of the signal separately [20], to satisfy the adaptive analysis of various frequencies, and then to realize the local analysis of any part of the signal, which overcomes the difficult problem of Fourier transform in signal processing. Wavelets are obtained from fundamental wavelets by mathematical transformation "stretching translation". The fundamental wavelet is a function with fast decay properties, and this function needs to mathematically satisfy the requirement of zero integration:

$$M = \sum_{i=1}^{n} X_i Y_i + \frac{1}{n}\left(\frac{x-\mu}{\sigma}\right). \tag{3}$$

Wavelet transform has the following good properties: (1) low entropy: due to the sparse nature of the WT coefficient distribution, the entropy of the signal after processing becomes very low; (2) multiresolution characteristics: wavelet transform can be a multiscale transform for processing local details, which can well retain the nonsmooth characteristics of the signal; (3) decorrelation: after the ECG signal is transformed by wavelet, the noise signal in it tends to be whitened, so it is easier to distinguish the two, making the wavelet; (4) flexibility of base selection: due to the diversity of wavelet basis functions, the wavelet transform method is more flexible in processing different signal data, so more suitable wavelet basis functions can be selected to improve the signal processing effect.

After wavelet decomposition of the ECG signal acquired by the device, the key features of the human ECG signal tend to be distributed and are on wavelet coefficients of high amplitude, while wavelet coefficients of smaller amplitude mostly contain various useless noises, while wavelet decomposition can also be corrected for the baseline drift of the signal. This topic is addressed by setting the signal with the original. Strongly correlated adaptive thresholds are used to zero out wavelet coefficients that are smaller than the threshold so that the ECG signal is the purpose of denoising. The main process is divided into three steps as shown in Figure 3.

Scale wavelet decomposition is as follows. Select a wavelet and determine the level of decomposition, and then carry out the decomposition calculation. Wavelet threshold processing is as follows. According to the signal-to-noise ratio of the original signal and the decomposed high-frequency coefficients, calculate the threshold value associated with it, screen the noise information by the threshold value, and then carry out quantization processing. Wavelet coefficient reconstruction is as follows. The decomposed wavelet coefficients are retransformed to a one-dimensional wavelet

RETRACTED

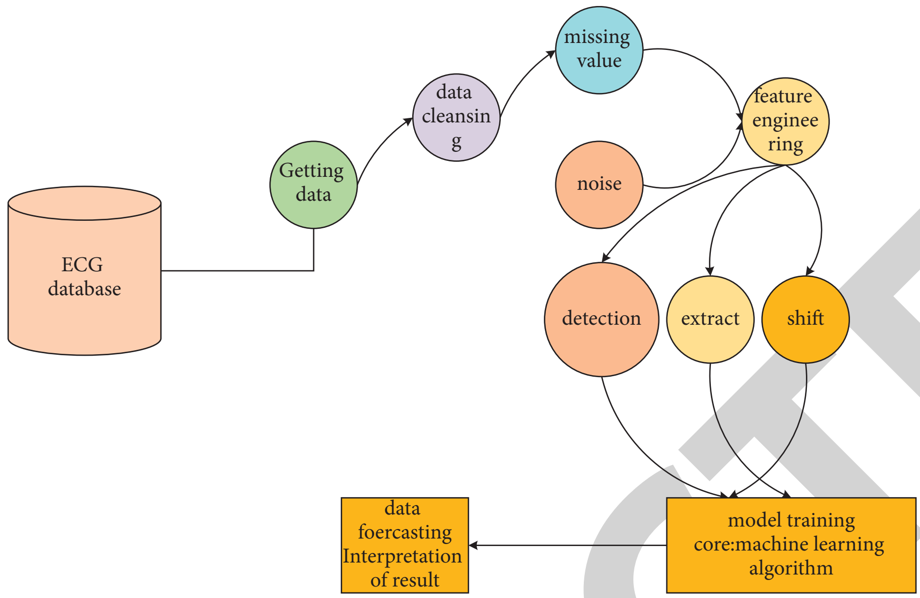

Figure 2: Algorithm model framework diagram.

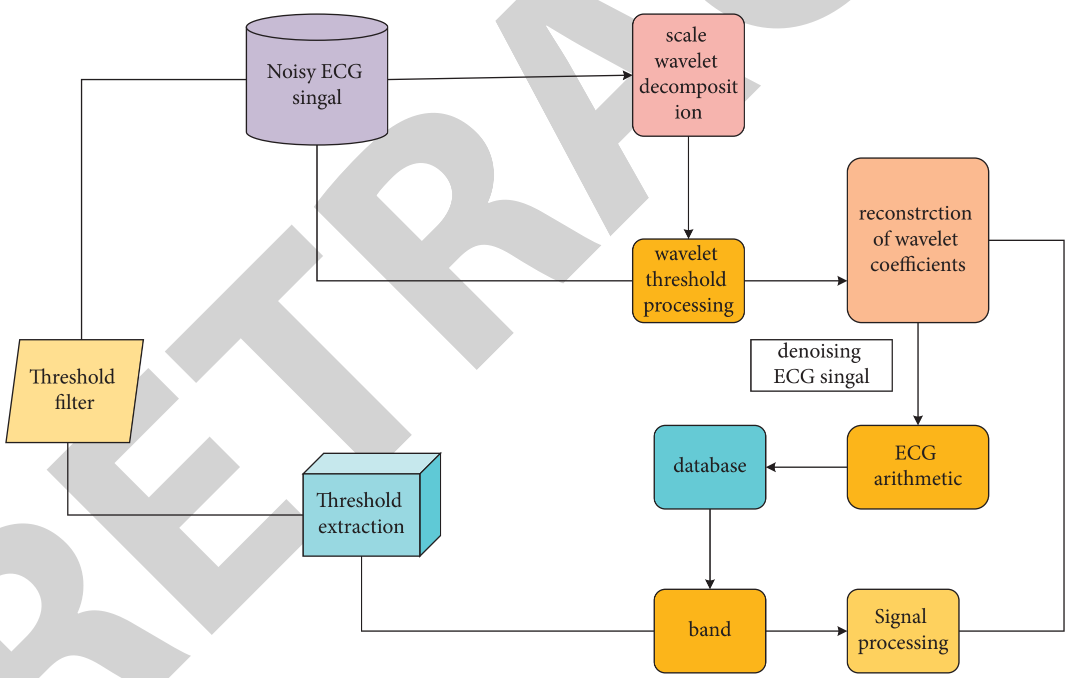

Figure 3: Wavelet filtering flow.

RETRACTED

reconstruction. In the whole process, the selection of wavelet basis, the determination of decomposition scale, and the setting of threshold are the key to the wavelet denoising process, which will directly affect the effectiveness of the signal after reconstruction. In signal processing, usually, these three key parameters do not have a fixed selection method. For different signals, the best experimental parameters need to be selected and experimented with according to the characteristics of the signal, the characteristics of the noise, and the actual needs. The improved wavelet filtering process is shown in Figure 4.

4. Experimental Results and Analysis

4.1. Experimental Results. The features extracted from the heartbeat waveform are mainly time-domain features and voltage amplitude features, and obtaining the main features has an important connection with the number of convolutional kernels. To investigate the effect of the number of convolutional kernels on the accuracy of the test set in the CNN model, this paper keeps the learning rate and training times constant and adjusts the number of convolutional kernels to observe the change in the accuracy of the test set

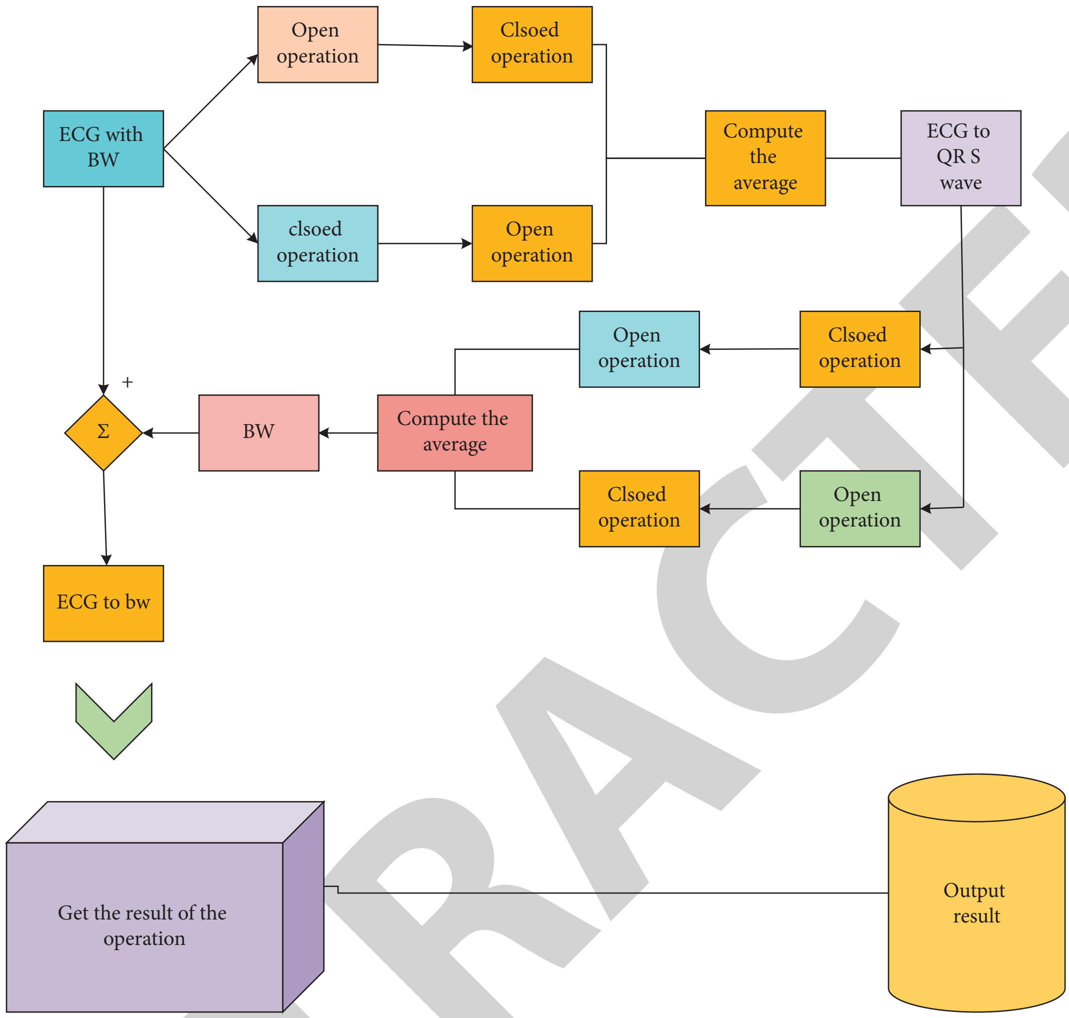

FIGURE 4: Improved wavelet filtering process.

with the number of network layers as 2. During the experiment, it is found that the time spent on training samples is positively related to the number of convolutional kernels. By comparison, it can be found that the number of convolutional kernels is more realistic when the number of convolutional kernels is 5. After the training is completed, the test set heartbeat data is used for testing, and the results obtained from the experiments are compared with the heart expert labeling results to construct a 1D CNN structure validation for heartbeats, which can obtain higher results for classifier performance evaluation metrics. To reflect the obvious advantage of 1D CNN network structure in the classification effect, a comparison test with the classical classifier SVM is performed. The coefficients of the wavelet transform are used as features of the classifier SVM, and its comparative efficiency graph is shown in Figure 5.

In this chapter, the ECG signal in the first channel of 119.dat in MIT-BIH data is selected to verify the filtering algorithm by extending the intercepted signal and adding a constant value to each sampling point in the signal, so that the S-T segment and P-T segment of the signal coincide with the baseline of the zero potential point, and, finally, the ECG signal will be considered pure without baseline drift interference, that is, signal S, where the horizontal coordinate is the number of sampling points, and the vertical coordinate is the voltage value/mV. The baseline drift noise is selected as the signal BW within the second channel of the baseline drift noise bw.dat in MIT-BIH, as shown in Figure 6, which is a plot of the number of experiments and the recognition rate.

To select a more effective feature extraction method, three feature extraction methods, wavelet feature extraction, improved RBP algorithm, and waveform features described earlier are applied to practical classification, and the classification results are compared in this paper. For the improved RBP features, 36 sets of experiments are conducted based on the parameters m-bit and interval, and the highest recognition rate is taken here. The average recognition rates achieved by the improved wavelet features and the improved RBP algorithm on the proposed multiorder classification algorithm are 78.8% and 64.5%, respectively. The efficiency of the three approaches is compared as shown in Figure 7.

However, often the recognition of one of the classes of heartbeats is not very good, resulting in being poor overall. Of course, there are also good classification results, like MSE,

RETRACTED

RETRACTED

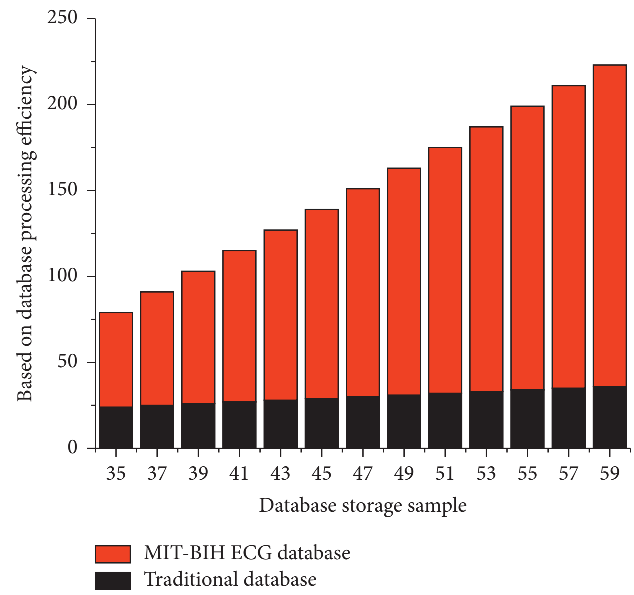

Figure 5: Efficiency comparison chart.

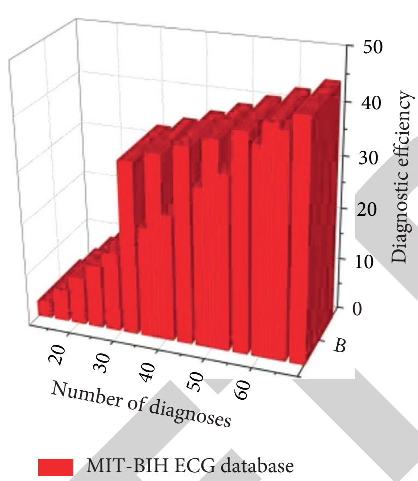

Figure 6: Number of experiments versus efficiency experimental analysis.

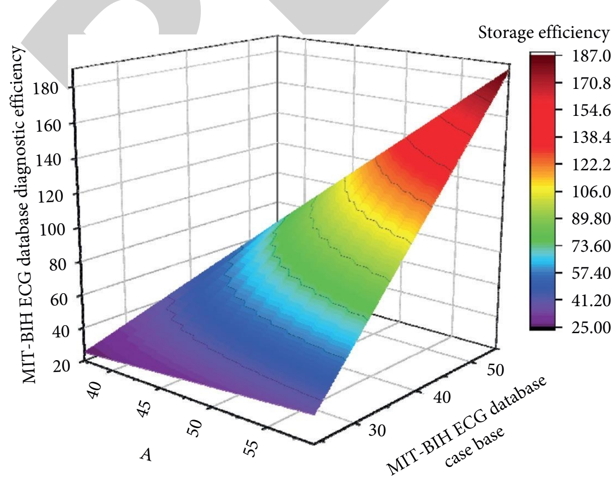

Figure 7: Comparison of the efficiency of the three approaches.

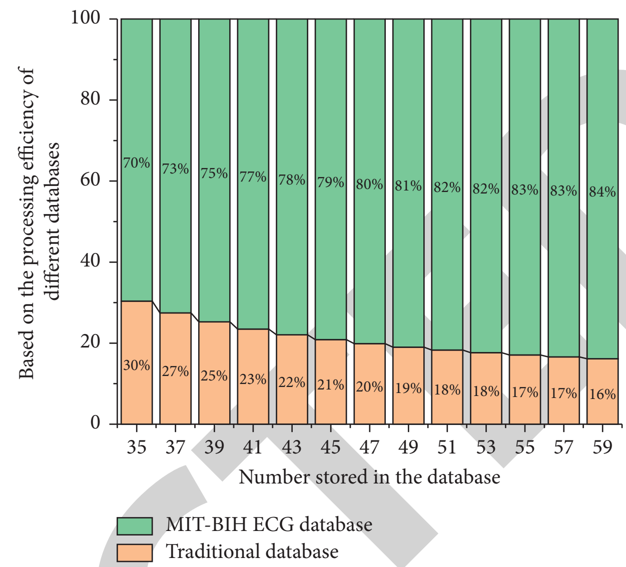

Figure 8: Electrocardiographic efficiency plot for the MIT-BIH approach.

NSE + MSE, MSE + RMSE, and NSE + MSE + RMSE. These feature sets have good classification results. It is observed that the MSE feature set is included in the above feature set, which indicates that the MSE feature set is more effective in classifying the heartbeats of this database. The last row of the table lists the multiorder classification recognition rate of this paper, and by comparison, it is found that although not every heartbeat has a higher recognition rate, the average recognition rate is higher than the other schemes, and it has a better recognition effect for every class of heartbeats as shown in Figure 8. Its representation shows the graph of its efficiency.

5. Conclusion

Cardiovascular diseases seriously damage the physical and mental health of the population and have a great impact on people's normal life. Therefore, it is important to prevent the occurrence of cardiovascular diseases in advance in daily life and to perform ECG examinations regularly. At the present stage, the diagnostic method of ECG still relies on the professional physician to implement the diagnosis using the observation method and this transmission. The conventional method consumes a lot of human and material resources and also greatly wastes the precious treatment time of doctors and patients, because it is particularly important to design an automated arrhythmia detection algorithm. Currently, some cardiac monitoring devices propose provided basic arrhythmia methods, but due to the different devices from different manufacturers and the poor immunity of some devices to interference, The diagnostic accuracy of arrhythmias is limited and there is no uniform algorithm that can identify all device signals. In recent years, as deep learning models have made good progress in various fields, they have been used to deal with some prediction and subclass of problems when obtaining high accuracy, as this

Hindawi
Journal of Healthcare Engineering
Volume 2023, Article ID 9817063, 1 page
https://doi.org/10.1155/2023/9817063

Retraction

Retracted: Interventional Treatment of Bronchiectasis Macrosomia Based on Multirow CT Tomography Monitoring

Journal of Healthcare Engineering

Received 5 December 2023; Accepted 5 December 2023; Published 6 December 2023

Copyright © 2023 Journal of Healthcare Engineering. This is an open access article distributed under the Creative Commons Attribution License, which permits unrestricted use, distribution, and reproduction in any medium, provided the original work is properly cited.

This article has been retracted by Hindawi, as publisher, following an investigation undertaken by the publisher [1]. This investigation has uncovered evidence of systematic manipulation of the publication and peer-review process. We cannot, therefore, vouch for the reliability or integrity of this article.

Please note that this notice is intended solely to alert readers that the peer-review process of this article has been compromised.

Wiley and Hindawi regret that the usual quality checks did not identify these issues before publication and have since put additional measures in place to safeguard research integrity.

We wish to credit our Research Integrity and Research Publishing teams and anonymous and named external researchers and research integrity experts for contributing to this investigation.

The corresponding author, as the representative of all authors, has been given the opportunity to register their agreement or disagreement to this retraction. We have kept a record of any response received.

References

[1] D. Lu, W. Chai, X. Gao, and X. Yan, "Interventional Treatment of Bronchiectasis Macrosomia Based on Multirow CT Tomography Monitoring," *Journal of Healthcare Engineering*, vol. 2021, Article ID 9116765, 12 pages, 2021.

Hindawi
Journal of Healthcare Engineering
Volume 2021, Article ID 9116765, 12 pages
https://doi.org/10.1155/2021/9116765

Research Article

Interventional Treatment of Bronchiectasis Macrosomia Based on Multirow CT Tomography Monitoring

DongDong Lu,[1] **Wenshu Chai**,[1] **Xue Gao**,[2] **and Xue Yan**[1]

[1]*Department of Respiratory Medicine, The First Affiliated Hospital of Jinzhou Medical University, Jinzhou, Liaoning 121000, China*
[2]*Department of Ophthalmology, The First Affiliated Hospital of Jinzhou Medical University, Jinzhou, Liaoning 121000, China*

Correspondence should be addressed to Xue Yan; yanxue@jzmu.edu.cn

Received 28 September 2021; Revised 3 November 2021; Accepted 5 November 2021; Published 9 December 2021

Academic Editor: Gu Xiaoqing

Copyright © 2021 DongDong Lu et al. This is an open access article distributed under the Creative Commons Attribution License, which permits unrestricted use, distribution, and reproduction in any medium, provided the original work is properly cited.

We present in this paper an in-depth study and analysis of bronchiectasis haemoptysis by multirow CT tomography and a multifaceted treatment and analysis of the interventions monitored by the scan. Although coronary CT is of great clinical value in the diagnosis and monitoring of coronary artery disease, the potential radiation damage caused by coronary CT should not be underestimated because CT imaging is based on X-rays and the actual effective dose is 5–30 mSv, which is reported in the literature to be high when using conventional imaging modalities for coronary CT. Although there is no direct evidence of a definite causal relationship between X-ray exposure during CT examinations and tumorigenesis, theoretically, even small doses of radiation exposure may pose some potential health risk. Therefore, in clinical practice, coronary CT examinations should be performed in strict compliance with the radiation protection rule "as low as reasonably achievable" (ALARA) recognized by the radiation industry. For longitudinal openings in the range of 0° to 59° and transverse openings in the range of 0° to 44°, the CB2 catheter is significantly more stable than the MIK catheter, and for longitudinal openings in the range of 60° to 119° and transverse openings in the range of 0° to 44°, the CB2 catheter is more stable than the MIK catheter. For longitudinal openings from 0° to 120° and lateral openings from 45° to 90°, there was no significant difference in cannulation stability between the CB2 and MIK catheters. There was a potential tendency for MIK cannulation stability to be higher than CB2 for longitudinal openings in the range of 120° to 180° and lateral openings in the range of 45° to 90°, but there was no significant difference.

RETRACTED

1. Introduction

The bronchial artery (BA) is the main trophoblastic vessel of the lung, which delivers blood to the trachea, extra- and intrapulmonary airways, supporting tissues, nerves, oesophagus, lymph nodes, and visceral pleura, and has numerous and cumbersome anastomosing structures with various capillaries at the end of the pulmonary arterial. It is involved during various congenital and acquired conditions in humans, congenital diseases such as bronchopulmonary isolation and pulmonary venous pressure syndrome, and acquired disorders such as tumours and inflammatory diseases [1]. Because of the significant angiogenic potential of BA, bronchial arteries thicken, twist, and increase blood flow in these conditions, making bronchial circulation a common source of haemoptysis. Given the degree of dilatation that can be achieved in the bronchial arteries, haemoptysis is often substantial and highly fatal, and its severity and natural course are clinically unpredictable [2]. The most common causes of haemoptysis in our country are mainly tuberculosis (active or its sequelae), bronchiectasis, primary bronchial carcinoma, hematogenous lung abscess, and less frequent etiologist such as chronic pneumonia, bronchial artery-pulmonary artery fistula due to pulmonary embolism, coronary artery-bronchial artery fistula, and rupture of aortic aneurysm [3]. Recently, most scholars believe that either primary or metastatic lung cancer is generally supplied by BA, which is the most common and important responsible vessel involved in lung cancer, while the pulmonary artery does not participate in blood supply, and only a few reports can have pulmonary circulation to participate in lung cancer blood supply [4]. In contrast, intermediate and advanced central lung cancer is a common and frequent disease, and their morbidity and mortality rates are extremely high. Bronchopulmonary sequestration and pulmonary venous pressure syndrome acquired diseases such as tumours and inflammatory diseases. The confirmation of the diagnosis is mainly based on imaging methods, and the treatment relies mainly on bronchial artery embolization. Therefore, it is crucial to understand the changes in BA to the chest (especially for tumour surgery). In addition, in patients with acute and severe haemoptysis who are considered for bronchial artery embolization, the anatomy of the bronchial arterial system must be understood for accurate and safe embolization [5]. In the past, evaluation of the bronchial circulation usually required invasive imaging with angiography to determine the location of the haemorrhage, which was limited by the fact that the origin, number, coaptation, course, diameter, and course of BA varied from person to person and textbook descriptions of the bronchial arteries were rather superficial and not carefully depicted, which limited their clinical use because of the obvious invasiveness, high surgical risk, high cost, and lack of stereoscopic images.

Haemoptysis is one of the many symptoms of lung disease and usually refers to bleeding from the trachea, bronchi, their branches, and lung tissue below the laryngopharynx, as well as the process of coughing up the airways. Haemoptysis of between 300 and 600 mL or more in a day is usually specified as macrohaemoptysis, and the mortality rate of conservatively treated macrohaemoptysis exceeds 50%. Recurrent small amounts of haemoptysis, with a duration of more than 3 days and average daily haemoptysis of more than 100 mL, are considered clinically significant [6]. Both occasional small amounts of blood in the sputum and life-threatening large amounts of coughing can cause some psychological stress and burden on the patient's life. Because haemoptysis can be life-threatening and affect the patient's quality of life, it is especially important to clarify its aetiology and the mechanism of its development, especially to show the anatomy of the responsible vessels associated with haemoptysis and its relationship with the lesion, which is crucial for the early intervention of those patients with haemoptysis whose medical treatment is unsatisfactory and who cannot tolerate surgical procedures. In recent years, with the rapid development of CT imaging equipment, the display of microstructures has reached the millimetre level; coupled with the continuous improvement of CT-related postprocessing technology, CTA has been recognized by increased physicians because of its powerful spatial display capability, especially for microvascular lesions, which can show the origin and course of dilated bronchial arteries and the relationship between vessels and lesions. It can also show whether there is extrapulmonary circulation involved in the haemoptysis supply so that the responsible vessels for the haemoptysis can be detected in a one-stop scan.

Bronchiectasis can be classified as congenital or secondary, congenital due to congenital bronchial dysplasia or other genetic disorders (e.g., pulmonary cystic fibrosis and congenital chondrodysplasia) and secondary due to recurrent bronchial infections and bronchial obstruction. The typical clinical presentation of bronchiectasis is frequent cough and profuse sputum production. Bronchial infections are the most common cause of bronchiectasis, and chronic inflammation leads to hypertrophy, distortion, and aneurysm formation in the bronchial arteries. Haemoptysis due to bronchiectasis occurs inconsistently, ranging from small amounts of sputum and blood to large amounts of haemoptysis, with approximately 50%–70% of patients having varying degrees of haemoptysis. In clinical practice, small amounts of haemoptysis tend to stop on their own after symptomatic treatment; if major haemoptysis occurs, it can lead to death due to ventricular rest or haemorrhagic shock, seriously endangering the patient's life. Vascular malformations are a common cause of haemoptysis and can be caused by congenital vascular malformations (e.g., congenital venous fistula), long-term chronic inflammatory infections, trauma, and diseases such as vasculitis. As the pressure in the pulmonary bronchial artery is higher than that in the pulmonary artery and pulmonary vein, rupture of the vessel occurs in the malformed vessel due to obstruction of blood flow leading to haemoptysis.

2. Related Work

The lungs are supplied with blood by two separate vascular systems, the bronchial arteries and the pulmonary arteries [7]. The pulmonary arteries supply 99% of the blood to the lungs, carry hypoxic blood at low pressure, and are involved in gas exchange in the alveolar capillaries; the bronchial arteries, on the other hand, carry oxygenated blood to the lungs at six times the pressure of the pulmonary arteries [8]. The bronchial arteries also provide the blood supply to the supporting structures of the lungs but are not generally involved in gas exchange [9]. The bronchial arteries coincide with the pulmonary arteries at the level of the alveoli and respiratory fine bronchi through several microvessels. In the fourth week of embryonic development, the 4th aortic arch gives off peribranchial vascular reticular tissue, which supplies the trachea and bronchi, and pulmonary vascular reticular tissue, which supplies the lung parenchyma [10]. Subsequently, the ventral root of the 6th aortic arch grows downward from the aortic bulb and fuses with the vascular network that grows dorsally from the pulmonary vascular reticular tissue to form the pulmonary arteries [11]. Thus, the primitive blood supply of the pulmonary vascular reticular tissue is transformed into the newly formed pulmonary artery, and the dorsal aortic vessels degenerate to form bronchial arteries. In early embryonic life, arteries of different origins on the pulmonary buds are connected to a common capillary network, and these capillary networks later differentiate into different arteries within and outside the lung that may remain connected to each other; that is, there are anastomoses between the pulmonary arteries and vessels of the body circulation, such as the bronchial arteries, these anastomosing branches are located in the bronchial wall, the pulmonary artery wall, and the pulmonary pleura,

RETRACTED

and during embryonic development, the pulmonary circulation must obtain blood through anastomosing branches with the body circulation and for gas exchange [12]. However, after birth, the body circulation has only bronchial arteries supplying blood to the intrapulmonary bronchi, and there are also many traffic branches between the bronchial arteries and pulmonary vessels at the capillary and precapillary levels, which become completely occluded as potential traffic after birth. The interaction between the two circulations through these anastomoses can result in both anatomic developmental abnormalities, that is, vascular malformations and so on, and anatomic snow remodelling, which can lead to altered hemodynamics.

In the past decade or so, with the rapid development of multilayer spiral CT technology, especially with the introduction of 64-layer and later 128-layer, 256-layer, and 320-layer CT, the temporal resolution and z-axis coverage of CT equipment have been greatly improved, making the image quality and diagnostic efficacy of coronary CTA reliably guaranteed. Literature reports have shown that the sensitivity of multilayer spiral CT coronary CTA is 82%–99%; the specificity is 93%–98% and has a high negative predictive value (95%–100%) compared with conventional coronary angiography, suggesting that coronary CTA has a very efficient and credible clinical value for the diagnosis and exclusion of coronary artery disease [13]. Physical examination is usually the first examination for patients, and by taking a detailed history and performing a thorough physical examination, the patient's condition can be quickly grasped and provide key clues for diagnosis [14]. At the time of intake, it is necessary to ask if there is a history of infection, respiratory system diseases, gastrointestinal symptoms, and bleeding disorders. The physical examination requires a detailed examination of areas such as the nose and throat [15]. The diagnosis of haemoptysis requires attention to differentiate haemoptysis from gastrointestinal bleeding and upper respiratory bleeding. Since upper respiratory and upper gastrointestinal bleeding can also be aspirated into the trachea and expelled from the mouth, it is easy to misdiagnose the same symptoms as haemoptysis. Gastrointestinal bleeding is usually dark red, often mixed with food debris, and is accompanied by nausea and vomiting [16].

Treatment for haemoptysis should be tailored to the cause, the patient's condition, and medical resources. The principles of emergency treatment for patients with haemoptysis are to keep the airway open and isolate the source of bleeding. The clinical first aid measures are to first clear the airway and encourage the patient to remove the blood in the airway by coughing to avoid asphyxia; otherwise, it is easy to cause hypoxemia due to respiratory distress, and tracheal intubation is needed immediately if the patient has respiratory distress. While clearing the blood in the airway, isolation of the source of bleeding is also needed to prevent blood clots from blocking the airway and affecting the patient's breathing. While carrying out the above emergency management measures, simultaneous treatment with haemostatic drugs can be used to speed up the formation of clots by reducing the blood flow rate and activating clotting factors. Also, in terms of care, patients with massive haemoptysis are asked to remain bedridden to avoid the aggravation of bleeding due to activity. Those with respiratory distress can be treated in a semirecumbent position and given oxygen.

3. Analysis of Bronchiectasis Macrohaemoptysis Monitored by Multirow CT Tomography

3.1. Multirow CT Tomography Monitoring Design for Large Bronchial Dilatation. After obtaining informed consent from the study subjects, 203 inpatients, aged 45–80 years, eligible for macrohaemoptysis from December 2019 to December 2020 in our hospital were selected according to the inclusion criteria. Each group of patients underwent bronchial artery embolization, and the bronchial artery embolus was a nonantigenic, absorbable medical gelatin sponge. Some of the study subjects used spring boluses with gelatin sponges. Inclusion criteria were as follows: generally, haemoptysis of ≥500 ml per day or more than 100 ml at one time was considered as massive haemoptysis [17]. The most common causes of haemoptysis are mainly pulmonary tuberculosis, bronchiectasis, primary bronchial carcinoma, blood-borne lung abscess, mycotoxin, and so on. The rare causes are chronic pneumonia, bronchial artery-pulmonary fistula caused by pulmonary embolism, coronary artery-bronchial fistula, arterial fistula, rupture of aortic aneurysm, and so on. In this trial, patients with daily haemoptysis >500 ml or haemoptysis more than 100 ml at one time, where the aetiology included pulmonary tuberculosis, bronchiectasis, vascular malformation, and pulmonary tumour, were selected, and the above-included subjects were diagnosed by a combination of clinical manifestations, laboratory tests, chest CT, and bronchial artery CTA. The vessels responsible for haemoptysis were all bronchial arteries treated with BAE. Exclusion criteria include patients with autoimmune diseases, severe hepatic, renal insufficiency, acrembolic diseases, and preoperative transfusion.

All patients underwent routine blood, coagulation, liver and kidney function, cardiac enzymology, calcitonin, electrolytes, CT scan of the chest, and CTA of the bronchial artery. Bronchial arteriography and BAE treatment: the CTA results of the bronchial arteries of the patients need to be read carefully before the procedure to understand the condition of the lesions and to clarify the location of the responsible vessels. After disinfection of the right inguinal region, local anaesthesia was performed, and the 5F vascular sheath was placed through a modified Salinger's procedure, and the 5F C3, 5F MiK, and 5F VERT catheters were introduced separately before the DSA machine fluoroscopy bronchial arteriography was performed. The diluted injection was injected through a high-pressure syringe, and angiography was performed. The responsible vessel was identified, and its alignment, diameter, terminal blood supply, and relationship with the surrounding vessels were observed. After identification of the responsible vessel, a step-by-step embolization of the diseased vessel was performed using microcatheter superselective angiography. The degree of embolization was determined by the presence

RETRACTED

of slowed blood flow or contrast spillage in the responsible vessel. After embolization is complete, the responsible vessel is again contrasted with iontophoresis injection, and successful embolization is judged by the fact that the terminal vessel is no longer visible. The patient was monitored throughout the procedure for cardiac, blood pressure, and finger pulse oxygen monitoring, and changes in vital signs and changes in subjective sensation were monitored [18]. After the procedure is completed, the puncture site is compressed for 15 minutes to stop bleeding, and the puncture site is bandaged with pressure. After returning to the ward, the patient needs to be placed in a flat position while the punctured limb is braked for 12 hours, and internal haemostasis and symptomatic treatment are required in case of bleeding, as shown in Figure 1.

Haemoptysis has numerous causes, not only respiratory diseases but also circulatory, hematologic, and traumatic diseases. The main underlying diseases of haemoptysis in our country include mainly bronchiectasis, pulmonary infections (tuberculosis, varicella, and other infections), and lung cancer. Another major underlying disease in Western countries is cystic fibrosis, which has ethnically inherited characteristics. Other rare underlying diseases include 5 areas: bronchopulmonary arteriovenous fistula, pulmonary isolation, ideology's disease (a rare submucosal arterial vasculopathy), anomalous somatic arteries supplying the basal segment of the normal lower lung, and true pulmonary aneurysms. Somatic arterial compensatory includes chronic pulmonary embolism, various congenital heart diseases such as tetralogy of Fallot, ventricular septal defect, patent ductus arteriosus, and pulmonary artery agenesis and pulmonary vein atresia; pulmonary contusions, stab wounds, rib fractures, postlung puncture biopsy, postradiofrequency ablation of lung tumours and postright heart catheterization chronic smoking haemoptysis; other rare diseases, such as pneumoconiosis, ruptured thoracic aortic aneurysm, idiopathic pulmonary hypertension, pulmonary endometriosis, and pulmonary-renal haemorrhagic syndrome.

The goal of minimally invasive techniques is to accomplish the same surgical results as traditional surgery, but with better visual detail, less tissue trauma, and smaller incisions. The advantages of minimally invasive techniques include less tissue damage (presumably with less probability of pain and inflammation), less perioperative bleeding, less need for postoperative analgesia, faster recovery of normal function, shorter hospital stays, and less reliance on rehabilitation. However, minimally invasive surgery cannot be performed in the presence of certain conditions, such as hemodynamic instability, sepsis, and coagulation disorders. In the past, the assessment of bronchial circulation usually requires invasive imaging of angiography to determine the location of bleeding because the origin, number, cointervention, course, diameter, and course of BA vary from person to person. The minimally invasive surgical technique involves the surgeon entering the patient from the dorsal side of the thoracolumbar segment, separating the spinal muscles at the location of the lesion, using a Casper cervical retractor to open and secure the wound, endoscopic access to the wound, endoscopic imaging to visualize the surgical site, and a long-necked microscraper to perform a hemisection of the intervertebral foramen for spinal cord decompression. Disc herniation/extrusion and subsequent spinal cord compression are common causes of clinical motor deficits in dogs. Chronic disc herniation is more severe because the disc herniation may be hard and dense and often adheres to the dura and intervertebral venous plexus. These factors make removal by conventional surgical methods difficult while increasing the risk of medically induced spinal cord injury and venous sinus bleeding. Minimally invasive techniques offer a way to treat chronic disc herniations as well as remove some of the remaining disc material left in the interspace while reducing spinal cord manipulation and allowing for nerve root inspection. Retrospective studies have demonstrated the feasibility of this technique, as shown in Figure 2.

The line generator is mainly connected to the cathode electron generator by a high-voltage power supply to generate high-voltage electrons. Electrons collide with the anode tungsten target under the acceleration of high pressure, and about 1% of its kinetic energy is converted into X-rays. The generator is divided into two types of fixed and rotating anode tubes, with the long axis of the fixed tube parallel to the detector and the long axis of the rotating tube perpendicular to the detector. Fixed and rotating anodes are used in different generations of CT. Collimators are used in CT to ensure good image quality and to reduce unnecessary radiation doses to the patient. The collimator is used to limit the angular distribution of radiation reaching the detector assembly and serves to spatially position it. It consists of a set of collimator blades made of highly absorbent material such as tungsten or molybdenum. The openings of these vanes are adjusted according to the selected slice width and the size and position of the focal spot. The slice thickness of a single layer CT is defined. The filter serves to constrain the X-rays emitted by the X-ray tube into a hard beam of uniform energy distribution. It is used to remove soft X-rays and low energy X-rays that radiate and scatter doses strongly to the patient but have less effect on the detection signal. Flat filters made of copper or aluminium are placed between the X-ray source and the patient. They allow a uniform distribution of the X-ray spectrum over the entire field of view. Since the cross section of the patient is mostly elliptical, these filters are thinner in the middle and thicker at the edges, making them hardly attenuate the radiation in the centre and have a strong signal at the periphery. In some machines, comb collimators near the detector array are used to reduce the effective detector element width and thus increase the achievable geometric resolution [19]. Detectors are energy conversion devices; their role is to detect analog signals for digital-to-analog signal conversion, converting analog signals to digital signals. The most important characteristics of detectors are high conversion efficiency, stability, fast response, and accuracy. Detectors are generally classified as gas detectors and solid-state detectors.

Selective bronchial arteriography, with its high spatial resolution, clearly shows the main trunk of the bronchial arteries and their branches, and it is worth emphasizing the digital subtraction angiography DSA technique, which has

RETRACTED

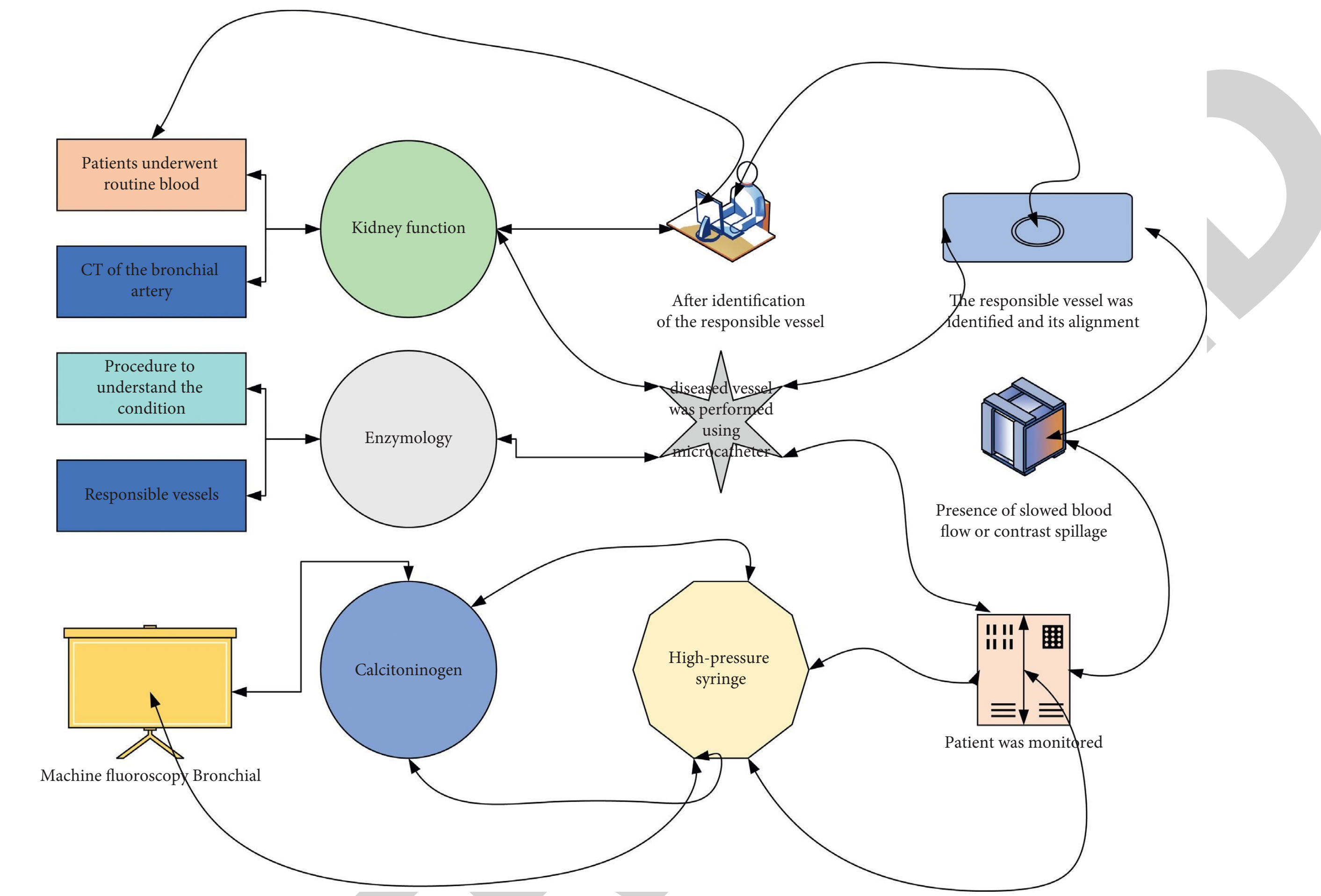

Figure 1: CT tomography monitoring framework.

been the gold standard in the in vivo study of bronchial arteries. Because haemoptysis can be life-threatening and affect the quality of life of patients, it is particularly important to understand its aetiology and the mechanism of its development. To show clearly the anatomy of the responsible blood vessels related to haemoptysis and its relationship with the disease is not effective for those medical treatments. Early interventional treatment of ideal patients with haemoptysis who cannot tolerate surgery is very important. It has obvious advantages in the direction of interventional treatment; for example, BAE, which is considered the main method of haemostasis in cases where medical treatment is ineffective and surgical procedures cannot be tolerated, is increasingly recognized clinically because of its rapid haemostasis, quick recovery, definite efficacy, and minimal trauma. DSA, as a confirmatory means of BAE, is considered the gold standard for the diagnosis of the vessel responsible for haemoptysis, and after clarifying the vessel responsible for haemoptysis, timely treatment with BAE treatment is very important for patients with haemoptysis. However, when selective bronchial arteriography is performed to reveal all bronchial arteries and some nonbronchial body arteries involved in the blood supply of the disease, the operation time, contrast dosage, and radiation dose are increased, which may lead to suboptimal intervention or secondary interventions if they are not detected or missed in time.

3.2. Experimental Design of Interventions for Bronchiectasis Macrosomia. CT bronchial arteriography: all patients must have 4 cardiac leads attached to the anterior chest wall in a standard position and a localization and enhancement scan performed after the normal appearance of heart rate. The scope of the scan is generally from top to bottom, from the entrance of the thorax to the level of the lumbar I vertebrae, and from the foot side to the head side. The scan parameters were tube ball voltage 80–120 kV (conventional 120 kV), current 250 mAs (increase milliamperes for body mass index over 28), layer thickness 1.0 mm, layer spacing 1.0 mm, and rotation speed 0.27 s; tiropramide (370 mg/ml) was injected via the anterior elbow vein and the total amount varied according to the patient's body mass (body mass ≤70 kg). Monitoring was started with a 15 s delay after drug injection, the scan was started when the region of interest reached the triggerable threshold, and the patient was instructed to hold his breath at the same time. The pitch of the chest biphasic enhanced CT is 0.16, the current is 250 mAs, the tube voltage is 120 kV, the matrix is 512 × 512, and the frame speed is 0.27 s/week. Tiropramide (370 mg/ml) was injected via the

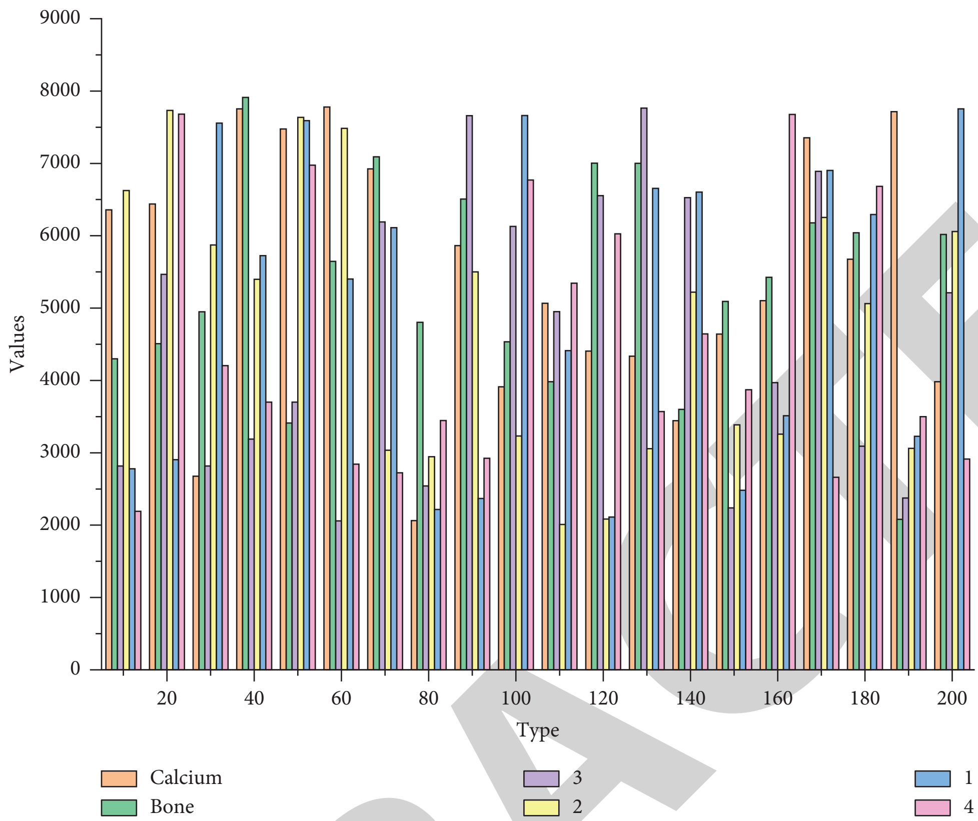

Figure 2: Bronchial dilatation macromonitoring.

anterior elbow vein and scanned from the level of the cervical 7 to lumbar I vertebrae, from the cephalad side to the pedicle side. The scan was started when the area of interest reached the triggerable threshold, and the patient was simultaneously instructed to hold his breath. At the end of the scan, the original image was reconstructed in the background, and the image layer thickness and layer spacing were 1.0 mm.

The degree of haemoptysis caused by bronchiectasis is inconsistent, from a small amount of sputum to a large amount of haemoptysis, and about 50%–70% of patients have different degrees of haemoptysis. Bronchial arteries originating from the thoracic aorta or intercostal arteries between the levels of the thoracic 5 and thoracic 6 vertebrae were coded as in situ arteries, and those originating beyond the expected level of origin (i.e., outside the descending aorta at levels T5 to T6) or from branch vessels of the thoracic aorta were coded as anomalous or ectopic openings, as shown in Figure 3.

CT has largely overturned traditional angiographic techniques. CT has been increasingly used in a wide range of clinical scenarios because it is noninvasive and easily accessible, combined with low radiation dose capacity and low noise, and provides good detail to determine the location and nature of lesions, driven by advances in technology and data showing improved results, and there is now a growing body of evidence that continues to refine and support the central role of CT in clinical care. The clinical application of CT is now gradually expanding to many noncoronary cardiovascular diseases and can demonstrate the spatial anatomy and lesion characteristics of BA from a variety of angles quite perfectly due to the good submillimetre isotropic spatial resolution and contrast resolution, which allows multiplanar reconstruction in any plane; also, CT relies on timed, fast volume scans with an open scanning field and wide availability. The ability to acquire images continuously during the first circulation venous contrast through the vessel of interest allows visualization of the aorta and other vascular systems such as pulmonary arteries, veins, and adjacent parenchymal organs in a single scan, aiding in the diagnosis and identification of other pathologies that may explain nonspecific symptoms.

Because of the realistic morphology and colour of VR, its display is closer to the anatomical structure, and it can image various arterioles, soft tissues, and bone structures in three dimensions, so it can not only visually and three-dimensionally display the origin and opening position of BA but also display the three-dimensional relationship between bronchial arteries and adjacent surrounding tissues in multiple angles and directions and restore the overall shape of bronchial arteries and their course, which can provide exquisite anatomical images, but it has a high demand on the intravascular diameter and contrast injection pressure, flow rate, and concentration. In this group, 17 cases of MPR + VR could not identify the origin of BA, and only 108 branches of BA alignment could be completely displayed, which was considered to be related to its small diameter (1~2 mm), tortuous alignment, and insufficient filling of contrast agent

RETRACTED

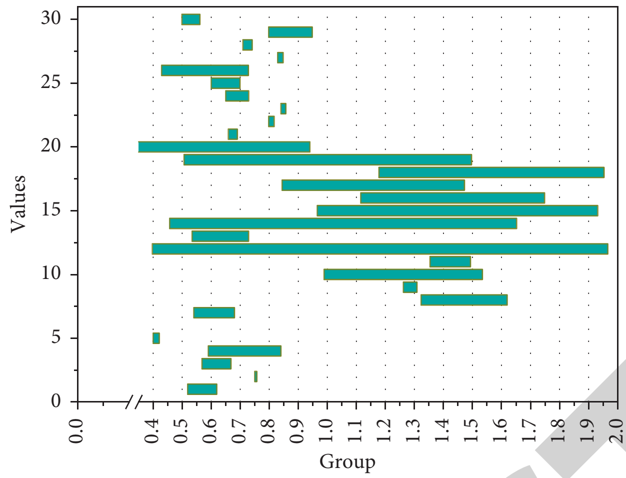

Figure 3: Results of display of bronchial artery origin.

RETRACTED

in the diameter, resulting in a reduced display of bronchial arteries; it may also be because the post-VR cutting operation process is very complicated and related to the operator's handling, and once the wrong identification is made, it is very easy to cut off the relevant [20]. Therefore, it is important to be careful during the postcropping process and to focus on the cross-axis images.

CPR is a special form of 2D reconstruction, which is of great significance for tracing the panoramic view of the BA, showing the curved vessels clearly by "spot seeding" and observing the contrast filling in the lumen. However, the accuracy and objectivity of the image are dependent on the image processor, and the wall may be jagged if the lines are not smooth. There were 8 cases in our group in which the origin of BA could not be determined by MPR + CPR, which may be related to the fact that BA is slenderer or the patient's respiratory and heart rate artifacts produce artifacts on BA.

Xu Xiaoping performed FIB and D-dimer assays on 150 patients with non-small-cell lung cancer grouped and found that the levels of FIB and D-dimer were significantly higher in the group with lung cancer complicated by pulmonary artery embolization than in the group with lung cancer and the levels of both substances were significantly higher in lung cancer patients than in healthy controls. BAE injects embolic material into the bronchial artery to occlude the vessel, generally by directly blocking the rupture of the vessel and haemostasis or by reducing pressure and blood flow in the distal vessel, which contributes to platelet aggregation at the distal rupture to form a thrombus to seal the rupture. In malformed blood vessels, the blood flow is blocked and the blood vessels rupture causing massive haemoptysis. In the present study, both FIB and D-dimer increased significantly in patients after surgery compared to preoperative levels, and the concentrations were positively correlated with the efficacy of surgery, suggesting that surgery in BAE activates the coagulation system and thrombus formation contributes to sealing the ruptured vessel, which is positively correlated with the efficacy of surgery. The results of this study indicate that fibrinogen and D-dimer concentrations can be used as clinical indicators to assess recurrent haemoptysis after BAE surgery, which has the advantages of being rapid, accurate, and inexpensive, does not require moving the patient, and is suitable for wide clinical application, as shown in Figure 4.

FIB and D-dimer can be detected by blood collection, which is simple to obtain and does not pose a serious risk to patients [21]. If FIB and D-dimer can be used to evaluate postoperative recurrent haemoptysis, with their advantages of simplicity, minimally invasive, and safety, clinicians can be guided to intervene promptly in patients at risk of recurrent haemoptysis and improve the cure rate. In this study, we found that patients' FIB and D-dimer concentrations were significantly higher after surgery compared with those before surgery, while there were significant differences between different efficacy groups, and the concentrations in the superior group were significantly higher than those in the poor group, indicating that both substances can be used as effective indicators to evaluate the effect of BAE.

4. Analysis of Results

4.1. CT Tomography Monitoring Performance Results. The bronchial arterial circulation has significant interindividual variability. The origin of the BA is thought to be either at the T5 and T6 vertebral levels of the descending aorta in the case of an in situ origin or at the level of a branch vessel from the thoracic aorta in the case of an ectopic origin, in addition to the expected origin (i.e., other than the T5 to T6 level of the descending aorta). Bronchial ectopic arteries originate most frequently from the thoracic aorta, aortic arch, subclavian artery, cephalic trunk, internal thoracic artery, and coronary arteries. For patients with haemoptysis exceeding 100 ml at a time, the causes include tuberculosis, bronchiectasis, vascular malformations, and lung tumours. The above-included subjects were diagnosed with comprehensive clinical manifestations, laboratory examinations, chest CT, and bronchial artery CTA. A total of 13 bronchial ectopic arteries were presented in the tumour group of this study, including 7 on the right and 6 on the left. Although the type VI BA was only 4.0%, it is critically important for finding BA during interventional procedures and plays a guiding role to avoid

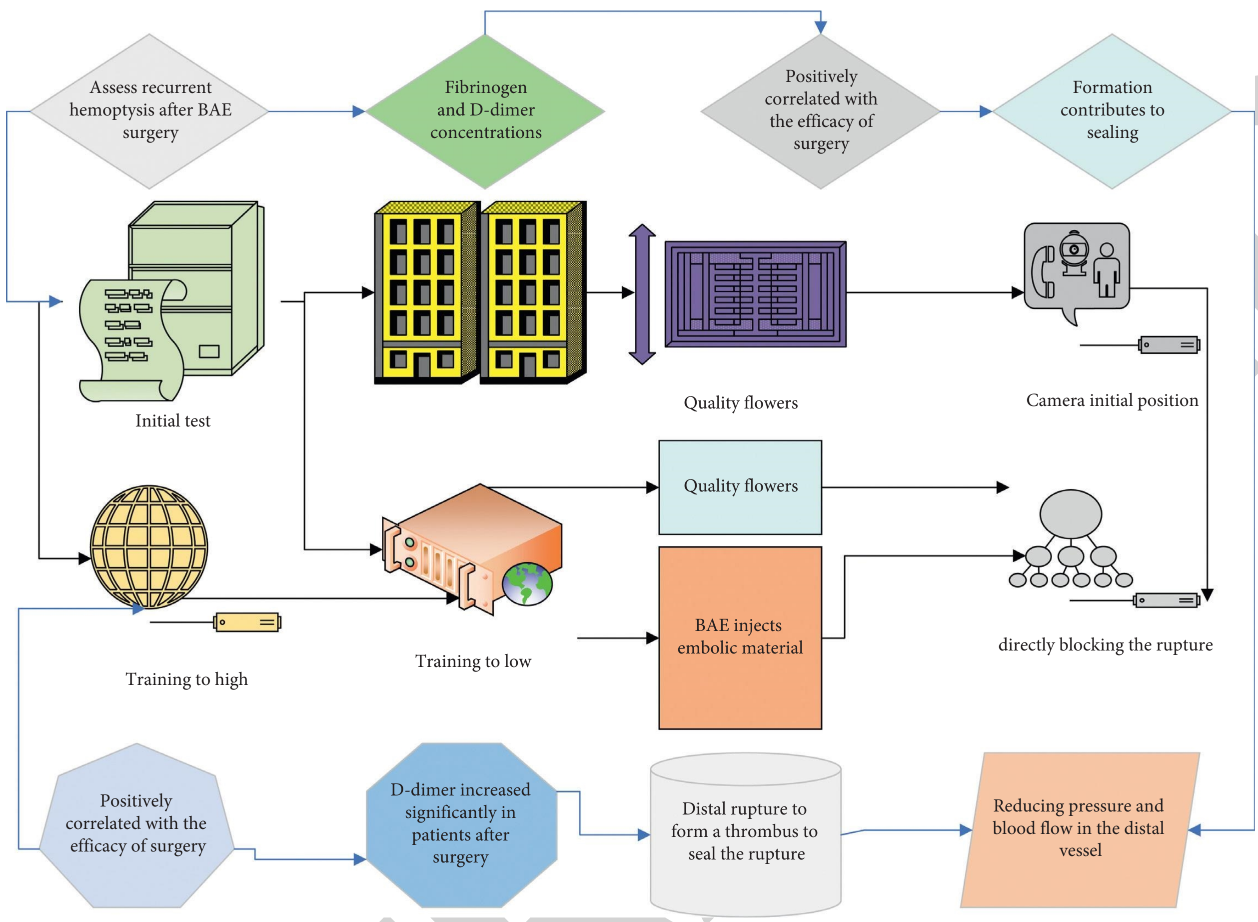

Figure 4: Interventional therapy experiment.

missing target vessels. For example, if a lung cancer or haemoptysis patient is successfully treated with interventional embolization and the mass enlarges or haemoptysis occurs again not long after, this is one of the possible causes. An issue of concern is that either BA originating from the coronary arteries or undercrossing with them is not an isolated case and has been reported in some cases, as Moberg and colleagues thought that some of these variants are present at birth but rarely lead to associated hemodynamic changes in humans.

At the same time, the radiation dose to the patient is reduced. The long scanning range, from the thoracic inlet to the lumbar I vertebral level, can be completed in a single scan, thus significantly expanding the examination range and depth of study. The submillimetre isotropic spatial resolution and contrast resolution have been greatly improved, and vessels with a diameter of less than 1 mm can be accurately displayed, thus making BA easier to develop. With powerful image postprocessing functions, multiplanar reconstruction of images in any plane becomes a reality. Previously, many researchers used MSCT chest double-phase enhancement scan to acquire the original image and then used MPR, MIP, VR, CPR, and other postprocessing methods to present the opening, number, and developmental variation of BA. The most important characteristics of the detector are high conversion efficiency, stability, fast response, and high accuracy. Detectors are generally divided into gas detectors and solid-state detectors. The introduced EWB 4.0.2.145 workstation is known for its display of images with high contrast resolution and has the advantage of one-click debulking and automatic extraction of blood vessels during postprocessing, which can provide convenient operation for radiologists; then, the number of bronchial arteries is determined using MPR thin-layer axial images, the origin and opening orientation of BA are observed on MIP with a layer thickness of 3 mm, BA is observed on MIP images with a layer thickness of 30 mm MIP image, and the z-axis orientation of the BA is observed at the beginning of the descending aorta on the VR image. This combination of postprocessing techniques helps to guide successful catheter cannulation and rapid embolization of bronchial ectopic arteries. As can be seen, the exploration and innovation of postprocessing procedures are indispensable to obtain excellent projections such as BA walk, but no procedures specifically for BA imaging have yet emerged, as shown in Figure 5.

In the initial phase of coronary CTA imaging, the clinical routine is to use a retrospective spiral scan with synchronized ECG monitoring for imaging, during which the CT device performs a spiral scan at a low pitch while the scan bed is continuously fed at a low speed to complete the acquisition of all cardiac data, while the CT device

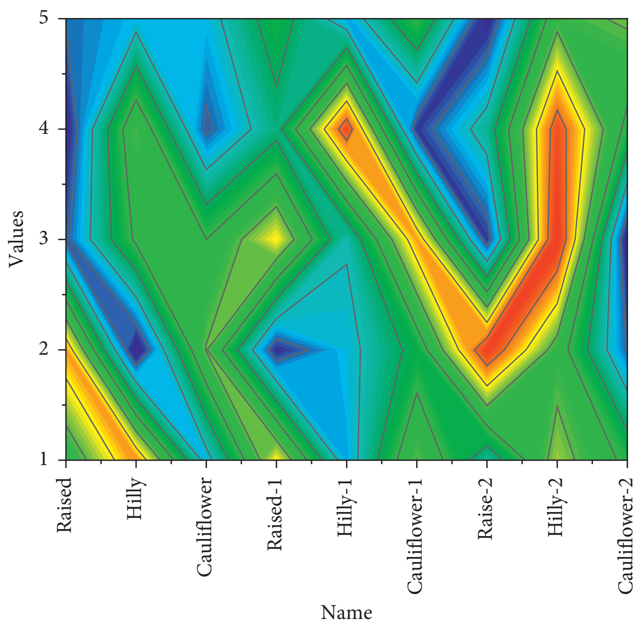

Figure 5: Distribution of severity of clinical signs.

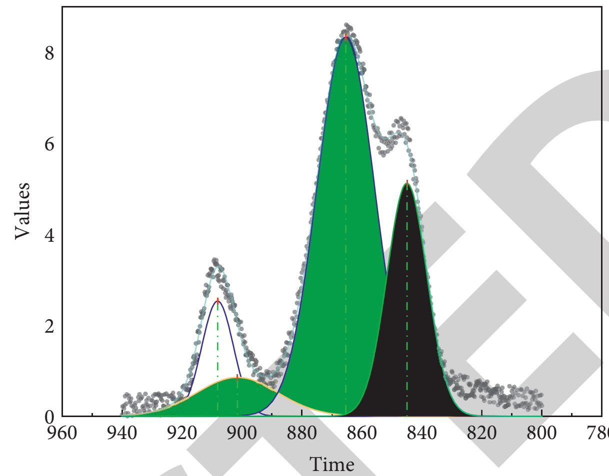

Figure 6: Comparison of success rates.

automatically records the patient's ECG information during the scan and after the completion of the scan. After the scan is completed, this ECG information is used to guide the reconstruction of the image data and the selection of the optimal image phase. This scanning modality allows for multiphase data reconstruction, a wide range of adaptations for heart rate and rhythm, and the ability to improve the image quality of coronary CTA by editing the ECG in patients with arrhythmias. However, this imaging modality also has the disadvantage that, to obtain a good image quality that satisfies the diagnosis, it is necessary to maintain a low bed feed speed during the spiral scan to achieve a high degree of overlap between the spiral data, and therefore this imaging modality requires a high radiation dose, as shown in Figure 6. When selective bronchial arteriography wants to show all bronchial arteries and some nonbronchial body arteries that are involved in the blood supply of the disease, the operation time, contrast medium dosage, and radiation dose will all increase. If it is not found in time, it may lead to unsatisfactory interventional treatment effects or the need for secondary interventional treatment.

At a reduction of nearly 1/3 of the radiation dose, there is no compromise in coronary image quality or diagnostic power. At 256-layer spiral CT, the use of the dose iterative reconstruction algorithm allows for a more than 50% reduction in radiation dose for retrospective spiral scan coronary CTA imaging. In dual-source CT, using the IRIS iterative reconstruction algorithm for coronary CTA imaging at a tube voltage of 80/100 kV resulted in a 62% reduction in radiation dose compared with coronary CTA imaging at a tube voltage of 120 kV using the conventional filtered inverse projection algorithm, while the noise level of the images was essentially the same and showed better for stents than the latter. For second-generation 128-layer dual-source CT, moreover, the SAFIRE iterative reconstruction method has been used to perform prospective large-pitch helical-scan coronary CTA imaging, which reduced the radiation dose to an ultralow level of less than 0.1 mSv. In addition to low radiation dose capability and low noise, it can also provide good details to determine the location and nature of the lesion, so it is increasingly used in clinical scenarios. This is due to the advancement of technology and the improvement of display results.

4.2. Experimental Results of Interventions for Bronchiectasis Macrosomia. Selective bronchial arteriography, with its high spatial resolution, clearly shows the main trunk of the bronchial arteries and their branches, and it is worth emphasizing the digital subtraction angiography DSA technique, which has been the gold standard in the in vivo study of bronchial arteries. DSA is considered the gold standard for diagnosing the responsible vessel for haemoptysis as a means of confirming the diagnosis of BAE. Patients with haemoptysis need to receive timely treatment after identifying the responsible vessel for haemoptysis. Selective bronchial arteriography is to show that all bronchial arteries and some nonbronchial arteries are involved in the blood supply of the disease. Selective bronchial angiography showed that the operation time, contrast dose, and radiotherapy dose all increased, and if they are not detected or missed in time, it may lead to unsatisfactory intervention or secondary intervention, as shown in Figure 7.

Pulmonary vascular diseases include nodular aortitis; diseases of the extrapulmonary system include cardiogenic hemoptysis and endometriosis. Among the 106 patients in this subject, 60 cases of bronchiectasis, 13 cases of bronchiectasis with old tuberculosis, 4 cases of destroyed lung, 8 cases of lung cancer, 8 cases of pneumonia, 2 cases of bronchial artery malformation, 1 case of idiopathic aortitis, and 10 cases of unknown cause were diagnosed. Most etiologists were still dominated by infectious and inflammatory airway diseases and cancer. The aorta and other vascular systems such as pulmonary arteries, veins, and adjacent parenchymal organs can be seen in a single scan, which helps in the diagnosis and identification of other pathologies, and

RETRACTED

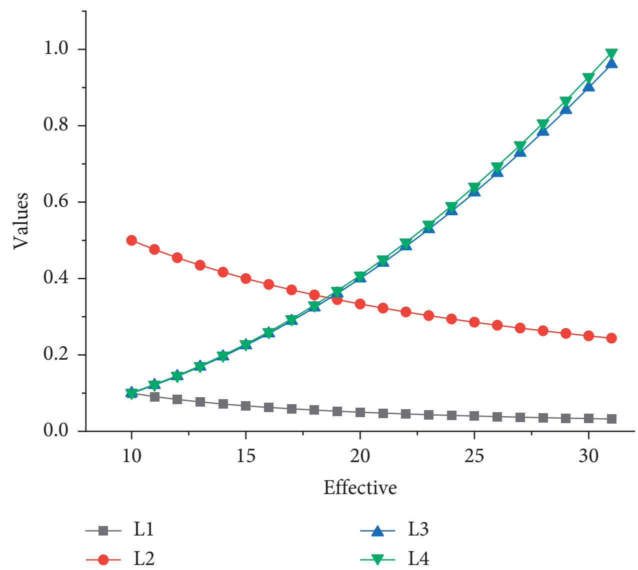

Figure 7: Preliminary results of treatment.

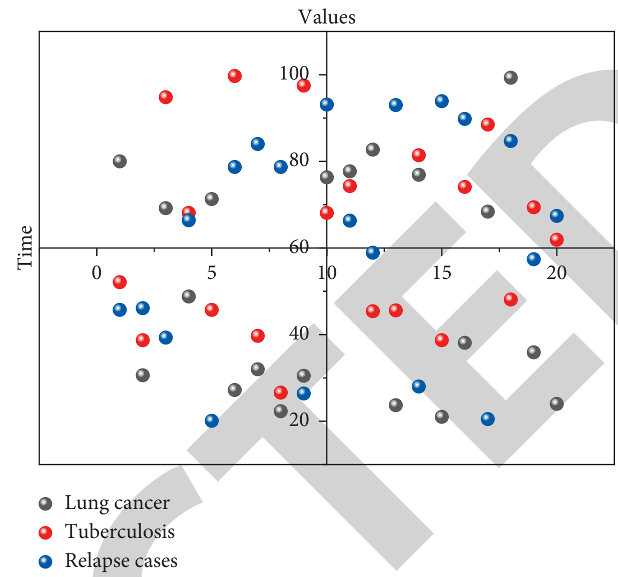

Figure 8: Statistics of recurrence cases at six months in the postoperative superiority group.

may explain nonspecific symptoms. It is generally believed that the imaging of abnormal BA is mainly of three types, showing obvious tortuous dilatation of the main trunk and poorly displayed peripheral branches, which are mostly seen in bronchial dilatation, and the degree of dilatation is positively correlated with the duration of the disease. BA main trunk and branches are dilated and thickened and may even reach below the lung segment, and the blood supply of multiple branches of BA can traffic anastomose with each other. The BA trunk and branches may be thickened and even reach below the lung segment. There are BA and extrapulmonary body circulation arteries supplying blood to the same lesion in the lesion area, and the extrapulmonary body circulation communicates with the intrapulmonary BA, which is mainly seen in tuberculosis. In the present study, bronchial artery CTA had a high quantitative ability to detect BA responsible for haemoptysis (93.55%, 145/155) but differed from DSA in terms of different imaging presentations. The direct signs of imaging macrohaemoptysis were manifested by spillage of contrast agent from the responsible vessel and indirect signs by thickening and distortion of the responsible vessel, aneurysmal dilatation, increased distal branch vascular disorder, B-P shunt or body-pulmonary circulation shunt, and aneurysm formation, as shown in Figure 8.

FIB is an acute-phase reactive protein, a coagulation factor, present in plasma, with an important role in platelet aggregation and changes in blood viscosity. Clinical studies have found that hyperfibrinogenaemia predicts the long-term risk of death after infarction. Statistics on European patients aged 40–79 years have found that FIB is associated with the long-term risk of death after cerebral infarction. Elevated concentrations of FIB Elevated FIB can be an independent risk factor for the development and progression of coronary artery disease. D-Dimers are degradation products resulting from the hydrolysis of fibrin monomers by fibrinolytic enzymes after the formation of crosslinks. The concentration of D-dimers in the peripheral blood of healthy individuals is very low and increases significantly in patients with thrombosis. D-Dimers can indicate fibrinolysis, which does not occur during primary fibrinolysis, and is significantly increased during thrombosis and secondary fibrinolysis, and its elevation can increase thrombin production. It has been shown that plasma D-dimer levels are significantly elevated in patients with acute cerebral infarction. In this study, there were 13 ectopic bronchial arteries in the tumour group, including 7 on the right side and 6 on the left side. Although type VI BA is only 4.0%, it is extremely important to find BA during interventional surgery. It plays a certain guiding role and can avoid missing target blood vessels.

Second, in terms of intraoperative contrast dosage, patients in group A underwent CTA preoperatively, and the operator could selectively cannulate normal and ectopic BAs directly by observing the reconstructed images after postprocessing, without the need to do thoracic aortography to clarify the location and number of responsible BAs. Group B underwent thoracic aortography before cannulation and then selectively cannulated after the location and number of responsible BAs were clarified; however, only relying on thoracic aortic angiography has limitations. However, simple thoracic aortography has limited ability to detect certain ectopic BAs, so an extended angiogram is also needed to find possible supply arteries. Finally, group A was higher than group B in terms of first embolization success rate.

5. Conclusion

Although bronchial artery vascular imaging has not been technically successful enough for widespread use, the application of 256-layer spiral CT cardiac gated scanning for bronchial artery vascular imaging is an ideal imaging modality, and the use of MPR + MIP is a stepwise combined postprocessing method that provides a good representation

RETRACTED

RETRACTED

of the anatomy of the bronchial artery, including its origin and general course. Spiral CT to familiarize oneself with the depiction of bronchial arteries can provide useful information and guidance for bronchial artery interventions, and the anatomic information it provides can help guide successful catheter cannulation and rapid embolization of bronchial ectopic arteries, as well as depicting and detect abnormal nonbronchial systemic arteries and helping focus on the artery in question. The use of multirow spiral CT before angiography reduces the failure rate of interventional catheter insertion and the number of patients requiring surgical intervention, reduces imaging time, contrast dosage, and radiation dose, and reduces false embolization and postembolization complications, such as transverse myelitis. Like reconstructive CT, it will show more information about the responsible vessels and can provide interventionalists with rapid morphological and spatial anatomical information about the responsible vessels associated with haemoptysis, which can play an important role in the diagnosis and treatment of patients and interventional embolization. In clinical practice, the scanning protocol of bronchial artery CT can be optimized to provide more comprehensive and clear images for surgical or interventional treatment of chest diseases.

Data Availability

The data used to support the findings of this study are available from the corresponding author upon request.

Conflicts of Interest

The authors declare that there are no conflicts of interest.

Acknowledgments

This work was supported by the Science and Technology Research Project of the Liaoning Education Department in 2020: Mechanism Research of CircFARSA as ceRNA Promotes Proliferation and Metastasis of NSCLC through mir-330-5p/EMP1 Molecular Axis (JYTJCZR2020057).

References

[1] Y. Zhao, Y. Ge, and Q. He, "Preoperative staging diagnosis of colorectal cancer based on multi-row spiral CT," *Journal of Medical Imaging and Health Informatics*, vol. 11, no. 6, pp. 1599–1607, 2021.

[2] W. Angthong, K. Jiarakoop, and K. Tangtiang, "Differentiation of benign and malignant ampullary obstruction by multirow detector CT," *Japanese Journal of Radiology*, vol. 36, no. 8, pp. 477–488, 2018.

[3] L. Jin, Y. Gao, A. Q. Jiang, Z. Li, P. Wang, and M. Li, "Can the coronary artery calcium score scan reduce the radiation dose in coronary computed tomography angiography?" *Academic Radiology*, vol. 28, no. 3, pp. 364–369, 2021.

[4] P. Cegła, A. Ciepłucha, M. Pachowicz, B. Chrapko, T. Piotrowski, and M. Lesiak, "Nuclear cardiology: an overview of radioisotope techniques used in the diagnostic workup of cardiovascular disorders," *Kardiologia Polska*, vol. 78, no. 6, pp. 520–528, 2020.

[5] H. Nagata, K. Murayama, S. Suzuki et al., "Initial clinical experience of a prototype ultra-high-resolution CT for assessment of small intracranial arteries," *Japanese Journal of Radiology*, vol. 37, no. 4, pp. 283–291, 2019.

[6] S. Mao, D. Li, D. Zhao et al., "Quantitative coronary calcium burden using ct scan with "as low as reasonably achievable" radiation dose and maintaining acceptable image quality," *Journal of Cardiovascular Computed Tomography*, vol. 14, no. 3, pp. S57–S58, 2020.

[7] C. G. Colip, V. Gorantla, C. A. LeBedis, J. A. Soto, and S. W. Anderson, "Extremity CTA for penetrating trauma: 10-year experience using a 64-detector row CT scanner," *Emergency Radiology*, vol. 24, no. 3, pp. 223–232, 2017.

[8] J.-Y. Hwang, K. S. Choo, Y. Y. Choi et al., "Subjective and objective image differences in pediatric computed tomography cardiac angiography using lower iodine concentration," *Pediatric Radiology*, vol. 47, no. 6, pp. 701–709, 2017.

[9] C. Zhang, M. Sun, Y. Wei, H. Zhang, S. Xie, and T. Liu, "Automatic segmentation of arterial tree from 3D computed tomographic pulmonary angiography (CTPA) scans," *Computer Assisted Surgery*, vol. 24, no. sup2, pp. 79–86, 2019.

[10] D. Spronk, Y. Luo, C. R. Inscoe, Y. Z. Lee, J. Lu, and O. Zhou, "Evaluation of carbon nanotube x-ray source array for stationary head computed tomography," *Medical Physics*, vol. 48, no. 3, pp. 1089–1099, 2021.

[11] A. Devaraj, B. van Ginneken, A. Nair, and D. Baldwin, "Use of volumetry for lung nodule management: theory and practice," *Radiology*, vol. 284, no. 3, pp. 630–644, 2017.

[12] M. M. Dawoud, A. A. Salama, T. A. El-Diasty, and M. Alhefnawy, "Diagnostic accuracy of computed tomography angiography in detection of post traumatic renal vascular injury," *The Egyptian Journal of Radiology and Nuclear Medicine*, vol. 49, no. 1, pp. 232–238, 2018.

[13] X. Lei, "Application of CT imaging in the analysis of thigh muscle morphology of athletes," *Journal of Medical Imaging and Health Informatics*, vol. 10, no. 4, pp. 853–858, 2020.

[14] T. K. Nowicki, K. Markiet, and E. Szurowska, "Diagnostic imaging of hepatocellular carcinoma - a pictorial essay," *Current Medical Imaging Reviews*, vol. 13, no. 2, pp. 140–153, 2017.

[15] L. Yang, S. Zhang, R. Gu, C. Peng, and M. Wu, "Imaging features of primary spinal osseous tumors and their value in clinical diagnosis," *Oncology letters*, vol. 17, no. 1, pp. 1089–1093, 2019.

[16] S. Lakshmanan, M. Holda, T. Joshi et al., "Measurement of liver fat by A novel 3d segmentation method of liver on non contrast cardiac ct in evaporate cohort: methods and reproducibility," *Journal of Cardiovascular Computed Tomography*, vol. 15, no. 4, pp. S37–S38, 2021.

[17] M. Boussoussou, B. Vattay, B. Szilveszter et al., "The role of left atrial wall thickness and pulmonary vein anatomy in success of pulmonary vein isolation using the close protocol," *Journal of Cardiovascular Computed Tomography*, vol. 15, no. 4, pp. S38–S39, 2021.

[18] M. K. A. Karim, A. Sabarudin, N. A. Muhammad, and K. H. Ng, "A comparative study of radiation doses between phantom and patients via CT angiography of the intra-/extra-cranial, pulmonary, and abdominal/pelvic arteries," *Radiological physics and technology*, vol. 12, no. 4, pp. 374–381, 2019.

[19] K. T. Flicek, W. VanBuren, K. Dudiak et al., "Borderline epithelial ovarian tumors: what the radiologist should know," *Abdominal Radiology*, vol. 46, no. 6, pp. 2350–2366, 2021.

[20] J.-B. Zhang, X.-Y. Li, W. Sun et al., "Multimode computed tomography evaluation of the efficacy and safety of an

Hindawi
Journal of Healthcare Engineering
Volume 2021, Article ID 4066415, 11 pages
https://doi.org/10.1155/2021/4066415

Research Article

Compressed Sensing Image Reconstruction of Ultrasound Image for Treatment of Early Traumatic Myositis Ossificans of Elbow Joint by Electroacupuncture

Yi Zhu,[1] **Mengyuan Sheng**,[2] **Yuanming Ouyang**,[3] **Lichang Zhong**,[4] **Kun Liu**,[5] **Tan Ge**,[6] **and Yaochi Wu**[1]

[1]*Department of Traumatology Acupuncture and Massage, Sixth People's Hospital Affiliated to Shanghai Jiaotong University, Shanghai 200233, China*
[2]*Innovation Base Hospital of Jiangxi University of Traditional Chinese Medicine, Jiangxi, Nanchang 330004, China*
[3]*Department of Orthopaedics, Sixth People's Hospital Affiliated to Shanghai Jiaotong University, Shanghai 200233, China*
[4]*Department of Medical Ultrasonics, Sixth People's Hospital Affiliated to Shanghai Jiaotong University, Shanghai 200233, China*
[5]*School of Information Engineering, Shanghai Maritime University, Shanghai 201204, China*
[6]*Department of Preventive Medicine, Guangming Traditional Chinese Medicine Hospital, Shanghai 201399, China*

Correspondence should be addressed to Tan Ge; badboygetan@163.com and Yaochi Wu; wuyaochi@sjtu.edu.cn

Received 28 September 2021; Accepted 1 November 2021; Published 7 December 2021

Academic Editor: Kaijian Xia

Copyright © 2021 Yi Zhu et al. This is an open access article distributed under the Creative Commons Attribution License, which permits unrestricted use, distribution, and reproduction in any medium, provided the original work is properly cited.

This article conducts a retrospective analysis of 500 patients with posttraumatic elbow dysfunction admitted to our department from March 2019 to September 2020. The average time from injury to operation is 11 months (2–20 months). We adopt a personalized treatment method to completely remove the hyperplastic adhesion tissue and heterotopic ossification around the joint, remove part of the joint capsule and ligament, and release it to achieve maximum function. After the operation, an external fixator was used to stabilize the loosened elbow joint, and the patient was guided to perform rehabilitation exercises with the aid of a hinged external fixator, and celecoxib was used to prevent heterotopic ossification. Mayo functional scoring system was used to evaluate the curative effect before and after surgery. The rapid realization of ultrasound imaging under the framework of compressed sensing is studied. Under the premise of ensuring the quality of ultrasound imaging reconstruction, the theory of ultrasound imaging is improved, and a plane wave acoustic scattering ultrasound echo model is established. On this basis, the theory of compressed sensing is introduced, the mathematical model of compressed sensing reconstruction is established, and the fast iterative shrinkage thresholding algorithm (FISTA) of compressed sensing reconstruction is improved to reduce the computational complexity and the number of iterations. This article uses FISTA directly to reconstruct medical ultrasound images, and the reconstruction results are not ideal. Therefore, a simulation model of FISTA training and testing was established using the standard image library. By adding different intensities of noise to all images in the image library, the influence of noise intensity on the quality of FISTA reconstructed images is analyzed, and it is found that the FISTA model has requirements for the quality of the images to be reconstructed and the training set images. In this paper, Rob's blind deconvolution restoration algorithm is used to preprocess the original ultrasound image. The clarity of the texture details of the restored ultrasound image is significantly improved, and the image quality is improved, which meets the above requirements. This paper finally formed a reconstruction model suitable for ultrasound images. The reconstruction strategy verified by the ultrasound images provided by the Institute of Ultrasound Imaging of a medical university has achieved a significant improvement in the quality of ultrasound images.

1. Introduction

The elbow joint is a hinged upper limb joint composed of multiple joints such as the brachial ulnar joint, the brachioradial joint, and the upper radioulnar joint [1]. At the same time, an elbow joint with a good range of motion is very important for people's daily life and work. In order to meet the basic needs of people's daily work and life, our elbow joint needs to have at least 100° of flexion and extension range of motion, and at least 100° of forearm rotation range of motion. Among them, the minimum angle that the elbow joint can reach is less than 30°, the maximum angle that can be achieved by flexion is greater than 130°, and the angle of pronation and supination of the forearm needs to be greater than 50°. When the minimum extension angle of the elbow joint is greater than 30°, or the maximum flexion angle of the elbow joint is less than 120°, we define it as elbow joint stiffness. However, as one of the most important joints in the whole body, the elbow joint cannot tolerate the complications and sequelae caused by trauma [2]. Studies have shown that if the range of motion of the elbow joint is reduced by 50°, 80% of the elbow joint function will be lost [3]. With the rapid development of science and technology in today's society, more and more patients suffer from elbow joint trauma. The contracture of the soft tissue around the elbow joint caused by immobilization can cause the stiffness of the elbow joint after trauma [4].

In recent years, sparse signal processing technology has gained great attention in signal processing [5]. The establishment and rapid development of sparse signal processing theory, especially compressed sensing theory, has laid a theoretical basis for using sparse signal processing technology to solve actual signal processing problems. More and more applications are used to solve practical problems such as the slow speed of MRI data acquisition [6]. Compressed sensing, as a new sparse signal processing theory, provides us with a framework for sparse signal reconstruction using a small amount of measurement data. Based on this theory, we can greatly reduce the sampling data in the Fourier transform domain, shorten the data scanning time, and increase the imaging speed. This not only reduces the patient's discomfort during the scanning process but also enables the reconstruction of high-quality images from less Fourier data. Compressed sensing is a linear incomplete signal acquisition method, which mainly involves the sparsity of the signal, the acquisition of perceptual signals, and the reconstruction of perceptual signals. It breaks through the limitations of traditional sampling methods and opens a new era of sparse signal research. Many scholars are committed to this area of research, and a series of research results have appeared in just a few years [7, 8]. These studies mostly focus on the sparseness analysis of the signal, the design of the measurement matrix, the optimization of the reconstruction algorithm, and the practical application.

In this study, we collected the case data of 500 patients with posttraumatic elbow joint dysfunction after surgical treatment, revisited the recovery effect of elbow joint function, and explored the surgical treatment of posttraumatic elbow joint dysfunction. Surgical treatment of posttraumatic elbow joint dysfunction is the only option. Individualized treatment is used during the operation. A combined lateral and posterior medial incision is routinely used to completely remove the heterotopic bone tissue that blocks joint movement. This paper studies the compressed sensing theory and sparse reconstruction algorithm. First, the compressed sensing theory is explained, and then two reconstruction algorithms suitable for solving large-scale observation matrices are introduced: SPGL1 and FISTA. We reduce its computational complexity, speed up the convergence speed, and verify that the improved FISTA algorithm is still suitable for ultrasound imaging reconstruction. The relevant factors affecting the reconstruction of ultrasound images are studied, the training set image types and training set image quality are discussed, and the relevant sensitive variables are adjusted and improved on the basis of the FISTA network. After verification, the PSNR value of the ultrasound image reconstruction using FISTA is higher than other algorithms, which shows that FISTA has a certain effectiveness in ultrasound image reconstruction.

2. Related Work

For the diagnosis of fractures, plain radiographs, CT, and MRI have become more mature. The diagnostic value of ultrasound for fractures makes up for the shortcomings of plain radiographs, CT, and MRI in some aspects. Due to the flexibility and real-time characteristics of ultrasound, for some fractures with irregular bones or unclear displacements, the fracture can be diagnosed quickly by changing the position or angle of the probe, and it can also guide the fracture technique in time. In the case of complex trauma fractures, it can help determine whether there is substantial visceral damage, and the CDFI technology can be used to diagnose whether the blood vessel has combined damage. For fracture healing monitoring, CDFI can be combined to help evaluate and predict the causes of delayed fracture union and nonunion.

The use of high-frequency ultrasound combined with CDFI technology to examine soft tissue hemangioma reveals tortuous and expanded tubular structures that communicate with each other and interspersed with moderately strong echoes or strong echoes with sound shadows. Related scholars believe that CDFI can more accurately indicate the source of the main blood vessel supply and the scope of invasion of hemangioma, so as to provide a reliable basis for surgery, and it is low cost and noninvasive, with no X-ray injury [9]. Although the nature of other soft tissue tumors cannot be clarified by ultrasound, the appearance, internal echo structure, peripheral boundary conditions, blood flow conditions, and whether there is infiltration into surrounding structures can be preliminarily treated by ultrasound for benign and malignant tumors. Relevant scholars summarized 53 cases of soft tissue masses in other parts of the maxillofacial area except for maxillofacial area using CDFI technology [10]. All the bleeding flow velocity and resistance index were measured, and they found that there was a significant difference in the maximum blood flow velocity around benign and malignant tumors. Related scholars summarized the CDFI test results of 35 cases of soft tissue masses in the limbs and finally concluded that the arterial flow velocity of the malignant tumor group was significantly higher than that of the benign tumor group, and the resistance index was also significantly higher than that of the benign tumor, with $Vs \geq 015\,m{\cdot}s^{-1}$ as the demarcation standard for judging benign and malignant tumors [11].

Signal sparsity is a prerequisite for the application of CS theory. Almost all signals in nature are not sparse. The research on signal sparsity is a major difficulty in the application of CS theory. Related scholars have proposed a method of using contourlet transform as an image sparse transformation [12]. First, the image is decomposed into multiple detail subbands of different resolutions and a low-frequency subband, and then Hilbert transform is performed on the detail subbands. Finally, the two-dimensional analysis signal is decomposed by a directional filter bank, and the contourlet transform with translation invariance is realized. Experimental results show that contourlet transform has obvious advantages in image denoising and compressed sensing sparse signal [13]. Related scholars have proposed a method of using nonsubsampled contourlet transform as the sparse representation of the image in compressed sensing image reconstruction [14]. This method needs to measure the transformed high-frequency subbands and retain the decomposition coefficients of the low-frequency approximation subbands. The method not only improves the speed of image reconstruction but also guarantees the quality of image reconstruction. In addition, some scholars have used mixed sparse basis to sparse the signal, reduce the calculation time, and improve the accuracy of signal reconstruction. Related scholars have designed an orthogonal dictionary, which is composed of multiple orthogonal bases, which can adaptively find the optimal orthogonal base that approximates a certain signal characteristic and select the most suitable orthogonal base according to the different signals [15].

With the increasing role and use of high-frequency ultrasound in the diagnosis of muscular, skeletal, and neurological diseases, CDFI has gradually been found to have its inherent limitations. For example, when the gain is too high or the threshold is too low, the noise can easily cover the blood streaming signals, as well as the dependence on the angle and the proneness to aliasing. Under this circumstance, a new detection technology, namely, PDI, came into being. Its dynamic range improves the sensitivity to blood flow. The above advantages of PDI technology broaden the clinical application of CDFI, enabling accurate display of low-velocity blood flow and extremely low-velocity blood flow that were difficult to detect in the past, especially the detection of blood flow in small blood vessels, which significantly improves the sensitivity of doppler blood flow detection. However, PDI technology has its own shortcomings. For example, the application of PDI is limited for organs with obvious movement. PDI cannot display the direction and speed of blood flow, as well as direct quantitative values such as resistance index and maximum systolic peak, so it can only be used as a supplement to CDFI [16–18]. However, with the in-depth study of CDFI and PDI in musculoskeletal neurological diseases, it has shown good prospects [19, 20]. It is believed that high-frequency ultrasound will be an indispensable imaging method for the diagnosis of musculoskeletal neurological diseases in the near future.

3. Materials and Methods

3.1. General Information. From March 2019 to September 2020, patients who received elbow joint adhesion release in our hospital, a total of 500 patients with elbow joint dysfunction, were included, aged 10 to 64 years old, with an average age of 35 years. There are 300 cases on the left and 200 cases on the right joints. There were 280 cases of fall injuries and 220 cases of car accident injuries (all combined injuries). The average operation time was 11 months (2–20 months) after trauma. Original cause was as follows: 8 cases of simple elbow joint dislocation, 24 cases of humeral fractures, 8 cases of radial head fractures, 16 cases of olecranon fractures, 12 cases of horror triad, and 7 cases of multiple elbow fractures.

Education level was as follows: 50 cases in elementary school, 50 cases in junior high school, 100 cases in high school, and 300 cases in university; these patients all received surgical treatment for posttraumatic elbow joint dysfunction. Patients with posttraumatic elbow joint dysfunction were treated at 3 months, 6 months, and 12 months after surgery. Follow-up was done monthly and at 24-month time points, using the Internet (QQ or Email), telephone, and outpatient services to conduct a return visit to record the recovery of elbow joint function, elbow joint flexion and extension angle, rotation angle, joint pain, and stability. The enrollment followup time was all >6 months.

3.2. Treatment Methods

3.2.1. Preoperative Preparation. We check the elbow joint flexion and extension range of motion, rotation range of motion, muscle strength, and neurological symptoms in detail and perform routine X-ray and CT plain scan + three-dimensional reconstruction before surgery to understand whether the articular surface is flat and whether the joint space is narrow and judge whether there is an ectopic position.

3.2.2. Surgical Method. All patients in this group underwent surgical treatment after hospitalization. Brachial plexus block anesthesia was used in the operation, the affected limb was placed on the hand rest, sterile airbag tourniquet was used at the proximal upper arm after disinfection and drape, and the combined lateral and posterior elbow approach was routinely used. For patients with elbow joint dysfunction after one-stage surgical treatment, we use the original surgical incision and make a posterior medial or lateral incision at the same time; for patients with the original posterior median incision, we use the original posterior median single incision to take care of both the medial and the lateral sides; the medial incision exposes the ulnar nerve. We loosen the triceps brachii tendon, open the rear olecranon fossa, remove the fibrous scar tissue and granulation tissue, and remove the heterotopic ossified bone in the fossa; the lateral incision is from the brachioradialis muscle and extensor carpi radialis longus muscle, exposing the front joint capsule, coronal fossa, exposing the brachioradial joint, clearing the hypertrophic joint capsule and fibrous scar tissue, and heterotopic ossification of bone. Obstacles undergo resection of the radial head or replacement of the radial head prosthesis. Old fractures of the ulna coronoid process cannot be anatomically reduced and fixed. We routinely use nonabsorbable sutures to repair the anterior joint capsule to enhance the anterior stability of the elbow joint. The injured medial and lateral collateral ligaments are often separated and repaired. In this group of 500 patients, both the internal and external collateral ligaments were repaired. If necessary, Anchor rivet ligament stops were reconstructed and sutured. At the same time, the ulnar nerve is released before (or the medial condyle osteotomy is performed in situ) and placed under deep fascia for protection to avoid postoperative rehabilitation exercises and compression of the ulnar nerve. After the wound is fully hemostatic, a negative pressure drainage tube is placed in the incision; two external fixation nails are injected into the upper middle 1/3 of the humerus and the middle and lower 1/3 of the ulna (or distal radius), respectively, and the hinged external fixation is connected. The average operation time is 160 min (120–180 min).

3.2.3. Postoperative Treatment. Routine use of dehydration drugs after surgery, local ice on the elbow that night, functional rehabilitation exercise under the guidance of a rehabilitation physician on the first day after surgery, active and passive functional exercises of the elbow joint with the aid of a hinged external fixator, and joint activities were performed. The scope depends on the patient's tolerance, and the elbow joint should not be moved under violence. Anti-inflammatory, swelling and pain relief oral celecoxib 200 mg/Bid prevents myositis ossificans. The drainage tube is placed for 10 to 12 days to fully drain the blood in the joint. The stitches were removed within 14 days, and the hinged external fixation bracket was removed for 6 to 8 weeks. Figure 1 shows a schematic diagram of a specific exercise plan after elbow joint dysfunction release.

4. Ultrasonic Imaging Reconstruction Algorithm under the Framework of Compressed Sensing

4.1. Compressed Sensing. According to the signal theory, the signal can be expressed by a set of base linear, namely,

$$x = \sum_{n=0}^{N-1} a_n \bullet \theta_n. \quad (1)$$

In the formula, a is a coefficient vector of $N * 1$. If there are only K nonzero coefficients (or coefficients far greater than zero) in the formula, then the signal x is said to be sparse (compressible) on the basis, and θ_n is called the sparse basis or sparse dictionary of the signal x, and K is the sparseness of the signal.

In the compressed sensing theory, the observation of the sparse signal x does not directly measure the signal x itself. Instead, the signal x is projected onto a set of low-dimensional measurement vectors through noncorrelated measurements, namely,

$$y = \eta x. \quad (2)$$

In the formula, y is the vector of $M * 1$, and η is the observation matrix of $M * N$.

Since the signal measurement value dimension M is much smaller than the signal dimension N, directly solving the above equation is an underdetermined problem, and generally speaking, there is no definite solution. Considering the sparsity of a, this problem is expected to find a definite solution. The finite isometric property gives the necessary and sufficient conditions for the existence of a definite solution. To fully reconstruct the signal, it must be ensured that the observation matrix will not map two different K-item sparse signals to the same sampling set. This requires that the matrix composed of every M column vector extracted from the observation matrix is nonsingular. Practice has proved that most uniformly distributed random matrices have this condition, such as a matrix that obeys the Gaussian distribution, a matrix that obeys the Bernoulli distribution, and a part of the Fourier matrix.

4.2. Determine the Reconstruction Algorithm. In actual ultrasound imaging, the number of linear ultrasound array elements can be selected as 128. Assuming that the number of sampling points in the frequency domain is 64–128, considering the complex number, the size of the observation matrix G required for a detection area of $256 * 256$ pixels is 8–16 GB (storage in double-precision mode). It is undoubtedly huge. On the one hand, the computer's memory is required to support so much data. On the other hand, even if a solid state drive SSD is used to transfer data from the disk to the memory RAM at a speed of 500 MB/s, it will take 16–32 s, and the speed of an ordinary SATA3.0 hard drive will be reduced to the order of a minute.

As the amount of data increases, the processing time of data will also increase. According to the definition of algorithm complexity, the calculation time of the same algorithm will increase exponentially as the amount of data increases. Therefore, the calculation time after increasing the amount of data will far exceed an $O(N2)$ complexity algorithm.

Therefore, in view of the characteristics of ultrasound imaging data, it is necessary to choose an algorithm that supports complex number operations, has lower algorithm complexity for large-scale matrices, and can converge as quickly as possible. We will focus on the SPGL1 algorithm and the FISTA algorithm. These two algorithms have a similar design basis, the gradient descent method, which belongs to the convex relaxation method in the reconstruction algorithm.

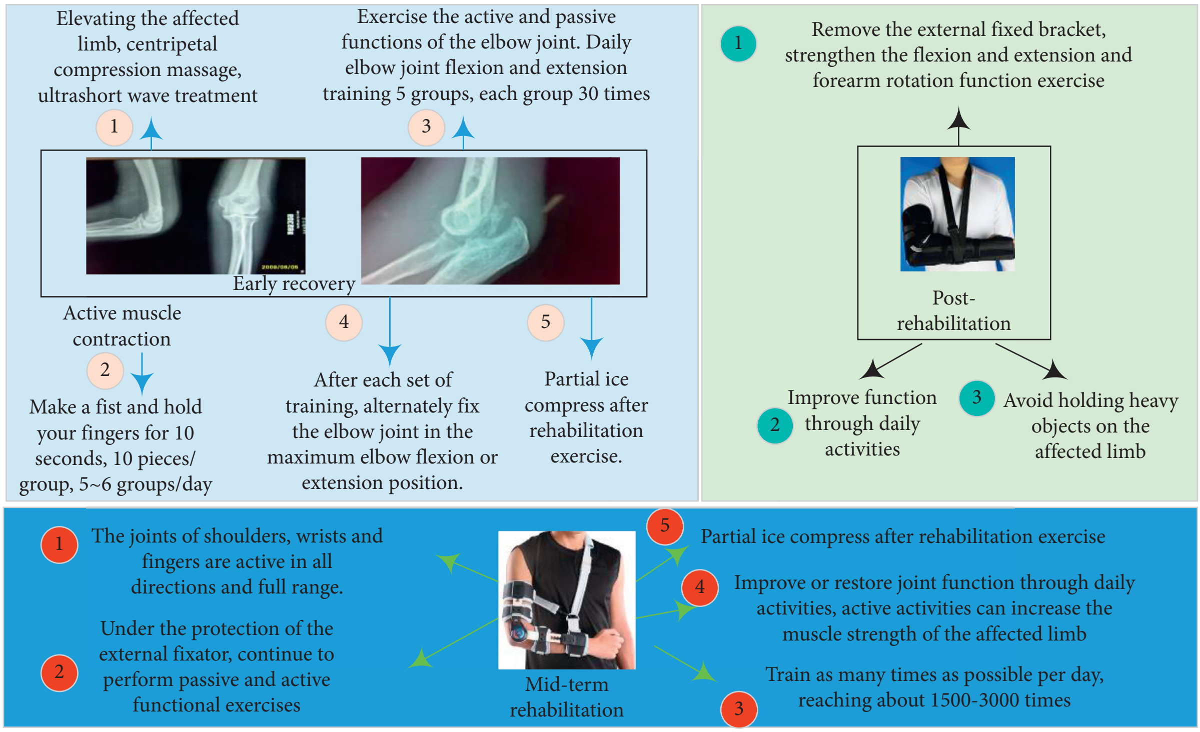

Figure 1: Schematic diagram of specific exercise plan after elbow joint dysfunction release.

4.2.1. SPGL1. It is mainly used to solve the BPDN (Basis Pursuit Denoising) problem. The BPDN problem is a variant of the BP problem. The expression is

$$\min \|a\|_1 \quad s.t. \quad y - \sigma \leq a\theta. \tag{3}$$

To solve the BPDN problem, the Least Absolute Shrinkage and Selection Operator (LASSO) problem is needed. The expression of the LASSO problem is

$$\min\|a\theta - y\|_2 \quad s.t. \quad \|a\|_1 \geq \tau\theta. \tag{4}$$

From the perspective of expression, the LASSO problem is a dual representation of the BPDN problem; that is, the objective function of LASSO is the constraint condition of BPDN, and the constraint condition of LASSO is the objective function of BPDN.

Every iteration needs to judge whether it drops. If it does not, the iteration step size must be reduced until the descending condition is met; after the iteration is completed, the iteration step size needs to be updated with the help of the Barzilai-Borwein (BB) algorithm to ensure the overall situation. The core part of the SPG algorithm is gradient projection. From the classic gradient descent method, we can see that the update of a is determined by the following formula:

$$a_k = a_{k-1} + g \bullet u \bullet \eta, \tag{5}$$

where g represents the gradient, u represents the iteration step size, and the gradient projection is to bring the right half of the above formula into the soft threshold iteration function $P()$, so that it satisfies

$$P(c) = \min\|2a - c\|_2 \quad s.t. \quad \|a\|_1 \geq \tau, \tag{6}$$

where c represents the soft threshold. After the soft threshold processing, the elements in a that are smaller than the threshold will be set to 0, and the nonzero information will be concentrated in a few nonzero points, and the sparsity will slowly manifest.

4.2.2. FISTA. It is an improved version of the iterative shrinkage threshold algorithm ISTA. The iterative shrinkage threshold algorithm is a very classic algorithm. It can solve the following regularization problems:

$$\min\left\{F(x) = \left[ay^2 - \theta\|\lambda a\|_2\right]\right\}, \tag{7}$$

where λ is called the regularization parameter.

The core of the ISTA algorithm is the gradient descent method, which is similar to SPGL1 in that it adds a threshold function $P()$:

$$a_{k+1} = P_{\lambda u}\left[a_k - u\theta\left(y - ua_{k-1}\right)\right]. \tag{8}$$

It can be a soft threshold or a hard threshold. This algorithm is very simple, but it has the same problems as the gradient descent method of slower convergence speed and uncertain global convergence. Therefore, what FISTA needs to do is to make the algorithm simple and fast convergent on the basis of ISTA, while ensuring global convergence. The flow of the FISTA algorithm is shown in Figure 2.

It can be seen from Figure 2 that the calculation process of FISTA is relatively simple, and there are three places that take time: one is to determine the iteration step size u; the other is to calculate the variable z when a matrix θ and a vector are multiplied. The variable u_k requires a conjugate transpose of the matrix θ and the vector multiplication

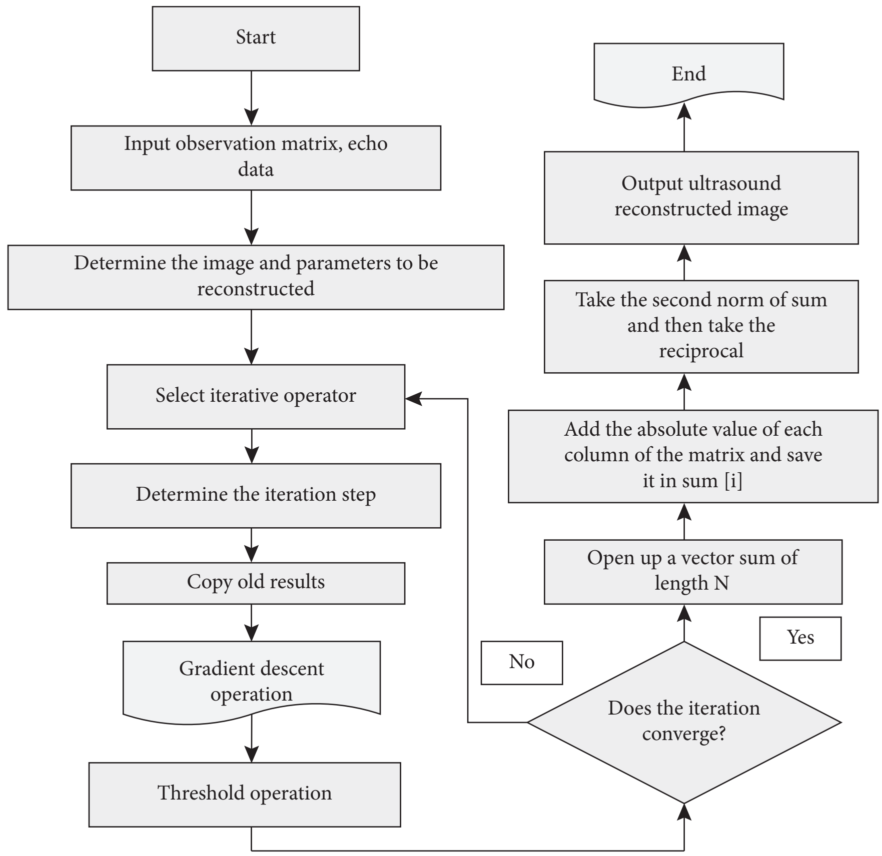

Figure 2: FISTA algorithm flow.

operation, which is similar to SPGL1 in terms of computational complexity. But the process of FISTA is much simpler than that of SPGL1. SPGL1 needs to do outer loop and inner loop, and there are many branches at the same time. This may improve the robustness of the algorithm, but the reconstruction speed will be slower than FISTA.

4.3. FISTA Algorithm Optimization

4.3.1. Optimization of Iteration Step Size. It can be seen in Matlab that if the SVD function is used to find the maximum singular value of the matrix, when the matrix dimension increases, the calculation time accounts for about 88%. From the perspective of algorithm time, it is the most time-consuming part. From the perspective of algorithm design, the iteration step size u taking the reciprocal of the largest singular value can ensure the fastest convergence speed, but it does not mean that the iteration step size is unique.

The optimization ideas for the iteration step size u are as follows: (1) open up a vector sum of length N; (2) add the absolute value of each column of the matrix θ and save it in sum$[i]$; (3) take sum of second norm, then take the reciprocal; this reciprocal is the estimated iteration step size u.

4.3.2. Optimization of the Number of Iterations. In the experiments in this paper, the iteration number can meet the iteration requirement at 100 times. Since each iteration requires two matrix and vector multiplications, when the matrix dimension is relatively high, the time increases exponentially. After the iterative step size is optimized, the most time-consuming process in the FISTA algorithm is undoubtedly the iterative process, so it is necessary to optimize the iterative process.

Considering that the characteristic of ultrasound images is to find the nonuniform area in the detection area, that is, the exact location of the lesion is what we want to know most, as for the amplitude information of the nonuniform area, it is relatively less important and can be passed through the image. From this point of view, the number of iterations can be appropriately reduced. The function of the threshold function is to set the threshold so that the number below the threshold is set to 0, and the number above the threshold is subjected to threshold processing. Therefore, appropriately increasing the threshold will be an effective way to reduce the number of iterations.

Blindly increasing the threshold will cause the effective information to be set to 0, and the result will be inaccurate. Therefore, it is necessary to select an appropriate threshold to meet the needs of different scenarios. In this paper, based on the approximate normalization of the observation matrix, the value range of λ is defined as $2e^4{\sim}4e^4$, and $0.5e^4$ is used as a step size to adapt to different amounts of data to obtain the best reconstructed image effect and the threshold that reconstructs the least sparse point can finally reduce the number of iterations to 30. After the improvement, the time of each part of the FISTA algorithm is shown in Table 1.

Table 1: Optimized FISTA algorithm running time.

Scene range	32 * 32	64 * 64	128 * 128
Estimated iteration step size (s)	0.26	0.31	0.48
30 iterations (s)	0.32	0.39	0.53
60 iterations (s)	0.37	0.43	0.56

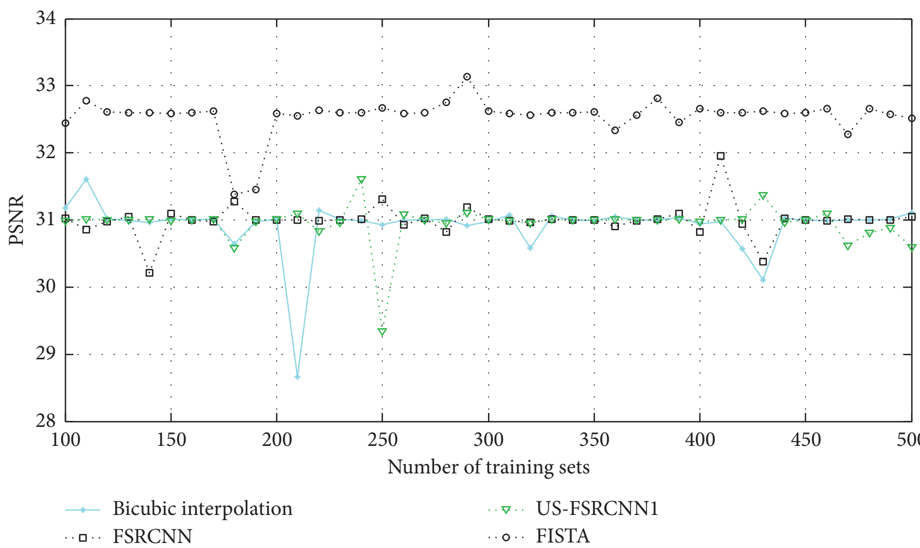

Figure 3: PSNR of ultrasound image reconstruction for different training sets.

5. Experiment and Analysis

5.1. The Impact of Training Set Image Types on Reconstruction Results. The experiment is divided into three groups: (1) the first group uses the 91-image library to train the FISTA network and then uses the trained network to perform superresolution reconstruction of the ultrasound images. (2) The second set of experiments uses Ultrasound Image Database to train the network. The database contains 84 ultrasound images from ten volunteers of different ages and weights. It is currently a common gallery in the field of ultrasound image research. (3) The third set of experiments uses the mixed training set of the previous two experiments to train the network. We compare the reconstruction effects of the trained network on ultrasound images in these three cases. Here is just to change the type of training set image, other experimental parameter settings, experimental schemes, etc. remain unchanged.

The experimental results are shown in Figures 3 and 4. Among them, US-FSRCNN1 represents a network trained using ultrasound images as a training set, FISTA represents a network trained using 91-image library as a training set, and FSRCNN represents a network trained using a mixed set.

It can be seen from Figures 3 and 4 that the PSNR and SSIM values of the ultrasound image reconstruction results obtained using the latter three methods based on compressed sensing are higher than those of the bicubic interpolation method. This shows that the ultrasound image reconstruction method based on compressed sensing is more effective than the general interpolation method. In addition, the network trained using ultrasound images as the training set has better reconstruction effects on ultrasound images than the network trained using the 91-image training set and the mixed training set. This fully proves that the network trained with a targeted training set has a better reconstruction effect on this type of image. Therefore, when training the network structure, a training set that is consistent with the type of image to be reconstructed should be used.

The comparison chart of the reconstruction results of ultrasound images is shown in Figure 5. From the visual point of view, we compare the reconstruction results of the four methods of bicubic interpolation, FSRCNN, US-FSRCNN1, and FISTA. We found that the first three methods have little difference in the reconstruction effect of ultrasound images. The network obtained by FISTA has the best reconstruction effect on ultrasound images. This verifies that the network trained with the FISTA ultrasound image training set can learn the characteristics of relevant ultrasound images in a targeted manner and is effective for ultrasound image reconstruction.

5.2. The Effect of Training Set Image Quality on the Results of Ultrasound Image Reconstruction. In the algorithm comparison experiment, this article adds speckle noise of different intensities to the 91-image training set to obtain multiple training sets of different qualities. By using these training sets to train the corresponding network, we discuss the impact of the training set under different intensities of noise on the effect of image reconstruction. The results show that FISTA has a certain antinoise ability.

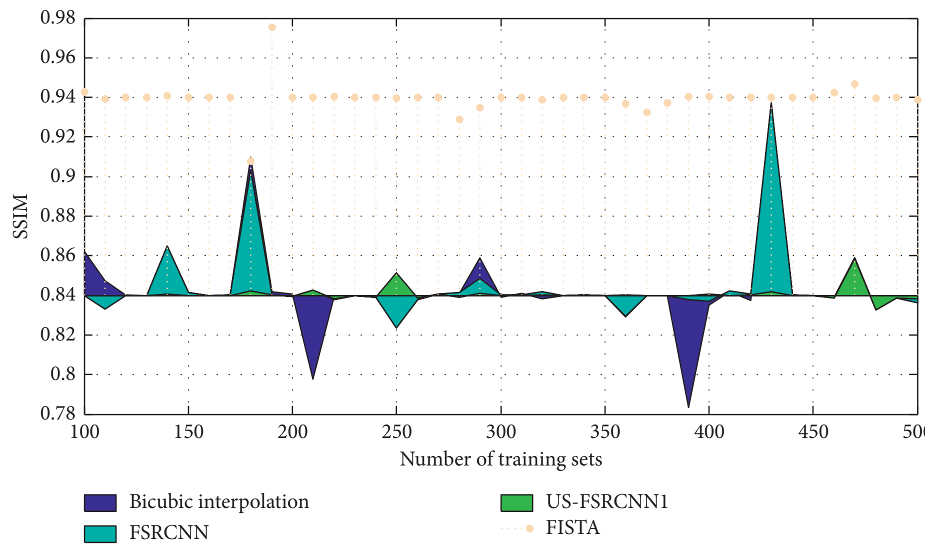

Figure 4: SSIM reconstruction of ultrasound images with different training sets.

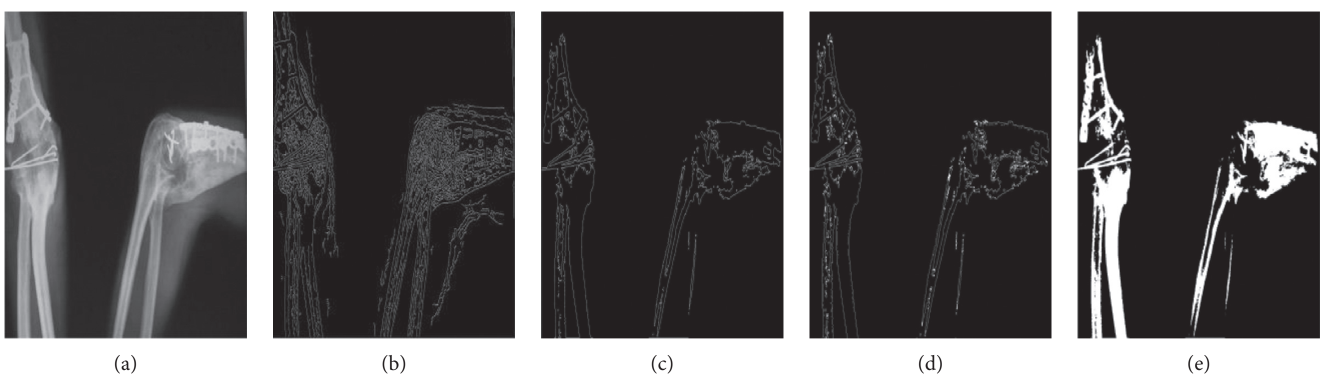

Figure 5: Comparison of ultrasound image reconstruction results of traumatic myositis ossificans of the elbow joint. (a) Original image. (b) Bicubic interpolation image. (c) FSRCNN image. (d) US-FSRCNN1 image. (e) FISTA image.

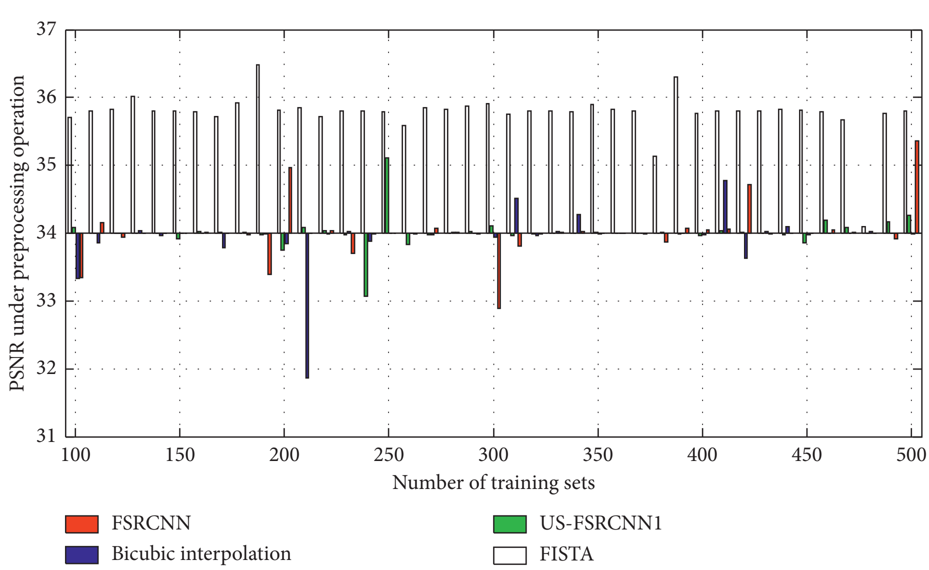

Figure 6: PSNR of ultrasound image reconstruction under preprocessing operation.

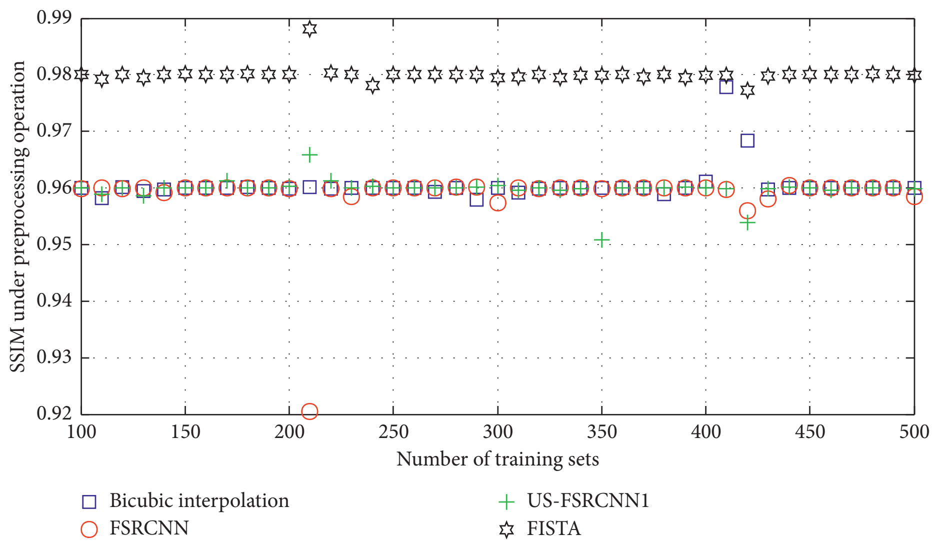

Figure 7: SSIM of ultrasound image reconstruction under preprocessing operation.

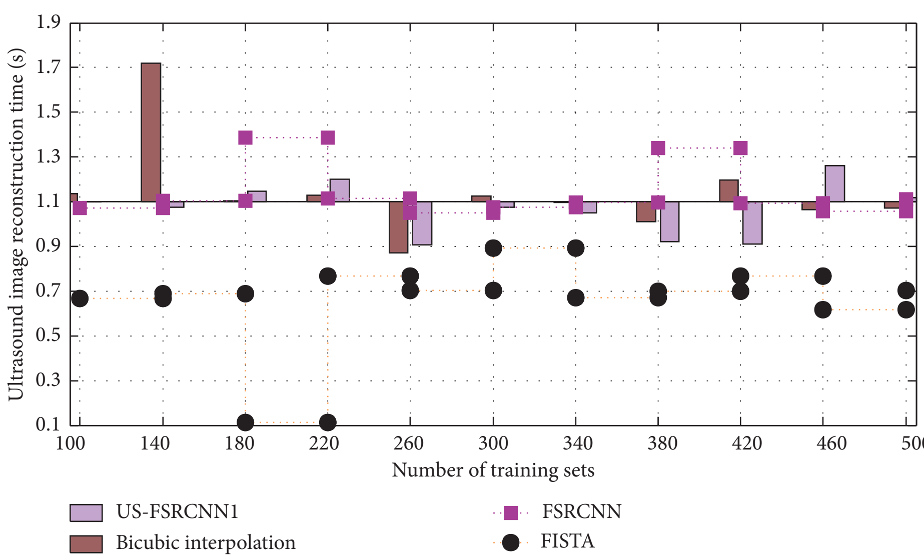

Figure 8: Comparison of the reconstruction time of the ultrasound image between the algorithm in this paper and other algorithms.

When the added noise variance is greater than 0.04, the reconstruction effect of FISTA is already not ideal. At this time, the PSNR value of the training set is about 28.1237 dB. We conclude that, in order to get a better reconstruction effect, the image quality of the training set should be similar to the quality of the test image to be reconstructed.

FISTA is the best for ultrasound image reconstruction. Therefore, the following experimental results are compared with FISTA. The experimental results are shown in Figures 6 and 7. Among them, US-FSRCNN1 represents the network trained using the preprocessed training set. It can be seen from the figure that the reconstruction effect of the ultrasound image obtained by the network trained with the preprocessed training set is better than that of the non-preprocessed training set. This verifies that the texture details of the training set images after preprocessing have been improved to meet the requirements, thereby improving the quality of the reconstructed image.

5.3. Comparison of Reconstruction Time with Other Algorithms. In order to verify the time efficiency of the ultrasound image superresolution reconstruction algorithm in this paper, the algorithm in this paper and the other three algorithms will be used to perform superresolution reconstruction on the ultrasound images of traumatic myositis ossificans of the elbow joint and compare them to ultrasound images.

It can be seen from Figure 8 that the time efficiency of ultrasound image reconstruction using the FISTA algorithm is the best among these four methods. This shows that the algorithm in this paper is effective in the reconstruction of ultrasound images.

6. Conclusion

With the increase of high-altitude operations and traffic accidents, the incidence of elbow joint dysfunction after trauma is on the rise, and the disability rate is quite high. The patient's elbow joint dysfunction affects the patient's physical and mental health such as life, work, and social interaction. Seeking the treatment of posttraumatic elbow joint dysfunction is the current clinical treatment difficulty. The treatment effect is not uniform, and the effect reports are quite different. In this article, from March 2019 to September 2020, 500 patients with posttraumatic elbow joint dysfunction were treated with personalized surgical treatment, followed by standardized rehabilitation exercises and celecoxib to prevent the occurrence of heterotopic ossification. From the perspective of the application of compressed sensing theory, we have carried out useful discussions on the problems faced by the compressed sensing theory and found solutions. We made a significant improvement to one of the algorithms, while retaining the advantages of compressed sensing for high-resolution and high-contrast signals or image information. It still has good resolution and contrast when the noise is large, which is beneficial to the recovery of ultrasound images. Using FISTA directly to reconstruct medical ultrasound images, the reconstruction results are not ideal. This paper uses the standard image library to establish a simulation model for FISTA training and testing. By adding different intensities of noise to all images in the image library, the influence of noise intensity on the quality of FISTA reconstructed images is analyzed, and it is found that the FISTA model has requirements on the quality of images and training set to be reconstructed. The original ultrasound image is preprocessed, and the clarity of the texture details of the restored ultrasound image is significantly improved, and the image quality meets the requirements. This article uses FISTA as the basic model, and the structure of FISTA is relatively large, which occupies a large part of the memory space. At the same time, a large model will also affect the processing time of the algorithm. Therefore, how to ensure the reconstruction quality of ultrasound images while reducing the network structure is a direction that can continue to be studied.

Data Availability

The data used to support the findings of this study are available from the corresponding author upon request.

Conflicts of Interest

The authors declare that there are no conflicts of interest.

Authors' Contributions

Y. Zhu and M. Sheng contributed equally to this work.

Acknowledgments

This work was supported by the Project of Three-Year Action Plan (2018–2020) of Shanghai Municipality for Further Accelerating the Development of Traditional Chinese Medicine (Grant no. ZY (2018-2020)-FWTX-8009), Construction of Plateau Discipline of Clinical TCM in Preventing Diseases of Pudong New Area Health and Family Planning Commission (Grant no. PDZY-2018-0605), and Three-Year Action Plan (2021–2023) of Shanghai Municipality for Further Accelerating the Innovation and Development of Traditional Chinese Medicine (Grant no. ZY (2021-2023)-0205-04).

References

[1] J. Z. Jijzhou Li, Y. J. Yongjin Zhou, Y. Yi Lu, G. Q. Guangquan Zhou, L. Yong-Ping Zheng, and Y. P. Zheng, "The sensitive and efficient detection of quadriceps muscle thickness changes in cross-sectional plane using ultrasonography: a feasibility investigation," *IEEE Journal of Biomedical and Health Informatics*, vol. 18, no. 2, pp. 628–635, 2014.

[2] W. Herzog, "Skeletal muscle mechanics: questions, problems and possible solutions," *Journal of NeuroEngineering and Rehabilitation*, vol. 14, no. 1, p. 98, Dec. 2017.

[3] G. Schwartz, B. C.-K. Tee, J. Mei et al., "Flexible polymer transistors with high pressure sensitivity for application in electronic skin and health monitoring," *Nature Communications*, vol. 4, no. 1, pp. 1859–1870, 2013.

[4] J. Zuniga, D. Katsavelis, J. Peck et al., "Cyborg beast: a low-cost 3d-printed prosthetic hand for children with upper-limb differences," *BMC Research Notes*, vol. 8, no. 1, p. 10, 2015.

[5] T. K. K. Koo, C. Wong, and Y. Zheng, "Reliability of sonomyography for pectoralis major thickness measurement," *Journal of Manipulative and Physiological Therapeutics*, vol. 33, no. 5, pp. 386–394, 2010.

[6] V. J. M. M. Schrier, S. Evers, J. G. Bosch, R. W. Selles, and P. C. Amadio, "Reliability of ultrasound speckle tracking with singular value decomposition for quantifying displacement in the carpal tunnel," *Journal of Biomechanics*, vol. 85, pp. 141–147, 2019.

[7] Y. Maeda, M. Sekine, and T. Tamura, "Relationship between measurement site and motion artifacts in wearable reflected photoplethysmography," *Journal of Medical Systems*, vol. 35, no. 5, pp. 969–976, 2011.

[8] A. Murgia, P. Kyberd, and T. Barnhill, "The use of kinematic and parametric information to highlight lack of movement and compensation in the upper extremities during activities of daily living," *Gait & Posture*, vol. 31, no. 3, pp. 300–306, 2010.

[9] Q. Zhang, K. Kim, and N. Sharma, "Prediction of ankle dorsiflexion moment by combined ultrasound sonography and electromyography," *IEEE Transactions on Neural Systems and Rehabilitation Engineering*, vol. 28, no. 1, pp. 318–327, Jan. 2020.

[10] M. B. Al-Harosh and S. I. Shchukin, "Peripheral vein detection using electrical impedance method," *Journal of Electrical Bioimpedance*, vol. 8, no. 1, pp. 79–83, 2017.

[11] X. Li, H. Li, J. Li, Y. Zhou, and J. Tan, "Real-time estimation of tibialis anterior muscle thickness from dysfunctional lower limbs using sonography," *Health Information Science*, vol. 8423, pp. 63–71, 2014.

[12] Q. Zhang, R. Liu, W. Chen, and C. Xiong, "Simultaneous and continuous estimation of shoulder and elbow kinematics from

surface EMG signals," *Frontiers in Neuroscience*, vol. 11, p. 280, May 2017.

[13] J. Liu, Y. Ren, D. Xu, S. H. Kang, and L.-Q. Zhang, "EMG-based real-time linear-nonlinear cascade regression decoding of shoulder, elbow, and wrist movements in able-bodied persons and stroke survivors," *IEEE Transactions on Biomedical Engineering*, vol. 67, no. 5, pp. 1272–1281, May 2020.

[14] Y. Zeng, J. Yang, C. Peng, and Y. Yin, "Evolving Gaussian process autoregression based learning of human motion intent using improved energy kernel method of EMG," *IEEE Transactions on Biomedical Engineering*, vol. 66, no. 9, pp. 2556–2565, Sep. 2019.

[15] Q. Li, D. Ni, W. Yi, S. Chen, T. Wang, and X. Chen, "Use of optical flow to estimate continuous changes in muscle thickness from ultrasound image sequences," *Ultrasound in Medicine and Biology*, vol. 39, no. 11, pp. 2194–2201, 2013.

[16] S.-M. Kim, J. H. Lee, S. Y. Park et al., "The study of pre-processing algorithm for improving performance of optical flow techniques on ultrasound image," *Journal of the Institute of Electronics Engineers of Korea S*, vol. 47, no. 5, pp. 24–32, 2016.

[17] G.-Q. Zhou and Y.-P. Zheng, "Automatic fascicle length estimation on muscle ultrasound images with an orientation-sensitive segmentation," *IEEE Transactions on Biomedical Engineering*, vol. 62, no. 12, pp. 2828–2836, 2015.

[18] X. Liang, Y. Sun, and H. Ren, "A flexible fabrication approach toward the shape engineering of microscale soft pneumatic actuators," *IEEE Robotics and Automation Letters*, vol. 2, no. 1, pp. 165–170, Jan. 2017.

[19] J. Tan, X. Li, W. Zhang, Y. Xie, and Y. Zhou, "Automatic estimation of muscle thickness in ultrasound images based on revoting hough transform (RVHT)," *Communications in Computer and Information Science*, vol. 484, pp. 392–401, 2014.

[20] E. Ozkan, C. Tanner, M. Kastelic, O. Mattausch, M. Makhinya, and O. Goksel, "Robust motion tracking in liver from 2D ultrasound images using supporters," *International Journal of Computer Assisted Radiology and Surgery*, vol. 12, no. 6, pp. 941–950, June 2017.

Hindawi
Journal of Healthcare Engineering
Volume 2023, Article ID 9827370, 1 page
https://doi.org/10.1155/2023/9827370

Retraction

Retracted: Artificial Intelligence-Based Echocardiographic Left Atrial Volume Measurement with Pulmonary Vein Comparison

Journal of Healthcare Engineering

Received 10 October 2023; Accepted 10 October 2023; Published 11 October 2023

Copyright © 2023 Journal of Healthcare Engineering. This is an open access article distributed under the Creative Commons Attribution License, which permits unrestricted use, distribution, and reproduction in any medium, provided the original work is properly cited.

This article has been retracted by Hindawi following an investigation undertaken by the publisher [1]. This investigation has uncovered evidence of one or more of the following indicators of systematic manipulation of the publication process:

(1) Discrepancies in scope
(2) Discrepancies in the description of the research reported
(3) Discrepancies between the availability of data and the research described
(4) Inappropriate citations
(5) Incoherent, meaningless and/or irrelevant content included in the article
(6) Peer-review manipulation

The presence of these indicators undermines our confidence in the integrity of the article's content and we cannot, therefore, vouch for its reliability. Please note that this notice is intended solely to alert readers that the content of this article is unreliable. We have not investigated whether authors were aware of or involved in the systematic manipulation of the publication process.

In addition, our investigation has also shown that one or more of the following human-subject reporting requirements has not been met in this article: ethical approval by an Institutional Review Board (IRB) committee or equivalent, patient/participant consent to participate, and/or agreement to publish patient/participant details (where relevant).

Wiley and Hindawi regrets that the usual quality checks did not identify these issues before publication and have since put additional measures in place to safeguard research integrity.

We wish to credit our own Research Integrity and Research Publishing teams and anonymous and named external researchers and research integrity experts for contributing to this investigation.

The corresponding author, as the representative of all authors, has been given the opportunity to register their agreement or disagreement to this retraction. We have kept a record of any response received.

References

[1] M. Zhu, X. Fan, W. Liu et al., "Artificial Intelligence-Based Echocardiographic Left Atrial Volume Measurement with Pulmonary Vein Comparison," *Journal of Healthcare Engineering*, vol. 2021, Article ID 1336762, 11 pages, 2021.

Hindawi
Journal of Healthcare Engineering
Volume 2021, Article ID 1336762, 11 pages
https://doi.org/10.1155/2021/1336762

Research Article

Artificial Intelligence-Based Echocardiographic Left Atrial Volume Measurement with Pulmonary Vein Comparison

Mengyun Zhu, Ximin Fan, Weijing Liu, Jianying Shen, Wei Chen, Yawei Xu, and Xuejing Yu

Department of Cardiology, Shanghai Tenth People's Hospital, Tongji University School of Medicine, Shanghai 200072, China

Correspondence should be addressed to Yawei Xu; xuyawei@tongji.edu.cn and Xuejing Yu; yuxuejing@aliyun.com

Received 28 September 2021; Revised 3 November 2021; Accepted 5 November 2021; Published 6 December 2021

Academic Editor: Gu Xiaoqing

Copyright © 2021 Mengyun Zhu et al. This is an open access article distributed under the Creative Commons Attribution License, which permits unrestricted use, distribution, and reproduction in any medium, provided the original work is properly cited.

This paper combines echocardiographic signal processing and artificial intelligence technology to propose a deep neural network model adapted to echocardiographic signals to achieve left atrial volume measurement and automatic assessment of pulmonary veins efficiently and quickly. Based on the echocardiographic signal generation mechanism and detection method, an experimental scheme for the echocardiographic signal acquisition was designed. The echocardiographic signal data of healthy subjects were measured in four different experimental states, and a database of left atrial volume measurements and pulmonary veins was constructed. Combining the correspondence between ECG signals and echocardiographic signals in the time domain, a series of preprocessing such as denoising, feature point localization, and segmentation of the cardiac cycle was realized by wavelet transform and threshold method to complete the data collection. This paper proposes a comparative model based on artificial intelligence, adapts to the characteristics of one-dimensional time-series echocardiographic signals, automatically extracts the deep features of echocardiographic signals, effectively reduces the subjective influence of manual feature selection, and realizes the automatic classification and evaluation of human left atrial volume measurement and pulmonary veins under different states. The experimental results show that the proposed BP neural network model has good adaptability and classification performance in the tasks of LV volume measurement and pulmonary vein automatic classification evaluation and achieves an average test accuracy of over 96.58%. The average root-mean-square error percentage of signal compression is only 0.65% by extracting the coding features of the original echocardiographic signal through the convolutional autoencoder, which completes the signal compression with low loss. Comparing the training time and classification accuracy of the LSTM network with the original signal and encoded features, the experimental results show that the AI model can greatly reduce the model training time cost and achieve an average accuracy of 97.97% in the test set and increase the real-time performance of the left atrial volume measurement and pulmonary vein evaluation as well as the security of the data transmission process, which is very important for the comparison of left atrial volume measurement and pulmonary vein. It is of great practical importance to compare left atrial volume measurements with pulmonary veins.

RETRACTED

1. Introduction

In recent years, the procedure has been gradually refined and matured and has demonstrated more outstanding safety and efficacy than traditional drug therapy, leaping to become the first-line treatment option for patients with atrial fibrillation [1]. The increase in the surgical base has also led to a relative increase in complications, which include pulmonary vein stenosis (PVS), pericardial effusion, arteriovenous embolism, and atrioventricular oesophageal fistula. The cardiac impedance signal is an impedance change signal measured directly from the body surface of the human chest using bioimpedance technology. Since the cardiac impedance signal has no negative waveform, it is often differentiated to reflect the pumping function of the heart from a hemodynamic perspective [2]. The pumping function of the heart can effectively reflect the location of the lesion in patients with cardiovascular diseases, the physical condition of the body, and the level of exercise training and is one of the important reference bases for the diagnosis of various cardiovascular diseases [3, 4]. Therefore, left atrial volume measurement and pulmonary vein assessment are of great importance for guiding treatment and assessing the functional status of the heart in patients with cardiovascular diseases. Artificial neural networks propose the concept of deep learning, which intends to make the machine simulate the multilayered information processing of the brain and automatically extract the intrinsic laws and representation levels of the input data through training [5]. With the rapid development of deep neural networks, their applications in the medical field are becoming more and more widespread, with relevant applications in disease diagnosis, medical image segmentation, drug tracking, medical text analysis, clinical aid diagnosis, treatment, and so forth. The launch of the AI intelligent imaging platform has brought new research ideas in human medical health assessment intelligence.

Some machine learning techniques help determine the sources and sequence variables that play an important role in the cause of the disease. In supervised learning, the algorithm consists of input and output, and the goal is to map input to output. It has a wide range of clinical applications, such as image recognition, interpretation of patients' electrocardiograms, chest X-rays, and CT results. In supervised learning, a set of databases containing observation data and their results can be used to build a predictive model that can classify the results from another set of given observation data [6]. The goal of unsupervised learning is to understand the internal relationships and patterns of the data itself. However, there is a lack of quantitative measurements of the relationship between parameters and prognostic status and a lack of comprehensive evaluation of the comparative ability of each parameter. Therefore, the development of a prognostic model for heart failure patients based on echocardiographic metrics is of great value to assist clinicians in the treatment of hospitalized patients and the daily management of patients after discharge. Comparative models were developed by applying machine learning algorithms with traditional statistical methods, that is, logistic linear regression, respectively, and, by comparing the values of the two models developed for the assessment of mortality and the risk of cardiovascular events in patients, it was concluded that comparative risk models with good comparative power and risk identification could be obtained by machine learning algorithms [7]. The purpose of this paper is to establish a comparative model based on the echocardiographic findings of the patients, by applying the BP neural network learning algorithm jointly by applying the 7 indicators reflecting the cardiac function of the patients obtained by echocardiography, and to conduct a comparative study on the comparative results of patients with reduced ejection fraction, that is, 1-year readmission and 3-year mortality, which has high clinical research and practical application significance.

The echocardiographic technique, as a clinical medical test for a comprehensive understanding of cardiac structure and function, has not been effectively used in left atrial volume measurement and pulmonary vein comparison. This study uses the echocardiographic technique for comprehensive observation of cardiac morphology and function, making the means of left atrial volume measurement and pulmonary vein comparison more accurate, efficient, and novel. Cardiac echocardiography is widely used in clinical medicine as the optimal test for determining the morphology and function of the heart. The first chapter firstly discusses the background and research significance of cardiovascular diseases, clarifies the main problems at the present stage, and clarifies the research plan and the chapter arrangement of the whole paper. The second chapter provides a brief review of the current state of development of domestic and international research on artificial intelligence for echocardiography, left atrial volume measurement and pulmonary vein assessment and detection methods, and deep learning. The third chapter proposes a 1D-CNN comparison model from deep neural networks, combining the characteristics of cardiac impedance differential signals themselves, to automatically learn the waveform features of cardiac impedance differential signals and avoid the manual feature selection process. Firstly, the cardiac impedance database is preprocessed, including signal denoising, feature point localization, and signal segmentation, to complete the data preparation work. The fourth chapter evaluates the model performance by test set samples and provides a detailed description and analysis of the experimental results. Then, the left atrial volume measurement and pulmonary vein classification in different states of the human body are evaluated by deeply mining the temporal connections between data points through long short-term memory networks. Finally, the validity of the model is verified by comparing the original data with the signal encoding features. The fifth chapter summarizes the research content of this paper.

2. Related Work

Echocardiography (UGG) is a noninvasive test that uses ultrasound echoes to examine the heart and large blood vessels to obtain relevant information. The echocardiogram provides information not only on the morphology and structure of the heart but also on the function of the heart and is an effective tool for evaluating the functional status of the heart. Quer et al. used X-ray fluoroscopy to find a strong heartbeat in humans and confirmed cardiac hypertrophy using X-ray until the introduction of echocardiography, which was a major step forward in the study of the heart [8]. Lai W T et al. began examining the heart using M-mode echocardiography and found that left ventricular hypertrophy was more common in humans in strength training programs [9]. Liu et al. further confirmed the enlargement of the heart ventricles in endurance training programs using two-dimensional echocardiography. Echocardiography not only allows for the evaluation of cardiac morphology and function but also allows for the accurate identification of cardiac and pathological hearts, which can effectively prevent the occurrence of sudden cardiac death in humans while guiding them through exercise training [10]. Cardiac enlargement and myocardial hypertrophy have been shown to occur in humans with prolonged exercise training, and the

RETRACTED

hypertrophy is often accompanied by an abnormal electrocardiogram, similar to that seen in clinical hypertrophic cardiomyopathy [11, 12].

Neural networks have been widely used in cardiovascular disease to quantify the complex relationships between the given data and have shown superior comparative ability in many areas such as diagnosis, response to treatment, and prognosis for patients suffering from various diseases [13]. Gearhart et al. used neural networks and cardiopulmonary function tests to compare the risk of cardiovascular-related mortality in patients who had heart failure with a left cardiopulmonary function test were followed up, and the results of the obtained tests and patient survival were composed into a sample set, which was randomly divided into a training set and a test set to compare cardiovascular-related mortality [14]. Olier et al. applied a cardiac hemodynamic monitor to measure left atrial volume measurements and pulmonary vein parameters by the cardiac impedance method in patients with coronary artery disease at different times to observe the effects of coronary artery disease on patients' left atrial volume measurements and pulmonary veins to further guide clinical diagnosis [15]. Chaturvedi et al. measured the hemodynamic indexes of heart failure patients by impedance hemogram detector and correlated them with BNP and left ventricular ejection fraction to explore their clinical significance in left atrial volume measurement and pulmonary vein assessment. Li et al. proposed BiLSTM-Attention neural network model with the heartbeat to improve the classification accuracy of heartbeat ECG signal [16]. La Porta E et al. used a 34-layer deep convolutional neural network trained on a dataset of 9123 ECG recordings from approximately 40,000 patients to achieve the classification of 15 rhythm types. From the above studies, it can be seen that, with the continuous development of deep learning, the use of deep learning methods in the medical field to mine the deep information of medical data and assist doctors in diagnosis and treatment has become a hot spot at home and abroad [17].

This paper adopts deep learning method to study and analyze the left atrial volume measurement and pulmonary vein status of the human body under the different intensity of exercise based on cardiac impedance differential signal and design a completely automatic feature learning model of cardiac impedance differential signal to reflect the effect of different intensity on the dynamic changes of cardiac blood flow and complete the automatic classification assessment of left atrial volume measurement and pulmonary vein function, which has the functions of real-time monitoring, predisease warning, and medical aid diagnosis [18, 19]. The db6 wavelet transform was used to decompose the signals in 8 layers, remove the signal noise at different frequencies, locate the signal characteristics and segment the signals, and establish the cardiac impedance database. The cross-validation method is used to divide 85% of the data samples into training and validation sets to test the model training, and the remaining 15% of the data samples are used as a separate test set to test the model generalization ability, evaluate the model performance, and complete the data preparation work [20, 21]. Finally, the deep left atrial volume measurement and automatic pulmonary vein assessment models are designed based on deep learning methods combined with one-dimensional cardiac impedance differential signal features [22]. According to the current experimental conditions, the use of cardiac echocardiography to compare the left atrium volume measurement with the pulmonary vein will provide experimental support and practical guidance for scientific exercise training monitoring and exercise plan formulation.

3. Artificial Intelligence-Based Echocardiographic Left Atrial Volume Measurement and Pulmonary Vein Comparison Study

3.1. Artificial Intelligence-Based Echocardiographic Parameter Building. After confirming that the electrodes and interfaces are correctly connected, the AcqKnowledge physiological signal acquisition software is used to synchronize the signal acquisition, convert the cardiac impedance signal and ECG signal into digital signals at the same time, and create a new channel to differentiate the cardiac impedance signal to obtain the cardiac impedance differential signal waveform. As shown in Figure 1, channel 2 is the cardiac impedance signal waveform, channel 10 is the cardiac impedance differential signal waveform, and channel 11 is the electrocardiographic signal waveform.

BP neural networks need to be trained before they can be used in comparison studies, to obtain networks with the ability to make accurate comparisons as well as associations with unknown data [23]. M is set as the input data and N is set as the output data, and the number of nodes in each layer is set as x, l, and y according to the provided sample data, after which the appropriate weights w_{ij} and w_{jk} between the layers are set according to the situation, and the thresholds x and y for the implicit and output layers are set, after which the learning rate and the relatively appropriate neuron excitation functions are selected according to the set target requirements.

The output Z of the intermediate hidden layer is obtained by basing on the input data M the threshold m of the next layer and w_{ij} between the two layers, as shown in the following equation:

$$Z_j = g\left(\sum_{i=1}^{n} w_{ij} * m_i - x_j\right) \quad j \subseteq [1,\ l]. \tag{1}$$

In equation (1), m is the excitation function of the implicit layer in the middle, multiple functions can be selected to execute. According to the research purpose of this paper, our definition is as follows:

$$\cos(m) = \frac{3 - \alpha * x}{1 + \exp(-3x)(mx - nx)}. \tag{2}$$

Based on Z obtained above, threshold y of the next layer, and w_{jk} between the two layers, the comparison result of this network is obtained after processing $P(k)$.

RETRACTED

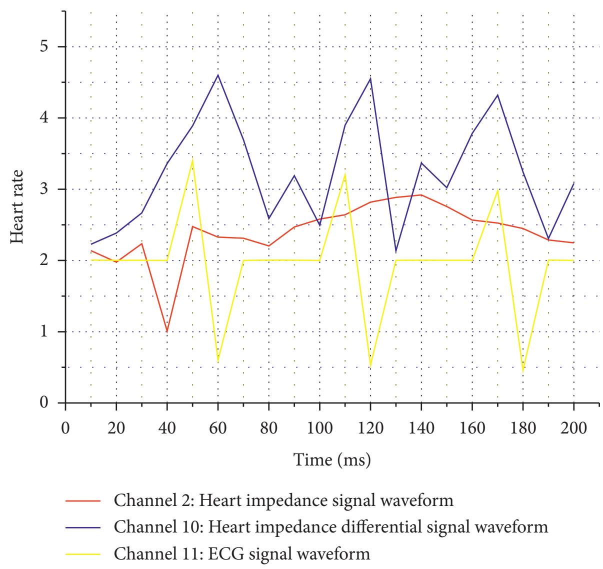

FIGURE 1: Cardiac synchronized cardiac impedance signal waveform.

$$P(k) = \sum_{j=1}^{l} \left(Z_j * w_{jk} - n_k \right), \quad k \subseteq [1,\ m]. \tag{3}$$

The new processed weights w_{ij} and w_{jk} are obtained by the error as in equation (4), and n is the set learning rate.

$$\begin{cases} w_{ij} = \psi * Z_j \left(1 - Z_j\right) * \sum_{j=1}^{n} w_{ij} * e_j, \\ w_{jk} = \psi * Z_j * e_k. \end{cases} \tag{4}$$

The errors are used to obtain the new threshold values x and y after processing, as in equation (5). Determine the current iteration of the algorithm to reach the target, the algorithm iterations, that is, the old values, are used to continuously recursively get new values, and the purpose of this process is to confirm whether the desired output can be reached. If the target is not reached, it returns to continue the training.

$$\begin{cases} x_j = \psi * Z_j \left(1 - Z_j\right) * \sum_{j=1}^{n} w_{ij} * e_j + m_j, \\ y_k = n_k + e_k. \end{cases} \tag{5}$$

Input parameters were selected for this study based on 7 relevant indices obtained by echocardiography: left ventricular end-diastolic internal diameter size, left ventricular ejection fraction size, pulmonary artery systolic pressure size, mitral regurgitation degree grouping, and tricuspid regurgitation degree grouping, with or without pericardial effusion and with or without pleural effusion confirmed by combined chest radiographs [24, 25]. Q (the number of neurons in the hidden layer) was determined based on equation (6). X and Y were the number of indicators of the input echocardiogram and the prognosis of the set heart failure patients, respectively.

$$Q = \max\left(X(Y+1), 2X, Y(X+1), 3Y\right). \tag{6}$$

Because of the large gap between the data of each echocardiographic index and the values of 1-year readmission and survival time as the results, the accuracy of the comparison results of heart failure patients may be affected during the network processing, so all the echocardiographic indexes and the prognostic results of patients should be normalized uniformly, and the data information of all patients should be transformed into a number between [0, 1], and the maximum-minimum method is applied here; min(B) is the smallest value among all data of each echocardiographic index, and max(B) is the largest value among all results of each prognostic condition, and the data obtained after the transformation can be directly used for the training of the following neural network:

$$AI = \frac{(B - \min(B))}{(\max(B) - \min(B))}. \tag{7}$$

After the weights and thresholds obtained through multiple trainings meet the identified target requirements, they are used as the parameters of the prognostic prediction model and placed in the network. It can better perform echocardiographic left atrial volume measurement and comparison with pulmonary veins. The next step is to set the training parameters of this heart failure prognostic comparison model: step size and learning rate. The learning rate should be set to a small value because a larger value will speed up the convergence at the beginning of the training, but it will not converge when it is close to the optimal value. Automatically extract the internal laws and representation levels of the input data through training.

3.2. Left Atrial Volume Measurement and Pulmonary Vein Comparison Method. After the subjects were identified through the questionnaire, the test time was determined through communication with the subjects to ensure that the subjects did not perform any training the day before, and the experimental group was allowed to sit still for at least 5 minutes before the test. A physician was in front of the computer and color printer to enter the information, record the data, and print the color echocardiography report form of the Hospital, and the control group was tested in the same way as the experimental group.

The left ventricular long-axis view measured the left atrial anterior-posterior diameter (LAAPD), left ventricular end-diastolic internal diameter (LVEDD), and left ventricular end-systolic internal diameter (LVESD); the apical four-chamber view measured the left atrial left-right diameter (LALRD) and left atrial upper and lower diameters (LASID); the real-time biplane method measured the left atrial maximum volume (LAVmax) at end-systole and the left atrial minimum volume (LAVmin) at end-diastole. LAVmax was measured at end-systole, LAVmin was measured at end-diastole, and LAVp was measured at the beginning of the P wave of the electrocardiogram, which could not be measured in PeAF patients without preoperative P wave. The shape of the pulmonary vein inlet is observed and

RETRACTED

measured by adjusting it at different angles. The disadvantage is that only one profile of the vessel can be displayed, so the accuracy of the operation affects the accuracy of the measurement results.

In pulmonary vein and left atrium imaging, the anatomical structure of the pulmonary vein vestibule can be directly observed by VE technique (comprehensive use of computer graphics systems and various reality and control interface devices to provide immersive technology in an interactive three-dimensional environment generated on a computer; among them, the computer-generated, interactive three-dimensional environment becomes a virtual environment), and the morphology and location of the intrapulmonary vein crest can be visualized, and the number of pulmonary vein openings can be clarified; it is also possible to clarify whether a small variant vein, which cannot be accurately displayed in postprocessing techniques such as VR and MPR, or a branch adjacent to the root of the pulmonary vein, is a variant by observing the location of the internal entrance of the vessel. The position of the interventricular ridge can also be used as an observation marker to further clarify whether the vein is a common pulmonary vein, which should project into the lumen of the left atrium if it is not a common pulmonary vein or deeper into the lumen of the pulmonary vein if it is a common pulmonary vein. The flow of left atrial volume measurements compared with pulmonary veins is shown in Figure 2. In patients with atrial electrical remodeling and an enlarged pulmonary vein inlet, atrial fibrillation cannot be completely cured by pulmonary vein isolation alone with atrial fibrillation ablation because of the presence of ectopic potential trigger points; and the enlarged pulmonary vein inlet may also affect the increase in electrical remodeling. The enlargement of the pulmonary vein inlet may lead to the easier formation of residual electrical conduction between the ipsilateral pulmonary veins and more likely to lead to ectopic trigger points outside the pulmonary veins. The increased diameter of the pulmonary vein entrance lengthens the ablation path; it becomes more difficult to keep all ablation points in the same plane during intraoperative ablation, resulting in a decreased success rate. The enlargement of the pulmonary vein entrance increases the number of atrial fibrillation trigger points and electrical activity, thus increasing the difficulty and complexity of the procedure and decreasing the success rate of the procedure.

A combination of postprocessing techniques and a comprehensive analysis is required for more objective and accurate observation and measurement of the pulmonary veins. When measuring the pulmonary vein inlet diameter in the transverse axis of the original image, it is difficult to observe the exact location of the opening because some of the left atrial walls are gently displaced from the pulmonary veins, and the presence of the left ventricle also makes it difficult to measure the left upper pulmonary vein. When measuring the pulmonary vein inlet diameter on VR images, although it can be rotated in multiple angles, it is difficult to select the starting and ending points for the measurement because it is modeled in three dimensions. When measuring the pulmonary vein inlet diameter on MIP images, care should be taken to avoid overlapping vascular images around the measurement results because of the density of the image. When measuring the pulmonary vein inlet diameter on MPR images, the division between the pulmonary vein inlet and the left atrium can be clearly shown, but because it is a two-dimensional reconstruction image, there is some image distortion on the image, which may affect the measurement results. When measuring the pulmonary vein inlet diameter on VE images, the structures within the pulmonary vein lumen can be seen, but because it is a real-time speculum image, care should be taken to determine the edge of the pulmonary vein inlet by rotating it at different angles.

In this study, both direct and indirect contrast methods were used to measure the narrowed pulmonary veins. The direct contrast method is the most classic method of PVS measurement, which has the advantage that preoperative and postoperative data can be retrieved and analyzed simultaneously to exclude the presence of preoperative PVS and pulmonary vein malformation; the disadvantage is that if the difference between the two imaging methods is large, the measurement results will be different, which will affect the PVS staging and the next treatment plan. The advantage of the indirect contrast method is that the presence of PVS can be inferred from postoperative CTA alone and the degree of stenosis can be calculated without obtaining additional preoperative data, which is suitable for patients with missing preoperative imaging data or with large differences between preoperative and postoperative imaging data. However, this method cannot exclude the existence of preoperative PVS and pulmonary vein malformation, and the conclusion is relatively one-sided. However, combined with the actual clinical situation, many patients were unable to provide preoperative imaging data at the time of follow-up due to the different locations of surgery and follow-up. Therefore, this study used both measurement methods to assess the degree of pulmonary vein stenosis and compared the two methods, aiming to demonstrate that, for patients who underwent CPVI for the first time, the occurrence of PVS can also be determined using only the indirect comparison method. However, the presence of special cases should also be considered in the clinical application, if the patient has missing preoperative data and develops postoperative chest tightness, cough, dyspnea, palpitations, difficult to specify etiology of recurrent pulmonary infections, and other symptoms; even if no obvious PVS is seen by indirect comparison method, the presence of PVS should be considered for further examination and follow-up.

4. Results and Analysis

4.1. Analysis of Simulation Results. First, the heart rate and the basic parameters of BSA and BV were calculated for each subject in the natural lying breathing state, as shown in Figure 3. The first 6 of the 20 subjects shown in Figure 3 were 12 female and the last 8 subjects were male. The mean heart rate of the female subjects was 76.74 beats/min and the mean heart rate of the male subjects was 74.12 beats/min, which were within the normal range of heart rate in the natural quiet state. In addition, because the heart volume of female

RETRACTED

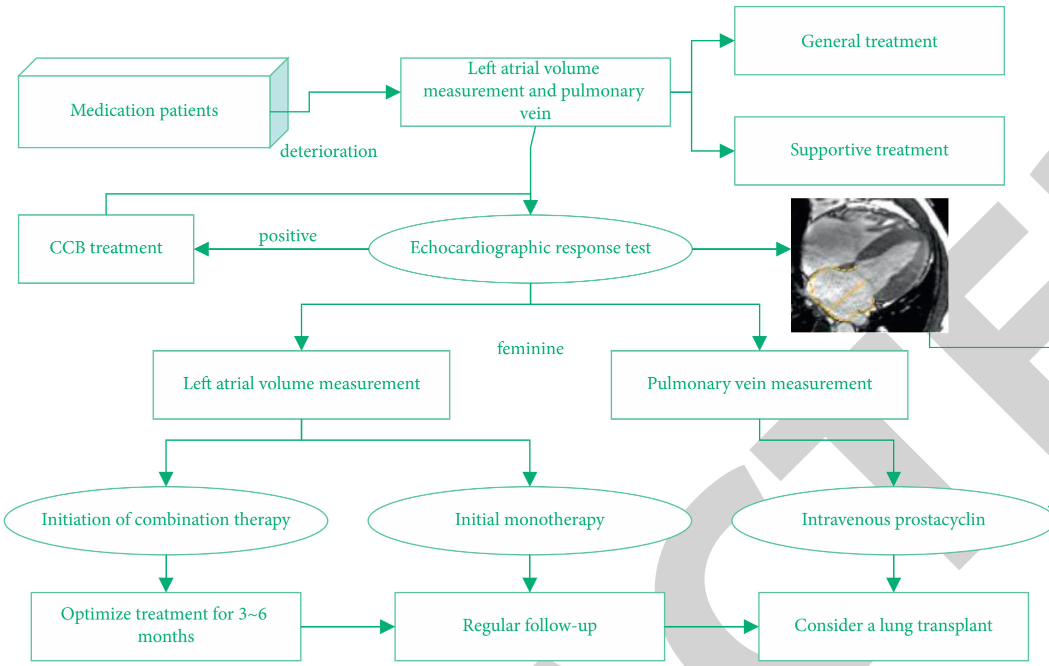

Figure 2: Left atrial volume measurements compared with pulmonary veins.

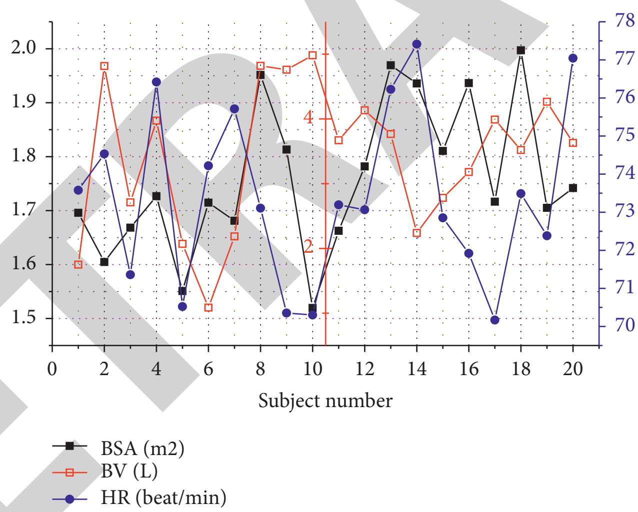

Figure 3: Calculated heart rate and BSA and BV parameters in the natural lying state.

subjects was slightly smaller than that of male subjects, the pumping capacity of the myocardium was relatively weaker, and the heart of female subjects needed to pump more times at the same time to ensure normal blood supply. Therefore, the average heart rate of female subjects was slightly faster than that of male subjects, and all measured data were within the normal heart rate reference range.

To further evaluate the effectiveness of convolutional self-coding structure as a signal compression method and signal coding features, and to facilitate the comparison and analysis of experimental results, two LSTM classification network models are prepared in this paper for comparison and evaluation. The only difference between the two networks is that the input signals are different. In the training phase of the model, the same tenfold cross-validation method is used to divide the training and validation sets for 85.14% of the data samples, and the remaining 15.14% are used for testing. Using the Adam optimizer, the batch size is 50.2; models are trained for 2000 iterations and the classification performance of the training model is evaluated using the test data, and the training results of the 2 models are presented in Figure 4.

The model test accuracy further verifies that the convolutional self-coding extracts effective coding features of the cardiac impedance differential signal. In terms of model training time, the former model takes 8635.12 seconds or 2.40 hours to achieve 10,000 iterations, while the latter only takes 1328.27 seconds or 0.37 hours, which is about 6.5 times longer than the latter. The greatly reduced model training time indicates that the CLSTM model can minimize storage

RETRACTED

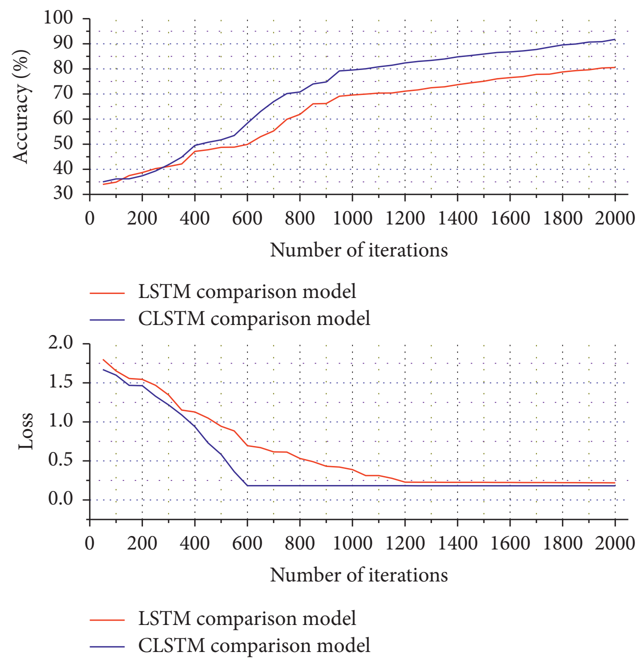

Figure 4: Training results of LSTM classification network with different inputs.

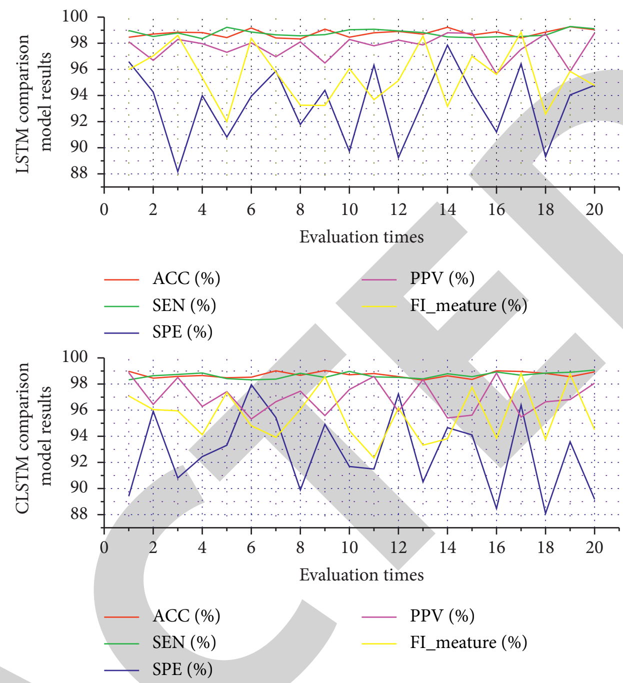

Figure 5: Relevant evaluation parameters of the network test set.

requirements, reduce data transfer costs and hardware configuration requirements, and improve real-time performance. In addition, the data is transmitted in encoded form to enhance data security. The evaluation parameters corresponding to each category are calculated based on the confusion matrix, as shown in Figure 5.

The model automatically learns the deep-level encoding features of the cardiac impedance differential signal through the convolutional autoencoder, which effectively compresses the cardiac impedance differential signal, reduces the model computational complexity, and decreases the model training time. Through a feedback mechanism, a 5-layer LSTM is used to integrate the valuable memories stored in the past and the contextual state of the current moment to deeply explore the strong correlation between the data points of the cardiac impedance differential signal and complete the classification assessment of cardiac function in different states of the human body. The average accuracy of the test set is 98.18% and 97.87%, and the training time of the model is reduced from 2.4 hours to 0.37 hours, indicating that the CLSTM model proposed in this paper has stronger real-time performance and lower hardware requirements.

4.2. Analysis of Comparative Results. For maximum diameter of pulmonary vein openings in the paroxysmal and continuous groups, LSPV was the largest, followed by RSPV, and LIPV and RIPV were the smallest; for the minimum diameter of pulmonary vein openings, RSPV and RIPV were the largest, followed by LSPV, and LIPV was the smallest; for the mean diameter, circumference, and area of pulmonary vein openings, RSPV and LSPV were the largest, followed by RIPV, and LIPV was the smallest; There were statistical differences in pulmonary vein openings ($P < 0.05$), as shown in Figure 6(a). In the normal control group, for the maximum diameter of pulmonary vein opening, RSPV and LSPV were the largest, followed by RIPV, and RSPV was the smallest; for the minimum diameter, mean diameter, circumference, and area of pulmonary vein opening, RSPV, RIPV, and LSPV were larger than LIPV; for the degree of incompatibility of pulmonary vein opening, LSPV and LIPV were the largest, followed by RSPV, and RIPV was the smallest; for the length of pulmonary vein trunk, LSPV and LIPV were the largest, followed by RSPV, and RIPV was the smallest. All of them were statistically different ($P < 0.05$), as shown in Figure 6(b).

For comparison of pulmonary vein opening sizes, the results of the maximum diameter, minimum diameter, mean diameter, circumference, and area of the LSPV and LIPV openings were statistically different among the three groups ($P < 0.05$), and the continuous group was larger than the normal and paroxysmal groups; the results of the above diameters of the RSPV and RIPV openings were not statistically different ($P > 0.05$). In the normal, paroxysmal, and persistent groups, the upper and lower left atrial diameters were 57.8 mm, 61.3 mm, and 62.6 mm, respectively, and there was a statistical difference between the three groups ($P < 0.05$), and the paroxysmal and persistent AF groups were larger than the normal group. The left atrial, left, and right diameters were 42.5 mm, 47.4 mm, and 43.4 mm, respectively; the anterior and posterior diameters were 32.2 mm, 36.4 mm, and 41.0 mm, respectively; and the left atrial volumes were 45.3 mm, 42.5 mm, and 48.5 mm, respectively. There was a statistical difference between the three groups ($P < 0.05$), and the sustained group was greater than the paroxysmal group and the normal group, as shown in Figure 7.

RETRACTED

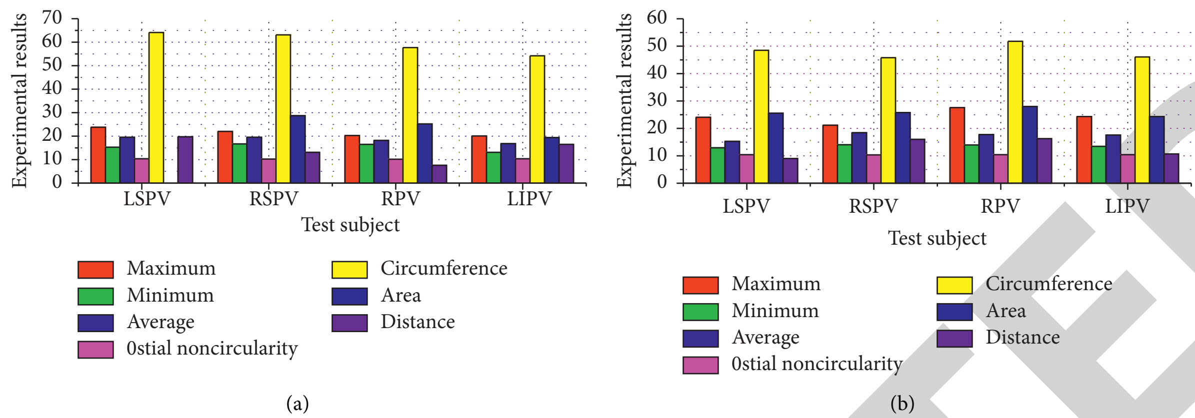

FIGURE 6: Maximum diameter of pulmonary vein opening. (a) Paroxysmal group and continuous group and (b) Normal control group.

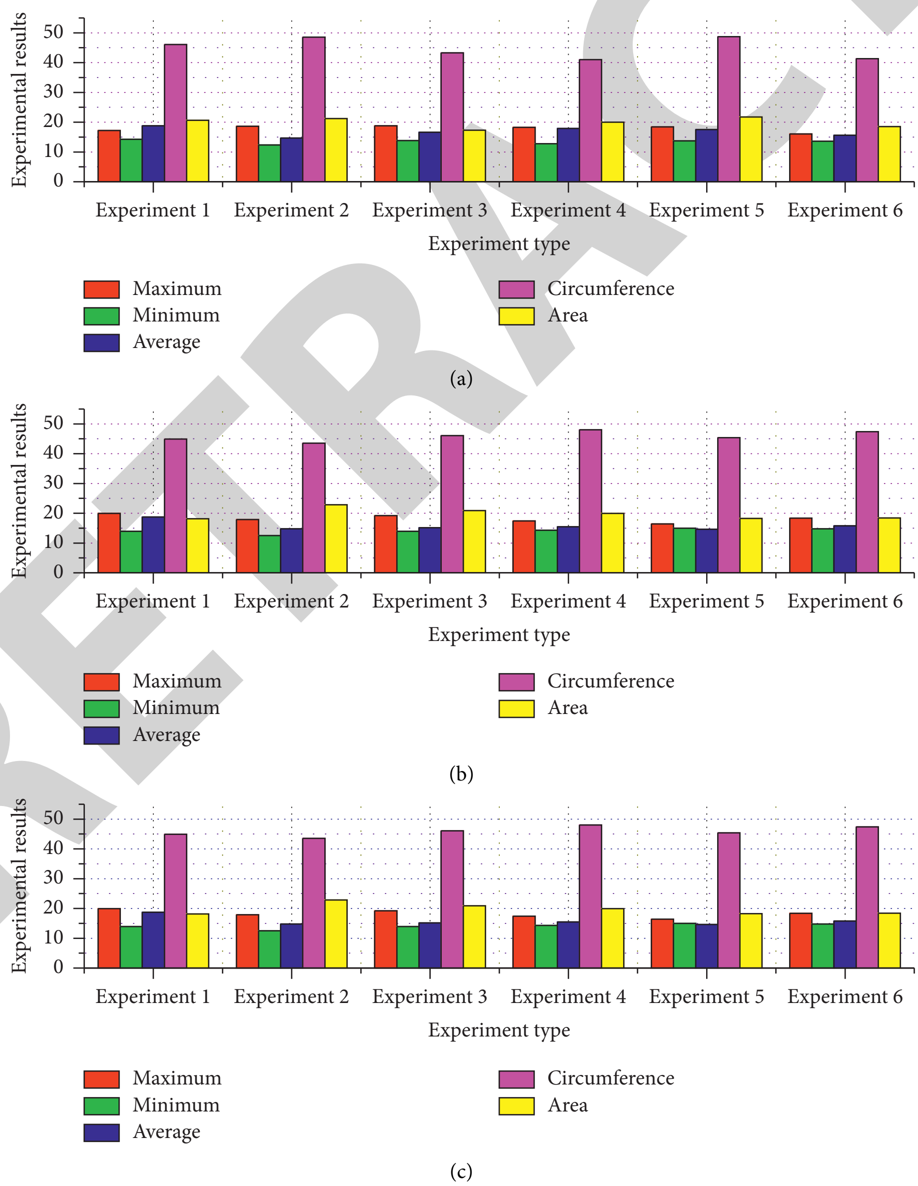

FIGURE 7: Comparison of pulmonary vein opening size and intergroup comparison of each diameter and volume of the left atrium (mm). (a) Normal group, (b) Burst group and (c) Continuous group.

RETRACTED

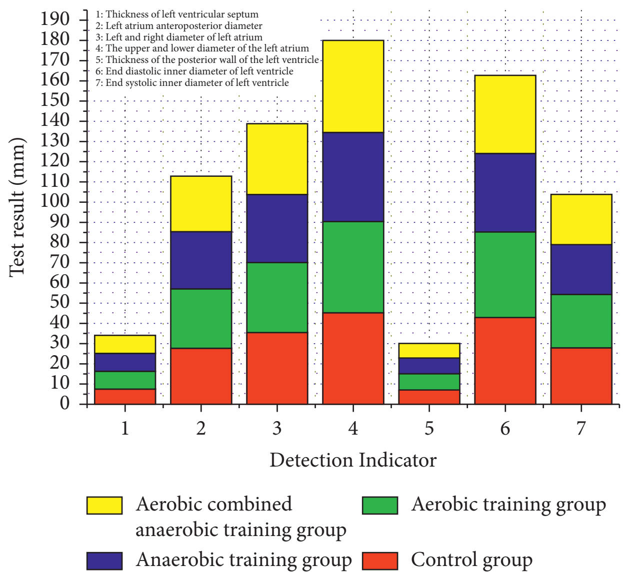

Figure 8: Echocardiographic results of morphological indicators of the heart (mm).

As shown in Figure 8, the cardiac echocardiographic results of female subjects in different groups showed highly significant differences ($P < 0.01$, $P < 0.01$, and $P < 0.01$) in the left ventricular septal thickness index, compared with the control group (C-F group), and in the A-F group, R-F group, and M-F group. For the left atrial anterior-posterior diameter index, the left ventricular anterior-posterior diameter was 30.3 mm in the M-F group with a highly significant difference ($P < 0.01$) compared with the control group (C-F group), and the left ventricular anterior-posterior diameter was 28.5 mm in the R-F group with a highly significant difference ($P < 0.01$) compared with the M-F group. Compared with the control group (C-F group), the left atrial, left, and right diameters in the A-F group and the R-F group were very significantly different ($P < 0.01$ and $P < 0.01$); compared with the A-F group, the R-M group, and the M-F group, they were very significantly different ($P < 0.01$ and $P < 0.01$); compared with the M-F group, the A-F group, and the R-F group, they were very significantly different ($P < 0.01$ and $P < 0.01$); compared with the M-F group, the A-F group, and the R-F group, the difference was highly significant ($P < 0.01$ and $P < 0.01$, respectively). Compared with the control group (C-F group), the upper and lower left atrial diameters were 47.4 mm in the A-F group, with a highly significant difference ($P < 0.01$), and in the R-F and M-F groups, with a highly significant difference ($P < 0.05$ and $P < 0.05$); compared with the A-F group, the R-F, and M-F groups, with a highly significant difference ($P < 0.05$, $P < 0.01$, and $P < 0.01$); compared with the A-F group, the R-F group, and the M-F group, there was a very significant difference ($P < 0.01$). For the left ventricular posterior wall thickness index, there were highly significant differences in the A-F, R-F, and M-F groups compared with the control group (C-F group) ($P < 0.01$, $P < 0.01$, and $P < 0.01$). Compared with the control group (C-F group), the left ventricular end-diastolic internal diameters of the A-F group and R-F group were significantly different ($P < 0.05$ and $P < 0.05$), and the left ventricular end-diastolic internal diameter of the M-F group was 45.6 mm, which was very significantly different ($P < 0.01$); compared with the M-F group, the left ventricular end-diastolic internal diameter of the R-F group was 43.6 mm, which was very significantly different ($P < 0.01$). The end-diastolic internal diameter of the left ventricle in the R-F group was 43.6 mm compared with that in the M-F group, with a highly significant difference ($P < 0.01$). Compared with the control group (C-F group), the left ventricular end-systolic internal diameter in the A-F group was 27.8 mm, with a significant difference ($P < 0.05$), and in the R-F and M-F groups, with a highly significant difference ($P < 0.01$ and $P < 0.01$).

Artificial intelligence technology, as a relatively new research direction, plays a role in several fields. At present, artificial intelligence technology has been widely used in the medical field and has demonstrated its value in many aspects such as diagnosis and treatment of acute or chronic diseases and prognosis evaluation. Neural network learning algorithm as one of the machine learning methods is also widely used. Neural networks are designed to analyze and process the given data by stimulating the activity of the human brain, and they have the same ability to learn by experience as that of the human brain. The echocardiographic left atrial volume measurement and pulmonary vein comparison model based on the neural network learning algorithm used in this study is suitable for dealing with the most complex nonlinear correlation problems seen in real practice, unlike the various risk comparison methods currently available, and provides a way to overcome the limitations of traditional statistical methods.

5. Conclusion

Echocardiographic indicators are of high value in determining the prognosis of patients, and neural network learning algorithms and other machine learning algorithms have proven their value in many fields of medicine. The MP160 multichannel physiologic meter can be used to measure the prognosis of heart failure patients. The MP160 multichannel physiological instrument was used to measure 20 subjects, and simultaneous data acquisition of cardiac impedance differential signals and ECG signals was performed. The noise interference sources contained in the collected cardiac impedance differential signals and ECG signals were analyzed, and the db6 wavelet function was selected to filter the noise within the collected data by comparing and analyzing the filtering of different wavelet bases on the collected data. The Mexican Hat wavelet transforms and the modal maximum threshold method were combined to locate the feature points of the acquired data. To further clarify the location of the feature points of the cardiac impedance differential signal, a secondary calibration of the feature points of the cardiac impedance differential signal was performed by the correspondence between the synchronized acquired ECG signal and the cardiac impedance differential signal in the time domain. The signal is segmented based on the cardiac period to increase the data sample size for the subsequent algorithm of fine identification. Finally, the data are organized and a database

RETRACTED

of cardiac impedance differential signals is established to complete the data preparation. In the future, through deep neural network and big data analysis technology, a large amount of data analysis will be carried out on the anatomy of the pulmonary veins to further clarify the relationship between the structure of the pulmonary veins and echocardiography and provide more powerful clues for medical prevention and treatment.

Data Availability

The data used to support the findings of this study are available from the corresponding author upon request.

Conflicts of Interest

The authors declare that there are no conflicts of interest.

Acknowledgments

The work in this paper was supported by Tongji University School of Medicine.

References

[1] A. Narang, V. Mor-Avi, A. Prado et al., "Machine learning based automated dynamic quantification of left heart chamber volumes," *European Heart Journal - Cardiovascular Imaging*, vol. 20, no. 5, pp. 541–549, 2019.

[2] D. Dey, P. J. Slomka, P. Leeson et al., "Artificial intelligence in cardiovascular imaging," *Journal of the American College of Cardiology*, vol. 73, no. 11, pp. 1317–1335, 2019.

[3] P. I. Dorado-Díaz, J. Sampedro-Gómez, V. Vicente-Palacios, and L. S. Pedro, "Applications of artificial intelligence in cardiol," *Revista Española de Cardiología*, vol. 72, no. 12, pp. 1065–1075, 2019.

[4] K. W. Johnson, J. Torres Soto, B. S. Glicksberg et al., "Artificial intelligence in cardiology," *Journal of the American College of Cardiology*, vol. 71, no. 23, pp. 2668–2679, 2018.

[5] S. Khoche, N. A. Silverton, J. Zimmerman et al., "The year in perioperative echocardiography: selected highlights from 2019," *Journal of Cardiothoracic and Vascular Anesthesia*, vol. 34, no. 8, pp. 2036–2046, 2020.

[6] K. B. Lee and H. W. Goo, "Comparison of quantitative image quality of cardiac computed tomography between raw-data-based and model-based iterative reconstruction algorithms with an emphasis on image sharpness," *Pediatric Radiology*, vol. 50, no. 11, pp. 1570–1578, 2020.

[7] N. Bernolian, R. U. Radiyati Umi Partan, S. Siti Nurmaini, fnm Cindy Kesty, and fnm Benedictus Wicaksono Widodo, "Congenital heart diseases in pregnancy," *Bioscientia Medicina: Journal of Biomedicine and Translational Research*, vol. 5, no. 4, pp. 988–1004, 2021.

[8] G. Quer, R. Arnaout, M. Henne, and R. Arnaout, "Machine learning and the future of cardiovascular care," *Journal of the American College of Cardiology*, vol. 77, no. 3, pp. 300–313, 2021.

[9] W. T. Lai, M. C. Hsiung, L. C. Lin, W. H. Yin, C. H. Hsu, and K. C. Huang, "Stepwise manipulation of cardiac computed tomography multi-planar reconstruction to mimic transesophageal echocardiography," *Echocardiography*, vol. 37, no. 9, pp. 1512–1523, 2020.

[10] X. Liu, L. Faes, A. U. Kale et al., "A comparison of deep learning performance against health-care professionals in detecting diseases from medical imaging: a systematic review and meta-analysis," *The lancet digital health*, vol. 1, no. 6, pp. e271–e297, 2019.

[11] J. C. Lam, D. B. Gregson, R. Somayaji et al., "Forgoing transesophageal echocardiogram in selected patients with complicated *Staphylococcus aureus* bacteremia," *European Journal of Clinical Microbiology & Infectious Diseases*, vol. 40, no. 3, pp. 623–631, 2021.

[12] D. Cao, R. Chandiramani, D. Capodanno et al., "Non-cardiac surgery in patients with coronary artery disease: risk evaluation and periprocedural management," *Nature Reviews Cardiology*, vol. 18, no. 1, pp. 37–57, 2021.

[13] K. Addetia, D. Muraru, L. P. Badano, and R. M. Lang, "New directions in right ventricular assessment using 3-dimensional echocardiography," *JAMA cardiology*, vol. 4, no. 9, pp. 936–944, 2019.

[14] A. Gearhart, S. Gaffar, and A. C. Chang, "A primer on artificial intelligence for the paediatric cardiologist," *Cardiology in the Young*, vol. 30, no. 7, pp. 934–945, 2020.

[15] I. Olier, S. Ortega-Martorell, M. Pieroni, and G. Y. H. Lip, "How machine learning is impacting research in atrial fibrillation: implications for risk prediction and future management," *Cardiovascular Research*, vol. 117, no. 7, pp. 1700–1717, 2021.

[16] A. Chaturvedi, H. Chengazi, and T. Baran, "Identification of patients with heart failure from test bolus of computed tomography angiography in patients undergoing preoperative evaluation for transcatheter aortic valve replacement," *Journal of Thoracic Imaging*, vol. 35, no. 5, pp. 309–316, 2020.

[17] E. La Porta, L. Lanino, M. Calatroni et al., "Volume balance in chronic kidney disease: evaluation methodologies and innovation opportunities," *Kidney & Blood Pressure Research*, vol. 46, no. 4, pp. 396–410, 2021.

[18] K.-L. Nguyen, P. Hu, and J. P. Finn, "Cardiac magnetic resonance quantification of structure-function relationships in heart failure," *Heart Failure Clinics*, vol. 17, no. 1, pp. 9–24, 2021.

[19] R. E. Leiter, E. Santus, Z. Jin et al., "Deep natural language processing to identify symptom documentation in clinical notes for patients with heart failure undergoing cardiac resynchronization therapy," *Journal of Pain and Symptom Management*, vol. 60, no. 5, pp. 948–958, 2020.

[20] I. D. Gregoric, P. Poredos, M. K. Jezovnik et al., "Use of transthoracic echocardiogram to detect left ventricular thrombi," *The Annals of Thoracic Surgery*, vol. 111, no. 2, pp. 556–560, 2021.

[21] J. Lv, T. Yang, X. Gu et al., "Differential diagnosis of fetal large ventricular septal defect and tetralogy of Fallot based on big data analysis," *Echocardiography*, vol. 37, no. 4, pp. 620–624, 2020.

[22] J. A. Leopold, B. A. Maron, and J. Loscalzo, "The application of big data to cardiovascular disease: paths to precision medicine," *Journal of Clinical Investigation*, vol. 130, no. 1, pp. 29–38, 2020.

[23] C. Luong, Z. Liao, A. Abdi et al., "Automated estimation of echocardiogram image quality in hospitalized patients," *The International Journal of Cardiovascular Imaging*, vol. 37, no. 1, pp. 229–239, 2021.

[24] J. R. Clark, S. C. Hoffman, N. A. Shlobin, A. Bavishi, and A. Narang, "Incidence of catheter-associated right atrial thrombus detected by transthoracic echocardiogram," *Echocardiography*, vol. 38, no. 3, pp. 435–439, 2021.

RETRACTED

Hindawi
Journal of Healthcare Engineering
Volume 2023, Article ID 9798509, 1 page
https://doi.org/10.1155/2023/9798509

Retraction

Retracted: Multicentre Study Using Machine Learning Methods in Clinical Diagnosis of Knee Osteoarthritis

Journal of Healthcare Engineering

Received 13 September 2023; Accepted 13 September 2023; Published 14 September 2023

Copyright © 2023 Journal of Healthcare Engineering. This is an open access article distributed under the Creative Commons Attribution License, which permits unrestricted use, distribution, and reproduction in any medium, provided the original work is properly cited.

This article has been retracted by Hindawi following an investigation undertaken by the publisher [1]. This investigation has uncovered evidence of one or more of the following indicators of systematic manipulation of the publication process:

(1) Discrepancies in scope
(2) Discrepancies in the description of the research reported
(3) Discrepancies between the availability of data and the research described
(4) Inappropriate citations
(5) Incoherent, meaningless and/or irrelevant content included in the article
(6) Peer-review manipulation

The presence of these indicators undermines our confidence in the integrity of the article's content and we cannot, therefore, vouch for its reliability. Please note that this notice is intended solely to alert readers that the content of this article is unreliable. We have not investigated whether authors were aware of or involved in the systematic manipulation of the publication process.

In addition, our investigation has also shown that one or more of the following human-subject reporting requirements has not been met in this article: ethical approval by an Institutional Review Board (IRB) committee or equivalent, patient/participant consent to participate, and/or agreement to publish patient/participant details (where relevant).

Wiley and Hindawi regrets that the usual quality checks did not identify these issues before publication and have since put additional measures in place to safeguard research integrity.

We wish to credit our own Research Integrity and Research Publishing teams and anonymous and named external researchers and research integrity experts for contributing to this investigation.

The corresponding author, as the representative of all authors, has been given the opportunity to register their agreement or disagreement to this retraction. We have kept a record of any response received.

References

[1] K. Zeng, Y. Hua, J. Xu et al., "Multicentre Study Using Machine Learning Methods in Clinical Diagnosis of Knee Osteoarthritis," *Journal of Healthcare Engineering*, vol. 2021, Article ID 1765404, 12 pages, 2021.

Hindawi
Journal of Healthcare Engineering
Volume 2021, Article ID 1765404, 12 pages
https://doi.org/10.1155/2021/1765404

Research Article

Multicentre Study Using Machine Learning Methods in Clinical Diagnosis of Knee Osteoarthritis

Ke Zeng ,[1,2] Yingqi Hua,[1] Jing Xu,[1] Tao Zhang,[1] Zhuoying Wang,[1] Yafei Jiang,[1] Jing Han,[1] Mengkai Yang,[1] Jiakang Shen ,[1] and Zhengdong Cai [1]

[1]*Department of Orthopedics, Shanghai General Hospital, Shanghai Jiao Tong University School of Medicine, Shanghai Bone Tumor Institution, Shanghai 200080, China*
[2]*Department of Orthopedics, Wuxi No. 2 People's Hospital, Nanjing Medical University, Wuxi, Jiangsu 214000, China*

Correspondence should be addressed to Jiakang Shen; shenjiakang2012@qq.com and Zhengdong Cai; caizhengdong@sjtu.edu.cn

Received 20 October 2021; Revised 14 November 2021; Accepted 15 November 2021; Published 3 December 2021

Academic Editor: Gu Xiaoqing

Copyright © 2021 Ke Zeng et al. This is an open access article distributed under the Creative Commons Attribution License, which permits unrestricted use, distribution, and reproduction in any medium, provided the original work is properly cited.

Knee osteoarthritis (OA) is one of the most common musculoskeletal disorders. OA diagnosis is currently conducted by assessing symptoms and evaluating plain radiographs, but this process suffers from the subjectivity of doctors. In this study, we retrospectively compared five commonly used machine learning methods, especially the CNN network, to predict the real-world X-ray imaging data of knee joints from two different hospitals using Kellgren-Lawrence (K-L) grade of knee OA to help doctors choose proper auxiliary tools. Furthermore, we present attention maps of CNN to highlight the radiological features affecting the network decision. Such information makes the decision process transparent for practitioners, which builds better trust towards such automatic methods and, moreover, reduces the workload of clinicians, especially for remote areas without enough medical staff.

RETRACTED

1. Introduction

Knee osteoarthritis (OA) is a chronic joint disease characterized by the degeneration, destruction, and bone hyperplasia of articular cartilage. It is the most common cause of joint pain, morning stiffness, and knee dysfunction. Currently, there is no effective conservative treatment that can completely cure knee OA. One of the main problems that limit the improvement of knee OA treatment is that there is no accurate, noninvasive inspection method that can monitor the progress of articular cartilage degeneration. As a traditional knee OA examination method, plain X-ray images cannot be directly used to evaluate cartilage changes, while its role in the early diagnosis of knee OA is also quite limited.

Medical imaging has different values and significance for clinical scientific research and diagnosis. For example, CT (Computed Tomography) scan can reflect the information of tomographic anatomy, which can effectively image the bones, breathing and digestive system, etc. MR (Magnetic Resonance) scan provides clear contrast imaging of soft tissues, without radiation damage to the human body, but has little effect on bones and internal voids. PET (Positron Emission Tomography) imaging is a molecular metabolic function imaging, which can screen suspected tumor cells at the molecular level. But, X-ray image is still the golden standard for knee OA diagnosis because of its safeness, cost effectiveness, and wide availability. Despite these advantages, X-ray images are not so sensitive when trying to detect early changes in OA. In addition, due to the lack of a precisely defined grading system, knee OA diagnosis is also highly dependent on the subjectivity of practitioners. The commonly used Kellgren-Lawrence (K-L) grading scale [1] is semiquantitative and has ambiguities, which reflects a large number of disagreements among readers (the secondary Kappa is 0.56 [2], 0.66 [3], and 0.67 [4]). This ambiguity makes early diagnosis of OA challenging and, therefore, affects millions of people worldwide. Fortunately, the current diagnostic accuracy of machine learning has reached the level of human being and may even surpass human experts in the future. Therefore, ultimately, the patient will get a more reliable diagnosis method. With these effective tools, radiologists and orthopedists can use them to supplement the diagnosis chain, which can reduce the focus on routine tasks such as image grading and focus more on accidental discoveries [5]. For all of the abovementioned reasons, we believe that clinical evaluation using machine learning methods can significantly improve the diagnosis of knee OA on plain radiographs.

Since 1989, the automatic diagnosis of knee OA has a long history [6]. Although the amount of data used in these studies was previously limited to hundreds of cases collected in one hospital [7–9], some research teams could still apply thousands of cases in their analysis process [10–12]. In recent years, the application of artificial intelligence in medical imaging has been developing rapidly, such as in tumor screening, qualitative diagnosis, radiotherapy organ delineation, efficacy evaluation, and prognosis. The application of artificial intelligence in medical image processing and analysis accompanied with big data can help reduce physicians' simple repetitive work, reduce the probability of human error, improve overall work efficiency, diagnosis, and treatment accuracy, and furthermore, promote precision medicine. Artificial intelligence (AI) has become a worldwide hot spot because it has demonstrated strong capabilities in image processing, language analysis, and knowledge understanding, relying on strong knowledge mastery and knowledge application. Much of the repetitive labor in the future could be replaced by AI.

AI's powerful advantages can effectively solve the current medical imaging field facing two major problems: first, more than 90% of the medical data is from medical imaging, but most of the current medical imaging relies on manual analysis. The disadvantages of manual analysis are obvious: doctors use the subjective experience to identify large amounts of image information are not only inefficient but also not conducive to timely and accurate positioning of lesions. Secondly, there is a shortage of medical imaging staff worldwide. Research shows that the annual growth rate of medical imaging data in China is about 30%, while the annual growth rate of radiologists is about 4%, which leads to a 26% gap between them. The growth in the number of radiologists is far less than the growth of imaging data. Meanwhile, the long training and practice required by radiologists indicate that the workload in dealing with medical imaging will be increasing, even unbearable in the future. Based on the current machine learning technology, AI can analyze and study historical medical image data and then identify some recurring characteristics of disease lesions, summarize the principles, combine the existing disease biology and other information, accurately predict the future variation of the disease, to intelligently identify disease lesions, and give effective recommendations in disease diagnosis, treatment plan design, and disease prognosis.

So, in this study, we retrospectively compared five commonly used machine learning methods (SVM, KNN, NB, RBF, and CNN) to predict the real-world X-ray imaging data of 407 knee joints from two different hospitals using Kellgren-Lawrence (K-L) grade of knee OA in order to help doctors choose proper auxiliary tools with much less time than usual, thus contributing to the promotion of machine learning-based automatic diagnosis methods.

2. Related Works

2.1. Data Collection. All data were collected with the informed consent of patients and ethical permission of both Shanghai Jiaotong University Affiliated Shanghai General Hospital and Nanjing Medical University Affiliated Wuxi No. 2 Hospital.

2.2. Clinical Features. There are 119 patients from Shanghai Jiaotong University Affiliated Shanghai General Hospital and 288 patients from Nanjing Medical University Affiliated Wuxi No. 2 Hospital with repeated pain, swelling, and limited range of motion (ROM) of knee joints. The symptoms get worse after going up and downstairs or walking for a long time, while some patients have joint locking. Meanwhile, all conservative treatments are ineffective.

2.3. Imageological Features. All patients have accepted anteroposterior and lateral axial X-ray examination (all of them were taken in standing weight-bearing positions while X-ray examiners from both hospital applicate the same procedure). There are varying degrees of bone hyperplasia, joint space narrowing, articular cartilage exfoliation, subchondral bone sclerosis, capsule degeneration, meniscus wear degeneration, synovial hypertrophy, joint capsule effusion, etc.

2.4. Region of Interest (ROI). We fixedly scale the original X-ray image to 256×256. After data expansion strategies such as translation, rotation, scaling, image brightness, and contrast adjustment, the image is passed through the ResNet-34 network backbone and the subsequent regression head network, using L1-loss regression optimization. The X, Y, and width values correspond to the ROI through this positioning method, and we can intercept a square region of interest of the original image for subsequent detection operations as shown in Figure 1.

According to the size of the joints in the captured image, the positioning model adaptively extracts the square area.

2.5. Kellgren-Lawrence (K-L) Grade. The Kellgren-Lawrence grading system for knee osteoarthritis is a grading method for evaluating the severity of knee osteoarthritis. According to the X-ray performance of the knee joint, it is divided into 0 (normal knee joint), I, II, III, and IV, as shown in Table 1.

The K-L grade of patients was evaluated by three senior doctors of the orthopedics department. Among 407 cases, 201 cases are classified as grade 0, while the other 206 cases are classified as grade 1 to 4.

RETRACTED

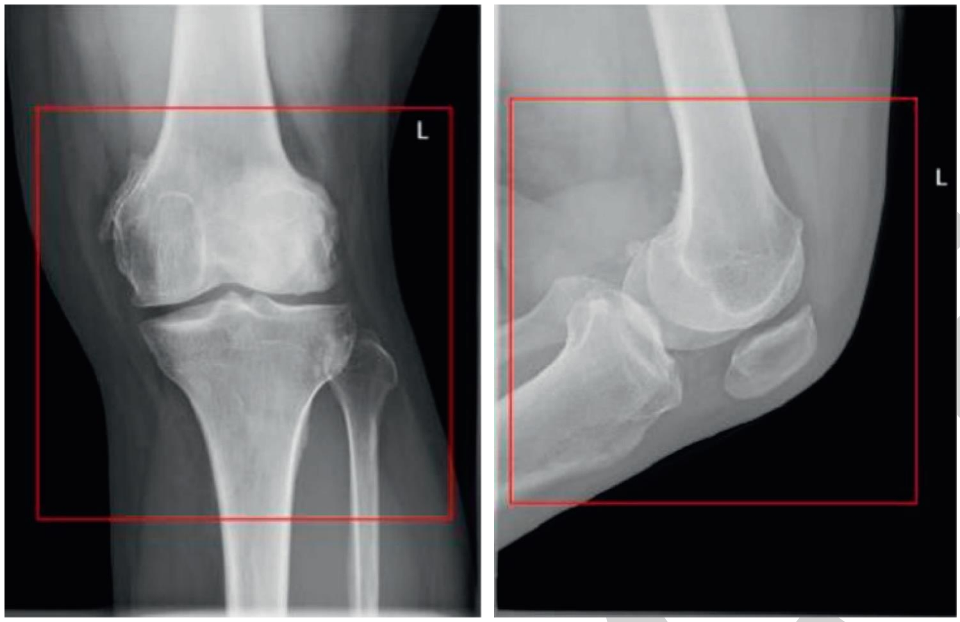

Figure 1: Sample graphs of ROI.

Table 1: Description and imageological features of Kellgren-Lawrence (K-L) grade.

Kellgren-Lawrence (K-L) grading scale					
Classification	Grade 0 normal	Grade 1 doubtful	Grade 2 mild	Grade 3 moderate	Grade 4 severe
Description	No signs of OA	Mild osteophyte: normal joint space	Specific osteophyte: normal joint space	Moderate joint space reduction	Joint space greatly reduced: subchondral sclerosis
X-ray image					

3. Automatic Diagnosis Methods

3.1. Traditional Methods. Imaging of osteoarthritis mainly involving technology will be understood mainly through Table 2.

3.2. Overall Design. First of all, we input X-ray images to perform feature extraction data preprocessing and then generate predictive samples using the data of 200 cases, which are used to train our models. Finally, the system will automatically perform ten repeat experiments using data from all cases and generate the ROC curve of the ten accuracy rates. The procedure is shown in Figure 2.

Features were first extracted from X-ray images according to the procedure mentioned before and then input into the five classifiers. Finally, ROC curve and accuracy rate were output and recorded.

3.3. Algorithm Modules

3.3.1. Naïve Bayes Algorithm. Naïve Bayes is a typical generation learning method based on the independent hypothesis of Bayes theology and conditions. The generation method is based on the training data to learn the joint probability distribution and then to find out the posttest probability. Specifically, using the training data to learn and estimate, its joint

RETRACTED

RETRACTED

Table 2: The five algorithms used in this study.

Algorithm	Introduction
Support vector machine, SVM	A class of generalized linear classifiers that binarizes data in supervised learning, with a decision boundary that is the maximum margin hyperplane for learning sample solving
Naïve Bayes, NB	The Naive Bayes classification (NBC) is based on the Bayes theology and assumes that the characteristic conditions are independent of each other, first through the given training set, with the characteristic words independent as the premise hypothesis, learning from the input to the output of the joint probability distribution, and then, based on the learned model, input X to find the output Y, which makes the interest probability the greatest
k-nearest neighbors, KNN	KNN's principle is that when predicting a new value x, it determines which category X belongs to, based on what category it is closest to the K point, and the general distance calculation method selects the European distance
Radial basis function neural network, RBF	There is one hidden node, including "n" input nodes, "p" hidden nodes, and "i" output nodes. The number of hidden nodes in the network is equal to the number of input samples. The activation function of this hidden node is usually a Gaussian radial basis function. All input samples are set as the center of the radial basis function, and each radial basis function agrees with the extended constant
Convolutional neural networks, CNNs	Convolutional neural network (CNN) is a type of feedforward neural network, which contains convolutional calculations with a deep structure and is one of the representative algorithms of deep learning. CNN has the ability to quantify learning and classify input information translation through class structure (displacement invariant classification), so it is also called "displacement invariant artificial neural network (SIANN)"

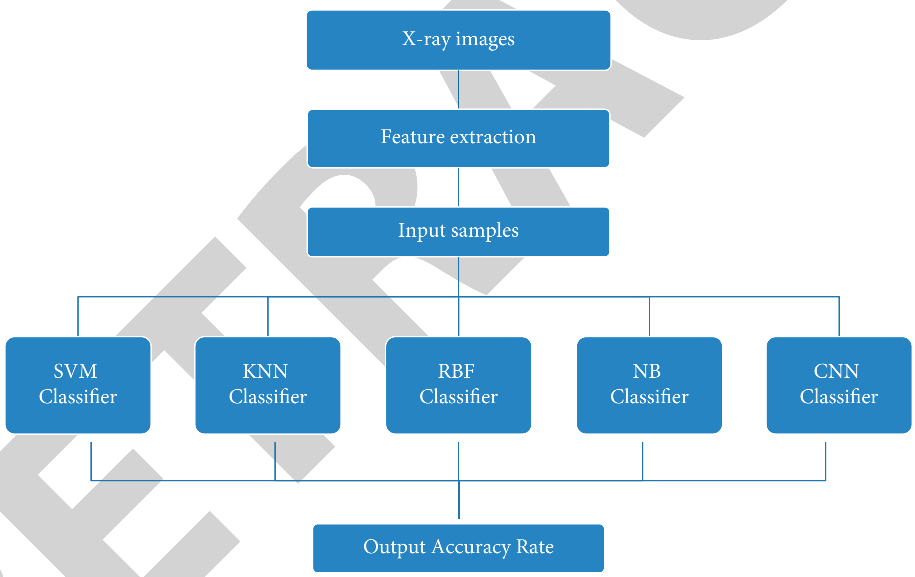

Figure 2: Flow diagram of the overall design.

probability distribution is obtained. The basic assumption of simple Bayes is conditional independence:

$$P(X = x \mid Y = C_k) = p\left(X^{(1)}, \ldots, X^{(n)} = x^{(n)} \mid Y = C_k\right) = \prod_{j=1}^{n} p\left(X^{(j)} = x^{(j)} \mid Y = C_k\right). \quad (1)$$

According to this hypothesis, the number of conditional probabilities contained in the model is greatly reduced, and the learning and prediction of simple Bayes is greatly simplified. Naïve simple Bayes uses Bayes and the learned joint probability model to classify the prediction.

$$P(Y \mid X) = \frac{P(X, Y)}{P(x)} = \frac{P(Y)P(X \mid Y)}{\sum_Y P(Y)(X \mid Y)}. \quad (2)$$

The resulting X is divided into classy.

$$y = \arg\max_{C_k} P(Y = C_k) \prod_{j=1}^{n} P\left(X_J = x^{(j)} \mid Y = C_k\right). \quad (3)$$

The expected risk is minimized when the probability of posttest is maximum equivalent to the 0-1 loss function.

3.3.2. The RBF Neural Network Algorithm. The RBF (Radial Basis Function) network is a single cryptographic feedforward neural network, as shown in the following figure: It is composed of three layers of neural networks, including an input layer, a hidden layer, and an output layer. The conversion from input space to lens space is nonlinear, while the conversion from implicit space to output layer space is linear. The radial basis function is used as the hidden neuron activation function, and the output layer is the linear combination of the hidden layer neuron output, as shown in Figure 3.

It is assumed that the input is a dimensional vector and the output is real, and then, the RBF network can be represented as

$$\varphi x = \sum_{i=1}^{q} w_i p(x, c_i), \tag{4}$$

where i is the number of recessive neurons, and the corresponding center and weight of the first criminal neuron are the radial base functions, which is some kind of radial symmetry of the standard function, usually defined as a monotony of the European distance between the sample and the data center, commonly used as Goss radial base functions such as

$$p(x, c_i) = e^{-1/2\sigma^2 \|x - c_i\|^2}. \tag{5}$$

RBF networks are usually trained in two steps: the first step is determining the center of neurons, and commonly used methods include immediate adoption and clustering, and the second step is, according to the least square loss function,

$$\eta = \min \sum_{j}^{m} \left\| t_j - p_j c_i \right\|^2. \tag{6}$$

The bias is obtained, so that it is equal to 0, and the formula can be simplified to

$$w = \exp\left(\frac{h}{c_{\max}^2} \left\| X_j - C_j \right\|^2\right), \quad j = 1, 2, \ldots m;\ i = 1, 2, \ldots, h. \tag{7}$$

3.3.3. Support Vector Machine (SVM). Support vector machine (SVM) is a binary classification model. Its basic model is to define the maximum interval of linear classifiers in the feature space. This maximum interval makes it different from the perceptron; the learning strategy of SVM is to maximize the interval, which can be its formalization is to solve the problem of convex quadratic programming, and it is also equivalent to minimizing the normalized hinge loss function. The learning algorithm of the support vector machine is an optimization algorithm for solving convex quadratic programming. The basic idea of SVM learning is to

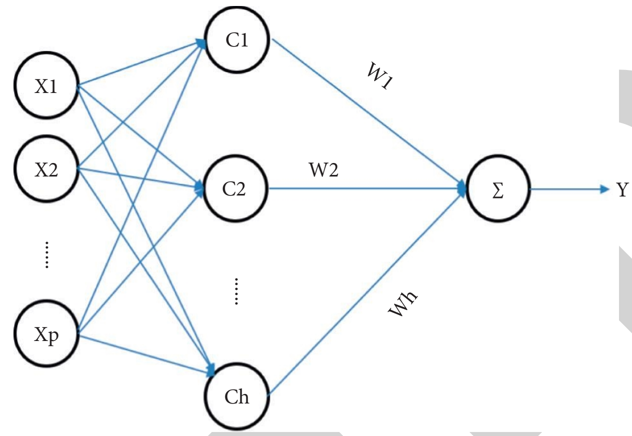

Figure 3: RBF network mode.

solve the separation hyperplane, which can correctly divide the training dataset and has the largest geometric interval. As shown in Figure 4, to separate hyperplanes, such hyperplanes have an infinite number (i.e., perceptrons) for the linearly divided dataset, but the separated hyperplane with the largest geometric interval is unique.

Given a training set, one of the regular SVM formulas can be expressed as

$$\begin{aligned} &\min \frac{1}{2}\|w\|^2 + C\sum_{i=1}^{N} \xi_i, \\ &s.t.\ y_i\left(w \cdot K\left(x_i, x_j\right) + b\right) \geq 1 - \xi, i = 1, 2, \ldots, N, \\ &\xi \geq 0, i = 1, 2, \ldots N. \end{aligned} \tag{8}$$

Y is the training data and X tag is the core function of the selection, commonly used is the Gauss nuclear. According to KKT conditions, the upper pair can be expressed as

$$\begin{aligned} &\min_{\alpha} \frac{1}{2} \sum_{i=1}^{N} \sum_{j=1}^{N} \alpha_i \alpha_j y_i y_j K\left(x_i, x_j\right) - \sum_{i=1}^{N} \alpha_i, \\ &s.t. \sum_{i=1}^{N} \alpha_i y_i = 0, \\ &0 \leq \alpha_i \leq C, i = 1, 2, \ldots, N. \end{aligned} \tag{9}$$

Among them is the Langrange calculator and C is the punishment parameter, and solving the abovementioned convex secondary planning problem, through 2 solutions, (1) the solution can be achieved by

$$\begin{aligned} w^* &= \sum_{i=1}^{N} \alpha_i^* y_i x_i, \\ b^* &= y_j - \sum_{i=1}^{N} y_i \alpha_i^* \left(x_i \cdot x_j\right). \end{aligned} \tag{10}$$

In the end, its classification decision function can be expressed as

RETRACTED

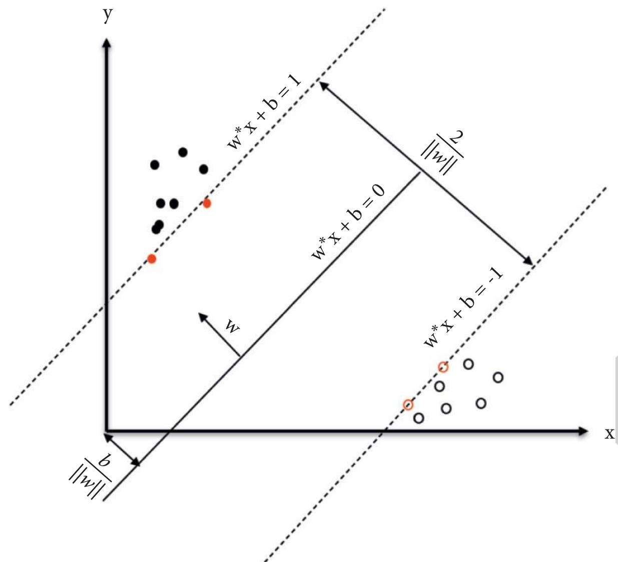

Figure 4: SVM network's separate superplanes.

$$f(x) = sign(w^* \cdot x + b^*). \tag{11}$$

3.3.4. K-Nearest Neighbor Algorithm (KNN). The K-nearest neighbor algorithm is a well-known statistical method for pattern recognition, which occupies an important position in machine learning classification algorithms. It is not only one of the simplest machine learning algorithms but also one of the most basic example-based learning methods and one of the best text classification algorithms. The basic idea of KNN is that if most of the K most similar instances in the feature space (that is, the nearest neighbors in the feature space) belong to a category, the instance also belongs to that category. The selected neighbor is an instance that has been correctly classified. The algorithm assumes that all instances correspond to points in N-dimensional space. We calculate the distance between a point and all other points, take out the K points closest to the point, and then, calculate the maximum proportion of the category belonging to the K points.

The European distance used here is expressed in two-dimensional space as

$$\rho = \sqrt{(x_2 - x_1)^2 + (y_2 - y_1)^2}. \tag{12}$$

The distance between the points $(x1, y1)$ and $(x2, y2)$ is represented in multidimensional space as

$$\rho = \sqrt{(x_1 - y_1)^2 + (x_2 - y_2)^2 + \ldots + (x_n - y_n)^2} = \sqrt{\sum_{i=1}^{n} (x_i - y_i)^2}. \tag{13}$$

This equation represents the distance between the point $(x1, x2, \ldots, x_n)$ and $(y1, y2, \ldots, y_n)$.

3.3.5. Convolutional Neural Networks (CNNs). Foreground and bone region extraction and background filling take the intercepted image, and the corresponding manually labeled foreground and bone mask image are taken as input. Through the basic semantic segmentation algorithm, the image is divided into bone, foreground, and background regions.

Here, we use the network structure of UNet-34 and use Tversky Loss and Focal Loss [13, 14] as the cost function for optimization. The segmented background area is filled with black to prevent the artificial marking in the background area from affecting the final classification result. The final output image size is 512×512, as shown in Figure 5.

Image segmentation is performed in the positioning area to complete the extraction of the foreground area and bone segmentation. Training the black-filled image in the background area helps to avoid the artificial identification of the background area and other additional information from interfering with the training of the classification and diagnosis model.

Classification and diagnosis of osteoarthritis based on images and supplementary patient information: we use cropped and filled front and side images plus the patient's supplementary information (age and gender) for classification diagnosis of osteoarthritis. Among them, the positive and lateral images use the ResNet-50 network with the

RETRACTED

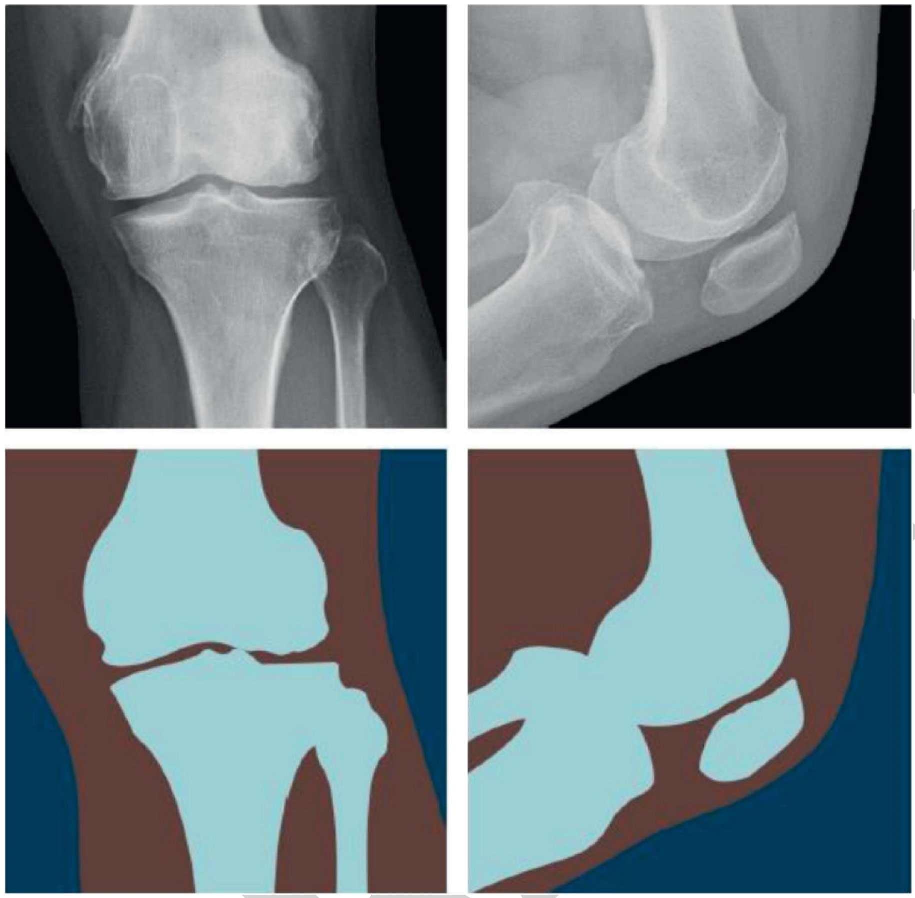

Figure 5: Foreground extraction of the knee joint.

spatial attention mechanism to obtain the corresponding description characteristics [15]. Age information is converted into a −1/1 multidimensional binary feature by setting different thresholds, plus gender features, as well as ROI and size information calculated by pixel spacing, and the features generated after the fully connected layer are merged with the image prediction features. Finally, the positive and negative samples and the prediction based on the Kellgren-Lawrence classification of osteoarthritis are carried out.

Visual diagnosis heat map display: since the final output only contains a positive and negative sample confidence value, it is not very intuitive. We use the Grad-CAM [16] method to visualize the main diagnostic basis areas for positive and negative samples, respectively, and improve the richness of information for auxiliary diagnosis, as shown in Figure 6.

Based on the results of the diagnosis and prediction, the basis for the prediction of the Grad-CAM visualization model is shown in the form of a heat map.

4. Results and Discussion

4.1. The Test Results of the Five Classifiers and ROC Curve. We used a dataset from more than 200 patients with knee X-ray positive and side-phase images, which were extracted and used to train our classifiers, followed by testing whether the five classifiers will work and what will work (ten times by default). As a result, the KNN, NB, SVM, and RBF classifiers can only figure out whether the X-ray image is grade 0 or grade 1–4 in K-L grade with the highest accuracy of 41.27%. By contrast, the CNN classifier can precisely figure out the K-L grade of the X-ray images with an accuracy of 99.68%.

4.1.1. KNN Classifier. The test result of the KNN classifier is shown in Figure 7.

4.1.2. NB Classifier. The test result of the NB classifier is shown in Figure 8.

4.1.3. SVM Classifier. The test result of the SVM classifier is shown in Figure 9.

4.1.4. RBF Classifier. The test result of the RBF classifier is shown in Figure 10.

4.1.5. CNN Classifier. The test result of the CNN classifier is shown in Figure 11.

4.2. Discussion. Knee X-ray examination is an important imaging method of knee osteoarthritis and a golden standard, which is the most common clinical imaging in medical

RETRACTED

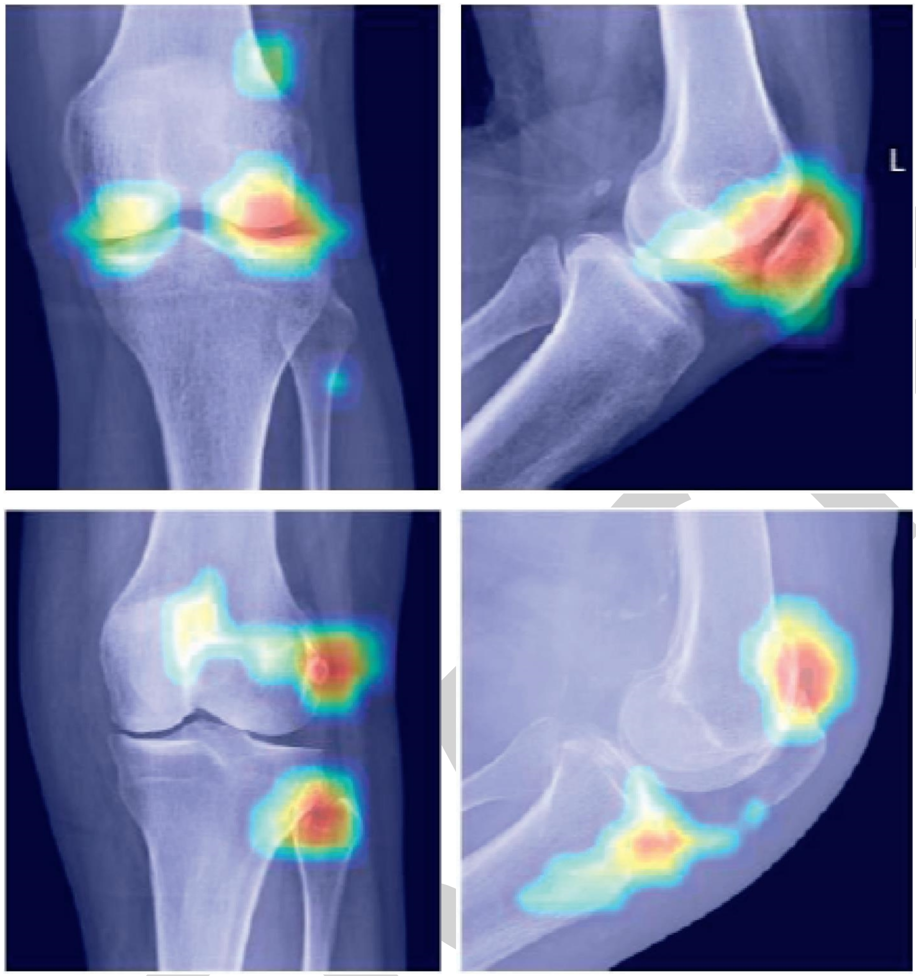

Figure 6: Sample graphs of the heat map.

RETRACTED

practice. In general hospitals, most routine checkups and OA screenings are preferred for knee OA, but there exists a large amount of false negative or false positive results in these diagnostic tasks [5]. The use of auxiliary diagnostic software can improve the efficiency of doctors, facilitate the optimization of workflow, and reduce the occurrence of missed diagnosis and misdiagnosis.

In the field of computer vision, the application of machine learning technology for data analysis shows a rapid growth trend. Especially, the application of Convolutional Neural Network (CNN) to learn to automatically obtain intermediate and high-level abstract features from images is widely used in various medical image analysis tasks. In some pieces of literature [17–19], the authors used MOST (http://most.ucsf.edu/) and OAI (https://oai.epi-ucsf.org/datarelease/) datasets for knee osteoarthritis diagnosis, but these datasets only use PA monologues for diagnosis, but the accuracy of diagnosis is not ideal. In clinical practice, in X-ray inspection of the patients' knee joints, it is routine to take an orthographic and lateral radiograph. However, due to the shooting habits of different radiologists and the compulsive posture caused by the pain of the patient, there are certain differences in the photographing posture of the patient. Moreover, it is difficult to train a robust knee joint prediction scheme due to the relatively limited image data generally available. So, we use multicenter X-ray images with a limited number of cases (407) to make our dataset more complicated to find out a better and universal machine learning method to help doctors make better clinical decisions.

The results of this study show that machine learning models can be used for the assisted diagnosis of OA, similar to previous studies. For the classification of medical images, the explanatory ability of the model is very important, which is helpful to evaluate the accuracy of the classification results of the model. This study used five machine learning methods, i.e., SVM, NB, KNN, RBF, and CNN [20], for classified model training of 407 knee imaging data of Shanghai Jiaotong University Affiliated Shanghai General Hospital and Nanjing Medical University Affiliated Wuxi No. 2 Hospital. Through the comparative analysis of the results, we have found out that the accuracy of the CNN classifier is 99.68%, while the accuracy of the NB classifier is 41.27%, 34.92% for the KNN classifier, 21.54% for the RBF classifier, and 29.93% for the SVM classifier. In addition, the CNN classifier provides a more detailed K-L rating (grade 0–5) of the patients' X-ray images and outputs the results in

RETRACTED

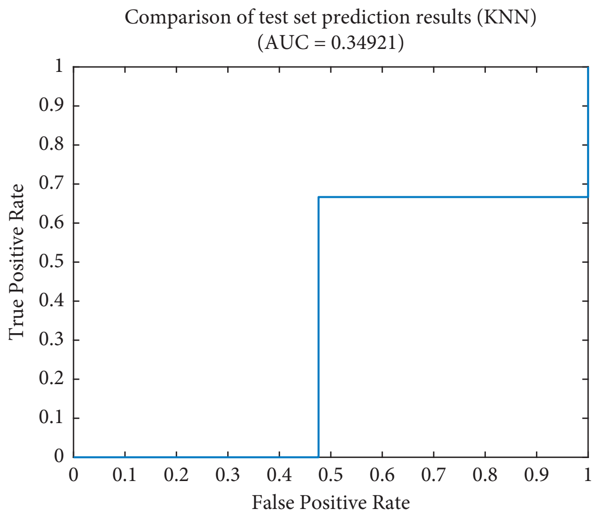

Figure 7: The ROC curve of the KNN classifier.

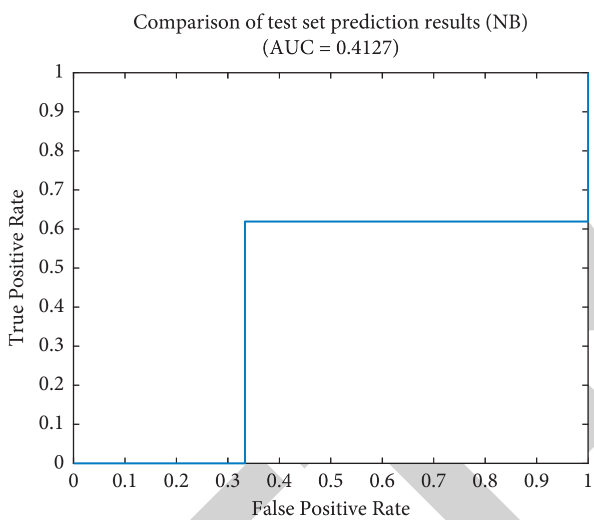

Figure 8: The results of the NB classifier.

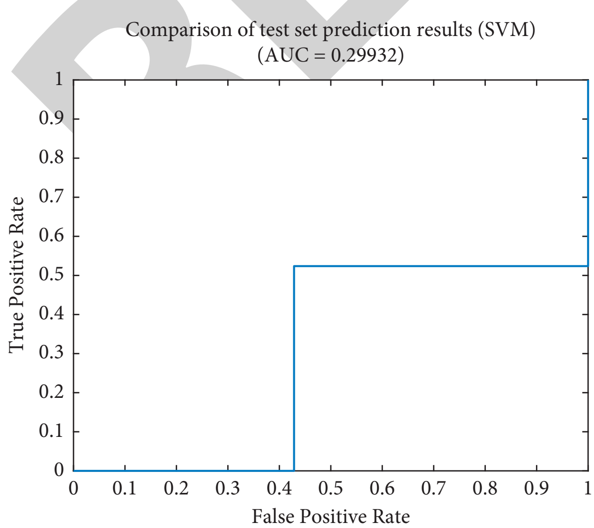

Figure 9: The results of the SVM classifier.

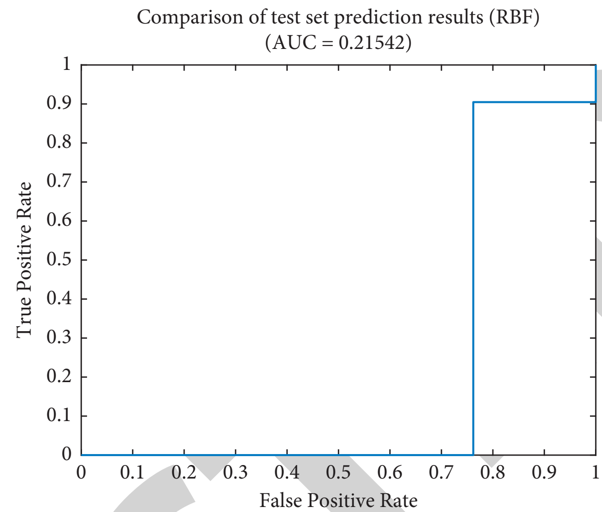

Figure 10: The results of the RBF classifier.

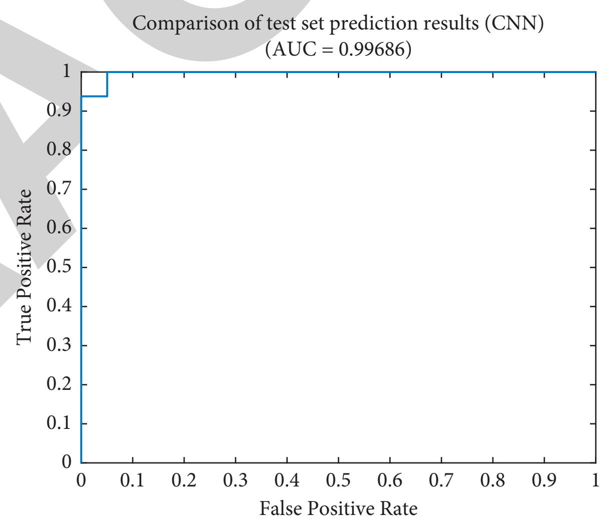

Figure 11: The results of the CNN classifier.

a probability manner, with more than 99% accuracy, accompanied by featured heat maps.

In medical image analysis, CNN is arguably one of the most successful applications of deep learning in the field of medical diagnosis. In 2015, researchers at the Chinese Academy of Sciences and the University of South Florida used one of CNN's variants, the multiscale convolution neural network, to enable computers to identify lung nodules (lung nodules are one of the bases for diagnosing lung cancer) from chest CT scans with 86.84% accuracy. In addition to lung cancer, CNN has been able to successfully detect breast cancer. Kooi trained CNN with more than 45,000 mammograms to bring diagnostic accuracy to the level of human experts. Another very common cancer, pancreatic cancer, was automatically identified by scholars at Huazhong University of Science and Technology using CNN, with a sensitivity of 89.85% and a specificity of 95.83

percent. Unlike previous studies, their CNN can use the original image directly as input without preediting the picture and other preprocessing.

In this study, we demonstrated five machine learning methods to diagnose and assess the K-L grade of knee OA from ordinary X-rays. Compared with previous studies, our model uses specific features related to the disease that can be compared with features used in clinical practice (for example, bone shape and joint space). The main advantage of the design of this study is that it demonstrates the ability of the model to transfer learning between different OA datasets [21, 22]. This clearly shows that our method is reliable for different "dummy data" and data collection settings. To create a clinically usable model, we considered several steps to enhance its robustness. First of all, we normalize the data to always have a constant area of interest and constrain the area of interest by considering only the area of interest used by the radiologist when making a decision. Secondly, we included a complete image queue containing X-ray image data from two centers of the same subject multiple times, which increases the size of the training dataset. Thirdly, we include X-ray beam angles of 5 degrees, 10 degrees, and 15 degrees, respectively, which helps standardize training and leads to more variability in the dataset. Moreover, we use rotation, jitter, contrast, and brightness data enhancement techniques, which make our training more powerful. Finally, we use a well-trained random seed network to introduce a small variance into the model decision.

In recent years, the relevant scholars have made a lot of explorations on the explanatory nature of the deep reel neural network model, in which the CAM method is to add weighting the feature maps generated by different types of reel layers and get the activation heat map, through which the results of the model classification can be explained [23]. Grad-CAM is an extension of CAM technology that can be applied to any CNN architecture. In this study, the K-L rating of OA used Grad-CAM to generate a classification activation heat map that shows which areas in the input image are important activation areas for obtaining the classification results. The data screening process for this study was completed by a retrospective study by a physician. Data screening was performed by imaging doctors and by senior orthopedic doctors to review the film again to determine image classification; although in the process of data cleaning, labor costs are higher, the results are better, with not too much data training to obtain the model, and accuracy is still very high [24].

Technical issues should be considered in the development and generalization of AI models [25]. In this study, the equipment was not filtered during model training, and continuous data were used. Knee imaging comes from a variety of DR equipment used by the unit in the actual clinical work, by different technicians to complete the filming work, not according to the equipment and personnel grouping. The results show that the images collected by different DR devices and technicians can be used for model training, and the metatheory comes from the images of DR devices, and the classification prediction of the verification set data has achieved good results. Knee X-ray inspection has clear technical specifications, and regularly trained technicians can complete daily work under the specifications and strong operational consistency, and modern DR equipment has automatic exposure function, can automatically set the best lighting conditions, and adjust the window level of the image, so the image preprocessing is not difficult, and it can be applied to a variety of AI model trainings. Because conventional X-rays can guarantee image quality, the image properties from different devices are not very different; from this point of view, in the process of generalization of the OA image diagnostic model, there is no risk of image acquisition technology.

A basic requirement for AI clinical applications is integration with clinical processes. By the regulatory and ethical framework, domestic and foreign technical personnel have conducted a lot of exploration, and all believe that the AI model is an independent third-party software used of the form which is not the optimal solution [26]. The author thinks that it is a better solution to return AI results directly to the structured report of clinical practice [27].

Of course, our research still has some limitations. Our validation set has filtered out relatively small amounts from clinical images. However, from a clinical point of view, in the OA case, our method has better classification performance than other methods in the comparison model. So, in future research, we will use a large amount of data to study the versatility of this method in multiple datasets. In addition, the images used in this study were obtained under standard settings (including positioning boxes).

5. Conclusions

As mentioned above, we recommend using the CNN classifier to evaluate knee OA patients' K-L rating. We believe that it can provide further information to practitioners about the severity of knee OA. By providing the probability of a particular K-L grade, the model mimics the decision-making process of practitioners by considering the one closest to the medical definition, and a choice is made between different K-L grades, which can benefit inexperienced practitioners and ultimately reduce their training time. Thus, builds better trust towards machine learning-based automatic diagnosis methods and, moreover, reduces the workload of clinicians, especially for remote areas without enough medical staff. All in all, we believe that the proposed method has several advantages. First, it can help patients with knee pain be diagnosed faster and more accurately. Secondly, in general, by reducing the workload of doctors, especially in remote areas, and reducing daily work costs, our medical services will benefit from it. Although the current research focuses on OA, our model can systematically assess the patient's knee condition and monitor other conditions, such as follow-up of ligament surgery and assessment of joint changes after knee removal. Third, research institutions will benefit from our method because it is a tool for analyzing large cohorts.

RETRACTED

RETRACTED

Data Availability

The labeled dataset used to support the findings of this study is available from the corresponding author upon request.

Conflicts of Interest

The authors declare no conflicts of interest.

Acknowledgments

This work was supported in part by the Special Youth Project for Clinical Research of Shanghai Health Commission under Grant 2018Y0247.

References

[1] J. H. Kellgren and J. S. Lawrence, "Radiological assessment of osteo-arthrosis," *Annals of the Rheumatic Diseases*, vol. 16, no. 4, pp. 494–502, 1957.

[2] L. Gossec, J. M. Jordan, S. A. Mazzuca et al., "Comparative evaluation of three semi-quantitative radiographic grading techniques for knee osteoarthritis in termsof validity and reproducibility in 1759 x-rays: report of the oarsi–omeract task force: extended report," *Osteoarthr. cartilage*, vol. 16, pp. 742–748, 2008.

[3] L. Sheehy, E. Culham, L. McLean et al., "Validity and sensitivity to change of three scales for the radiographic assessment of knee osteoarthritis using imagesfrom the multicenter osteoarthritis study (most)," *Osteoarthritis and Cartilage*, vol. 23, pp. 1491–1498, 2015.

[4] A. G. Culvenor, C. N. Engen, B. Elin Øiestad, L. Engebretsen, and M. Arna Risberg, "Defining the presence of radiographic kneeosteoarthritis: a comparison between the kellgren and lawrence system and oarsi atlas criteria," *Knee Surgery, Sports Traumatology, Arthroscopy*, vol. 23, pp. 3532–3539, 2015.

[5] T. Drew, M. L.-H. Vo, and J. M. Wolfe, "The invisible gorilla strikes again: sustained inattentional blindness in expert observers," *Psychol. science*, vol. 24, pp. 1848–1853, 2013.

[6] J. Dacree and E. Huskisson, "The automatic assessment of knee radiographs in osteoarthritis using digital image analysis," *Rheumatology*, vol. 28, pp. 506–510, 1989.

[7] L. Shamir, D. T. Felson, L. Ferrucci, and I. G. Goldberg, "Assessment of osteoarthritis initiative–kellgren and lawrence scoring projectsquality using computer analysis," *J. Musculoskelet. Res.*, vol. 13, pp. 197–201, 2010.

[8] T. Woloszynski, P. Podsiadlo, G. Stachowiak, and M. Kurzynski, "A dissimilarity-based multiple classifier system for trabecular bone texturein detection and prediction of progression of knee osteoarthritis," *Proceedings - Institution of Mechanical Engineers Part H: J. Eng. Medicine*, vol. 226, pp. 887–894, 2012.

[9] L. Shamir, S. M. Ling, W. Scott, M. Hochberg, L. Ferrucci, and I. G. Goldberg, "Early detection of radiographic knee osteoarthritis using computer-aided analysis," *Osteoarthritis and Cartilage*, vol. 17, pp. 1307–1312, 2009.

[10] J. Thomson, T. O'Neill, D. Felson, and T. Cootes, "Automated shape and texture analysis for detection of osteoarthritis fromradiographs of the knee," in *Proceedings of the International Conference on Medical Image Computing and Computer-Assisted Intervention*, pp. 127–134, Springer, Switzerland AG, November 2015.

[11] J. Antony, K. McGuinness, N. E. Connor, and K. Moran, "Quantifying radiographic knee osteoarthritis severity using deepconvolutional neural networks," in *Proceedings of the 2016 23rd International Conference on Pattern Recognition (ICPR)*, IEEE, Cancun, Mexico, December 2016.

[12] J. Antony, K. McGuinness, K. Moran, and N. E. O'Connor, "Automatic detection of knee joints and quantification of knee osteoarthritisseverity using convolutional neural networks," in *Proceedings of the International Conference onMachine Learning and Data Mining in Pattern Recognition,Lecture Notes in Computer Science*, pp. 376–390, Springer, Cham, Switzerland AG, July 2017.

[13] Abraham and N. Mefraz Khan, "A novel focal TverskyLoss function with improved attention U-net for lesion segmentation," in *Proceedings of the 2019 IEEE 16th International Symposium on Biomedical Imaging*, IEEE, Venice, Italy, April 2019.

[14] T.-Yi Lin, P. Goyal, R. Girshick, K. He, and P. Dollar, "Focal loss for dense object detection," in *Proceedings of the IEEE International Conference on Computer Vision (ICCV)*, pp. 2980–2988, IEEE, Venice, Italy, October 2017.

[15] F. Wang, M. Jiang, C. Qian et al., "Residual attention network for image classification," in *Proceedings of the IEEE Conference on Computer Vision and Pattern Recognition (CVPR)*, pp. 3156–3164, IEEE, Honolulu, HI, USA, July 2017.

[16] R. R. Selvaraju, M. Cogswell, A. Das, R. Vedantam, D. Parikh, and D. Batra, "Grad-CAM: visual explanations from deep networks via gradient-based localization," in *Proceedings of the IEEE International Conference on Computer Vision (ICCV)*, pp. 618–626, IEEE, Venice, Italy, October 2017.

[17] J. Antony, K. McGuinness, K. Moran, and N. E. O'Connor, "Feature learning to automatically assess radiographic knee osteoarthritis severity," *Deep Learners and Deep Learner Descriptors for Medical Applications*, vol. 186, pp. 9–93, 2020.

[18] M. Górriz, J. Antony, K. McGuinness, X. Giró-i-Nieto, and N. E. O'Connor, "Assessing knee OA severity with CNN attention-basedend-to-end architectures," *Proceedings of the 2nd International Conference on Medical Imaging with Deep Learning, PMLR*, vol. 102, pp. 197–214, 2019.

[19] J. Abedin, J. Antony, K. McGuinness et al., "Predicting knee osteoarthritis severity: comparative modeling based on patient's data and plain X-ray images," *Scientific Reports*, vol. 9, p. 5761, 2019.

[20] C. von Tycowicz, "Towards shape-based knee osteoarthritis classification using graph convolutional networks," in *Proceedings of the 2020 IEEE 17th International Symposium on Biomedical Imaging (ISBI)*, pp. 750–753, IEEE, Iowa City, IA, USA, April 2020.

[21] Y. Jiang, Y. Zhang, C. Lin, and D. Wu, "Chin-teng lin, EEG-based driver drowsiness estimation using an online multi-view and transfer TSK fuzzy system," *IEEE Transactions on Intelligent Transportation Systems*, vol. 22, no. 3, pp. 1752–1764, 2021.

[22] Y. Jiang, X. Gu, D. Wu et al., "A novel negative-transfer-resistant fuzzy clustering model with a shared cross-domain transfer latent space and its application to brain CT image segmentation," *IEEE/ACM Transactions on Computational Biology and Bioinformatics*, vol. 18, no. 1, pp. 40–52, 2021.

[23] B. Zhou, A. Khosla, A. Lapedriza, A. Oliva, and A. Torralba, "Learning deep features for discriminative localization[C]," in *Proceedings of the Las Vegas: IEEE Conference on Computer Vision and Pattern Recognition (CVPR)*, pp. 2921–2929, IEEE, Las Vegas, NV, USA, June 2016.

[24] D. Jia, D. Wei, S. Richard, L. Li-Jia, L. Kai, and L. Fei-Fei, *Lmagenet: A Large-Scale Hierarchical Image Database in*

Hindawi
Journal of Healthcare Engineering
Volume 2023, Article ID 9817018, 1 page
https://doi.org/10.1155/2023/9817018

Retraction

Retracted: Prediction and Analysis of Length of Stay Based on Nonlinear Weighted XGBoost Algorithm in Hospital

Journal of Healthcare Engineering

Received 10 October 2023; Accepted 10 October 2023; Published 11 October 2023

Copyright © 2023 Journal of Healthcare Engineering. This is an open access article distributed under the Creative Commons Attribution License, which permits unrestricted use, distribution, and reproduction in any medium, provided the original work is properly cited.

This article has been retracted by Hindawi following an investigation undertaken by the publisher [1]. This investigation has uncovered evidence of one or more of the following indicators of systematic manipulation of the publication process:

(1) Discrepancies in scope
(2) Discrepancies in the description of the research reported
(3) Discrepancies between the availability of data and the research described
(4) Inappropriate citations
(5) Incoherent, meaningless and/or irrelevant content included in the article
(6) Peer-review manipulation

The presence of these indicators undermines our confidence in the integrity of the article's content and we cannot, therefore, vouch for its reliability. Please note that this notice is intended solely to alert readers that the content of this article is unreliable. We have not investigated whether authors were aware of or involved in the systematic manipulation of the publication process.

Wiley and Hindawi regrets that the usual quality checks did not identify these issues before publication and have since put additional measures in place to safeguard research integrity.

We wish to credit our own Research Integrity and Research Publishing teams and anonymous and named external researchers and research integrity experts for contributing to this investigation.

The corresponding author, as the representative of all authors, has been given the opportunity to register their agreement or disagreement to this retraction. We have kept a record of any response received.

References

[1] Y. Chen, "Prediction and Analysis of Length of Stay Based on Nonlinear Weighted XGBoost Algorithm in Hospital," *Journal of Healthcare Engineering*, vol. 2021, Article ID 4714898, 9 pages, 2021.

Hindawi
Journal of Healthcare Engineering
Volume 2021, Article ID 4714898, 9 pages
https://doi.org/10.1155/2021/4714898

Research Article

Prediction and Analysis of Length of Stay Based on Nonlinear Weighted XGBoost Algorithm in Hospital

Yong Chen

The Affiliated Hospital of Chengde Medical College, Chengde, Hebei 067000, China

Correspondence should be addressed to Yong Chen; chenyong2655@cdmc.edu.cn

Received 22 October 2021; Revised 19 November 2021; Accepted 20 November 2021; Published 1 December 2021

Academic Editor: Gu Xiaoqing

Copyright © 2021 Yong Chen. This is an open access article distributed under the Creative Commons Attribution License, which permits unrestricted use, distribution, and reproduction in any medium, provided the original work is properly cited.

An improved nonlinear weighted extreme gradient boosting (XGBoost) technique is developed to forecast length of stay for patients with imbalance data. The algorithm first chooses an effective technique for fitting the duration of stay and determining the distribution law and then optimizes the negative log likelihood loss function using a heuristic nonlinear weighting method based on sample percentage. Theoretical and practical results reveal that, when compared to existing algorithms, the XGBoost method based on nonlinear weighting may achieve higher classification accuracy and better prediction performance, which is beneficial in treating more patients with fewer hospital beds.

RETRACTED

1. Introduction

Hospital beds are one of the important medical resources, and these beds are usually used as an important indicator to measure the hospital service level, which can objectively reflect the development level of local medical system [1]. Due to the limited number of beds in most hospitals, the length of stay of patients is also closely related to the cost of hospitalization. Therefore, shortening the length of stay can not only increase the turnover of inpatients but also reduce the medical cost and the social medical burden [2]. For the medical system, it is very important to identify the relevant risk factors related to patient recovery and length of stay. Therefore, how to improve the allocation of hospital beds and alleviate the shortage of hospital beds is a major problem currently faced by hospital managers [3].

In the case of limited medical resources in hospitals and various uncertain factors in the treatment process, the problem of bed allocation has not been effectively resolved, and many hospital beds are still in short supply. Therefore, accurately predicting the length of stay will help to allocate hospital beds rationally and increase the utilization rate of beds [4].

The length of hospital stay is an important indicator of hospital management. Specifically, its prediction is to use statistical methods to summarize, analyze, and study its change rule and its distribution law and use machine learning algorithms [5, 6] to build models to predict the length of hospital stay [7]. Not only are these important key technology that need to be broken through in theoretical research, but they also have a certain engineering value for hospital bed scheduling arrangements and the improvement of hospital rescue capabilities [8]. Therefore, domestic and foreign scholars have conducted in-depth studies on the length of hospitalization of patients [9–11]. The research content is mainly divided into distribution fitting and parameter estimation. In the study of distribution fitting, some scholars use different distribution function to fit the length of stay of patients and compare their fitting effects. For example, Kong et al. [12] selected three widely used models, log-normal model, Weibull model, and Gamma model, used these three models to fit the distribution of length of stay in hospital, and evaluated the applicability of these three models. Coskun et al. [13] used the Markov process to analyze the hospitalization process of patient, which is divided into short, medium, and long hospital stays. The PH distribution is used to fit the distribution of the length of stay, and the maximum likelihood estimation method is used to obtain the estimated value of the parameter. The study also pointed out the inadequacy of choosing lognormal distribution and gamma distribution to fit the length of hospital stay. The empirical analysis results show that the use of the 6-phase Markov model to fit the length of stay is better than other distribution, but there is also overfitting phenomenon. Lazar et al. also described the hospitalization process as a Markov state so as to analyze the whole process of the patient from admission to discharge [14].

In the study of parameter estimation, most scholars adopt Expectation-Maximization (EM) algorithm to estimate the model parameters of the length of hospital stay. Reed et al. [15] used the convolution operation of two distributions to establish the model of hospitalization length variable, which is a well-known technology in the field of signal processing. The particularity of the model is that the variables of interest are considered to be the sum of two random variables with different distributions. One of the variables will take the recovery of patients from hospitalization as the model, while the other variable will take the hospital management process (such as discharge process) as the model. A novel improved model based on the classical maximum likelihood estimation and the EM algorithm is used to fit a group of real data in the hospital, where the results show that the effect of the proposed model is good. Since the average length of stay cannot well reflect the distribution characteristics, some references have studied the distribution of length of stay based on probability distribution. Ingeman et al. [16] studied the length of stay distribution of patients on the basis of the data of medical insurance center, fitted the probability distribution of length of stay with different probability distribution, and evaluated the fitting effect of different distributions according to KL indicators. Finally, the Coxian distribution is selected to divide the length of hospitalization into decision trees through three variables: age, gender, and hospital level. It provides an empirical basis for the traditional operations research model, verifies the common service time distribution of the queuing model through data, and provides help for hospital management decision-making.

Although these research methods based on inpatient data have achieved good results in the daily operation of the hospital, there is still an overfitting problem in establishing the superposition distribution based on a single continuous model. Therefore, some scholars began to design two or more distribution models to fit a group of hospitalization data, so as to make the fitting effect of the tail better. This overlay model not only makes the tail closer to the actual distribution but also better adjusts the fitting effect of other parts and solves the problem of insufficient fitting of a single distribution. Literature [16] established a prediction model of hospitalization duration based on SVM regression, analyzed the chaotic characteristics of time series from admission to discharge, and constructed the input vector of support vector regression model by phase-space reconstruction. Literature [17] adopts Naive Bayes (NB) methods to extract the characteristics of hospital resource data and patient data and establish the prediction model of length of stay. Literature [18] constructed the prediction model based on C4.5 decision tree. However, most of the existing research methods are for small data samples. When dealing with high-dimensional samples, data dimensionality reduction is required, which makes it easy to cause information loss and affect the accuracy of prediction [19].

The continuous emergence of big data analysis and processing methods in the field of data science provides an effective tool for massive data mining and data law learning. Extreme gradient boosting (XGBoost [20]) is a parallel integration algorithm suitable for large-scale datasets. It has the characteristics of multicore parallel operation, regularization promotion, and user-defined objective function, is suitable for processing structured data, and has high accuracy and interpretability. At present, XGBoost algorithm has been widely used in the field of data science [21–23].

In this paper, a nonlinear weight XGBoost algorithm is proposed to predict the length of hospitalization. Aiming at the problem of unbalanced data samples, the proposed algorithm uses the sample proportion and Sigmoid function to determine the sample weight and improve the objective function, so as to realize the effective learning of unbalanced data samples and improve the prediction accuracy.

The length of stay is an important basis for the rational allocation of hospital beds, and an important embodiment of the operation speed, medical level, and work quality of the hospital. However, the simple average length of stay cannot reflect its internal distribution characteristics, which is not reasonable as the basis of hospital bed management. In the case of asymmetric data distribution of patient length of stay, the decisions made by hospital managers based on the average length of stay may lead to unreasonable allocation of hospital beds and unnecessary losses. Therefore, this paper will select an appropriate model to fit the length of stay and find out the distribution law of the length of stay, which is of great significance to the improvement of hospital bed management and hospital rescue ability. In addition, by constructing the prediction model of inpatient length of stay, this paper discusses the application of the improved algorithm in the prediction of inpatient length of stay, hoping to bring some help to hospital managers in the scheduling and arrangement of hospital beds.

2. Related Works

XGBoost model is a machine learning algorithm implemented under the gradient boosting framework. It is a representative algorithm in boosting-based integrated algorithms [24]. The integrated algorithm constructs multiple weak-evaluators on dataset and summarizes the modeling results of all weak-evaluators to obtain better regression performance than a single model. The idea of XGBoost model is the process of continuously adding trees. Adding a tree every time is to learn a new function $f(x)$ to fit the residual of the last prediction. After training, k trees will be obtained. Each tree will fall to a corresponding leaf node, and each leaf node corresponds to a score. Adding up the scores corresponding to each tree is the predicted value of the sample. In other words, XGBoost model generates a new tree through continuous iteration to fit the residual of the previous tree, as shown in Figure 1. With the increase of

RETRACTED

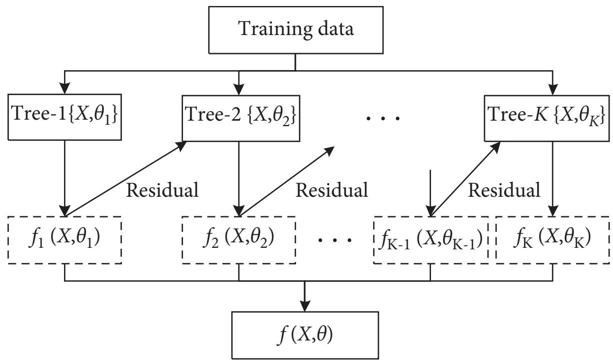

Figure 1: Framework of XGBoost model.

iteration times, the accuracy continues to improve. Therefore, XGBoost model can fit the inpatient data better, so as to reduce the prediction error and achieve high prediction accuracy.

The tree model used in this paper is CART regression tree model. It is assumed that there are n trees in the model, and the prediction results of the whole model on the sample can be shown in the following formula:

$$\widehat{y}_i = \sum_{i=1}^{n} f_i(x_i), \quad f_i \in F, \tag{1}$$

where n is the number of trees, f_i is a function in function space F, $\widehat{y}_i$ is the predicted value, x_i is the first x_i data entered by users, and F is all possible CART sets.

XGBoost has achieved good results in inventory and sales prediction, physical-event classification, web-text classification, customer-behavior prediction, click-through-rate (CTR) prediction, stock prediction, and other tasks, but it is rarely used in hospital length-of-stay prediction [25]. XGBoost provides scalable functions in all scenarios and can adopt external memory to ensure the calculation of big data, which can process a large amount of data with a small amount of node resources. XGBoost algorithm has the following advantages: XGBoost adds a regularization term to the objective function, reduces the variance of the model, makes the learned model simpler, and can effectively prevent overfitting; XGBoost carries out the second-order Taylor expansion of the loss function, which makes the model more accurate; XGBoost supports parallelization and column sampling, which has fast training speed [26]. Therefore, this paper will use XGBoost to predict the length of stay and treat more patients with limited medical beds.

Scholars at home and abroad mostly fit the distribution of inpatient length of stay [27]. However, the fitting of distribution only describes its distribution form through the length-of-stay data and cannot reflect what factors affect the length of stay of patients. This paper will use the improved XGBoost algorithm to establish the prediction model for the prediction of the length of stay. Firstly, preprocess the data, then extract the features from the patient data, take the medical features as the input variable to predict the length of stay, and finally realize the classified prediction of the length of hospitalization. In order to compare the prediction performance of different algorithms on the length of stay, the advantages and disadvantages of different methods in predicting the length of stay were experimentally discussed, so as to provide technical support for the prediction of the length of stay.

3. Nonlinear Weighted XGBoost Algorithm for Prediction of Length of Stay

As we all know, the traditional XGBoost algorithm aims to reduce the overall error, so it pays more attention to the classification and prediction performance of most class samples in the process of model learning, which will lead to the insufficient training of the classification performance of a few class samples [28, 29]. In the problem of length-of-stay prediction, this will also affect the prediction effect of the model for the allocation of hospital beds with relatively less frequency but more serious practical impact.

XGBoost model generates a new tree through continuous iteration to fit the residual of the previous tree. With the increase of iteration times, the accuracy continues to improve. At each iteration, the original model remains unchanged and a new function is added to the model. Since a function corresponds to a tree, the newly generated tree fits the residual of the last prediction. The iterative process is written as follows:

$$\begin{cases} \widehat{y}_i^{(0)} = 0, \\ \widehat{y}_i^{(1)} = f_1(x_i) + \widehat{y}_i^{(0)}, \\ \widehat{y}_i^{(t)} = \widehat{y}_i^{(t-1)} + f_t(x_i). \end{cases} \tag{2}$$

The objective function of XGBoost is as follows:

$$F(y) = \sum_{i=1}^{n} l(y, \widehat{y}) + \sum_{i=1}^{n} \Omega(f_k), \tag{3}$$

$$\Omega(f_k) = \gamma T + 0.5\lambda \sum_{i=1}^{T} \varpi_j^2 \Bigg), \tag{4}$$

where $l(y, \widehat{y})$ is used to measure the difference between the predicted score and the real score and $\sum_{i=1}^{n} \Omega(f_k)$ is a regularization term. In (4), T is the number of leaf nodes, r is the score of leaf nodes, γ is used to control the number of leaf nodes, and λ is to ensure that the score of leaf nodes is not too large. The goal of regularization is to select a simple prediction function to prevent overfitting of the model [30]. When the regularization parameter is zero, XGBoost degenerates into a traditional boosting model. The iteration operation adopts the additive training to further optimize the objective function. In each iteration, the following strategy is adopted to update the objective function:

$$\tau^{(t)} = \sum_{i=1}^{n} l\left(y_i, \widehat{y}_i^{(t-1)}\right) + f_t(X_i) + \Omega(f_t). \tag{5}$$

In order to minimize the objective function, XGBoost first expands the Taylor second-order expansion at $f_t = 0$ and extends the Taylor series of the loss function to the

RETRACTED

second-order. The objective function is approximate to the following equation:

$$\tau^{(t)} \approx \sum_{i=1}^{n}\left[l\left(y_i, \hat{y}_i^{(t-1)}\right) + f_t\left(X_i\right) + 0.5h_i f_t^2\left(x_i\right)\right] + \Omega\left(f_t\right). \tag{6}$$

If the loss function values of each data are added up, the final objective function can be rewritten as follows:

$$\begin{aligned} X_{obj} &\approx \sum_{i=1}^{n}\left[g_i f_t\left(x_i\right) + 0.5h_i f_t^2\left(x_i\right)\right] + \Omega\left(f_t\right) \\ &= \lambda T + \sum_{i=1}^{n}\left[g f_{t0.0.5}\left(X_i\right) + 0.5h_i f_t^2\left(x_i\right)\right] + \Omega\left(f_t\right) + 0.5\lambda\sum_{j=1}^{T} w_j^2 \\ &= \sum_{j=1}^{T}\left[\sum_{i\in I} g_i w_j^2 + 0.5\left(\sum_{i\in I} h_i + \lambda) w_j^2\right)\right] + \lambda T, \end{aligned} \tag{7}$$

where X_{obj} is the loss function, $g_i = \partial\hat{y}^{t-1} l\left(y_i, \hat{y}^{(t-1)}\right)$ is the first derivative, and $h_i = \partial^2\hat{y}^{t-1} l\left(y_i, \hat{y}^{(t-1)}\right)$ is the second derivative.

It can be seen that (7) rewrites the objective function into a quadratic function about the leaf node fraction, and the optimal value is $g_i = \partial\hat{y}^{t-1} l\left(y_i, \hat{y}^{(t-1)}\right)$, so objective function values can be obtain as follows:

$$\begin{aligned} w_j^* &= -\frac{G_j}{\left(H_j + \lambda\right)}, \\ X_{\text{obj}} &= -0.5\sum_{j=1}^{T}\frac{G_j}{\left(H_j + \lambda\right)} + \lambda T, \end{aligned} \tag{8}$$

where $G_j = \sum_{i\in I} g_i \; H_j = \sum_{i\in I} h_i$.

It can be seen that the weight w_j^* will also affect the prediction effect of the model for the allocation of hospital beds with relatively less frequency but more serious practical impact. Therefore, this paper proposes a nonlinear weighting method to improve the performance of XGBoost model under data imbalance. The basic idea is to use heuristic function to nonlinear weight different categories of samples, and the number of samples is negatively correlated with the sample weight. The weight can be calculated as follows:

(1) Calculate the sample proportion.

$$v_k = \frac{d_k}{D}, \tag{9}$$

where D is the total number of samples, d_k is the number of samples of the $k-$th categories, and v_k is the proportion of the $k-$th categories sample in the total samples.

(2) Calculate the nonlinear weighting function.

Generally speaking, the weighting idea based on sample proportion can use the reciprocal of v_k in (10) as the weight. Although the reciprocal of v_k can improve the weight of a few samples, the weight of the categories accounting for the majority of samples decreases greatly, which may lead to excessive weight difference. In addition, if the proportion of most samples is much higher than that of a few samples, the weight of most samples may be very small, and the weight of a few samples may be too high, which may lead to low model training efficiency. Therefore, a nonlinear weighting function based on sample proportion is proposed in this paper.

$$w_k = 0.5 + \frac{\alpha}{\left(1 + e^{v_k}\right)}. \tag{10}$$

The nonlinear weighting function shown in (9) has two advantages: (1) the weighting function based on Sigmoid function is smooth and differentiable; (2) since too small weight will affect the training efficiency of the model and lead to overfitting, the constant 0.5 is added to the weighting function shown in (9) which can ensure that the weight will not be too small. According to (7), the value range of the function is $[0.5 + \alpha/(1 + e), 0.5 + \alpha/2]$, where α is the weight range control parameter.

Negative-log-likelihood (NLL) loss function is selected as the loss function to predict the length of stay. For samples x with the $k-$th categories, the NLL-based loss function can be denoted as $l\left(y_i, \hat{y}_i\right) = -\sum_k y(k)\log\hat{y}(k)$. Therefore, the difference between the predicted score and the real score can be rewritten as follows:

$$l\left(y_i, \hat{y}_i\right) = -w_k \log\hat{y}(k). \tag{11}$$

In this paper, a hospital length-of-stay prediction algorithm based on nonlinear weighted XGBoost algorithm is proposed. The algorithm is divided into model training and test verification stages. In the model training stage, a new classifier is gradually added to fit the training error in the current iteration and optimize the fitting effect of the model on the training samples [15, 31]. In the test verification stage, the test set is used to verify the classification prediction performance of the model. The algorithm flow is shown in Table 1.

4. Experiment Results and Analysis

4.1. Parameter Settings. In our experimental, there are 114,209 real patient datasets from an open-source database, where 75% of them are training sets and 25% are test sets. In order to compare the model performance, the nonlinear weighted XGBoost algorithm is compared with Naive Bayes (NB) [32], decision tree (DT) [33], SVM [34], KNN [32], and XGBoost algorithm [20].

XGBoost algorithm has many parameters. Generally speaking, the initialization settings of parameters are as follows: *n_estimators, Gamma, Subsample, colsample-bytree*, and *learning rate* are set to 1000, 0, 0.8, 0.8, and 2, respectively. To improve the generalization ability of the model, optimizing the model parameters is also an essential step.

As for our improved XGBoost, three parameters need to be determined in the process of the length-of-stay prediction and have a great impact on the performance, including the learning rate, the maximum height of the tree, and the random sampling ratio. Since the maximum height of the

RETRACTED

Table 1: Pseudocode for nonlinear weighted XGBoost algorithm.

Model: nonlinear weighted XGBoost algorithm
Input: high-dimensional patient medical data
Output: hospital length-of-stay
$X_{\text{Obj}} \leftarrow 0$, $G \leftarrow \sum_{i \in I} g_i$, $H \leftarrow \sum_{i \in I} h_i$, and $\hat{y}_i^{(0)} = 0$
For $k = 1$ to m do
$G_L \leftarrow 0$, $H_L \leftarrow 0$
For j in sorted(I, by x_{kj})
$\hat{y}_i^{(t)} \leftarrow \hat{y}_i^{(t-1)} + f_t(x_i)$
$\Omega(f_k) \leftarrow \gamma T + 0.5\lambda \sum_{i=1}^{T} \varpi_j^2)$
$w_k \leftarrow 0.5 + \alpha/(1 + e^{v_k})$
$l(y_i, \hat{y}_i) \leftarrow -w_k \log \hat{y}(k)$
$X_{\text{obj}} \leftarrow \sum_{j=1}^{T} [\sum_{i \in I} g_i w_j^2 + 0.5(\sum_{i \in I} h_i + \lambda) w_j^2] + \lambda T$
End
End

tree affects the final result, this parameter should be tuned first. The tuning method first gives an initial value to other parameters, where important parameters are set to common typical values. Other parameters are set to default values.

In the model training stage, the grid search method is used to search all possible parameter combinations of each algorithm. For each parameter combination, the 3-fold cross validation experiment is used to determine the optimal parameters of each algorithm according to the cross validation results. The experimental algorithm is mainly implemented based on Python 3.7.7 and scikit-learn toolkit, and the hardware configuration is Intel Core i5-8300h CPU@2.3 GHz processor, 16-G memory. The parameters setting for different classifiers can be found in Table 2.

Table 2: Parameters setting for different classifiers.

The adopted classifiers	The setting of the predefined parameters
The proposed method	Number of trees: [10, 30, 50, 100] Maximum depth of tree: [3, 5, 8, 10] Minimum leaf node weight sum: [1, 3, 6, 9] Learning rate parameters: [0.05, 0.1, 0.15, 0.2]
Naive Bayes	Weight control parameters: [0.5, 1, 1.5, 2, 2.5]
XGBoost	Default parameters Smoothing parameters
SVM	Kernel function: RBF Penalty coefficient: [0.01, 0.1, 1, 10] Kernel parameter: [0.01, 0.001, 0.0001]
KNN	Number of nearest neighbors: [3, 5, 8, 10] Maximum number of leaves: [5, 8, 10, 30]
Decision tree	Number of trees: [10, 30, 50, 100] Maximum depth range: [3, 5, 8, 10] Learning rate range: [0.05, 0.1, 0.15, 0.2]

4.2. Data Preprocessing. As we all know, it is very important to select appropriate influencing factors in the prediction system for patient length of stay. Too few parameters will easily lead to overgeneralization, and the omission of key information will increase the error of final prediction. Too much parameters will increase the complexity of the model, and in the same case, the increase of the complexity of the model will often reduce the accuracy of the final result. Therefore, this paper tries to find a balance between the two in preprocessing stage so as to achieve satisfactory results: firstly, the selected influencing factors must not be too few and must be able to fully represent the problem. Secondly, the selected factors should not be too many; at least irrelevant influencing factors cannot be included. Similar to literature [23], we processed the adopted dataset.

4.3. Evaluation Indexes. In order to evaluate the performance of different models, this paper compares the performance of different models based on the relevant statistical indexes and performance curves of confusion matrix, including accuracy (ACC), Root Mean Square Error (RMSE), F1-score, and kappa coefficient. Performance curves include receiver operating characteristic (ROC) curve, precision recall (PR) curve, and learning curve.

ROC curve and PR curve can intuitively evaluate the performance of the classifier, where the ROC curve reflects the relationship between the true positive rate (TPR) and the false positive rate (FPR), and the PR curve reflects the relationship between the accuracy rate and the recall rate. At the same time, the classification performance of the model can be evaluated by comparing the size of the Area under the Curve (AUC) of different models. The true positive rate and false positive rate are shown as follows:

$$
\begin{aligned}
\text{FPR} &= \frac{\text{FP}}{\text{FP} + \text{TN}} \times 100\%, \\
\text{TPR} &= \frac{\text{TP}}{\text{TP} + \text{FN}} \times 100\%.
\end{aligned}
\tag{12}
$$

4.4. Performance Analysis

4.4.1. Distribution for Length of Stay. Our proposed nonlinear weighted XGBoost can rank the relative importance of feature variables. It reflects the value of each feature variable when training the model. The greater the value of the feature variable when training the model, the higher its relative importance. The results showed that the variables that had the greatest impact on the length of stay were the number of operations, transfer status, and age. From a common sense point of view, the more surgeries there are, the longer it takes to be hospitalized for treatment. The older the age, the longer the hospital stay, which is also consistent with the results of medical research. In addition, the status of transfer, discharge outcome, and discharge diagnosis are closely related to the length of stay in the hospital. However, factors such as gender and number of rescues do not have much influence on the length of the patient's hospital stay. The analysis of important characteristics not only is of great significance for predicting the length of stay but also can bring important reference opinions to medical staff.

A descriptive statistical analysis was made on the length of stay from the perspective of the gender of the patients. The results of the statistical analysis are shown in Table 3.

RETRACTED

Table 3: Gender distribution.

	Number of patients	Mean	Median	Standard deviation	Kurtosis	Skewness
Total	1986	9.10	8	14.25	9.55	2.289
Male	1028	9.69	8	14.68	7.18	2.158
Female	958	8.26	9	13.01	15.67	2.731

As shown in Table 3, the shortest and longest hospitalization days of patients in the hospitalization data record are 1 day and 73 days, where 99.49% of the patients were hospitalized for less than 25 days. The average length of stay was 9.1 days, and the median length of stay was 8 days. The total length of hospitalization skewness coefficient was 2.289 and kurtosis coefficient was 9.55. Therefore, the length of stay distribution of patients showed a right deviation. Figure 2 shows the distribution of the length of stay of patients, where there is a "long tail" phenomenon in the number of samples with different length of stay. In other words, the distribution of sample is unbalanced. Due to the difference in the number of samples, the "normal" category with a large number will be fully trained, while the number of samples with long length is relatively small.

From the perspective of gender, there are 1028 male patients, accounting for 57.1% of the total number, and 958 female patients, accounting for 42.9% of the total number. The ratio of male to female patients is 1.3 : 1. The youngest male patient was 11 years old, the oldest was 91 years old, and the average age was 62 years old. The youngest female patient was 7 years old, the oldest was 89 years old, and the average age was 65 years old. Overall, the average length of stay of male patients was 0.93 days longer than that of female patients and was greater than the overall average length of stay. The skewness coefficients of male and female patients were positive, so the length of hospitalization showed a right skewness. The kurtosis of the length of stay of female patients is much greater than that of male patients, and greater than the overall kurtosis.

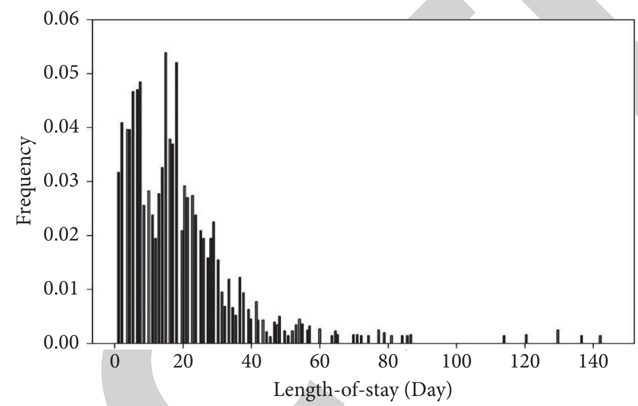

Figure 2: Distribution of the length of stay of patients.

Table 4: Quantitative prediction indicators of different algorithms.

Model	ACC	RMSE	F1-score	Kappa coefficient
Naive Bayes	0.7912	2.211	0.725	0.8017
Decision tree	0.8247	1.885	0.829	0.8182
SVM	0.8661	1.592	0.865	0.8611
KNN	0.8117	1.721	0.773	0.8482
XGBoost	0.7958	1.807	0.782	0.8251
The proposed model	0.8211	1.523	0.851	0.8622

4.4.2. Predictive Performance Analysis. After feature processing, the characteristic variables of patient hospitalization are used as the feature input of machine learning model, and the model is trained, verified, and predicted on the training set and test set. In order to verify the effect of the improved CGBoost algorithm on predicting the length of stay, we compare it with the traditional classical algorithm and analyze the performance indicators of the prediction models for different algorithms.

Table 4 shows the quantitative prediction indicators of different algorithms. It can be seen that the accuracy (ACC), Root Mean Square Error (RMSE), F1-score, and kappa coefficient of our proposed algorithm are 0.8211, 1.823, 0.8501, and 0.8122, respectively, which has good practical performance. In other words, it is indicated that our proposed XGBoost model is feasible in predicting the length of stay. The accuracy (ACC), Root Mean Square Error (RMSE), F1-score, and kappa coefficient of the decision tree algorithm are 0.824, 0.806, 0.829, and 0.818, respectively. The prediction effect is general. The performance of decision tree model in predicting the length of stay is not as good as our improved XGBoost model. The quantitative performance indexes of the KNN are 0.811, 1.721, 0.773, and 0.848, respectively. The prediction accuracy is not as high as XGBoost model and decision tree model. However, the AUC of the model is higher, which shows that the logical regression model is more robust than the decision tree model. The AUC value and accuracy of the XGBoost algorithm are higher than those of decision tree and KNN, which means that the prediction effect of XGBoost model is better and the stability of the model is stronger.

According to the above results, the hospital length-of-stay prediction of our proposed model has achieved good results. Compared with the traditional model, it has a good improvement in stability and accuracy and has a certain practical value.

Figure 3 shows the comparison of AUC values of classifier PR curve and PR curve. It can be seen that our proposed XGBoost algorithm has higher AUC values and is better than other comparative classifiers.

As can be seen from Figure 4, our proposed algorithm has the fastest convergence accuracy, followed by *XGBoost algorithm* and *Naive Bayes* algorithm, respectively. *KNN* algorithm has the lowest score on the training set and cross

RETRACTED

RETRACTED

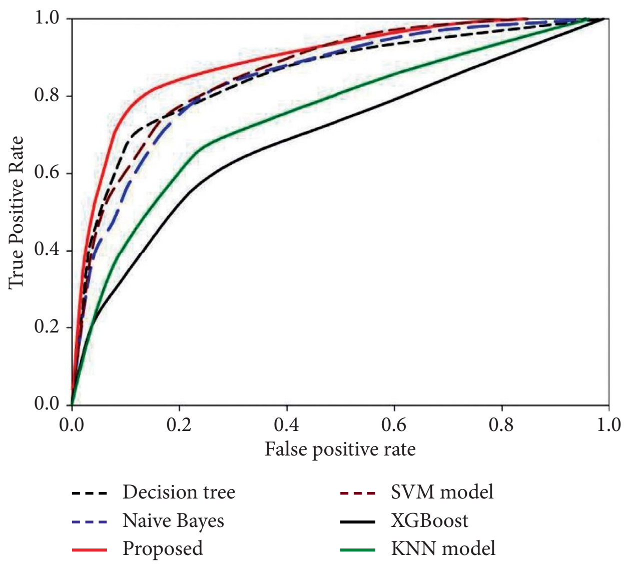

Figure 3: Comparison of ROC curve for different models.

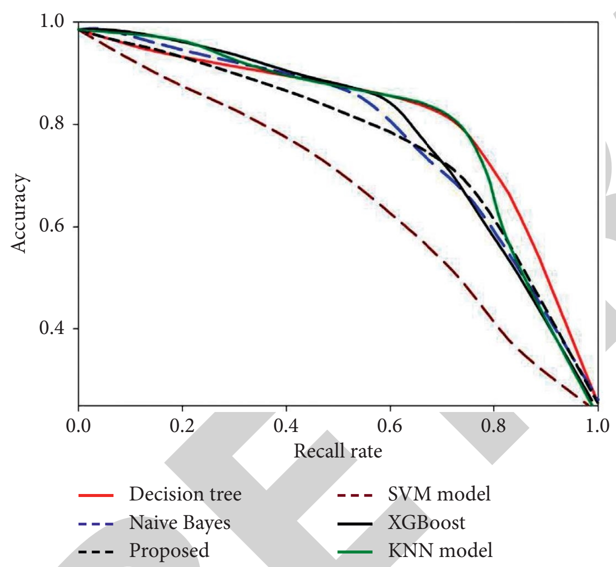

Figure 4: Comparison of PR curve for different models.

validation set, and the other algorithms have the overfitting state for unbalance data. At the same time, it can be seen from Figure 4 that our algorithm has the highest score on the cross validation set, which is consistent with the experimental results in Table 4.

According to the results of various indicators and performance curves, it can be seen that our proposed algorithm can achieve good classification and prediction performance for length of stay in hospital. The nonlinear weighting method can not only ensure the overall accuracy but also improve the classification accuracy. In addition, the improved XGBoost algorithm also shows its advantages in convergence speed and learning ability compared with traditional classifiers in Figure 5. It should be noted that the proposed algorithm increases the weight control parameter

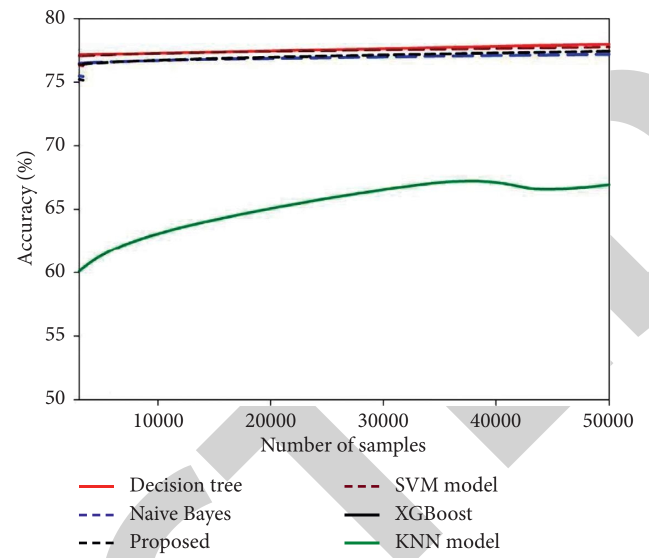

Figure 5: Comparison of learning curve for different models.

α compared with XGBoost algorithm, and there are five possible values in its parameter range. Therefore, in the process of parameter optimization, the parameter combination of our algorithm is five times that of XGBoost algorithm, which requires more parameter optimization time.

In general, the purpose of this paper is to use the proposed algorithm to predict the length of hospitalization based on the limited bed resources of the hospital. We need to not only obtain accurate prediction accuracy but also obtain the optimal bed scheduling.

5. Conclusion

The resources that hospitals can provide are often unable to meet the needs of hospitalization. Accurately predicting the number of days a patient will stay in the hospital can improve the efficiency of hospital operations. This paper proposes to use a nonlinear weighted XGBoost algorithm to predict and analyze patient hospitalization data. Due to the imbalance of real case data, the XGBoost algorithm used improves the objective function based on the idea of sample ratio and nonlinear weighting, which improves the classification and prediction ability of the algorithm in the case of imbalanced data samples. In order to verify whether the prediction performance of the proposed algorithm can meet actual application requirements, the experimental part uses multiple comparison algorithms for experimental verification. The experimental results show that the algorithm proposed in this paper has obvious advantages for unbalanced data. This further shows that the research work in this paper can be applied to real application. There are still some shortcomings in this research. For large datasets, the processing performance of the algorithm used is not good. However, with the passage of time and the increase in case data, the amount of data will inevitably increase gradually. How to improve the processing time and accuracy of the algorithms used for big data is the direction that our team will continue to study in the future. In addition, we also need

RETRACTED

to consider how to use predictive information to optimize the use of resources in hospitals when encountering some emergencies and the surge in case data. This is what we need to study in the future.

Data Availability

The dataset used to support the findings of this study are available from the corresponding author upon request.

Conflicts of Interest

The author declares no conflicts of interest.

Acknowledgments

This work was supported by the Affiliated Hospital of Chengde Medical College.

References

[1] G. Vandersteen, H. V. Hamme, and R. Pintelon, "General framework for asymptotic properties of generalized weighted nonlinear least-squares," *IEEE Transactions on Automatic Control*, vol. 2, no. 58, pp. 458–477, 1996.

[2] P. Guillaume and R. Pintelon, "A Gauss-Newton-like optimization algorithm for 'weighted' nonlinear least-squares problems," *IEEE Transactions on Signal Processing*, vol. 25, no. 125, pp. 35–41, 1996.

[3] M. Medina, G. M. Gallego, M. S. Arenas, and M. D. Rodríguez, "[Risk factors and length of stay attributable to hospital infections of the urinary tract in general surgery patients]," *Enfermedades Infecciosas y Microbiología Clínica*, vol. 15, no. 6, pp. 310–315, 1997.

[4] P. Appelros, "Prediction of length of stay for stroke patients," *Acta Neurologica Scandinavica*, vol. 116, no. 1, pp. 09–12, 2010.

[5] Y. Jiang, K. Zhao, K. Xia et al., "A novel distributed multitask fuzzy clustering algorithm for automatic MR brain image segmentation," *Journal of Medical Systems*, vol. 43, no. 5, pp. 118-119, 2019.

[6] Y. Jiang, Y. Zhang, C. Lin, D. Wu, and C.-T. Lin, "EEG-based driver drowsiness estimation using an online multi-view and transfer TSK fuzzy system," *IEEE Transactions on Intelligent Transportation Systems*, vol. 22, no. 3, pp. 1752–1764, 2021.

[7] L. H. Cohn, D. Rosborough, and J. Fernandez, "Reducing costs and length of stay and improving efficiency and quality of care in cardiac surgery," *The Annals of Thoracic Surgery*, vol. 64, no. 6, pp. 180–221, 1997.

[8] N. M. Katz, R. L. Hannan, R. A. Hopkins, and R. B. Wallace, "Cardiac operations in patients aged 70 years and over: mortality, length of stay, and hospital charge," *The Annals of Thoracic Surgery*, vol. 60, no. 1, pp. 96–101, 1995.

[9] S. T. Engelter, J. M. Provenzale, J. R. Petrella, D. M. DeLong, and M. J. Alberts, "Infarct volume on apparent diffusion coefficient maps correlates with length of stay and outcome after middle cerebral artery stroke," *Cerebrovascular Diseases*, vol. 15, no. 3, pp. 188–191, 2003.

[10] L. L. Holland, L. L. Smith, and K. E. Blick, "Reducing laboratory turnaround time outliers can reduce emergency department patient length of stay," *American Journal of Clinical Pathology*, vol. 124, no. 5, pp. 672–674, 2005.

[11] M. R. Williams, R. B. Wellner, E. A. Hartnett et al., "Long-term survival and quality of life in cardiac surgical patients with prolonged intensive care unit length of stay," *The Annals of Thoracic Surgery*, vol. 73, no. 5, pp. 1472–1478, 2002.

[12] G. K. Kong, M. J. Belman, and S. Weingarten, "Reducing length of stay for patients hospitalized with exacerbation of COPD by using a practice guideline," *Chest*, vol. 111, no. 1, pp. 89–94, 1997.

[13] D. Coskun, J. Aytac, A. Aydınlı, and A. Bayer, "Mortality rate, length of stay and extra cost of sternal surgical site infections following coronary artery bypass grafting in a private medical centre in Turkey," *Journal of Hospital Infection*, vol. 60, no. 2, pp. 176–179, 2005.

[14] H. L. Lazar, C. Fitzgerald, S. Gross, T. Heeren, G. S. Aldea, and R. J. Shemin, "Determinants of length of stay after coronary artery bypass graft surgery," *Circulation*, vol. 92, pp. 20–24+26, 1995.

[15] S. D. Reed, D. K. Blough, K. Meyer, and J. G. Jarvik, "Inpatient costs, length of stay, and mortality for cerebrovascular events in community hospitals," *Neurology*, vol. 1, no. 12, pp. 89–93, 2001.

[16] A. Ingeman, G. Andersen, H. H. Hundborg, M. L. Svendsen, and S. P. Johnsen, "In-hospital medical complications, length of stay, and mortality among stroke unit patients," *Stroke*, vol. 42, no. 11, pp. 3214–3218, 2011.

[17] C. Winslow, R. K. Bode, D. Felton, D. Chen, and P. R. Meyer, "Impact of respiratory complications on length of stay and hospital costs in acute cervical spine injury," *Chest*, vol. 121, no. 5, pp. 1548–1554, 2002.

[18] S. Tanuja, D. U. Acharya, and K. R. Shailesh, "Comparison of different data mining techniques to predict hospital length of stay," *Journal of Pharmaceutical & Biomedicalences*, vol. 12, no. 24, pp. 120–128, 2011.

[19] D. A. Wentworth and R. P. Atkinson, "Implementation of an acute stroke program decreases hospitalization costs and length of stay," *Stroke*, vol. 27, no. 6, pp. 1040–1043, 1996.

[20] Y. Lu, E. Forlenza, M. R. Cohn et al., "Machine learning can reliably identify patients at risk of overnight hospital admission following anterior cruciate ligament reconstruction," *Knee Surgery, Sports Traumatology, Arthroscopy*, vol. 29, pp. 1–9, 2020.

[21] B. L. Hoh, Y.-Y. Chi, M. A. Dermott, P. J. Lipori, and S. B. Lewis, "The effect of coiling versus clipping of ruptured and unruptured cerebral aneurysms on length of stay, hospital cost, hospital reimbursement, and surgeon reimbursement at the university of Florida," *Neurosurgery*, vol. 64, no. 4, pp. 614–621, 2009.

[22] M. Soares, J. I. F. Salluh, V. B. L. Torres, J. V. R. Leal, and N. Spector, "Short- and long-term outcomes of critically ill patients with cancer and prolonged ICU length of stay," *Chest*, vol. 134, no. 3, pp. 520–526, 2008.

[23] A. V. Straten, J. H. V. D. Meulen, G. A. V. D. Bos, and M. Limburg, "Length of hospital stay and discharge delays in stroke patients," *Stroke*, vol. 28, no. 1, pp. 137–140, 1997.

[24] D. Morel, K. C. Yu, A. L. Ferrara, A. J. C Suriel, S. G. Kurtz, and Y. P. Tabak, "Predicting hospital readmission in patients with mental or substance use disorders: a machine learning approach," *International Journal of Medical Informatics*, vol. 139, Article ID 104136, 2020.

[25] J. Liu, J. Wu, S. Liu, M. Li, K. Hu, and K. Li, "Predicting mortality of patients with acute kidney injury in the ICU using XGBoost model," *PLOS ONE*, vol. 16, no. 121, pp. 5120–5131, 2021.

Hindawi
Journal of Healthcare Engineering
Volume 2023, Article ID 9852487, 1 page
https://doi.org/10.1155/2023/9852487

Retraction

Retracted: Spiral Computed Tomography in the Quantitative Measurement of the Adjacent Structure of the Left Atrial Appendage in Patients with Atrial Fibrillation

Journal of Healthcare Engineering

Received 10 October 2023; Accepted 10 October 2023; Published 11 October 2023

Copyright © 2023 Journal of Healthcare Engineering. This is an open access article distributed under the Creative Commons Attribution License, which permits unrestricted use, distribution, and reproduction in any medium, provided the original work is properly cited.

This article has been retracted by Hindawi following an investigation undertaken by the publisher [1]. This investigation has uncovered evidence of one or more of the following indicators of systematic manipulation of the publication process:

(1) Discrepancies in scope
(2) Discrepancies in the description of the research reported
(3) Discrepancies between the availability of data and the research described
(4) Inappropriate citations
(5) Incoherent, meaningless and/or irrelevant content included in the article
(6) Peer-review manipulation

The presence of these indicators undermines our confidence in the integrity of the article's content and we cannot, therefore, vouch for its reliability. Please note that this notice is intended solely to alert readers that the content of this article is unreliable. We have not investigated whether authors were aware of or involved in the systematic manipulation of the publication process.

In addition, our investigation has also shown that one or more of the following human-subject reporting requirements has not been met in this article: ethical approval by an Institutional Review Board (IRB) committee or equivalent, patient/participant consent to participate, and/or agreement to publish patient/participant details (where relevant).

Wiley and Hindawi regrets that the usual quality checks did not identify these issues before publication and have since put additional measures in place to safeguard research integrity.

We wish to credit our own Research Integrity and Research Publishing teams and anonymous and named external researchers and research integrity experts for contributing to this investigation.

The corresponding author, as the representative of all authors, has been given the opportunity to register their agreement or disagreement to this retraction. We have kept a record of any response received.

References

[1] Z. Zhang and W. Yan, "Spiral Computed Tomography in the Quantitative Measurement of the Adjacent Structure of the Left Atrial Appendage in Patients with Atrial Fibrillation," *Journal of Healthcare Engineering*, vol. 2021, Article ID 9893358, 10 pages, 2021.

Hindawi
Journal of Healthcare Engineering
Volume 2021, Article ID 9893358, 10 pages
https://doi.org/10.1155/2021/9893358

RETRACTED

Research Article

Spiral Computed Tomography in the Quantitative Measurement of the Adjacent Structure of the Left Atrial Appendage in Patients with Atrial Fibrillation

Zhen Zhang and Wei Yan

Department of Cardiovascular Medicine, Affiliated Hospital of Youjiang Medical College for Nationalities, Guangxi Baise 533000, China

Correspondence should be addressed to Wei Yan; 2227@ymun.edu.cn

Received 18 October 2021; Revised 10 November 2021; Accepted 11 November 2021; Published 30 November 2021

Academic Editor: Gu Xiaoqing

Copyright © 2021 Zhen Zhang and Wei Yan. This is an open access article distributed under the Creative Commons Attribution License, which permits unrestricted use, distribution, and reproduction in any medium, provided the original work is properly cited.

Cardiac arrhythmias are common clinical cardiovascular diseases. Arrhythmias are abnormalities in the frequency, rhythm, site of origin, conduction velocity, or sequence of excitation of the cardiac impulses. Arrhythmia mechanisms include foldback, altered autonomic rhythm, and triggering mechanisms. It can cause palpitations, dizziness, black dawn, syncope, and angina pectoris and can worsen a preexisting cardiac disease, reduce the quality of life, and increase mortality. Also, by making it one of the constant challenges for the clinical cardiovascular physician, we can get more information. The study included 94 patients with atrial fibers, including 56 men and 38 women aged 57, 46, 11, and 68 years. There are 80 patients with nonatrial fibers, including 44 men and 36 women aged 56, 10, and 83 years. Those who can perform a normal coronary angiography and exclude congenital heart disease, heart valve disease, and other cardiovascular diseases. In both groups, a 256-layer spiral CT examination was performed. A pulmonary vein scanning protocol was applied to the patients with atrial fibrillation, and this can perform normal coronary angiography and exclude those with cardiovascular diseases such as congenital heart disease and valvular heart disease. The purpose of this study is to investigate the anatomical changes of the left atrium and its adjacent structures by applying the 256 nm spiral CT imaging to visualize the left atrium and its adjacent structures and by applying the MPR technology, VR technology, and simulation endoscope techniques.

1. Introduction

Antiarrhythmic drugs are the traditional treatment for arrhythmias, but they are less effective and have more side effects [1]. In particular, since the publication of CAST trial results in the late 1980s, the arrhythmogenic effect of antiarrhythmic drugs has been widely recognized, i.e., antiarrhythmic drugs may induce or aggravate arrhythmias while treating arrhythmias. 1986 saw the first application of radiofrequency energy ablation in basic experiments, and the reports of radiofrequency ablation in canine hearts were also published. It was possible to achieve ablation by changing the temperature and energy [2]. In 1986, the first application of radiofrequency energy ablation was performed in basic experiments, and the first report of radiofrequency ablation in the canine heart was published. After the publication of these two studies, the radiofrequency ablation of the catheters gradually gained attention and developed rapidly, and it was soon applied to humans, ushering in the era of the radiofrequency ablation of cardiac arrhythmias. Radiofrequency ablation is a form of electric current that can be converted into electrical energy. It mainly produces an impedance thermal effect on the local tissues, evaporating and drying the water in cardiomyocytes, forming a small, well-defined circular or oval coagulative necrosis to achieve the purpose of ablation [3]. After more than 20 years of development, improvement, and clinical popularity, radiofrequency ablation has gradually become the main way of the radical treatment of cardiac arrhythmias and the first-line clinical treatment modality [4]. It can cure a variety of arrhythmias, including atrial tachycardia, atrial tachycardia, paroxysmal ventricular tachycardia, early atrial fibrillation, and atrial tachycardia. In the treatment of some arrhythmias, radiofrequency ablation can be the method of choice. At the same time, the development of radiofrequency ablation has also enriched and expanded the understanding of arrhythmia, i.e., "learning by burning" [5].

The clinical electrophysiology practice has found that some atrial arrhythmias, such as atrial tachycardia, or ventricular arrhythmias, such as ventricular premature and ventricular tachycardia, are more difficult to be successfully ablated using a conventional endocardium, while they can be successfully ablated in the vicinity of the aortic sinus [6]. However, the anatomy of the aortic root is very complex, and a full understanding of the adjoining and anatomical structures of the aortic root is very important for the successful ablation of arrhythmias and the reduction of complications. Basic studies have found that the aortic sinus includes three sinuses: the noncoronary sinus (NS). More commonly, the ablation of the noncoronary sinus can eradicate some right atrial tachycardia, and the ablation of the left coronary sinus orifice region can eradicate some left ventricular idiopathic/ventricular premature/ventricular tachycardia [7]. This led us to consider how the aortic sinus and its adjoining structures become arrhythmogenic substrates and how the ablation of the aortic sinus and its adjoining structures can eradicate arrhythmias. It relies on the further understanding of the anatomy of the aortic sinus and its frequent adjacent tissues. At present, there are a few studies in China and abroad, and most of them focus on animal observation, autopsy, or visual observation during cardiac surgery, which lacks clinical guidance [8]. This is achieved by the slip ring technology and a continuous flat movement of the scanning bed [9]. The subjects underwent selective pulmonary venography (CPV) during the subsequent ablation of atrial fibrillation to measure the entrance diameter of each pulmonary vein, and these data were used as a control group [10]. Patients with a positive contrast allergy test, patients with decompensated neurological insufficiency, patients with severe cardiac and renal insufficiency (creatinine >10 μmol/L), and patients who were unable to cooperate with poor breath-holding during the respiratory training were excluded from the pulmonary venous and left atrial angiography using a 320-slice spiral CT; all patients signed an informed consent form before the examination. If a patient had a pulmonary vein variant detected after successful examination, that patient was also excluded [11]. All patients were required to fast for at least 6 h before performing the pulmonary venous left atrial angiography. Then, venous access was established and an indwelling cannula was placed in the anterior elbow vein.

The patient's weight is routinely measured for an accurate contrast dosage, and an electrocardiogram is performed. The patient should be placed in a supine position with the scanning direction on the front of the foot. The electrodes should be placed correctly in the standard position with the ECG leads connected and the ECG signal confirmed to be received before the scan; the patient is then trained to breathe to minimize the artifacts caused by the respiratory movements so that he can cooperate with the examination.

2. Related Work

94% of ectopic electrical activity originates from the pulmonary veins. Abnormal extracardiac potentials are the main cause of paroxysmal atrial fibrillation [12]. Clinically, radiofrequency ablation for pulmonary vein isolation is currently an effective treatment for patients in whom antiarrhythmic drugs are ineffective. However, because of the complex anatomical structure of the pulmonary veins, individual variability, and more variability, the accurate placement of the marker device and the ablation effect can be affected by many of these factors [13]. However, different imaging techniques have their advantages and disadvantages. With the continuous updating of the CT imaging equipment, CT angiography has been widely used for noninvasive vascular imaging before the ablation of atrial fibrillation [14].

Ventricular arrhythmias are one of the more common critical illnesses in clinical work. There are many types of ventricular arrhythmias, including ventricular tachycardia, ventricular fibrillation, premature ventricular contractions, ventricular flutter, and supraventricular arrhythmias, such as atrial fibrillation, supraventricular tachycardia, and preexcitation syndrome [15]. Most arrhythmias are associated with heart diseases. However, some patients without organic heart disease also develop ventricular arrhythmias. Such cases account for approximately 10% of the patients with arrhythmias and idiopathic ventricular arrhythmias. Atrial fibrillation is the most common persistent arrhythmia in clinical practice, and its prevalence increases with age, seriously affecting people's health. In recent years, the incidence of AF has been increasing significantly with age. The number of patients with AF is gradually increasing as the number of aging people in China further increases. Its high morbidity and disability rate have caused more and more clinical; epidemiological statistics found that the adult prevalence of AF in China is approximately 0.77%. There are approximately more than 8 million patients with AF, and the incidence is similar to that of Western countries [16]. The current treatment strategy for idiopathic ventricular arrhythmias is guided by the severity of the patient's clinical symptoms and the risk of sudden death. Although the use of antiarrhythmic drugs can reduce the patient's symptoms to some extent, the effect is less satisfactory in reducing the patient's risk of sudden death. The placement of cardioverter-defibrillators in the patients can effectively terminate and reduce the mortality rate to an extent, but only for some. The cardioverter-defibrillator is effective in terminating and reducing mortality, but only in certain populations, and it is not effective in reducing arrhythmias [17].

Multiple abnormal potential trigger points in the pulmonary veins play an important role in the development and progression of AF. The myocardial tissue of the left atrium extends into the outer layer of the pulmonary vein wall, which, in turn, forms a myocardial sleeve. This extended myocardial sleeve is the release point for the abnormal

RETRACTED

potential activity, and it has been demonstrated that approximately 94% of the abnormal potential triggers are from the pulmonary veins [18]. Supraventricular arrhythmias, such as atrial fibrillation, generally have a long history, significant myocardial fibrosis, more complications, high risk of stroke with drug therapy, poor efficacy, and arrhythmogenic effects with the long-term application of antiarrhythmic drugs in such patients. Therefore, there is much interest in the clinical effectiveness and safety of transcatheter ablation for the treatment of AF [19]. Current studies suggest that most cases of paroxysmal AF are triggered or driven by the extracardiac abnormal potential sites and the pulmonary veins are the most common sites of origin for such arrhythmias that often cause paroxysmal AF. Therefore, it is believed that the effective treatment of paroxysmal AF can be achieved by implementing the electrical isolation of the pulmonary veins to terminate the ectopic potential generation.

The radiofrequency ablation of the pulmonary veins causing arrhythmia can lead to the eradication of paroxysmal atrial fibrillation [20]. The purpose of the catheter radiofrequency ablation of atrial fibrillation is to form an effective electrical isolation between the pulmonary veins and the atria. The necessary tool for the electrical isolation of the pulmonary veins in radiofrequency ablation, the annulus, is the marker electrode, which is placed at the entrance of the pulmonary veins via a catheter after performing an atrial septal puncture. The annular plane is placed parallel to the entrance of the pulmonary veins. The most used electrode diameters in clinical practice are 1.5 cm and 2.0 cm, and the diameter of the calibrated electrode chosen during the procedure should be slightly larger than the diameter of the pulmonary vein to be ablated [21]. The normal anatomy of the pulmonary veins has four pulmonary veins, and when anatomical variations occur, the number of pulmonary veins varies. A normal pulmonary vein's anatomy accounts for about 70% of the total in the studied population while the pulmonary vein's anatomical variations occur in about 19–30% of the normal population. Different pulmonary vein branches in the same patient and the same pulmonary vein branch in different patients have very different morphology, diameter, angle, and branches at the entrance of their pulmonary veins. There are also differences in the angle and branch of the same pulmonary vein in different patients.

3. Helical Tomography of Structures Adjacent to the Left Heart Ear

3.1. Left Atrial Angiography. A total of 105 subjects were selected who underwent the 320-slice spiral CT pulmonary vein and left atrial angiography in the radiology department from November 2017 to March 2021. 58 were male and 47 were female. The mean age was 58 ± 12 years. The patients with positive contrast allergy test, patients with decompensated neurological insufficiency, patients with severe cardiac and renal insufficiency (creatinine >10 μmol/L), and patients with poor breath-holding ability to cooperate were excluded. All patients signed an informed consent form before the examination. The patients were also excluded if the pulmonary vein variation was detected after a successful examination.

All patients were required to fast for at least 6 h before performing the pulmonary venous left atrial angiography. Then, intravenous access was established with an indwelling cannula placed in the anterior elbow vein. If the patient's heart rate is > 70 beats/min, the patient should be advised to breathe steadily and be reassured with words to keep the patient as calm as possible. The heart rate should be controlled to less than 70 beats per minute.

The patient should be placed in a supine position with the scanning direction in the direction of the head of the foot. Before scanning, the electrodes should be placed correctly with the ECG leads connected in the standard position and the ECG signal should be confirmed. Toshiba AQULION ONE TSX-304A 320-slice spiral CT with cardiac gating technology was used. The scan was performed in a calm breathing state with breath-holding from 5 mm below the tracheal bifurcation to 10 mm below the diaphragmatic surface of the heart using a whole-heart volume scan. The subject was placed in the supine position with the foot and head orientation to confirm that the ECG signal was received as shown in Figure 1; a Toshiba AQULION ONE TSX-304A 320-row spiral CT was used to perform the scan using cardiac gating technology. The pulmonary vein and left atrial CTV scan sequences were selected and the sure start software intelligently triggered the scan with the trigger point range set at the level of the root of the ascending aorta and a trigger threshold of 320 HU. The scan was performed in a calm breathing state with breath-holding from 5 mm below the tracheal bifurcation to 10 mm below the diaphragmatic surface of the heart using the whole-heart volume scanning. The tube voltage was 100 kV, tube current was 600 mA, full heart volume acquisition range was 320 rows × 0.5 mm, frame speed was 350 ms, and the rotational scan time was 140 ms. The area of interest was set in the left atrium at the mitral level and the enhancement scan was automatically triggered. The average scan time was 2.5 s. The resulting data were reconstructed at 75% of the RR interval. The images are uploaded to a postprocessing workstation and reconstructed using postprocessing techniques, such as multiplanar reconstruction, volume reproduction, maximum density projection, and simulated endoscopy, which showed a long-axis image of the left atrium and pulmonary veins, with the pulmonary vein trunk intact. The patients undergoing atrial fibrillation ablation should have a clinical diagnosis of atrial fibrillation that has failed to respond to the antiarrhythmic drug therapy.

3.2. Spiral Tomography-Based Ablation of Atrial Fibrillation. The subjects were patients with clinically diagnosed atrial fibrillation for whom antiarrhythmic drug therapy had failed. The patients with severe cardiac insufficiency and untreated valvular disease, pulmonary hypertension, coagulation abnormalities, severe hyperthyroidism, and multi-organ failure of the liver and kidneys were excluded, preoperatively. All patients signed an informed consent

RETRACTED

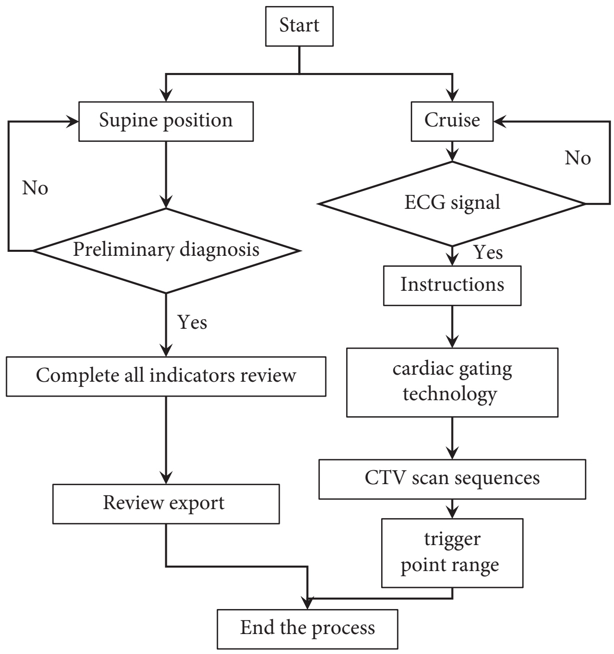

Figure 1: Spiral tomographic process under atrial fibrillation.

form and a surgical protocol. The patients should be admitted for routine investigations: screening for infectious diseases, laboratory tests (blood and urine routine, coagulation function, thyroid function, liver and kidney function, electrolytes, NT-pro BNP), and cardiac echocardiography to understand the left ventricular systolic function, clarify the size of each atrium and left atrial diameter, routine electrocardiogram, monitoring of 24-hour heart rate by 24-hour ambulatory electrocardiogram, and pulmonary CT or X-ray chest orthopantomogram. Pulmonary CT or X-ray chest frontal and lateral radiographs were performed for routine pulmonary examination. The patients taking warfarin INR at the preoperative level should be tested for intraoperative heparin dosage that must be reduced appropriately. The patients taking new anticoagulant drugs should discontinue the drugs 12–24 hours before the surgery. Intraoperative heparin dosage (80–100 μ/kg) should be accurate and adjusted in a timely manner based on intraoperative clotting time.

The patient is placed flat on the angiographic C-arm bed and the position of the patient's heart is confirmed to be in the center of the C-arm bulb before the procedure. The left femoral vein and the left subclavian vein are punctured, and the target catheter is placed into the coronary sinus and the right ventricle, respectively. The atrial septal puncture needle is fed through the left femoral vein catheter. The septum is penetrated and contrast is sprayed to visualize the image of the left atrium. Heparin (100 μ/kg) is injected when the septal puncture is completed, and additional heparin (1000 μ/hour) is added intraoperatively to prevent thrombosis. The catheter is fed through the femoral vein, pointed at the target vein, and after sufficient venting, a high-pressure syringe is connected and the contrast agent (1.2 ml/kg) is injected. The C-arm rotational imaging mode is selected with the tube ball in the starting position and the delayed acquisition time at 0. After the high-pressure syringe triggers the linkage to inject the contrast agent, the images are acquired by rotating the patient at a rate of 30 frames/second with a rotation time of 4-5 seconds. The catheter is perfused with cold saline via the Swartz sheath, and the loop electrode is delivered to the left atrium.

3.3. Quantitative Results of the Main Left Auricular Adjacent Connection Structure. The observation and analysis of MSCT imaging data of 100 patients revealed that there was a connection structure between the three sinus walls of the aortic sinus (coronary sinus, left coronary sinus, and right coronary sinus) and atrium/ventricle (coronary sinus), as shown in Figure 2. The number of cases connected and the percentage of the total number of connected cases were as follows: 48 patients (21.82%) had aortic sinus-right ventricle tissue connections, 23 patients (10.45%) had aortic sinus -left ventricle tissue connections, 20 patients (9.09%) had aortic sinus-right atrium tissue connections, 25 patients (11.36%) had the right coronary sinus-right ventricular tissue connection, 23 patients (10.45%) had the right coronary sinus-left ventricular tissue connection, 16 patients (7.27%) had the left coronary sinus-right ventricular tissue connection, 20 patients (9.09%) had the left coronary sinus-left ventricular tissue connection, and 45 patients (20.45%) had the left coronary sinus-left ventricular tissue connection. No connection structure was found between the coronary sinus and the ventricle. The most common connection was between the coronary sinus and the atrium. After x2 analysis, there was a significant difference in the connection between the left coronary sinus, the right coronary sinus, and the coronary sinus and peripheral tissues ($P < 0.01$). Thus, according to the connection structure, they were divided into groups without coronary sinus, left coronary sinus group, and right coronary sinus group. The connections were defined as the presence of a contact between the aortic sinus and the endocardia of the atrial ventricular tissue or of tissue connections. Figure 2 shows the presence of a connection to the peripheral atrium and ventricle from the aortic sinus under 3D reconstruction. The lower table shows the number of cases where the aortic sinus is connected to the surrounding tissue and the lower X2 is applied. Analyze whether there is a difference.

The aortic root was reconstructed by the MSCT software, scanned from 10 levels. The distance between the left coronary sinus without a right ventricular sinus and right coronary sinus and atrial/ventricular connection structure was measured and averaged. As shown in Figure 3, the distance between the coronary sinus and the atrium: the distance between the coronary sinus and the right atrium was significantly smaller than the distance between the coronary sinus-left atrium (1.77 ± 0.85 mm versus 2.22 ± 0.92 mm, $P < 0.01$). For the distance between the left coronary sinus and the atrium/ventricle, the left coronary sinus-right ventricle distance is significantly greater than the left coronary sinus-left coronary sinus and the left coronary sinus-left ventricle distance. We compared the left coronary sinus-left ventricle distance and the left coronary sinus-left

RETRACTED

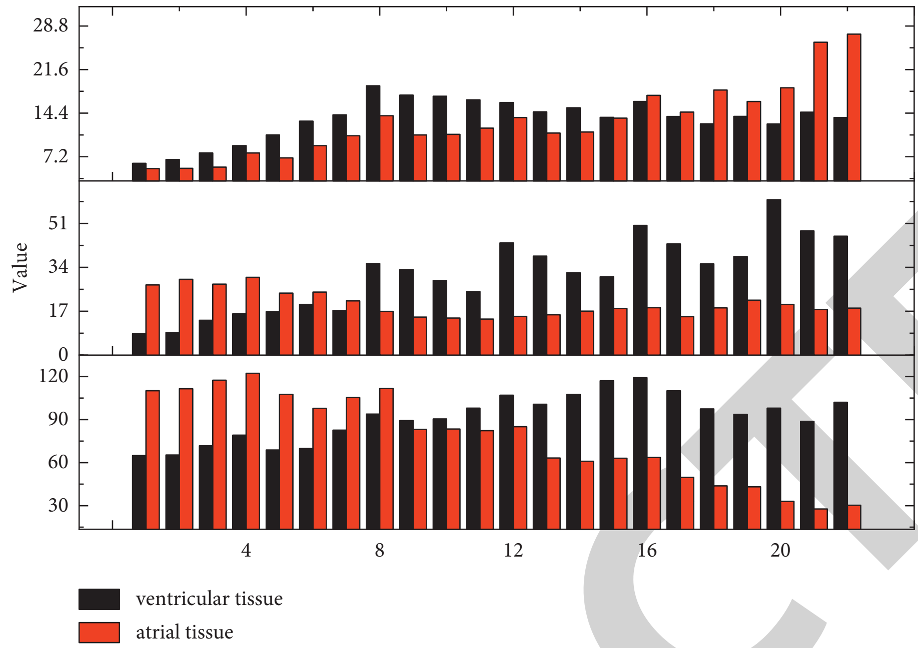

FIGURE 2: Analysis of aortic sinus connection to atrial or ventricular tissue.

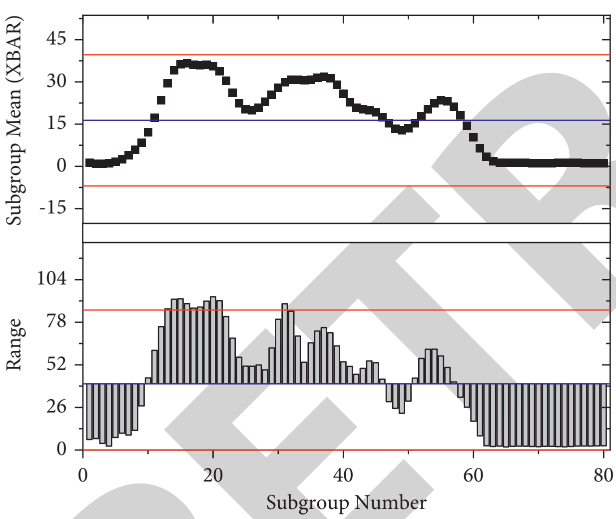

FIGURE 3: Analysis of variance for the left atrial distance row.

ventricle distance ($P < 0.01$). For the right coronary sinus atrial/ventricular distance, the right coronary sinus-right ventricle distance is significantly smaller than the right coronary sinus-right ventricle distance. The distance between the coronary sinus and the right coronary sinus-left ventricle was significantly greater than that of the right coronary sinus and left ventricle ($P < 0.05$). However, there was no significant difference between the right coronary sinus and the right ventricle and the right coronary sinus and the left ventricle.

There were tissue connections between the aortic sinus and the atria and ventricles, which could be fatty connections, fibrous connections, etc.: the aortic sinus-right atrium connection was present in 48 patients, the aortic sinus-left atrium connection in 23 patients, the right coronary sinus-right atrium connection in 20 patients, the right coronary sinus-right ventricle connection in 25 patients, the right coronary sinus-left ventricle connection in 23 patients, the left coronary sinus-right ventricle connection in 16 patients, the left coronary sinus-left ventricle connection in 20 patients, and the aortic sinus-right ventricle connection in 45 patients. The right ventricular connection was present in 23 patients, the left coronary sinus-right ventricular connection was present in 16 patients, the left coronary sinus-left atrial connection was present in 20 patients, and the left coronary sinus-left ventricular connection was present in 45 patients. The right coronary sinus-right ventricle was significantly shorter than the right coronary sinus-right atrium and right coronary sinus-left ventricle distances (1.85 ± 0.93 mm vs. 2.16 ± 0.99 mm, 2.01 ± 0.77 mm, $P < 0.05$), respectively, and the right coronary sinus-right atrium distance was significantly greater than the right coronary sinus-left ventricle ($P < 0.05$).

4. Experiments and Results Analysis

4.1. Anatomical Features of the Left Auricular Connection. The left coronary sinus is located posteriorly above the right ventricular outflow tract, adjacent to the root of the pulmonary artery and the left atrium. The right coronary sinus is located above the atrioventricular junction, posterior to the area of the bundle of Hitchcock and is connected to the atrioventricular node, adjacent to the right ventricle and right atrium. In this study, the right and left coronary sinuses were found to be connected mainly to the ventricular tissue, and the left coronary sinus was most commonly connected to the left ventricle, with 45 (20.45%) connected cases. Can it be stated that the ventricular arrhythmias associated with the aortic sinus can be successfully ablated by the ablation of the left coronary sinus? 44 patients with idiopathic ventricular

RETRACTED

arrhythmias associated with the aortic sinus (including ventricular premature and ventricular tachycardia) were studied, and the results showed that of all 44 patients, 24 patients were successfully ablated in the left coronary sinus, 14 patients were successfully ablated in the right coronary sinus, only 1 patient was successfully ablated in the non-coronary sinus, and 5 patients had a successful ablation in the left and right coronary sinus junctions. It showed that ventricular arrhythmias associated with the aortic sinus were mostly seen in the left coronary sinus. However, the relationship between the aortic sinus and the interventricular junction is poorly studied. Most cases are reported on a case-by-case basis, and there is a lack of relevant imaging evidence.

In the ablation of frequent ventricular premature or ventricular tachycardia associated with the aortic sinus, ventricular arrhythmias originating in the left coronary sinus were the most common. The analysis of 7 cases of frequent ventricular premature or ventricular tachycardia associated with the aortic sinus led to the conclusion that 5 of them were successfully ablated in the left coronary sinus and the remaining 2 in the right coronary sinus. The mean distance from the left coronary sinus to the left trunk opening was 12.2 ± 3.2 mm. 12 cases of ventricular tachycardia were successfully ablated in the aortic sinus, and 9 cases were successfully ablated in the left coronary sinus. The majority of ventricular tachycardias were successfully ablated in the left coronary sinus, which may be related to the closer proximity of the left coronary sinus to the left ventricle in this study. Histological studies also revealed crescentic myocardial tissue connections between the aortic sinuses, especially the left and right coronary sinuses, and the right and left ventricular myocardium. These connecting structures may be the extensions of the ventricular myocardium to the aortic sinus and may be the ectopic points of origin for ventricular arrhythmias originating from the aortic sinus. In this study, the presence of connecting structures in the right coronary sinus-right ventricle, right coronary sinus-left ventricle, left coronary sinus-right ventricle, and left coronary sinus-left ventricle was confirmed from an imaging perspective by applying MSCT. These connecting structures may serve as conduction channels between the aortic sinus-ventricle, making the aortic sinus a substrate for ventricular arrhythmias. Consistent with the results of previous studies, the present study showed that the left coronary sinus-left ventricle connection was the most common, which could explain the predominance of the aortic sinus-related ventricular arrhythmias associated with the left coronary sinus as shown in Figure 4. In addition, during the ablation of the left and right coronary sinus, to prevent complications in addition to the strict control of RF energy, it is also important to clarify the anatomical relationship between the coronary artery opening and the ablation target. Many scholars believe that the ablation of the aortic sinus should ensure a distance greater than 1 cm from the left and right coronary orifices, but others believe that this distance of 5–8 mm is considered safe. Therefore, most centers at home and abroad should routinely perform coronary angiography to place contrast catheters before the ablation of the left and right coronary sinuses to mark the coronary openings and avoid coronary opening or intracoronary discharge ablation to reduce the occurrence of complications such as coronary syndrome. The coronary sinus-right atrial distance was significantly smaller than the coronary sinus-left atrial distance (1.77 ± 0.85 mm vs. 2.22 ± 0.92 mm, $P < 0.05$). The left coronary sinus-right ventricular distance was significantly greater than the left coronary sinus-left atrial distance and the left coronary sinus-left ventricular distance (2.66 ± 0.57 mm vs. 2.05 ± 0.91 mm, 1.90 ± 0.45 mm, $P < 0.05$).

4.2. Comparison of Information between Atrial Fibrillation Group and Control Group. In this study, a total of 174 patients, including 94 patients with atrial fibrillation and 80 patients with normal rhythm, included a comparison of age, gender, height, and weight among the groups of atrial fibrillation and nonatrial fibrillation ($P < 0.05$), while the body weight was higher in the atrial fibrillation group than in the nonatrial fibrillation group ($P < 0.05$). The difference in gender and height was statistically significant ($P > 0.05$). The incidence of male patients with atrial fibrillation was significantly higher than that of the female patients. The ratio of left atrial fibrillation was different between atrial fibrillation and control. In the atrial fibrillation group, we considered the number of cases of type A I, type A II, type B, and type C and the proportions of the cases were 10 (10.6%), 38 (40.4%), 38 (40.4%), and 8 (8.5%), respectively. There were 12 (15.0%), 51 (78.8%), 8 (10.0%), and 9 (11.3%) in the number of cases of type A I, type A II, type B, type C in nonatrial fibrillation group, respectively. As shown in Figure 5, the percentages of type A I, type A II, and type C were lower in the atrial fibrillation group than in the control group, and the percentage of type B was higher than the control group.

Quantitative analysis of the left upper pulmonary vein and the mitral ring atrial fibrillation group and nonatrial fibrillation group was performed by comparing the minimum distance from the left atrium to the left upper pulmonary vein and left atrial branch, the width of the crista, the upper margin of the left atrium, the middle edge, the lower edge, and the opening of the left atrium. The data were compared between the two groups (Figure 6). The minimum distance from the left atrium to the upper pulmonary vein and the distance from the opening of the left atrium to the opening of the left upper pulmonary vein and the mitral ring increased in the atrial fibrillation group in comparison with nonatrial fibrillation. In the atrial fibrillation group, the minimum distance from the left atrium to the left gyral branch, the top length of the left atrium, and the width of the top of the apex were reduced in comparison with the nonatrial fibrillation group ($P < 0.05$).

The left auricle is generally located in the atrioventricular sulcus of the free wall of the left atrium and has a complex relationship with the surrounding adjacent structures. The anterior wall is close to the proximal coronary artery gyrus and travels upward close to the root of the pulmonary artery. The left auricle and the left auricular crest are highly variable, and some studies have shown that an excessive ablation in

RETRACTED

RETRACTED

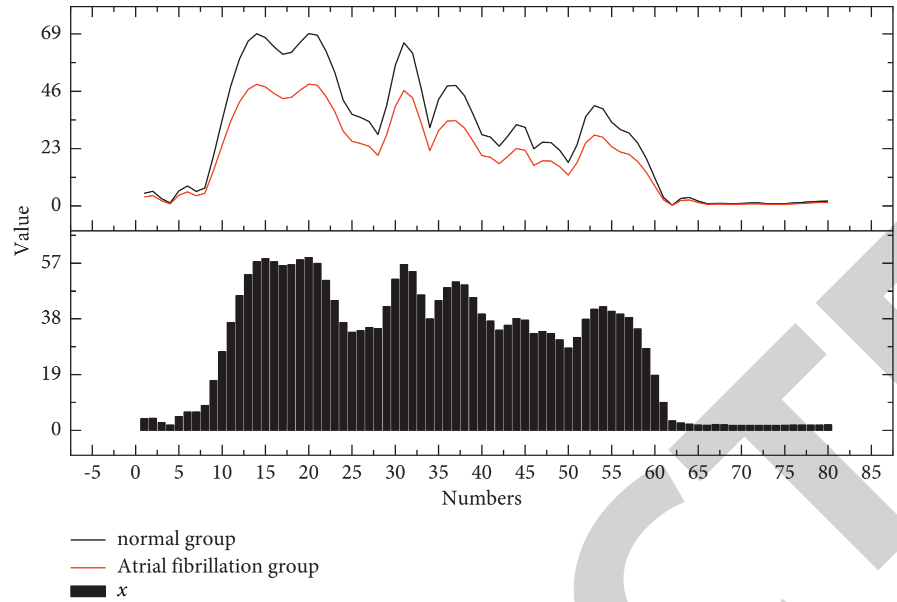

FIGURE 4: χ^2 analysis of the number of cases in which the aortic sinus was connected to the atrium and ventricle.

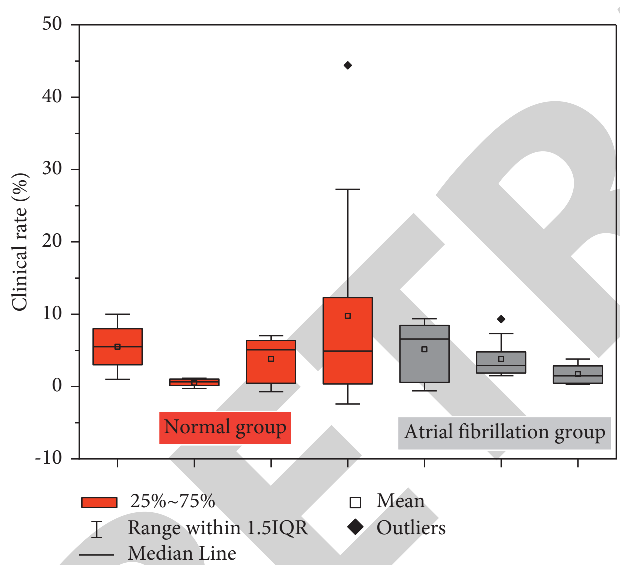

FIGURE 5: Comparison of clinical data between the atrial fibrillation group and control group.

the left auricular crest has the risk of causing pulmonary vein stenosis. There are also case reports of patients with atrial fibrillation in whom the ablation of the base of the left auricle was performed, improperly resulting in a perforation, and possibly, it resulted in a left gyral branch-left atrial fistula. A multilayer spiral CT examination has an obvious superiority in observing the display of cardiac structures. Coronary CT angiography (CTA) is mostly used in clinical practices to observe the cardiovascular lesions, while pulmonary vein scanning parameters are mostly used in patients with atrial fibrillation.

A 256-layer spiral CT can clearly observe the anatomical structure of the heart by a powerful image posttreatment technique. It follows the understanding of certain anatomical structures of the left atrium and pulmonary veins before the surgery, atrial fibrillation, and follow-up of the presence of pulmonary vein stenosis after RF ablation. The incidence of atrial fibrillation was high in the middle-aged and elderly subjects. The average age of the subjects in both experimental and control groups was higher in this study, 57.46 ± 11.68 and 56.10 ± 7.83 years in the atrial fibrillation group. As shown in Figure 7, there was no significant difference in the age between the two groups in the nonatrial fibrillation group ($P < 0.05$). The weight of patients in the atrial fibrillation group was found to be an independent risk factor for the development of atrial fibrillation by the nonatrial fibrillation group and follow-up study. The high-frequency ablation therapy may exacerbate the symptoms and the load of atrial fibrillation. The frequency of radiofrequency ablation therapy is also suitable for obese patients.

In addition, the results of the study found that the crest length and the width of the superior margin of the crest were shorter and statistically different in the patients with atrial fibrillation than in the control group. The patients with atrial fibrillation should pay attention to the morphology and diameter of the left auricular crest when performing the circumferential pulmonary vein spot isolation to avoid damage to other structures or tissues during the operation and to make the scope of the procedure more precise. The left anterior descending coronary and gyral branches are very close to the left auricle or its opening and are susceptible to trauma during percutaneous device implantation, especially when the device is greater than 20% to 40% OS. The results of this study show that the minimum distance from the left auricle to the left gyral branch is small in patients with atrial fibrillation compared to controls, and the majority of the patients have a close distance between the base of the left auricle and the gyral branch of the coronary artery. When performing the radiofrequency ablation of the left auricle, the operator needs to be more careful to prevent the

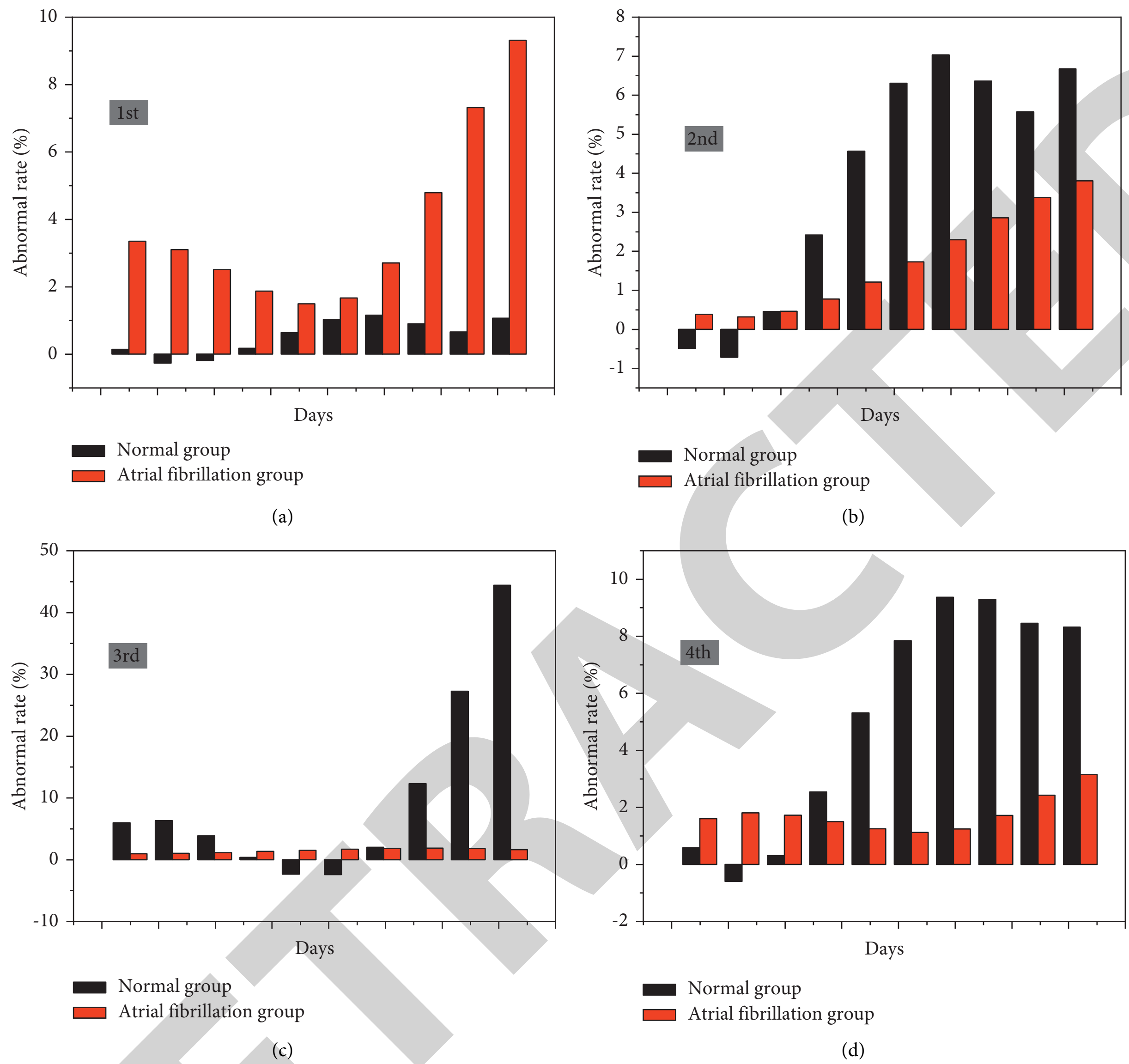

FIGURE 6: Comparison of left atrial crest fractions in the atrial fibrillation group and control group.

RETRACTED

perforation of the left auricle with damage to the left gyral branch because of improper operation. The operator has to be careful to not cause a left auricle-left gyral branch fistula. There is also a risk of compression of the left gyral branch by an oversized blocking device when performing a left auricular occlusion as shown in Figure 8. This study mainly focused on patients with and without atrial fibrillation. Other cardiovascular system diseases were not included in the grouping criteria of the atrial fibrillation group. It may produce errors in the experimental results, but this can be a direction for future studies to understand the pathogenesis of atrial fibrillation more carefully.

Atrial fibrillation, which is common in the elderly, can be classified according to the characteristics of episodes as paroxysmal (lasting <7 hours, self-resetting rate), persistent (meaning lasting >7d, generally not self-resetting), and permanent (failure of resetting to maintain sinus rhythm or no indication for resetting) atrial fibrillation. Irregular atrial fibrillation and ventricular rate derangement can cause a series of clinical symptoms such as dyspnea, palpitations, chest tightness, etc. In severe cases, it can cause heart failure and stroke. A large number of studies have shown that the left auricle (LAA) is closely related to the occurrence and development of atrial fibrillation. In 90% of the patients with atrial fibrillation, the cardiogenic thrombus forms in the left auricle, the atria lose their rhythmic contraction, the pumping capacity decreases, and the ability of the left auricle to drain the blood decreases, making it easy to form a thrombus. In addition, recent studies have found that the left heart ear can act as a trigger point for atrial arrhythmias. To treat atrial fibrillation, restore the normal rhythm of the atria, prevent the formation of thrombus and help patients improve their quality of life, pharmacological and surgical treatments are mostly used in clinical practices.

At present, radiofrequency ablation and left ear occlusion are a new trend of development that is mostly applied to

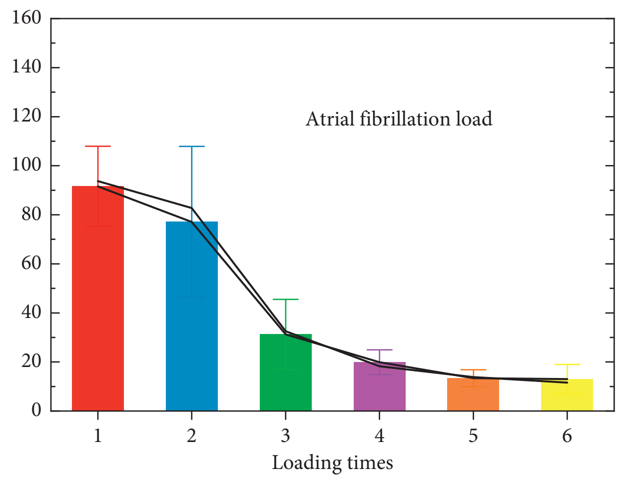

Figure 7: Atrial fibrillation load in the atrial fibrillation group versus the control group.

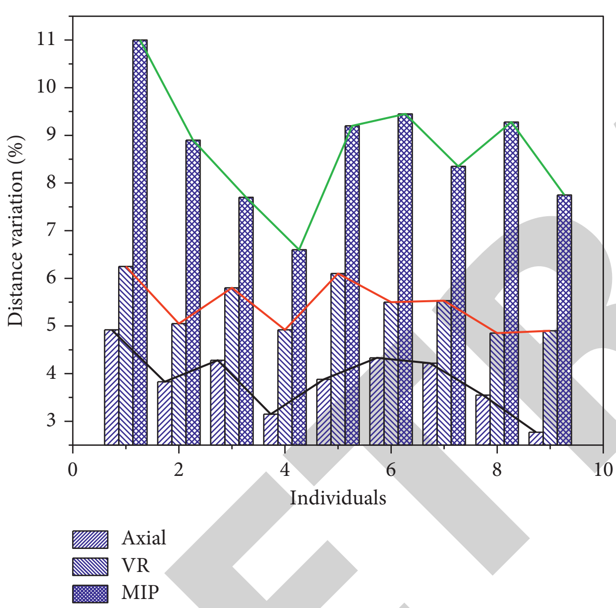

Figure 8: Variation in left auricular-left gyral distance.

treat patients with atrial fibrillation for whom drug therapy is ineffective. Radiofrequency ablation can ablate the rapid conduction or specific areas of cardiomyocytes in the patients with atrial fibrillation to reduce the symptoms of atrial fibrillation. The left ear occlusion is used to occlude the left ear by selecting a suitable occluder, which is mostly used to prevent the formation of left ear thrombus in the patients with atrial fibrillation or to prevent the dislodgement of the formed thrombus to reduce the risk of ischemic stroke. The implementation of both procedures requires precise observation and measurement of the left ear and its surroundings. Therefore, the quantitative study of the anatomy and function of the left auricle in the patients with atrial fibrillation can provide an objective imaging basis for the clinical treatment of patients with atrial fibrillation by initially exploring the clinical significance of the left auricle on the development and progression of atrial fibrillation. With the advancement of technology, multilayer spiral CT (MSCT) is widely used in various clinical examinations and has its unique advantages in diagnosing cardiovascular diseases and evaluating the anatomical structure of the heart. The images obtained from MSCT are of high quality and can evaluate the anatomical structure and function of the heart more objectively using various postprocessing techniques.

5. Conclusion

The purpose of this study is to investigate the anatomical changes of the left atrium and its adjacent structures by applying the 256 nm spiral CT imaging to visualize the left atrium and its adjacent structures and by applying the MPR technology, VR technology, and simulation endoscope techniques. This has a large clinical value in the preoperative evaluation of patients with atrial fibrillation. It can provide an objective morphological reference of radiofrequency ablation and left atrial obstruction in patients with atrial fibrillation. In the quantitative CT study of 612 patients, with or without AF, the left auricular opening was found to be oval (68.9%), pedunculated (10%), triangle (7.7%), and tear drop (7.7%). It is suggested that the diameter calculated from the circumference of the left auricular opening of the MSCT image is more reliable than directly measuring the diameter and area of the left ear opening. In most cases, it is difficult to accurately measure the diameter of the left ear opening because the plane of the left auricular opening obtained by tee or MRCT may not be parallel to the true left ear opening even if MDCT multiplane reconstruction is used. As the shape of the opening is very irregular, it is difficult to reconstruct the cross-section of the left ear opening. The patient was lying flat on the angiography bed, and the preoperative position of the patient's heart was confirmed to be in the central region of the C-arm tube bulb. The left femoral vein and the left subclavian vein were punctured, and the catheter was placed into the coronary sinus and the right ventricle, respectively.

Data Availability

The data used to support the findings of this study are available from the corresponding author upon request.

Conflicts of Interest

The authors declare that there are no conflicts of interest.

Acknowledgments

This work was supported by Affiliated Hospital of Youjiang Medical College for Nationalities.

References

[1] T. Lyu, J. Wang, S. Cao, L. Song, X. Tong, and Y. Zou, "Radiofrequency ablation guided by cone beam computed tomography for hepatocellular carcinoma: a comparative study of clinical results with the conventional spiral computed

RETRACTED

Hindawi
Journal of Healthcare Engineering
Volume 2023, Article ID 9865097, 1 page
https://doi.org/10.1155/2023/9865097

Retraction

Retracted: Analysis of Influencing Factors on Hospitalization Expenses of Patients with Breast Malignant Tumor Undergoing Surgery: Based on the Neural Network and Support Vector Machine

Journal of Healthcare Engineering

Received 27 June 2023; Accepted 27 June 2023; Published 28 June 2023

Copyright © 2023 Journal of Healthcare Engineering. This is an open access article distributed under the Creative Commons Attribution License, which permits unrestricted use, distribution, and reproduction in any medium, provided the original work is properly cited.

This article has been retracted by Hindawi following an investigation undertaken by the publisher [1]. This investigation has uncovered evidence of one or more of the following indicators of systematic manipulation of the publication process:

(1) Discrepancies in scope
(2) Discrepancies in the description of the research reported
(3) Discrepancies between the availability of data and the research described
(4) Inappropriate citations
(5) Incoherent, meaningless and/or irrelevant content included in the article
(6) Peer-review manipulation

The presence of these indicators undermines our confidence in the integrity of the article's content and we cannot, therefore, vouch for its reliability. Please note that this notice is intended solely to alert readers that the content of this article is unreliable. We have not investigated whether authors were aware of or involved in the systematic manipulation of the publication process.

In addition, our investigation has also shown that one or more of the following human-subject reporting requirements has not been met in this article: ethical approval by an Institutional Review Board (IRB) committee or equivalent, patient/participant consent to participate, and/or agreement to publish patient/participant details (where relevant).

Wiley and Hindawi regrets that the usual quality checks did not identify these issues before publication and have since put additional measures in place to safeguard research integrity.

We wish to credit our own Research Integrity and Research Publishing teams and anonymous and named external researchers and research integrity experts for contributing to this investigation.

The corresponding author, as the representative of all authors, has been given the opportunity to register their agreement or disagreement to this retraction. We have kept a record of any response received.

References

[1] J. Zhang and L. Sun, "Analysis of Influencing Factors on Hospitalization Expenses of Patients with Breast Malignant Tumor Undergoing Surgery: Based on the Neural Network and Support Vector Machine," *Journal of Healthcare Engineering*, vol. 2021, Article ID 9268660, 7 pages, 2021.

Hindawi
Journal of Healthcare Engineering
Volume 2021, Article ID 9268660, 7 pages
https://doi.org/10.1155/2021/9268660

Research Article

Analysis of Influencing Factors on Hospitalization Expenses of Patients with Breast Malignant Tumor Undergoing Surgery: Based on the Neural Network and Support Vector Machine

Jing Zhang [1,2,3] and Lin Sun [2,3,4]

[1] *West China School of Public Health, Sichuan University, Chengdu 610041, Sichuan, China*
[2] *West China School of Medicine, Sichuan University, Chengdu 610041, Sichuan, China*
[3] *Institute for Hospital Management West China Hospital, Sichuan University, Chengdu 610041, Sichuan, China*
[4] *West China Hospital, Sichuan University, Chengdu 610041, Sichuan, China*

Correspondence should be addressed to Jing Zhang; 2019224020154@stu.scu.edu.cn

Received 23 September 2021; Revised 14 October 2021; Accepted 19 October 2021; Published 24 November 2021

Academic Editor: Gu Xiaoqing

Copyright © 2021 Jing Zhang and Lin Sun. This is an open access article distributed under the Creative Commons Attribution License, which permits unrestricted use, distribution, and reproduction in any medium, provided the original work is properly cited.

Objective. Analyze the influencing factors of hospitalization expenses of breast cancer patients in a tertiary hospital in Chengdu and provide a basis and suggestion for controlling the unreasonable increase of medical expenses. *Methods*. The first pages of all inpatient medical records of patients with breast malignant tumor from 2017 to 2020 were extracted, and the descriptive analysis, single-factor analysis, and multifactor analysis were conducted by using the statistical method and data mining method to explore the influencing factors of hospitalization expenses. *Results*. In 2017–2020, the average hospitalization cost and the average surgical treatment cost increased year by year, and the number of operations, actual hospitalization days, and CCI were the important influencing factors. *Conclusion*. It is suggested to strengthen the supervision of medical rationality and eliminate the waste of medical resources; and we should improve the efficiency of diagnosis and treatment services, so as to shorten the actual length of hospitalization; at the same time, the combination of DRG grouping and fine management can be used to control the hospitalization expenses.

RETRACTED

1. Introduction

In recent years, with the rapid development of social economy, people's demand for health has been increasing, and the problem of waste of health resources is becoming more and more serious in the world. As an important part of medical expenses, hospitalization expenses are paid more and more attention.Slowing down the growth rate of hospitalization costs is the key to solving the problem of overall medical cost growth. At the same time, the treatment of cancer is more likely to incur high medical costs than other diseases. Breast cancer has become one of the most common malignant tumors among women in China [1 , 2]. The annual growth rate of breast cancer-related expenses in China is 2.3%–2.4%, which causes heavy economic burden to individuals and society. How to effectively and reasonably control the growth of medical expenses is of great significance to reduce the disease burden and economic burden of inpatients and society. At present, the management of breast cancer in Chengdu is too extensive, which is not conducive to the reasonable control of hospitalization expenses. Based on the results of this study, the classification of breast cancer in Chengdu area can be further subdivided; at the same time, research idea about this study can be provided for research of other disease, and it also provides theoretical basis and suggestions for improving service efficiency, controlling medical costs, and rationally optimizing medical resources; therefore, it has become an urgent and realistic research topic to explore the important factors that affect the hospitalization expenses of breast cancer patients and to provide a scientific basis for establishing a scientific and reasonable reimbursement mechanism and standard for the hospitalization expenses of breast cancer patients.

2. Information and Methods

(1) Source of information: the data of this study came from the medical record information management system of a general third-class hospital in Chengdu. In order to ensure the integrity and systematicness of the data,the relevant data information on the first page of medical records of all discharged patients diagnosed with breast malignant tumors in the hospital from January 1, 2017, to December 31, 2020, were derived from the system, and then the patients undergoing breast malignant tumor surgery were selected according to the diagnostic code and operation code. Finally, the selected data were used to establish the initial patient database. The patients with malignant breast tumor were selected, and the initial patient database was established. Finally, the repeat cases, main information missing cases, and the abnormal cases whose hospitalization days <1 or >60 were eliminatedor the total hospitalization cost was beyond P1–P99.

(2) Method: Excel was used to analyze the composition ratio and development trend of hospitalization expenses, and then a single-factor analysis was performed to determine the relationship between different demographic characteristics, disease characteristics, and total hospital costs for breast cancer patients. Based on the results of the normality test and related literature, the total cost of hospitalization and the single cost all present a skewness distribution. Therefore, nonparametric test was used to analyze the cost of hospitalization under each influencing factor. In the non-parametric test, Mann–Whitney U test was used for two independent samples, and Kruskal–Wallis H test was used for many independent samples. The test level $\alpha = 0.05$ was used to screen out the influential factors which had statistical significance on hospitalization expenses ,finally multi-factor analysis was used to further analyze the degree of influence of each factor on hospitalization expenses, and then the important influencing factors are explored." Regression analysis has been widely used in the previous analysis of influencing factors, but many studies using regression analysis have not reported in the paper whether it meets the preconditions of regression analysis: normality, independence, linearity, variance equality, etc. hospitalization cost is a kind of medical big data. Compared with the general data, the information of hospitalization cost has the characteristics of skewness and correlation among variables. Therefore, the traditional regression analysis method often has the limitation in the study of hospitalization cost and is no longer sufficient for analysis. Some research studies show that the fitting result of the data mining method may be more suitable for medical big data [3], such as artificial neural network (ANN) and support vector machine (SVM) [4]. This study used the above two methods to carry out the multifactor analysis on the influencing factors of the hospitalization expense, compared the forecast performance of the two results, and chose the suitable model as the final result. In the above factor analysis, CC method was used to analyze the coincidence and complications quantitatively [5], and the CCI of each case was calculated as a new variable in the factor analysis.

3. Results

(1) Descriptive statistics of hospital expenses: the results, as shown in Table 1 and Figure 1, were 33% for diagnosis and 31% for surgery, and the rates of medical materials, drugs, nonoperative treatment, and service were 11%, 8%, 7%, and 3%, respectively. The trend of the average cost was evaluated by the line graph drawn by Excel, and the results are shown in Figure 2: in 2017–2020, the average cost was 21239.01489RMB, 22057.25477RMB, 23050.40358RMB, and 23048.36969RMB, respectively. The cost of operation was 29.56%, 29.67%, 31.20%, and 32.60%, respectively. The cost of diagnosis was 34.97%, 35.18%, 33.73%, and 30.80%, respectively. And the cost of medical materials was 11.09%, 11.15%, 08.30%, and 12.49%, respectively.

(2) Calculation of CCI (score of complications): the following steps are included: (1) calculate the frequency of each complication, and combine the complications with frequency less than 5 into others; (2) establish the complication table of patients: count the complications of each patient; (3) calculate the weight coefficient of complications: take the total cost after logarithmic conversion as the dependent variable and the presence or absence of complications (0/1) of patients as the independent variable to establish a multiple linear regression model. The regression coefficient in the model output result is the weight coefficient of complications, indicating the impact of this CC category on medical resources. If the coefficient is negative or $P \geq 0.05$, it means that the CC category has no impact on the consumption of medical resources, and its weight value is treated as 0; (4) calculate the patient's complication score CCI: the sum of the corresponding weight coefficients of the complications of the case. The results are shown in Tables 2 and 3.

(3) Single-factor analysis of hospitalization expenses: because the cost of hospitalization does not satisfy the conditions of the parameter test, we used nonparameter test to analyze the cost of hospitalization under each influencing factor, and Kruskal–Wallis test was used to test the data from multiple independent samples. The test level was $\alpha = 0.05$. The influencing factors of hospitalization expenses were analyzed. The results are shown in Table 4. The influencing factors that have statistical significance on hospitalization expenses are age, mode of payment, length of stay, number of operations, operative grade, and CCI.

RETRACTED

Table 1: Composition of hospitalization expenses of patients with breast malignant tumor undergoing surgery.

	Service charge	Diagnostic fee	Nursing expenses	Surgical expenses	Nonsurgical expenses	Medical expenses	Cost of blood products	Cost of medical materials	Other expenses
Total cost	2143819	23236847.69	846926.18	21657109.73	4931820.27	5364841.26	66712.65	7292302.98	4119887.88
Percentage	3.077534831	33.35739077	1.215795185	31.08961602	7.079818148	7.701436474	0.095768581	10.46838209	5.914257897

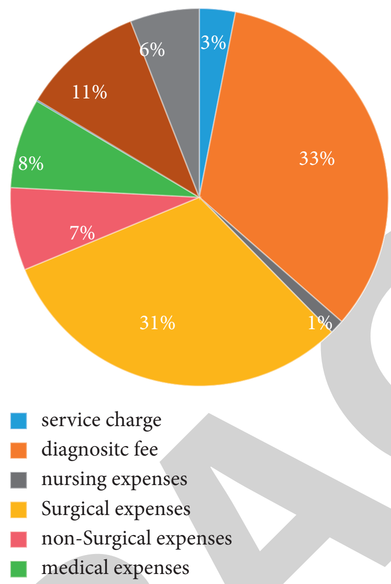

Figure 1: Chart of inpatient costs for breast cancer surgery.

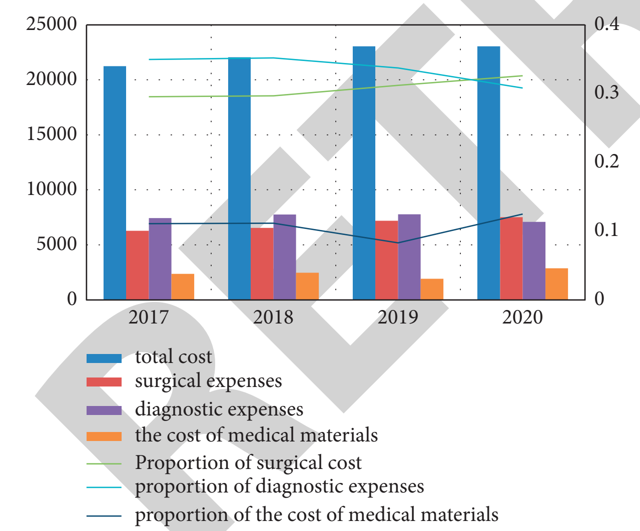

Figure 2: Trend of average cost per hospitalization in patients undergoing breast cancer surgery.

(4) Multifactor analysis of hospitalization expenses: artificial neural network can be regarded as a computer-intensive classification method. Theoretically, artificial neural networks should have considerable advantages over standard statistical methods, such as allowing double nonlinear relationships between independent variables and dependent variables and all possible interactions between dependent variables [6]. Support vector machine is a new general learning method developed on the basis of statistical learning theory. Based on the VC dimension theory of statistical learning theory and the principle of structural risk minimization, it seeks the best compromise between the complexity of the model and learning ability according to the limited sample information, so as to obtain the best generalization ability [7]. In this study, the neural network and support vector machine were used simultaneously to explore the factors that had the greatest impact on hospital costs. According to the results of univariate analysis, the input variables included age, mode of payment, length of stay, number of operations, operative grade, and CCI. Using SPSS Modeler software to build the model and using the indexes of error and correlation coefficient, the model with good fitting effect was selected as the result of multifactor analysis. The results are shown in Table 5. In each evaluation index, the average absolute error represents the proximity between the predicted value and the real value. The smaller the value, the higher the prediction accuracy of the model. The correlation coefficient is the index to evaluate the goodness of fit of the model. The larger the value, the better the model fitting. The correlation coefficient and error showed that the fitting effect of the neural network model is better than that of the support vector

RETRACTED

RETRACTED

Table 2: Weight coefficient of complications in patients undergoing breast cancer surgery.

Variable (code for complications)	Coefficient	*t*	Statistical significance
Constant		1201.422	0.000
C77.301	0.102	5.904	0.000
N39.000	0.116	6.810	0.000
D24.x00	0.101	5.614	0.000
Z51.103	0.104	6.123	0.000
J94.804	0.082	4.813	0.000
E77.801	0.070	4.077	0.000
N60.201	0.076	4.216	0.000
C50.100	0.061	3.657	0.000
R94.303	−0.052	−3.080	0.002
In the news	0.062	3.600	0.000
K76.000X011	−0.054	−3.177	0.002
J34.300	0.066	3.611	0.000
Z85.300	−0.048	−2.836	0.005
M50.201	−0.055	−3.240	0.001
N63.x00	0.054	3.122	0.002
D61.101	0.051	2.994	0.003
D05.100x001	0.048	2.839	0.005
C79.800X809	0.059	3.349	0.001
N64.802	0.045	2.672	0.008
N64.500	0.045	2.671	0.008
D69.600	−0.043	−2.575	0.010
T85.400	0.044	2.585	0.010
D48.601	0.042	2.503	0.012
J34.200	−0.041	−2.280	0.023
I 82.804	0.042	2.481	0.013
N63.X01	0.040	2.290	0.022
C50.300	0.039	2.296	0.022
R90.000x002	0.037	2.211	0.027
J47.x00	−0.035	−2.062	0.039
J47.x03	−0.036	−2.134	0.033
C50.200	0.036	2.157	0.031
D72.800x002	0.036	2.136	0.033
C77.002	0.036	2.111	0.035
C50.800	0.035	2.072	0.038
F41.101	0.034	2.024	0.043
R22.201	0.038	2.226	0.026
C79.827	−0.044	−2.456	0.014
M48.901	0.038	2.209	0.027
N64.503	0.034	1.994	0.046

Table 3: CCI of breast cancer surgery patients in a hospital in Chengdu from 2017 to 2020.

Period	ID code	CCI
202010	00001	0.376190627
202012	00002	0.361690004
201911	00003	0.360015743
202001	00004	0.360015743
201807	00005	0.336938059
202004	00006	0.333024001
202010	00007	0.332539654
201801	00008	0.332539654
201906	00009	0.332539654
201803	00010	0.332539654
201807	00011	0.332539654
201908	00012	0.332539654
201904	00013	0.332539654
201904	00014	0.332539654
202012	00015	0.332539654
201812	00016	0.329251529
202004	00017	0.317962384
202009	00018	0.317962384
201911	00019	0.317962384

Table 4: Results of univariate analysis.

Variable	Mean value	Number of cases	Standard deviation	Median	Percentage	P
Age						<0.01
≤20	32690.335	2	19054.86605	32690.335	0.10%	
20–40	25901.0894	510	11065.29952	22159.69	1660	
40–60	21960.9184	1999	8141.2137	20451.57	65.10%	
60–80	21875.2406	549	8520.29518	20260.46	1790	
>80	43268.0291	11	69149.33435	23239.59	0.40%	
Native place						0.143
Unknown	19341.674	5	2741.14545	19720.7	0.20%	
Southwest	22658.015	2878	9858.99858	20671.02	93.70%	
Northwest	23791.9147	58	8828.24487	21380.105	1.90%	
East China	23717.2767	43	10817.21822	21175.99	1.40%	
Central China	22486.9883	35	6097.92305	21411.29	1.10%	
North China	24536.2174	23	9262.9743	21481.48	0.70%	
Northeast	21610.6044	18	9009.82898	18054.66	0.60%	
South China	19422.6918	11	5458.59496	18884.54	0.40%	
Nation						0.324
Han nationality	22771.8336	2755	10061.9057	20701.26	89.70%	
Tibetan	21321.5037	54	5155.2445	20224.15	1.80%	
Others	22032.4616	262	7269.37178	20308.155	8.50%	
Occupation						0.204
Farmers	21743.1218	393	8285.32421	20478	1280	
Staff	23347.5746	276	8349.4663	20900.1	9.00%	
Technical expertise	23687.8992	194	10295.17455	20883.69	6.30%	
Retiree	21977.3684	187	7338.63312	20163.83	6.10%	
Civil servants	23720.3678	129	10649.82274	20764.4	4.20%	
Others	22677.6651	1892	10342.75743	20684.605	61.60%	
Payment method						<0.01
Others	22426.4669	2019	10437.36182	20472.57	65.70%	
Town employee	23297.1823	890	8726.14502	20970.715	29.00%	
Urban and rural residents	22510.7327	162	6230.07858	21368.69	5.30%	
Length of stay						<0.01
≤5	19413.8759	192	9231.37935	18080.63	6.30%	
5–10	22163.7347	2711	7072.05057	20566	88.30%	
10–15	29557.7026	139	11623.11149	26396.88	4.50%	
>15	59944.759	29	51470.89992	44091.36	0.90%	
Mode of discharge						0.835
Doctor's orders	22682.5627	3060	9800.73906	20681.395	99.60%	
Transfer on doctor's orders	23104.706	10	6806.35353	23218.545	0.30%	
Death	20578.81	1	.	20578.81	0.00%	
Pathological diagnosis						0.173
Not subdivided	22393.1364	2062	7561.24753	20752.235	67.10%	
Noninvasive	21711.0832	37	12369.74946	19623.81	1.20%	
Invasive special carcinoma	21745.2973	48	8192.17301	20354.835	1.60%	
Invasive nonspecific carcinoma	23464.1058	901	13552.86947	20595.15	29.30%	
Others	21625.0744	23	8582.79677	19170.54	0.70%	
Number of operations						<0.01
≤2	20105.6137	1311	5798.30993	19396.58	42.70%	
3–5	23171.5636	1422	7833.40981	21445.445	46.30%	
>5	30626.7595	338	19838.96913	26006.47	11.00%	
Surgical grade						<0.01
Level 1	26477.6325	4	9519.5442	23846.445	0.10%	
Level 2	22797.0614	7	6439.33718	21836.76	0.20%	
Level 3	20577.9487	780	5128.11815	20074.74	25.40%	
Level 4	23396.4814	2280	10855.72205	20950.575	74.20%	
Readmission status						0.3
Yes	24688.615	453	17439.8389	20919.71	1480	
No	22322.3023	2614	7655.06889	20633.945	85.10%	
Unknown	31456.6875	4	19889.14619	21774.065	0.10%	

RETRACTED

Table 4: Continued.

Variable	Mean value	Number of cases	Standard deviation	Median	Percentage	*P*
CCI						<0.01
0	20700.5261	1013	5843.80473	19872.92	33.00%	
0–0.1	22070.1947	729	8176.88359	20012.11	23.70%	
0.1–0.2	23492.7826	1160	8921.19155	21512.5	37.80%	
0.2–0.3	31261.7223	146	22471.80424	25929.435	4.80%	
0.3–0.4	34157.5413	23	34880.01899	25107.19	0.70%	
Rh						0.07088
Unknown	22014.4542	704	7794.55932	20411.13	0.229	
Positive	22882.3501	2347	10329.55077	20750.74	0.764	
Negative	22860.81	20	6557.75538	21618.945	0.007	
Allergies						0.005164
Yes	22210.7861	1568	6655.0434	20969.485	0.511	
No	23176.151	1503	12215.7928	20278.69	0.489	

Table 5: Comparison of neural network and support vector machine fitting.

	Support vector machine		Neural network	
	Training set	Test set	Training set	Test set
Minimum error	−0.95	−0.894	−0.22	−0.505
Maximum error	1.064	0.892	0.221	0.528
Mean error	−0.007	−0.006	−0.006	−0.004
Mean absolute error	0.213	0.217	0.067	0.081
Standard deviation	0.274	0.273	0.084	0.113
Correlation	0.331	0.263	0.741	0.474
Occurrence rate	2,422	649	2,422	649

Table 6: Importance ranking of neural network variables.

Nodes	Importance
The mode of payment	0.0024
Age	0.0334
Level of operation	0.034
CCI	0.1428
Actual length of stay	0.3533
Number of operations	0.4341

machine. Therefore, the output of the neural network model was selected as the final result of the multifactor analysis, as shown in Table 6. As you can see from the neural network output, the order of importance of the factors influencing the hospitalization expenses of patients with breast malignant tumor was the number of operations (0.49), the actual length of stay (0.35), the CCI (0.14), the age (0.03), the level of operation (0.03), and the mode of payment (0.01).

4. Conclusion

(1) The general situation of hospitalization expenses of patients with breast malignant tumor operation: the highest proportion of hospitalization expenses is diagnosis expenses, which is 33%, followed by operation treatment expenses and medical material expenses, which are 31% and 11%, respectively; the remaining service fees, drug fees, nonsurgical treatment fees, and other fees account for a relatively low proportion. The operation fees and diagnostic fees account for a large proportion of the cost of cancer in line with the current structure of the common situation in China. In the trend chart, the average total cost and the large proportion of the average cost of surgical treatment increased year by year, while the average cost of medical materials decreased significantly in 2019; the reason may be related to the management upgrade of medical consumables in the 2019 medical reform and the cancellation of the consumable bonus in public hospitals [8].

(2) According to the results of neural network analysis, the most important influencing factor is the number of operations, and there is a positive correlation between the number of operations and the cost of hospitalization. The more the operations, the higher the cost of hospitalization, for the surgical treatment of malignant tumors, the more complicated the disease is, and the more surgery is often needed at the same time or successively in order to achieve the desired therapeutic effect; multiple operations represent high operating and hospitalization costs and should also pay attention to whether there are unreasonable treatment and waste of medical resources. Therefore, the number of operations is an important influencing factor for hospitalization costs. When grouping related diseases, the number of operations should also be taken into account, so as to make fine segmentation. Secondly Less important was the actual length of stay, which showed that the longer the stay, the higher the cost. The reasons for this situation have their rationality and irrationality. For example, it is normal for difficult cases to have relatively long hospitalization days and relatively high hospitalization expenses, but it is not reasonable if the hospitalization time is deliberately prolonged; therefore, it is suggested that reducing the average length of stay is an effective way to control the cost of

RETRACTED

Hindawi
Journal of Healthcare Engineering
Volume 2023, Article ID 9781637, 1 page
https://doi.org/10.1155/2023/9781637

Retraction

Retracted: Diagnosis and Etiological Analysis of Gastroesophageal Reflux Disease by Gastric Filling Ultrasound and GerdQ Scale

Journal of Healthcare Engineering

Received 10 October 2023; Accepted 10 October 2023; Published 11 October 2023

Copyright © 2023 Journal of Healthcare Engineering. This is an open access article distributed under the Creative Commons Attribution License, which permits unrestricted use, distribution, and reproduction in any medium, provided the original work is properly cited.

This article has been retracted by Hindawi following an investigation undertaken by the publisher [1]. This investigation has uncovered evidence of one or more of the following indicators of systematic manipulation of the publication process:

(1) Discrepancies in scope
(2) Discrepancies in the description of the research reported
(3) Discrepancies between the availability of data and the research described
(4) Inappropriate citations
(5) Incoherent, meaningless and/or irrelevant content included in the article
(6) Peer-review manipulation

The presence of these indicators undermines our confidence in the integrity of the article's content and we cannot, therefore, vouch for its reliability. Please note that this notice is intended solely to alert readers that the content of this article is unreliable. We have not investigated whether authors were aware of or involved in the systematic manipulation of the publication process.

In addition, our investigation has also shown that one or more of the following human-subject reporting requirements has not been met in this article: ethical approval by an Institutional Review Board (IRB) committee or equivalent, patient/participant consent to participate, and/or agreement to publish patient/participant details (where relevant).

Wiley and Hindawi regrets that the usual quality checks did not identify these issues before publication and have since put additional measures in place to safeguard research integrity.

We wish to credit our own Research Integrity and Research Publishing teams and anonymous and named external researchers and research integrity experts for contributing to this investigation.

The corresponding author, as the representative of all authors, has been given the opportunity to register their agreement or disagreement to this retraction. We have kept a record of any response received.

References

[1] B. Wang, Q. Sun, Y. Du, K. Mu, and J. Jiao, "Diagnosis and Etiological Analysis of Gastroesophageal Reflux Disease by Gastric Filling Ultrasound and GerdQ Scale," *Journal of Healthcare Engineering*, vol. 2021, Article ID 5629067, 6 pages, 2021.

Hindawi
Journal of Healthcare Engineering
Volume 2021, Article ID 5629067, 6 pages
https://doi.org/10.1155/2021/5629067

Research Article

Diagnosis and Etiological Analysis of Gastroesophageal Reflux Disease by Gastric Filling Ultrasound and GerdQ Scale

Bo Wang,[1] Qian Sun,[1] Yonghong Du,[1] Kexiao Mu,[2] and Jingxia Jiao[1]

[1]*Department of Physical Diagnostics, West Hospital District of Qingdao Multicipal Hospital, Qingdao 266002, China*
[2]*Department of Ultrasound, the Second Affiliated Hospital of Shandong University of Traditional Chinese Medicine, Jinan 250000, China*

Correspondence should be addressed to Jingxia Jiao; jiaojingxiaqd@163.com

Received 11 September 2021; Revised 13 October 2021; Accepted 21 October 2021; Published 15 November 2021

Academic Editor: Gu Xiaoqing

Copyright © 2021 Bo Wang et al. This is an open access article distributed under the Creative Commons Attribution License, which permits unrestricted use, distribution, and reproduction in any medium, provided the original work is properly cited.

Objective. To investigate the diagnosis and etiological analysis of GERD by gastric filling ultrasound and GerdQ scale. *Methods*. The clinical data of 100 suspected GERD patients were selected for retrospective analysis. The selection time was from June 2016 to June 2019. According to the gold standard (endoscopy) results, they were divided into the gastroesophageal reflux group (positive, $n = 62$) and the nongastroesophageal reflux group (negative, $n = 38$); both gastric filling ultrasound and GerdQ scale examination were performed to compare the positive predictive value and negative predictive value, evaluate the abdominal esophageal length, His angle, and GerdQ scale score, and analyze the AUC value, sensitivity, specificity, and Youden index of His angle, length of abdominal esophagus, combined ultrasound parameters, and GerdQ scale in the diagnosis of GERD. *Results*. 100 patients with suspected GERD were diagnosed as GERD by endoscopy; in a total of 62 cases, the percentage was 62.00%. Among them, 28 cases were caused by the abnormal structure and function of the antireflux barrier, accounting for 45.16%, 18 cases were caused by the reduction of acid clearance of the esophagus, accounting for 29.03%, and 16 cases were caused by the weakening of the esophageal mucosal barrier, accounting for 25.81%. After ultrasound detection, the positive predictive value was 88.71% and the negative predictive value was 81.58%; after the GerdQ scale was tested, the positive predictive value was 71.43% and the negative predictive value was 54.05%. The length of the abdominal esophagus in the gastroesophageal reflux group was lower than that of the nongastroesophageal reflux group, while the scores of His angle and GerdQ scale were higher than those in the gastroesophageal reflux group ($P < 0.05$). ROC curve analysis showed that the AUC values of His angle, length of abdominal esophagus, combined ultrasound parameters, and GerdQ scale to diagnose GERD were 0.957, 0.861, 0.996, and 0.931 ($P < 0.05$), their sensitivity was 93.5%, 98.40%, 98.40%, and 90.30%, and the specificity was 92.10%, 63.20%, 100.00%, and 92.10%, respectively. *Conclusion*. Both gastric filling ultrasound and GerdQ scale have a certain application value in the diagnosis of GERD, but the former has a higher accuracy rate, and it is more common for gastroesophageal reflux caused by abnormal structure and function of antireflux barrier in etiological analysis.

RETRACTED

1. Introduction

Gastroesophageal reflux disease (GERD) is a functional disease caused by the reflux of duodenal contents into the esophagus with lesions of esophageal mucosa and extra-esophageal tissues [1]. The clinical manifestations of the disease are complex and varied, with acid reflux, antifeeding, and burning pain under xiphoid or substernum as the typical clinical symptoms. In patients with obvious clinical manifestations, the diagnosis can be made by typical symptoms, but there are also some patients with atypical clinical symptoms; in this case, the use of auxiliary examination is particularly important. The most reliable method for the diagnosis of gastroesophageal reflux and gastroesophageal reflux disease is 24-hour pH detection, which can not only detect reflux but also understand the relationship between the degree of reflux and symptoms, body position, and feeding. However, the application of the pH detection method is limited because it has not been widely used in China [2]. At present, the diagnosis of gastroesophageal reflux disease in

RETRACTED

China uses a combination of clinical, endoscopic, and physiological parameters. Based on the inner diameter manifestations of esophagitis, long Barrett's esophagus, or digestive stenosis, the diagnosis of pathological reflux esophageal connective tissue can be made [3]. Clinically, endoscopy is regarded as the golden standard for the diagnosis of this disease. However, as this method is invasive and intolerable for some patients and is not suitable for promotion in primary hospitals [4], it is very important to find a non-invasive examination method with high accuracy. The GerdQ scale has been suggested by clinical scholars for examination. The GerdQ scale was found by Dent et al. in 2007 and optimized by three scales called Reflux Disease Questionnaire (RDQ), Gastroesophageal Reflux Disease Impact Scale (GIS), and Gastrointestinal Symptom Grade Scale (GSRS), widely used in clinical practice [5, 6], At the same time, some scholars suggest the use of ultrasound examination. However, there are few comparative studies on the above two methods, and it is not clear which method has high accuracy and specificity. Therefore, the clinical data of 100 suspected GERD patients were selected for retrospective analysis in order to discuss the diagnosis of GERD by gastric filling ultrasound and GerdQ scale and analyze its etiology. They are now reported in the following.

2. Data and Methods

2.1. Clinical Data. Clinical data of 100 suspected GERD patients diagnosed and treated from June 2016 to June 2019 were retrospectively analyzed. Diagnostic criteria: the diagnosis was confirmed by esophageal reflux monitoring and upper gastrointestinal endoscopy in accordance with the diagnostic criteria of "multidisciplinary diagnosis and treatment consensus of gastroesophageal reflux disease in China" [7]. Inclusion criteria:(1) age ≥18 years; (2) at least one of the clinical manifestations such as reflux, acid reflux, or heartburn in the past 4 weeks. Exclusion criteria:(1) recent dysphagia, weight loss, and other symptoms; (2) after physical examination, there are abnormalities such as rebound pain and mass in the abdomen; and (3) accompanied by serious heart, liver, kidney, and other diseases. There was no significant difference in general data between the two groups ($P > 0.05$), as given in Table 1.

2.2. Methods. The data of 100 patients with suspected GERD undergoing ultrasound examination and GerdQ scale assessment were retrospectively analyzed.

2.2.1. Ultrasonic Detection Method. Color Doppler ultrasound diagnostic instrument is produced by Siemens GE 4D convex array probe, probe frequency of 3.5–5.5 mhz. Pretest routine fasting should be 8–12 h and 5 min before testing guide patients with oral gastric ultrasound help agent 500 ml, guide the patient to sitting, dynamic scan end of the esophagus and cardia, gastric, gastric body, gastric antrum, pylorus, duodenum, and observe whether the stomach wall form changes, changes of peristaltic frequency, contents emptying condition, the existence of a reverse flow, echo property, and vascular distribution of lesion were recorded. Then, assist the patient to take the supine position, select the oblique section of the left costal margin under the xiphoid process, instruct the patient to maintain the breath-holding state after forcibly inhaling, put the probe toward the left lobe of the liver septum, and gently press the abdominal wall. The angle between the parallel line of the long axis of the feeding tube and the tangent line of the fundus of the stomach was His angle. The distance between the esophageal hiatus and the place was taken as the length of the abdominal esophagus, and the mean value was taken as the final result.

2.2.2. Gastroesophageal Reflux Disease Questionnaire (GerdQ) Scale [8]. The scale was used to assess the patients' symptoms in the last week, The assessment included 6 items, including frequency of reflux attacks, frequency of gastric burning attacks, frequency of nausea, frequency of upper abdominal pain, frequency of self-medication for sleep disorders, and frequency of using OTC drugs. The frequency of nausea and the frequency of upper abdominal pain are assessed inversely, that is, 0 d is 3 points, 1 d is 2 points, 2-3 d is 1 point, and 4–7 d is 0 points; the others are positive scores, that is, 0 d is 0 point, 1 d is 1 point, 2-3 d is 2 points, and 4–7 d is 3 points. Finally, the total score of 6 items ≥8 points is judged as positive, that means suffering from GERD.

2.3. Observation Index

- The positive predictive value and negative predictive value of 100 subjects were measured by ultrasound and GerdQ scale, using the four-cell table method
- The length of abdominal esophagus, His angle, and GerdQ scale scores of 2 groups were evaluated
- His angle, abdominal esophageal length, combined ultrasound parameters, AUC value, sensitivity, specificity, and Youden index of GERD were evaluated. Combined ultrasound parameters = abdominal esophagus length + (β His angle/β abdominal esophagus length) × His angle, where β was used as the dependent variable, and abdominal esophagus length and His angle were used as independent variables to carry out the regression coefficient of binary logistic regression.

2.4. Statistical Method. SPSS22.0 software was used to analyze the data. Measurement data were represented by ($\overline{x} \pm s$), and the independent sample T-test was performed. Counting data were represented by (n; %), the χ^2 test was performed. The predictive value was analyzed by the ROC curve. $P < 0.05$ was considered as a statistically significant difference.

3. Result

3.1. Etiological Analysis. Among the 100 suspected GERD patients, 62 cases (62.00%) were confirmed to be GERD by endoscopic examination. Among them, 28 cases (45.16%) were caused by the abnormal structure and function of

Table 1: Comparison of general information.

Group	Gender (%)		Mean age	BMI index (kg/m^2)
	Male	Female		
GERD ($n = 62$)	32 (51.61)	30 (48.39)	45.23 ± 3.52	22.32 ± 2.02
Non-GERD ($n = 38$)	19 (50.00)	19 (50.00)	45.28 ± 3.50	22.36 ± 1.95
χ^2/t	0.025		0.069	0.097
P	0.876		0.945	0.923

antireflux barrier, 18 cases (29.03%) were caused by the reduced function of esophageal scavenging acid, and 16 cases (25.81%) were caused by the reduced function of esophageal mucosal barrier.

3.2. Comparison of Positive and Negative Predictive Values. The positive predictive value and negative predictive value of 100 suspected GERD patients were 88.71% and 81.58% after ultrasonic examination. The positive predictive value was 71.43% and the negative predictive value was 54.05%. Table 2 provides the details.

Table 2: The positive and negative predictive values of the two methods were compared.

Golden standard	Ultrasound		GerdQ		Sum
	Positive	Negative	Positive	Negative	
GERD	55	7	45	17	62
Non-GERD	7	31	18	20	38
Sum	62	38	63	37	100

Note. The gold standard is endoscopic examination; the GERD group was positive and the non-GERD group was negative.

3.3. Comparison of Abdominal Esophageal Length, His Angle, and GerdQ Scale Scores. The abdominal esophageal length of the GERD group was lower than that of the non-GERD ultrasound group, while His angle and GerdQ scale scores were higher than those of the GERD group ($P < 0.05$). Table 3 provides the details.

3.4. Diagnostic Performance Analysis. ROC curve analysis showed that the AUC values of His angle, abdominal esophageal length, combined ultrasound parameters, and GerdQ scale for GERD diagnosis were 0.957, 0.861, 0.996, and 0.931 ($P < 0.05$). According to AUC and standard error, the difference of AUC was tested by Z, and the results showed that His angle vs. abdominal esophageal length $Z = 2.26$, $P = 0.024$; His angle vs. ultrasonic combined parameters $Z = -1.985$, $P = 1.953$; His angle vs. GerdQ scale score $Z = 0.828$, $P = 0.408$; abdominal esophageal length vs. ultrasound combined parameters $Z = -3.522$, $P = 2.00$; abdominal esophageal length vs. GerdQ scale score $Z = -1.539$, $P = 1.876$; and ultrasound combined parameters vs. GerdQ scale score $Z = 2.55$, $P = 0.011$. According to the optimal critical value, when His angle was higher than 58.135°, the sensitivity and specificity were 93.5% and 92.1%, respectively. When the length of abdominal esophagus was higher than 3.295 cm, the sensitivity and specificity were 98.4% and 63.2%, respectively. When the ultrasonic combination parameter is lower than −4.40702, the sensitivity is 98.4% and the specificity is 100%. When GerdQ score was higher than 7.31, the sensitivity and specificity were 90.3% and 92.1%, respectively. Table 4 provides the details. ROC curves are shown in Figures 1 and 2.

4. Discussion

According to the epidemiological investigation [9], the prevalence of GERD is about 5.77%. The prevalence of GERD in European countries is as high as 10%–20%, while the prevalence of GERD in Asia is less than or slightly lower. In recent years, with the economic and social development, people's living habits and diet structure have been improved to some extents, the aging degree has increased, and the unhealthy lifestyle has led to the increase in the incidence of GERD. The incidence of disease will be increasing with people's living habits and diet structure [10]. Clinically, it is believed that the occurrence of this disease is related to the abnormal structure and function of the antireflux barrier, the reduced function of esophageal acid clearance, and the weakened role of esophageal mucosal barrier [11–13]; at the same time, esophageal mucosa inflammation and motor disorders are also associated with the severity of GERD [14]. Previous studies have shown that the proportion of GERD caused by the first etiology is the highest, and the abnormal structure and function of the antireflux barrier are mostly related to dietary habits and living habits, such as obesity, which lead to the damage of the lower esophageal sphincter structure by promoting the increase of abdominal pressure [15]. Studies have also pointed out that long-term use of calcium channel blockers, aminophylline, diazepam, and other drugs will also cause esophageal motor dysfunction and lower esophageal sphincter pressure drop [16]. Studies have also pointed out that long-term use of calcium channel blockers, aminophylline, diazepam, and other drugs will also cause esophageal motor dysfunction and lower esophageal sphincter pressure drop. The above research results indicate that maintaining good living habits and eating habits is particularly important to reduce the incidence of GERD. In the past, X-ray barium meal examination was mostly used for clinical diagnosis of this disease, which provided important information for clinical diagnosis by comprehensively observing the shape of the stomach, length of the abdominal cavity and esophagus, His angle, and frequency of gastroesophageal reflux. However, due to the limitation of instantaneous performance, it was difficult to distinguish physiological reflux from pathological reflux. Some studies have pointed out that the reflux rate detected by X-ray barium meal in normal population is about 20% or even higher, while the detection rate in the diagnosis of pathological acid reflux is

RETRACTED

Table 3: Comparison of abdominal esophageal length, His angle, and GerdQ scale scores between the two groups.

Group	*n*	Ultrasound		GerdQ
		Length of abdominal esophagus (cm)	His angel (°)	
GERD	62	2.36 ± 0.75	68.23 ± 6.52	8.35 ± 2.85
Non-GERD	38	3.49 ± 0.60	52.45 ± 5.09	5.75 ± 1.02
T		7.867	12.723	5.407
P		<0.001	<0.001	<0.001

Table 4: ROC curve analysis of the four detection methods.

Test result variable	AUC	Standard error	*P*	95% confidence interval		Cutoff	Youden' index	Sensitivity	Specificity
				Lower limiting value	Higher limiting value				
His angel	0.957	0.019	<0.001	0.920	0.993	58.135	0.856	93.50	92.10
Length of abdominal esophagus	0.861	0.038	<0.001	0.787	0.934	3.295	0.616	98.40	63.20
Ultrasonic combination parameter	0.996	0.005	<0.001	0.987	1.000	−4.4070	0.984	98.40	100.00
GerdQ score	0.931	0.025	<0.001	0.882	0.980	7.31	0.824	90.30	92.10

Note. The parameters of ultrasonic combination are His angle and abdominal esophagus length, and its formula is calculated as ultrasonic combination parameter = abdominal esophagus length + 0.360/2.791 * His angle.

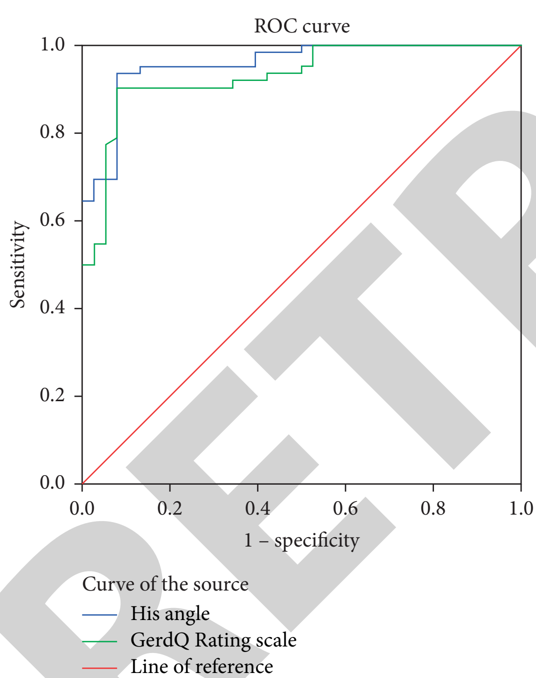

Figure 1: ROC curve analysis of His angle and GerdQ scale scores.

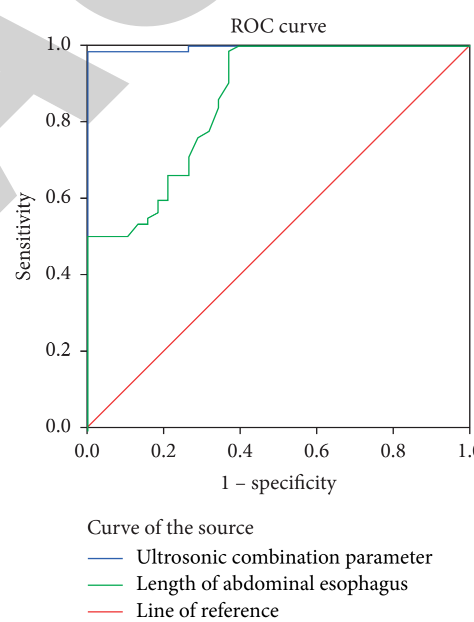

Figure 2: ROC curve analysis of abdominal esophagus length and ultrasonic combined parameters.

RETRACTED

only 26%, indicating its low sensitivity and specificity [17]. With the further development of imaging technology, clinical ultrasound examination of GERD can not only dynamically and intuitively observe esophageal peristalsis, length of abdominal esophagus, His angle, and other information but also measure gastric empty. With advantages of good repeatability, simple operation, and convenience, it has been widely used and promoted in clinical practice [18].

The results of this study showed that the positive predictive value and negative predictive value of GERD in gastric filling ultrasound diagnosis were 88.71% and 81.58%, respectively. The results are close to the gold standard. In addition, when measuring the length of the abdominal esophagus and His angle, it was found that the length of the abdominal esophagus in the GERD group was shorter than that in the non-GERD group, while His angle was higher than that in the non-GERD group, which may be related to the anatomical abnormalities of the lower gastroesophageal segment. Under normal circumstances, the anatomical structure of the lower segment of the stomach and esophagus can play an antireflux role. For example, His angle connecting the esophagus and stomach is a one-way valve to prevent reflux, while the abdominal esophagus is affected by

RETRACTED

abdominal pressure and plays an antireflux role by promoting the wall of the tube to converge [19–21]. However, when His angle increases, it means that the diaphragmatic angular clamp is weakened and cannot prevent the occurrence of reflux symptoms. Studies [22] pointed out that under the stomach esophagus period of abnormal anatomical structure is a common cause of gastroesophageal reflux, and in the GERD group, it was found that the ventral segment esophageal length shorter than the general population prompt the stomach esophagus in patients with the gastroesophageal reflux period of abnormal change in anatomy, and ultrasound examination can directly observe the stomach esophagus connection department of anatomy. It can provide quantitative or semiquantitative index for the degree of reflux. Some scholars also suggest the use of the GerdQ scale, which is a newly developed new diagnostic method, and provide information for clinical diagnosis by understanding the frequency and severity of symptoms [23, 24]. However, in this study, it was found that the specificity of GERD was relatively low, so the GerdQ scale can only be used as a preliminary screening diagnostic tool. In addition, in ROC curve analysis, it was found that the AUC value of the GerdQ scale was lower than that of His angle and abdominal esophageal length, indicating that its predictive value was lower than that of ultrasound. In addition, this study proposed "ultrasound combined parameter," that is, His angle combined with abdominal esophageal length to diagnose GERD. Its AUC value and specificity are significantly higher than His angle and abdominal esophageal length alone, indicating that combined diagnosis has a higher predictive value and can provide more accurate reference information for GERD diagnosis, thus reducing the rate of misdiagnosis and missed diagnosis.

In conclusion, both gastric filling ultrasound and the GerdQ scale have a certain application value in the diagnosis of GERD, but the diagnostic value of gastric filling ultrasound is higher, especially the combination of His angle and abdominal esophageal length can further improve the diagnosis and confirmation rate.

Data Availability

The dataset used to support the findings of this study are available from the corresponding author upon request.

Conflicts of Interest

The authors declare that they have no conflicts of interest.

Acknowledgments

This study was supported by Shandong Province Medical and Health Technology Development Plan (2019WS561) and Qingdao Medical Research Guidance Plan for 2017 (2017-WJZD093).

References

[1] K. Wang, H. Tao, Q. Wang et al., "Analysis of clinical and esophageal function detection characteristics of refractory gastroesophageal reflux disease," *Chinese Journal of Internal Medicine*, vol. 59, no. 11, pp. 880–886, 2020.

[2] B. Marta, A. Sanchez Angel, S. R. Garcia, D.-R. Manuel, and E. Rey, "Weight gain and somatization are associated with the onset of gastroesophageal reflux diseases: results of two 5-year follow-up studies," *Journal of Clinical Gastroenterology*, vol. 50, no. 3, 2016.

[3] S. Ilia and S. Daniel, "Editorial: inconclusive diagnosis of GERD-are new parameters in impedance-pH-metry ready for clinical use?" *Alimentary Pharmacology and Therapeutics*, vol. 54, no. 4, 2021.

[4] S. Ma, M. Deng, Y. Liu et al., "Application and clinical value of gastric filling ultrasound in gastric diseases," *Cancer Prevention and Treatment*, vol. 33, no. 11, pp. 881–886, 2020.

[5] H. Suzuki, M. Juntaro, S. Okada, K. Hirata, S. Fukuhara, and H. Toshifumi, "Validation of the GerdQ questionnaire for the management of gastro-oesophageal reflux disease in Japan," *United European gastroenterology journal*, vol. 1, no. 3, 2013.

[6] Z.-G. Miguel Angel, A. A. Azamar-Jacome, A. Meixueiro-Daza et al., "Validation and diagnostic usefulness of gastroesophageal reflux disease questionnaire in a primary care level in Mexico," *Journal of neurogastroenterology and motility*, vol. 20, no. 4, 2014.

[7] Chinese Medical Care International Exchange Promotion Association Gastroesophageal Reflux Multidisciplinary Branch, "Consensus on multidisciplinary diagnosis and treatment of gastroesophageal reflux disease in China," *Frontier Journal of Chinese Medicine (Electronic Edition)*, vol. 11, no. 9, pp. 30–56, 2019.

[8] L. Ju, J. Miao, L. Zi, Q. Jingtian, and Y. Hongxia, "Correlation study between spleen and stomach weakness score and GerdQ in patients with gastroesophageal reflux disease," *Chinese Journal of Integrated Traditional Chinese and Western Medicine on Digestion*, vol. 27, no. 6, pp. 411–414, 2019.

[9] H. Q. Hu, H. K. Li, and Y. Xiong, "Peroral endoscopic cardial constriction in gastroesophageal reflux disease," *Medicine*, vol. 97, no. 15, p. 169, 2018.

[10] A. Argyrou, E. Legaki, C. Koutserimpas et al., "Risk factors for gastroesophageal reflux disease and analysis of genetic contributors," *World Journal of Clinical Cases*, vol. 6, no. 8, pp. 176–182, 2018.

[11] Y. Cui, L. Jiang, and P. Bu, "Comparison of clinical features between reflux esophagitis and non-erosive gastroesophageal reflux disease," *Chinese Physician Journal*, vol. 20, no. 8, pp. 1151–1154, 2018.

[12] R. Wang, J. Wang, and S. Hu, "Application of gastroesophageal reflux disease questionnaire in the diagnosis of reflux esophagitis," *Chinese Medical Records*, vol. 19, no. 7, pp. 103–105, 2018.

[13] T. Huang, Y. Li, Q. Huang, and Y. Jing, "Analysis of the clinical characteristics of refractory gastroesophageal reflux disease in the elderly," *Medical Journal of Chinese People's Liberation Army*, vol. 43, no. 6, pp. 514–517, 2018.

[14] R. Mentore and S. Edoardo, "Exploring the association between esophageal mucosal inflammation, impaired motility, and GERD severity," *Neurogastroenterology and motility: The Official Journal of the European Gastrointestinal Motility Society*, vol. 33, 2021.

[15] R. Shao, L. Yang, S. Ge et al., "The clinical diagnostic value of gastric contrast-enhanced ultrasound in the anatomical etiology of gastroesophageal reflux," *Journal of Bengbu Medical College*, vol. 44, no. 1, pp. 101–103, 2019.

[16] B. Zhao, H. Jiang, L. Wang, and W. Hong, "Clinical study on esophageal motility and reflux characteristics of patients with

Hindawi
Journal of Healthcare Engineering
Volume 2023, Article ID 9891612, 1 page
https://doi.org/10.1155/2023/9891612

Retraction

Retracted: Analysis of the Diagnostic Effect of EUS-RTE on Giant Cystic Tumours of the Oesophagus Based on Cluster Analysis

Journal of Healthcare Engineering

Received 5 December 2023; Accepted 5 December 2023; Published 6 December 2023

Copyright © 2023 Journal of Healthcare Engineering. This is an open access article distributed under the Creative Commons Attribution License, which permits unrestricted use, distribution, and reproduction in any medium, provided the original work is properly cited.

This article has been retracted by Hindawi, as publisher, following an investigation undertaken by the publisher [1]. This investigation has uncovered evidence of systematic manipulation of the publication and peer-review process. We cannot, therefore, vouch for the reliability or integrity of this article.

Please note that this notice is intended solely to alert readers that the peer-review process of this article has been compromised.

Wiley and Hindawi regret that the usual quality checks did not identify these issues before publication and have since put additional measures in place to safeguard research integrity.

We wish to credit our Research Integrity and Research Publishing teams and anonymous and named external researchers and research integrity experts for contributing to this investigation.

The corresponding author, as the representative of all authors, has been given the opportunity to register their agreement or disagreement to this retraction. We have kept a record of any response received.

References

[1] H. Yang, Z. Zhang, Y. He et al., "Analysis of the Diagnostic Effect of EUS-RTE on Giant Cystic Tumours of the Oesophagus Based on Cluster Analysis," *Journal of Healthcare Engineering*, vol. 2021, Article ID 1395826, 11 pages, 2021.

Hindawi
Journal of Healthcare Engineering
Volume 2021, Article ID 1395826, 11 pages
https://doi.org/10.1155/2021/1395826

Research Article

Analysis of the Diagnostic Effect of EUS-RTE on Giant Cystic Tumours of the Oesophagus Based on Cluster Analysis

Huizhen Yang [1,2], Zhenghang Zhang [1,2], Yingbi He [1,2], Bin Tian [1,2], Xiaozhen Zhang [1,2], Yingying Hao [1,2], Shuang Lu [1,2] and Yanhua Tian [1,2]

[1]*Department of Endoscopy, The Second People's Hospital of Jiaozuo City, Jiaozuo, Henan 454003, China*
[2]*The First Affiliated Hospital of Henan Polytechnic University, Jiaozuo, Henan 454003, China*

Correspondence should be addressed to Huizhen Yang; yanghuizhen@hpu.edu.cn

Received 17 August 2021; Revised 14 September 2021; Accepted 15 September 2021; Published 3 November 2021

Academic Editor: Gu Xiaoqing

Copyright © 2021 Huizhen Yang et al. This is an open access article distributed under the Creative Commons Attribution License, which permits unrestricted use, distribution, and reproduction in any medium, provided the original work is properly cited.

This paper presents an in-depth analysis and study of the diagnostic effectiveness of EUS-RTE in giant cystic tumours of the oesophagus utilizing cluster analysis. A new form of interval data expression was designed based on the cluster analysis algorithm, as well as a new way of updating the cluster radius and cluster centre. Feature triads are defined, eliminating the need to access all historical data at the time of update. It also prevents the case of overfusion of clusters and outputting only one cluster. If there exist a very low number of clusters, the newly merged clusters are reclustered according to the density clustering method for the internal data objects based on the cluster segmentation so that the data objects in the same cluster have a high similarity as possible. All accumulated electronic files of oesophageal cancer cases were collected and comprehensively organized, and all clinical data of 129 eligible cases with a total of 356 consultations were screened in strict accordance with inclusion and exclusion criteria. A database of oesophageal cancer cases was established using Visual FoxPro software, and frequency distribution, cluster analysis, association rule, and chi-square test were used to focus on mining the association between symptoms, disease mechanisms, prescriptions, and medications. The results were analysed and summarized. Overall, the therapeutic efficacy and safety of the three groups of treatment modalities for gastric mesenchymal tumours were positive, and the preoperative endoscopic treatment modalities should be selected based on the EUS-RTE characteristics of the tumour, the site, and the operator's skill level in a comprehensive manner.

RETRACTED

1. Introduction

Oesophageal cancer occurs in all five continents of the world. The wide distribution and concentration of oesophageal cancer are its characteristics. Oesophageal cancer is often widely distributed in a region and concentrated to form a high incidence area, and there are also low incidence areas in the high incidence area, showing the relationship between geography and the occurrence of oesophageal cancer. The incidence level of oesophageal cancer varies widely among different regions and populations, with rural areas having a higher incidence than urban areas [1]. The aetiology of oesophageal cancer is still unclear, and with the development of epidemiology, it is found that the incidence of oesophageal cancer involves multiple factors, each of which can play different roles due to differences in their exposure opportunities and dose intake caused by differences in geography, customs, and lifestyle behavioural habits, and the main prevalence factors may vary from region to region [2]. Adverse psychological factors such as the history of mental stimulation, frequent depression, and long-term mental depression have a close relationship with the occurrence of oesophageal cancer. Experiments show that adverse psychological factors can cause a series of adverse physiological changes through the combined effects of intermediary mechanisms such as the vegetative nervous system, endocrine system, neurotransmitters, and immune system, which can disrupt the "self-stability" of the immune system and cause disorders of the immune system, thus triggering the occurrence of cancer. Therefore, the significance of some factors should be further explored through cross-regional comparison or long-term monitoring and observation; the development of prevention and treatment measures for oesophageal cancer should also be based on local conditions [3]. The development of oesophageal cancer prevention and control measures should also be tailored to local conditions.

Data mining techniques not only help people to obtain and deeply apply the surface information of data from data warehouses but also obtain the implicit information of data and help people to determine the trend of future data changes. Clustering analysis is one of the main data mining techniques, which usually groups data objects according to some similarity measure and under certain criteria. There is always the problem of K-value selection and initial clustering centroid selection, and these problems can also affect the effect of clustering. In order to avoid these problems, we can choose another more practical clustering algorithm, the hierarchical clustering algorithm. After clustering, the data can be divided into sets with special meanings, and then the data can be analysed to get the implied information. Tumour treatment has entered a period of multidisciplinary, multipathway, and multimethod integrated treatment, which still cannot be cured. The recurrence rate of oesophageal cancer after surgery is high, and even for early lesions, the overall survival rate in the postoperative years is still very low; some patients have serious destruction of organ function and immunity during radiotherapy and chemotherapy, and the toxic side effects are strong and intolerable [4]. A more adapted comprehensive treatment is being explored, and TCM treatment is indispensable. TCM focuses on holistic concepts, and treatment is centred on humans rather than the tumour. The immune function of the body is regulated by mobilizing the patient's potential to participate in the regulation of the tumour or timely correction of too much or too little in the regulation and timely elimination of residual tumour cells. Reversing precancerous lesions will prolong or stop recurrence, improve the quality of life, and achieve the goal of survival with tumors.

At present, most clustering algorithms are oriented to static offline data with definite data size and scale. These algorithms firstly store all the data to be processed in memory and obtain the approximate optimal clustering results through multiple iterations. However, increasingly uncertain data are being generated from various industries, making uncertain data gradually become an important object for data mining, and it is an important issue to better obtain and apply valuable information from uncertain data for judgment and prediction. Uncertain data is different from general data from the beginning of generation, so it is necessary to extend the existing clustering algorithms for deterministic data to generate clustering algorithms that are truly applicable to uncertain data. The size of data is growing exponentially with the increasing volume of data, and what kind of representation and efficient storage should be used is a very important issue; secondly, the data objects are no longer single-dimensional but multidimensional. It considers the requirements of the characteristics of multidimensional data on mathematical models and related calculation methods.

2. Related Work

The clustering analysis technique is an integral part of the machine learning field and belongs to the unsupervised learning model [5]. In the era of big data, it is not practical to rely only on manual mining of the value behind the massive amount of information, and clustering is an effective data processing method that can help people discover some correlations within the data and even make predictions about future trends based on the existing data. In recent years, clustering analysis has played a key role in many fields [6]. Taking regional economic development as an example, by extracting representative economic indicators to cluster analysis of regional economic development, we can have clearer understanding of the status of economic development in different regions, to facilitate the formulation of measures to further promote good and rapid economic development. At the same time, cluster analysis is also applied in medical, chemical, computer vision, pattern recognition, and other fields, and its advantages cannot be ignored [7]. Lu et al. combined the minimum spanning tree principle with k-means to find a reasonable initial centre of clustering [8]. Malheiros combined a region-limited strategy with a k-means algorithm to achieve adaptive selection [9].

In rare patients with liquefied tissue within the tumour, ultrasound may suggest the presence of fluidic dark areas or cystic echogenicity. Currently, the main ancillary test for preoperative diagnosis of GIST patients is endoscopy [10]. The endoscopic appearance of the gastric mucosa is mainly oval hemispherical or bulbous, with a wide base in most cases and a smooth mucosal bulge with clear demarcation from the surrounding area. However, the endoscopic presentation of GIST is not very specific; therefore, it is difficult to distinguish GIST from other tumours by the microscopic features alone, and there are limitations of endoscopy for exophytic GIST because the lesions are often located in the submucosa, so it is difficult to obtain biopsies [11]. Ultrasound endoscopy can better compensate for the shortcomings of ordinary endoscopy, with the advantage of being able to distinguish between various layers of the gastric wall, as well as determine the origin of the mass lesion, that is, the specific layer and specific tissue structure of the gastric wall from which it originates and detect exophytic GIST, which is difficult to detect by ordinary endoscopy. In addition, ultrasound endoscopy can also determine the cystic solidity of the tumour by its echogenicity [12]. In addition, ultrasound endoscopy can also determine the cystic solidity of the tumour by its echogenicity, thus further differentiating it from some other gastric tumours [13]. However, the application of RECIST morphological criteria based only on the change of tumour size does not accurately reflect the effect of tumour treatment, and there are limitations in using it to evaluate the targeted treatment of gastrointestinal mesenchymal tumours [14]. The Choi criterion combines

RETRACTED

two indicators, tumour length and CT value change, and has been proved to have high application value in evaluating the efficacy of tumour treatment. However, tumour changes on imaging are often overestimated and sometimes do not coincide with pathological changes, so assessment of efficacy by imaging is controversial.

To retain the real-time online processing feature of the ECM algorithm, this paper designs a new way of updating cluster centres and cluster radii based on the ECM algorithm and MU-ECM algorithm and proposes an evolutionary clustering algorithm with adaptive interval width: MU-SAECM algorithm. To satisfy the property of scanning once, a feature triad is defined for each cluster, which makes the algorithm perform the radius and centroid update calculation only for the updated cluster radius and cluster centre once, satisfying the processing of each data based on reduced computation. New determination rules are added to the categorization to prevent changes occurring due to clustering from affecting the dissimilarity between classes. At the same time, to avoid the excessive fusion of clusters that can lead to a low number of clusters, the idea of density-based partial clustering is introduced to improve the accuracy by partitioning the relatively large clusters internally into several different clusters.

2.1. Cluster Analysis of EUS-RTE in Giant Cystic Tumours of the Oesophagus Designed for Diagnostic Effectiveness

2.1.1. Analysis of EUS-RTE Algorithm for Cluster Analysis. Collaborative filtering technology is widely used in recommendation systems due to its advantages of simple operation and high recommendation efficiency, and it has become one of the most popular recommendation techniques in the field of personalized recommendation. The cold start problem mainly includes user cold start and item cold start. The user cold start is based on new users, and new users are a major challenge in the recommendation field. The situation is similar for new items in the system, which do not receive any feedback from users at the initial stage, so they are almost impossible to be recommended and in most cases are ignored [15]. The traditional collaborative filtering algorithm calculates similarity based on rating data to form the final recommendation, and the richer the data, the higher the accuracy of the recommendation, which directly affects user satisfaction. The number of items in the system is increasing, but the number of items faced by a single user is limited, and a few users can make valid ratings for items, so the ratings in the system mostly exist as null values which has a great impact on the accuracy of recommendations.

Collaborative filtering technology is based on a large amount of data information to provide users with reliable recommendations. With the rapid development of network technology, the number of users and products is increasing, and the corresponding amount of rating data is also increasing. The computation of various data needed to generate recommendations based on all data information in the whole recommendation system is large and time-consuming, which makes the recommendation efficiency low, the recommendation real-time poor, and the accuracy of the recommended results limited [16]. The division-based clustering first needs to specify the number of clusters k. Assuming that the sample contains n data objects, $k< n$ needs to be satisfied, and then k initial centroids are selected from the data samples and iterated until the initial threshold is satisfied or the maximum number of iterations is reached so that the distance between data samples within the class is small and the similarity is high, and the distance between data between classes is large and the similarity is low. The most widely cited method is the k-means algorithm, which divides the data set into k disjoint clusters according to the specified k-values, with a small distance between data in the same cluster and high data similarity and a large distance between data in different clusters and low data similarity.

$$E = \frac{\sum_{i=1}^{k} \sum_{x \in c_i} \|x\|^2}{\sum_{i=1}^{k} \sum_{x \in c_i} \|\mu_i\|^2}. \quad (1)$$

The distance measure between data is the core step of the clustering algorithm, which is necessary for clustering the data. When clustering, data with small distances are classified into the same class of clusters, and data with large distances are classified into different classes of clusters. The traditional user-based collaborative filtering technique mainly calculates the similarity between users based on their past behavioural data and then selects the nearest users for rating prediction and recommendation generation based on the similarity size. However, new users do not generate behavioural data that can be used for recommendations, and recommendations are hampered; at the same time, as user data and project data continue to grow, the scalability problem poses a growing challenge. At the same time, the soft clustering algorithm replaces the hard clustering algorithm, and the affiliation degree replaces the hard division of either/or, which is closer to real life. Secondly, based on the user's attribute data, we combine the improved clustering algorithm to cluster the users, so that new users can also be classified into the corresponding class clusters based on the attribute data information at the time of registration. Finally, the weighted similarity calculation of the similarity of user attributes is carried out in the clusters to which the user belongs, to improve the accuracy of user similarity calculation. At the same time, for new users with missing behavioural data, the nearest-neighbour selection and rating prediction can also be carried out based on the similarity of user attributes, to form recommendations and alleviate the drawbacks brought about by user cold start. At the same time, the selection of nearest-neighbour users in the cluster to which they belong reduces the scope of user search, reduces the amount of computation, and alleviates the disadvantages of recommendation scalability problems, as shown in Figure 1.

The digitized user attribute values are further normalized, and the normalization calculation is shown in

$$x^* = \frac{x - x_{\min}}{x_{\max} + x_{\min}}. \quad (2)$$

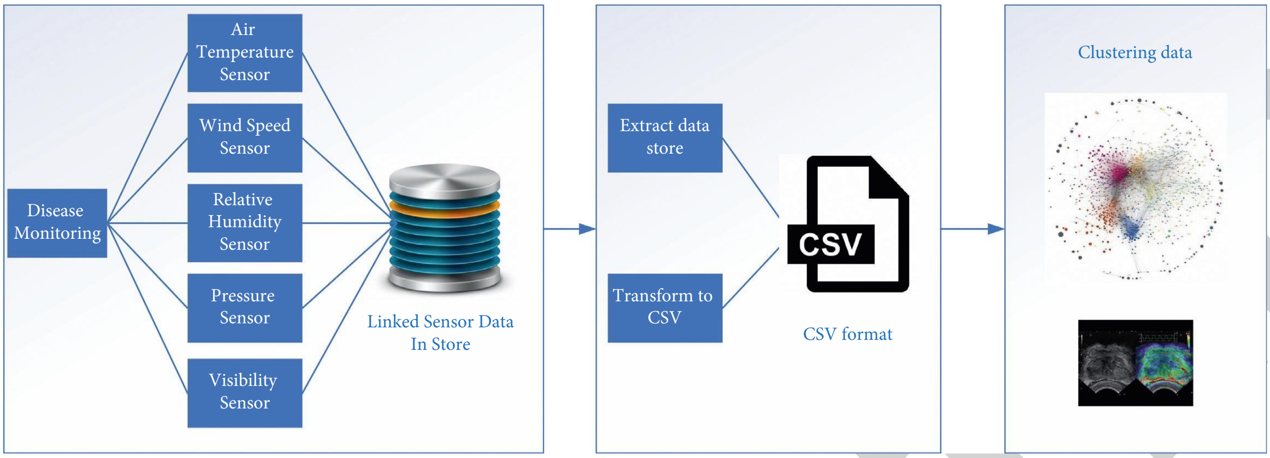

Figure 1: Framework of EUS-RTE algorithm for clustering analysis.

Based on the normalized user attribute data for the calculation of user attribute similarity, the Euclidean distance is first selected for the initial calculation, which is shown in

$$\text{distance} = \sqrt{\sum_{i=1}^{n} (x - \mu_i)^2}. \quad (3)$$

Based on the obtained Euclidean distance between users, the user attribute similarity is further calculated as shown in

$$\text{sim}_d(u, v) = \frac{1}{1 - \text{distance}(u, v)}, \quad (4)$$

$$\text{sim}_d(u, v) = \frac{\sum (p + \overline{p})}{\sqrt{(p + \overline{p})}}. \quad (5)$$

ECM algorithm is a real-time online scanning algorithm for data streams, which can also be understood as a clustering algorithm for online data. The algorithm presets a real number threshold of cluster radius Dr, and based on the property that the distribution of data in the data stream changes over time, the ECM algorithm makes a clustering of the new data every time it enters the system. The ECM algorithm always controls the upper limit of the cluster radius utilizing a parameter threshold; that is, the cluster radius of a cluster stops growing when it increases to the value of Dr. Thus, the threshold value Dr controls the size of each clustering cluster by controlling the radius size and the size of each cluster, which affects the number of clusters and the clustering performance.

$$d(x, y) = \sqrt{\frac{\sum_{i=1}^{n} (x - y_i)^2}{q}}. \quad (6)$$

In the clustering process, the data for the ECM algorithm originates from a continuous stream of online data. The ECM algorithm starts from an empty set and determines whether the data in the new data stream belongs to a currently existing cluster: if the new data belongs to an existing cluster, the cluster centre and the cluster radius of that cluster are updated; if the new data does not belong to any of the existing clusters, a new cluster is created. When a new cluster is created, the new data is used as the initial cluster centre of the new cluster, and the cluster radius R of the new cluster is initialized. The ECM algorithm dynamically increases the number of clusters, adjusts the cluster centres and the cluster radius in real-time regarding parameter thresholds, and may increase the cluster radius with each clustering, but when the cluster radius reaches the threshold, the cluster radius of the cluster is not updated. In modern technology, data streams have uncertainty in some aspects due to physical measurement limitations, interference from the surrounding environment, and other factors, such as frequent sexual instability or anomalies in some data streams [17]. The uncertainties contained in data streams can be divided into two categories: uncertainty of existence and uncertainty of attribute values. Therefore, the above two types of uncertainty based on uncertain data can usually be represented by statistics such as interval number or probability density function, and in this paper, multidimensional uncertain data streams are represented by interval numbers.

The ECM algorithm clusters deterministic data streams, and for achieving evolutionary clustering of multidimensional uncertain data, the ECM algorithm is not applicable. The MU-ECM algorithm uses the Euclidean distance between the data object and the centre of the clusters as the basis for determining the similarity between the data object and the clusters, and the smaller the distance, the greater the similarity. The smaller the distance value, the greater the similarity. The relationship between the distance value and the cluster radius is used as an important factor to determine whether the cluster radius is updated or not and whether the cluster centre is rediscovered or not, to obtain more accurate clustering results.

Also, clustering clusters may intersect with each other after formation because each cluster usually has an increasing cluster radius throughout the clustering process of the MU-ECM algorithm; that is, it is getting closer to the edges of other clusters in each dimension. As clustering continues, the increasing cluster radius also leads to larger intersection regions between neighbouring clusters. For

RETRACTED

example, triangles and circles represent samples in two different clusters, and their distributions are shown in Figure 2.

Although triangular objects and circular objects belong to two different clusters, there is an intersection of their edge points, and the objects within the intersection of the clusters are within the radius of both clusters. The intersection region is the similar region of two clusters and tends to expand continuously, which will make the number of data objects falling in the intersection region increasingly similar. Since different clusters have different sizes and different density fractions of objects within the clusters, the location distribution is also different, and it is not accurate to measure the similarity of two clusters by the distance between the centres of the two clusters or the distance of the closest samples. Therefore, the number of data objects in the cluster within the intersection range as a percentage of the total number of data objects in the cluster is used to characterize the degree of fusion to other clusters. The magnitude of the fusion degree indicates the degree of similarity between the most adjacent clusters of the cluster and can determine whether to fuse the two clusters. The clusters with high similarity can be selected for fusion, which ultimately ensures the accuracy of the final clustering results. Suppose that, for any cluster Ci, its fusion degree to any other cluster is calculated in the form shown in

$$\text{fus}(i, j) = \frac{h_{ij}}{h_i^2}. \tag{7}$$

If the value of the shortest distance is less than the cluster radius value of the corresponding cluster, it is directly categorized; if the value of the shortest distance is greater than the cluster radius value of the corresponding cluster but close to some clusters, the corresponding cluster with the smallest difference between the distance value and the radius can be searched for to categorize. The data object is defined as the cluster centre of this cluster to create new clusters. Then, after getting multiple clusters, considering the possible intersection between clusters, the fusion degree between clusters is calculated and the degree of each fusion degree value is used to determine whether they should be fused into one cluster.

2.1.2. Diagnostic Effect Experiment in Giant Cystic Tumour of the Oesophagus. All data were statistically analysed using SPSS 22.0 software. The correlates affecting recurrence metastasis and/or survival of GIST patients after preoperative imatinib adjuvant therapy were analysed using COX univariate and multifactorial analysis. The optimal threshold of pathological responsiveness after adjuvant therapy was investigated using ROC curves by maximizing the sum of sensitivity and specificity, minimizing the total error, and minimizing the distance between the cut-off value and the upper left corner of the ROC curve. The correlation between pathological responsiveness and each clinicopathological factor was analysed comparatively using the chi-square test. The Kaplan–Meier survival curve and log-rank method were used to analyse the relationship between tumour pathological responsiveness and recurrence-free survival and overall survival after adjuvant therapy [18]. The ROC curve actually represents a stochastic classifier. The faster the TPR grows and the larger the slope is, the better the classification performance of the model is reflected. The closer the ROC curve to the upper left corner, the higher the sensitivity and the lower the false positive rate. The point on the ROC curve closest to the upper left corner has the largest sum of sensitivity and specificity, and this point or its neighbouring points are often referred to as the diagnostic reference value. The recurrence-free survival time was calculated from the date of completion of surgery to the recurrence of surgical resection site or distant metastasis at other sites. Overall survival time was determined by counting the date of patient death from the date of completion of surgery. All statistical tests were two-sided in this paper, and a p value < 0.05 indicated a statistical difference.

Clinical symptoms of GIST patients may include gastrointestinal bleeding, obstruction, abdominal pain, and abdominal masses. GIST located in the oesophagus often shows symptoms of dysphagia, and malignant GIST may be accompanied by weight loss, liver metastases, abdominal implants, and so on. Some patients may come to the hospital for intestinal perforation [19]. The clinical symptoms of GIST patients are highly variable and lack their clinical specificity, and the symptoms are related to many factors, such as the location of the tumour, the size of the tumour, the malignancy of the tumour, and whether the tumour is ruptured or perforated. In the early stage of GIST, there may be no symptoms, and the symptoms appear relatively late, so it is not easy to attract the attention of the patients themselves. GIST tumours vary in size, and their clinical manifestations are variable and related to tumour size and location. Small tumours often have no clinical manifestations and are mostly detected during physical examination or laparotomy. The most common clinical symptom is gastrointestinal bleeding, which is caused by ulceration of the mucosal surface of the tumour, and patients present with vomiting blood, black stools, and anemia due to occult blood loss. Other symptoms include abdominal pain, abdominal masses, and debility. This may be accompanied by loss of appetite, fever, and weight loss. Frequent and scanty urination is seen in individual patients with rectal GIST. Individual cases with spontaneous rupture of the tumour and diffuse peritonitis as the first presentation have been reported. When the tumour diameter is relatively small, the first symptom is upper gastrointestinal bleeding, because the tumour diameter is small, but the mucosal surface often has ulcer formation, so there will be cystic necrosis, bleeding, and other manifestations, resulting in clinical symptoms of gastrointestinal bleeding. When the GIST tumour gradually increases and compresses the stomach and intestinal cavity, the symptoms of upper abdominal discomfort may appear, and when the tumour causes ulcers to form on the mucosal surface, the symptoms of peptic ulcer may appear. When GIST tumour ruptures, acute upper gastrointestinal bleeding symptoms may occur. When GIST has a long course, it may lead to weight loss, anemia, and other wasting symptoms, as shown in Figure 3.

RETRACTED

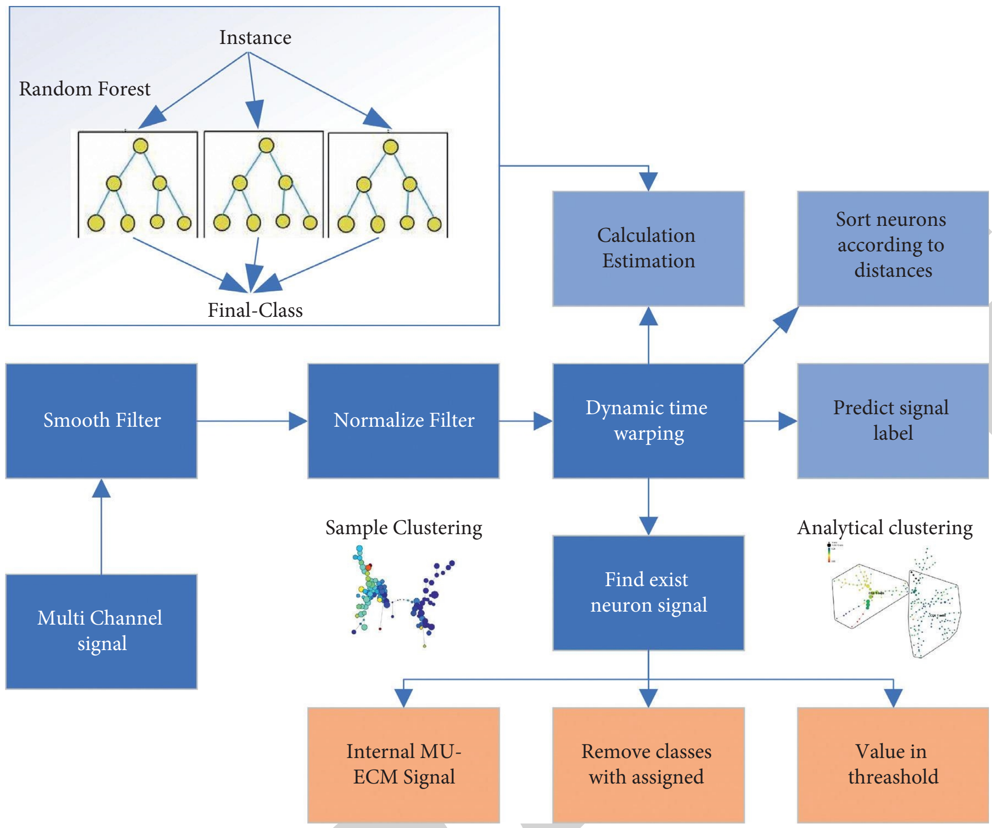

Figure 2: Two clusters with a certain similarity.

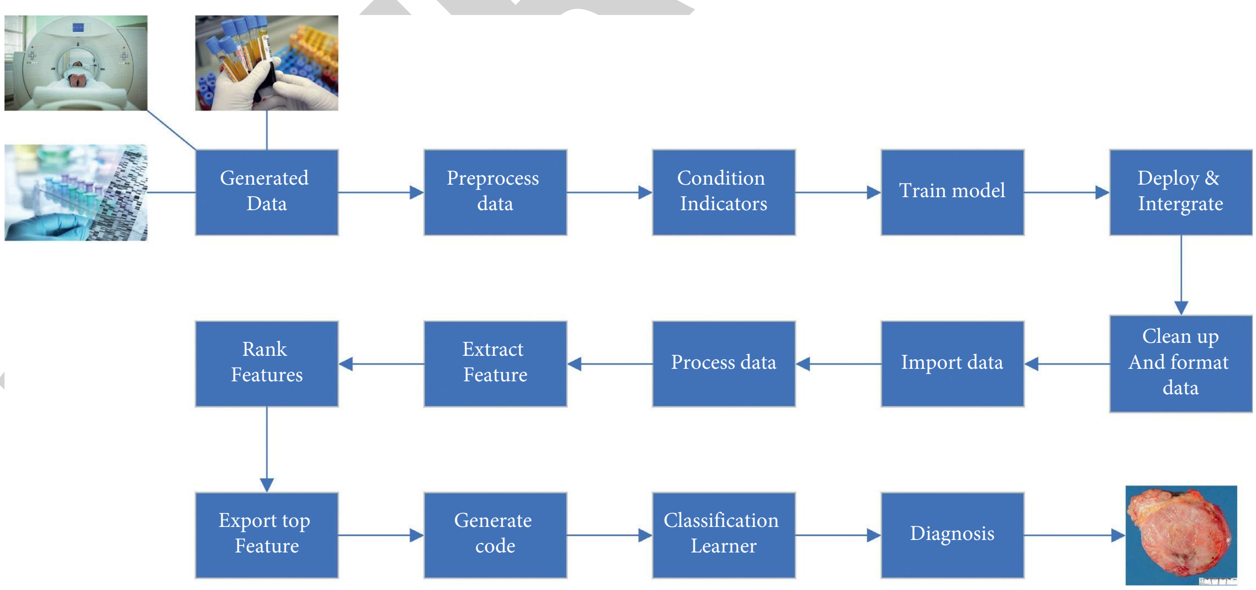

Figure 3: Diagnostic features.

Ultrasound endoscopy can better compensate for the shortcomings of general endoscopy and has the advantage of distinguishing the various layers of the gastric wall and the origin of the mass, that is, the specific layers and tissues of the gastric wall, as well as detecting exophytic GISTs that are difficult to detect by general endoscopy. GIST can be differentiated from other gastric tumours by ultrasound endoscopy, and if the tumour grows towards the lumen or mixed growth inside and outside the lumen, it can show displacement, separation, or even unfolding of the gastric mucosa due to compression, and at the same time, barium radiography can indicate destruction of the mucosa of the gastric wall, filling defect, disorder or even ulcer formation, and so on; however, barium radiography also has its drawbacks. However, barium radiography also has the drawback that it is difficult to diagnose GIST with extraluminal growth, and therefore the diagnostic rate is not high. This ancillary test was not used in the present study.

The tumour diameter of gastric mesenchymal tumour and small intestinal mesenchymal tumour can be compared by the chi-square test, and the tumour diameter of gastric mesenchymal tumour is smaller, while the tumour diameter of small intestinal mesenchymal tumour is larger. In contrast, small intestinal mesenchymal tumours with a small diameter or obvious clinical symptoms are often difficult to be detected. Meanwhile, when comparing the postoperative NIH risk ratings of gastric mesenchymal tumour and small intestinal mesenchymal tumour, 38 patients with gastric mesenchymal tumour were at very low risk, 31 patients at low risk, 32 patients at intermediate risk, and 19 patients at high risk, while 3 patients with small intestinal mesenchymal tumour were at very low risk, 8 patients at low risk, 4 patients at intermediate risk, and 20 patients at high risk. By comparing the risk classification results of both, it can be found that small intestinal mesenchymal tumour has a higher risk compared with gastric mesenchymal tumour, as shown in Figure 4.

Therefore, it is necessary to distinguish between the priority of evil and deficiency and to choose the priority and sequence of treatment to support and eliminate evil. This is the key to improve the efficacy of difficult diseases; from the pathogenesis, we can also see that such patients often have damp-heat or cold-heat mismatch, and the treatment should be warming and clearing [20]. Among them, there were 53 patients with very low risk, 42 patients with low risk, 42 patients with medium risk, and 65 patients with high risk. A total of 69 high-risk patients were followed up, among whom 26 patients were taking imatinib adjuvant therapy after surgery, with a dosing rate of 37.68%. In comparison with other studies with larger sample sizes, the postoperative imatinib dosing rate in patients with intermediate to high risk was 60.47%, 68.35%, 49.06%, and 52.86%, respectively. The reason for the low rate of postoperative imatinib in the high-risk patients in this study may be related to the poor economic conditions of patients in the region and their inability to afford the drug. Gastrointestinal lesions occurring in combination with small GIST were predominantly malignant, mostly carcinomas, including adenocarcinoma, and squamous cell carcinoma, with high to moderate differentiation in squamous cell carcinoma and moderate to low differentiation in adenocarcinoma, which is generally consistent with the literature [21]. One case of oesophageal carcinoma was a mixed squamous cell carcinoma and small cell carcinoma, and the other was a basal cell-like squamous cell carcinoma; in addition, other rare types were lymphoma (MALT lymphoma in this group, which was also combined with a hyperplastic polyp of the appendix in this case) and squamous epithelial atypical hyperplasia, the latter two being rarely reported combined tumours. The benign tumours were juvenile polyps and hyperplastic polyps, which were also rarely reported. The benign tumours are juvenile polyps and hyperplastic polyps which are also rarely reported. The onset of the disease is mainly concentrated in the stomach and oesophagus. Treatment is based on digestive system lesions, especially in cases with combined digestive system cancer. Tumour compression symptoms are commonly found in the intracranial, cervical, mediastinal, retroperitoneal, and intravertebral canal. For example, intracranial tumours compressing the brain parenchyma cause increased intracranial pressure, which may cause headache, nausea, vomiting, and visual disturbance. The tumour of the thyroid gland may press the laryngeal nerve and cause hoarseness. If it presses on the trachea or esophagus, it causes difficulty in breathing or swallowing.

2.2. Analysis of Results

2.2.1. Algorithm Performance Analysis. In the experimental process, to observe the influence of the different proportion of similarity of user attributes and similarity of ratings and category preferences on the experimental results, the parameter values of r and ω were adjusted continuously during the experimental process, the value of k was also adjusted continuously to select the optimal nearest neighbours, and the final experimental results were compared and analysed with the traditional correlation algorithm after parameter tuning. The experimental results are shown in Figure 5, which shows that the MAE value is the lowest when the R-value is 0.9 and the experimental results are the best.

Different items have different attribute characteristics, which will affect the size of the final user rating to a certain extent. The existing data set has high-dimensional item attributes, so we first introduce PCA technology to reduce the dimensionality of the item attribute data and do the calculation of item similarity based on the reduced dimensional attribute data. Secondly, the item similarity is fused with the WSO algorithm for prepopulation of ratings, and then the user rating similarity is further calculated. In addition to tumour size, the primary site and the number of nuclear schwannomas are also key factors in determining the prognosis of the disease. The NIH subsequently developed a standard for assessing the malignancy of gastrointestinal mesenchymal tumours by combining tumour size and the number of nuclear schwannomas and assessed the malignancy of this tumour by the risk of invasion, which is classified into four grades: very low, low, moderate, and high risk of invasion. Currently, the common grading diagnosis for gastrointestinal mesenchymal tumours is the NIH criteria. The WSO algorithm uses the number of users who jointly rates the items as the corresponding weights for the weighted rating prediction but does not consider the effect of interitem similarity on user rating differences. Taking movies as an example, most female friends like literary and family movies, while they have a low preference for war crime movies, so when these two types of movies are rated together, there is a large difference in ratings.

As can be seen from Figure 6, the average running time of the MU-SAECM algorithm in the test dataset is

RETRACTED

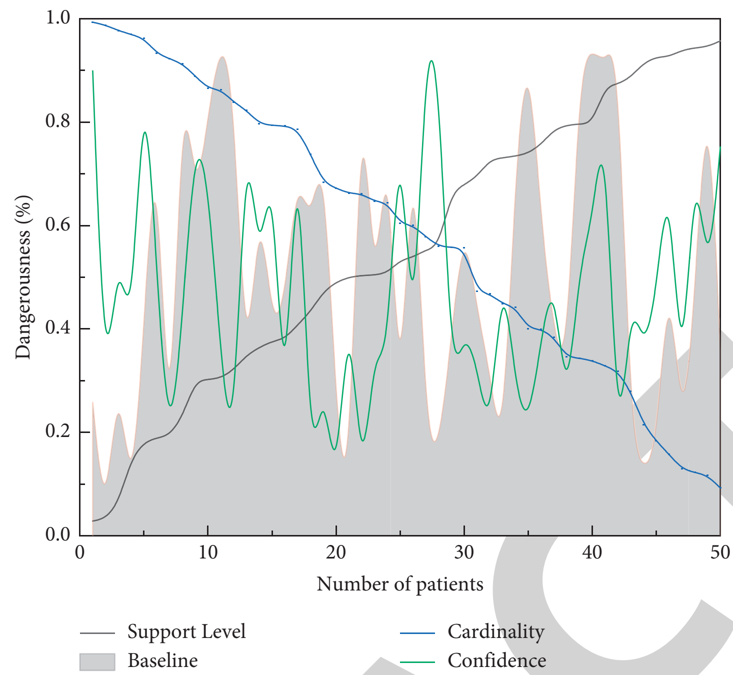

Figure 4: Relationship between symptoms.

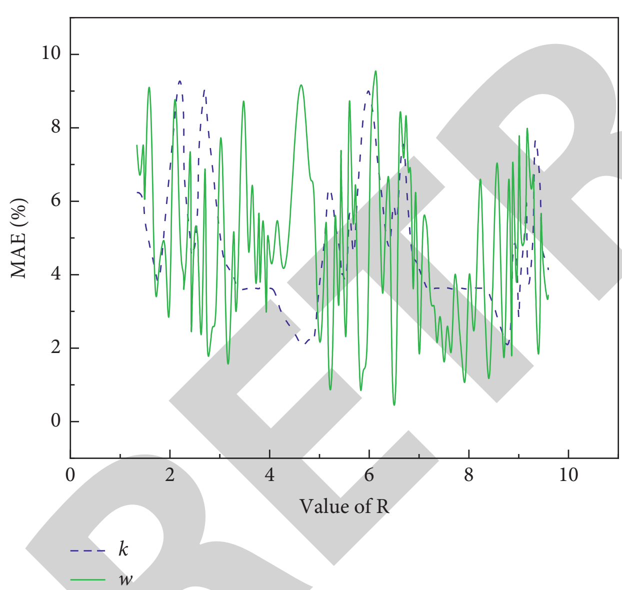

Figure 5: Effect of R-value on MAE.

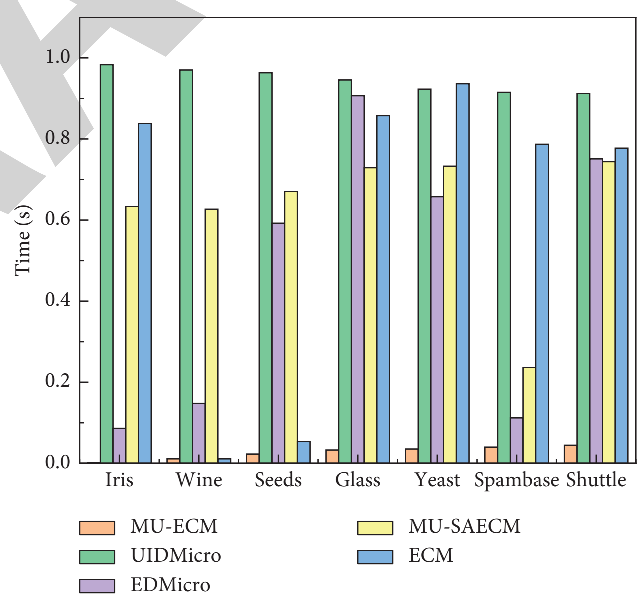

Figure 6: Running time of the five algorithms with different data sets.

RETRACTED

significantly lower than that of the other four algorithms, and the variation is relatively small. This is because in the later clustering of the data, along with the increase of the cluster radius, the distance between the data object and the cluster centre is increasingly likely to be smaller than the cluster radius, so it is increasingly likely that it can be directly classified into the clusters. The MU-SAECM algorithm also uses the number of intervals and distance calculation to represent the uncertainty of the data, which avoids the problem of large computation caused by the integral operation and improves the algorithm's efficiency. In contrast, the UIDMicro algorithm has a large impact on the number of members' threshold, which makes the clustering model update with a large delay or too frequent clustering update; the EDMicro algorithm requires more iterative steps, which requires more time overhead to update the microcluster structure in the form of MBR in each step. The MU-ECM algorithm and the ECM algorithm require multiple accesses to the historical data in one execution. The MU-ECM algorithm and the ECM algorithm require multiple accesses to historical data at one time, and the efficiency of the ECM algorithm is susceptible to the threshold value as the number of data increases. The time advantage of the MU-SAECM algorithm over the other four algorithms becomes increasingly obvious when the number of uncertain data becomes larger.

The MU-SAECM algorithm has improved the clustering efficiency by incorporating feature triples while making the clustering of interval-type data closely related to its characteristics. It is suitable for clustering analysis of data streams, and the new computational form of interval-type data combines two elements of intervals simultaneously, which can reflect the influence of uncertainties in the clustering results. The MU-SAECM algorithm is proposed to solve the clustering problem in multidimensional uncertain data streams. The representation of the interval number is improved so that the algorithm is highly adaptive to the interval width, and a new formula combining the interval number and the Euclidean distance formula is used as a new calculation method to calculate the spacing between clusters and between clusters and data elements. Also on data object categorization, the interval number and distance calculation are combined to propose a new method of similarity categorization based on Euclidean distance. In the case that intersection may be generated between multiple clusters generated by preclustering, the fusion of two clusters with greater similarity is realized at the same time to prevent the case that cluster fusion is excessive to generate only one cluster. The idea of internal partitioning of clusters using density clustering is proposed to ensure the reliability of clustering results.

2.2.2. Diagnostic Effect Results. Gastroscopy and ultrasound endoscopy are common tests for gastric mesenchymal tumours and are valuable in the diagnosis of mesenchymal tumours and in helping to assess the risk of malignancy of the lesion. Data clustering, on the other hand, analyses and divides data that would otherwise have no category reference into different groups, that is, derives class labels from these data. Cluster analysis itself is to discover information about data objects and their relationships based on the data and to group these data. The objects within each group are similar to each other, while the objects between the groups are unrelated. It is easy to understand that the higher the similarity within groups and the higher the dissimilarity between groups, the better the clustering. Gastric mesenchymal tumours appear gastroscopically as hemispherical, fusiform, or irregularly shaped submucosal masses with a smooth surface mucosa, sometimes with erosions, ulcers, and bleeding. EUS is the most used tool to identify submucosal masses in the GI tract by scanning the wall of the GI tract with a miniature high-frequency ultrasound probe mounted on top of the endoscope, which can clearly show the level and echogenicity of the wall. The first, third, and fifth layers are high echogenic bands, which correspond to the superficial mucosal layer, submucosal layer, and plasma layer, while the second and fourth layers are low echogenic bands, which correspond to the mucosal muscle layer and intrinsic muscle layer. As a basis for determining the likelihood of tumour recurrence after

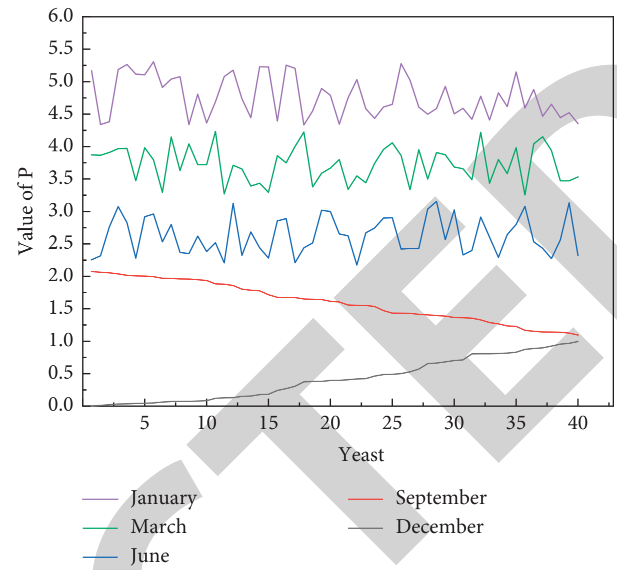

Figure 7: Functional changes at different times.

surgery and predicting treatment outcome and prognosis, positive circumferential margins, presence of vascular infiltration and perineural infiltration, poor response to neoadjuvant therapy, BRAF gene mutation, and microsatellite stability can be considered as indicators of high recurrence rate and poor prognosis, which also indicate the need for more aggressive and comprehensive adjuvant therapy after surgery. Gastric mesenchymal tumours appear endoscopically as hypoechoic homogeneous masses, which may be accompanied by punctate hyperechoic and cystic echogenicity, most of which originate from the lamina propria and a few from the submucosa. Smooth leiomyosarcoma appears as a round or oval hypoechoic endoscopic mass with clear borders, originating from layer 2 or layer 4 of the gastric wall. Ectopic pancreatic echogenic endoscopy showed hypoechoic or mixed echogenicity, sometimes with tubular structures, and could originate from layers 2–5 of the gastric wall, as shown in Figure 7.

In a large sample size study, CD117 expression was detected in 985 of 1040 GIST patients, representing an expression rate of approximately 94.7%. In addition, CD117 is barely expressed in smooth muscle tumours, smooth muscle sarcomas, nerve sheath tumours, etc., suggesting that CD117 is indeed a highly sensitive and specific marker for GIST, as shown in Figure 8.

For the evaluation of pathological response after preoperative adjuvant therapy for tumours, TRG aims to grade the pathological response of tumours after adjuvant therapy and to assess the effect of patients on preoperative adjuvant therapy and has been applied to rectal cancer, oesophageal cancer, and gastric cancer. In contrast, PCR is still more often used in clinical practice with a focus on PCR because it can ensure the prognostic safety of patient survival and is also following relevant ethical norms. In our study, the pathological response after adjuvant therapy was taken as a threshold of 40%, which can accurately distinguish the

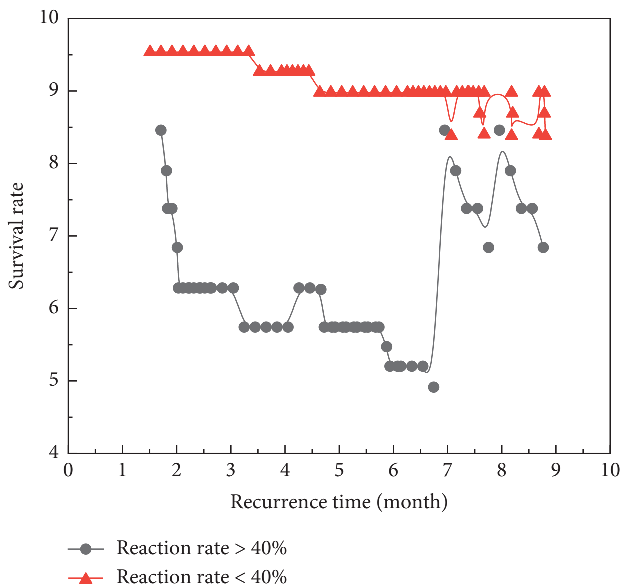

Figure 8: Comparison of patient outcomes in different groups.

prognosis of patients. We believe that the effectiveness of imatinib treatment varies among patients, that patients with a pathological response of >40% after imatinib treatment have a better prognosis, and that such patients are more effective for imatinib adjuvant therapy, which is important for guiding individualized treatment after surgery.

3. Conclusion

Firstly, an evolutionary clustering algorithm for clustering multidimensional uncertain data streams is proposed: the MU-ECM algorithm. Then, we improve the Euclidean distance calculation method in the ECM algorithm to consider the information of each dimension when dealing with multidimensional data, so that we can find the clear degree of similarity between data objects. This rule does not need to rely on predefined thresholds as in the ECM algorithm and avoids the situation that thresholds affect the final clustering results. The present study did not compare microwave ablation with other thermal ablation techniques (e.g., radiofrequency ablation), and the efficacy of microwave ablation in clinical practice can be further demonstrated in a controlled trial. Due to the limitations, the pathological evaluation in this study could also be more convincing if the material was punctured from each patient at each time point for its control.

Data Availability

The data used to support the findings of this study are available from the corresponding author upon request.

Conflicts of Interest

The authors declare that there are no conflicts of interest.

Acknowledgments

This work was supported by the Project of Henan Provincial Medical Science and Technology Tack Plan in 2020-Study on the Diagnostic Value of EUS-RTE in Giant Cystic Tumors of the Esophagus (LHGJ20200832).

References

[1] Y. Zhao, R. Wang, Y. Wang et al., “Application of endoscopic ultrasound-guided-fine needle aspiration combined with cyst fluid analysis for the diagnosis of mediastinal cystic lesions,” *Thoracic cancer*, vol. 10, no. 2, pp. 156–162, 2019.
[2] D. Navas-Carrillo, J. Manuel Rodriguez, S. Montoro-García, and E. Orenes-Piñero, “High-resolution proteomics and metabolomics in thyroid cancer: deciphering novel biomarkers,” *Critical Reviews in Clinical Laboratory Sciences*, vol. 54, no. 7-8, pp. 446–457, 2017.
[3] Y. Qi, J. Ding, L. Li et al., “Application of endoscopic ultrasound image analysis in the treatment of digestive tract diseases and nursing,” *Journal of Medical Imaging and Health Informatics*, vol. 10, no. 9, pp. 2211–2216, 2020.
[4] A. Abdelkader, B. Hunt, C. P. Hartley, N. C. Panarelli, and T. Giorgadze, “Cystic lesions of the pancreas: differential diagnosis and cytologic-histologic correlation,” *Archives of Pathology & Laboratory Medicine*, vol. 144, no. 1, pp. 47–61, 2020.
[5] D. Xu, W. Dang, S. Wang, B. Hu, L. Yin, and B. Guan, “An optimal prognostic model based on gene expression for clear cell renal cell carcinoma,” *Oncology letters*, vol. 20, no. 3, pp. 2420–2434, 2020.
[6] M. Noë, N Niknafs, C. G Fischer et al., “Genomic characterization of malignant progression in neoplastic pancreatic cysts,” *Nature Communications*, vol. 11, no. 1, p. 4085, 2020.
[7] F. Andreiuolo, P. Varlet, A. Tauziède-Espariat et al., “Childhood supratentorial ependymomas with YAP1-MAMLD1 fusion: an entity with characteristic clinical, radiological, cytogenetic and histopathological features,” *Brain Pathology*, vol. 29, no. 2, pp. 205–216, 2019.
[8] J. Lu, Y. Ding, Y. Chen et al., “Whole-exome sequencing of alpha-fetoprotein producing gastric carcinoma reveals genomic profile and therapeutic targets,” *Nature Communications*, vol. 12, no. 1, pp. 3946–3964, 2021.
[9] D. C. Malheiros, S. Canberk, D. N. Poller, and F. Schmitt, “Thyroid FNAC: causes of false-positive results,” *Cytopathology*, vol. 29, no. 5, pp. 407–417, 2018.
[10] M. P. Kumarasinghe, M. J. Bourke, I. Brown et al., “Pathological assessment of endoscopic resections of the gastrointestinal tract: a comprehensive clinicopathologic review,” *Modern Pathology*, vol. 33, no. 6, pp. 986–1006, 2020.
[11] M. H. Lee, M. G. Lubner, J. K. Peebles et al., “Clinical, imaging, and pathologic features of conditions with combined esophageal and cutaneous manifestations,” *RadioGraphics*, vol. 39, no. 5, pp. 1411–1434, 2019.
[12] R. Liu, C. Chen, X. Huang, Q. Zhu, and Y. Xia, “Ultrasonography of extrathyroidal diseases mimicking intrinsic thyroid lesions,” *Ultrasound Quarterly*, vol. 35, no. 3, pp. 301–307, 2019.
[13] D. Ai, J. Yao, F. Yang et al., “TRPS1: a highly sensitive and specific marker for breast carcinoma, especially for triple-negative breast cancer,” *Modern Pathology*, vol. 34, no. 4, pp. 710–719, 2021.

RETRACTED

Hindawi
Journal of Healthcare Engineering
Volume 2023, Article ID 9851032, 1 page
https://doi.org/10.1155/2023/9851032

Retraction

Retracted: The Promise for Reducing Healthcare Cost with Predictive Model: An Analysis with Quantized Evaluation Metric on Readmission

Journal of Healthcare Engineering

Received 27 June 2023; Accepted 27 June 2023; Published 28 June 2023

Copyright © 2023 Journal of Healthcare Engineering. This is an open access article distributed under the Creative Commons Attribution License, which permits unrestricted use, distribution, and reproduction in any medium, provided the original work is properly cited.

This article has been retracted by Hindawi following an investigation undertaken by the publisher [1]. This investigation has uncovered evidence of one or more of the following indicators of systematic manipulation of the publication process:

(1) Discrepancies in scope
(2) Discrepancies in the description of the research reported
(3) Discrepancies between the availability of data and the research described
(4) Inappropriate citations
(5) Incoherent, meaningless and/or irrelevant content included in the article
(6) Peer-review manipulation

The presence of these indicators undermines our confidence in the integrity of the article's content and we cannot, therefore, vouch for its reliability. Please note that this notice is intended solely to alert readers that the content of this article is unreliable. We have not investigated whether authors were aware of or involved in the systematic manipulation of the publication process.

In addition, our investigation has also shown that one or more of the following human-subject reporting requirements has not been met in this article: ethical approval by an Institutional Review Board (IRB) committee or equivalent, patient/participant consent to participate, and/or agreement to publish patient/participant details (where relevant).

Wiley and Hindawi regrets that the usual quality checks did not identify these issues before publication and have since put additional measures in place to safeguard research integrity.

We wish to credit our own Research Integrity and Research Publishing teams and anonymous and named external researchers and research integrity experts for contributing to this investigation.

The corresponding author, as the representative of all authors, has been given the opportunity to register their agreement or disagreement to this retraction. We have kept a record of any response received.

References

[1] K. Teo, C. W. Yong, F. Muhamad et al., "The Promise for Reducing Healthcare Cost with Predictive Model: An Analysis with Quantized Evaluation Metric on Readmission," *Journal of Healthcare Engineering*, vol. 2021, Article ID 9208138, 10 pages, 2021.

Hindawi
Journal of Healthcare Engineering
Volume 2021, Article ID 9208138, 10 pages
https://doi.org/10.1155/2021/9208138

Research Article

The Promise for Reducing Healthcare Cost with Predictive Model: An Analysis with Quantized Evaluation Metric on Readmission

Kareen Teo,[1] **Ching Wai Yong**,[1] **Farina Muhamad**,[1] **Hamidreza Mohafez**,[1] **Khairunnisa Hasikin**,[1] **Kaijian Xia**,[2] **Pengjiang Qian**,[3] **Samiappan Dhanalakshmi**,[4] **Nugraha Priya Utama**,[5] **and Khin Wee Lai**[1]

[1]*Department of Biomedical Engineering, Faculty of Engineering, Universiti Malaya, 50603 Kuala Lumpur, Malaysia*
[2]*The Affiliated Changshu Hospital of Soochow University (Changshu No.1 People's Hospital), Changshu, Jiangsu 215500, China*
[3]*School of Artificial Intelligence and Computer Science, Jiangnan University, Wuxi 214122, China*
[4]*Department of Electronics and Communication Engineering, SRM Institute of Science and Technology, Kattankulathur 603203, India*
[5]*School of Electrical Engineering and Informatics, Institut Teknologi Bandung, Bandung 40132, Indonesia*

Correspondence should be addressed to Khin Wee Lai; lai.khinwee@um.edu.my

Received 1 July 2021; Accepted 15 October 2021; Published 2 November 2021

Academic Editor: Antonio Gloria

Copyright © 2021 Kareen Teo et al. This is an open access article distributed under the Creative Commons Attribution License, which permits unrestricted use, distribution, and reproduction in any medium, provided the original work is properly cited.

Quality of care data has gained transparency captured through various measurements and reporting. Readmission measure is especially related to unfavorable patient outcomes that directly bends the curve of healthcare cost. Under the Hospital Readmission Reduction Program, payments to hospitals were reduced for those with excessive 30-day rehospitalization rates. These penalties have intensified efforts from hospital stakeholders to implement strategies to reduce readmission rates. One of the key strategies is the deployment of predictive analytics stratified by patient population. The recent research in readmission model is focused on making its prediction more accurate. As cost-saving improvements through artificial intelligent-based health solutions are expected, the broad economic impact of such digital tool remains unknown. Meanwhile, reducing readmission rate is associated with increased operating expenses due to targeted interventions. The increase in operating margin can surpass native readmission cost. In this paper, we propose a quantized evaluation metric to provide a methodological mean in assessing whether a predictive model represents cost-effective way of delivering healthcare. Herein, we evaluate the impact machine learning has had on transitional care and readmission with proposed metric. The final model was estimated to produce net healthcare savings at over $1 million given a 50% rate of successfully preventing a readmission.

RETRACTED

1. Introduction

The decision-making process in healthcare is much more complex in reality, requiring significant number of considerations and research before arriving at best interventions that provide high-quality care. Current shared decision-making model often involves stakeholders from multiple levels, such as care providers, policy makers, and patients. Different opinions in arriving appropriate course of action have been the subject of controversy in decision-making. The challenge is further complicated by medical complexity [1, 2] and exponentially expanding clinical knowledge [3]. The use of predictive models is likely to improve clinical decision process and achieve better outcome without increasing costs.

Predictive modeling is used to identify patients at high risk of developing certain conditions. Intervention can then be implemented to mitigate the risk, thus preventing them from becoming high cost. Various predictive models have been devised to aid clinical decision-making [4–7]. Modeling tool that is tailored to certain conditions or health institutions may be more useful, as there exists no single model that generally addresses all use cases [8]. Readmission is a clinical outcome that requires modeling to identify likelihood of a patient gets readmitted after previous discharge. Readmission is problematic especially in Intensive Care Unit (ICU) where it is associated with high risk of in-hospital mortality and incurs more cost [9]. Authorities like the Centre for Medicare and Medicaid Services (CMS) consider readmission rate as a proxy to measure quality of care since it could be due to improper treatment or premature discharge [10]. Prediction of readmission risk can support decision on whether a patient is ready for discharge or needs further interventions.

Different time frames have been employed for readmission analysis in medical literature. However, most researchers typically refer to hospital admissions within 30 days following the initial discharge [11]. The implementation of Hospital Readmission Reduction Program by CMS since 2012 imposed financial penalties to hospitals with excessive readmission rate. Penalties are levied on hospitals depending on their performance with respect to readmission rate. Such penalties cost healthcare providers an amount of over $500 million annually, or $200k per hospital [12, 13]. Thus, it is advantageous for hospitals to conduct advance care planning during patient stays and discharge in contributing to the efforts of reducing readmission rate.

Recent exponential growth in machine learning (ML) driven by improved computing power and more advanced algorithms allows more accurate prediction not only in clinical domain, but also in other domains [14–16]. With the aforementioned predictive modeling, ML has been used as a mean of identification of patients at higher risk for hospital readmission. Predictive models can be broadly classified into three main categories in ML: (1) statistical learning, (2) classical ML, and (3) neural networks. The two key statistical prediction methods are logistic regression (LR) and survival analysis. Traditional regression analysis is usually constructed to study the effects of each clinical predictor/variable on the event of interest such as readmission. Survival model is the method of choice when the objective is to analyze time to readmission by relating features to the time that passes before readmission occurs. Unlike traditional statistical learning, classical ML has the ability of handling high dimensional datasets, especially when the number of features is more than the sample size. Examples are Naive Bayes (NB), Support Vector Machines (SVM), and tree-based approach. As classical ML setting requires extensive feature derivation and engineering, the use of neural networks for readmission modeling has just emerged in recent year. Neural network is a promising ML tool that tries to mimic the human brain, which has the capability to process and learn complex data and solve complicated tasks based on the input. Multilayer perceptron, recurrent neural network (RNN), and convolutional neural network (CNN) are three major deep learning related models being applied in structured data modeling. Despite the emergence of more advanced predictive model, simple scoring model based on clinical knowledge remains as a preferable tool for most of the healthcare providers. LACE and HOSPITAL models have been proven to work pretty well in readmission prediction [17, 18]. For any score-based model, higher score is directly proportional to higher risk of readmission. A specific threshold value can be set where patients with risk scores over this threshold are flagged as "high risk." The major concern associated with its clinical utility is model's applicability to another study population needs to be validated at different cutoff score that leads to best discrimination.

2. Related Works

The ability of predictive models to identify high-risk individuals among patient populations has been determined through performance analysis. In order to evaluate the performance of learning approach, models or algorithms are often assessed using the area under the curve receiver operating characteristic (AUC). This test quantifies a model's ability to distinguish between two classes, that is, "readmission" versus "no readmission." If the confidence of distinguishing a positive event from population is 50%, the AUC is 0.5, which indicates a very poor model. A good model is indicated by AUC value close to 1.

Many models have been developed based on clinical data to predict risk of readmission. The LACE index predicts the risk of nonelective readmission or death within 30 days after discharge from a hospital based on length of stay, acuity of admission, Charlson Comorbidity Index, and the number of emergency visits made by a patient during the previous 6 months [19]. Using AUC as evaluation metric, the benchmark score for the original article was 0.68. Predictive power of LACE score is however varied greatly as different hospitals have different socioeconomical and patient characteristics. Few researchers have achieved an AUC of above 0.7 [20]; some papers report results as low as <0.6 [21, 22]. HOSPITAL score is another similar readmission scoring system with internally validated AUC of 0.71 [23]. Both LACE and HOSPITAL score require validation when applied to different clinical settings, as there is no single model that performs well in all the scenarios, and inconsistent performance was reported across multiple studies.

A second expanding readmission research area uses ML models tailored to each health institution. LR is the most used linear classifier that models the probability of readmission. Being a tool that is easy to use and implement, LR and other advanced ML models could have comparable performance. Some researchers found no significant differences in terms of AUC of models developed using regression and ML [24, 25]. SVM is another classifier, which attempts to find decision boundaries that maximize classification margins. Recent SVM models have mostly reported moderate prediction performance (AUC ≤ 0.7) [17, 26, 27]. Tree-based models are the most frequently used (~77%) classification techniques among those using ML for prediction [11]. Decision trees have also been successfully shown to perform similarly or slightly better than other prediction techniques [28, 29]. NB is simple probabilistic classifier that is known to be able to classify an instance extremely fast. Using unstructured data as training source, researchers have observed good results for predicting readmission with NB [30]. Wolff and Graña [26] recommended the use of NB as the most robust prediction model for their pediatric readmission prediction.

RETRACTED

The potential of deep neural network (DNN) to model readmission has been extensively explored in recent years [31, 32]. Wang and Cui [33] proposed the use of CNN to automatically learn features, and the AUC of the proposed model was 0.70. Rajkomar and Oren [18] used patients' entire raw electronic medical records (EMR) for prediction and their models achieved good accuracy (AUC 0.75–0.76). Min and Yu [17] demonstrated that the state-of-the-art deep learning models fail to improve prediction accuracy, with 0.65 being the best AUC. Huang and Altosaar [27] developed a deep learning model that processes clinical notes and predicts the associated risk score of readmissions (AUC = 0.694 for RNN). Without relevant data, more complicated learning algorithms may not outperform traditional simple model.

Existing studies have reported clinical prediction performance with AUC. However, one important question remains unanswered by these prior works. AUC metric may be less meaningful and end users might find it to be unclear on how to translate these performance benefits into cost and resource allocation. While prior research proved prediction improvement over chance, a more relevant concern is clinical impact of predictive models to healthcare providers: what is the cost-effectiveness of predictive model being applied to clinical setting, and does the model help to reduce healthcare cost?

To address such research questions, we leveraged both clinical notes and predictive models for modeling all-cause 30-day readmission. We proposed a quantized evaluation metric that could assist healthcare providers in comparing cost before and after model implementation, as well as guiding decision-making particularly on optimizing hospital resources in efforts to reduce readmission rate.

3. Methods

3.1. Data. The quantity and quality of data source determine the robustness of predictive model. MIMIC-III is a publicly available real-world EMR repository of critical care cohort [34]. Unstructured clinical notes were used as a primary data, due to the ease of extraction from EMR system. Figure 1 illustrates the patient selection process. Of 58,976 distinct patient admissions, 7,863 were admissions pertaining to the patient's birth, 5,792 admissions were inpatient hospital deaths, and 1,441 were admissions without clinical notes. The final cohort consists of 43,880 (~75%) inpatient stays with patients discharged alive from hospital. Of selected inpatient stays, 2,971 (~7%) were readmitted within 30 days.

3.2. Predictive Model. The primary outcome of this study was all-cause unplanned hospital readmission within 30 days of index admission. Ground truth label for all instances was obtained by computing the binary readmit label associated with each hospital admission. Preparing clinical notes to be analyzable and predictable requires a combination of text representation and prediction model. Our previous work [35, 36] showed that Word2vec embeddings with CNN and

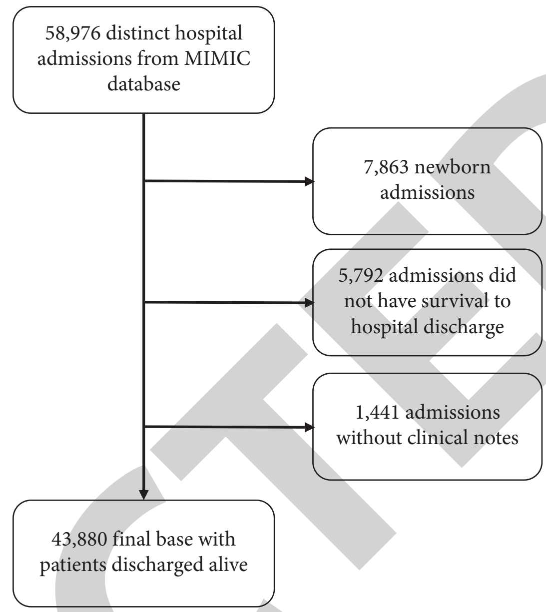

Figure 1: Study population selection flowchart.

ensemble model of CNN with LACE index work well for predictive tasks on MIMIC-III clinical notes. After exploring several architectures, we composed CNN with a 1D shallow network structure that achieved the highest AUC. Therefore, the final model consists of an embedding layer initialized with pretrained Word2vec, a CNN layer with 256 hidden units, and a dense output label sigmoid. The filter size of 5 produces the best result for CNN with a max pooling layer right after the convolution structure. CNN was trained for 25 epochs with a batch size of 64 in Keras. Both models were trained on 80% of data and the remaining 20% were withheld for validation and testing, respectively.

3.3. Model Evaluation. The most common evaluation metric of binary classification performance is AUC. Another common measure is sensitivity, which indicates the ability of model to detect readmission (proportion of readmission predicted as True). The use of AUC as a performance evaluation metric has shown inconsistent results reported by researchers [11]. Some researchers highlighted the inappropriate use of AUC to evaluate the performance of classification systems [37]. Cost as a performance metric may offer more meaningful insights. Thus, we evaluated cost effectiveness of predictive models at two time points: (1) during hospitalization and (2) at discharge as depicted in Figure 2. This is crucial as after readmission prediction, implementation of both pre- and postdischarge interventions is needed to reduce readmission rate.

3.4. Cost as Performance Metric. We proposed a quantized evaluation metric to identify the economic benefits that could be generated by predictive models for selecting patients for interventions based on readmission risk. Given a set of N patients, it is not possible to implement interventions on all patients with predicted positive readmission.

RETRACTED

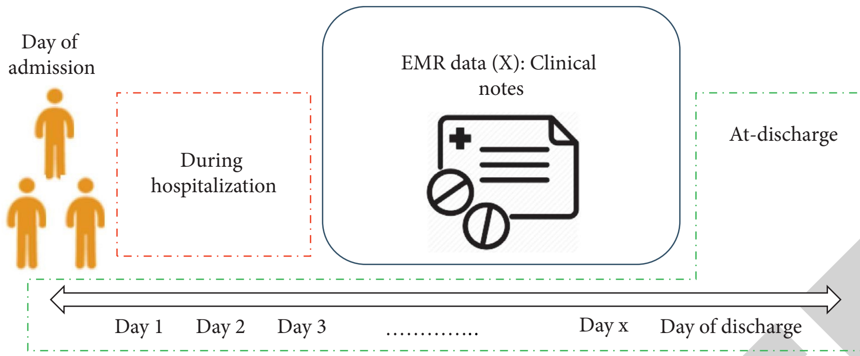

Figure 2: The predictive model is built for two time points: during hospitalization and at discharge.

Thus, small subset of study population should be chosen for intervention targeting. Before computation of cost can be performed, every patient must have a probability score generated from the model, and the score is ranked from 0 to 1 in that particular population. There are 3 factors associated with the effort to maximize cost savings with optimal intervention threshold: (1) readmission cost, (2) expected intervention cost, and (3) effectiveness of intervention (intervention might not be effective to prevent readmission). The expected savings after model implementation can be calculated as follows:

$$\text{Savings} = C_r\left(N_{act} - \lambda_{fn}\right) - N_s\rho_r C_i, \quad (1)$$

where C_r is the average readmission cost per patient, N_{act} is the number of actual readmission before model implementation, λ_{fn} is the false negative prediction, N_s is the number of patients of whom predicted positive, ρ_r is intervention threshold, and C_i represents intervention cost.

After the classification threshold for intervention can be decided, we took into consideration the intervention success rate/response rate, that is, the rate of successfully preventing a readmission after applying intervention to a patient predicted as high risk. For example, the response rate of 50% means another 50% of patients who underwent interventions would still be readmitted within 30 days. Thus, the net saving can be calculated using the following equations:

$$\text{Net savings} = C_r\left(N_{act} - \lambda_{fn}\right)\delta - \left(N_{TP} + N_{FP}\right)C_i, \quad (2)$$

$$\text{Net savings} = C_r N_{TP}\delta - \left(N_{TP} + N_{FP}\right)C_i, \quad (3)$$

where N_{TP} is the number of true positive, δ is the intervention success rate, and $N_{TP} + N_{FP}$ is the number of predicted positives.

4. Results

Our previous studies proved that the predictive model, that is, CNN, with the combination of LACE leads to very accurate predictions of 30-day readmissions both during hospitalization and at discharge [35, 36]. After identifying high-risk patients accurately, healthcare providers need to plan on the cost-effective interventions based on the discrimination threshold that maximize the projected cost saving.

For the purpose of cost simulation, the estimation of actual values might be difficult; thus, we adopted the values established in past literature for cost calculation in US dollar ($). Readmission cost per patient was $9655, and intervention cost per patient was $1500 [38]. Two better performing models, CNN, CNN + LACE, in our prior research were chosen to identify an optimal intervention threshold with metric in Equation (1). Figure 3 evaluates the economic benefits that could be produced by the two models computed for each classification threshold (with 0.05 separation). When using convention threshold, that is, 0.5 for discriminating high-risk instance, CNN + LACE did not mark superior performance over ML model alone. Only when threshold was at 0.65, positive cost reduction rose slowly as the threshold rose to a higher value. There was no large turbulence in the AUC performance for both prediction models. The CNN + LACE model exceeded CNN in cost reduction at the threshold of 0.8. The second and third better results were obtained at the threshold of 0.85 and 0.90. CNN demonstrated the maximum savings at $16.9 million; however, targeting patients with probability score of 0.95 and above can barely reduce readmission rate. This is undesirable as the aim for most of the hospitals is to curb the increased readmission rate.

At-discharge model offers few opportunities to reduce the chance of readmission because the target patient might have already been discharged. Preventive measure during hospitalization holds valuable potential for mitigating readmission risk. Thus, identifying high-risk readmission early during hospitalization is crucial. Figures 3 and 4 illustrate that ensemble classification selected more correctly identified patients for readmission intervention at the threshold ≤0.8, as proven by better AUC and higher cost reduction. At the 0.5 cutoff, CNN + LACE demonstrated lesser economic benefits compared to CNN. Notably, it is interesting to find out that using 0.85 as threshold, the ensemble model had an AUC that is 0.01 lower, but it generated higher saving than CNN model alone.

After estimation of cost reduction, the intervention cost required to achieve targeted saving and model's impact on readmission rate remains unknown. Figure 5 shows the projected intervention cost and readmission rate, calculated by changing the number of patients for interventions with the classification threshold. Assumption was made that

RETRACTED

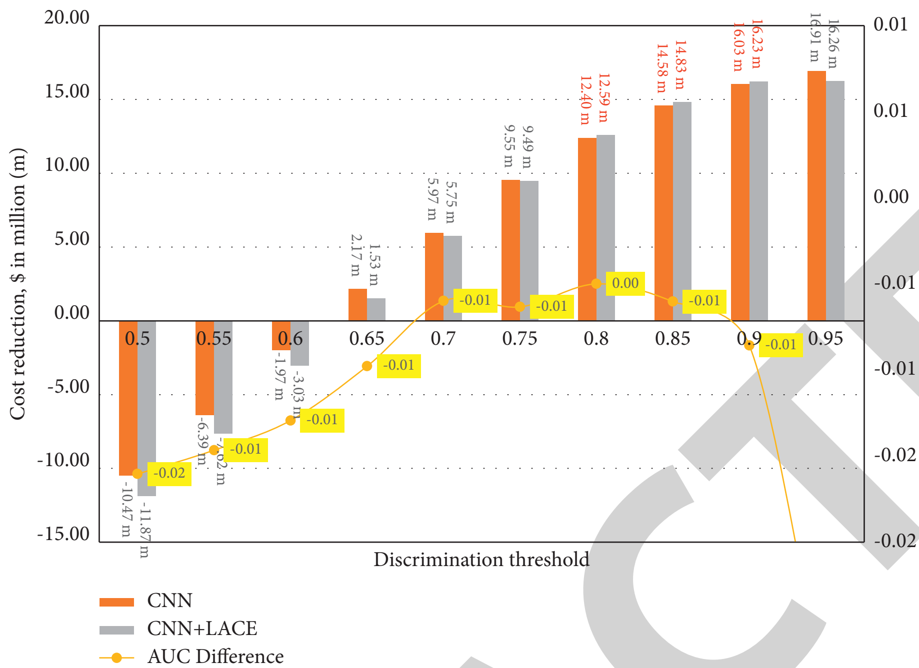

Figure 3: The projected saving values as a function of classification threshold for CNN versus CNN + LACE models for at-discharge prediction. AUC difference indicates the performance of CNN + LACE against CNN model alone.

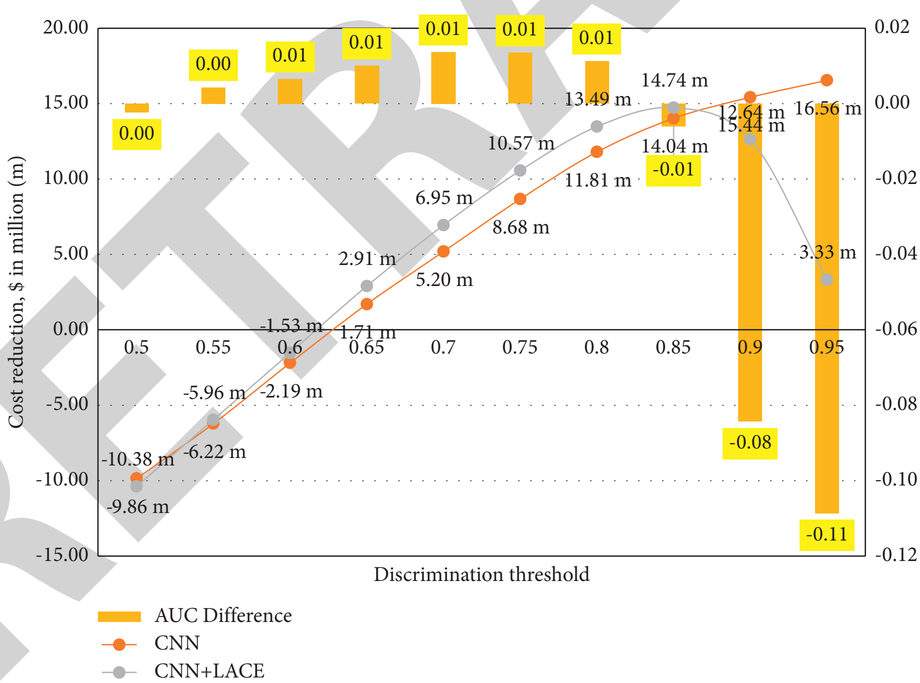

Figure 4: The projected saving values as a function of classification threshold for CNN versus CNN + LACE models for during hospitalization prediction. AUC difference indicates the performance of CNN + LACE against CNN model alone.

intervention could successfully prevent 50% of readmissions by applying special care to patients who would be readmitted within 30 days. The decline trend in intervention cost is in line with the findings shown in Figure 3, as lesser intervention cost corresponds to greater savings. The series of line chart represents the readmission rate after implementation of predictive model. The ensemble model was shown to have contributed to a lower readmission rate for the threshold of <0.9. This could be explained by the ability of CNN + LACE model in identifying higher number of true positive compared to CNN.

Figure 6 illustrates results on the intervention cost required during early admission. Unlike findings presented in Figure 5, readmission rate is higher for the ensemble model,

RETRACTED

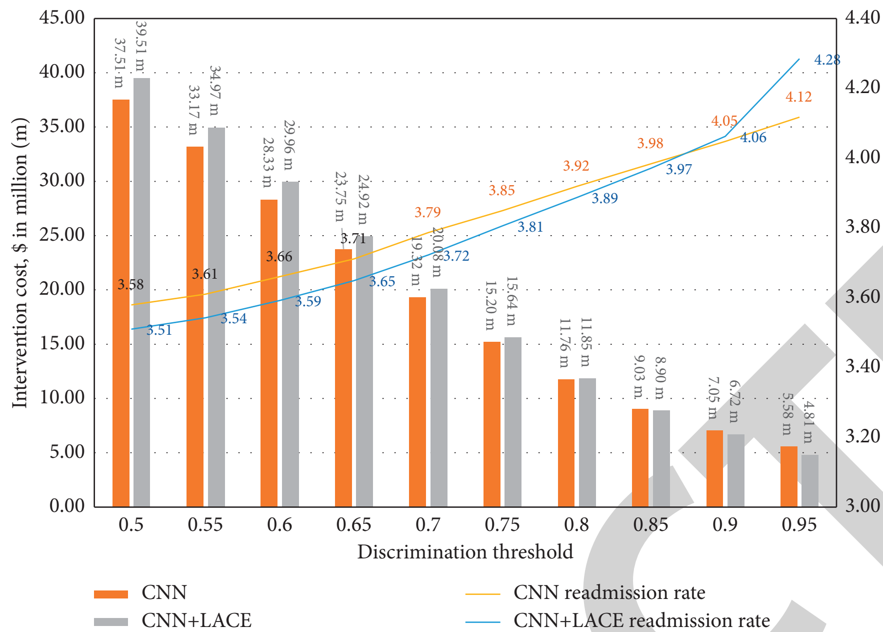

Figure 5: The projected intervention cost over various discrimination threshold for CNN vs. CNN + LACE at-discharge models.

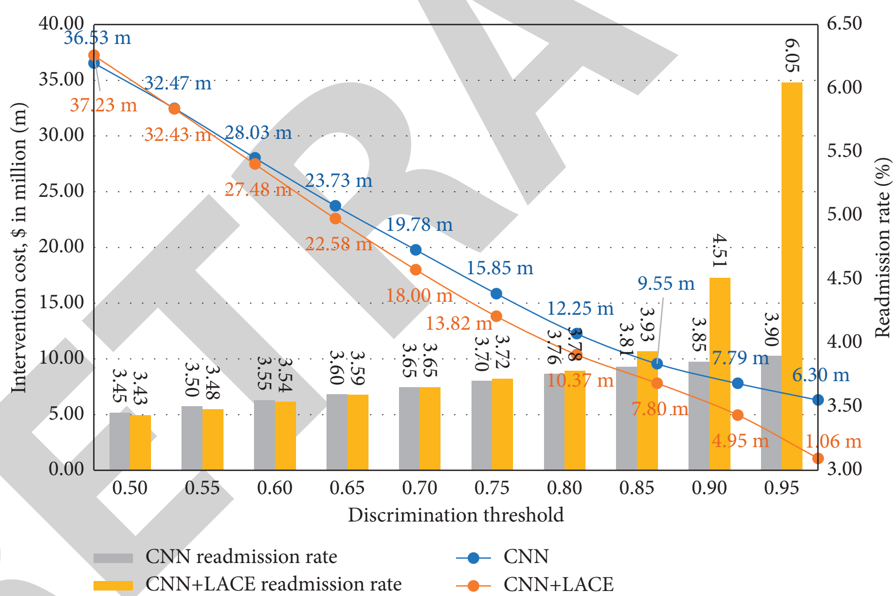

Figure 6: The projected intervention cost over various discrimination threshold for CNN vs. CNN + LACE during hospitalization models.

despite the fact that the model has the highest incremental AUC at the threshold of 0.7, 0.75, and 0.80. This suggests that although AUC is commonly used as metrics to measure classification performance, readmission prediction task needs to be supplemented by objective/use case of model that depends on different proportion of readmission/intervention cost, as well as the balance between false positive and false negatives. In addition, it is important to identify a threshold that matches the hospital's resources for targeted interventions. This also affects the decision to choose which model to put into production.

We also looked at final net savings by setting the number of intervention enrollees at 0.8 classification threshold. The metrics in equations (2) and (3) calculate the estimated cost considering various possibilities of successfully preventing a readmission. Table 1 shows the maximum net savings from readmission reduction considering the intervention success rate from 10% to 100%. When evaluating from CNN perspective, we need to achieve a 60% response rate to ensure a positive saving. The CNN + LACE was shown to be able to maintain positive saving at a lower response rate 50%.

Another analysis was carried out with intervention implemented after discharge. We reported the result of cost saving in Table 2. We can find that if healthcare providers were able to prevent as much readmission through interventions, the more savings can be generated, provided a

RETRACTED

Table 1: Net savings from readmission reduction by selecting patients for predischarge intervention at different success rates.

Intervention success rate (%)	CNN net saving, $	CNN + LACE net saving, $
10	−9,847,474	−7,982,250
20	−7,441,448	−5,596,499
30	−5,035,422	−3,210,749
40	−2,629,396	−824,998
50	−223,370	1,560,753
60	2,182,656	3,946,503
70	4,588,682	6,332,254
80	6,994,708	8,718,004
90	9,400,734	11,103,755
100	11,806,760	13,489,505

Table 2: Net savings from readmission reduction by selecting patients for postdischarge intervention at different success rates.

Intervention success rate (%)	CNN net saving, $	CNN + LACE net saving, $
10	−9,346,354	−9,401,820
20	−6,929,707	−6,958,139
30	−4,513,061	−4,514,459
40	−2,096,414	−2,070,778
50	320,233	372,903
60	2,736,879	2,816,583
70	5,153,526	5,260,264
80	7,570,172	7,703,944
90	9,986,819	10,147,625
100	12,403,465	12,591,305

minimum response rate of 50% is achieved for both models. Extra 2.5 mil of saving can be projected with every increase in the success rate by 10%. On the other hand, ensemble of CNN and LACE was expected to contribute to higher net saving than single classifier. This proves that it is still useful to readmission prediction task.

5. Discussion

This was a retrospective study which applied machine learning to unstructured clinical prose from EMR to construct a risk prediction model for 30-day readmission. As most studies used AUC evaluation metrics, this metric only provides theoretical mean of how well a model performs. To overcome such challenge, our proposed metric evaluates model's impact on the financial performance and offers an analysis metric that is more meaningful to hospital management.

Readmission prediction has been challenging. Artetxe and Beristain [11] found that a direct comparison on models across different studies with AUC is challenging because the performance of the models varies greatly with the target population. Another more recent review focused on the use of EMR for the development of risk prediction model [25]. In their reported outcome, most models failed to interpret with reasonable diagnostic test other than AUC or clinical usefulness of the proposed models. We were able to identify only two readmission studies which reported cost evaluation results. Jamei and Nisnevich [39] showed the highest projected saving values of $750k at 20% intervention success rate. However, the ratio of readmission to intervention cost was 20, as compared to 6.5 used in this study. Huge ratio could have potentially overestimated the actual cost saving. With similar ratio as in this study, Goals and Shibahara [38] proposed a deep learning technique and the model demonstrated net savings at 3.4 million at 50% intervention success rate.

To the best of our knowledge, there is no study that has specifically addressed the clinical impact of developed models on MIMIC dataset; however, there are quite a number of readmission models [18, 27, 40–43]. While applying risk models can help to identify patients who would benefit most from clinical interventions, a better performing model does not necessarily contribute much to cost saving. Therefore, two models that produced the same AUC may have different cost potentially. This is due to the fact that misclassification costs associated with false positive and false negative are different. This is proven in Figures 3 and 4 where classifier with better AUC is not necessarily resulting in greater cost reduction. The CNN + LACE model obtained a slight lower AUC but generated more savings at specific classification threshold. This suggests that the proportion of false positive and false negative prediction is more important than AUC. As a means of comparing models associated with these two false predictions, the tradeoff between precision and recall could be a better metric. In Figure 7, we display precision-recall curve for during hospitalization and at-discharge models. The impact on overall cost reduction obtained from Tables 1 and 2 is $1.5 million and $350k for the two predictions, respectively (CNN + LACE). Indeed, model associated with early prediction showed larger improvement in terms of the area under the precision recall curve in Figure 7.

RETRACTED

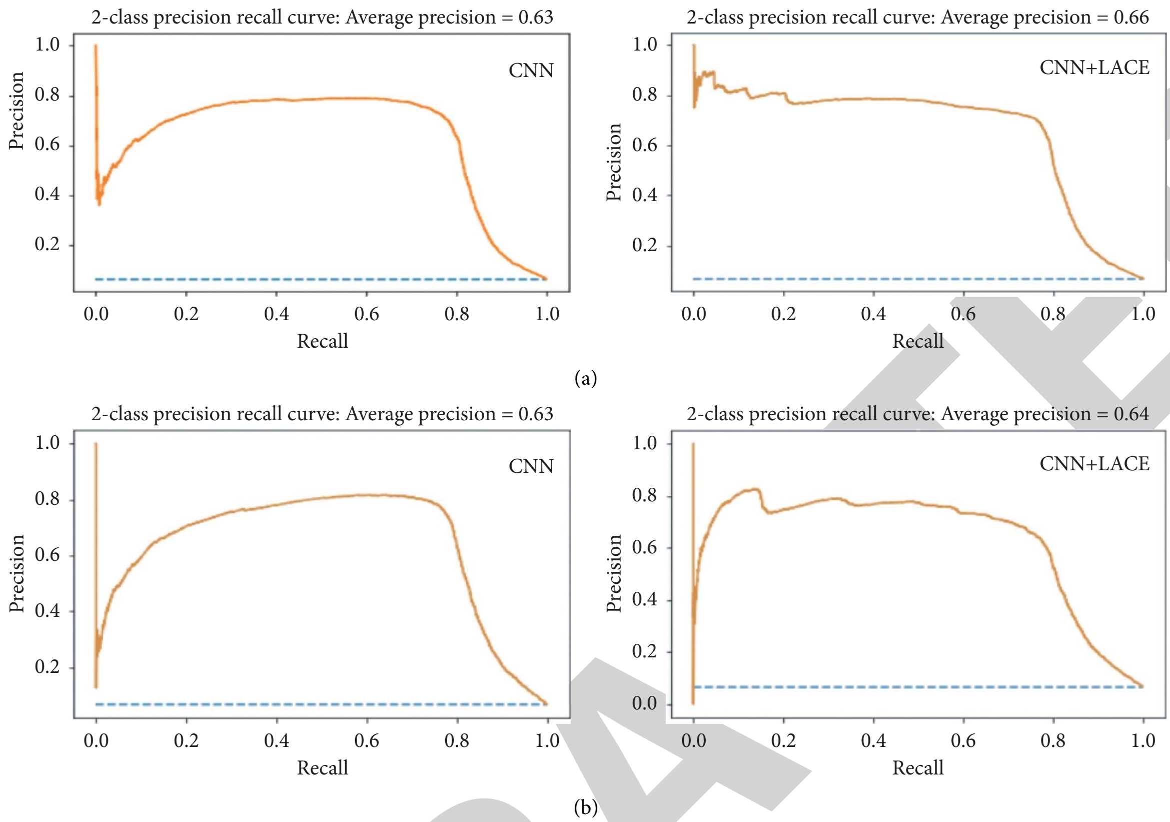

FIGURE 7: Precision-recall curve for CNN and CNN + LACE models at prediction (a) during hospitalization for predischarge intervention and (b) at discharge for postdischarge intervention.

RETRACTED

A fair comparison of our results with existing literature is not feasible, because no previous study has considered cost as evaluation metric on MIMIC population. The cost estimation was done based on models developed in our prior research [36]. The primary factor that influences how much healthcare cost can be saved is definitely the effectiveness or success rate of intervention. We need to understand that a number of patients will still need hospital readmission even after intervention. However, increasing the intervention success rate has a positive impact on net cost saving. To maintain positive benefit, we showed that intervention success rate must be kept at least 50%. Predischarge intervention was believed to be able to contribute greater cost benefit compared to at-discharge model. An approximate 1.5 million of healthcare cost could potentially be saved at the current ratio of readmission to intervention cost, provided a 50% success rate is achieved for in-hospital intervention. Higher ratio of readmission to intervention cost would generate more cost saving.

Our proposed metric hints an opportunity to improve model evaluation in clinical settings by presenting potential healthcare cost saving together with intervention cost and model's impact on readmission rate. By including all possible factors that affect the economical benefit, strength of this study is the generalizability of the metric to encounter any other readmission predictive models. We also noted several limitations in considering our results. First, the metric considers only clinical factors into cost analysis. Other nonclinical factors such as hiring of ML expert and procurement of workstation remain to be established. Second, this study was conducted on EMR data from MIMIC; future works should consider national level hospital admissions to build a more comprehensive analysis. Still, this proposed metric can still be applied to carry out predictive modeling evaluation on clinical data from completely new entities.

6. Conclusion

The value of this study is its ability to evaluate clinical usefulness of readmission risk prediction model regardless of type of modeling technique. This enables healthcare providers and hospital management to plan targeted interventions at their budget and improve overall patient outcomes, which is important in curbing increased readmission rate and healthcare cost. Our evaluation metric has also shown that simply improving predictive model is often not sufficient as traditional way of measuring performance does not necessarily bring positive impact on cost reduction. Integrating cost into model evaluation has shown a significant reduction in costs by selecting patients who will benefit most from intervention without causing extra burden on healthcare resources, intervention success rate thus becoming the key to be monitored to ensure positive impact of adopting predictive modeling into clinical settings. It is also important for care teams to evaluate which of the false predictions can be more detrimental: false positive or negative. The cost ratio between these two predictions and between readmission and intervention determines the final benefits of any classification system.

Data Availability

MIMIC-III is a publicly available real-world EMR repository of critical care cohort [34], and it can be found at the list of references.

Conflicts of Interest

The authors declare that they have no conflicts of interest.

Acknowledgments

This work was supported by the 2020 EBC-C (Extra-Budgetary Contributions from China) Project on Promoting the Use of ICT for Achievement of Sustainable Development Goals and University Malaya under Grant IF015-2021.

References

[1] B. Khizar and R. H. Harwood, "Making difficult decisions with older patients on medical wards," *Clinical Medicine*, vol. 17, no. 4, pp. 353–356, 2017.

[2] Y. Zhang, Y. Jiang, L. Qi, M. Z. Alam Bhuiyan, and P. Qian, "Epilepsy diagnosis using multi-view & multi-medoid entropy-based clustering with privacy protection," *ACM Transactions on Internet Technology*, vol. 21, no. 2, 2021.

[3] K. E. Miller, H. Singh, R. Arnold, and G. Klein, "Clinical decision-making in complex healthcare delivery systems," in *Clinical Engineering Handbook*, E. Iadanza, Ed., pp. 858–864, Academic Press, Cambridge, UK, Second Edition, 2020.

[4] Y. Zhang, S. Wang, K. Xia, Y. Jiang, and P. Qian, "Alzheimer's disease multiclass diagnosis via multimodal neuroimaging embedding feature selection and fusion," *Information Fusion*, vol. 66, pp. 170–183, 2021.

[5] K. Jiang, J. Tang, Y. Wang, C. Qiu, Y. Zhang, and C. Lin, "EEG feature selection via stacked deep embedded regression with joint sparsity," *Frontiers in Neuroscience*, vol. 14, p. 829, 2020.

[6] F. Wang, L. P. Casalino, and D. Khullar, "Deep learning in medicine-promise, progress, and challenges," *JAMA Internal Medicine*, vol. 179, no. 3, pp. 293-294, 2019.

[7] A. Spooner, E. Chen, A. Sowmya et al., "A comparison of machine learning methods for survival analysis of high-dimensional clinical data for dementia prediction," *Scientific Reports*, vol. 10, no. 1, p. 20410, 2020.

[8] S. den Boer, N. F. de Keizer, and E. de Jonge, "Performance of prognostic models in critically ill cancer patients - a review," *Critical Care*, vol. 9, no. 4, pp. R458–R463, 2005.

[9] M. Hammer, S. D. Grabitz, B. Teja et al., "A tool to predict readmission to the intensive care unit in surgical critical care patients—the RISC score," *Journal of Intensive Care Medicine*, vol. 36, no. 11, pp. 1296–1304, 2020.

[10] C. K. McIlvennan, Z. J. Eapen, and L. A. Allen, "Hospital readmissions reduction program," *Circulation*, vol. 131, no. 20, pp. 1796–1803, 2015.

[11] A. Artetxe, A. Beristain, and M. Graña, "Predictive models for hospital readmission risk: a systematic review of methods," *Computer Methods and Programs in Biomedicine*, vol. 164, pp. 49–64, 2018.

[12] C. Boccuti and G. Casillas, *Aiming for Fewer Hospital U-Turns: The Medicare Hospital Readmission Reduction Program*, Kaiser family Foundation, Menlo Park, CA, USA, 2015.

[13] G. J. Hoffman and O. Yakusheva, "Association between financial incentives in medicare's hospital readmissions reduction program and hospital readmission performance," *JAMA Network Open*, vol. 3, no. 4, Article ID e202044, 2020.

[14] M. A. Al-Garadi, M. R. Hussain, N. Khan et al., "Predicting cyberbullying on social media in the big data era using machine learning algorithms: review of literature and open challenges," *IEEE Access*, vol. 7, pp. 70701–70718, 2019.

[15] L. W. Qin, M. Ahmad, M. Ali, R. Mumtaz, M. Ahsan Raza, and M. Tahir, "Precision measurement for industry 4.0 standards towards solid waste classification through enhanced imaging sensors and deep learning model," *Wireless Communications and Mobile Computing*, vol. 2021, pp. 1–10, Article ID 9963999, 2021.

[16] J. Huang, J. Chai, and S. Cho, "Deep learning in finance and banking: a literature review and classification," *Frontiers of Business Research in China*, vol. 14, no. 1, p. 13, 2020.

[17] X. Min, B. Yu, and F. Wang, "Predictive modeling of the hospital readmission risk from patients' claims data using machine learning: a case study on COPD," *Scientific Reports*, vol. 9, no. 1, p. 2362, 2019.

[18] A. Rajkomar, E. Oren, K. Chen et al., "Scalable and accurate deep learning with electronic health records," *Npj Digital Medicine*, vol. 1, no. 1, p. 18, 2018.

[19] C. van Walraven, I. A. Dhalla, C. Bell et al., "Derivation and validation of an index to predict early death or unplanned readmission after discharge from hospital to the community," *Canadian Medical Association Journal*, vol. 182, no. 6, pp. 551–557, 2010.

[20] C. van Walraven, J. Wong, and A. J. Forster, "LACE+ index: extension of a validated index to predict early death or urgent readmission after hospital discharge using administrative data," *Open Medicine : A Peer-Reviewed, Independent, Open-Access Journal*, vol. 6, no. 3, pp. e80–e90, 2012.

[21] I. F. Caplan, P. Z. Sullivan, D. Kung et al., "LACE+ index as predictor of 30-day readmission in brain tumor population," *World Neurosurgery*, vol. 127, pp. e443–e448, 2019.

[22] A. M. Ibrahim, C. Koester, M. Al-Akchar et al., "HOSPITAL Score, LACE Index and LACE+ Index as predictors of 30-day readmission in patients with heart failure," *BMJ Evidence-Based Medicine*, vol. 25, no. 5, pp. 166-167, 2020.

[23] J. Donzé, D. Aujesky, D. Williams, and J. L. Schnipper, "Potentially avoidable 30-day hospital readmissions in medical patients," *JAMA Internal Medicine*, vol. 173, no. 8, pp. 632–638, 2013.

[24] A. Allam, M. Nagy, G. Thoma, and M. Krauthammer, "Neural networks versus Logistic regression for 30 days all-cause readmission prediction," *Scientific Reports*, vol. 9, no. 1, p. 9277, 2019.

[25] E. Mahmoudi, N. Kamdar, N. Kim, G. Gonzales, K. Singh, and A. K. Waljee, "Use of electronic medical records in development and validation of risk prediction models of hospital readmission: systematic review," *BMJ*, vol. 369, p. m958, 2020.

[26] P. Wolff, M Graña, S. A Ríos, and M. B Yarza, "Machine learning readmission risk modeling: a pediatric case study," *BioMed Research International*, vol. 2019, Article ID 8532892, 9 pages, 2019.

[27] K. Huang, J. Altosaar, and R. J. A. Ranganath, "Clinicalbert: modeling clinical notes and predicting hospital readmission," 2019, https://arxiv.org/abs/1904.05342.

RETRACTED

Hindawi
Journal of Healthcare Engineering
Volume 2023, Article ID 9849317, 1 page
https://doi.org/10.1155/2023/9849317

Retraction

Retracted: The Factors Affecting Orthodontic Pain with Periodontitis

Journal of Healthcare Engineering

Received 27 June 2023; Accepted 27 June 2023; Published 28 June 2023

Copyright © 2023 Journal of Healthcare Engineering. This is an open access article distributed under the Creative Commons Attribution License, which permits unrestricted use, distribution, and reproduction in any medium, provided the original work is properly cited.

This article has been retracted by Hindawi following an investigation undertaken by the publisher [1]. This investigation has uncovered evidence of one or more of the following indicators of systematic manipulation of the publication process:

(1) Discrepancies in scope
(2) Discrepancies in the description of the research reported
(3) Discrepancies between the availability of data and the research described
(4) Inappropriate citations
(5) Incoherent, meaningless and/or irrelevant content included in the article
(6) Peer-review manipulation

The presence of these indicators undermines our confidence in the integrity of the article's content and we cannot, therefore, vouch for its reliability. Please note that this notice is intended solely to alert readers that the content of this article is unreliable. We have not investigated whether authors were aware of or involved in the systematic manipulation of the publication process.

In addition, our investigation has also shown that one or more of the following human-subject reporting requirements has not been met in this article: ethical approval by an Institutional Review Board (IRB) committee or equivalent, patient/participant consent to participate, and/or agreement to publish patient/participant details (where relevant).

Wiley and Hindawi regrets that the usual quality checks did not identify these issues before publication and have since put additional measures in place to safeguard research integrity.

We wish to credit our own Research Integrity and Research Publishing teams and anonymous and named external researchers and research integrity experts for contributing to this investigation.

The corresponding author, as the representative of all authors, has been given the opportunity to register their agreement or disagreement to this retraction. We have kept a record of any response received.

References

[1] Y. Peng and S. Tang, "The Factors Affecting Orthodontic Pain with Periodontitis," *Journal of Healthcare Engineering*, vol. 2021, Article ID 8942979, 11 pages, 2021.

Hindawi
Journal of Healthcare Engineering
Volume 2021, Article ID 8942979, 11 pages
https://doi.org/10.1155/2021/8942979

Research Article

The Factors Affecting Orthodontic Pain with Periodontitis

Yuzhi Peng [1] and Songjiang Tang [2]

[1] *Department of Stomatology, First Affiliated Hospital of Guizhou University of Traditional Chinese Medicine, Guiyang 550001, China*
[2] *Department of Anesthesiology, First Affiliated Hospital of Guizhou University of Traditional Chinese Medicine, Guiyang 550001, China*

Correspondence should be addressed to Yuzhi Peng; pengyuzhi705@gzy.edu.cn

Received 19 August 2021; Revised 18 September 2021; Accepted 20 September 2021; Published 1 November 2021

Academic Editor: Gu Xiaoqing

Copyright © 2021 Yuzhi Peng and Songjiang Tang. This is an open access article distributed under the Creative Commons Attribution License, which permits unrestricted use, distribution, and reproduction in any medium, provided the original work is properly cited.

The occurrence of pain is often closely related to the psychological status, and the threshold for pain tolerance varies from patient to patient. In short, the factors affecting orthodontic pain are diverse and have individual differences. Tooth pain after the first force of intraoral malocclusion orthodontic treatment is one of the common complications of fixed orthodontic treatment, which often affects the outcome of treatment of patients with malocclusion and their subjective satisfaction with fixed orthodontic treatment. The purpose of the paper was to investigate the basic patterns and influencing factors of dental pain in fixed orthodontic patients within seven days after the initial wearing of straight arch aligners and the analysis of the effect of psychological intervention on dental pain using the visual simulation scoring method. According to the inclusion criteria of the experimental design, 89 patients who visited the Department of Orthodontics of Hospital for malocclusion were randomly divided into observation group and control group, and the observation group used chewing gum as psychological intervention, while the control group did not use any intervention. The effect of psychological intervention on periodontal pain was analyzed. The results of the paper were that all but 3 of the 89 patients had no pain, and all the patients had different degrees of dental pain at different points in time.

RETRACTED

1. Introduction

With the development of society, the progress of technology, and the improvement of living conditions, people are no longer just satisfied with the level of subsistence but have higher and higher requirements for the quality of life and also have higher and higher requirements for aesthetics [1]. In order to make oneself more beautiful and confident, the treatment of maxillofacial deformities has entered people's vision and attracted widespread attention. In recent years, the prevalence of maxillofacial malocclusion in China has shown an increasing trend, and according to the latest research data, it can be as high as 72.92% [2]. Dental and maxillofacial malocclusion is a congenital or externally acquired abnormality in the morphology and structure of the teeth and jaws and the function of the accompanying oromandibular system, which has become one of the most important diseases threatening the physical and mental health of the nation, and the World Health Organization has positioned oral and maxillofacial malocclusion as one of the three major symptoms of oral diseases [3]. Malocclusion not only affects the physiological function of the oral cavity but also has an impact on other oral diseases such as endodontic disease and periodontal disease.

Nowadays, with the change of the medical model, the definition of health not only includes the physiological health of the human body but also the psychological perfection state [4]. The low-level goal is to restore and reconstruct the normal anatomical structure of the patient's maxillofacial tissues without affecting the patient's mastication, swallowing function and breathing, and other physiological functions and to achieve the maximum degree of aesthetics, while the high-level goal is to understand the psychological state of the patient and family as much as possible, help them overcome their psychological fears, and improve their self-confidence, so that they can get a higher degree of cooperation from the patient [5–8], thus ensuring that orthodontic treatment is carried out effectively and smoothly. Studies have been done on patients with malocclusion and have shown that orthodontic therapeutic pain not only affects patients with malocclusion in fixed orthodontic treatment but also causes patients with fixed orthodontic treatment to fail to attend follow-up appointments or even to terminate their orthodontic treatment, and other studies have shown that about eight percent of patients give up the pursuit of aesthetics because of the severe pain caused by orthodontic treatment [9].

Therefore, the pathogenesis of dental pain, its development, the factors influencing it, and the relief of orthodontic pain have always been of interest. The transmission of pain is analyzed biologically, the tooth is stimulated, capillaries in the pulp are dilated and filled with blood, the osmotic pressure in the pulp cavity is increased, plasma extravasation and microcirculatory disorders increased pressure in the pulp tissue, and conduction via C and A-δ nerve fibers in the pulp cavity induced tooth pain. After periodontal membrane stimulation, the periodontal ligament is compressed or stretched. Mast cells release various inflammatory factors and pain-causing substances. A series of edema and inflammatory reactions are as follows: vasodilatation and congestion, an increase in capillary osmotic pressure, an increase in sensitivity of receptors in the periodontal membrane, and a decrease in the body's threshold for dental pain response [10]. Early pain often occurs after the application of orthodontic forces, causing changes in the osmotic pressure in the periodontium; delayed pain is an allergic state of the periodontium, probably related to the stimulation of the nerve endings of the periodontium by inflammatory mediators, which in turn stimulates the release of neuropeptides from the pain receptors, usually within a few hours after the force is applied. The pain stimulus signals from the tooth and periodontal membrane continue to transmit pain stimulus signals to the center on the one hand and release neuropeptides (enkephalins, histamine, interleukins, substance P, dopamine, gamma-aminobutyric acid, serotonin, glycine, prostaglandins, calcitonin gene-related peptide CGRP, neurofilament protein NEP, vasoactive intestinal peptide, neuropeptide, etc.) to the periphery to regulate orthodontic pain, and these released neuropeptides are also involved in local blood flow regulation, which facilitates the reconstruction of dental tissue [11].

A person's psychological state can affect his or her perception of orthodontic pain during the treatment process, so psychological interventions can be used to improve patient cooperation, relieve orthodontic pain, ensure the smooth and effective implementation of orthodontic fixed orthodontic treatment, and improve patients' oral health-related quality of life under the modern biopsychosocial medicine model. Quality of life should be improved to find a simple, effective, easy-to-implement method with few side effects for orthodontic treatment pain relief and to provide some theoretical basis for psychological interventions affecting orthodontic dental pain. The purpose of this experiment is to investigate the changes in the pattern of dental pain, the factors affecting the pain, and the psychological intervention on dental pain within one week after the first force application of straight wire orthodontic appliances in patients with malocclusion by means of a clinical questionnaire, so as to provide a theoretical basis for the development of orthodontic clinical work.

2. Related Work

Over the years, the study of pain response to fixed orthodontic treatment has become a hot research topic in orthodontic medicine. Clinical research focuses on the manifestation of pain, influencing factors, and how to relieve the symptoms of pain, while basic research focuses on the causes, influencing factors, and pathogenesis of orthodontic therapeutic pain, such as the relevant factors causing dental pain, conduction mediators, and pain receptors [12]. At present, domestic and foreign scholars have started to study the mechanism of fixed orthodontic therapeutic pain at the molecular and cellular levels and found that therapeutic pain-related factors play an important role in both the peripheral and central mechanisms of fixed orthodontic pain. Since there are no specific pain receptors in the enamel, there is no pain sensation during orthodontic treatment, while the pulp and dentin contain many tiny nerve fibers, which contain mainly C-fibers and A-δ fibers [13]. The hypothesis proposed that any sensory nerve endings could produce some signals to conduct pain that was later given theoretical support [14].

It has been demonstrated that under orthodontic forces, the peripheral tissues contain small bundles of nerve fibers (C-fibers and A-delta fibers) that transmit information about the pain state to the nucleus of the pulpal ridge, some of which are dedicated to the transmission of pain signals and some of which are responsible for the transmission of both pain and general sensory signals. The pulp and periodontal tissues contain a large number of small nerve fiber bundles, mainly C-fibers and A-delta fibers, which are insulated and have a much faster conduction speed (10–30 m/s) than C-fibers (2.5 m/s), which are not insulated [15]. As the A-delta fibers (10–30 m/s) conduct faster, the pain sensation is mainly sharp, so the first sharp pain is perceived at the beginning of the first force application, and the C nerve fibers start to produce signals only after the sharp pain, resulting in a dull pain that is subjectively described as a "burning sensation". The nerve fibers of the C nerve begin to produce signals only after the first sharp pain has been applied, producing a dull pain that the body subjectively describes as a "burning sensation" [16].

Burstone divided orthodontic pain into early pain and delayed pain. Early pain often occurs after the application of orthodontic forces, causing changes in the osmotic pressure in the periodontium; delayed pain is an allergic state of the periodontium, probably related to the stimulation of the nerve endings of the periodontium by inflammatory mediators, which in turn stimulates the release of neuropeptides from the pain receptors, usually within a few hours after the

RETRACTED

force is applied. It usually occurs within a few hours after the force is applied [17]. Recent studies have found that the effect and role of neuropeptides in the expression of orthodontic treatment of pain focus on neurokinin A (NKA), substance P (SP), neuropeptide Y (NPY), and calcitonin gene-related peptide CGRP.

The pain produced after the first force of a fixed orthodontic appliance does not only depend on the sensitization state of the periodontal membrane and the change in osmotic pressure caused by the stimulation but is also related to many factors, such as tooth separation, the value of the orthodontic force given, and other medical factors, as well as the sex and age of the individual, the variability of pain thresholds, and the psychological quality of the individual. In short, orthodontic pain after the first force is influenced not only by medical factors but also by psychological factors such as concentration, emotion, and the expected effect. Orthopedic pain after the first force is a series of reactions, both psychological and physiological, triggered by the action of a harmful stimulus on the body [18].

Therefore, how to relieve the pain caused by orthodontic treatment becomes the first consideration and problem for patients and practitioners [19]. At present, the commonly used methods to relieve orthodontic pain are reduction of orthodontic force, transcutaneous electrical nerve stimulation, oral analgesics, and certain low-dose laser irradiation [20]. The orthodontic force needs to reach a certain threshold in order to produce tooth movement, so it is impossible to reduce the orthodontic force indefinitely; oral analgesics have certain adverse effects, and it has been reported that analgesics also slow down the rate of movement of the malocclusion teeth and induce certain physical diseases; laser irradiation with a certain low dose must be operated by the physician and the pain relief has a certain time limit [21].

3. Introduction and Survey of Patients with Periodontal Disease

3.1. Clinical Information. One hundred patients with periodontal disease from October 2020 to May 2021 were treated with fixed orthodontic appliances and given orthodontic pain questionnaires. 11 invalid questionnaires were excluded (including those whose parents or patients did not complete the questionnaire, those who did not chew gum regularly as required, and those whose L factor T value in the Eysenck Personality Questionnaire was >60, i.e., highly masked and poorly credited). The remaining valid questionnaires were 89, with an effective rate of 89%. As shown in Figure 1, the pain transmission of the signals could be started to study the mechanism of fixed orthodontic therapeutic pain at the molecular and cellular levels and found that therapeutic pain-related factors play an important role in both the peripheral and central mechanisms of fixed orthodontic pain. There were 44 patients in the observation group, 18 males and 26 females; 34 were minors and 10 were adults. In the control group, there were 45 patients, including 19 males and 26 females; 34 were minor patients and 11 were adult patients.

Inclusion criteria for study subjects are as follows:

(1) Patients with bimaxillary orthodontic treatment using straight wire orthodontic appliances
(2) Both use Japanese TOMY straight wire arch brackets
(3) Uniform use of Green Arrow chewing gum
(4) Those who agree to participate in the survey and voluntarily fill out the questionnaire

Exclusion criteria are as follows:

(1) Those with auxiliary devices such as bevel guides and implant supports in the oral cavity
(2) Those with obvious endodontic and periodontal diseases
(3) Pain caused by surgical procedures for maxillofacial deformities and oral soft tissue injuries caused by the interaction between brackets and bands
(4) In addition to the observation group, patients in the control group who had chewing gum behavior during the experiment
(5) Those who took antianxiety, analgesic, or sedative medication 4 days before wearing the aligner

4. Materials and Devices

The Short Form Mc Gill Pain Questionnaire (SF-MPQ) is a simplified version of the McGill Pain Questionnaire (MPQ), which was developed by Melzack and Torgerson in the 1970s to assess the intensity, characteristics, nature, and concomitant status of pain, and is one of the multifactor scoring methods for investigating pain. However, the content was cumbersome, abstract, and difficult to understand, so a simple, sensitive, and reliable pain assessment method, the Simplified McGill Pain Questionnaire (SF-MPQ), was proposed. The commonly used SF-MPQ includes pain index rating (PRI), pain intensity rating (PPI), and visual analog rating (VAS), among which the visual analog rating (VAS) is sensitive and reliable and is commonly used to assess dental pain in clinical practice, with the following steps: a line segment of about 100 mm long, 0 mm, and 100 mm is marked on both sides of the end. 0 mm is described as no pain and 100 mm is described as unbearable severe pain. 100 mm is described as intolerable severe pain. Between 0 mm and 100 mm, the tooth pain gradually increases and can be expressed as "soreness, swelling pain, mild pain, swelling pain, severe pain". The point of the patient's tooth pain is marked on this line segment. This patient pain intensity rating value is the distance from 0 to this point. This method of assessing pain is simple, easy to understand, and highly feasible to operate.

The Eysenck Personality Questionnaire (EPQ) was developed by Professor H. J. Eysenck, a famous British psychologist, and the current version is available in two formats for children (7–15 years old) and adults (16 years old and above), covering a total of four parts respectively: E scale: measuring internal and external tendencies of personality; N scale: measuring emotional stability or

RETRACTED

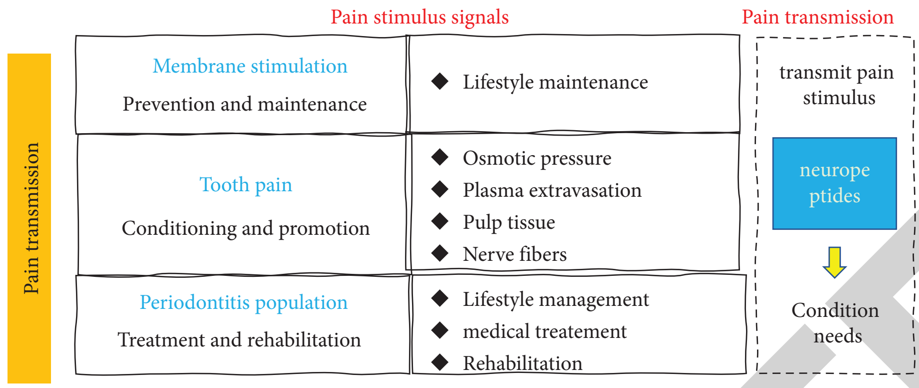

Figure 1: Pain transmission in periodontal disease.

neuroticism; *P* scale: measuring mental quality; *L* scale: testing the authenticity of the subject. This questionnaire has the advantages of being easy to understand and easy to test and having high validity and is one of the most influential psychological scales in the fields of psychology, medicine, education, and justice.

Psychotherapy and psychological interventions were first applied in the field of medicine by the famous psychologist Sigmund Freud in the 1920s, when he proposed the theory of "conscious and unconscious influence on their behavior". The concept of psychological intervention is the process of using theoretical knowledge of psychology to systematically influence the psychological factors and personality traits of a given subject to bring about a change in their behavior toward the desired goal. Dental pain is the most common complication of orthodontic treatment; the main step in the implementation of psychological intervention in the treatment process is to inform the patient in detail of each step in the treatment process, the cooperation he needs to make, and the possible problems and solutions to problems, so that he can relax, eliminate his anxiety and panic, and reduce or eliminate the possible pain in the orthodontic process, so that he can better cooperate with the treatment. The treatment will be carried out in the following way.

The following methods of psychological interventions are commonly used in current clinical studies:

(1) Psychological interventions for distraction.
(2) Group-based psychological interventions.
(3) Educational psychological interventions.
(4) Cognitive a behavioral psychological intervention, etc. This study proposes using the distraction method; the so-called distraction is to shift their attention through some behavioral methods.

It has been reported in the literature that chewing gum can make people feel relaxed and in a more relaxed state physically and mentally, diverting the attention of patients from the pain caused by the orthodontic appliance and also better cooperating with the treatment. Therefore, this study used the chewing gum method, which has the advantages of easy implementation, low cost, safety, no side effects, good taste, and clean mouth.

5. Test Method

5.1. Investigation of Factors Influencing Pain. Before treatment, the orthodontist first made a record of some basic information of the patients and eliminated the samples that did not fit the requirements of this study. Patients who met the requirements of this experiment and participated voluntarily were given EPQ assessment questionnaires and tested by the physician. The patients were then randomly divided into two groups according to the order of consultation: the control group (conventional treatment mode) and the observation group (psychological intervention on top of the conventional treatment mode).

The patients selected for treatment with fixed orthodontic appliances in this experiment were cases of malocclusion with mild (moderate) crowding of the teeth, and all patients were required to keep a notational model after the initial visit and to take photographs of the oral and maxillofacial surfaces, which were printed and perfected for preservation to verify and ensure that all cases met the requirements of this experiment. For patients included in this experiment to cement the brackets and bands of the aligners, the labial and buccal surfaces were the first acids etched for 40 seconds, the acid etchant was rinsed, the labial and buccal surfaces were chalky, blown dry, and insulated, the brackets and buccal tubes were cemented with a small cotton ball coated with 3M bonding agent, and a 0.012-inch titanium-nickel round wire was placed on the first archwire. All brackets were lightly ligated with 0.020 mm stainless steel ligature wire to ensure that the same force was released from the archwire, the end of the archwire was bent back at the end with a needle holder, individual teeth that were tilted or twisted very significantly were not forcibly ligated into the slot first, and a light force was taken to suspend the ligature to avoid excessive force on the teeth causing pain to the patient already interfered with this experiment.

After the patients finished the initial orthodontic sticky wear, the professional staff immediately communicated with the patients and parents in the control group, introducing the knowledge about the treatment plan, precautions, and the maintenance of oral hygiene during the treatment period after wearing in, to relieve the patients' anxiety or nervousness, and explaining to them the purpose and significance of this experiment. All participating patients fully understood the purpose of this clinical study, voluntarily participated in this research study, could fully understand the questionnaire, and could accurately and honestly answer the pain reflections caused by wearing their own orthodontic appliances. The questionnaire required the patients to record the changes in pain at home for 2 h, 6 h, 24 h, 48 h, 72 h, 96 h, and 7 d after wearing the orthoses. The visual analog scales (VASs) were used to measure the intensity of dental pain to quantify the patients' pain level for the orthodontic treatment. 0 cm is described as "no pain", 10 cm is described as "unbearable severe pain", and between 0 cm and 10 cm, the pain increases gradually and can be described as "soreness, swelling, mild pain". Patients marked the point on the line where the patient's tooth pain level was indicated, and the pain intensity was rated as the distance from 0 to that point. This questionnaire is to be filled out by the patient according to the preset time points and can be taken home. If there are minor patients, they can be supervised by their parents to complete this test together to ensure that no items are missed. Please bring the questionnaire with you when you return to the clinic so that it can be collected.

5.2. Introduction to Statistical Methods. The orthodontists involved in this experiment were all orthodontists with rich clinical experience, who fully understood the pain questionnaire and the Eysenck Personality Questionnaire, and were able to explain the issues related to the questionnaire carefully and accurately. Under the premise of establishing a good doctor-patient relationship, all patients should participate voluntarily and understand the purpose of the experiment and its clinical and scientific significance and have no interest in the relationship with themselves. All participating doctors should remind them to fill in the survey form and chew gum on time by telephone follow-up, respectively, and keep the test results confidential to protect patients' privacy, eliminate the subjects' concerns and worries, and ensure the authenticity of the test results. The physician regularly reminded all the participating patients by telephone to fill in the questionnaire form and chew the gum on time, as shown in Figure 2. In the curing satisfaction, pain contains not only pathophysiological factors and sensory effects but also multidimensional experiences, such as psychological factors, emotional effects, and individual subjective factors in the pain experience and the individual's unique experience. The measurement scores and data entry were done by one person, and another person was allowed to verify them.

After the questionnaires were returned, the same physician used the same ruler to measure the length of the pain point marked by the patient on the VAS from the 0 cm end:

(1) Use of SPASS 11.0 (WINDOWS version) statistical software
(2) Measures are expressed as mean ± standard deviation ($x \pm s$)
(3) One-way ANOVA was used between groups, and the significance level was set at $\alpha = 0.05$, with $P < 0.05$ as a significant difference

6. Experimental Results

6.1. Influence of Gender and Age Factors. Some scholars have found that the pain caused by the first orthodontic force is more pronounced in female patients than in male patients, while others have found that there is no significant gender difference. In terms of sensitivity to dental pain caused by orthodontic treatment after the first force, it is generally believed that there are gender differences in orthodontic pain mainly due to the following considerations: first, there are three essential differences in the physiological structure of men and women, namely, differences in the reproductive system, differences in the occurrence of changes in hormone levels, and differences in hormonal composition; second, there are also differences in the function and structure of sympathetic nerve tissue between men and women; third, it is influenced by the social and psychological factors. The experimental group lies in asking patients to chew gum (uniformly Green Arrow gum) regularly after the initial orthodontic appliances. The professional staff issued orthodontic pain questionnaires to the patients and then explained to the patients and their families the method of filling them out so that they could fill out the questionnaires accurately, timely, and without errors:

(1) Different upbringing, living environment, and social experiences make men and women express pain differently
(2) Men and women have different levels of sensitivity to pain for physiological reasons
(3) Differences in sociooccupational status of men and women result in different types of pain and different risks
(4) Men and women have had different experiences of pain in the past

In this study, there was no significant difference in pain between the control group and the test group by gender ($P > 0.05$). The reason why this result is inconsistent with the results of previous studies may be that although women are prone to anxiety and fear of pain in many cases, they have a high demand for beauty and are also very tolerant. Therefore, women's requirements for appearance and their awareness and acceptance of orthodontics may lower their pain threshold. In this study, due to time, manpower, and financial constraints, the sample content selected for this study was small and the observation time of the patients was relatively short, and in future work, it will be necessary for the latter to increase the information of large samples for further study. The pattern of influence of sociodemographic factors between the control and observation groups is as follows. The sociodemographic factors of the control and observation groups were compared, and no statistically significant differences were found between the two groups in terms of gender ($P = 0.412$) and age ($P = 0.723$) (as shown in Figure 3).

RETRACTED

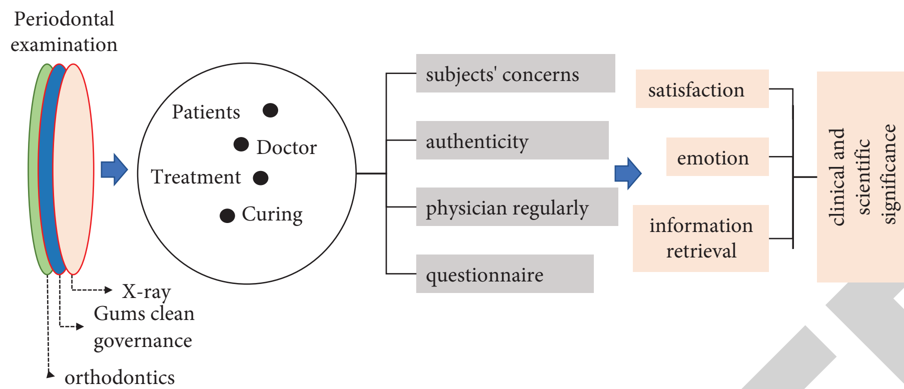

Figure 2: Examination procedure for patients with periodontal disease.

The basic pattern: no pain was felt; pain developed and gradually increased (the onset of tooth pain ranged from 1 h to 11 h, with an average time of 2 h) in 89 patients with the exception of 3 patients who did not experience pain. Reaching the peak (around 24 h), the pain gradually decreases, and then, there is no pain (see Figure 4) (pain scores at different time points in both groups of patients).

6.2. Factors Influencing Tooth Pain after Stressing with Meals. Comparing the pain values in one week between the two groups of patients of both sexes, the difference was not statistically significant ($P > 0.05$), which shows that dental pain is not related to gender. Comparing the pain values within one week between the two groups of patients of age, the difference was statistically significant ($P < 0.05$), which shows that dental pain is related to age (see Figure 5).

The International Society for the Study of Pain has standardized the definition of pain as follows: "pain is an unpleasant sensory and emotional sensation associated with substantial or underlying tissue damage". In this definition, pain contains not only pathophysiological factors and sensory effects but also multidimensional experiences, such as psychological factors, emotional effects, and individual subjective factors in the pain experience and the individual's unique experience. Pain as a subjective experience varies greatly among individuals, as evidenced by their perception and tolerance of pain, and orthopedic pain is also influenced by the patient's mental attention, emotions, pain experience, and genetics, making it difficult to evaluate. In psychology, the visual analog scale (VAS) was the first to quantify emotion as a method of evaluating acute and chronic pain, and its sensitivity is outstanding. Therefore, the visual analog scale was chosen to assess orthopedic pain in this experiment.

The Eysenck Personality Questionnaire (EPQ) is one of the most influential psychological scales in the fields of psychology, medicine, education, and justice because it is easy to understand, is simple to administer, and has high validity. The EPQ questionnaire consists of yes or no questions, and after the test is completed, the total score is calculated and converted into a standard score, where L is a validity scale, and if $L > 60$, the patient has strong masking

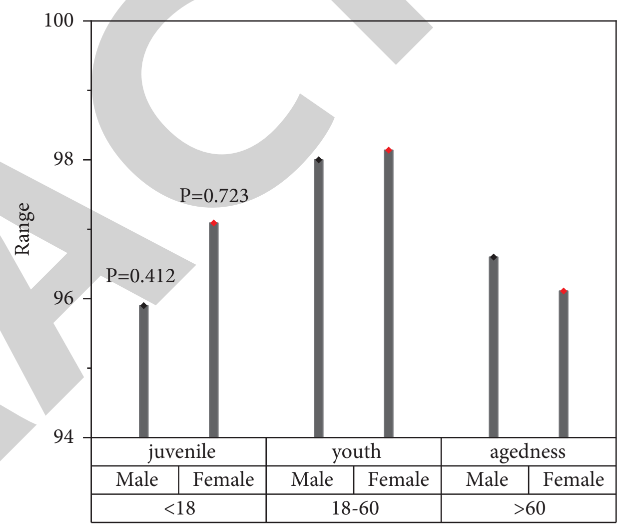

Figure 3: Comparison of sociodemographic factors between the two groups of patients.

information and is excluded. Since this experiment is a multifactor questionnaire, this study was conducted by testing the balance of sociodemographic factors between the control group and the experimental group, which to some extent reduces the unfavorable factors affecting the accuracy of this study and avoids research bias.

6.3. Influence of Psychological Factors. The pain levels of the observation group and the control group were different at different time points, the pain value of the control group was greater than that of the observation group at each time point, the difference was statistically significant ($P < 0.05$), and the specific scores of pain are shown in Figure 6. However, the trend of pain time change was basically the same in both groups, and the pain started to appear at about 2 h, and then, the pain time was gradually prolonged and the pain gradually increased until the pain level at 24 h. The intensity of pain gradually decreased until it disappeared completely on the seventh day.

Orthodontic pain is chronic pain with a short period, low intensity, and obvious individual differences. 90% to 95% of

RETRACTED

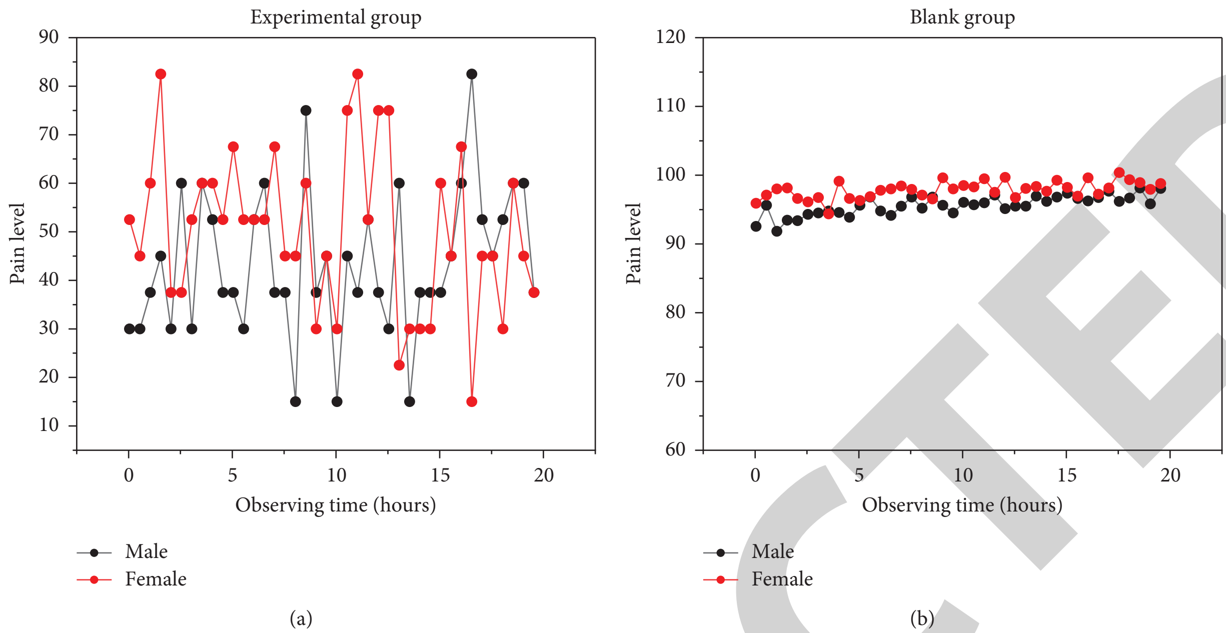

FIGURE 4: Pain scores at different time points for both groups of patients. (a) Experimental group. (b) Blank group.

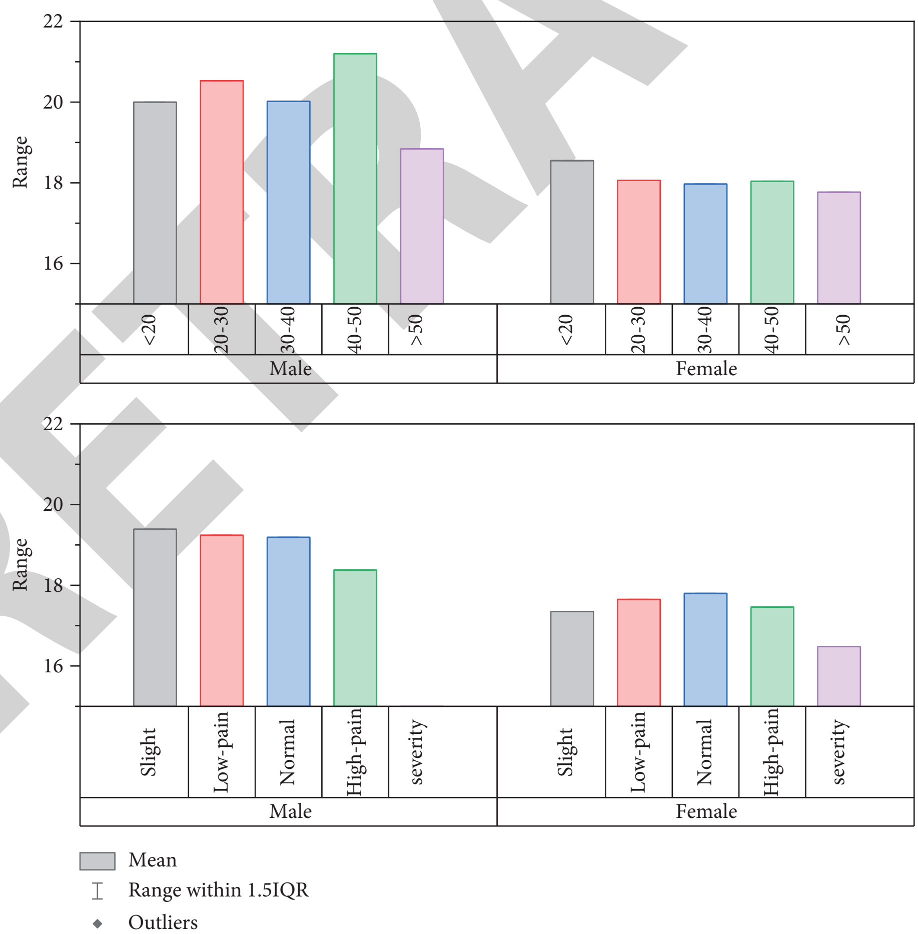

FIGURE 5: Changes in pain index by gender and age.

RETRACTED

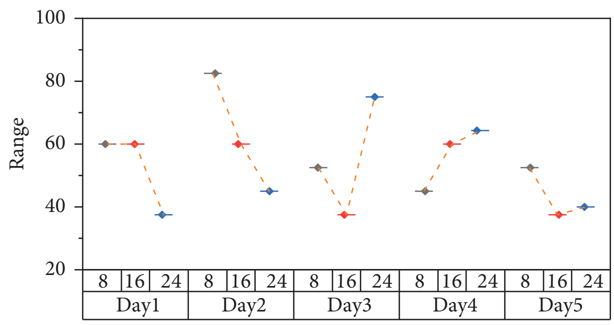

Figure 6: Effect of fear on pain rating.

orthodontic patients have experienced varying degrees of pain or discomfort during the orthodontic treatment process. The study showed that, at the beginning of the first force of the fixed orthodontic treatment, up to 94% of the population felt varying degrees of tooth pain, which usually manifested itself as tooth pain and discomfort in 2–3 h after the force was applied to the orthodontic patient, with the tooth pain peaking in 1–2 d. Then, the pain gradually disappeared in 3–7 d. The majority of orthodontic patients basically felt no pain on the 7th day. In this experiment, 2 h, 6 h, 24 h, 48 h, 72 h, 96 h, and 7 d after the initial orthodontic braces were selected as the observation time, mainly because the pain-related factors and pain mediators and pain receptors will change differently over time at these different time points of orthodontic therapeutic pain. A questionnaire was administered to the patients to obtain clinical information about their perceived pain after wearing orthodontic appliances. After data processing and statistical analysis, it was found that 3 of the 89 patients who wore straight wire orthodontic appliances with valid questionnaires complained of no pain, while the remaining patients complained of pain of varying degrees from 1 h to 11 h, with the average time of pain perception being more than 2 h, with the peak of pain perception occurring approximately 24 h after wearing the appliances, followed by a gradual decrease in pain by the seventh day. The majority of patients complained of no more pain, as shown in Figure 7. The results of this experiment are generally similar to those reported in the literature above. Now, it has been confirmed that this pain pattern affects the synthesis and secretion of neural factors, and the orthodontic therapeutic pain pattern is as follows: no pain felt, pain generated and gradually increased, peaked, the pain gradually decreased, and no pain. The pain gradually decreases and no pain.

The mechanisms involved, according to available literature and experimental reports, are probably:

(1) After wearing the orthodontic appliance, the tensioned fibers on the tensioned side of the tooth impact the peripheral nerve fiber endings and the nerve endings of the periodontal membrane and fail to conduct the pain sensation, which is restored after about 2 hours.

(2) Wearing the orthodontic appliance may cause temporary local ischemia or aseptic necrosis, resulting in a decrease in the threshold of pain perception and an increase in pain after about 1 day, and then, with the extension of wearing time and completion of tooth movement, the actual force exerted by the orthodontic appliance on the teeth decreases, the pain receptors of the teeth and periodontium regain their function, and the pain threshold rises and approaches the original level, but the receptors fully regain their ability to discriminate between painful stimuli. The ability to discriminate between painful stimuli requires the end of orthodontic treatment to be reached.

(3) The periodontal ligament is stretched to release some chemical mediators, which are distributed in different concentrations in the periodontal membrane at different times, producing different painful stimuli.

(4) The pain produced by the force exerted on the teeth after wearing the orthodontic appliance is divided into immediate pain and delayed pain depending on the time of generation. Immediate pain may be related to the pressure response to the periodontal ligament caused by the force exerted after wearing the orthodontic appliance; delayed pain may be due to the periodontal membrane nerve fiber endings being in a hypersensitive state, often produced several hours after the first force is exerted. The occurrence of delayed pain is mainly related to the chemical mediators produced by the nerve endings in the periodontium after stimulation by force and the neuropeptides released by the periodontal pain receptors after stimulation by orthodontic force.

6.4. Factors Influencing Pain during Treatment. With the awareness that patients with malocclusion are primarily interested in the aesthetics of their teeth, there is a significant difference in the response of adult and adolescent patients to orthodontic pain. Medical experts also have different opinions regarding the age-related differences in therapeutic pain and the age-related differences in tooth pain caused by the first force applied to orthodontic treatment. The theoretical basis for these opinions may be the fact that adolescent patients are more likely than adults to experience pain after the first force, probably because adolescents are not yet psychologically developed and are prone to psychological discomfort from orthodontic pain; on the other hand, it may be that adolescent patients' newly erupted teeth are young permanent teeth and their dental and periodontal tissues are not yet mature, so they are more active in the tissue alterations caused by orthodontic force. On the other hand, it may be due to the fact that the periodontal and periodontal tissues of the young permanent teeth have not yet developed and are not mature enough for the tissue alteration caused by the orthodontic force, or that there is a difference in the level of perceptual threshold of periodontal and pulpal tissues to the tooth pain caused by the force in different age groups, or that the psychological tolerance of different age groups is different. In this experiment, there

RETRACTED

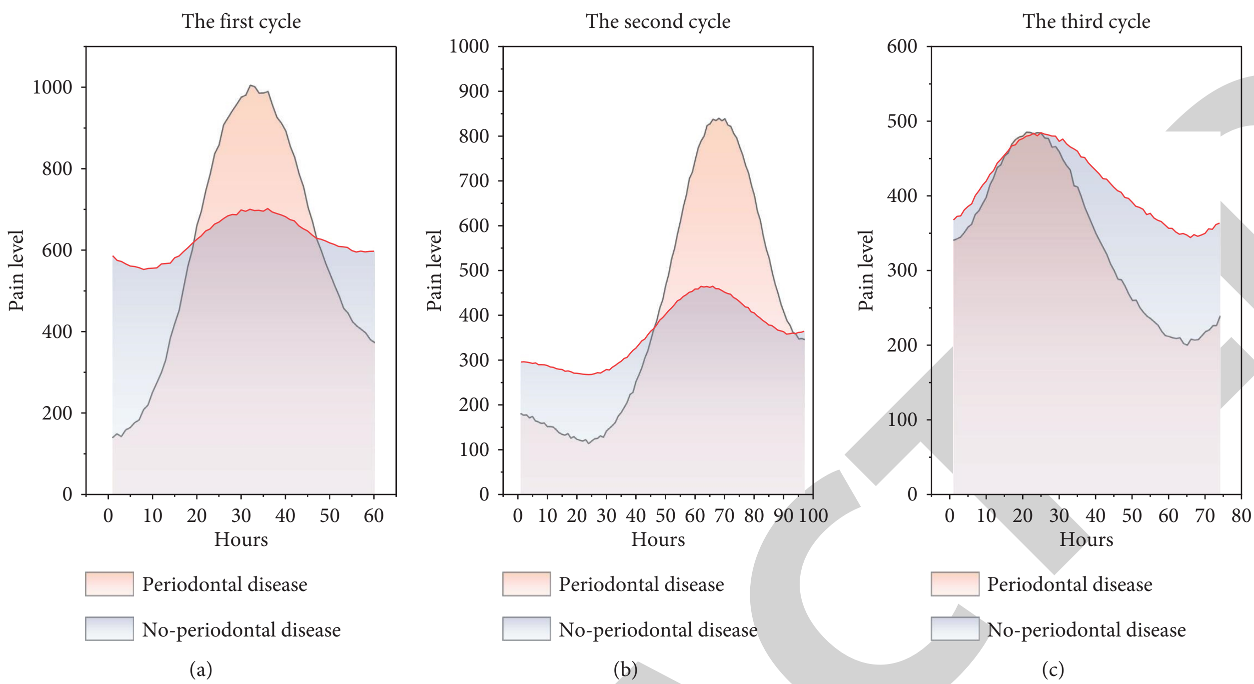

Figure 7: Cycle of pain change. (a) The first cycle. (b) The second cycle. (c) The third cycle.

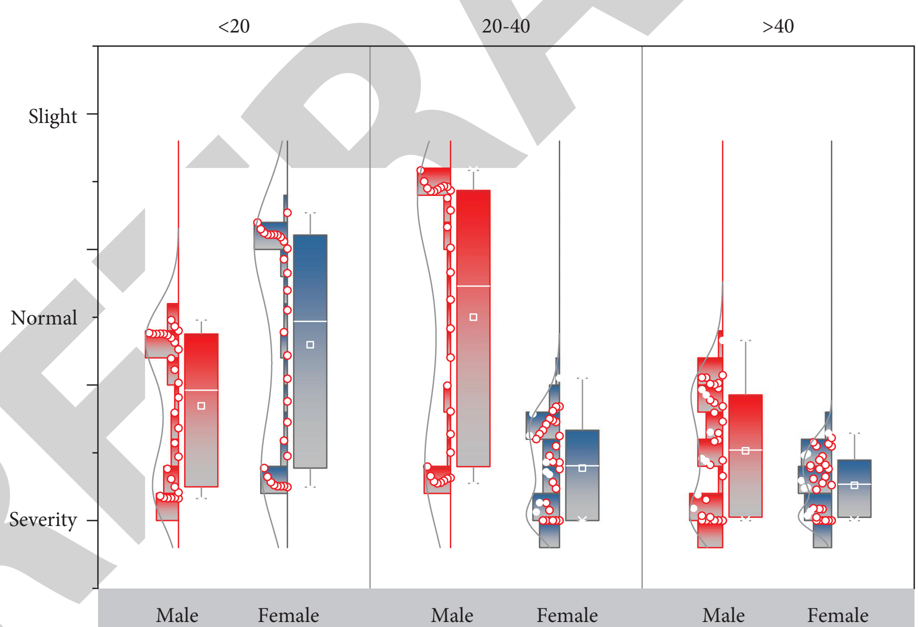

Figure 8: Pain levels in patients of different ages.

was a significant difference ($P < 0.05$) in the pain level between the two groups of patients of different ages, as shown in Figure 8, where the pain level of adult patients was higher than that of adolescent patients. This may be due to the fact that although adult patients have mature dental pulp and periodontal tissues and are in a social environment with better compliance and self-control than adolescents, they show more concern about the treatment course, efficacy, and possible risks of the whole orthodontic treatment process, repeatedly consult the doctor about everything, and sometimes lack trust in the doctor and are under great psychological pressure, which leads to the perception of pain by periodontal tissues and dental pulp. This leads to a lower threshold of pain perception in the periodontal tissues and dental pulp and thus a stronger sensitivity to pain than in adolescents. The pain caused by the first orthodontic force contains not only pathophysiological factors and sensory effects but also multidimensional experiences, such as psychological factors, emotional effects, individual subjective factors, and unique experiences in the pain experience.

RETRACTED

Recent research data suggest that the psychological fluctuations caused by tooth movement after force may precede the pain sensation induced by the pain receptors and that the psychological stress experienced by the patient during the treatment may also have an impact on the pain perception. Chewing gum can distract patients and is one of the methods of psychological intervention. In this experiment, the chewing gum method was used to test the effect of psychological factors on pain, and from the comparison of the control and experimental groups, it was seen that chewing gum significantly reduced the level of pain that occurs during orthodontic treatment. Therefore, psychological factors are one of the most important factors influencing dental pain after orthodontic stress.

The results of this experiment showed that the pain pattern using chewing gum changed in the same trend as the control group and was not statistically significant, but this psychological intervention method was able to reduce the intensity of orthodontic therapeutic pain. Therefore, chewing gum did not change the essence of the process of perceived pain and the basic pattern of occurrence and progression of pain in patients after the first force of the initial orthodontic appliance, but it could alleviate the degree of pain. The reasons for this may be the following:

(1) Chewing gum can make people feel relaxed and in a more relaxed state physically and mentally, diverting the patient's attention from the pain caused by the orthodontic appliance and also better cooperating with the treatment

(2) Chewing gum can accelerate the blood circulation inside and outside the periodontal membrane, promote periodontal lymphatic circulation, further reduce and prevent the production of inflammatory chemical mediators and neuropeptides, and reduce the occurrence of tissue edema

(3) Chewing gum to accelerate blood flow can also block the transmission of pain signals via nerve impulses to relieve pain

7. Conclusion

The purpose of the paper was to investigate the basic patterns and influencing factors of dental pain in fixed orthodontic patients within seven days after the initial wearing of straight arch aligners and the analysis of the effect of psychological intervention on dental pain using the visual simulation scoring method. According to the inclusion criteria of the experimental design, 89 patients who visited the Department of Orthodontics of Hospital for malocclusion were randomly divided into observation group and control group, and the observation group used chewing gum as psychological intervention, while the control group did not use any intervention. The effect of psychological intervention on periodontal pain was analyzed. The results of the paper were that all but 3 of the 89 patients had no pain, and all the patients had different degrees of dental pain at different points in time. Dental pain was related to age, $P < 0.05$, and the difference was statistically significant; it was not related to gender, $P > 0.05$, and the difference was not statistically significant. The trend of pain change was the same in the observation and control groups, and the control group was greater than the observation group at all time points, $P < 0.05$; the difference was statistically significant.

Data Availability

The data used to support the findings of this study are available from the corresponding author upon request.

Conflicts of Interest

The authors declare that there are no conflicts of interest.

Acknowledgments

This work was supported by the First Affiliated Hospital of Guizhou University of Traditional Chinese Medicine.

References

[1] F. Y. S. Basha, D. Ganapathy, and S. Venugopalan, "Oral hygiene status among pregnant women," *Research Journal of Pharmacy and Technology*, vol. 11, no. 7, pp. 3099–3102, 2018.

[2] T. Dietrich, P. Ower, M. Tank et al., "Periodontal diagnosis in the context of the 2017 classification system of periodontal diseases and conditions - implementation in clinical practice," *British Dental Journal*, vol. 226, no. 1, pp. 16–22, 2019.

[3] M. Sanz, A. Ceriello, M. Buysschaert et al., "Scientific evidence on the links between periodontal diseases and diabetes: consensus report and guidelines of the joint workshop on periodontal diseases and diabetes by the International Diabetes Federation and the European Federation of Periodontology," *Journal of Clinical Periodontology*, vol. 45, no. 2, pp. 138–149, 2018.

[4] R. J. Lamont, H. Koo, and G. Hajishengallis, "The oral microbiota: dynamic communities and host interactions," *Nature Reviews Microbiology*, vol. 16, no. 12, pp. 745–759, 2018.

[5] A. A. Alhassani, F. B. Hu, Y. Li, B. A. Rosner, W. C. Willett, and K. J. Joshipura, "The associations between major dietary patterns and risk of periodontitis," *Journal of Clinical Periodontology*, vol. 48, no. 1, pp. 2–14, 2021.

[6] M. Sanz, A. Marco del Castillo, S. Jepsen et al., "Periodontitis and cardiovascular diseases: consensus report," *Journal of Clinical Periodontology*, vol. 47, no. 3, pp. 268–288, 2020.

[7] T.-J. Oh and S.-H. Yu, "Treatment of stage I-iii periodontitis-the EFP S3 level clinical practice guideline," *Journal of Clinical Periodontology*, vol. 47, no. 47, pp. 4–60, 2020.

[8] A. A. Alhassani, F. B. Hu, E. B. Rimm et al., "Dietary flavonoid intake and risk of periodontitis," *Journal of Periodontology*, vol. 91, no. 8, pp. 1057–1066, 2020.

[9] D. M. Proctor, K. M. Shelef, A. Gonzalez et al., "Microbial biogeography and ecology of the mouth and implications for periodontal diseases," *Periodontology 2000*, vol. 82, no. 1, pp. 26–41, 2020.

[10] F. D'Aiuto, N. Gkranias, D. Bhowruth et al., "Systemic effects of periodontitis treatment in patients with type 2 diabetes: a 12 month, single-centre, investigator-masked, randomised trial," *The Lancet Diabetes & Endocrinology*, vol. 6, no. 12, pp. 954–965, 2018.

RETRACTED

Hindawi
Journal of Healthcare Engineering
Volume 2023, Article ID 9870814, 1 page
https://doi.org/10.1155/2023/9870814

Retraction

Retracted: Spinal Biomechanical Modelling in the Process of Lumbar Intervertebral Disc Herniation in Middle-Aged and Elderly

Journal of Healthcare Engineering

Received 10 October 2023; Accepted 10 October 2023; Published 11 October 2023

Copyright © 2023 Journal of Healthcare Engineering. This is an open access article distributed under the Creative Commons Attribution License, which permits unrestricted use, distribution, and reproduction in any medium, provided the original work is properly cited.

This article has been retracted by Hindawi following an investigation undertaken by the publisher [1]. This investigation has uncovered evidence of one or more of the following indicators of systematic manipulation of the publication process:

(1) Discrepancies in scope
(2) Discrepancies in the description of the research reported
(3) Discrepancies between the availability of data and the research described
(4) Inappropriate citations
(5) Incoherent, meaningless and/or irrelevant content included in the article
(6) Peer-review manipulation

The presence of these indicators undermines our confidence in the integrity of the article's content and we cannot, therefore, vouch for its reliability. Please note that this notice is intended solely to alert readers that the content of this article is unreliable. We have not investigated whether authors were aware of or involved in the systematic manipulation of the publication process.

In addition, our investigation has also shown that one or more of the following human-subject reporting requirements has not been met in this article: ethical approval by an Institutional Review Board (IRB) committee or equivalent, patient/participant consent to participate, and/or agreement to publish patient/participant details (where relevant).

Wiley and Hindawi regrets that the usual quality checks did not identify these issues before publication and have since put additional measures in place to safeguard research integrity.

We wish to credit our own Research Integrity and Research Publishing teams and anonymous and named external researchers and research integrity experts for contributing to this investigation.

The corresponding author, as the representative of all authors, has been given the opportunity to register their agreement or disagreement to this retraction. We have kept a record of any response received.

References

[1] X. Zhang, Z. Zhao, C. Niu et al., "Spinal Biomechanical Modelling in the Process of Lumbar Intervertebral Disc Herniation in Middle-Aged and Elderly," *Journal of Healthcare Engineering*, vol. 2021, Article ID 2869488, 12 pages, 2021.

Hindawi
Journal of Healthcare Engineering
Volume 2021, Article ID 2869488, 12 pages
https://doi.org/10.1155/2021/2869488

RETRACTED

Research Article

Spinal Biomechanical Modelling in the Process of Lumbar Intervertebral Disc Herniation in Middle-Aged and Elderly

Xinyu Zhang,[1] **Zhe Zhao**,[2] **Chunlei Niu**,[1] **Zengbiao Ma**,[1] **Jianlei Hou**,[1] **Guanjun Wang**,[2] **and Miao Tang**[3]

[1]*The Department of Orthopedics, The Third Medical Center of PLA General Hospital, Beijing 100039, China*
[2]*Senior Department of Orthopedics, The Fourth Medical Center of PLA General Hospital, Beijing 100048, China*
[3]*The Department of Orthopaedics, Suzhou Hospital of Anhui Medical University, Suzhou, Anhui 234099, China*

Correspondence should be addressed to Guanjun Wang; doctorwxa@163.com and Miao Tang; tangmiao@ahmu.edu.cn

Received 26 August 2021; Revised 9 October 2021; Accepted 11 October 2021; Published 29 October 2021

Academic Editor: Kaijian Xia

Copyright © 2021 Xinyu Zhang et al. This is an open access article distributed under the Creative Commons Attribution License, which permits unrestricted use, distribution, and reproduction in any medium, provided the original work is properly cited.

Lumbar disc herniation is one of the common clinical diseases of the lower lumbar spine in orthopedics. The purpose is to remove the herniated disc nucleus pulposus tissue, remove the compressed part of the disease, and relieve symptoms, such as nerve pain. In the past, biomechanics research mostly relied on in vitro measurements, but the complicated internal environment of the human body prevented us from further measurement and research. However, with the development of computer technology, the use of computer CT scanning, software three-dimensional reconstruction, and displacement study three-dimensional spine biomechanics method makes the research of biomechanics into in vitro simulation stage and has gradually become the focus of current research. The postoperative biomechanics was simulated and the comparison model was established at the same time. At the same time, we combined the clinical follow-up data and studied the clinical data for the treatment of postoperative recurrence of lumbar disc herniation. We compared and analyzed the initial operation method and the experimental results and obtained the prevention of recurrence. The results showed that when one inferior articular process was removed, the lumbar spine appeared unstable to rotate to the opposite side; when one inferior articular process was completely removed, the movement of the lumbar spine in all directions was unstable. Better research on the biomechanical properties of the spine will help the diagnosis and treatment of clinical lumbar disc herniation. Therefore, when performing posterior lumbar spine surgery, not only should the exposure of the surgical field and thorough decompression be considered, but also the biomechanical properties of the lumbar spine should be comprehensively evaluated.

1. Introduction

Lumbar disc herniation is one of the common clinical lower lumbar diseases in orthopedics. Severe pain and inconvenience not only affect the quality of life of the patient, but also bring a huge burden to the family and society. The most fundamental reason for this symptom is the disease of the intervertebral disc. After degeneration, the nucleus pulposus is degenerated and frees the rear dural sac, nerve roots, and other tissues [1]. With the development of computer technology, the use of computer CT scanning, three-dimensional reconstruction, spine biomechanics segmentation and assignment analysis, mechanical loading, stress analysis, and displacement study of three-dimensional spine biomechanics methods makes the research of biomechanics enter the stage of in vitro simulation and gradually become current research hotspots [2]. Spinal biomechanics method, also known as spine biomechanical analysis, is a commonly used and efficient numerical calculation method for the design, analysis, and experiment of continuous physical systems in engineering technology. It is suitable for solving problems with complex physical and geometric conditions [3]. The lumbar spine is a heterogeneous structure with irregular shape and complex mechanical characteristics. The traditional method of using specimens will be subject to many restrictions, and the internal stress changes of the intervertebral disc cannot be measured. The platform can give the intervertebral disc superelasticity, bony structure elastoplasticity, and ligament viscoelastic material properties [4]. Mitchell et al. [5] applied the spinal biomechanics analysis method to spinal biomechanics for the first time, but their model had no posterior structure and only involved complete intervertebral joints. Desmoulin et al. [6] made up for this shortcoming in the later stage, adding the posterior structure to the biomechanical model of the lumbar spine and carrying out the biomechanical analysis of the spine. As one of the research methods of biomechanics, spinal biomechanical analysis has been widely used in the biomechanical analysis of various tissues of the spine and has become a research hotspot in lumbar spine biomechanics [7].

Biomechanical studies have shown that in the process of applying cyclic loads, not giving the necessary time for the recovery of the intervertebral disc can lead to cumulative damage. Lumbar disc disease causes low back pain and other uncomfortable symptoms, which have seriously affected the quality of life of humans [8]. Spinal biomechanics analysis method is currently the most popular tool for studying spinal biomechanics. The more important point is that it can change the input parameters and analyze the results [9]. At present, a variety of biomechanical models of the lumbar spine have been gradually established, which can fully and accurately reflect the internal stress of the lumbar spine, so that the modeling method based on medical images has been widely used [10, 11]. Wu et al. [12] changed the elastic modulus and Poisson's ratio to establish L3-L4 degenerative intervertebral discs and applied an axial load of 0.3 MPa, which was compared with the normal intervertebral discs in the data review. Widyasari et al. [13] established the L4-L5 normal spine biomechanical model and the intervertebral disc herniation model, applied loads under five working conditions including flexion, extension, and torsion, and found that the contact force of the facet joints of the herniated disc model was greater than normal model. Suśtersic et al. [14] proved that the load of the facet joints increases and the bearing capacity of the herniated intervertebral disc decreases, which leads to a decrease in the stability of the lumbar spine. Jezek et al. [15] considered the osmotic pressure change characteristics of the intervertebral disc as one of the key considerations when establishing a three-dimensional spine biomechanical model, and the tissue expansion pressure determines part of the osmotic pressure. The stress of the liquid substance in the intervertebral disc increases, but the stress of the solid substance decreases accordingly. The previous research believed that the water was completely pressed out and would not bear the pressure, and the pressure was fully borne by the solid [16–19]. These studies can visually observe the stress and strain characteristics of intervertebral disc degeneration and deepen the understanding of the mechanism of low back pain and lower extremity pain caused by the protrusion of the nucleus pulposus after the rupture of the annulus fibrosus and the pain of the lower limbs and provide necessary supplements to clinical research [20–22]. Wang et al. [23] studied the load transfer mode and stress distribution with the help of a two-dimensional spine biomechanical model. This simplified intervertebral disc degeneration model shows a slight degeneration of the intervertebral disc. Although it fails to explain the changes that occurred early in the process of intervertebral disc degeneration, the study shows the initial stage of the degeneration process [24–27].

In order to better solve the existing problems, this article intends to use Magnetic Resonance Imaging (MRI) and CT images for 3D reconstruction and then use the finite element method to analyze the stress and displacement of the spine model. This article simulates various surgical methods for the treatment of lumbar disc herniation, removing the bone and ligament structure at the back of the spine and studying the changes in the stability of the spine under different conditions. After re-sampling, layer-by-layer division, filling, filtering, and smoothing of the images, all layers of images are combined to build a three-dimensional model of the spine. In the project, the young normal spine, the young diseased spine, and the elderly normal spine were modeled separately. Different models have differences in material properties and physical forms. After modeling, the spine biomechanical analysis is performed on the model. After modeling, the same load should be applied to different models to simulate various movements of the spine, and the results obtained should be analyzed. This article discusses which surgical method will simulate spinal instability and provides a certain theoretical basis for the selection of surgical methods. The main analysis process involves the comparison of the stress and displacement of the young normal spine model and the young diseased spine model under the same load and the comparison of the old normal spine model and the young normal spine model under the same load.

2. Construction of a Biomechanical Model of the Spine in the Process of Lumbar Disc Herniation in Middle-Aged and Elderly People

2.1. The Distribution of Lumbar Disc Herniation. The lumbar intervertebral disc is located between the two lumbar vertebral bodies. It is a very flexible viscoelastic tissue between the vertebral bodies. It forms lumbar motion segments with the surrounding ligaments, muscles, and fascia to maintain the mobility and stability of the lumbar spine. The lumbar intervertebral disc can transfer the load, balance the body, and stabilize the spine. Figure 1 shows a schematic diagram of the structure distribution of lumbar disc herniation.

However, the main function of the spine also depends on the integrity of the intervertebral disc. The understanding of the stress and strain distribution of the lumbar spine will help the clinical diagnosis and treatment of the lumbar intervertebral disc. Compared with other parts of the spine, the intervertebral disc bears more pressure, which leads to the extremely common lumbar disc herniation.

$$f(x) = \{x(1), x(2), \ldots, x(n) \mid n \in R\}. \quad (1)$$

When the material to be studied is certain, the basic variables of mechanics should include the following: displacement, stress, and strain. The equations established

RETRACTED

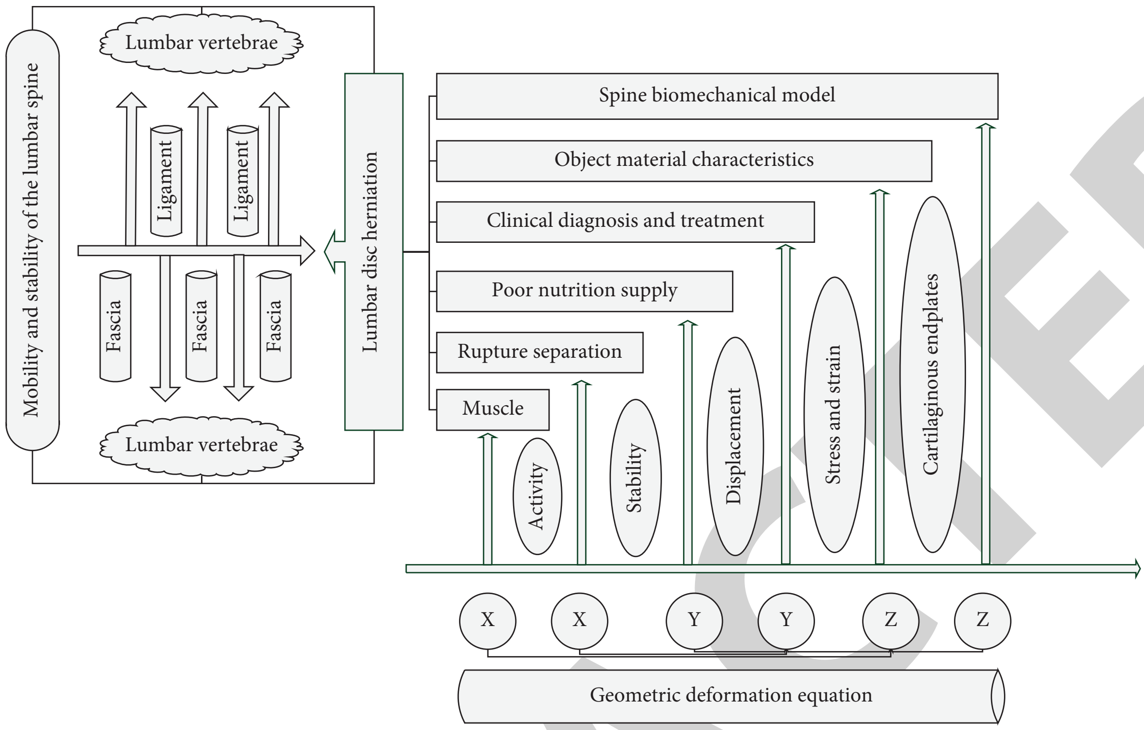

Figure 1: Schematic diagram of the structure distribution of lumbar intervertebral disc herniation.

during the research should be universal equations. Therefore, the small voxel is usually used as the research content. The basic variables used in the description of spine biomechanics analysis should include displacement, stress, and strain.

$$\begin{cases} u(x,y) = \overline{u}(x,y) \\ v(x,y) = \overline{v}(x,y) \end{cases}, x, y \in \overline{S}(\overline{u}). \tag{2}$$

We study the relationship between various variables when the tiny voxels are subjected to external forces, including the displacement, stress, and strain of the tiny voxels, and construct equations. The equation includes three major categories, namely, balance equation, geometric equation, and physical equation. Among them, the main focus of the balance equation is the force condition, the geometric equation is the embodiment of the deformation of the object:

$$\begin{gathered} \frac{\partial u}{\partial x} + \frac{\partial v}{\partial y} + \frac{\partial w}{\partial z} = 0, \\ \sigma(x,y) = \frac{1}{E} \times (\varepsilon(x,x) - t(\varepsilon(y,y))). \end{gathered} \tag{3}$$

In order to describe the complex geometric characteristics of the object, the material characteristics of the object, and the given force and constraint conditions, variables, equations for description, and the boundary of the object are used. The commonly used three types of equations in spine biomechanics analysis refer to equations that describe the balance between forces, geometric deformation equations, and physical equations that describe material properties. The boundary conditions are divided into two categories, namely, the displacement boundary and the external force boundary.

$$\begin{cases} \varepsilon(x,x) = \dfrac{\partial u}{\partial x} \\ \varepsilon(y,y) = \dfrac{\partial v}{\partial y}. \\ \varepsilon(z,z) = \dfrac{\partial w}{\partial z} \end{cases} \tag{4}$$

The intervertebral disc is composed of cartilaginous endplates (CEP), annulus fibrosus (AF), and nucleus pulposus (NP). Once the intervertebral disc is under abnormal pressure, the permeability of the endplate and cancellous bone will change, which will affect the nutrient supply of the annulus fibrosus, which in turn leads to the degeneration of the intervertebral disc. If the pressure of the lumbar spine is high and concentrated in this area, the annulus fibrosus will rupture due to poor nutrient supply, and then the nucleus pulposus will be separated along the ruptured area, and finally the intervertebral disc will be squeezed out.

2.2. Spinal Biomechanical Model. There are three methods for spine biomechanics modeling: geometric modeling, three-dimensional coordinate instrument modeling, and image modeling. Geometric modeling is quick and simple. It is constructed by geometric form and size, which is suitable for objects with relatively regular shapes; 3D coordinate instrument modeling is constructed based on the spatial

RETRACTED

coordinates of the specimen. Image modeling obtains image data through CT, MRI, etc., which is suitable for the construction of irregular models, and this method is widely used.

$$\partial h(\partial x, \partial y, \partial z) = \begin{bmatrix} \dfrac{\partial h}{\partial x \partial x} & 0 & \cdots & \dfrac{\partial h}{\partial x \partial y} \\ 0 & \dfrac{\partial h}{\partial x \partial x} & \cdots & 0 \\ \cdots & \cdots & \cdots & \cdots \\ \dfrac{\partial h}{\partial x \partial y} & 0 & \cdots & \dfrac{\partial h}{\partial x \partial x} \end{bmatrix}. \quad (5)$$

The initial finite element analysis was used to analyze aircraft structural problems, and later engineers defined it and extended it to large structures. A structure can theoretically be decomposed into many small and discretized regions. These small regions are called finite elements. If an object moves relative to its interior when subjected to an external force, such an object is called a deformed body, which is closely related to the material properties of the deformed body itself.

Figure 2 shows the spine biomechanical model architecture. The composition of each element is called a unit, and the unit is composed of the nodes that make up the unit. We can use the computer to define the material properties of the element, deal with the nodes of the element, and at the same time constrain and load the nodes, define the boundary conditions, calculate the element equations mathematically, and establish the equations of the object to be solved so that for complex materials, we approximately solve the internal and external structural mechanics problems of objects such as structures.

$$\{\sigma(x,x), \sigma(y,y), \sigma(z,z)\} \longrightarrow \{\varepsilon(x,y), \varepsilon(y,z), \varepsilon(z,x)\},$$
$$\frac{p'(x) - p(x)}{p(x)} = \frac{\partial u/\partial x dx}{dx} = \frac{\partial u}{\partial x}. \quad (6)$$

If the deformable body is divided according to the angle of the geometric complexity of the object, it can be divided into two categories: one is the deformable body of simple shape, and the other is the deformable body of arbitrary shape. Arbitrary deformable body is the main research content, mainly studying its variables and equations. The earliest biomechanical model of the spine was a two-dimensional linear model. Later, with the development of computer software and hardware, nonlinear models were developed, and various analysis software versions gradually improved, which further extended the two-dimensional linear model to the three-dimensional nonlinear model.

At the same time, the spine biomechanics method itself is no longer a relatively independent study of the mechanical properties of the spine, but cleverly combined with other disciplines and other methods to make the research results more accurate and reliable. Table 1 shows the unit properties of the spine biomechanics model. Spine mobility and displacement can be measured in vitro using experimental methods, but internal stress changes can only be measured by mathematical methods such as spine biomechanics, such as stress changes inside the vertebral body, cancellous bone deformation inside the vertebral body, and microfractures. At the same time, spine biomechanics analysis can also evaluate the effectiveness of internal fixation and effectively modify the internal fixation to reduce stress concentration and fatigue.

However, other details must be described in addition to this, such as symmetrical sliding boundaries and other special situations that often require special descriptions, which cannot be expressed by using units alone. Other methods, such as coupling equations or constraint equations, can be used to establish special connections to make up for the details of the degree of freedom connection that the element cannot express. When performing spine biomechanical analysis on actual problems, sometimes it is necessary to show, although the value of the degree of freedom is unknown, the value of multiple degrees of freedom is equal. Coupling can be used to realize this relationship. There are not only main degrees of freedom but also other degrees of freedom in the concentration of coupled degrees of freedom, and the analysis matrix has only main degrees of freedom. The value of the main degree of freedom can be calculated, and the obtained value can be assigned to other degrees of freedom.

2.3. Model Weight Factor Optimization. This article is to directly read the CT image into Simpleware and then use this software to segment and process the image to generate a three-dimensional model of the spine. The biomechanical model of the spine is an abstract representation of the actual object to be studied, which can abstract the nature of the object to be studied. In ANSYS, the model needs to be meshed, and the model is divided into units. The construction process of the spine biomechanics model can be subdivided into the following steps: first, we name the working files and then define the unit type of the model. Here, the properties of all materials must be clarified, and finally the spine biomechanics model is constructed. The following tasks can be done in the processor: we clarify the type of solution this time, set the spinal biomechanics analysis options, apply the load, select the load step, and complete the calculation solution. The steps of loading and solving can also be subdivided. After the spine is strong internally fixed, the stress shielding effect appears, and the damaged front column structure loses the function of bearing the main load. These are the results of stress concentration. We must clarify the analysis type and analysis options, then apply a load on the object to be analyzed, and finally select the load step option and perform the solution calculation.

In the 3D view, we can generate a preview, preview the generated three-dimensional model, and export the three-dimensional model after confirming that the model does not

RETRACTED

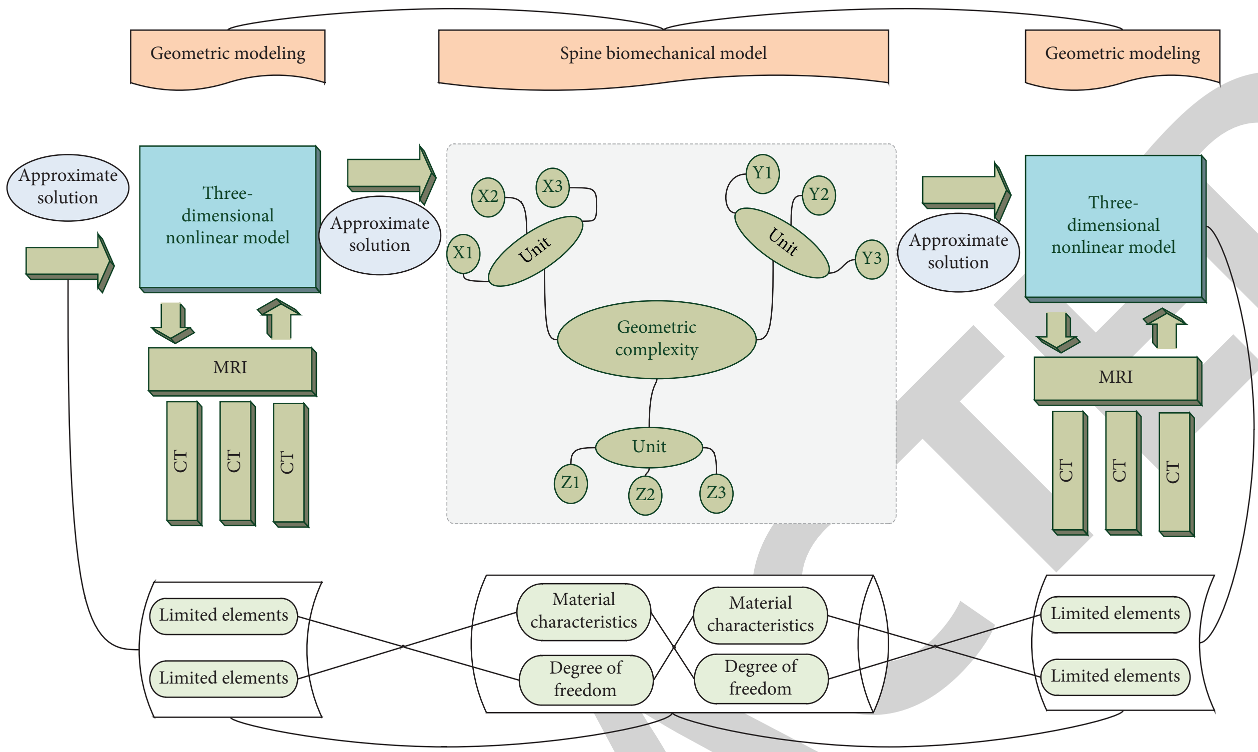

Figure 2: The architecture of the spine biomechanical model.

Table 1: Unit attributes of the spine biomechanical model.

Organizational material	Density (10^{-6} kg/mm^3)	Young's modulus (MPa)	Poisson's ratio
Posterior longitudinal ligament	1.12	9.41	0.41
Anterior longitudinal ligament	1.20	10.91	0.39
Annulus	1.32	5.71	0.49
Cancellous bone	1.81	292	0.27
Compact bone	1.23	14320	0.41

need to be modified. Presmoothing can be done according to the default settings of the options, and then the model can be exported. In ScanIP, only the surface of the spine model is meshed, and the interior of the model body is not partitioned. Therefore, after the model exported from ScanIP is imported into ScanFE, the smoothing and meshing must be optimized first. Figure 3 shows a fan chart of the degree of freedom of the spine biomechanical model. By setting model smoothing parameters, a smooth, volume meshed three-dimensional model can be obtained. All the degrees of freedom and nodes in the model should appear, and the situation where any node or degree of freedom does not appear should be avoided. If there are degrees of freedom at a node, this node should be connected to other elements with the necessary degrees of freedom. The command can be used to derive a new set of equations from the existing constraint equations. In order to generate a new constraint equation here, a new node number will appear in the existing set of constraint equations, but the coefficients and labels should remain the same as the original ones. It is also necessary to pay attention to the constraint equation: the theory of small rotation is the theoretical basis of the constraint equation. Therefore, when there is a large rotation, the major changes in the degree of freedom should be restricted to avoid unexpected situations.

Table 2 shows the weighting factor distribution of the spine biomechanics model. After completing the spine biomechanics calculations, we need to view the results of the calculations. At this time, a postprocessor is used to view the calculation results. The postprocessing here is to observe and analyze the calculation results, and the results can be used to judge whether the calculation is correct, so this step is also very important. There are two types of postprocessors, one is to view static results, that is, general-purpose processors. Another type of processor is to view the dynamic results, that is, the time postprocessor. For the stability of the internal fixation system, the better the screw implantation, the better, but if it is too deep or even penetrates the cortical bone, it will greatly increase the incidence of complications. It is considered that 80% is more appropriate depth. The former is abbreviated as POST1, to view the results over a certain period of time or the results under a certain frequency. The latter is abbreviated as POST2, and what you view is the result of specifying a certain point, and this result changes

RETRACTED

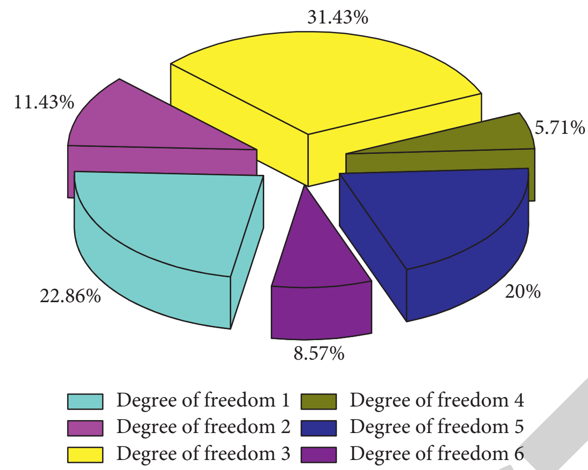

FIGURE 3: Fan chart of the proportion of degrees of freedom of the spine biomechanical model.

RETRACTED

dynamically over time. Therefore, it can be seen that the results viewed by the general post-processor are the results at a fixed point in time, but the results viewed by the time history postprocessor are the results that dynamically change with time.

3. Results and Analysis

3.1. Data Processing of Lumbar Intervertebral Disc Detection. In this paper, SPSS 13 statistical software is used, and the data obtained are expressed. The comparison of the sample means between each group uses a one-way analysis of variance. We analyze whether there are significant changes in the status of various simulated operations compared with normal spine specimens. The main tool used for data processing is Simpleware software, which consists of three parts. Here, two modules, ScanIP and ScanFE, are mainly used. After the modeling is completed, the material of the spine model is set according to the physical characteristics of the actual human spine so that the model is as close to the actual human spine as possible. Because ANSYS has a very good openness, it can take advantage of this feature of ANSYS to carry out secondary development, modify and expand the functions of ANSYS, and develop a special spine biomechanical analysis tool for the human spine model. Finally, the model is imported into ANSYS, and different loads and constraints are applied to the spine model according to the analysis steps to simulate the movement of the spine. The calculation results of each model are analyzed in the results and experimental conclusions are drawn.

The data used in this article are 60 frames of continuous format data obtained by continuous scanning of the human body. The data are read into ScanIP for viewing and processing. First, we adjust the resolution to achieve the purpose of adjusting the accuracy of the model. This step is called resampling. In this project, the imported CT data are trimmed, and data resampled in ScanIP so that only useful data are retained, and the number of grids is reduced. In ScanIP, the part of interest is segmented by observing the different gray values. There are many factors that affect the internal pressure of the intervertebral disc, such as whether the intervertebral disc is originally degenerated, the range of motion of the segment, muscle tension, ligament tension, abdominal pressure, and so on. The bone tissue is easily observed on the CT image, so it is easier to divide the boundary between them. Then, we use the confidence region connection method to fill in the divided regions to obtain plane models of different parts of the fault. Unlike the spine, the characteristics of the intervertebral disc are closer to soft tissue, so it is not very clear on the CT image. We can use all knowledge of medical anatomy to outline the general outline of the intervertebral disc and then fill it. Next, we must perform filtering processing, boundary region processing, threshold segmentation, and other operations on the plane model, and finally generate a three-dimensional spine model based on the multilayer tomographic plane model.

Figure 4 shows the histograms of the changes in vertebrae expansion and contraction of different specimen numbers. With the increase in the resection of the posterior structure in different surgical methods of the lumbar spine, the range of motion of the lumbar spine specimens in flexion/extension is increasing. From specimen B to specimen C, compared with specimen A, the average increase in flexion range was 3.3%, 5.0%, 9.5%, 16.9%, and 30.2%, respectively. The average increase in extension range was 6.6%, 8.0%, 13.7%, 22.6%, and 32.3%. According to statistical analysis, compared with specimen A, specimens B, C, and D have no significant difference in flexion/extension changes, specimen D has significant differences in flexion/extension, and specimen C has a significant difference in flexion/extension.

3.2. Simulation of the Biomechanical Model of the Spine. This article is mainly aimed at CT plain scans of normal patients without disease, using Mimics software and ANSYS software to establish a three-dimensional spine biomechanical model of the normal spine, and simulate, stress, load loading, and other conditions on the three-dimensional finite element model of the normal spine. For digital simulation of surgery, etc., we establish a three-dimensional spine biomechanical model after surgery and other different surgical plans and perform stress analysis, and at the same

Table 2: Weighting factor distribution of spine biomechanics model.

Model index	Tissue site	Unit type	Number of units	Number of nodes	Elastic modulus (MPa)
1	Cortical bone	3D solid	1171	1427	11542
2	Cancellous bone	3D solid	1102	1305	721
3	Fiber tube	3D solid	342	537	5.91
4	Ligament	3D solid	132	327	3124
5	Endplate	2D planar	87	104	11.71

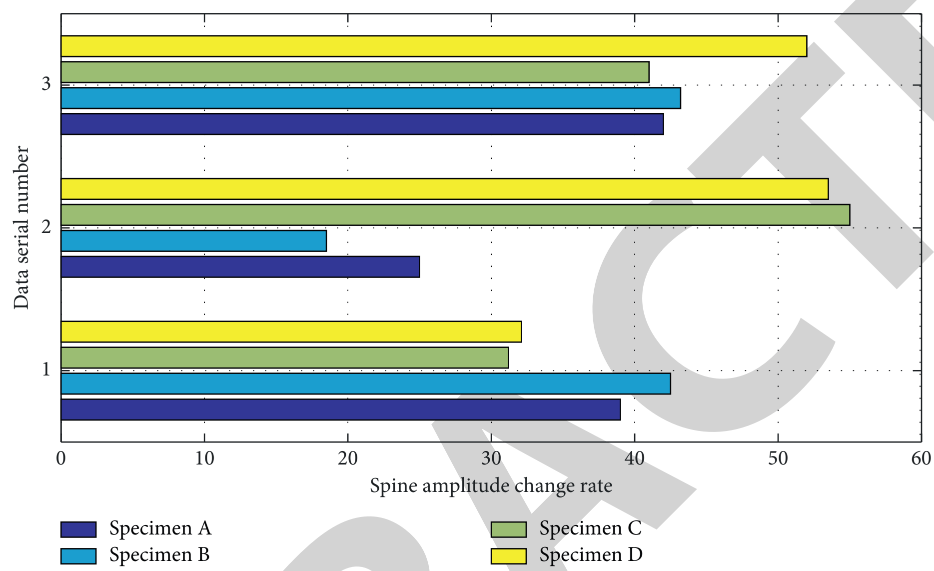

Figure 4: Histogram of changes in vertebral extension of different specimen numbers.

time analyze and compare the data. Sixty-one patients diagnosed with postoperative recurrence of lumbar disc herniation and surgical treatment were selected, and the initial surgical plan for recurrence and the reason for the re-operation were counted. According to the treatment method of re-operation, 50 patients in the observation group were divided into the observation group, and the control group was fixed with posterior approach. There were 50 patients undergoing fusion surgery. Figure 5 shows the line comparison chart of the visual simulation score of the spine biomechanics model. Statistics of the blood loss during the second operation, operation time, postoperative score, Visual Analogue Scale (VAS) score, etc., of the two treatment methods were calculated using SPSS 13 to perform statistical analysis. The observation group and the control group had significant differences in intraoperative blood loss and operation time, but there was no significant difference in postoperative score and VAS score.

The steps of spine biomechanics analysis mainly include preprocessing, loading and solving, and postprocessing. The work that can be completed in the preprocessing includes building the model, setting the properties of the material, applying different loads and boundary conditions, and defining various contact relationships. The establishment of the biomechanical model of the spine and the setting of the material properties have been completed before. Now only the load and boundary conditions of the model and the contact relationship need to be defined, the stress and strain of the lumbar spine can be simulated and simulated. Loads in ANSYS can be divided into two categories: one is boundary conditions, and the other is excitation. The function of ANSYS is to apply different excitations and different boundary conditions to the model to be analyzed for spine biomechanics, and then we perform the analysis to obtain the response. Figure 6 shows the linear fitting of the coupling ratio of the model nodes. The maximum stress between the different models increases with the increase of the punch diameter, but all are below the lower limit of the 95% confidence interval of the endplate failure strength, and the difference between the models is not obvious, and the difference is not much from the normal value, so the endplate fracture risk is low. According to the previous introduction, here for the contact relationship, the coupling operation is used to simulate so that the calculation maintains a linear relationship so that the nodes of the contact parts of different materials are set to be the same. In this paper, manual point selection is used to select points between nodes at the same location so that various materials connecting nodes are automatically coupled together.

We use a high-resolution Philips 64-slice CT machine to scan the lower lumbar spine with 140 kV, 200 mA conditions, and 0.9 mm intervals. The scan length is about 84 cm to obtain 1000 pictures in DICOM format. The CD completes the data collection. We use the image import function to select the CD-ROM drive; the system will automatically recognize the DICOM format pictures and sequences in the disc and generate

RETRACTED

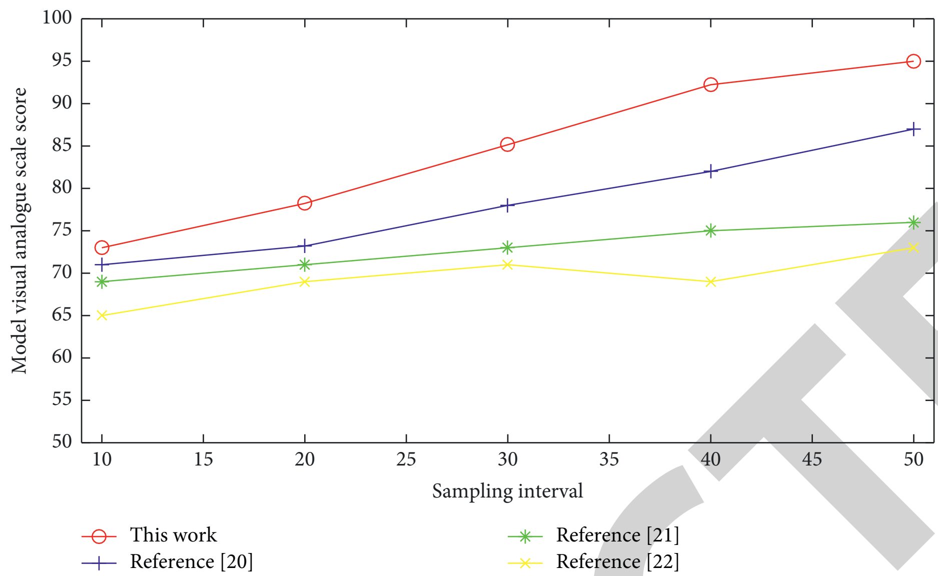

Figure 5: Comparison chart of spine biomechanics model visual simulation score line.

RETRACTED

three window pictures including sagittal, coronal, and transverse positions. We select the L4 to be studied on the scanned CT film. By using the method of setting CT threshold on the skeletal plain scan to distinguish between bone and surrounding soft tissues, we use profile line to select StartThresholding option and select Apply option to start rendering, and get the system. The area of the CT threshold range is selected by default, and the edit button is used to depict the selected area, fill in the glitch space in the default range, erase the area that does not need to be studied, and click calculate 3D to obtain a three-dimensional mask.

We perform proper wrapping and smoothing operations on the masked three-dimensional model to obtain a normal three-dimensional model containing the L4 vertebral body and intervertebral disc. Importing it into FEA for processing, we use surface spine biomechanical meshing, automatically reduce the mesh and adjust the number of meshes to obtain a triangular mesh pattern, and use a free division mode to convert the triangular mesh into a tetrahedral mesh to get the volume mesh model. The material assignment is carried out through the material that comes with Mimics, and the empirical formula assignment method is used, the model is assigned to the material, the formula is used to assign the value and compared with the empirical results, the elastic modulus and Poisson's ratio are modified, and a complete normal human L4 vertebral body and intervertebral disc model is established.

3.3. Example Application and Analysis. This article adopts the method of three-dimensional spine biomechanics through Mimics l0 and ANSYS 13 software to study the biomechanics of changes in spinal stability after treatment of lumbar disc herniation. *Methods.* (1) Select normal healthy adult volunteers, no history of lumbar spine disease, male, height 175 cm, weight 70 kg, and perform thin-slice CT scans of 0.9 mm on their lumbar spine to obtain CT data in DICOM format. (2) Importing it into the Mimics l0 software for modeling, divide the surface mesh, build the volume model, assign the material, and get the in vitro model of the normal lower lumbar spine L4-5 including the intervertebral disc. (3) Through Boolean shearing and other functions, by setting the shearing area to simulate L4-5 intervertebral disc removal surgery respectively, we establish A, B, and C including normal model, removal surgery model, small fenestration surgery model, and articular process removal surgery model. (4) Import the four groups of models into ANSYS 13 software for stress load simulation, and obtain the corresponding total displacement vector sum, total mechanical strain, and statistical cloud graph data for application SPSS 20 to analyze the data.

Figure 7 shows a box diagram of the range of spinal pressure load values. A normal human L4 vertebral disc model will be established. There are 40 finite elements, of which there are 45 nodes. We import it into ANSYS 13 software and simulate normal people by applying 500 N pressure load on the upper end plate surface node of waist, and restricting movement in X, Y, and Z directions on the bottom surface node of waist. Spinal pressure process: a torsional load of 8 N in the X direction is applied to the transverse process and the upper surface of the spinous process of the waist, and other constraints remain unchanged, and the numerical value of the spine in flexion and extension is obtained. Torque is applied to the reference points to simulate the six motion states of cervical spine flexion, extension, left-right rotation, and left-right scoliosis. The range of motion of each segment of the cervical spine is measured and compared with the results of previous in vitro and finite element experiments. It is basically similar to the research conducted in the literature verification, and the relevant values are compared. The results of this experiment are compared with the three groups of values, $P > 0.05$, indicating that there is no significant difference between the

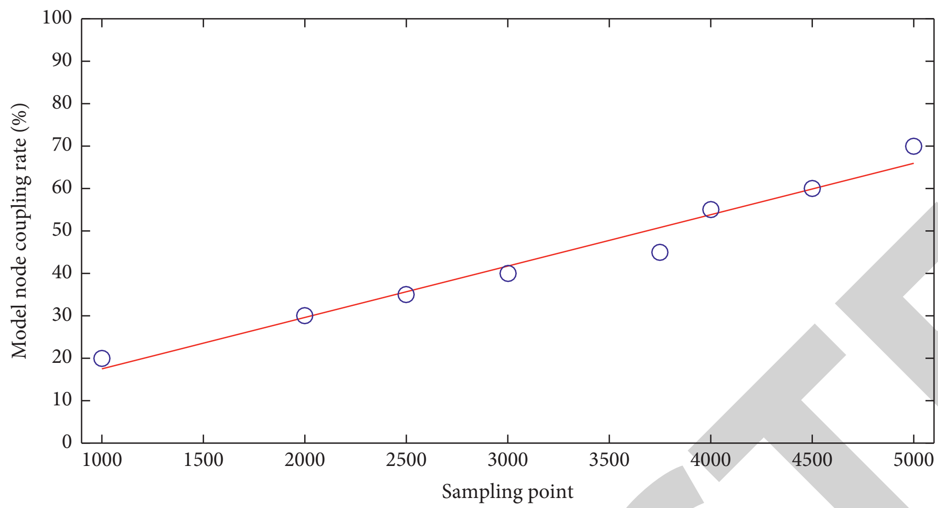

FIGURE 6: Linear fitting of model node coupling ratio.

results of this experiment and the other three groups of experiments. The verification confirms that the model is consistent with previous studies. The current stress cloud images in the three directions of X, Y, and Z are consistent with the actual situation, and the appearance conforms to the physiological anatomy, and it is accurate and usable.

We performed flexion/extension, left/right flexion and left/right axial rotation on the experimental specimens on the mechanical testing machine to measure the maximum range of different motions. The data obtained are represented, and the single-factor analysis of variance is performed under the SPSS 13 statistical software in the microcomputer. In the simulated operation, the movement of the spine specimens in all directions was not significantly different from that of the normal control group ($P > 0.05$); the simulated hemilaminectomy chain nucleus extraction was performed simply. After the interlaminar and inferior articular processes were removed, the movement of the specimen in all directions was not significantly different from that of the normal control group except for the right rotation ($P > 0.05$).

After all the inferior articular processes were removed, the movement in all directions is significantly different from that of the normal control group ($P < 0.05$ for right rotation); under the simulated total laminectomy, the movement of the specimen in all directions is very different from that of the normal control group ($P < 0.01$). Figure 8 shows the statistical distribution of disc sensitivity deviation. The intervertebral disc tissue is most sensitive to pressure. Group A showed that the pressure sensitive area was located on the posterior edge of the intervertebral disc. The pressure sensitivity of the three groups B, C, and D was located on the fibrous annulus of the posterior edge of the intervertebral disc after resection. The sensitivity of the front edge subsided. As the decompression range increases, the pressure sensitivity of the value becomes larger. The simulated resection group B was smaller than the other operation groups in terms of displacement, pressure, and stress sensitivity.

The maximum principal strain data of the upper endplate were extracted from the two groups of models, and the unit with the maximum principal strain was defined as the unit with high fracture risk. Both the intact vertebral body and group B have 3 high-risk units for vertebral body endplate fractures, accounting for 0.15% of the total number of endplate units. We selected the sidewall of the bone tunnel where the stress is concentrated in the vertebral body as the research object and measured the change trend of von Mises stress distribution along the path from the ventral side to the dorsal side of the vertebral bone tunnel sidewall with different perforation diameters. In group A, the high-risk units for fractures of models appear in the endplates. Around the damage margin, consistent with the von Mises stress concentration position, the fracture high-risk units of the model are widely distributed in the residual area of the anterior endplate. The fracture risk prediction was performed on the upper endplate of each model, and the results indicated that there were different numbers of high-risk fracture units in the upper endplate of the A group model, while the upper endplate of the group B model is low. Figure 9 shows a comparison chart of the significance level of the spine biomechanical model. The stress data of the anterior and posterior upper endplates of the vertebral body in groups A and B were analyzed by one-way analysis of variance with the normal model data. Both bone tunnels have an effect on the endplate stress distribution ($P = 0.01$). Among them, the stress value of the upper endplate of the model A has no significant difference compared with the normal model ($P > 0.05$), and the stress value of the upper endplate of the model B has no significant difference compared with the normal model ($P > 0.05$). Compared with the normal model, the end plate stress data of the model are significantly different.

RETRACTED

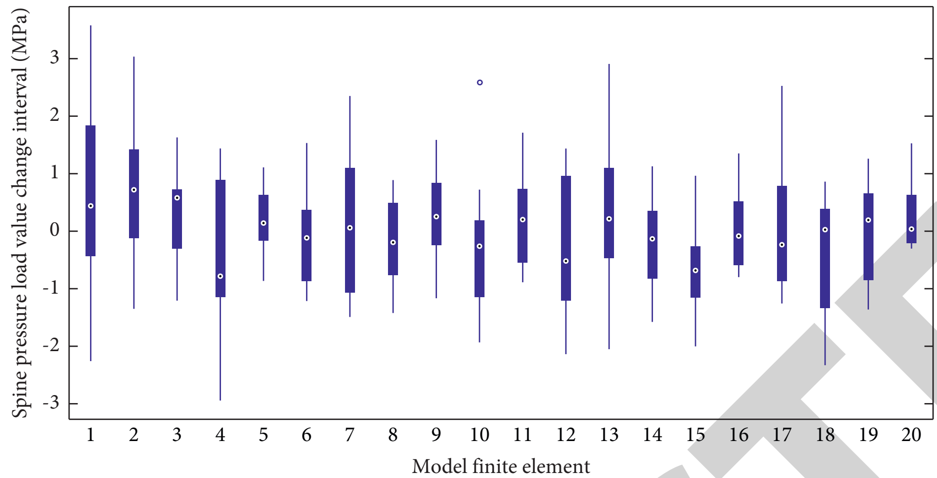

Figure 7: Box diagram of spine pressure load value change interval.

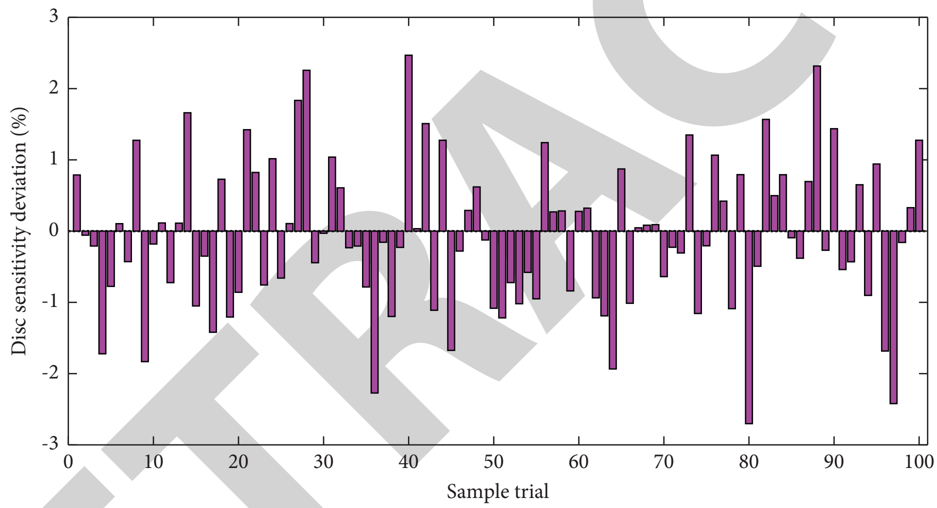

Figure 8: Statistical distribution of disc sensitivity deviation.

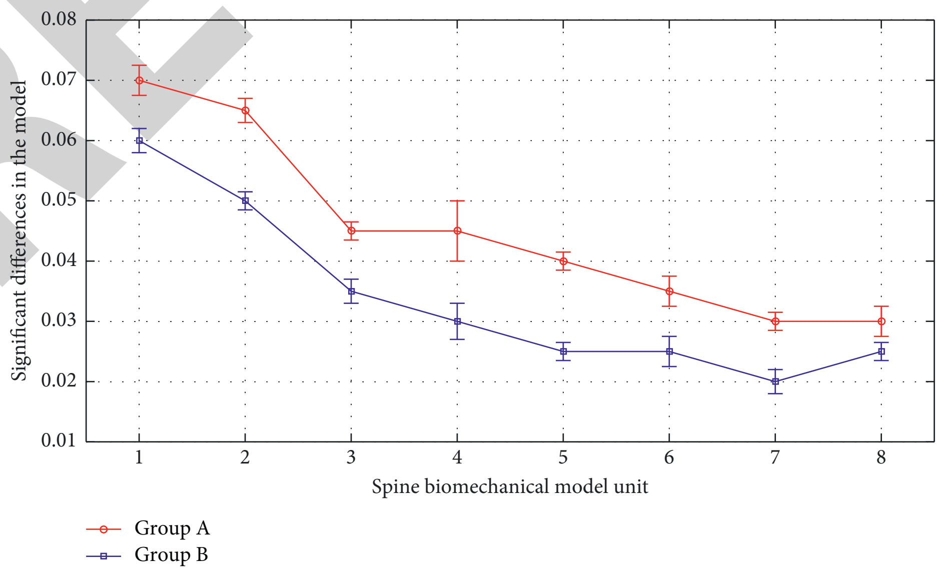

Figure 9: Comparison of the significance level of the spine biomechanical model.

RETRACTED

4. Conclusion

The spinal biomechanics analysis method can perform stress and strain analysis on complex shapes, and the mechanical performance test is comprehensive and objective. The application of biomechanical analysis of the spine to the lumbar spine is the current research hotspot. Lumbar degeneration is usually caused by a variety of cumulative injuries to the motor segments of the spine. The spine biomechanical model can simulate extremely complex tissues and load systems and can accurately simulate complex lumbar spine geometric models, study the stress and strain analysis of spinal motion segments under complex cyclic loads, and help us understand the biomechanical properties of the intervertebral disc and disc retraction. By comparing stress data and displacement data, this paper can analyze the differences between different spine models, which is of great significance to the research of the spine and the treatment of spine diseases. The computer simulation model can control the experimental conditions and calculate the contact area and stress of the vertebral body and the intervertebral disc. By comparing the stress data and the displacement data, the differences between different spine models can be analyzed, which has important guiding significance for the research of the spine and the treatment of spine diseases. In this way, the operation process can be simulated before the operation, and the purpose of helping the doctor to formulate a reasonable operation plan is achieved. After the operation, the effect of the operation can also be analyzed and appropriate recommendations can be given to the patient. This article reviews the data of patients with recurrence, using retrospective analysis method to make statistics on the patient's age, initial operation time, operation method, operation segment, recurrence interval, recurrence reason, second operation method, etc. At the same time, the patients after the operation were followed up, JOA score, VAS score, and other conditions were performed, statistical analysis was performed, and relevant conclusions were drawn. Finally, compared with the previously established three-dimensional spine biomechanics model, analysis of the need for improvement and prevention and other prognostic measures are given.

Data Availability

The data used to support the findings of this study are available from the corresponding author upon request.

Conflicts of Interest

The authors declare that there are no conflicts of interest regarding the publication of this paper.

Acknowledgments

This work was supported by Suzhou Hospital of Anhui Medical University.

References

[1] N. Hareni, F. Strömqvist, B. Strömqvist, B. E. Rosengren, and M. K. Karlsson, "Predictors of satisfaction after lumbar disc herniation surgery in elderly," *BMC Musculoskeletal Disorders*, vol. 20, no. 1, pp. 594–596, 2019.

[2] C. Zhao, H. Zhang, Y. Wang et al., "Nomograms for predicting recurrent herniation in PETD with preoperative radiological factors," *Journal of Pain Research*, vol. 14, pp. 2095–2109, 2021.

[3] R. Menezes-Reis, G. P. Bonugli, C. E. G. Salmon, D. Mazoroski, C. F. P. da Silva Herrero, and M. H. Nogueira-Barbosa, "Relationship of spinal alignment with muscular volume and fat infiltration of lumbar trunk muscles," *PLoS One*, vol. 13, no. 7, p. 198, 2018.

[4] D. M. Stewart, L. A. Monaco, and D. E. Gregory, "The aging disc: using an ovine model to examine age-related differences in the biomechanical properties of the intralamellar matrix of single lamellae," *European Spine Journal*, vol. 26, no. 1, pp. 259–266, 2017.

[5] U. H. Mitchell, J. A. Bowden, R. E. Larson, D. L Belavy, and P. J Owen, "Long-term running in middle-aged men and intervertebral disc health, a cross-sectional pilot study," *PLoS One*, vol. 15, no. 2, Article ID e0229457, 2020.

[6] G. T. Desmoulin, V. Pradhan, and T. E. Milner, "Mechanical aspects of intervertebral disc injury and implications on biomechanics," *Spine*, vol. 45, no. 8, pp. E457–E464, 2020.

[7] P. Suri, E. J. Boyko, S. D. Rundell, N. L. Smith, and J. Goldberg, "Do ical conditions predispose to the development of chronic back pain? A longitudinal co-twin control study of middle-aged males with 11-year follow-up," *BMC Musculoskeletal Disorders*, vol. 19, no. 1, pp. 1–10, 2018.

[8] M. D. Zhixiang Huang, M. D. Guochao Li, M. D. Weiming Deng et al., "Lumbar disc herniation is a nonnegligible factor for the degeneration of sacroiliac joints," *Pain Physician*, vol. 24, pp. 357–365, 2021.

[9] Y. Chen, J. Bao, Q. Yan, C. Wu, H. Yang, and J. Zou, "Distribution of Modic changes in patients with low back pain and its related factors," *European Journal of Medical Research*, vol. 24, no. 1, pp. 34–39, 2019.

[10] T. Liu, "Design of hospital embedded system and the treatment of cervical spondylopathy," *Microprocessors and Microsystems*, vol. 81, p. 17, 2021.

[11] L. E. Miller, R. T. Allen, B. Duhon, and K. E. Radcliff, "Expert review with meta-analysis of randomized and nonrandomized controlled studies of Barricaid annular closure in patients at high risk for lumbar disc reherniation," *Expert Review of Medical Devices*, vol. 17, no. 5, pp. 461–469, 2020.

[12] W. Wu, S. Yang, W. Diao et al., "Analysis of clinical efficacy of endo-LIF in the treatment of single-segment lumbar degenerative diseases," *Journal of Clinical Neuroscience*, vol. 71, pp. 51–57, 2020.

[13] N. N. Widyasari, E. D. Martadiani, M. W. Asih et al., "Correlation between loss of cervical lordosis and the degree of cervical disc herniation," *IJBS*, vol. 15, no. 1, pp. 43–47, 2021.

[14] T. Suśtersic, V. Ranković, M. Peulić, and A. Peulic, "An early disc herniation identification system for advancement in the standard ical screening procedure based on Bayes theorem," *IEEE journal of bioical and health informatics*, vol. 24, no. 1, pp. 151–159, 2019.

[15] J. Jezek, J. Sepitka, M. Daniel et al., "The role of vascularization on changes in ligamentum flavum mechanical properties and development of hypertrophy in patients with lumbar spinal

Hindawi
Journal of Healthcare Engineering
Volume 2023, Article ID 9831620, 1 page
https://doi.org/10.1155/2023/9831620

Retraction

Retracted: Study on the Correlation Factors of Tumour Prognosis after Intravascular Interventional Therapy

Journal of Healthcare Engineering

Received 27 June 2023; Accepted 27 June 2023; Published 28 June 2023

Copyright © 2023 Journal of Healthcare Engineering. This is an open access article distributed under the Creative Commons Attribution License, which permits unrestricted use, distribution, and reproduction in any medium, provided the original work is properly cited.

This article has been retracted by Hindawi following an investigation undertaken by the publisher [1]. This investigation has uncovered evidence of one or more of the following indicators of systematic manipulation of the publication process:

(1) Discrepancies in scope
(2) Discrepancies in the description of the research reported
(3) Discrepancies between the availability of data and the research described
(4) Inappropriate citations
(5) Incoherent, meaningless and/or irrelevant content included in the article
(6) Peer-review manipulation

The presence of these indicators undermines our confidence in the integrity of the article's content and we cannot, therefore, vouch for its reliability. Please note that this notice is intended solely to alert readers that the content of this article is unreliable. We have not investigated whether authors were aware of or involved in the systematic manipulation of the publication process.

In addition, our investigation has also shown that one or more of the following human-subject reporting requirements has not been met in this article: ethical approval by an Institutional Review Board (IRB) committee or equivalent, patient/participant consent to participate, and/or agreement to publish patient/participant details (where relevant).

Wiley and Hindawi regrets that the usual quality checks did not identify these issues before publication and have since put additional measures in place to safeguard research integrity.

We wish to credit our own Research Integrity and Research Publishing teams and anonymous and named external researchers and research integrity experts for contributing to this investigation.

The corresponding author, as the representative of all authors, has been given the opportunity to register their agreement or disagreement to this retraction. We have kept a record of any response received.

References

[1] L. Zheng, H. Feng, L. Yin et al., "Study on the Correlation Factors of Tumour Prognosis after Intravascular Interventional Therapy," *Journal of Healthcare Engineering*, vol. 2021, Article ID 6940056, 11 pages, 2021.

Hindawi
Journal of Healthcare Engineering
Volume 2021, Article ID 6940056, 11 pages
https://doi.org/10.1155/2021/6940056

RETRACTED

Research Article

Study on the Correlation Factors of Tumour Prognosis after Intravascular Interventional Therapy

Lei Zheng[1] **Hua Feng**[2] **Limin Yin**[2] **Jun Wang**[2] **Wei Zhou**[2] **Sunin Tang**[2] **and Mingming Li**[3]

[1]*Taizhou Hospital of Traditional Chinese Medicine, Taizhou Jiangsu 225300, China*
[2]*Taixing People's Hospital, Taizhou, Jiangsu 225400, China*
[3]*First Affiliated Hospital of Soochow University, Suzhou Jiangsu 215000, China*

Correspondence should be addressed to Hua Feng; zyajun512@126.com and Mingming Li; mmli@suda.edu.cn

Received 17 August 2021; Revised 17 September 2021; Accepted 20 September 2021; Published 27 October 2021

Academic Editor: Gu Xiaoqing

Copyright © 2021 Lei Zheng et al. This is an open access article distributed under the Creative Commons Attribution License, which permits unrestricted use, distribution, and reproduction in any medium, provided the original work is properly cited.

Noninvasive or minimally invasive interventional surgery was selected, and the complications were less and had no significant impact on the quality of life of patients. Tumour patients are often accompanied by cerebrovascular diseases, metabolic diseases, and other basic diseases, which more or less adversely affect the surgical efficacy of tumour. In this paper, endovascular remobilization was used to treat tumour; the basic condition of patients before operation and the interventional operation plan were introduced. Through the analysis of clinical data and prognosis evaluation results of tumour patients receiving intravascular interventional therapy, the patients were divided into good prognosis group and poor prognosis group according to the modified Rankin scale score at discharge. The relationship between gender, age, history of hypertension, tumour width, tumour size, preoperative Hunt-Hess grade, interventional surgery method, and prognosis related to intravascular interventional therapy was explored. The results showed that intravascular interventional therapy for tumour patients can obtain a good prognosis, which provides a reference for the future preoperative assessment of treatment risk and possible prognosis and provides a theoretical basis for the formulation of treatment plan to improve prognosis.

1. Introduction

Combined tumour therapy includes surgery, radiotherapy, and chemotherapy. With the development of advanced technologies such as imaging, microcatheters, and stents, interventional therapy is providing new treatments for diseases that were previously untreatable or ineffective. Tumour therapy has entered the noninvasive or minimally invasive era. The purpose of digital subtraction angiography intravascular interventional therapy of tumour is to improve the therapeutic effect of local tumour and overcome the disadvantages of traditional treatment such as intravenous systemic chemotherapy, such as adverse reactions, radiation damage, and severe injury. Preoperative tumour interventional therapy can reduce tumour staging, improve surgical resection rate and survival rate, and reduce postoperative recurrence and metastasis. Interventional therapy for patients with advanced cancer can improve the quality of life and prolong the overall survival time of patients with cancer [1–3]. Therefore, interventional therapy has become one of the important means of comprehensive tumour therapy. However, there are still many weak links in the relevant basic and clinical research, especially the study of pharmacokinetics.

With the development of medicine, interventional surgery has been applied more and more widely, not only in medical treatment, but also in surgery. Interventional therapy is appropriate for patients with severe bleeding due to trauma or whose tumours are unsuitable for major surgery. The intervention not only has less trauma and bleeding, but also recovers quickly. As long as there is a risk of surgery, interventional surgery is the same; different primary disease interventional complications are also different. The operation of interventional surgery has been greatly developed, so it has become a major minimally invasive surgical therapy not only applied to the back circulation but also widely applied to tumours. It has been recognized and accepted by the majority of patients for its accurate surgical efficacy, high success rate, and good prognosis. By adopting elastic yellow ring or stent-assisted embolization experience and clinical data, interventional embolization is safe and has a good curative effect of new treatments [4, 5], especially for some tumours that be treated with open surgical operation or difficult high risk patients, intravascular interventional embolization has become a preferred therapy. Interventional surgery is a modern, high-tech, and minimally invasive treatment method, which is introduced into the body by using professional catheter or guide wire and other instruments, combined with medical imaging equipment, to judge and treat diseases. Interventional therapy is an advanced science and technology developed in recent years. It has the advantages of small trauma and effective and rapid recovery by interventional therapy on the premise of no operation. Interventional therapy is now widely used. In the past, many operations that cannot be done clinically or are very difficult can be operated simply and effectively through interventional surgery. Now, it is mostly used for tumours, cardiovascular and cerebrovascular diseases, nervous system, gynaecological problems, all kinds of bleeding, stones, and so on. Especially in liver cancer and liver haemangioma effect is very significant; in addition to myocardial infarction this effect is very significant.

As a relatively new treatment method, the prognosis of intravascular interventional therapy for IA has attracted much attention. Under the guidance of imaging equipment, doctors send a special catheter to the tumour's supplying artery and then inject embolization material through the catheter to completely embolize the tumour's supplying artery. B. Taslakian et al. studied the related factors that may affect the prognosis of invasive surgery, including the basic information of patients, such as gender, age, etc., which are thought to be associated with tumour incidence that is closely related to the basic diseases such as hypertension, tumour size, tumour related specific morphological features, such as neck width, and different ways of interventional surgery, the patient's clinical status classification, etc. [5]. At present, prognostic factors have not been clearly defined. O. Sutte et al. listed simple coil embolization, preoperative Hunt-Hess grade III-IV, and tumour diameter >10 mm as independent risk factors affecting the prognosis of tumour patients after endovascular intervention, while age, sex, underlying diseases, tumour neck width, and other indicators had no significant correlation with prognosis [6]. Lee et al. believe that Hunt-Hess grade of patients, tumour location and size, and other factors are independent risk factors affecting interventional efficacy and postoperative tumour rupture [7]. L. Wang et al. believe that most patients are complicated with atherosclerosis, arteriosclerosis, and other vascular diseases and are more prone to mini-ischemia [8]. Chang study showed that aneurysm diameter ≥7 mm and tumour neck size ≥4 mm were significantly correlated with symptomatic cerebral microischemia and DWI (+). The size and shape of aneurysms are also associated with increased thromboembolic events detected by Diffusion Weighted Imaging (DWI) [9]. Larger or wide-necked aneurysms usually require more coils or the use of double catheters, balloon reconstruction, or stent-assisted techniques, theoretically increasing the risk of thromboembolic complications. However, different research data support that the ratio of tumour length to tumour neck width (AR) and hypertension are included as prognostic factors. L. Tselikas pointed out that, due to different locations, the prognosis of anterior and posterior circulation tumours is significantly different after interventional therapy [10]. However, most previous studies related to prognostic factors involve multisite tumours and lack pertinence to the location of tumours.

2. Data and Methods

2.1. Preoperative Data. In this study, clinical data of tumour patients undergoing intravascular intervention therapy in a hospital were selected, including age, smoking history, hypertension history, diabetes history, hyperlipidemia, aneurysm location and size, whether it was a wide-necked aneurysm, stent use, platelet suppression 1 day before surgery, and operation duration. All patients were diagnosed with intracranial aneurysm by CT angiography (CTA) and digital subtraction angiography (DSA). Magnetic Resonance Imaging (MRI) of the head was completed 3 days after surgery. All signed informed consent forms: patients with systemic infectious diseases, severe organ dysfunction, and other surgical contraindications; dissecting aneurysm, pseudoaneurysm and intracranial multiple aneurysm; pregnancy with intracranial aneurysm; intracranial and extracranial artery stenosis; intraoperative acute thrombosis and intraoperative aneurysm rupture. After admission, the patient was closely monitored in the neurological care unit, with absolute bed rest, appropriate sedation, and analgesia treatment, and stool was kept unapparent. Blood pressure was regulated to keep systolic pressure within 160 mmHg, while ensuring that the mean arterial pressure is higher than 90 mmHg. According to the patient's condition, drugs to relieve cerebral vasospasm, dehydration to reduce cranial pressure, lumbar puncture cerebrospinal fluid replacement, lateral ventricle drainage, and other treatments were used, and further interventional therapy was performed after preoperative examination was completed and the condition was stabilized [11]. The preoperative procedure is shown in Figure 1.

2.2. Interventional Therapy. Simple core embolization, double microcatheter remobilization, or stent-assisted core-remobilization was selected according to the patient's condition, the situation of pulsar tumour, and the patient's willingness. During the operation, the patient was placed in the supine position. After tracheal intubation and general anaesthesia, the puncture site with the most obvious pulse 1.5 cm below the right inguinal ligament was selected as the puncture site. After routine skin disinfection for three times,

RETRACTED

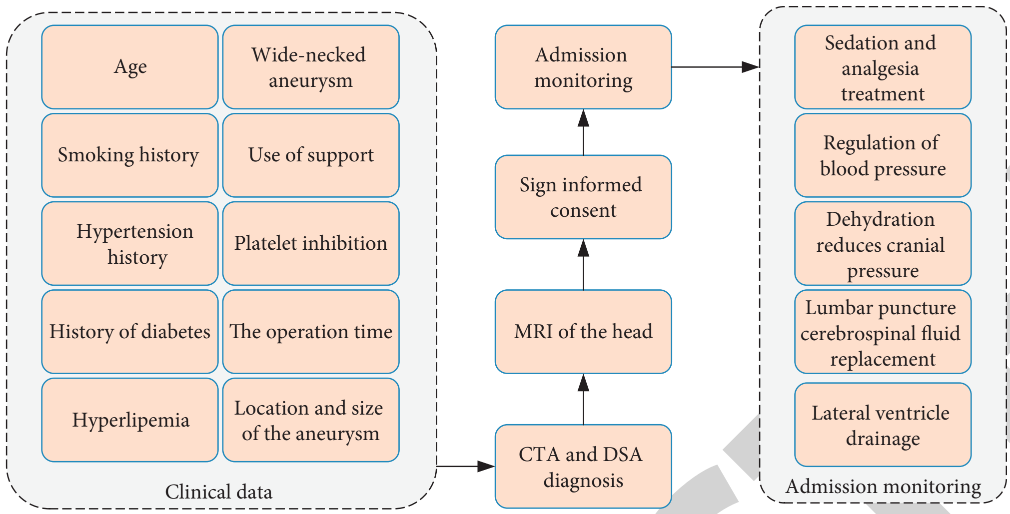

Figure 1: Preoperative flowchart.

sterile towel was covered. After percutaneous femoral artery puncture and catheter sheath placement, the catheter was guided from the femoral artery all the way up to the internal carotid artery. Microguide wires and microcatheters were used in the operation, and the appropriate working angle was selected in combination with the 3D reconstruction image during the operation. Remobilization with simple coil is to send a microcatheter to the tumour cavity under the guidance of a microguide wire and to deliver a certain number of microcoils through the microcatheter to fill according to the tumour size and shape nad width of the tumour neck and the parent artery.

For relatively broad neck tumours or broad neck tumours with difficult stent placement, double microcatheter technology was adopted. Under the operation of two microcatheters, spring coils were, respectively, transported into the tumour cavity, and remobilization effect was achieved by winding the spring coils together into a basket. Stent-assisted coiling remobilization (SAC) is to perform coiling remobilization in the tumour cavity on the basis of placing stents in the tumour neck with absolute or relatively wide neck by microcatheter, so as to close the tumour neck and avoid coiling displacement [12]. The therapeutic objective and ideal state of all treatment methods are that there is no development in the tumour and there is spring coil tamping in the neck of the tumour immediately after treatment.

During the operation, the patient's whole body heparin was maintained, and high pressure heparin saline was administered to continuously flush the lumen to avoid thrombosis in the lumen guided by the catheter. It was expected that patients using stents would be given clopidogrel tablets 75 mg/d and enteric-coated aspirin tablets 100 mg/d 3 days before surgery. In case of emergency, preoperative disposable clopidogrel tablets 300 mg and enteric-coated aspirin tablets 300 mg were used.

The above operations are performed by skilled people. 24 hours after the operation, strict ECG monitoring, and give anticerebral vasospasm, anti-inflammatory, fluid replacement, expansion, dehydration, and other treatments. After 3 days of subcutaneous injection of low molecular weight heparin sodium, patients were treated with oral clopidogrel 75 mg/d and enteric-coated aspirin 100 mg/d for 6 months and then maintained with enteric-coated aspirin 100 mg/d or clopidogrel 75 mg/d.

All interventional procedures were performed by the same neurosurgeon via femoral artery approach under general anaesthesia. A complete set of thromboelastography (AA% and ADP%) was completed for all patients 1 day before surgery. Both patients received dual antiplatelet therapy (aspirin 300 mg and clopidogrel 300 mg) 2 hours before surgery. After successful general anaesthesia, heparinization was performed on the whole body, the dosage was 1 mg/Kg, and the dosage was reduced to 50% of the previous dosage 1 hour later until the reduction was maintained at 10 mg/hour. Procaine and heparin were given at the end of the operation if only coiling embolization of the tumour was performed. If stent-assisted embolization of the tumour is used intraoperatively, no heparin is obtained. After the operation, the coagulation image was examined immediately. If the coagulation result reached the indication of blood transfusion, plasma was given to improve the coagulation function. If stent-assisted embolization of tumour is used, subcutaneous anticoagulant injection of low molecular weight heparin should be used according to the preoperative inhibition of TEG platelet [13]. If aspirin and/or clopidogrel resistance, low liver 4000IU Q12 h is given. If both aspirin and clopidogrel were sensitive, the liver was lower than 2000IU q12 h. After 3 days, it was changed to double therapy. If no stents were used, hypohepatic and double-antitumor therapy was not used after surgery. The procedure of interventional surgery is shown in Figure 2.

2.3. Prognostic Data Collection. In this study, the relevant data of the included patients during outpatient, inpatient, or telephone follow-up 6 months to 1 year after surgery were collected, and the prognosis of the patients was evaluated according to the scores of the modified Rankin scale, as shown in Table 1. Disability and death mentioned in the

RETRACTED

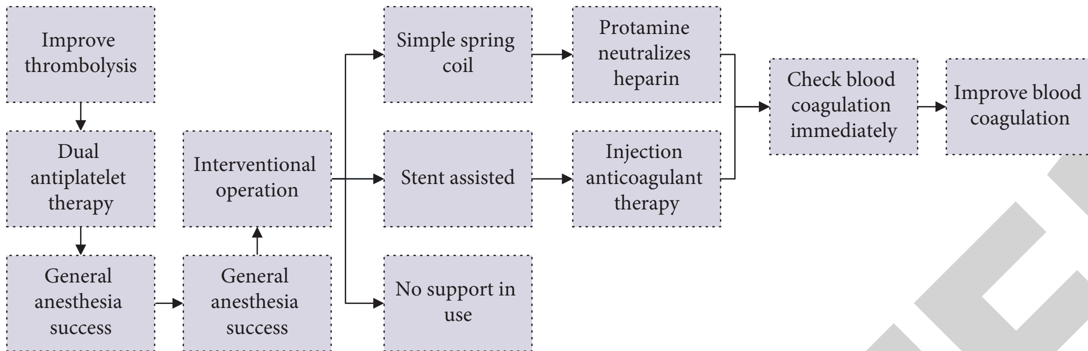

Figure 2: Flowchart of interventional surgery.

Table 1: mRS scoring criteria.

Scale of marks Project	Scope	Score
Age	≤40	0
	41–50	1
	51–69	2
	≥70	3
NIHSS scores	0–4	0
	5–9	1
	10–15	2
	>15	3
Defect of field vision	—	2
Decreased level of consciousness	—	3
The onset lasts more than 3 hours	—	2

criteria are related to responsible tumours, excluding heart disease, cirrhosis, and other factors. The patients were grouped according to the mRS score, with 0–2 points included in the good prognosis group and 3–6 points included in the poor prognosis group [14, 15].

2.4. Statistical Method. SPSS21 statistical software was used for statistical analysis. The data of normal distribution were represented by mean ± standard deviation, and the data of nonnormal distribution was represented by median ± quartile interval. The counting data are expressed by frequency and percentage. University analysis was performed on indicators that may affect prognosis, including gender, age, history of hypertension, tumour neck width, tumour diameter size, preoperative Hunt-Hess grade, and interventional surgery. The continuous variables were converted into classified variables, and Pearson chi-square test (sample size $n \geq 40$ and theoretical frequency $T \geq 5$) or corrected chi-square test ($n \geq 40$, $1 \leq T \leq 5$) or Fisher exact probability method ($n < 40$ or $T < 1$) was used. $P < 0.05$ was considered statistically significant. The factors with statistical significance in univariate analysis were further analyzed by multivariate analysis: logistic regression analysis; $P < 0.05$ was considered statistically significant [16, 17].

3. Result

3.1. Basic Information of the Patient. A total of 63 patients, including 23 males and 40 females, were enrolled in the Body Mass Index (BMI) study. The investigation and analysis of patients took into account the factors of previous pathological history, hypertension, smoking history, and diabetes. Thirty-one patients had a history of hypertension, 22 had a history of diabetes, and 21 had a history of smoking. The highest age was 62 years, the lowest age was 20 years, and the average age was 57.3 ± 10.3 years. BMI ranged from 36.3 to 16.7, with a mean value of 24.0 ± 3.3. The statistical results are shown in Figure 3.

Sixty-three patients had a total of 68 tumours, of which 60 were treated with interventional therapy and 8 were untreated. Among them, there were 66 responsible tumours (as shown in Table 2): 23 anterior traffic tumours, 5 anterior brain tumours, 16 brain tumours, 18 intracranial tumours of internal carotid artery, and 14 posterior traffic tumours.

3.2. Interventional Therapy. Among the 63 cases of anterior circulation responsible tumours receiving intravascular interventional therapy, 43 cases received simple coiling embolization therapy, 1 case received double microcatheter embolization therapy, and 19 cases received stent-assisted coiling embolization therapy. The distribution of interventional therapy methods is shown in Figure 4.

3.3. Postoperative Angiography and Clinical Results. The total immediate dense embolization rate was 80.2%, and the rate of subcomplete and incomplete embolization was 17.6%. Because the follow-up time of each patient is not consistent, the follow-up embolization degree has no statistical value and was not analyzed. In terms of clinical results, one patient with superior cerebella artery tumour frequently vomited after stent-assisted embolization, and the second angiography showed that the parent artery was preserved without thrombosis. Another patient with superior cerebella artery tumour had blurred vision due to parent artery occlusion. 1 case of posterior inferior cerebella artery dissection tumour underwent stent-assisted coiling embolization with reduced muscle strength in the left limb. A patient with a large middle cerebral artery tumour undergoing parent artery occlusion showed reduced muscle strength in the left limb after surgery. Postoperative rebreeding occurred in 2 cases, including 1 in inferior posterior cerebella artery and 1 in middle cerebral artery, and parent artery occlusion was performed in both cases. Microischaemic lesions occurred in 34 of the 63 patients. The statistical results are shown in Figure 5.

RETRACTED

RETRACTED

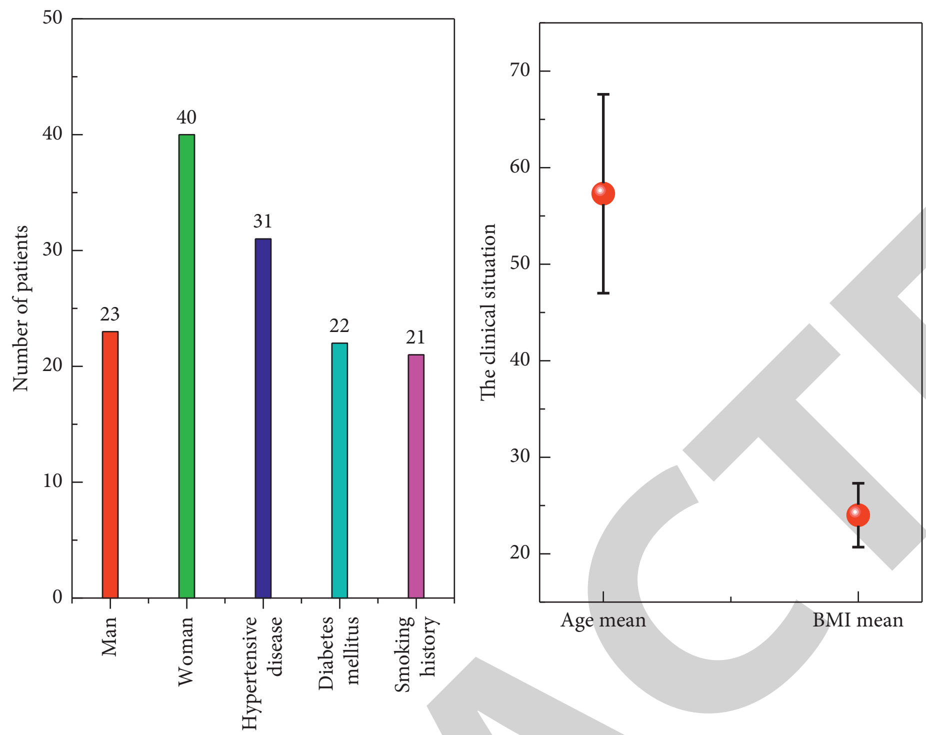

FIGURE 3: The basic situation of the patient statistical graph. Basic information of tumour.

TABLE 2: Responsible for the location of the tumour distribution.

Position	Number of cases	Percentage rate (%)
Anterior communicating artery	23	34.85
Anterior cerebral artery	5	7.58
Middle cerebral artery	16	24.24
ICA	8	12.12
Posterior communicating artery	14	21.21

3.4. Prognostic Factor Analysis

3.4.1. Relationship between Age, Sex, Hypertension, and Prognosis. The age of patients was divided into three segments by 40 and 60. In the intravascular intervention group, the poor prognosis rate of patients <40 years old was 6.00%, that of patients 40–59 years old was 7.89%, and that of patients ≥60 years old was 30.00%. There was no statistical significance between the poor prognosis rates. In the vascular intervention group, the poor prognosis rate of male patients was 13.16%, and the poor prognosis rate of female patients was 6.67%. There was no statistical significance between the poor prognosis rates. In the vascular intervention group, the poor prognosis rate of patients with hypertension history was 19.36%, and that of patients without hypertension history was 4.48%, and the difference between the poor prognosis rates was statistically significant. The relationship between age at onset, sex, hypertension, and prognosis is shown in Figure 6.

Statistical analysis showed that there was no statistically significant difference in prognosis between male and female patients, so gender difference was not an independent risk factor affecting the prognosis of tumour interventional therapy. Endovascular interventional therapy is a minimally invasive surgery, which has less tissue trauma and surgical impact on patients than craniotomy and clipping surgery, and the endurance of the elderly is relatively improved. Elderly patients can give priority to endovascular interventional therapy, and old age is not an absolute contraindication for interventional surgery.

Hypertension is regarded as a common risk factor by most scholars. Long-term hypertension can lead to damage of vascular endothelial cells, apoptosis of vascular smooth muscle cells in the media, rupture and disappearance of elastic fibbers, and gradual thinning of vascular walls. On this basis, changes in hemodynamics promote the formation of lesions. High vascular wall shear stress and high blood flow velocity have a strong blocking effect on local tumour thrombosis. Meanwhile, hypertension can also affect the hemodynamic parameters and increase the shear force of the vascular wall at the intracranial artery bifurcation, causing damage to the vascular wall and aggravating the condition of intracranial aneurysm. In the process of intravascular interventional therapy, the lesion site cannot be thromboses and the healing of the tumour is hindered. In addition, the high speed blood flow can also lead to microspring

RETRACTED

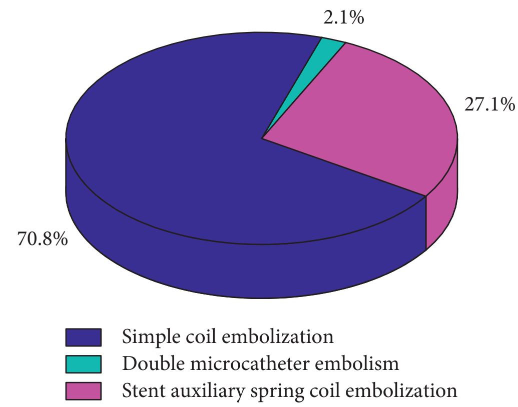

Figure 4: Distribution of interventional therapy.

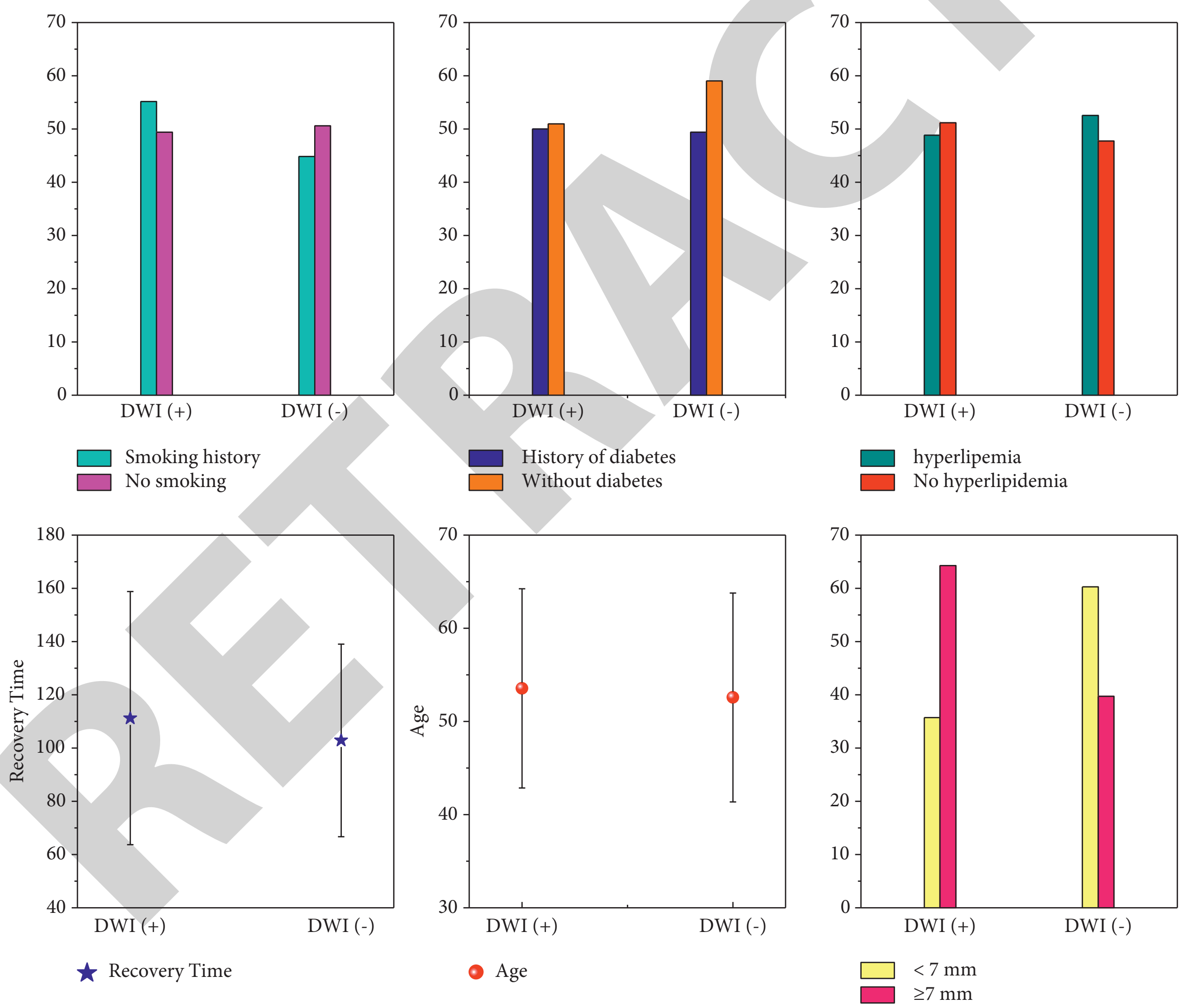

Figure 5: Single-factor analysis diagram.

compression and increase the risk of recurrence, which is unfavourable before and after tumour [18, 19]. Avoiding large fluctuations in blood pressure can prevent exacerbation and progression of the disease, and even patients with hypertension can obtain a good prognosis.

3.4.2. Relationship between Preoperative Hunt-Hess Grade, CT-Fisher Grade, and Prognosis. In the endovascular intervention group, the prognostic rates of grade I, II, III, and IV patients were 0%, 9.09%, 8.33%, and 80.00%, respectively, with statistically significant differences. In the vascular intervention

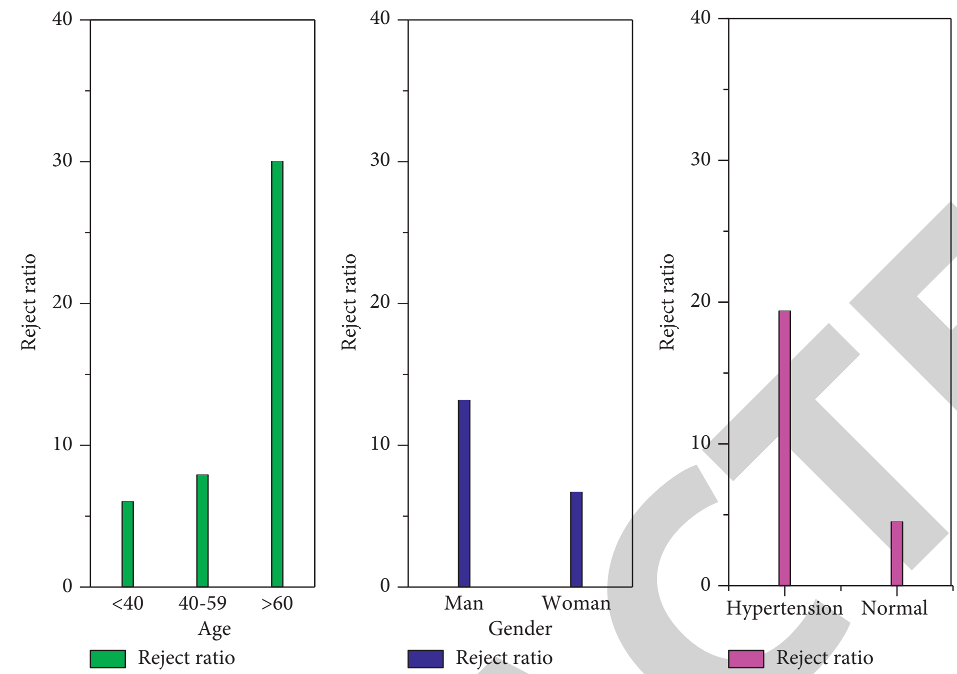

Figure 6: Patient age, sex, and prognosis diagram analysis.

RETRACTED

group, the preoperative CT-Fisher grade poor prognosis rate of grade I was 0.00%, grade II was 1.69%, grade III was 8.33%, and grade IV was 13.64%, with statistically significant differences in the poor prognosis rate. The relationship between preoperative Hunt-Hess grade, CT-Fisher grade, and prognosis was shown in Figure 7.

Hunt-hess grade is an objective index reflecting the clinical status of patients, which evaluates patients according to headache degree, meanings irritation, consciousness state, nervous system function state, etc. [18]. There was no statistically significant difference in prognosis among patients with different Hunt-Hess grades. It was considered that some patients with high Hunt-Hess grade were not included in this study because of their serious condition and high risk of intervention therapy, and they died before receiving treatment or finally decided to receive conservative treatment, give up treatment or surgical clamping treatment, or transferred to hospitals according to the wishes of their families. Therefore, in this study, the number of cases with lower Hunt-Hess grade was significantly more than those with higher Hunt-Hess grade, and there was a certain selection bias. Although Hunt-Hess grade IV and V cases were combined into one group for statistical analysis, the results still showed no statistically significant difference in prognosis. In addition, the intervention before the operation, to stabilize their condition, provides the operation conditions on the Hunt-Hess rank higher in patients with lumbar puncture cerebrospinal fluid replacement, lateral ventricle drainage, and other treatments; the treatment operation to some extent reduced the degree of hydrocephalus, relieved the intracranial pressure, and dredged the cerebrospinal fluid pathway, a positive influence on the prognosis of patients. Therefore, in this study, the rate of poor prognosis did not increase with the increase of Hunt-Hess grade, and no positive results were obtained by statistical analysis.

3.4.3. Relationship between Tumour Size, Tumour Width, and Prognosis. Figure 8 shows the relationship between tumour size, tumour width, and prognostics in enrolled patients. According to the results of Fisher's exact probability test, it was believed that the difference of prognosis among different tumour sizes and widths was statistically significant.

Tumour size is considered to be an independent risk factor for postoperative ischemic events. Thrombosis is more likely to occur in large aneurysms, making it difficult for the spring coil to fill the area occupied by the thrombus, and the residual cavity will be exposed and enlarged after thrombus dissolution, leading to aneurysm recurrence. In addition, oversized aneurysms may also have the problem of space occupying. Even if the space occupying effect caused by blood pulsation is relatively reduced after complete embolization, the aneurysm volume does not change significantly after embolization, and the space occupying effect of the tumour itself is not relieved, which can still cause clinical symptoms. The tumour diameter <7 mm was more prone to intraoperative rupture during endovascular therapy. Tumours larger than 7 mm had a higher incidence of thromboembolic events, but tumour size had no significant effect on intraoperative rupture. Statistical analysis showed that there was a statistically significant difference in prognosis between tumour size <7 mm and tumour size >7 mm, and tumour size >7 mm was a risk factor for poor prognosis.

Tumour neck width and tumour body neck ratio (AR) are important indexes to reflect the geometric characteristics of tumour. The tumour neck size has a controlling effect on the eddy current velocity in the tumour cavity. Wide-neck tumours usually have larger blood flow and complex stress gradient, which affects the filling effect of spring coil [19]. Therefore, the treatment of wide-neck tumours is relatively difficult. Related studies have found that broad neck tumours show a lower

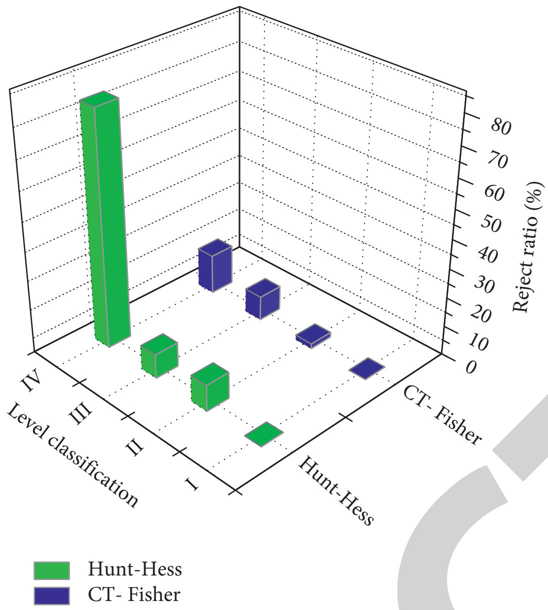

Figure 7: Diagram of relationship between preoperative Hunt-Hess grade, CT-Fisher grade, and prognosis.

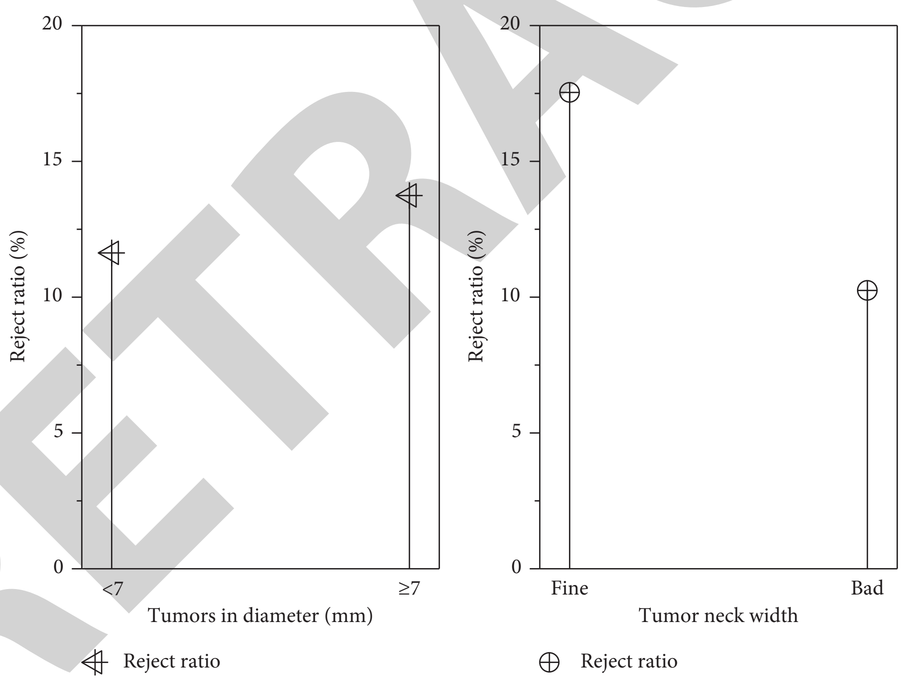

Figure 8: The relationship between tumour size, tumour width, and prognosis in patients.

complete occlusion rate in both immediate postoperative angiography and follow-up angiography [20], and broad neck tumours have a higher decimalization rate than narrow neck tumours. With the progress of embolization technology and materials, the problems such as the insertion of tamped spring coil into the parent artery through a wide neck can be solved, and even wide-necked aneurysms can obtain a relatively ideal effect [21].

Tumour diameter, tumour neck width, and multiple tumours are risk factors for recurrence of intracranial aneurysms treated by intravascular intervention. The tumours with larger diameter were more irregular, and the tamping degree of the tumour neck with larger width was lower, so recurrence was easy to occur. In addition, thrombus is more common in tumour lumen in patients with large tumour diameter, and it is difficult to completely occupy part of the space of thrombus in the process of embolization of microspring coil. With the absorption of thrombus in tumour lumen, it is easy to cause the expansion of residual lumen and relapse. Patients with multiple

RETRACTED

TABLE 3: Univariate analysis of relationship statistics.

Element	X^2	P
Age	1.303	0.075
Gender	0.526	0.468
Hypertension	3.982	0.056
Hunt-Hess	0	0.001
CT-Fisher	0	0.001
Tumours in diameter	0	0.002
Tumour neck width	0.987	0.388

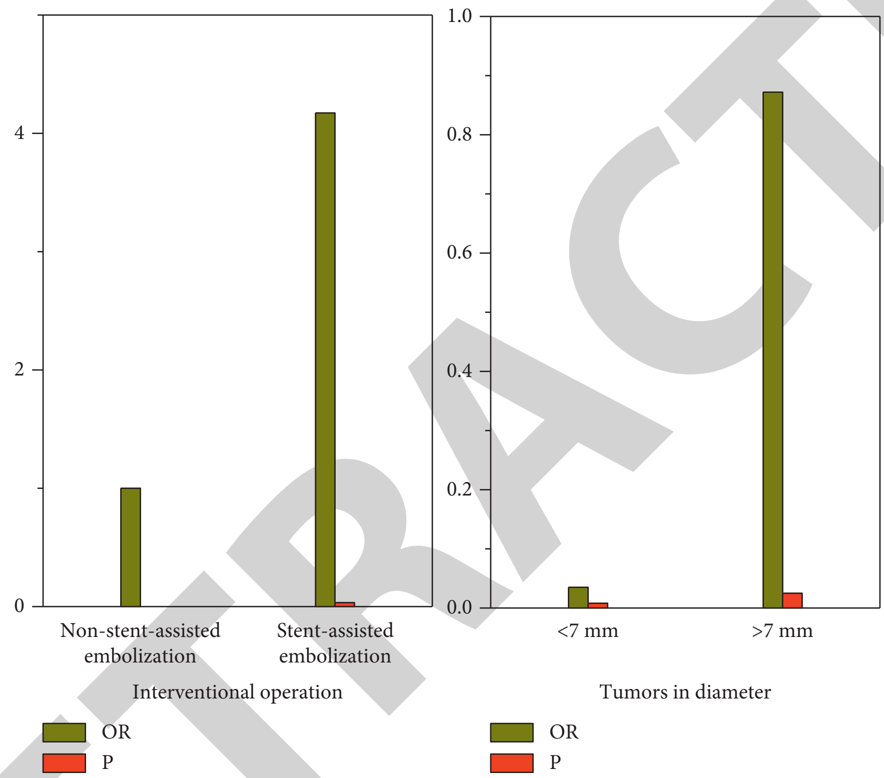

FIGURE 9: Multivariate binary logistic regression analysis.

tumours have more tumours, more complex disease, and more difficult intravascular interventional therapy, so the prognosis is poor and the risk of recurrence is greater.

3.5. Single-Factor Analysis. Univariate analysis showed that patients with a history of hypertension, large tumour diameter, clopidogrel resistance, and stent-assisted embolization had a higher incidence of postoperative microischemia. Age, smoking history, diabetes history, hyperlipidemia, aspirin resistance, tumour neck size, tumour location, and surgical duration were not statistically different between the two groups. The Chi-square test and Fisher's exact probability method were used in the univariate analysis, as shown in Table 3. Aneurysm size, aneurysm morphology, aneurysm neck morphology, aneurysm treatment, aneurysm embolization degree, follow-up time, and other factors are related to aneurysm recurrence. $P < 0.05$ was considered as statistically significant.

3.6. Multiple-Factor Analysis. Multivariate binary logistic regression analysis was conducted for the above two statistically significant indicators, as shown in Figure 9. The results showed that tumour size and interventional surgery method were the influencing factors for the prognosis of tumour interventional therapy. Tumour size > 7 mm and stent-assisted embolization are independent risk factors for the prognosis of patients with anterior circulation rupture. The risk of poor prognosis in patients receiving stent-assisted embolization was 4.172 times that of patients receiving non-stent-assisted embolization. The risk of poor prognosis in patients with <7 mm tumour was 0.035 times that in patients with >7 mm tumour, respectively.

The essence of the tumour lies in the local lesion of the arterial wall of the parent artery. Both stent-assisted embolization and non-stent-assisted embolization are mainly for the filling of the tumour cavity, while the treatment of the parent artery is neglected. The application of stents can effectively increase the density of tumour embolization and reconstruct

RETRACTED

the parent artery wall to surround the tumour neck. Stents improve hemodynamics and thus promote endometrial hyperplasia to cover the neck of the tumour. Multivariate logistic regression analysis showed that stent-assisted embolization had a 4.172-fold higher risk of poor outcome than non-stent-assisted embolization. In the process of stent-assisted embolization, the control and operation of stents are complicated. Once there is poor stent adherence and resistance to antiplatelet aggregation drugs, it is easy to induce platelet aggregation, promote stent thrombosis, and increase the incidence of cerebral infarction. On the one hand, choosing the stent with appropriate radial force and avoiding stimulating endothelial proliferation can reduce the chance of stinting stenosis. On the other hand, preoperative and postoperative ant platelet therapy should not be ignored. Therefore, in clinical work, the sensitivity of patients to ant platelet drugs should be well grasped, and individualized ant platelet therapy should be achieved, so as to maximize the advantages of stent-supported therapy.

4. Conclusion

Endovascular interventional therapy is a minimally invasive surgery, which has less tissue trauma and surgical impact than craniotomy clipping surgery. In this paper, endovascular embolization was used to treat tumour; the basic condition of patients before operation and the interventional operation plan were introduced. Through the analysis of clinical data and prognosis evaluation results of tumour patients receiving intravascular interventional therapy, the patients were divided into good prognosis group and poor prognosis group according to the modified Rankin scale score at discharge. The relationship between gender, age, history of hypertension, tumour width, tumour size, preoperative Hunt-Hess grade, interventional surgery method, and prognosis related to intravascular interventional therapy was explored. Conclusion: tumours >7 mm are a risk factor for poor prognosis. Age, sex, history of hypertension, tumour neck width, and preoperative Hunt-Hess grade were not independent risk factors affecting the prognosis of interventional therapy for tumours with anterior circulation rupture. The prognosis of tumour after intravascular intervention was related to the age, Hunt-Hess grade, and hypertension. The recurrence of the disease is related to the patient's age, Hunt-Hess grade, diabetes, hypertension, tumour diameter, tumour neck width, surgical methods, and embolization. Clinical attention should be paid to the influence of these factors, and corresponding measures should be taken to reduce the recurrence rate and improve the prognosis. Further studies are needed to determine whether preoperative control of blood pressure levels will reduce the incidence of microthromboembolic complications.

Data Availability

The data used to support the findings of this study are available from the corresponding author upon request.

Conflicts of Interest

The authors declare that there are no conflicts of interest.

Acknowledgments

The work in this paper was supported by First Affiliated Hospital of Soochow University.

References

[1] Z. Xianxian, Y. Chengsong, M. Qiang et al., "The efficiency analysis of thrombolytic rt-PA combined with intravascular interventional therapy in patients with acute basilar artery occlusion," *International Journal of Biological Sciences*, vol. 13, no. 1, p. 57, 2017.

[2] E. T. Warkentin and M. Pai, "Shock, acute disseminated intravascular coagulation, and microvascular thrombosis: is 'shock liver'the unrecognized provocateur of ischemic limb necrosis?" *Journal of Thrombosis and Haemostasis*, vol. 14, no. 2, pp. 231–235, 2016.

[3] R. Arghandeh, A. V. Meier, L. Mehrmanesh, and L. Mili, "On the definition of cyber-physical resilience in power systems," *Renewable and Sustainable Energy Reviews*, vol. 58, pp. 1060–1069, 2016.

[4] V. Y. Liu, A. M. Agha, and J. Lopez-Mattei, "Interventional cardio-oncology: adding a new dimension to the cardio-oncology field," *Frontiers in cardiovascular medicine*, vol. 5, p. 48, 2018.

[5] B. Taslakian, M. G. Sebaaly, and A. Al-Kutoubi, "Patient evaluation and preparation in vascular and interventional radiology: what every interventional radiologist should know (part 2: patient preparation and medications)," *CardioVascular and Interventional Radiology*, vol. 39, no. 4, pp. 489–499, 2016.

[6] O. Sutte, J. Calvo, and G. N'Kontchou, "Safety and efficacy of irreversible electroporation for the treatment of hepatocellular carcinoma not amenable to thermal ablation techniques: a retrospective single-center case series," *Radiology*, vol. 284, no. 3, pp. 877–886, 2017.

[7] J. H. Lee, M. U. Kim, and E. T. Kim, "Prevalence and predictors of peripherally inserted central venous catheter associated bloodstream infections in cancer patients: a multicentre cohort study," *Medicine*, vol. 99, no. 6, Article ID e19056, 2020.

[8] L. Wang, W. Wang, and W. Rong, "Postoperative adjuvant treatment strategy for hepatocellular carcinoma with microvascular invasion: a non-randomized interventional clinical study," *BMC Cancer*, vol. 20, no. 1, pp. 1–13, 2020.

[9] J. C. Chang, "Disseminated intravascular coagulation: is it fact or fancy?" *Blood Coagulation and Fibrinolysis*, vol. 29, no. 3, pp. 330–337, 2018.

[10] L. Tselikas, S. Champiat, and R. A. Sheth, "Interventional radiology for local immunotherapy in oncology," *Clinical Cancer Research*, vol. 27, no. 10, pp. 2698–2705, 2021.

[11] S. Pascual, I. Herrera, and J. Irurzun, "New advances in hepatocellular carcinoma," *World Journal of Hepatology*, vol. 8, no. 9, p. 421, 2016.

[12] M. L. Ellis, S. Okano, and A. McCann, "Catheter-related thrombosis incidence and risk factors in adult cancer patients with central venous access devices," *Internal Medicine Journal*, vol. 50, no. 12, pp. 1475–1482, 2020.

[13] B. C. Case, C. Yerasi, and B. J. Forrestal, "Intravascular lithotripsy facilitated percutaneous endovascular intervention of the aortic arch: a single-center experience," *Cardiovascular Revascularization Medicine*, vol. 21, no. 8, pp. 1006–1015, 2020.

Hindawi
Journal of Healthcare Engineering
Volume 2023, Article ID 9897527, 1 page
https://doi.org/10.1155/2023/9897527

Retraction

Retracted: Modified Look-Locker Inverse-Recovery (MOLLI) Sequence of Quantitative Imaging in Dirty Magnetic Resonance Longitudinal Relaxation Time Diagnostic Value of GE Combined with Longitudinal Relaxation Time Quantitative Imaging for Myocardial Amyloidosis

Journal of Healthcare Engineering

Received 10 October 2023; Accepted 10 October 2023; Published 11 October 2023

Copyright © 2023 Journal of Healthcare Engineering. This is an open access article distributed under the Creative Commons Attribution License, which permits unrestricted use, distribution, and reproduction in any medium, provided the original work is properly cited.

This article has been retracted by Hindawi following an investigation undertaken by the publisher [1]. This investigation has uncovered evidence of one or more of the following indicators of systematic manipulation of the publication process:

(1) Discrepancies in scope
(2) Discrepancies in the description of the research reported
(3) Discrepancies between the availability of data and the research described
(4) Inappropriate citations
(5) Incoherent, meaningless and/or irrelevant content included in the article
(6) Peer-review manipulation

The presence of these indicators undermines our confidence in the integrity of the article's content and we cannot, therefore, vouch for its reliability. Please note that this notice is intended solely to alert readers that the content of this article is unreliable. We have not investigated whether authors were aware of or involved in the systematic manipulation of the publication process.

In addition, our investigation has also shown that one or more of the following human-subject reporting requirements has not been met in this article: ethical approval by an Institutional Review Board (IRB) committee or equivalent, patient/participant consent to participate, and/or agreement to publish patient/participant details (where relevant).

Wiley and Hindawi regrets that the usual quality checks did not identify these issues before publication and have since put additional measures in place to safeguard research integrity.

We wish to credit our own Research Integrity and Research Publishing teams and anonymous and named external researchers and research integrity experts for contributing to this investigation.

The corresponding author, as the representative of all authors, has been given the opportunity to register their agreement or disagreement to this retraction. We have kept a record of any response received.

References

[1] Q. Lao, W. Xia, J. Jin, Y. Jia, and J. Feng, "Modified Look-Locker Inverse-Recovery (MOLLI) Sequence of Quantitative Imaging in Dirty Magnetic Resonance Longitudinal Relaxation Time Diagnostic Value of GE Combined with Longitudinal Relaxation Time Quantitative Imaging for Myocardial Amyloidosis," *Journal of Healthcare Engineering*, vol. 2021, Article ID 2800891, 12 pages, 2021.

Hindawi
Journal of Healthcare Engineering
Volume 2021, Article ID 2800891, 12 pages
https://doi.org/10.1155/2021/2800891

RETRACTED

Research Article

Modified Look-Locker Inverse-Recovery (MOLLI) Sequence of Quantitative Imaging in Dirty Magnetic Resonance Longitudinal Relaxation Time Diagnostic Value of GE Combined with Longitudinal Relaxation Time Quantitative Imaging for Myocardial Amyloidosis

Qun Lao,[1] **Wenping Xia**,[2] **Jing Jin**,[2] **Yuzhu Jia**,[3] **and Jianju Feng**[4]

[1]*Department of Radiology, Hangzhou Children's Hospital, Hangzhou, Zhejiang 310014, China*
[2]*Department of Radiology, Yin Zhou Second Hospital, Ningbo, Zhejiang 315040, China*
[3]*Department of Radiology, Tongde Hospital of Zhejiang Province, Hangzhou, Zhejiang 310012, China*
[4]*Departments of Radiology, Zhuji Affiliated Hospital of Shaoxing University, Zhuji People's Hospital, Zhuji, Zhejiang 311800, China*

Correspondence should be addressed to Jianju Feng; fengjj@usx.edu.cn

Received 17 August 2021; Revised 15 September 2021; Accepted 18 September 2021; Published 19 October 2021

Academic Editor: Kaijian Xia

Copyright © 2021 Qun Lao et al. This is an open access article distributed under the Creative Commons Attribution License, which permits unrestricted use, distribution, and reproduction in any medium, provided the original work is properly cited.

The pathological changes of myocarditis include degeneration and necrosis of myocardial cells and infiltration of inflammatory cells in the myocardial interstitium, accompanied by obvious myocardial fibrosis. Myocardial fibrosis is a determinant of ventricular remodeling and an important indicator of the classification of clinical risk factors and has an important value in evaluating the prognosis of heart disease. Cardiac magnetic resonance (CMR) is the "gold standard" for evaluating the shape and function of the heart, and it can show the characteristic pathological changes of myocardial tissue. The traditional gadolinium imaging agent delays the enhanced sequence images to visually show the extent of the affected myocardial fibrosis, but it cannot effectively identify small focal fibrosis or widespread diffuse fibrosis. The CMR longitudinal relaxation time quantitative technique can directly measure the relaxation time (T1) determined by the myocardial tissue and does not depend on the signal strength of the reference tissue and can quantitatively analyze the affected myocardium. In this study, the initial and enhanced quantitative imaging techniques of CMR were used to measure the magnetic value of the myocardium in patients with myocarditis, to explore the diagnostic value of myocardial fibrosis, and to analyze the correlation between cardiac fibrosis and cardiac function.

1. Introduction

Myocardial fibrosis is a determinant of cardiac pathological remodeling caused by various cardiovascular diseases [1], is the pathological basis of abnormal cardiac mechanical function and electrical activity [2], and eventually leads to heart failure and increases patient mortality [3]. A large number of clinical studies have shown that [4, 5] the abnormal expansion of myocardial extracellular matrix (ECM) is reversible, and the therapeutic targets of some new research drugs are mainly for fibrosis or myocardial extracellular matrix expansion. Therefore, it is important to detect myocardial fibrosis and evaluate its extent or the degree of extracellular matrix expansion.

At present, clinical imaging tests commonly used in the clinic include echocardiography, cardiac CT, cardiac magnetic resonance (CMR), cardiovascular angiography, and myocardial radionuclide examination. What are the different examination methods? They have their advantages and values in the morphology, function, diagnosis, and differential diagnosis of myocardial lesions but they also have certain limitations. In recent years, CMR imaging technology has developed more and more rapidly, and clinical applications have become more and more widely used. It has become a routine examination method in cardiovascular centers and large hospitals. CMR has a good temporal and spatial resolution, arbitrary plane imaging, good repeatability, and other advantages. It can play cardiac morphology, function, myocardial tissue characteristics, and myocardial activity in heart disease. The "one-stop" inspection function has a unique value in the cause diagnosis, risk stratification, and prognosis judgment of cardiomyopathy, and it has become the most ideal noninvasive examination method for cardiomyopathy [6]. From a histological point of view, myocardial tissue includes intracellular components, intravascular components, and interstitial spaces. The extracellular matrix space of myocardium is surrounded by cardiomyocytes, capillaries, and nerves, and the gap is filled with the extracellular matrix. After activation of myofibroblasts, a series of processes lead to the deposition. According to the distribution, myocardial fibrosis can be divided into localized fibrosis and diffuse fibrosis. Localized fibrosis is more common in myocardial infarction. Diffuse fibrosis includes reactive fibrosis and interstitial fibrosis, and diffuse interstitial fibrosis is more seen in cardiomyopathy. CMR has unique advantages in the evaluation of myocardial histological features. In recent years, magnetic mapping technology has been gradually applied in clinical practice. In 2013, the Cardiac Magnetic Resonance Association and the European Radiological Society's Cardiac Magnetic Resonance Working Group issued an expert consensus to define magnetic mapping as a CMR method to directly measure the magnetic value of myocardial tissue before or after injection of the contrast agent. The signal strength of each pixel is encoded by the size of the pixel, and the parameter schematic diagram is drawn through computer postprocessing. According to previous reports, the gas magnetic mapping technology is divided into the initial magnetic (noncontrast agent or magnetic before injection of contrast agent) and the enhanced magnetic. Native magnetic value can noninvasively find the pathological changes of the heart such as changes in iron content because it does not require the injection of contrast agents and can be used in patients with severely impaired renal function. The magnetic value is obtained from a fitting curve of at least 6–10 time points, and the magnetic time needs to be measured in multiple cardiac cycles. At present, different manufacturers and equipment have different magnetic mapping sequences. Magnetic mapping can be implemented using inversion recovery (IR) or saturation recovery (SR) pulse sequences. The clinically used reversed recovery pulse sequence in the modified magnetic mapping technique is the MOLLI sequence. Under gating, a specific cardiac cycle (often at the end of diastole) is selected for data collection. An image is obtained every cardiac cycle, and a set of images can be obtained by continuously increasing the IR sequence of magnetics. MOLLI used preparation sequences to reconstruct images with different inversion times in one breath-hold in 17 cardiac cycles. The readout sequence adopts steady-state free precession (steady-state prediction, SSP), which can reduce the loss of the magnetization vector in the reverse recovery. The acquisition time is less than 200 ms, and there are few motion artifacts. It has high accuracy, repeatability, and spatial resolution [7–9]. It is currently the most commonly used in magnetic mapping technology, as shown in Figure 1. However, the MOLLI breath-holding time is longer, with heart rate dependence, and there are T2 dependence and other factors. The result of SSP reading is the recovery time magnetic, which is lower than the true value of myocardium. The magnetic value needs to be corrected.

In this study, segments accounted for 5.9%, mostly located in the inferior sidewalls. Previous work summarized the results of the multicenter study and speculated that the myocardial segmental magnetic value difference was not caused by different myocardial composition. The main reason why the MOLLI sequence affects the image quality classification is magnetically sensitive artifacts and respiratory and motion artifacts. The reading of MOLLI adopts an SSP sequence, which can produce magnetic sensitive artifacts similar to the movie sequence. 3.0 T magnetic resonance has higher signal-to-noise ratio and contrast-to-noise ratio, which can provide higher temporal and spatial resolution and shorten the scanning time. However, it is easy to produce a series of problems related to the unevenness of the main magnetic field and the RF field, such as the detuned resonance artifacts of the SSP sequence. But this does not fully reflect the extent of myocardial disease involvement. In this study, there was no statistically significant difference in apical image quality compared with the central and basal parts; and it is indicated that magnetic value can be measured and different sections of left ventricular myocardium can be obtained if the thickness of the apical myocardium is allowed. The magnetic value of the segment completely evaluates the fibrosis of all myocardium.

2. Research Methods and Objects

2.1. Materials and Methods. We collected 12 healthy volunteers who underwent CMR magnetic mapping technique scans between January 2015 and December 2016. The scanning sequence includes movie sequence and gadolinium contrast agent delayed enhancement; and magnetic mapping scanning includes more patients (before and after injection contrast agent scanning). The scan adopts the MOLLI sequence. After the scanning is completed, the time is automatically generated. The mentioned method was used to analyze the tapping parameters of the left ventricular myocardium. The mentioned portrayal and measurement are all done by Spin Lite software. Here, we use the Pearson correlation analysis to explore the correlation between each parameter and age. Finally, according to the coronary artery blood supply area, electrical currents were divided into three groups for comparison.

2.2. Health Conditions. According to the position statement of the European Society of Cardiology in 2015 [10], direct clinic mention (DCM) is defined as left ventricular (LV) or

RETRACTED

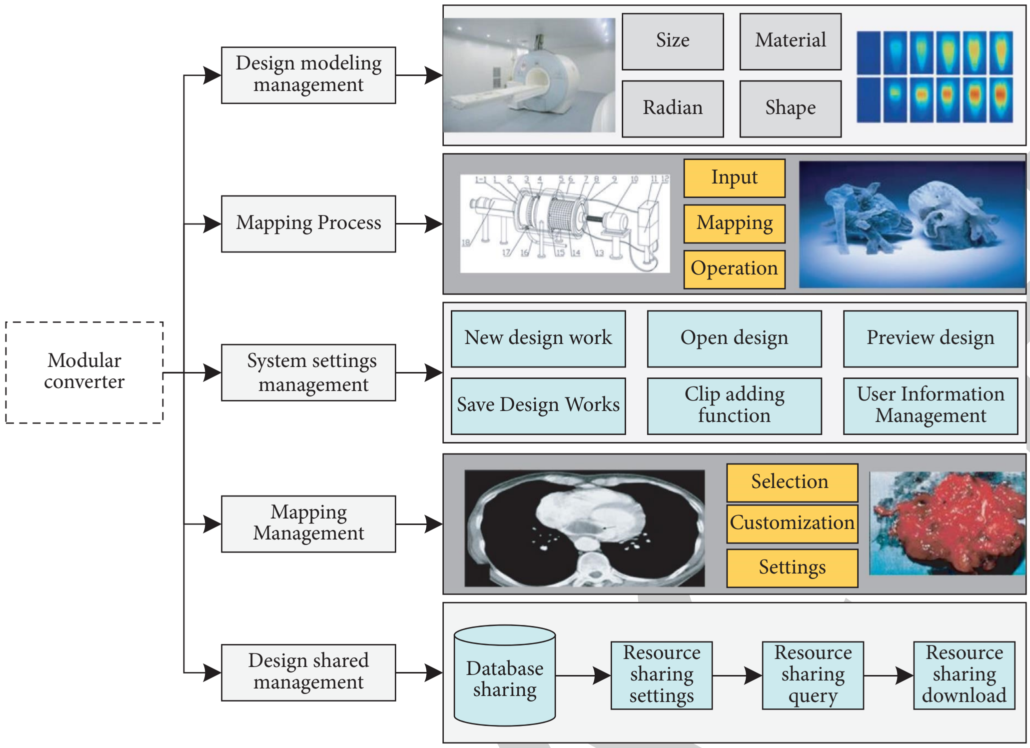

Figure 1: Magnetic mapping technology for the modular mapping.

biventricular dilatation or systolic insufficiency and excludes abnormalities such as hypertension and valvular disease and causes large-scale contractile dysfunction coronary artery disease. Causes include genetic or nongenetic factors. The clinical manifestations are left ventricular or bilateral ventricular enlargement and reduced ventricular systolic function, with or without congestive heart failure and arrhythmia, and complications such as embolism and sudden death can occur, as shown in Figure 2. The condition is progressively worse, the prognosis is very poor, and death can occur at any stage of the disease. The 5-year mortality rate reported abroad is 50%, and the domestic epidemiological survey found that the 5-year mortality rate is 80%. DCM ranks third among common causes of heart failure and ranks first among heart transplants [11]. According to Laplace's law, increased intraventricular wall tension leads to increased oxygen consumption and decreased myocardial contractile function. Decreased cardiac function forms a vicious cycle, progressive ventricular dilation, and relative thinning of the wall, and enlargement of the ventricular sphere eventually leads to ventricular remodeling, as well as microvascular damage, abnormal myocardial blood flow, and left ventricular block; and abnormal right ventricular pacing is also exacerbated. CMR imaging technology has developed more and more rapidly, and clinical applications have become more and more widely used. It has become a routine examination method in cardiovascular centers and large hospitals. CMR has a good temporal and spatial resolution, arbitrary plane imaging, good repeatability, and other advantages. It can play cardiac morphology, function, myocardial tissue characteristics, and myocardial activity in heart disease.

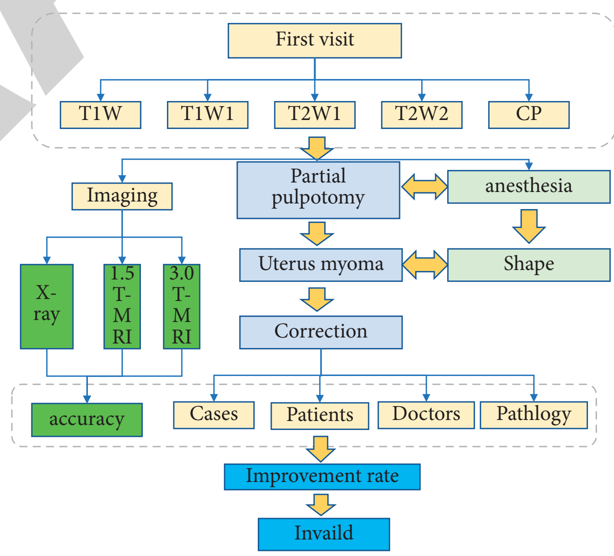

Figure 2: Health conditions measured by a series of imaging processes.

The process of ventricular remodeling eventually leads to direct clinical mention (DCM). The magnetic mapping technique can improve the sensitivity of CMR diagnosis of myocarditis and can be used as an effective means for the assessment of myocarditis condition and efficacy. The fibers of DCM are tandem hyperplasia and eccentric hypertrophy of the heart, the heart is significantly enlarged, the wall thickness is normal or slightly thickened, and the ventricles on both sides are excessively trabeculated. The left

RETRACTED

ventricular myocardial thickness is increased or thinned due to the enlargement of the heart cavity. Occasionally a subendocardial thrombus can be seen in the heart cavity. DCM has no specific histological manifestations and cardiomyocytes vary in size, cytoplasmic vacuolation, abnormal nuclei, and abnormal chromatin arrangement [12]. Alternative fibrosis in the middle layer can extend from the interventricular septum to the free wall or diffuse fibrosis. Some inflammatory DCM may have focal lymphocyte infiltration [13]. There are often thickened fibers under the endocardium. The cause of fibrosis in the interventricular septal muscle is unknown. Myocardial fibrosis leads to increased wall rigidity, reduced ventricular contraction, and diastolic function, leading to hemodynamic changes. Myocardial fibrosis can also cause fatal arrhythmias, leading to serious complications. The myocardial interstitial fibrosis in DCM patients is extensive, and the extracellular matrix is enlarged. The gadolinium contrast agent is concentrated outside the cell, showing delayed enhancement. CMR's problem has certain advantages for the detection of early moderate myocardial fibrosis. The problem may be a potential tool for predicting the risk stratification of DCM cardiac risk events.

The degree of myocardial diffuse fibrosis in patients with hypertensive heart disease and left ventricular hypertrophy is higher than that in simple hypertensive heart disease group and normal control group, and an electrical current is positively correlated with left ventricular myocardial mass index. It has a significant correlation with cardiovascular mortality, sudden cardiac death, and heart failure hospitalization rates. It is an independent predictor of cardiovascular death and heart transplant events. But myocardial diffuse fibrosis, lack of fibrosis, and normal myocardium, leading to mild fibrosis lesions, cannot show these problems [13]. Studies have confirmed [14] that the distribution of fibrotic tissue in DCM patients has a high degree of consistency with delayed enhancement sites, mainly manifested as intermuscular wall enhancement, which is related to poor prognosis, as shown in Figure 3. Fifty percent of patients present with negative performance. Coronary artery-negative myocardium [15] is likely to have undergone diffuse fibrosis in pathology. The negative coronary artery does not rule out myocardial disease. Previous studies [16] have shown that coronary artery can be associated with adverse cardiac events or arrhythmias but not with cardiac function. A study by Reiter et al. [17] has shown that, in patients with dilated cardiomyopathy, the value of Natal is related to left ventricular remodeling and myocardial contractile function. Stromp et al. [18] performed CMR examination and endocardial biopsy on 47 patients with cardiomyopathy, and 13 normal controls were used as the control group. The results showed that the magnetic values of the control group were greater than those with a negative coronary artery or accompanied by the obvious coronary artery.

Magnetic value is negatively correlated with histological fibrosis, similar to the above study results; and magnetic value can be used to noninvasively assess diffuse endocardial fibrosis in patients with cardiomyopathy. Schaefer et al.'s [19] study shows that the electrical current of DCM patients

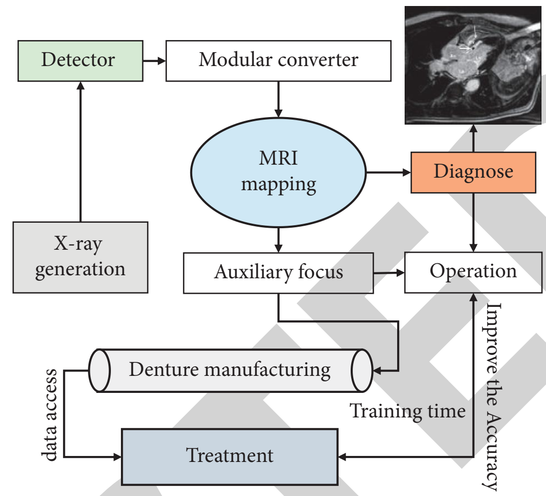

Figure 3: Distribution of the fibrotic tissue in DCM patients.

is higher than that of normal people, and it is related to cardiac function [20]. 45 cases of early DCM (mild cardiac function impairment and enlarged heart cavity, between 45% and 55%), 29 cases of DCM (impaired cardiac function, EF < 45% and enlarged heart chambers), and 56 healthy controls underwent CMR examination, showing that early DCM electrical current (25% ± 4%) and DCM electrical current (27% ± 3%) increased, higher than the healthy control (23% ± 3%), and there was a statistical difference (>0.05). Four patients with DCM underwent endocardial biopsy, and there was a significant correlation between CVF and electrical current ($r = 0.85$, $p = 0.01$), indicating that the early DCM electrical current can be increased, and the electrical current value can be reflected myocardial collagen deposition. Electrical current can be used as a noninvasive method and quantitative tool for the detection of myocardial fibrosis and can be used to monitor the response and risk stratification of DCM treatment.

2.3. Complications. The tissue characteristics of myocarditis include myocardial edema, hyperemia, and necrosis or fibrosis. The subendocardial biopsy is an important method to diagnose myocarditis, but it may cause complications or adverse consequences, and the tissue intensity can be summarized as in Figure 4. Patients with acute myocarditis have increased water content of myocardial cells due to inflammation. Myocardial ischemia leads to changes in the distribution of sodium and potassium inside and outside the cell, affecting free proton movement, resulting in a significant increase in magnetic relaxation time compared with normal people. Studies have shown that the accuracy of the magnetic mapping technique in the diagnosis of myocarditis is significantly higher than the "Lake" diagnostic criteria. Other studies have shown that the Postel value and electrical current value can identify the potential myocardial damage in the "normal" myocardium of children with myocarditis. The other 25 patients with acute myocarditis and normal controls underwent black blood mapping and coronary artery scans, respectively, and it was found that the magnetic

RETRACTED

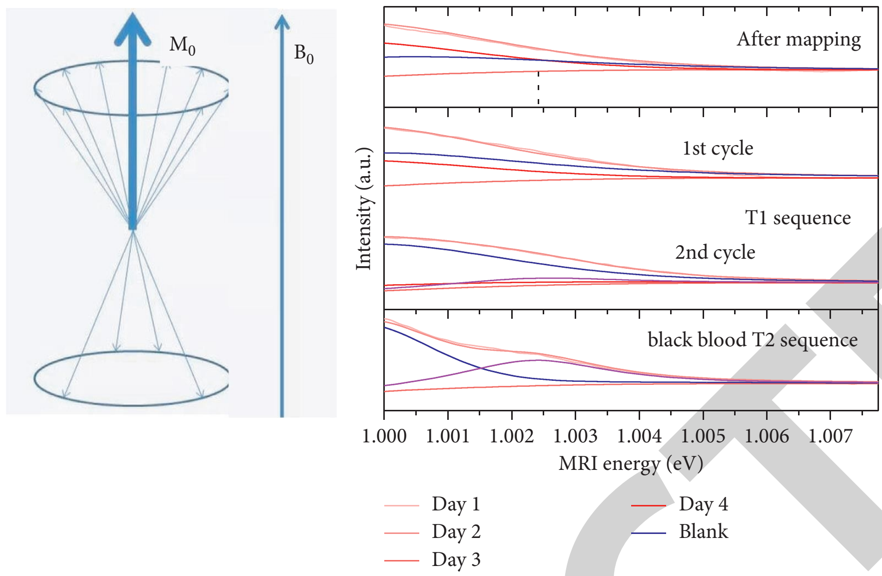

Figure 4: Tissue characteristics of myocarditis based on the MRI energy.

value of patients with acute myocarditis was significantly higher than that of the control group, and there was a statistical difference. Myocarditis sensitivity (91.5%) and accuracy (90.4%) were significantly higher than black blood T2 sequence (50.3% and 64.2%) and coronary artery sequence (73.1% and 83.0%). The specificity (89.2%) is lower than acute myocarditis (96.3%) and higher than the black blood sequence (88.5%) and has a good diagnostic value for acute myocarditis, especially. It is a diffuse lesion and a small focal lesion, which is similar to the results of Ferreira and other studies, and the quantitative advantage is more significant.

Tapping can be used to quantitatively evaluate the degree of myocardial diffuse fibrosis in patients with hypertension and heart disease, especially the magnetic value and electrical current value. The degree of myocardial diffuse fibrosis in patients with hypertensive heart disease and left ventricular hypertrophy is higher than that in simple hypertensive heart disease group and normal control group, and an electrical current is positively correlated with left ventricular myocardial mass index. Patients with hypertensive heart disease and left ventricular hypertrophy with diastolic dysfunction have higher magnetic and electrical current values than patients with hypertensive heart disease and hypertensive heart disease and left ventricular hypertrophy without cardiac dysfunction, suggesting that the myocardial diffuse interstitial fibers as shown in Figure 5 are more serious. Electrical current can also identify myocardial fibrosis in patients with hypertension and heart disease at an early stage and is an independent predictor of arrhythmia (atrial fibrillation), diastolic heart failure, and death in patients with hypertension and heart disease. The pathological change is the deposition of amyloid in the extracellular space, which leads to an increase in the volume of the extracellular space. After enhanced scanning, gadolinium is deposited in the enlarged extracellular space, and delayed enhancement may occur. The typical acute myocarditis manifestations are as follows: (1) acute myocarditis diffuse full-thickness subendocardial or transmural enhancement; (2) contrast medium being cleared quickly from the blood pool, and the heart cavity having dark blood pool performance; and (3) magnetic medium scan.

The myocardium is inhibited earlier than the heart cavity. Not only can acute myocarditis be used for diagnosis but also it reflects the distribution of amyloid, suggesting that the myocardial load of amyloid is an independent prognostic factor. The characteristic enhancement pattern of acute myocarditis can also be distinguished from scars of ischemic cardiomyopathy and myocardial fibrosis of non-ischemic cardiomyopathy. The coronary artery's acute myocarditis also tends to develop from normal no enhancement to subendocardial enhancement to transmural enhancement. Therefore, the enhancement pattern changes greatly, and the typical performance occurs in the late stage of the disease, and early lesions can be without acute myocarditis. Many patients with immune light chain amyloidosis (ALCH) have kidney involvement at the same time and cannot perform enhanced scans. The initial magnetic mapping technique does not require contrast agents and can be used for the detection of amyloidosis infiltration degree and efficacy. The electrical current value is significantly higher than that of cardiomyopathy patients and normal control groups, and the distribution of electrical current and acute myocarditis segments is consistent. The value of Natl can diagnose coronary artery. Here we found that the threshold value of AL type is 1020 ms and the diagnostic accuracy is 92%, which has a significant correlation with systolic and diastolic dysfunction. The magnetic value with significantly improved accuracy can reflect the cardiac amyloid load. In the study, the coronary artery's national magnetic value is higher than that of normal volunteers. Our research shows that the magnetic value is about 16% higher than normal and is related to cardiac systolic and diastolic function. Native value is more sensitive to early changes of

RETRACTED

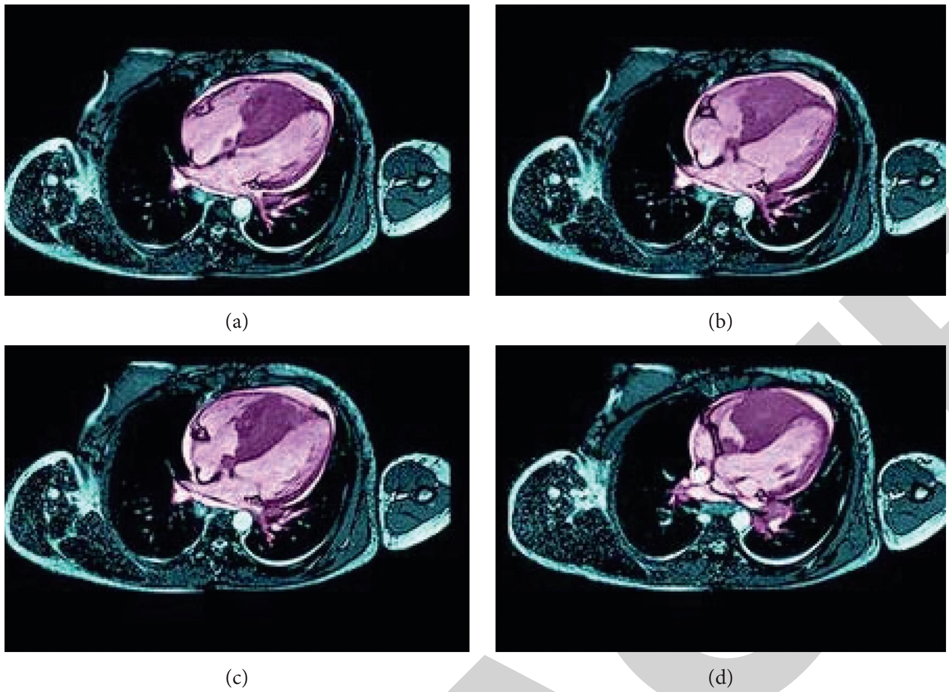

Figure 5: Hypertensive heart disease and left ventricular hypertrophy with diastolic dysfunction.

RETRACTED

the disease and prolonged magnetic value, and increased electrical current precedes changes in cardiac hypertrophy. The increase of magnetic value can reflect the severity of the disease and myocardial load. The magnetic value can also be used for treatment monitoring. Studies such as paintings have found that the left ventricular myocardial mass (LVM) of 7 patients who took green tea extract for 12 months decreased, accompanied by a decrease in magnetic value and electrical current, suggesting a decrease in myocardial load of amyloid. Studies have shown that electrical current >0.45 has a significant correlation with mortality (>4.41). Electrical current can be used as a biological indicator for predicting the prognosis of AL.

3. Clinical Manifestations

3.1. Extracellular Matrix and Myocardial Fibrosis. Myocardial fibrosis is a determinant of cardiac pathological remodeling caused by various cardiovascular diseases, is the pathological basis of abnormal cardiac mechanical function and electrical activity, and eventually leads to heart failure and increases patient mortality. A large number of clinical studies have shown that the abnormal expansion of the myocardial extracellular matrix is reversible, so the therapeutic targets of some new research drugs are mainly aimed at fibrosis or myocardial extracellular matrix expansion. Therefore, it is important to detect fibrosis and evaluate the extent of myocardial fibrosis or the degree of expansion of the extracellular matrix. Myocardial tissue includes three components: (1) cellular components, including cardiomyocytes, fibroblasts, epithelial cells, smooth muscle cells; (2) intravascular components, namely, blood; and (3) interstitial space, except for cells and vascular cells. The outer matrix is partially filled. In normal myocardial tissue, myocardial cells are closely packed, and there is little extracellular matrix. The extracellular interstitial space is a complex, mesh-like three-dimensional space surrounded by cardiomyocytes, capillaries, and nerves; it is mainly composed of collagen scaffolds, of which the first situation is 85% and the second is 11%, as shown in Figure 6. It is clinically suspected that the increase of electrical current during the coronary artery is early. Period involvement is more sensitive than acute myocarditis, and the change in electrical current is more obvious than magnetic value, which can be used as a new indicator to assess the severity of the coronary artery. Besides, it surrounds cardiomyocytes and the coronary artery between muscles maintains the dynamic balance, support, and integrity of the myocardial structure and has the function of preventing the myocardial fibers from slipping and supporting the mechanical function of the myocardial tissue; there are various proteins and information molecules (signaling molecules) in the interstitial space. The intracellular scaffold proteins and intercellular proteins establish links and transmit biochemical signals. Extracellular matrix affects myocardial fibrosis and secondary cardiac tissue structure and cardiac function changes. After activation of myofibroblasts, a series of processes lead to the deposition, mainly the formation of thick and ductile collagen, which forms various forms of fibrosis visible to the naked eye, resulting in abnormal heart function or conduction.

The extracellular matrix is damaged under the action of matrix magnetic metalloproteinases (MMPs). The relative levels of tissue inhibitors of metalloproteinases determine the rate of damage. Inflammatory cells and other cytokines also affect the process of myocardial fibrosis. Myocardial

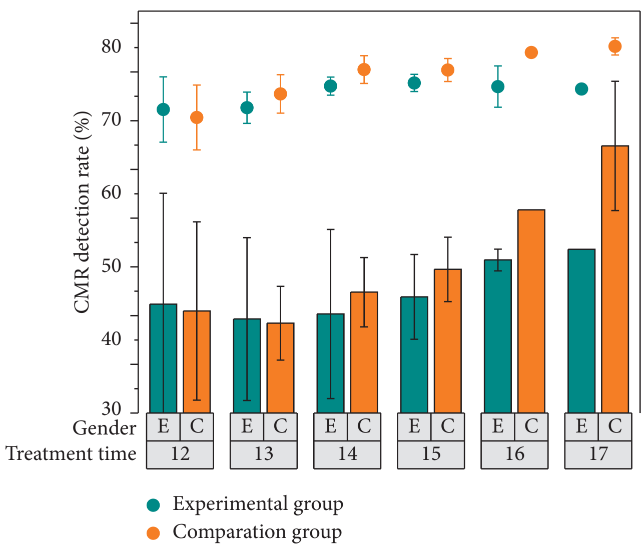

Figure 6: Collagen scaffolds in the mesh-like three-dimensional space.

fibrosis includes alternative fibrosis and interstitial fibrosis, and the former can be seen in patients with myocardial cell necrosis or myocardial infarction; and the latter can be seen in nonischemic cardiomyopathies, such as sarcoidosis, myocarditis, and chronic renal insufficiency. Interstitial fibrosis can be diffuse, including reactive fibrosis and infiltrating interstitial fibrosis. Reactive fibrosis is seen in aging, high blood pressure, and diabetes. Myocardial fibrosis is a complex process that leads to aggregation/expansion of extracellular matrix and stiff ventricular wall, affects diastolic function, and ultimately damages cardiac contractile function and also affects normal cell activities such as myocardial electrophysiology.

3.2. Myocardial Fibrosis Evaluation Tool

3.2.1. Contrast Agent-Delayed Strengthening. An endocardial biopsy is the “gold standard” for diagnosing myocardial fibrosis, but it is an invasive test and may have sampling errors, which limits clinical application. Acute myocarditis is considered to be the “gold standard” for noninvasive detection of myocardial focal fibrosis. The gadolinium contrast agent is an extracellular space contrast agent, which cannot enter the cell through the intact cell membrane. Its function is to shorten the magnetic relaxation time of the tissue. Myocardial fibrosis deposits in extracellular interstitial collagen, causing the body to expand. A gadolinium contrast agent is deposited and concentrated in the extracellular matrix, and the capillary density in the affected area is reduced, and the outflow rate is slowed which shortens the relaxation time of myocardial fibrosis magnetic and is more obvious than the normal myocardial shortening. Delayed scanning adopts magnetic-weighted inversion recovery sequence imaging. The inversion time is artificially set so that the normal myocardial signal is 0 (black), and the fibrotic tissue is a local high signal (showing white), which is in obvious contrast with the surrounding normal tissue. Acute myocarditis is the “gold standard” for imaging scars and fibrosis, especially for focal fibrosis, which has good repeatability. Acute myocarditis of different diseases has different manifestations of myocardial fibrosis, so it can be prompted and identified. However, acute myocarditis also has corresponding problems; and the coincidence rate can be realized into continuous growth, as shown in Figure 7. The pathogenesis of DCM is caused by stress load, volume load, and neurohormonal hyperresponsiveness, leading to apoptosis, death, and fibrosis of myocardial cells, and myocardial cells are rarely regenerated and renewed. The myocardium is damaged and the cytoskeleton is dissolved, and the ventricular cavity is enlarged. In the early stage of the disease, acute myocarditis’s performance characteristics can indicate the faults, but, in the late stage of the disease, acute myocarditis is diffusely distributed and the performance is not specific. It is difficult to identify the cause. Currently, acute myocarditis is mainly judged visually, and there is no unified threshold; and it depends on fibrosis and surrounding normal tissues. Compared with the signal, the boundary of the lesion area is generally not clear enough. There is no objective standard when judging the edge of acute myocarditis and measuring the range of acute myocarditis. When the window width and window position are changed, the range also changes, especially in ischemic cardiomyopathy. Before the acute myocarditis scan, you must first perform a sequence scan to find the appropriate magnetic time for normal myocardial tissue suppression.

If the myocardium is diffusely fibrotic, the scanner will mistakenly think that the fibrotic myocardium is normal and incorrectly set the reverse. At the time of transfer, acute myocarditis will display diffuse fibrosis lesions as black, causing its false normalization. However, it will not display diffuse fibrosis, resulting in missed diagnosis, such as diseases with volume load or pressure load overload. There is no abnormal signal delayed enhancement, abnormal heart changes cannot be ruled out. It can be seen that there is no optimal threshold for acute myocarditis on CMR which can well reflect myocardial fibrosis. The signal strength of acute myocarditis cannot accurately identify the type of fibrosis. In patients with renal dysfunction, the gadolinium contrast agent will aggravate the change of renal fibrosis and increase the occurrence of contrast agent nephropathy and cannot be enhanced. Therefore, the quantitative technique based on the inherent properties of the tissue and the direct measurement of the magnetic value and the electrical current technique of extracellular interstitial volume fraction have become research hotspots in recent years. Such techniques can more sensitively detect early and diffuse myocardial fibrosis and improve the diagnostic efficacy of CMR. In October, our working group put forward the consensus of quantitative evaluation of magnetic mapping and extracellular mesenchymal volume fraction (extracellular, fractional, electrical current).

3.2.2. Magnetic Mapping Sequence. After using inversion recovery (IR) or saturation recovery (SR) pulse sequence scanning, the magnetic mapping parameter map of the heart

RETRACTED

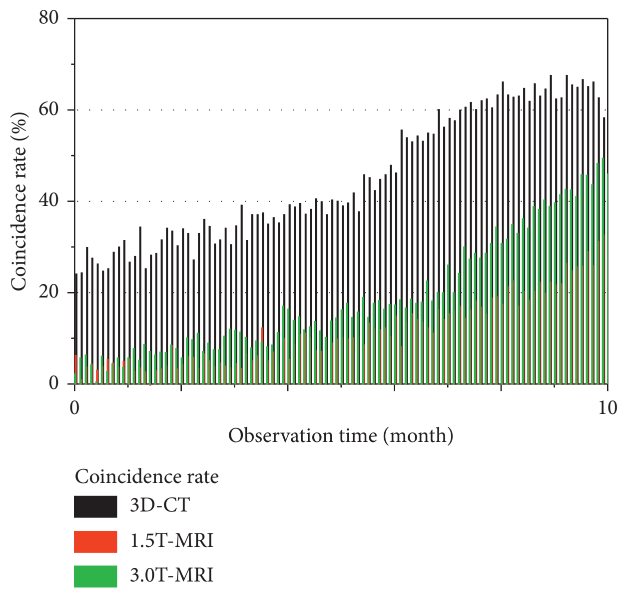

Figure 7: Coincidence rate under a continuous observation time.

is generated by each pixel in the magnetic value coding map. In the reverse recovery sequence, the magnetic mapping technology and the improved Look-Locker magnetic mapping technology are commonly used. The Loop-Locker magnetic mapping technology periodically applies a series of low flip angle (<35°) RF pulses to generate gradient echoes. After the magnetization vector is reversed, it uses gradient echoes to read out after each RF pulse. The MR signal quantifies the magnetic value according to the rate of change of the signal amplitude. This sequence can be acquired multiple times under multiple magnetic values, and the imaging speed is fast. The disadvantage is that the gradient echo readout signal causes the inversion recovery curve to change which may lead to inaccurate magnetic measurement and is not suitable for a beating heart. MOLLI technology utilizes balanced steady-state precession (SSP) sequence to read out the signal which can reduce the loss of magnetization vector during reverse recovery and has a smaller impact on the longitudinal magnetization vector recovery curve and can obtain a higher signal-to-noise ratio. From this result, we can use mapping-gating to perform selective image acquisition at the end of diastole, effectively reducing the impact of a heartbeat on image acquisition. The sequence generates a data set that increases the number of samples in the relaxation curve, thereby making the measurement accuracy of magnetic higher in 3.0 T MRI compared to the CT and 1.5 T MRI mappings as shown in Figure 8. The scan was completed within 17 cardiac cycles, and 5 single acquisitions were performed with 3 cardiac cycles without data acquisition between each acquisition. The initial magnetic time is the time from the application of the inversion pulse to the acquisition of the first image in k-space. The effective magnetic time is the length of the cardiac cycle from the beginning of the first image acquisition at the initial time.

MOLLI can collect all tapping data of a single layer of the heart in a breath-holding process. The collection time is less than 200 ms, and there are few motion artifacts. High accuracy, repeatability, and spatial resolution are currently the most commonly used technologies. However, breath-holding time is longer. With heart rate dependence, there are factors such as dependence, magnetization transfer, inversion efficiency, and loss of magnetization vector. The result of SSP reading is the recovery time magnetic, which is lower than the true value of myocardium. Therefore, magnetic mapping needs to be corrected. Common saturation recovery (SR) sequence acquisition method is saturation recovery single-shot acquisition, which is not subject to the measurement within 10 cycles of a heartbeat cycle, and the A-frame measurement is performed within 10 cycles. The SSP sequence read signal is not affected by the loss of the longitudinal magnetization vector and is also not affected by the absolute magnetic value, heart rate, and flip angle. It is more accurate than MOLLI, but the signal noise is lower and the artifacts are more than the latter. Therefore, by this method, the accuracy is reduced.

4. Simulation Experiment and Result Analysis

4.1. Longitudinal Relaxation Time. Magnetic mapping technology includes the initial (before enhancement) magnetic mapping and enhanced magnetic mapping. The initial magnetic mapping is to measure the magnetic value of the myocardium by scanning the noninjected contrast agent. This technique is highly repeatable and is not affected by contrast injection. It is suitable for patients with renal insufficiency or contrast allergy. After enhancement, time-mapping is usually injected with a contrast agent at a dose of 0.15–0.220 mm/kg. After 15–20 minutes of injection, an image is collected to measure the myocardial posttime value, but the posttime value is affected by a variety of factors, such as contrast agent dose, concentration, injection rate, and collection time after injection. The increase in the value could be found in the following factors: (1) cell necrosis caused by myocardial injury or myocardial inflammation and (2) myocardial amyloidosis or fibrosis (myocardial infarction scar, hypertrophic cardiomyopathy, dilated cardiomyopathy, etc.). The decrease in the value is seen in myocardial fat infiltration (such as Anderson-Fabry disease) and myocardial iron deposition disease. However, the magnetic value is dependent on heart rate. Due to the cardiac cycle, the magnetic value in diastole is slightly higher than that in systole, which may be due to the difference in myocardial blood volume between systole and diastole. The magnetic value is also affected by the myocardial segment. Here, we found that the apex is larger than the basal and central native measurements, which may be related to the thinner wall of the apex and the greater proportion of extracellular interstitial. Also, it may be related to the apical image being more susceptible to partial volume effect interference. Moreover, we summarized the results of the multicenter study and speculated that the difference in myocardial segmental magnetic value was not caused by different myocardial composition. But the magnetic field uniformity could be reached into the highest point in a certain time as shown in Figure 9. When there is a difference between the measurement segments, it is necessary to

RETRACTED

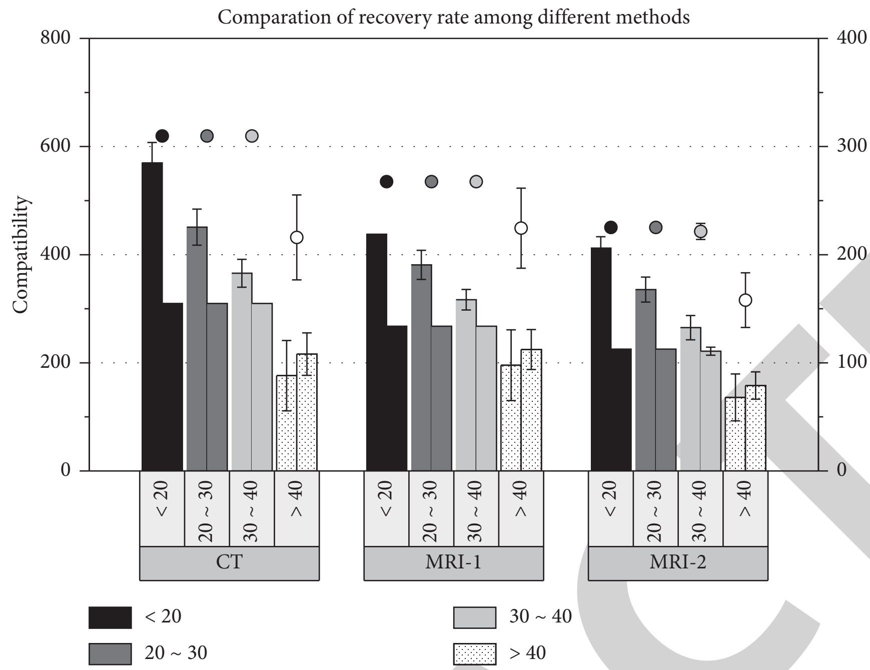

Figure 8: Compatibility of magnetic measurement in the MRI and CT mappings.

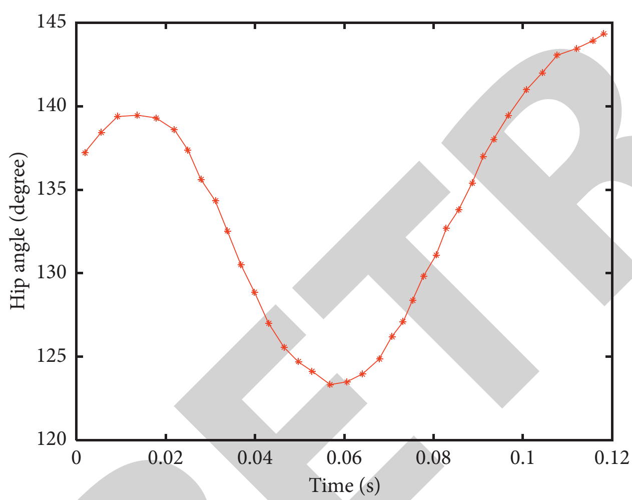

Figure 9: Magnetic value-respective hip angle changes with time.

consider the existence of these objective factors, rather than direct judgment as myocardial injury. Gender and age are also physiological factors that affect the magnetic value, but the conclusion is not uniform.

4.2. Extracellular Matrix Volume Fraction. The magnetic value is affected by the strength of the magnetic field and the accuracy of the measurement method, and these effects may exceed the difference between the normal myocardium and diseased myocardium, making it difficult to directly compare the value under different conditions. Moreover, the magnetic value includes two parts: the interstitial part and cardiomyocytes part. The electrical current of the myocardium reflects the volume fraction of the myocardial tissue that is not occupied by the cells. The electrical current value can be calculated by adjusting the myocardial value and the magnetic value of the myocardium through the blood cell volume, and the electrical current map is generated accordingly. Electrical current measures the space occupied by extracellular interstitium and is correlated with the collagen volume fraction (collapse evolution, CVF).

The typical characteristics of acute myocarditis in HCM patients are patchy or large acute myocarditis between muscles, which are common in the anterior wall, the right ventricular insertion part of the base, the anterior septum, and the area of myocardial hypertrophy, and nonhypertrophic areas appear. In the case of noninvasive disease and edema, electrical current can be used as a biological marker of myocardial fibrosis. The electrical current value is less affected by changes in magnetic field strength. It is affected by the dose of contrast agent, delay time, glomerular filtration rate, hematocrit, and body fat content. Contrast agent injection methods include continuous intravenous infusion and a single bolus injection of contrast agent. From this, we can achieve a dynamic equilibrium state of distribution between plasma and interstitial. We compared two injection methods of normal volunteers, and the difference was not statistically significant. The accuracy of MRI in the first sample is higher than the second value and the third value as shown in Figure 10. But the individual varies greatly. Here we found that electrical current in females is higher than that in males. If itself is high, there are statistical differences, which may be inherent. Most of the current literature also supports this view. An electrical current map can intuitively provide the electrical current value of each pixel, which significantly shortens the measurement time compared to manual measurement, but it may affect the measurement due to poor registration and image correction.

RETRACTED

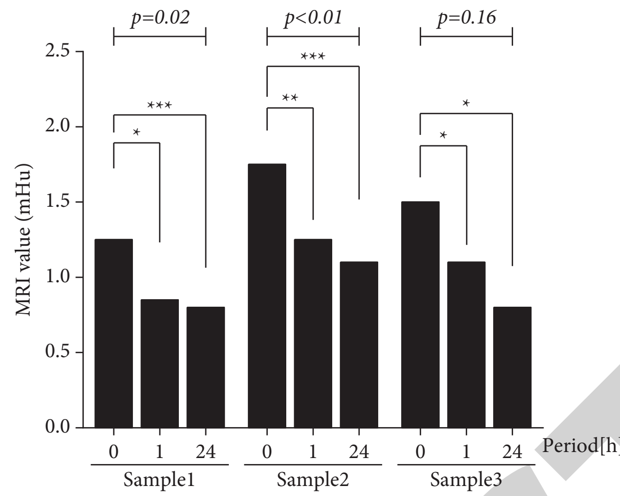

Figure 10: Accuracy of MRI value in the different samples.

4.3. Clinical Application. The study of the magnetic value before and after infarction found that the initial magnetic mapping can detect myocardial infarction; and the acute myocardial infarction native value (1197 ± 76 ms) is higher than the old myocardial infarction native value (1060 ± 61 ms). Magnetic mapping sensitivity and specificity for the diagnosis of acute myocardial infarction can reach 96% and 91%, which is more sensitive than second mapping. Compared with acute myocardial infarction, the abnormal area of the magnetic value of old myocardial infarction is closer to the range of acute myocarditis display infarction and has a good consistency. However, the abnormal area of magnetic value is larger than the range of acute myocarditis, suggesting that the mapping can be used. Screening for acute myocardial infarction is not suitable for assessing infarct size. Magnetic mapping can quantify the value of myocardial edema of acute myocardial infarction (AMI), reflecting the scope of edema. Magnetic mapping technique combined with acute myocarditis can accurately determine the inversion of myocardial infarction. The value of mapping can also identify the microvascular obstruction. The microvascular area is higher than the distal myocardium but lower than the infarcted myocardium. Magnetic mapping technology can evaluate the degree and severity of the myocardial injury. Here, by using acute myocarditis and mapping as a tool, it was found that native magnetic is significantly related to the severity of the myocardial injury, and magnetic value can predict the recovery of cardiac function. Calculating electrical currents can also accurately diagnose the range of myocardial infarction. The electrical current range of normal myocardium is 24%. In another part, the electrical current of patients with acute myocardial infarction at 1 week was 58.5% ± 7.6%. Our research shows that the electrical current of old myocardial infarction reached 68.5% ± 8.6%. After myocardial infarction, apoptosis is widespread in the infarct area and the noninfarct area. The myocardial cell apoptosis in the noninfarct area and the late ventricular remodeling are mutually causal, leading to the continuous deterioration of cardiac function.

The increase of electrical current indirectly suggests that the apoptosis and displacement of the noninfarct area may be related to the mechanism of myocardial remodeling in the noninfarct area. Studies also show that magnetic value in the noninfarct area is heart failure after myocardial infarction. Independent variables are related to cardiac adverse events and death. Although acute myocarditis is still the most important method for detecting acute and old myocardial infarction, magnetic mapping and electrical current can further quantitatively evaluate noninfarct myocardium and the area around the infarct from different angles, which can provide more pathophysiology for the diagnosis and treatment of myocardial infarction information. The new guideline of the European Society of Cardiology in 2014 expanded the definition of hypertrophic cardiomyopathy, which can be regarded as the newfound when the patient has left ventricular wall thickening and increased cardiac load as a nonindependent pathogenic factor. This definition includes not only cardiac muscle. Autosomal dominant genetic diseases caused by mutations in globulin genes also include metabolic and neuromuscular genetic diseases, chromosomal inheritance, and genetic syndromes, as well as aging and amyloidosis. Hypertrophic cardiomyopathy is characterized by ventricular wall hypertrophy, mainly involving the left ventricle. The incidence is about 1/500 and the case fatality rate is nearly 1/1000, which is one of the main causes of sudden death in young adults. Hypertrophic histological cardiomyopathy showed that myocardial cells were hypertrophic and the nuclei were abnormal under the microscope. They were arranged in an irregular, chaotic, herringbone pattern. In asymmetric ventricular septal hypertrophic cardiomyopathy, the increase in myocardial cells also exacerbates ventricular septal hypertrophy. The abnormalities of extracellular interstitial include interstitial fibrosis and alternative fibrosis; in particular, plexiform fibrosis can be seen in the chaotically arranged areas. Interstitial fibrosis can be seen around normal or abnormal

RETRACTED

cardiomyocytes; alternative fibrosis can extend to areas where cardiomyocytes are missing.

Occasionally, there are abnormalities in the intermural coronary arteries, the development of small intermural arteries, the thickening of the intima, and intima with a structural disorder of the intima. Hypertrophic cardiomyopathy fibrosis may be related to two reasons: (1) model caused by abnormal myocardial cells, as well as interstitial and plexiform fibrosis caused by histopathological reactions, and (2) narrowed coronary artery lumen stenosis caused by small abnormalities. Chronic infarction impairs hypertrophic myocardial perfusion and reduces coronary reserve capacity. Previous studies have shown that the interventricular septal area is more common to the intermural arterioles, and the areas with obvious fibrosis are more common than the areas with no or light fibrosis. This result indicates the stage of disease progression. End-stage acute myocarditis patients have a wider range than those who preserve cardiac function. Acute myocarditis is associated with the occurrence of ventricular arrhythmias. Extensive acute myocarditis is associated with an increased risk of sudden cardiac death (SCD) and decreased end-stage systolic function. Acute myocarditis is a risk factor for sudden cardiac death. Acute myocarditis is expected to provide a basis for the risk stratification of SCD and guide implantable cardioverter-defibrillator (ICD) implantation treatment. Histopathologically, the acute myocarditis region reflects alternative fibrosis and end-stage hypertrophic cardiomyopathy fibrosis. Acute myocarditis generally does not appear in the mild fibrosis zone, because the signal in the small fibrosis zone can be completely suppressed. Hypertrophic cardiomyopathy fibrosis is common and the degree of fibrosis of the affected myocardium is different through 48 hypertrophic cardiomyopathy patients and 18 normal controls. Magnetic mapping technique can be used to determine the severity of myocardial fibrosis in hypertrophic cardiomyopathy patients. The evaluation shows that there are different degrees of fibrosis in the surrounding area of acute myocarditis, suggesting that lesions in the early stage of fibrosis can be found. Native magnetic value is valuable for detecting this part of the anomaly without acute myocarditis, and the electrical current value is significantly higher than normal control. We analyzed the results of magnetic mapping's assessment of myocardial fibrosis with the results of high-throughput gene sequencing and endocardial biopsy and found that the mapping values of hypertrophic cardiomyopathy-related gene carriers were significantly shortened after a delay. The decrease of the value is significantly related to the patient's left ventricular diastolic dysfunction, suggesting that the diffuse fibrosis measured by mapping can be used as a powerful tool to link the phenotype and genotype of the patient.

5. Conclusion

This shows that the application of magnetic mapping and electrical current techniques in CMR examination can improve the accuracy of coronary artery diagnosis, quantify amyloid load, distinguish coronary artery types, and predict prognosis. In summary, magnetic mapping technology and electrical current technology can detect early and can quantitatively evaluate the lesions. It has good application prospects in the diagnosis, risk assessment, efficacy, and prognosis evaluation of various myocardial diseases. However, magnetic mapping technology and electrical current technology are affected by many factors. At present, there is a lack of a unified normal reference value. Moreover, large-scale and multicenter research is still required.

In the future, electrical current can be used as a biological marker of myocardial fibrosis. The electrical current value is less affected by changes in magnetic field strength. It is affected by the dose of contrast agent, delay time, glomerular filtration rate, hematocrit, and body fat content.

Data Availability

The data used to support the findings of this study are available from the corresponding author upon request.

Conflicts of Interest

The authors declare that there are no conflicts of interest.

Acknowledgments

This work was supported by Zhuji Affiliated Hospital of Shaoxing University, Zhuji People's Hospital.

References

[1] A. Reister Schultz, T. Jacob, C. A. Eide et al., "Characterizing phsignaling changes in chronic myeloid l stem and progenitor cells upon combined treatment with i inhibitors using quantitative single cell p-imaging," *Blood*, vol. 132, no. 1, p. 4248, 2018.

[2] B. D. Nam, S. M. Kim, H. N. Jung, Y. Kim, and Y. H. Choe, "Comparison of quantitative imaging parameters using cardiovascular magnetic resonance between cardiac amyloidosis and hypertrophic cardiomyopathy: inversion time scout versus T1 mapping," *The International Journal of Cardiovascular Imaging*, vol. 34, no. 11, pp. 1769–1777, 2018.

[3] B. Marty, R. Gilles, M. Toussaint et al., "Comprehensive evaluation of structural and functional myocardial impairments in Becker muscular dystrophy using quantitative cardiac magnetic resonance imaging," *European Heart Journal-Cardiovascular Imaging*, vol. 20, no. 8, pp. 906–915, 2019.

[4] O. Mesubi, K. Ego-Osuala, J. Jeudy et al., "Differences in quantitative assessment of myocardial scar and gray zone by LGE-CMR imaging using established gray zone protocols," *The International Journal of Cardiovascular Imaging*, vol. 31, no. 2, pp. 359–368, 2015.

[5] L. Barisoni, C. Gimpel, R. Kain et al., "Digital pathology imaging as a novel platform for standardization and globalization of quantitative nephropathology," *Clinical Kidney Journal*, vol. 10, no. 2, pp. 176–187, 2017.

[6] M. J. Wilhelm, H. H. Ong, S. L. Wehrli et al., "Direct magnetic resonance detection of myelin and prospects for quantitative imaging of myelin density," *Proceedings of the National Academy of Sciences*, vol. 109, no. 24, pp. 9605–9610, 2012.

RETRACTED

Hindawi
Journal of Healthcare Engineering
Volume 2023, Article ID 9836495, 1 page
https://doi.org/10.1155/2023/9836495

Retraction

Retracted: Intracavitary Electrocardiogram Guidance Aids Excavation of Rhythm Abnormalities in Patients with Occult Heart Disease

Journal of Healthcare Engineering

Received 5 December 2023; Accepted 5 December 2023; Published 6 December 2023

Copyright © 2023 Journal of Healthcare Engineering. This is an open access article distributed under the Creative Commons Attribution License, which permits unrestricted use, distribution, and reproduction in any medium, provided the original work is properly cited.

This article has been retracted by Hindawi, as publisher, following an investigation undertaken by the publisher [1]. This investigation has uncovered evidence of systematic manipulation of the publication and peer-review process. We cannot, therefore, vouch for the reliability or integrity of this article.

Please note that this notice is intended solely to alert readers that the peer-review process of this article has been compromised.

Wiley and Hindawi regret that the usual quality checks did not identify these issues before publication and have since put additional measures in place to safeguard research integrity.

We wish to credit our Research Integrity and Research Publishing teams and anonymous and named external researchers and research integrity experts for contributing to this investigation.

The corresponding author, as the representative of all authors, has been given the opportunity to register their agreement or disagreement to this retraction. We have kept a record of any response received.

References

[1] Y. Wei, Y. Zhu, X. Wen, Q. Rui, and W. Hu, "Intracavitary Electrocardiogram Guidance Aids Excavation of Rhythm Abnormalities in Patients with Occult Heart Disease," *Journal of Healthcare Engineering*, vol. 2021, Article ID 2230383, 11 pages, 2021.

Hindawi
Journal of Healthcare Engineering
Volume 2021, Article ID 2230383, 11 pages
https://doi.org/10.1155/2021/2230383

RETRACTED

Research Article

Intracavitary Electrocardiogram Guidance Aids Excavation of Rhythm Abnormalities in Patients with Occult Heart Disease

Yanli Wei,[1] **Ying Zhu**,[1] **Xin Wen**,[1] **Qing Rui**,[2] **and Wei Hu**[1]

[1]*Department of Critical Care Medicine, Affiliated Hangzhou First People's Hospital, Zhejiang University School of Medicine, Hangzhou, Zhejiang 370000, China*
[2]*Department of Critical Care Medicine, The First People's Hospital of Chang Zhou, Changzhou, Jiangsu 213003, China*

Correspondence should be addressed to Wei Hu; paolohu929@zju.edu.cn

Received 19 August 2021; Revised 15 September 2021; Accepted 16 September 2021; Published 15 October 2021

Academic Editor: Gu Xiaoqing

Copyright © 2021 Yanli Wei et al. This is an open access article distributed under the Creative Commons Attribution License, which permits unrestricted use, distribution, and reproduction in any medium, provided the original work is properly cited.

In this paper, the analysis of intracavitary electrocardiograms is used to guide the mining of abnormal cardiac rhythms in patients with hidden heart disease, and the algorithm is improved to address the data imbalance problem existing in the abnormal electrocardiogram signals, and a weight-based automatic classification algorithm for deep convolutional neural network electrocardiogram signals is proposed. By preprocessing the electrocardiogram data from the MIT-BIH arrhythmia database, the experimental dataset training algorithm model is obtained, and the algorithm model is migrated into the project. In terms of system design and implementation, by comparing the advantages and disadvantages of the electrocardiogram monitoring system platform, the overall design of the system was carried out in terms of functional and performance requirements according to the system realization goal, and a mobile platform system capable of classifying common abnormal electrocardiogram signals was developed. The system is capable of long-term monitoring and can invoke the automatic classification algorithm model of electrocardiogram signals for analysis. In this paper, the functional logic test and performance test were conducted on the main functional modules of the system. The test results show that the system can run stably and monitor electrocardiogram signals for a long time and can correctly call the deep convolutional neural network-based automatic electrocardiogram signal classification algorithm to analyze the electrocardiogram signals and achieve the requirements of displaying the electrocardiogram signal waveform, analyzing the heartbeat type, and calculating the average heart rate, which achieves the goal of real-time continuous monitoring and analysis of the electrocardiogram signals.

1. Introduction

According to statistics, cardiovascular disease accounts for about one-third of all deaths worldwide each year and has become the biggest threat to human health. Today, the incidence of heart disease and cardiovascular disease is increasing due to the fast pace of life and the pressure of work and life. Therefore, the prevention and diagnosis of heart disease and cardiovascular disease are particularly important [1]. Heart disease is a chronic disease and is characterized by chronic morbidity and memory onset [2]. Patients with heart disease are mobile and scattered and do not stay in one place, so they may die at some point before they can be treated. Therefore, if we can provide timely relief measures and treatment when physiological signals such as an electrocardiogram are abnormal, we can greatly reduce the mortality rate and other accidents caused by heart disease [3]. If people can check their physiological signals at any time and know their physical condition clearly according to the results obtained from the analysis of physiological signals, then they can take the initiative to prevent some heart diseases before they occur [4]. By selecting the deep convolutional neural network as the basic framework of the algorithm, the first and second points in the proposed problem can be solved well. Also, for those patients who have just finished rehabilitation surgery and returned home, it is necessary to monitor their body changes at any time, so that they can seek medical attention at any time in case of special circumstances [5]. Of course, people can also save their physiological signals so that they are not lost and can be used as an important reference for the doctor when they seek medical attention. Therefore, the ability to collect human electrocardiogram signals and analyze them automatically is essential, which will certainly promote the rapid development of medicine in the diagnosis of heart disease and cardiovascular diseases [6].

Due to the presence of noise in the collected electrocardiogram signal such as frequency interference, electromyographic interference, and baseline drift, the preprocessing stage of the electrocardiogram signal is mainly to remove the noise by filtering the electrocardiogram signal [7]. The current electrocardiogram signal noise removal methods are quite mature. Baggish et al. proposed the use of wavelet transform coefficients to determine the denoising threshold, which has a very good noise reduction effect on electrocardiogram signal denoising [8]. Hadeed et al. used IIR and FIR filters to remove the three main types of noise from electrocardiogram signals and compared the two noise removal filters. Hadeed et al. proposed an automatic classification method for arrhythmia detection by implementing a robust classifier using a neural network on a Bayesian framework [9]. Shapiro et al. classify electrocardiogram signals by proposing a method using a least-squares support vector machine, which can distinguish between normal and abnormal heartbeats [10]. Burchill propose a forward neural network-based backpropagation algorithm for cardiac arrhythmias by Artificial Neural Network (ANN) automatic classification recognition [11]. The basic level of the entire network structure consists of 11 layers. The meaning of each layer of the structure diagram will be briefly explained below. The first is the input layer, which takes an ECG signal cycle as a data sample as the input of the network; then three layers of the same structure are connected. Cuomo et al. proposed an algorithm to classify electrocardiogram arrhythmias by using Discrete Wavelet Transformation (DWT) and ANN, with a final recognition accuracy of 87.01% [12]. With the increasing capability of computers, PC-based electrocardiogram monitoring systems have been developed [9]. By sending the electrocardiogram data of the human body to the PC terminal, then the PC terminal does the preliminary analysis and diagnosis, display, and storage of electrocardiogram data locally using some electrocardiogram signal analysis algorithms and electrocardiogram signal analysis software [13]. Later, due to the rapid development of the Internet, the electrocardiogram signal collected by the PC terminal is transmitted to the cloud server and processed by some electrocardiogram signal automatic analysis algorithms, and the server returns the analysis results to the user, which not only strengthens the analysis of electrocardiogram signal but also reduces the pressure of processing in one PC terminal and speeds up the response speed [14].

Although the research on electrocardiogram monitoring systems has indeed made great progress in recent years, there are still some shortcomings. For example, the cardiac Holter machine can collect and display electrocardiogram data from the human body, but it cannot transmit and analyze them. Although the cardiac BP machine solves the problem of communication data transmission, it requires user participation, and the signal acquisition period is too short, so it can only be worn when the heart feels uncomfortable, but not when some undetectable heart rhythm abnormalities occur. Although the PC-based and Internet-based approach perfectly solves the problem of real-time monitoring and analysis of electrocardiogram signals, it is limited in application and promotion due to its lack of mobility. For example, surrounding lighting equipment and various electronic instruments are interference sources, and the frequency of such interference is mainly concentrated in 50–60 Hz. It is eliminated by designing a band notch filter or digital smoothing filter algorithm, and the frequency of the ECG signal is mainly 5–20 Hz. The research and analysis of the development of automatic electrocardiogram signal classification algorithms and the state-of-the-art electrocardiogram signal monitoring and analysis systems show that current electrocardiogram monitoring systems are not able to perform convenient and long-term monitoring of human electrocardiogram signals nor can they give real-time physiological signal analysis data. In this thesis, an improved weight-based deep convolutional neural network framework is used to study the automatic classification of electrocardiogram signals, and the algorithm model is embedded in a mobile platform to design an electrocardiogram analysis system that can perform mobile monitoring and real-time analysis of electrocardiogram signals conveniently. We analyze the current state of research on automatic electrocardiogram signal classification algorithms as well as the history of electrocardiogram monitoring systems and possible problems at various stages, propose a general plan for system design, and analyze the need for monitoring software for automatic electrocardiogram signal analysis based on a mobile platform. The basic characteristics of electrocardiogram signals are studied, and the algorithm that can correctly classify and identify electrocardiogram signals based on deep convolutional neural networks is designed and improved, and the algorithm model is saved to run on the mobile platform.

2. Design of Intracavitary Electrocardiogram-Guided Procedure to Assist in Mining Heart Rate Abnormalities

2.1. Design Analysis of Intracavitary Electrocardiogram Guidance. Abnormal heart rhythms are an important group of cardiovascular disorders [15]. There are a wide variety of cardiac rhythm abnormalities, with an irregular, rapid, or slow heartbeat. Among the more common types of heart rhythm abnormalities are the following: left bundle-branch block, right bundle-branch block, ventricular premature beats, and atrial premature beats [16]. The maximum APC weight value can be 7.8, so the corresponding normal weight value is within (0, 0.26). For the other three types of PVC, the sample size is about 4 times that of APC, so when choosing the weight value of these three categories, it is set to 1/4 of APC. The types of normal rhythms and these common types of abnormal heart rhythms will be described next. Normal rhythm is the predominant type of electrocardiogram signal, with P-wave, QRS wave, T-wave, and tiny U-wave in the waveform pattern, and occurs when there is a blocking delay

RETRACTED

or interruption in the left bundle-branch conduction system, which is a typical left bundle-branch block in the database. The incidence of these abnormalities is age-dependent, with the incidence increasing with age [17].

The S-T direction is opposite to that of the QRS main wave, and the S-T segment is elevated. On the waveform characteristics, the QRS wavelength is greater than 0.12 seconds, and the R peak is longer than or equal to 0.06 seconds. This kind of abnormality occurs when the right bundle-branch prolongation occurs, causing the right bundle-branch conduction system to suffer from blocking conduction delay or interruption. This is a typical right bundle-branch block in the database [18]. The right bundle-branch conduction block is a typical right bundle-branch block in the database [19]. The waveform pattern of the right bundle-branch conduction block reflects that the waveform before the QRS wave is relatively normal, the S wave widens and extends more downward, a small depression appears between the S and T segments, and the T wave is inverted. In terms of waveform characteristics, the QRS wave is longer than or equal to 0.12 seconds and the S wave is longer than or equal to 0.04 seconds, as shown in Figure 1.

The subjects selected for screening included both newborns and children already enrolled in school, both males and females, both urban and rural hukou populations, both cities with higher air pollution and cities with cleaner air quality, and randomly screened children with a positive diagnosis of congenital heart disease, whose screening criteria met the entry criteria for this study, since a total of 877 children with congenital heart disease were randomly screened from January 1, 2018, to December 31, 2019, and 877 children with congenital heart disease were screened for early detection of arrhythmias and follow-up for simple congenital heart disease conditions including septal defect, ventricular septal defect, unobstructed foramen oval, unobstructed ductus arteriosus, not included aortic torsion, tetralogy of Fallot, single ventricle, and other complex congenital heart disease. The abovementioned children did not have dizziness, headache, palpitations, and other symptoms before the screening of congenital heart disease (the same kind of symptoms due to the decline in cardiac function caused by congenital heart disease are not an exclusion criterion) or confirmed diagnosis of arrhythmias or hospitalization due to arrhythmias [20]. It can be found that the classification accuracy of the ECG signal after denoising processing is higher than the classification accuracy without denoising processing. The classification accuracy of the other four categories is similar, indicating that the ECG signal after denoising can improve the accuracy of the classification.

For patients with congenital heart disease who need to be hospitalized, electrocardiogram monitoring and 12-lead electrocardiogram examination were routinely performed during the hospitalization, and some patients underwent 24-hour dynamic electrocardiogram examination; for patients with abnormal electrocardiogram, they were rechecked two to three times in a week on average. For patients whose condition is not suitable for medical intervention, open thoracic surgery will be performed as the surgical group, while some patients whose condition is not suitable for surgical treatment or who have not undergone surgery for various reasons will be treated as the nonoperative group. Patients with congenital heart disease (both operated and unoperated children) who are discharged from the hospital are followed up for arrhythmias (outpatient follow-up after discharge) for about 3–12 months (average about 0.5 years).

2.2. Abnormal Heart Rate Design Analysis for Occult Heart Disease. The basis of abnormal heart rhythm detection lies in accurate heartbeat interception, the abnormal heartbeat on the electrocardiogram performance, that is, the appearance of more abnormal patterns.

The first step in the detection of abnormal heart rhythms is to intercept the heartbeat, splitting a section of the electrocardiogram signal into a single heartbeat, and then feature extraction of the segmented heartbeat, and then you can detect abnormal heart rhythms through machine learning. In today's social situation, as people's lives are getting faster and faster, the pressure on work and life is gradually increasing, resulting in the increasing incidence of heart disease and cardiovascular disease. If the length of the segmented heartbeats is too long, there will be a lot of data redundancy, and the accuracy of feature extraction will be affected [21]. On the other hand, if the segmented centroid is too short, some important data may be missed, which will cause errors in feature extraction. The width of the QRS wave group is known to be in the range of 0.05 s–0.l2 s, and because the data frequency in the MIT-BIH is 360 Hz, the heartbeat intercepted in this paper will be centered on the R peak, with 45 samples backward and 25 samples forward, as shown in Figure 2.

After all, subjects signed the informed consent form, intracardiac electrophysiologic study (EPS) was performed, and radiofrequency ablation was performed after the diagnosis was confirmed [22]. Intracardiac electrophysiologic measurement + ablation procedure: after the relevant surgical instruments and patients are well prepared, the patients are sterilized in the cardiac catheterization interventional room and sterile precautions such as towel laying are taken. Under local anesthesia, the left subclavian vein, left femoral vein, and right femoral vein are punctured and the 10-pole electrode catheter is placed in the coronary venous sinus (CS) area under X-ray fluoroscopy, the 4-pole electrode catheter is placed in the His bundle (HBE) area, and the 2-pole electrode catheter is placed in the right ventricle/right atrium (right ventricular, RV/right atrial, RA) in the corresponding site, adjusting the stimulation parameters to perform routine intracardiac electrophysiological examination. Through the atrial and ventricular procedures and incremental stimulation, the left and right bypasses are excluded one by one [23], and the diagnosis of AV node dual pathway can be confirmed by the presence of typical jumping phenomenon and tachycardia episodes or echoes during the procedure, followed by slow pathway improvement of the AV node [24]. When the AV node double pathway is associated with concealed conduction, it is easy to develop AV block (AVB) in the sinus rhythm state, and the

RETRACTED

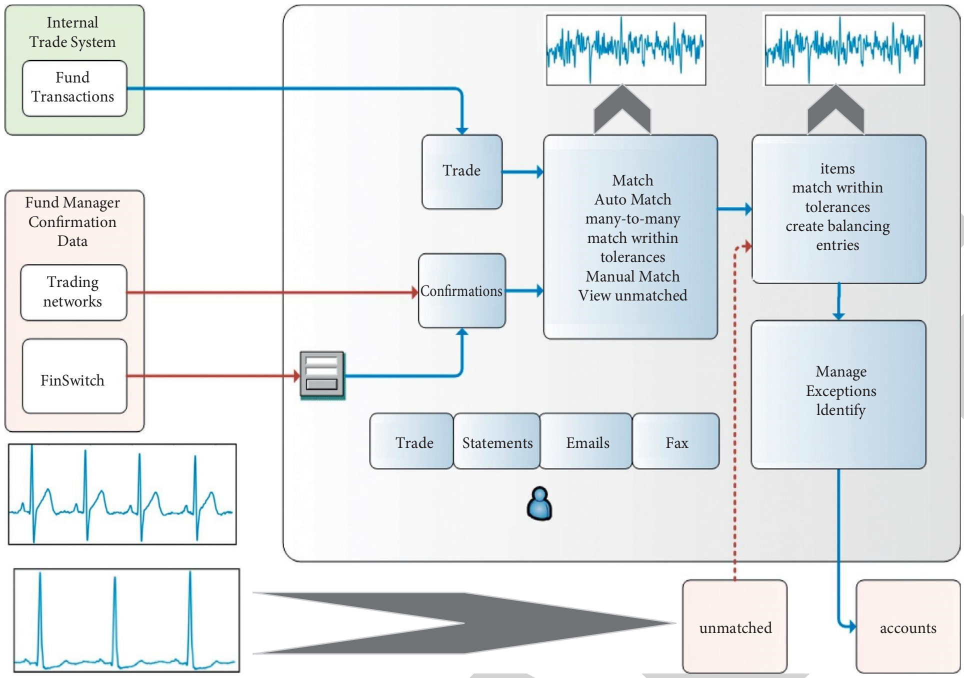

Figure 1: Intracavitary electrocardiogram guidance design framework.

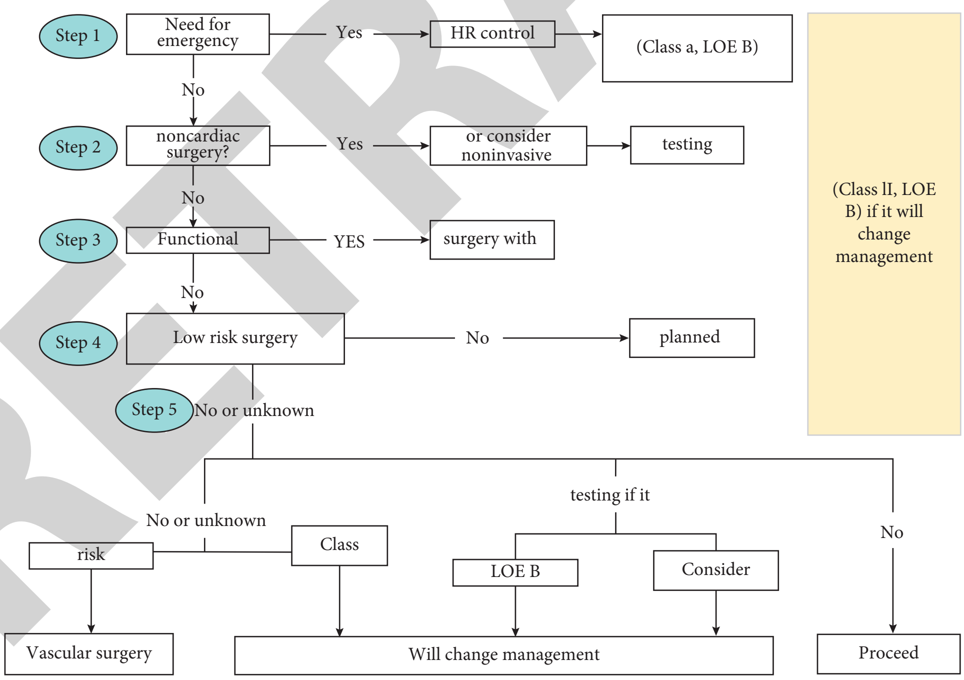

Figure 2: Heartbeat interception diagram.

RETRACTED

etiology of this phenomenon is usually unknown, which may cause the clinician to misjudge and give incorrect treatment. If the physiological signals such as electrocardiogram (ECG) and other physiological signals are abnormal, timely relief measures and treatment can be provided, which can greatly reduce the mortality and other accidents caused by heart disease. There have been reports of patients who were misdiagnosed as having AVB in the clinical diagnosis and had a permanent pacemaker implanted. Pacemaker implantation due to misdiagnosis is often associated with unforeseen risks, such as intraoperative bleeding, postoperative infection, and even complications such as irreversible cardiac rupture. The clinical and electrophysiological characteristics of the 11 patients included in this paper were

RETRACTED

observed and followed up to analyze the factors associated with AVB.

The MIT-BIH arrhythmia database is the most authoritative and extensive database for the study of arrhythmias and is provided by the Massachusetts Institute of Technology (MIT). Electrocardiogram data were from individuals, 47 of whom consisted of 25 males and 22 females, for a total of 48 recordings (data 201 and 202 were taken from the same male individual). These 48 records were sampled at a frequency of 360 HZ, in two leads, for approximately 30 minutes. Each record is annotated by more than two electrocardiogram experts, and each beat cycle of electrocardiogram signal is analyzed, independently annotated, and then verified and reviewed, and the rhythm type of electrocardiogram signal is decided by final consensus. The arrhythmia database is used as an authority to study abnormal heart rhythm data. The correspondence between the annotation information of MIT-BIH is shown in Table 1.

Through the investigation and analysis of the requirements of the common abnormal electrocardiogram signal mobile platform analysis system, including the whole process from the acquisition of the electrocardiogram signal, through the Bluetooth transmission to the end for analysis and the result visualization, this paper determines the direction and goal of the whole system implementation. Although the PC-based and Internet-based methods perfectly solve the problem of real-time monitoring and analysis of ECG signals, because they are not mobile, they will be greatly restricted in application and promotion. The monitored person is connected to the electrocardiogram acquisition terminal through the way of three leads, collecting the human body's electrocardiogram signal, sending the data through Bluetooth module after signal processing means, and receiving the human body's electrocardiogram data through Bluetooth in real time in the client. Analysis and the results of the analysis determine the need to alarm the relevant personnel. The monitored personnel will be able to view their physiological health status in real time through the client.

According to the data flow diagram of the system, the main functional requirements of the system are electrocardiogram data collection and transmission, electrocardiogram data reception, and real-time electrocardiogram display, electrocardiogram signal waveform detection, automatic analysis, alarm judgment, and electrocardiogram data preservation and management.

2.3. Evaluation Index Design Analysis. In the MIT-BIH arrhythmia database, 75.25% of the electrocardiogram signals are normal electrocardiogram signal types, while the four abnormal signal types account for only about 24.75%. Therefore, an imbalance problem arises in the data processed in the MIT-BIH arrhythmia database. The so-called data imbalance problem refers to the highly skewed distribution of the classification samples. In this paper, the normal type is much more than the other four types of abnormal electrocardiogram signals, which will cause a large error in the classification of abnormal electrocardiogram signals. How to improve the algorithm framework for data imbalance is the most important issue in the algorithm design process, which is the main improvement of the algorithm in this paper.

From the above analysis, deep convolutional neural networks can be carried out together with sample feature extraction and classification identification in the classification identification process. When transplanted to the platform, the developer only needs to care about the input and output of the model, and the work of intermediate waveform localization and feature extraction can be eliminated, minus the complexity caused by the transplantation of the algorithm model, so the deep convolutional neural network as an algorithm framework can be conveniently applied in the platform. By choosing a deep convolutional neural network as the algorithm framework, the first and second points of the proposed problem can be well solved. For the third point of data imbalance problem, the basic deep convolutional neural network framework cannot solve such problems, so the algorithm framework needs to be improved, as shown in Figure 3.

After the above specific analysis of each level, analyzing the characteristics of each level in the deep convolutional neural network and the abnormal electrocardiogram signal classification problem to be solved in this paper and the specific hierarchical structure of the input and output layers as well as the intermediate basic levels of convolutional, pooling, and fully connected layers are determined. As shown in Figure 4, the basic network structure of the deep convolutional neural network electrocardiogram signal classification algorithm is proposed in this paper, and the whole network structure contains 11 layers. Study the basic characteristics of the ECG signal, according to the characteristics of the deep convolutional neural network, design and improve the algorithm that can correctly classify and recognize the ECG signal, and save it as an algorithm model running on the mobile platform. The first layer is the input layer, which takes an electrocardiogram signal period as a data sample as the input of the network; then it is followed by three similar layers, which include a convolutional layer, a convolutional block composed of a convolutional layer, a normalization process, and an excitation function Rely, and a pooling layer, which can complete the extraction of electrocardiogram signal features and avoid inaccurate waveform localization and artificial selection. The errors of the eigenvalues are then connected to three fully connected layers to map the eigenvectors to the labels, and the final output layer is used to obtain the output results of the five heart rhythm types.

3. Results and Analysis

3.1. Analysis of Experimental Data Processing Results. This system enables automatic analysis of electrocardiogram signals by using a convolutional neural network model framework. However, training the network model requires a large number of data samples, i.e., the input of the network, and there are two ways to obtain the general deep learning dataset: the first one can use the public dataset on the Internet, which eliminates the steps of dataset

Table 1: MIT-BIH annotation code correspondence table.

Comment code	Symbol	Remarks	Values
0	—	Normal beating	3
1	L	Left bundle-branch block	3
2	R	Right bundle-branch block	3
3	a	Abnormal atrial premature beats	4
4	V	Ventricular premature beats	4
5	F	Ventricular fusion heartbeat	3
6	J	Borderline premature beats	2
7	S	Atrial premature beats	2
9	g	Supraventricular premature contractions or abnormalities	3
10	j	Ventricular escape	3
11	1	Borderline escape	2
12	—	Heartbeat	4
13	L	Uncategorized heartbeat	2

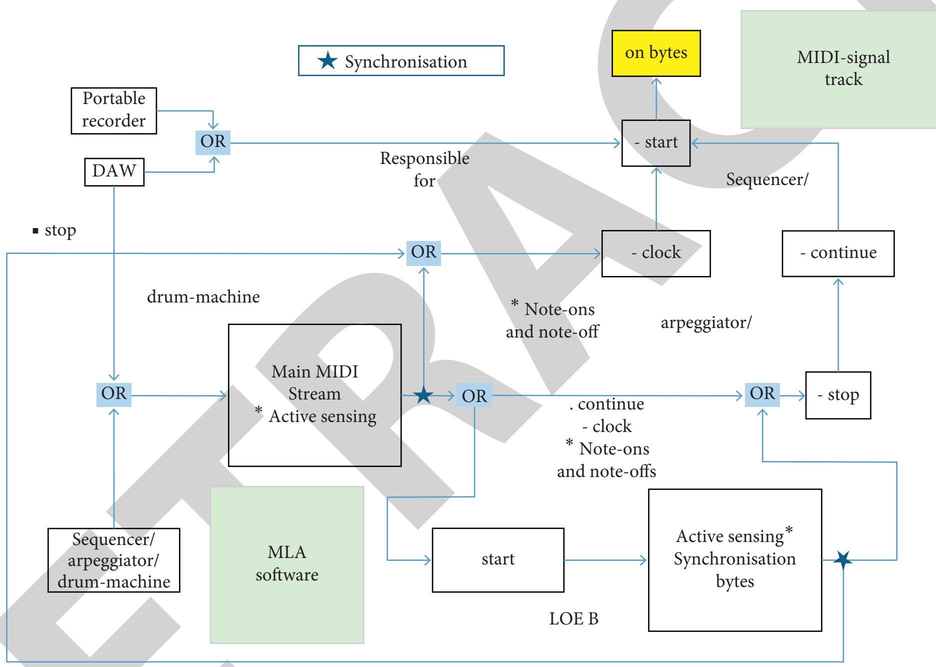

Figure 3: Evaluation process design.

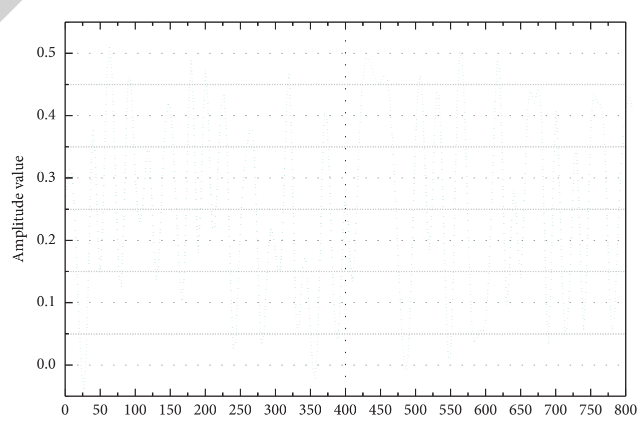

Figure 4: Schematic diagram of a continuous segment of the electrocardiogram signal.

RETRACTED

processing, and the second one is that the data is publicly available on the Internet or there is no corresponding dataset, which requires manual hands-on production of the dataset. The MIT-BIH database contains 60 groups of signals with a sampling frequency of 360 Hz, and each group of signals is sampled continuously for nearly 32 minutes. Figure 4 shows a continuous waveform of the electrocardiogram signal from the intercepted MIT-BIH database 101 data, but the doctor's analysis of the electrocardiogram is based on one heartbeat, so the electrocardiogram signal is divided into one heartbeat. Therefore, although there are 48 sets of MIT-BIH arrhythmia data, they still cannot be used as the input of the convolutional neural network model, so we need to preprocess the 48 sets of data first, and the preprocessing process mainly includes MIT-BIH data parsing, electrocardiogram signal denoising, and beat division.

The first line of the record represents the record as data number 101, which contains two signals and the sampling frequency is 360 Hz with 650,000 sampling points. In the waveform shape, there are P-wave, QRS wave, T-wave, and tiny U-wave in sequence. This kind of abnormality occurs when there is a delay or interruption of block conduction in the left bundle-branch conduction system, which is a typical left beam of the database. The next two lines record information for two sets of signals, respectively, which represent data number 101 and are stored in the "212" mode. 200 refers to the ADC gain, 11 refers to the ADC resolution, the ADC zero value is set to 1024, and the first value of the sampled signal is 955. And the next two large integers indicate the number of checks that were performed on the sampling sites. The fourth-row records patient information, with age, gender, and record data, respectively. The last row records the patient's medication history.

In the MIT-BIH record reading process, each record is firstly read as a file, and then the parameters of each record are parsed according to the previous record format; after the format parsing, the MLII channel of the two groups of signals is selected, and then all the original records are read according to "212" format, including atrial septal defect, ventricular septal defect, patent foramen oval, and patent ductus arteriosus. After getting the record-sampled raw data, the next step is to denoise the electrocardiogram signal for each record. However, considering the special characteristics of the convolutional neural network, the data samples can be directly inputted into the network without denoising, and the network also has a certain denoising effect, so this paper divides two data sets on whether the electrocardiogram signal is denoised or not and carries out the simulation experiments respectively, as shown in Figure 5.

The frequency distribution of the main components is between 20Hz and 5000Hz. power frequency interference is a common interference in the power network; for example, surrounding lighting equipment and a variety of electronic devices are interference sources, and such interference frequency is mainly concentrated in the 50–60 Hz. Through the design of a band trap filter or digital smoothing filter algorithm, the elimination was performed, while the cardiac signal frequency was mainly in the range of 5–20 Hz.

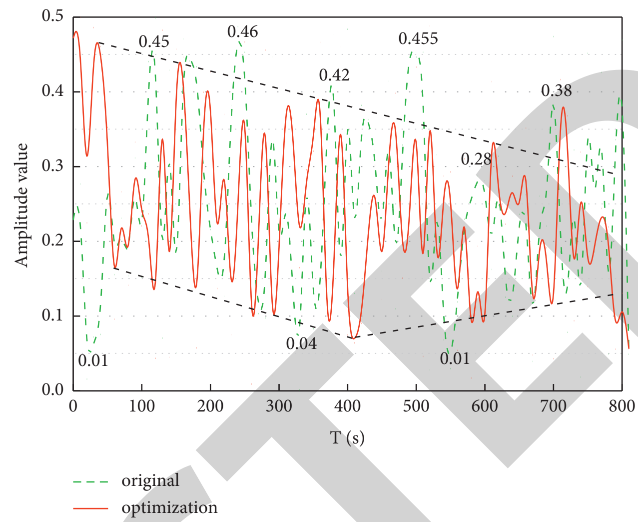

Figure 5: Simulation experiment results.

After determining the specific steps of the heartbeat division method, the two groups of data use this method to divide the heartbeat separately to obtain two data sets. First of all, the 48 groups of data without denoising are divided into five categories, and the corresponding heartbeats are placed in one category to obtain the data set Set1; similarly, the 48 groups of data after denoising are divided to obtain the data set Set2; the final results of the two data sets are shown in Figure 6.

The experimental data taken in this paper is from the MIT-BIH arrhythmia database; in the experimental data processing step, the data from the database has been converted into the input of the network, followed by the simulation experiments, and the results of the model simulation experiments are analyzed and discussed (Figure 7).

In this paper, the algorithmic framework without adding weights is used as the improvement algorithmic model, but the network, which will be improved according to the improvement strategy, will be used as a deep convolutional neural network based on weights, i.e., the improved algorithmic model. The original dataset Set1 is now used as the experimental data to perform the experiments separately. Before conducting the experiments, we need to set the weights of the improved deep convolutional network model Cross-Entropy first.

Firstly, since the sample size of Normal is about 30 times that of APC, the corresponding weight of Normal is set to 1/30 of APC, and the maximum APC weight is 7.8, so the corresponding weight of Normal is in the range of (0,0.26). For the other three types of RBBBB, LBBBB, and PVC, the sample size is about 4 times the APC sample size, so the weight of these three types is set to 1/4 of the APC, and according to the determined Normal weight range, the step size is 0.02, and the weight with the highest accuracy is the final weight.

RETRACTED

RETRACTED

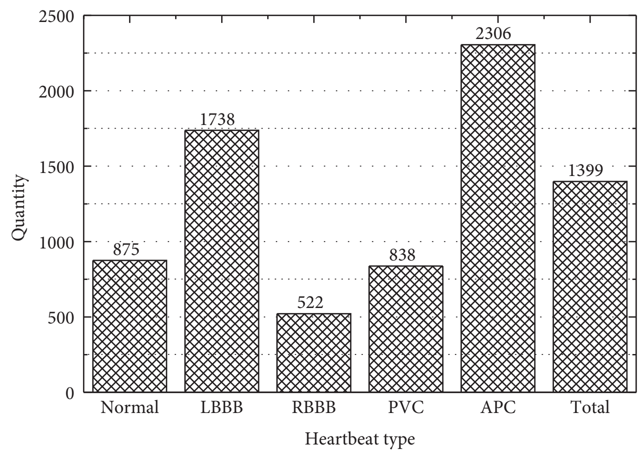

Figure 6: Five types of results.

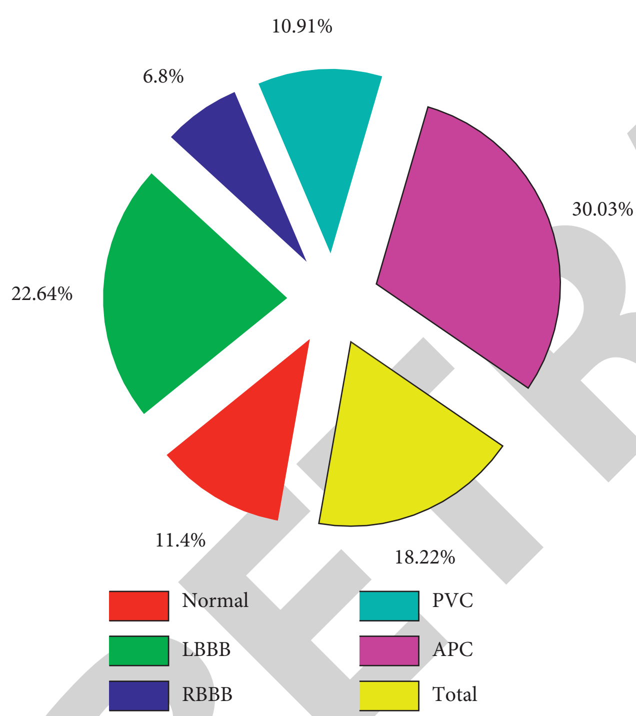

Figure 7: Setting range of weights.

3.2. Analysis of Excavation Results. According to the specific idea of weight setting, take the step length of 0.02 and perform the experiment in the range of (0, 0.26), and the specific experimental results are shown in Figure 8, where the horizontal axis represents the Normal weight setting value and the vertical axis represents the overall accuracy of the network model.

After the experiment, it is found that the overall accuracy is the highest when the Normal weight is set to 0.2, so the final Normal-type weight is set to 0.2, each type is calculated according to the idea of weight setting, and the final weight setting value is shown in Figure 8.

The datasets all use the original dataset Set1, and the two network models keep the same parameters except for the difference in the Cross-Entropy weights. The network learning rate is set to 0.001 and the number of learning iterations is set to 250. Figure 9 shows the overall accuracy of the network model before and after the 250 iterations, and Figure 9 shows the loss of the network model before and after the 250 iterations.

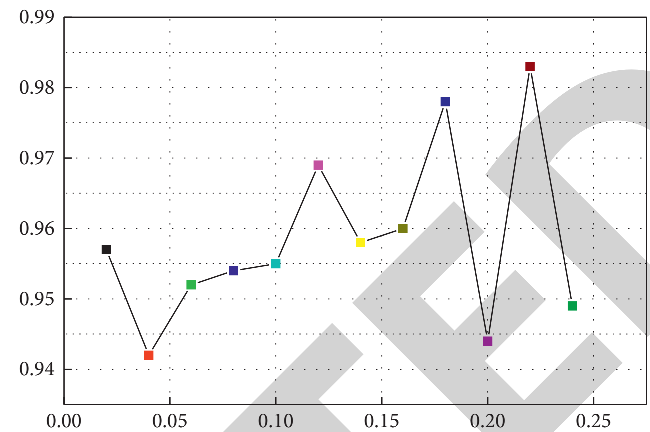

Figure 8: Experimental results of weight setting.

From Figure 9, we can see that the overall accuracy of the improved network model is significantly higher than the curve before the improvement, which is better than before; from Figure 9, we can see that the loss before the improvement is above 0.01, and the loss after the improvement is down to about 0.001, which is much lower than the model loss. Some of the patients underwent 24-hour dynamic electrocardiogram examination. For those with abnormal electrocardiogram, reexamination was performed 2 to 3 times in an average of 1 week. However, these two figures can only show that the overall classification identification rate of the network model with increased weights is better than before, but this paper is mainly concerned with the classification and identification accuracy of the four types of abnormal electrocardiogram signals, so the following is the specific classification of each type of situation and evaluation index results.

The main content of the test is the test of the data receiving module and the overall system function module. The data receiving module test is mainly Bluetooth pairing connection test, and data parsing processing test, to ensure the correctness and integrity of the received data. After a series of testing and debugging, the overall system function can be stable and run for a long time.

In the experimental data processing stage, two data sets, Set1 and Set2, were made according to whether to denoise the electrocardiogram signal data. The network model results for the original dataset Set1 are shown in Figure 10, and the following experiments are conducted on the denoised dataset Set2 using the improved model. The experimental classification results are shown in Figure 10, where the vertical axis represents the actual heartbeat type and the horizontal axis represents the model prediction results. The results of the classification evaluation metrics are shown in Figure 10.

From Figure 10, it can be seen that the experimental results of the algorithmic network model for the denoised data set Set2 are all above 95% except for the APC type, and

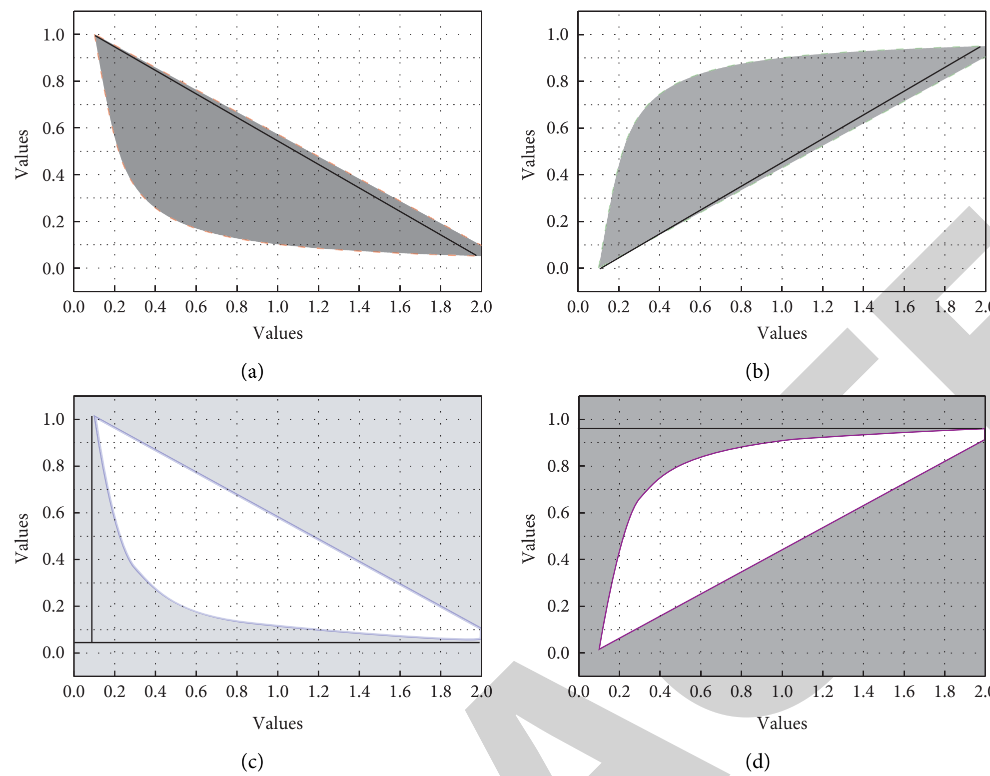

Figure 9: Comparison of the overall accuracy change of the network model before and after improvement.

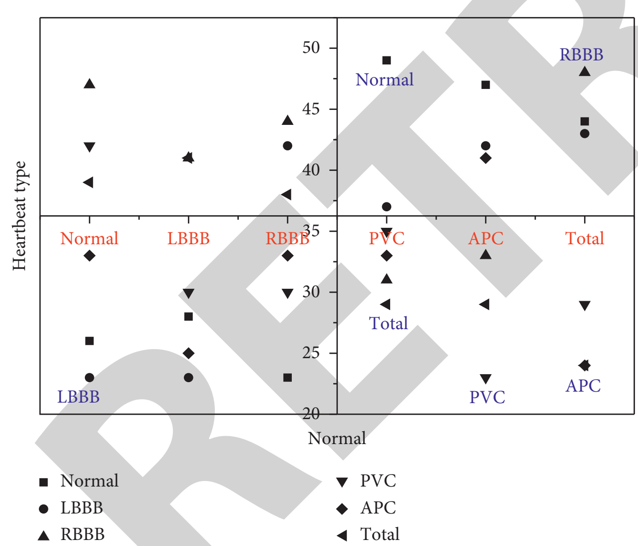

Figure 10: Identification results.

although the recognition rate of the APC type does not reach the same as the other types, it is also improved compared to the data before denoising. Comparing the data set after denoising with the data set without denoising, there is a small improvement in all three indicators of APC type, but the improvement is not significant for the other four types because the APC type is like Normal-type in waveform morphology. The reason the classification accuracy is still so high is that the number of normal heartbeats accounts for a very large proportion of the dataset, thus the classification accuracy can be maintained at a relatively high level. Comparing the simulation results of Set1 and Set2, it is found that the classification accuracy of the denoised electrocardiogram signal is improved for APC types compared with that of the nondenoised one, and the classification accuracies of the other four types are similar, indicating that the denoised electrocardiogram signal can improve the recognition accuracy of APC types and will not affect the classification of the other types. Therefore, in this paper, denoising is firstly performed on the collected electrocardiogram signal, and then the classification and identification are performed on the denoised electrocardiogram signal.

4. Conclusion

This paper fully investigated the research content and research status of common abnormal electrocardiogram signals, summarized some algorithms in the automatic classification of electrocardiogram signals, elaborated on the specific measures taken by these traditional classification algorithms in the process of automatic classification of electrocardiogram signals as well as their shortcomings, and determined the research ideas and relevant technical theoretical knowledge. Besides, for the electrocardiogram signal mobile platform analysis system, the development history of the electrocardiogram monitoring system is analyzed, and the direction and goal of the mobile platform analysis system are determined in this paper after analysis and comparison. The functional and performance requirements of the mobile

RETRACTED

platform system for common abnormal electrocardiogram signals were designed, and the functional modules and the links between them were identified. To address the shortcomings of traditional electrocardiogram signal classification algorithms and their inconvenience in engineering applications, this paper proposes a weight-based deep convolutional neural network as a framework for electrocardiogram signal classification algorithms, which eliminates the need for manual feature extraction, reduces the complexity of the algorithm, and can be deployed quickly and invoked on the end. Two datasets were constructed using data from the public database MIT-BIH, and the classification results of the two datasets were compared to finalize the process of denoising the electrocardiogram signals before analyzing and processing them.

Data Availability

The data used to support the findings of this study are available from the corresponding author upon request.

Conflicts of Interest

The authors declare that there are no conflicts of interest.

Authors' Contributions

Y. Wei and Y. Zhu contributed equally to this work.

Acknowledgments

This work was supported by Affiliated Hangzhou First People's Hospital, Zhejiang University School of Medicine.

References

[1] C. D. No-diabetes, "Asymptomatic patients without known heart disease have markers of occult heart disease left ventricular dysfunction is a sig," *The American Journal of Cardiology*, vol. 125, no. 1449, pp. 1449–1453, 2020.

[2] B. Sassone, D. Muser, M. Casella et al., "Detection of concealed structural heart disease by imaging in patients with apparently idiopathic premature ventricular complexes: a review of current literature," *Clinical Cardiology*, vol. 42, no. 12, pp. 1162–1169, 2019.

[3] G. Cioffi, F. Ognibeni, A. Dalbeni et al., "High prevalence of occult heart disease in normotensive patients with rheumatoid arthritis," *Clinical Cardiology*, vol. 41, no. 6, pp. 736–743, 2018.

[4] A. B. Fernandez and P. D. Thompson, "Exercise training in athletes with heart disease," *Progress in Cardiovascular Diseases*, vol. 60, no. 1, pp. 121–129, 2017.

[5] K. Averin, R. Hirsch, M. D. Seckeler, W. Whiteside, R. H. Beekman, and B. H. Goldstein, "Diagnosis of occult diastolic dysfunction late after the Fontan procedure using a rapid volume expansion technique," *Heart*, vol. 102, no. 14, pp. 1109–1114, 2016.

[6] J. D. Arroja, H. Burri, C. I. Park, P. Giraudet, and M. Zimmermann, "Electrophysiological abnormalities in patients with paroxysmal atrial fibrillation in the absence of overt structural heart disease," *Indian Pacing and Electrophysiology Journal*, vol. 16, no. 5, pp. 152–156, 2016.

[7] S. I. Im, H. B. Gwag, Y. Park et al., "Electrocardiographic features of the presence of occult myocardial disease in patients with VPD-induced cardiomyopathy," *Journal of Arrhythmia*, vol. 36, no. 3, pp. 485–492, 2020.

[8] A. L. Baggish, M. J. Ackerman, and R. Lampert, "Competitive sport participation among athletes with heart disease," *Circulation*, vol. 136, no. 17, pp. 1569–1571, 2017.

[9] N. N. Hadeed, D. A. Ahmad, F. M. Lolan et al., "Angiographic assessment of exercise treadmill test-detected occult coronary artery disease in type 2 diabetics," *Iraqi Journal of Medical Sciences*, vol. 14, no. 3, pp. 215–222, 2016.

[10] H. Shapiro, S. Meymandi, K. Shivkumar, and J. S. Bradfield, "Cardiac inflammation and ventricular tachycardia in Chagas disease," *HeartRhythm Case Reports*, vol. 3, no. 8, pp. 392–395, 2017.

[11] L. J. Burchill, "Heart transplantation in adult congenital heart disease," *Heart*, vol. 102, no. 23, pp. 1871–1877, 2016.

[12] J. R. Cuomo, S. P. Javaheri, G. K. Sharma, D. Kapoor, A. E. Berman, and N. L. Weintraub, "How to prevent and manage radiation-induced coronary artery disease," *Heart*, vol. 104, no. 20, pp. 1647–1653, 2018.

[13] A. Taqatqa, J. Bokowski, M. Al-Kubaisi et al., "The use of speckle tracking echocardiography for early detection of myocardial dysfunction in patients with Duchenne muscular dystrophy," *Pediatric Cardiology*, vol. 37, no. 8, pp. 1422–1428, 2016.

[14] M. Yokokawa, K. C. Siontis, H. M. Kim et al., "Value of cardiac magnetic resonance imaging and programmed ventricular stimulation in patients with frequent premature ventricular complexes undergoing radiofrequency ablation," *Heart Rhythm*, vol. 14, no. 11, pp. 1695–1701, 2017.

[15] T. L. Braber, A. Mosterd, N. H. Prakken et al., "Occult coronary artery disease in middle-aged sportsmen with a low cardiovascular risk score: the Measuring Athlete's Risk of Cardiovascular Events (MARC) study," *European journal of preventive cardiology*, vol. 23, no. 15, pp. 1677–1684, 2016.

[16] S. I. Mavrogeni, P. P. Sfikakis, T. Dimitroulas et al., "Can cardiovascular magnetic resonance prompt early cardiovascular/rheumatic treatment in autoimmune rheumatic diseases? Current practice and future perspectives," *Rheumatology International*, vol. 38, no. 6, pp. 949–958, 2018.

[17] T. A. Danwade, S. Devidutta, A. B. Shelke et al., "Prognostic value of fluorine-18 fluoro-2-deoxyglucose positron emission computed tomography in patients with unexplained atrioventricular block," *Heart Rhythm*, vol. 15, no. 2, pp. 234–239, 2018.

[18] A. H. Tennøe, K. Murbræch, J. C. Andreassen et al., "Left ventricular diastolic dysfunction predicts mortality in patients with systemic sclerosis," *Journal of the American College of Cardiology*, vol. 72, no. 15, pp. 1804–1813, 2018.

[19] Y. N. V. Reddy, M. Obokata, B. J. Gersh, and B. A. Borlaug, "High prevalence of occult heart failure with preserved ejection fraction among patients with atrial fibrillation and dyspnea," *Circulation*, vol. 137, no. 5, pp. 534-535, 2018.

[20] P. K. Mehta, C. Bess, S. Elias-Smale et al., "Gender in cardiovascular medicine: chest pain and coronary artery disease," *European Heart Journal*, vol. 40, no. 47, pp. 3819–3826, 2019.

[21] J. F. Huizar, K. A. Ellenbogen, A. Y. Tan, and K. Kaszala, "Arrhythmia-Induced cardiomyopathy," *Journal of the American College of Cardiology*, vol. 73, no. 18, pp. 2328–2344, 2019.

[22] M. Packer, C. S. P. Lam, L. H. Lund, and M. M. Redfield, "Interdependence of atrial fibrillation and heart failure with a preserved ejection fraction reflects a common underlying

RETRACTED

Hindawi
Journal of Healthcare Engineering
Volume 2023, Article ID 9864805, 1 page
https://doi.org/10.1155/2023/9864805

Retraction

Retracted: Regression Analysis of Factors Based on Cluster Analysis of Acute Radiation Pneumonia due to Radiation Therapy for Lung Cancer

Journal of Healthcare Engineering

Received 10 October 2023; Accepted 10 October 2023; Published 11 October 2023

Copyright © 2023 Journal of Healthcare Engineering. This is an open access article distributed under the Creative Commons Attribution License, which permits unrestricted use, distribution, and reproduction in any medium, provided the original work is properly cited.

This article has been retracted by Hindawi following an investigation undertaken by the publisher [1]. This investigation has uncovered evidence of one or more of the following indicators of systematic manipulation of the publication process:

(1) Discrepancies in scope
(2) Discrepancies in the description of the research reported
(3) Discrepancies between the availability of data and the research described
(4) Inappropriate citations
(5) Incoherent, meaningless and/or irrelevant content included in the article
(6) Peer-review manipulation

The presence of these indicators undermines our confidence in the integrity of the article's content and we cannot, therefore, vouch for its reliability. Please note that this notice is intended solely to alert readers that the content of this article is unreliable. We have not investigated whether authors were aware of or involved in the systematic manipulation of the publication process.

In addition, our investigation has also shown that one or more of the following human-subject reporting requirements has not been met in this article: ethical approval by an Institutional Review Board (IRB) committee or equivalent, patient/participant consent to participate, and/or agreement to publish patient/participant details (where relevant).

Wiley and Hindawi regrets that the usual quality checks did not identify these issues before publication and have since put additional measures in place to safeguard research integrity.

We wish to credit our own Research Integrity and Research Publishing teams and anonymous and named external researchers and research integrity experts for contributing to this investigation.

The corresponding author, as the representative of all authors, has been given the opportunity to register their agreement or disagreement to this retraction. We have kept a record of any response received.

References

[1] X. Zhang, B. Lv, L. Rui, L. Cai, and F. Liu, "Regression Analysis of Factors Based on Cluster Analysis of Acute Radiation Pneumonia due to Radiation Therapy for Lung Cancer," *Journal of Healthcare Engineering*, vol. 2021, Article ID 3727794, 12 pages, 2021.

Hindawi
Journal of Healthcare Engineering
Volume 2021, Article ID 3727794, 12 pages
https://doi.org/10.1155/2021/3727794

Research Article

Regression Analysis of Factors Based on Cluster Analysis of Acute Radiation Pneumonia due to Radiation Therapy for Lung Cancer

Xiaofeng Zhang[1], **Beili Lv**[1], **Lijun Rui**[1], **Liming Cai**[1], and **Fenglan Liu**[1,2]

[1]*Respiratory Department, The Affiliated Hospital of Jiangnan University, Wuxi Jiangsu 214062, China*
[2]*Medical School Liaocheng University, Shandong Liaocheng 250200, China*

Correspondence should be addressed to Liming Cai; cailm180728@163.com and Fenglan Liu; 6172806002@stu.jiangnan.edu.cn

Received 18 August 2021; Revised 17 September 2021; Accepted 24 September 2021; Published 13 October 2021

Academic Editor: Joon Huang Chuah

Copyright © 2021 Xiaofeng Zhang et al. This is an open access article distributed under the Creative Commons Attribution License, which permits unrestricted use, distribution, and reproduction in any medium, provided the original work is properly cited.

We conducted in this paper a regression analysis of factors associated with acute radiation pneumonia due to radiation therapy for lung cancer utilizing cluster analysis to explore the predictive effects of clinical and dosimetry factors on grade ≥2 radiation pneumonia due to radiation therapy for lung cancer and to further refine the effect of the ratio of the volume of the primary foci to the volume of the lung lobes in which they are located on radiation pneumonia, to refine the factors that are clinically effective in predicting the occurrence of grade ≥2 radiation pneumonia. This will provide a basis for better guiding lung cancer radiation therapy, reducing the occurrence of grade ≥2 radiation pneumonia, and improving the safety of radiotherapy. Based on the characteristics of the selected surveillance data, the experimental simulation of the factors of acute radiation pneumonia due to lung cancer radiation therapy was performed based on three signal detection methods using fuzzy mean clustering algorithm with drug names as the target and adverse drug reactions as the characteristics, and the drugs were classified into three categories. The method was then designed and used to determine the classification correctness evaluation function as the best signal detection method. The factor classification and risk feature identification of acute radiation pneumonia due to radiation therapy for lung cancer based on ADR were achieved by using cluster analysis and feature extraction techniques, which provided a referenceable method for establishing the factor classification mechanism of acute radiation pneumonia due to radiation therapy for lung cancer and a new idea for reuse of ADR surveillance report data resources.

RETRACTED

1. Introduction

Lung cancer, also known as primary bronchopulmonary cancer, is a malignant tumour that occurs mainly in bronchial mucosal epithelial cells, with a few occurring in alveolar tissue. Patients with lung cancer often have no obvious clinical symptoms in the early stage of the disease and are often neglected. As the disease worsens and develops to the middle and late stage, they start to show clinical symptoms such as haemoptysis and pain. Most of the patients have already developed to the middle and late stages when their disease is discovered, and the best time for surgical treatment is lost [1]. The diagnosis of lung cancer is relatively easy. Combining clinical symptoms, imaging (CT, MRI, etc.), and biochemical indexes can make a preliminary diagnosis of the patient's disease status, and for patients suspected of having lung cancer, the pathological examination can make a definite diagnosis. Radiotherapy is one of the main treatment methods for lung cancer, and clinical statistics show that more than 70% of lung cancer patients need radiotherapy during treatment, indicating the important value of radiotherapy in lung cancer treatment [2]. For measurement data, independent-sample t-test or non-parametric rank-sum test is used in multivariate analysis of variance. The main treatment mechanism of radiotherapy is to irradiate tumour tissues and cells with high doses of radiation to kill cancer cells and prevent their continued proliferation and differentiation [3]. However, during radiotherapy, a large area of noncancerous lung tissue will be exposed to radiotherapy, normal lung tissues do not have good tolerance to high-dose radiation, and the normal lung tissues will be damaged to different degrees under high-dose radiation. The lung tissue damage caused by radiotherapy is a kind of value-added death damage. After high-dose radiation irradiation, cell damage immediately appears and a series of cytokine synthesis increases, which triggers a series of pathophysiological reactions with the transmission and amplification of intercellular signals, thus causing radiation pneumonia. The occurrence of radiation pneumonia not only affects the normal effect of radiotherapy but also has a serious impact on the patient's recovery, leading to a decrease in the patient's quality of life.

The main goal of cluster analysis is to divide the samples or feature variables into a data set by distance so that the distance between elements in the same class is closer than the distance between elements in other classes, or the elements in the same class are more similar than other classes so that the homogeneity of elements within classes and the heterogeneity of elements between classes can be maximized at the same time [2]. Image cutting uses the Image Segmented tool software in the MATLAB software, using a semiautomatic method. After the approximate range is manually outlined, the software automatically iteratively calculates. A good clustering model can solve the problem of large data size [4]. Cluster analysis divides the given data by its inherent characteristics, to better grasp the data characteristics of each cluster after the division, reduce the size of the data, and obtain simpler and more intuitive data from the relatively complex original data. It is also possible to obtain simpler and more intuitive data from the relatively complex original data and uncover the hidden data value behind the huge data volume. Therefore, cluster analysis has become a very important part of big data analysis, and it has been successfully applied to many practical problems in social and natural sciences. For example, in the financial industry, cluster analysis can be used for bank customer segmentation and financial investment; in traffic management, cluster analysis can be used for traffic control and traffic accident analysis; in the biomedical field, cluster analysis can study the nature and function of genes and proteins, thus helping us to explore the mystery of life.

At present, the incidence of acute radiation pneumonia after radiotherapy for lung cancer patients is relatively high, which not only affects the effect of radiotherapy but also increases the incidence of complications and increases the risk of radiotherapy. Taking reasonable measures to reduce the incidence of acute radiation pneumonia after radiotherapy for lung cancer patients is an important research topic for clinical workers, which becomes a major clinical complication. The occurrence of acute radiation pneumonia will hinder normal treatment, leading to the inability to increase the radiation dose, the clinical treatment effect is very poor, and the patient's quality of life is not ideal. This study aims to investigate the risk factors associated with acute radiation pneumonia in lung cancer patients after radiotherapy and to guide clinicians to take reasonable treatment measures to prevent the occurrence of acute radiation pneumonia according to the actual situation of patients, to improve the clinical effect of lung cancer radiotherapy and reduce the risk of radiation pneumonia. It is important to improve the clinical effect of radiotherapy and reduce the occurrence of complications.

2. Related Work

Many clinical factors have been reported to influence the development of radiation pneumonia, including age, gender, smoking history, and history of chronic obstructive pulmonary disease (COPD). Wang et al. reported that age was an influential factor in the development of radiation pneumonia and that patients of advanced age were at a higher risk of developing radiation pneumonia [5]. Tinkle et al. showed that smoking history was a protective factor against radiation pneumonia and that smoking could prevent radiation pneumonia [3]. The risk and severity of radiation pneumonia are higher in patients with a history of severe COPD [6]. The effect of concurrent radiotherapy on the occurrence of radiation pneumonia has been inconsistently concluded in different studies, which mainly lies in the different toxic effects on lung tissues by using different chemotherapeutic drugs [7]. Many drugs for oncology cause an increased risk of developing radiation pneumonia, such as methotrexate, bleomycin, and mitomycin, which have pulmonary toxicity and can increase the risk of radiation pneumonia [8]. There is no solid evidence to support the fact that classical oncology chemotherapy drugs such as cisplatin and carboplatin increase the risk of radiation pneumonia. However, more chemotherapeutic agents such as paclitaxel and gemcitabine show greater pulmonary toxicity in concurrent radiotherapy sensitization therapy, which can lead to an increased risk of radiation pneumonia. Therefore, try to avoid the use of these drugs with pulmonary toxicity during radiotherapy to reduce the risk of radiation pneumonia.

Among the many dosimetry parameter studies reported so far, dosimetry parameters such as V5, V20, and V30 have the greatest value in predicting the risk of radiation pneumonia and are now used in clinical practice to improve the ability to predict the risk of radiation pneumonia, but Pradhan et al. reported in a review study of current clinically applied dosimetry assessment parameters that, even at lower dosimetry reference values, radiation pneumonia still occurs, and it is not yet possible to accurately predict the occurrence of radiation pneumonia [9]. In clinical practice, we observed that, with the increase of radiotherapy dose, the radiation dose and irradiation volume of the lung lobe of the primary focus were higher than those of the adjacent lobe and the chance of radiation pneumonia in the lung lobe of the primary focus was higher than that of the adjacent lobe [10]. There are few reports in the domestic and international literature about the relationship between the volumetric dosimetry of radiation and radiation pneumonia in the lung lobe where the primary focus of lung cancer is located; therefore, this topic will explore the clinical factors and dosimetry factors on radiotherapy-induced radiation pneumonia in lung cancer [11]. Therefore, this study will investigate the predictive role of clinical and dosimetry factors on the development of ≥2-grade radiation pneumonia due to lung cancer radiotherapy and refine the effect

RETRACTED

of the ratio of the volume of the primary foci to the volume of the lung lobes in which they are located on ≥2-grade radiation pneumonia, to refine the factors that are clinically effective in predicting the development of ≥2-grade radiation pneumonia and provide a basis for better guiding lung cancer radiotherapy, reducing the risk of ≥2-grade radiation pneumonia, and improving the safety of radiotherapy [12]. It has been pointed out that many factors are leading to acute radiation pneumonia in lung cancer radiotherapy patients, including patients' clinical factors, physical factors of radiotherapy, and biological factors. However, at this stage, the research on factors related to acute radiation pneumonia in lung cancer patients after radiotherapy lacks systematicity and cannot provide good scientific guidance for clinical prevention.

The BIRCH algorithm uses clustering features and CF trees instead of cluster descriptions, thus achieving efficiency and scalability in large datasets, making the method suitable for incremental and dynamic clustering. On the other hand, it is based on the idea of representative points, which is a good solution to the problem of clustering preference for spherical shapes and similar cluster sizes and is also more robust in dealing with isolated points. And to solve the problem that the divisional clustering method cannot effectively deal with complex-shaped datasets, a density-based clustering algorithm DBSCAN algorithm was proposed, which does not use the conventional method of measuring data similarity by distance but divides the dataset by sparsity of density, and such an approach can discover clusters of various shapes in complex datasets with noise. With the development of clustering algorithms, grid-based and density-based clustering algorithms also emerged later and have been well studied and maturely applied. The classification results of the first two types of flowers are ideal, while the third type of flowers has a higher misjudgement. There is a small overlap between the latter two categories. This may be related to the size of the data. Too small data size causes the clustering algorithm to fail. Learn all kinds of characteristics more effectively. The GA indicator of clustering effectiveness based on generalization ability is proposed, and the method of determining the optimal number of clusters for K-means based on the GA indicator is proposed by combining the indicator with the K-means algorithm. Through experiments, it is proved that the method works well in determining the optimal number of clusters.

3. Regression Analysis of Factors for Acute Radiation Pneumonia due to Radiation Therapy for Lung Cancer by Cluster Analyses

3.1. Clustering Analysis Algorithm Design. Cluster analysis is a type of unsupervised learning, also known as unguided learning, and a common method in multivariate statistical analysis, which is an important research element in the fields of data mining, machine learning, and pattern recognition [13]. The difference between cluster analysis and supervised learning methods is that the samples used in cluster analysis are not labelled in advance, and the categories to which the samples belong are determined automatically by the cluster analysis algorithm, which is a process of dividing the data set into clusters according to the similarity of the samples' characteristics without training data so that the samples within the same cluster have high similarity and the samples in different clusters have high dissimilarity. Although cluster analysis has a history of several decades, there is no unified definition of cluster analysis so far because different clustering methods end up with a variety of output patterns of the cluster structure. Among the various ways of defining cluster analysis, the one that is accepted by most people is the mathematical description given based on the most common form of output in cluster analysis, the K-split of the sample data.

Let the dataset $X = \{x_1, x_2, \ldots, x_n\}$ and R be the clusters defined on the dataset X . Split X into m set classes $C_1, \ldots, C_m$, if these m set classes satisfy the following three conditions:

$$\begin{gathered} C_i \neq \phi, \\ \cup_{i=1}^{m} C_i = X, \\ C_i \cap C_j = \phi. \end{gathered} \tag{1}$$

Then, it is said to be a cluster on dataset X. Among the above three conditions, condition 1 restricts that all set classes are nonempty, condition 2 restricts that all sample points in dataset X have set classes to which they belong, and condition 3 constrains that each set class does not intersect with each other. From these three constraints, it can be summarized that any sample point in dataset X will be classified into an ensemble class and can belong to at most one ensemble class [14]. Finally, based on the obtained risk grading results and the signal proportion sum, the pharmacological correlation of each drug category was analysed and evaluated by the drugs of each risk level to further verify the rationality and feasibility of this experiment. Although the diversity of clustering criteria leads to different clustering results obtained by different clustering methods, basically all clustering methods need to follow the following four steps. Preprocess the data and feature engineering to retain as much information as possible in the processed data. The clustering algorithm is selected according to the structure of the data; the validity of the clustering results is checked by selecting the appropriate clustering validity index; the clustering results are analysed together with other experimental data to understand the clustering results; and the final correct conclusion is obtained, as shown in Figure 1.

Based on this study, cluster analysis is an exploration of the intrinsic association of adverse reactions to antibiotics, but no specific number of clusters is specified, and the number of clusters needs to be determined artificially for a more stable and reasonable clustering effect. In this study, the elbow rule was used to determine the clustering values [15]. The main idea of the elbow rule is to record and plot the objective function value of each clustering value. As the objective function value increases, the average distortion decreases; each category contains fewer objects accordingly, so the objects will be closer to their centres; however, as the number of clusters increases, the level of change of the average distortion continues to decrease. As the number of clusters increases, the clustering value corresponding to the

RETRACTED

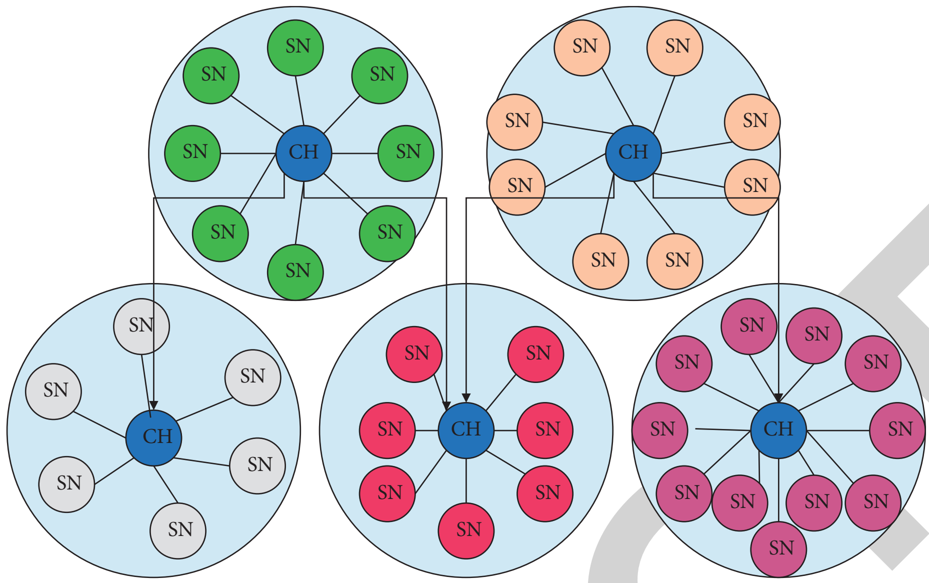

Figure 1: Framework of the clustering analysis algorithm.

RETRACTED

place where the level of aberration decreases the most is the elbow, and the clustering value corresponding to the elbow can be used as the best clustering value for cluster analysis. To derive the best clustering number more intuitively, this paper proposes to use the method of calculating the angle between two lines, and the absolute value of the tangent of the angle is the best clustering number. The tangent formula for the angle is as follows:

$$\mathrm{EI}_{\mathrm{drug}} = \sum_{n=1}^{s} \frac{N_{\mathrm{yn}}}{N_{\mathrm{tn}}} k_n^2. \tag{2}$$

We scored each type of antibiotic based on the severity of adverse reactions. General adverse reaction type was rated as 1 point, and severe adverse reaction type was rated as 3 points. Adverse drug reaction injury index is defined as follows:

$$\mathrm{DI}_{\mathrm{ADR}} = \frac{\sum_{n=1}^{s} N_{\mathrm{yn}}/N_{\mathrm{tn}} k_n^2}{m}, \tag{3}$$

where n denotes the number of adverse reactions where the reported type of each drug is average, n denotes the number of adverse reactions where the reported type of each drug is serious, and n denotes the number of drugs in each category [16]. Because of the existence of drugs with a serious number of 0, this study intends to score the adverse reaction impairment index for such drugs as 1. According to the sensitivity and misjudgement rate of the whole lung V20 at each point on the ROC curve, the values of all cut-off points (sensitivity + specificity) are calculated. The diagnostic index corresponding to the maximum cut-off point is that the best diagnostic threshold is 25.9%. In the definition of adverse reaction severity score, the higher the severity of adverse reactions which scored higher, the higher the calculated adverse drug reaction impairment index and the higher the risk level of the corresponding class of drugs.

There are three main types of internal validity metrics, namely, metrics based on sample geometry of datasets, metrics based on dataset partitioning, and metrics based on statistical information of datasets. There are many internal validity metrics, including Want metric, CH metric, Hart metric, KL metric, DB metric, and IGP metric. They are more commonly used. Among them, the In-Group Proportion (IGP) indicator is based on the statistical information of the dataset, while all other indicators are based on the structure of the sample set of the dataset. These internal validity indicators are not based on external characteristics as a reference standard, but on the statistical characteristics of the dataset itself to assess the validity of the clustering results, so these clustering validity indicators can be used as the selection criteria for the optimal number of clusters. The idea of the CH indicator is to represent the separation by the class matrix and the tightness by the intraclass deviation matrix.

$$\mathrm{CH}(k) = \frac{\mathrm{tr}B(k)/k}{\mathrm{tr}W(k)/n}. \tag{4}$$

Although there are many existing clustering algorithms, most of them need to determine the number of clusters in advance, and the number of clusters as a hyperparameter in the clustering algorithm often has a great influence on the clustering results. In the early days of cluster analysis, the number of clusters was often set artificially by data analysts through experience or by combining background and knowledge from other fields, which was too crude and subjective to obtain the best clustering results. At present, the optimal number of clusters is mostly determined by combining the clustering algorithm with the internal validity index, the internal validity index is used to evaluate the clustering results under different clustering numbers, and the number of classes corresponding to the best clustering validity is selected as the optimal number of clusters for the data set, as shown in Figure 2.

An overview of cluster analysis is given, including the definition of cluster analysis, the basic steps, and the five classes of clustering algorithms. Then the evaluation of cluster validity is introduced, and several classical external validity indicators, as well as internal validity indicators, are presented, respectively. Finally, the method for determining the optimal number of clusters is described in detail, and the algorithmic steps for determining the optimal number of clusters are expressed in the form of an algorithmic flowchart. As the disease worsens, it progresses to the middle and late stages and begins to show clinical symptoms such as haemoptysis and pain. Most patients have already progressed to the middle and late stages when the disease is discovered and have lost the best period of surgical treatment. This chapter introduces the relevant knowledge background to pave the way for the subsequent chapters and provides the theoretical basis for the algorithm simulation experiments in the future.

Clustering validity analysis generally refers to the process of evaluating the merit of clustering results. Intuitively, the merit of clustering results lies in the accuracy of the clustering of samples in the dataset, and most of the existing external validity evaluation metrics are proposed for this point. However, in practical applications, the real clustering of samples in the dataset is difficult to obtain, and this limitation makes it difficult to ensure the practicality of external validity metrics. Unlike external validity indexes, internal validity indexes are often used to test whether the clustered dataset can reflect the intrinsic structure of the dataset, that is, whether the dataset can be as similar as possible while the samples between classes are as different as possible after clustering. Therefore, internal validity metrics are mostly based on the idea of the maximum-minimum distance of sample points, and the objective function is to minimize the intraclass distance and maximize the interclass distance in the clustering results.

$$X_{\text{tr}} = \left\{x_{\text{tr}}^1, x_{\text{tr}}^2, \ldots, x_{\text{tr}}^m\right\}. \tag{5}$$

The GA metric evaluates clustering results in terms of generalization ability in guided learning based on the current clustering results; that is, it considers the merit of clustering results to be related to their generalization ability to predict unknown samples and therefore differs from existing clustering validity metrics, whether external or internal. The clustering results of the training set are used for machine learning to build a classifier, and this classifier is used to predict the test set and compare the prediction results with the clustering results. Therefore, GA metrics are like external validity metrics, but the difference is that it is difficult to obtain the true category of the dataset with the commonly used external validity metrics, while GA metrics solve the problem of difficulty in obtaining the true category of the dataset by constructing a classifier and replacing the true category of the test dataset with the predicted result of the classifier.

3.2. Factor Regression Experiment of Acute Radiation Pneumonia due to Radiation Therapy for Lung Cancer. The relevant medical records of all study subjects were retrieved using the electronic medical record system: general information (gender, age, smoking history, history of chronic lung disease, combined diabetes mellitus, and prechemotherapy FEV1), disease (clinical stage, pathological type, and tumour location), albumin and haemoglobin levels, and relevant treatment (chemotherapy cycle before radiotherapy, whether radiotherapy was applied simultaneously, mean lung dose (MLD), V5, V20, V30, etc.). According to the occurrence of acute radiation pneumonia, the study subjects were divided into the acute radiation pneumonia group and the normal radiotherapy group, and the differences in the indexes between the two groups were compared to analyse the risk factors associated with the development of acute radiation pneumonia after radiotherapy in lung cancer patients [17]. The differences between the two groups in terms of general information, disease, albumin and haemoglobin levels, and related treatment were observed and compared. Patients were followed up for 6 months, and the treatment status of both groups was recorded in detail. Follow-up visits included telephone calls and a review of patients' imaging information. The follow-up included the patients' clinical symptoms and chest CT imaging performance.

The data involved in this study were analysed and processed using SPSS 20.0 statistical software. For the count data, the data were expressed in the form of percentages (%), and the results of comparison between the data were tested using 2, with $P < 0.05$as a statistically significant difference; for the measurement data, the data were expressed using, the results of comparison between the data were tested using t, and 0.05 was considered statistically significant. The unconditional logistic regression model was used to analyse the risk factors for acute radiation pneumonia after radiotherapy in lung cancer patients, and the OR values and their confidence intervals (95% CI) were calculated [18]. In the acute radiation pneumonia group, the percentages of patients with lower middle lobe lung cancer, history of chronic lung disease, combined diabetes mellitus, and the percentages of patients with smoking history were significantly lower than those in the normal radiotherapy group. The percentage of patients with a smoking history was significantly lower than that of the normal radiotherapy group, and the comparison was statistically significant. However, there were no significant differences between the two groups in terms of gender, age, clinical stage, pathological type, albumin, and haemoglobin levels, as shown in Figure 3.

The diagnosis of radiation pneumonia is mainly exclusionary and must be accompanied by the following conditions: history of previous lung irradiation; chest CT imaging mainly shows patchy images, ventilated bronchial signs, striae, solid lung images, or honeycomb-like changes confined to the radiation field, the lesions do not correspond to the anatomical structure of normal lung tissue (not distributed according to lung fields or lung segments), and a small number of patients in the acute phase of the injury may have imaging changes outside the radiation field in addition

RETRACTED

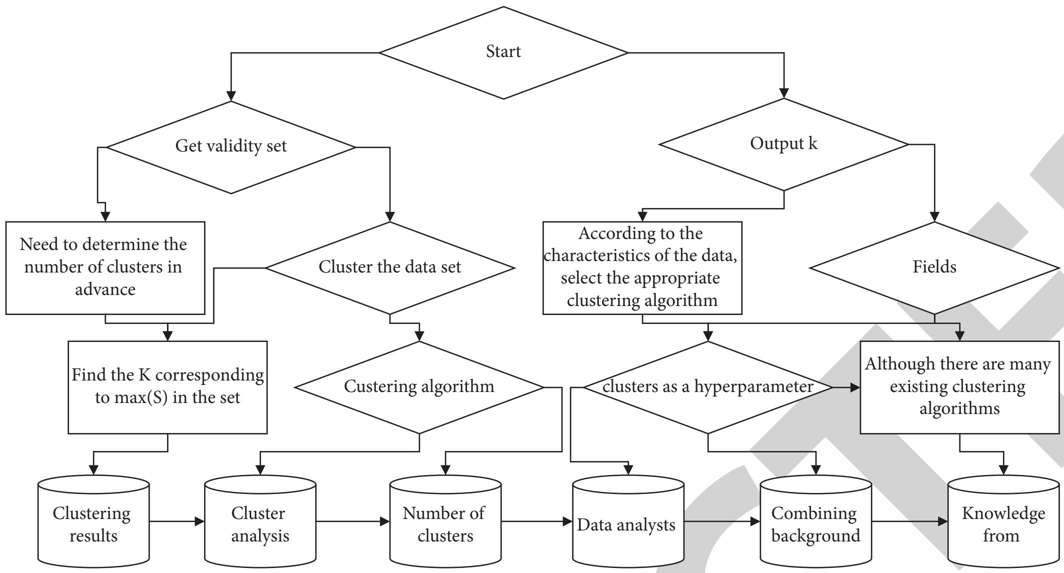

Figure 2: Flow of the algorithm for determining the optimal number of clusters.

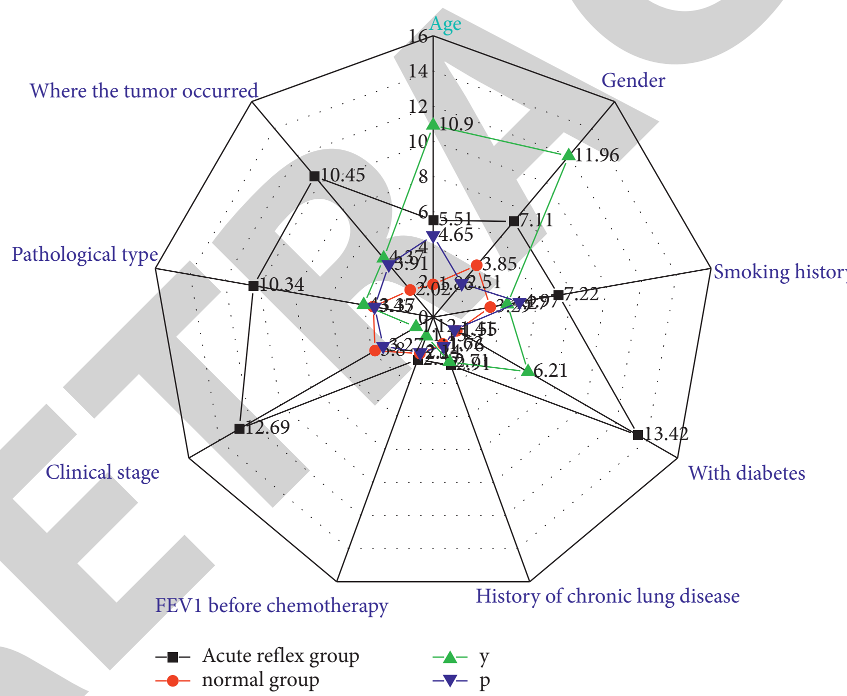

Figure 3: Comparison of relevant indexes between patients in acute radiation pneumonia group and normal radiotherapy group.

to those in the irradiated area. In addition to changes in the irradiated area, a few patients may also have imaging changes outside the radiation field; patients with severe lung injury have clinical symptoms such as cough, shortness of breath, and fever. Cough is the most common, followed by shortness of breath; patients with mild lung injury have shortness of breath after activity; patients with severe lung injury also feel shortness of breath in a calm state; about 50% of patients have a fever; the above symptoms are excluded due to the following factors [19]. Under high-dose radiation, normal lung tissues will be damaged to varying degrees. The above symptoms are excluded from the following factors: tumour progression, lung infection (bacterial, fungal, or viral), acute exacerbation of COPD, cardiogenic disease, pulmonary infarction, anaemia, and drug-related pneumonia.

The first radiation treatment was used as the starting time point, the occurrence of acute radiation pneumonia was recorded within 90 days, and grade 2 radiation pneumonia was used as the endpoint of this study. In the one-way ANOVA, the independent binary chi-square test was chosen for the analysis of count data, and the independent-sample t-test or nonparametric rank-sum test was used for the analysis of measurement data; in the multifactor ANOVA,

RETRACTED

the binary logistic regression analysis was chosen to determine the test level $a = 0.05$, and $P < 0.05$ was taken as statistically significant.

The dose drop rate at the edge of the target area is faster, and to improve the resolution of the dose by the spatial information model, the outward expansion step in the direction of all endangered organs is smaller in the range closer to the target area. Since the dose outside the target area had different dose drop ranges in the bladder, small bowel, rectum, and femoral head directions, the dose drop rate was faster in the rectum and femoral head directions compared to the bladder and small bowel directions, and therefore, their outward expansion steps were smaller relative to the bladder and small bowel directions. All images for texture cut were in 2D mode, and CT image cut was selected by scanning the largest level, measuring the CT value of the lesion and the diameter of the lesion, and then performing image cut. After high-dose radiation exposure, cell damage appears immediately, followed by a series of cytokine synthesis increases. With the transmission and amplification of signals between cells, a series of pathophysiological reactions are triggered, which leads to radiation pneumonitis. The Image Segmented tool within the MATLAB software introduced in the previous chapter was used to perform the image segmentation in a semiautomatic manner, with the approximate extent outlined manually and then iterated automatically by the software, paying attention to the structures adjacent to the chest wall vessels, mediastinum, and atelectasis, as shown in Figure 4.

With the increasing level of awareness of radiation pneumonia, people began to pay attention to the risk factors that induce acute radiation pneumonia and tried to take effective measures in clinical treatment to reduce the incidence of acute radiation pneumonia and ensure the clinical treatment effect. Some foreign researchers have taken lung cancer patients receiving radiotherapy as study subjects and formulated radiotherapy regimens for them according to the target population's characteristics, with targeted restrictions on radiotherapy dose and volume, resulting in a significant reduction in the incidence of acute radiation pneumonia [20]. No matter what kind of radiotherapy will inevitably cause damage to good cells and tissues, the incidence of various complications in radiotherapy patients is high, such as hair loss, skin reaction, immunosuppression, bone marrow suppression, nephrotoxicity, pulmonary toxicity, gastrointestinal toxicity, and radiotherapy pneumonia.

In recent years, the incidence of acute radiation pneumonia after radiotherapy treatment for lung cancer patients is high and has become a major complication in clinical practice. The occurrence of acute radiation pneumonia will hinder the normal treatment, resulting in the inability to enhance the radiation therapy dose, poor clinical treatment effect, and unsatisfactory life quality of patients. In severe cases, it may even lead to interruption of treatment and induce death.

4. Analysis of Results

4.1. Cluster Analysis Results. The data in the original database included the drug classification, drug name, ADR name, the number of reports of both the target drug and the target ADR in the database a value, the total number of all other ADRs for the target drug b value, the total number of targets ADRs for drugs other than the target drug in the database c value, and the total number of reports other than the target drug and the target ADR in the entire databased value. The corresponding PRR values, IC values, and binary values were calculated by substituting each value into the formula in the previous chapter, and the information obtained is shown in Figure 5.

To cluster the drugs, this paper builds a vector space model with the selected drugs and the signal detection values of the adverse reactions as features and outputs the results as a cross-tabulation table. The following is the cross-wizard table generated with the binary value data, IC value data, and PRR value data as features, respectively. The vector space model was established with the antibiotic name as the row label and each type of adverse reaction as the column label, where the binary value of the adverse reaction-antibiotic combination without signal was set as 0. The clustering results were compared with the category to which the original samples belonged, and it was found that 136 samples were accurately classified out of all 150 samples. The classification results were more satisfactory for the first two flowers, while the misclassification was higher for the third flower.

There was a small overlap between the latter two categories, which may be related to the size of the data volume, too small to cause the clustering algorithm to learn the features of each category more effectively, thus leading to misclassification of the clustering results. The basic structure of these three datasets is briefly introduced before the experiment. The BUPA dataset has 345 samples with sample dimension 6 and correct class number 2; the PID dataset has 768 samples with sample dimension 8 and correct class number 2; the BCW dataset consists of 699 samples with sample dimension 9 and correct class number 2.

The data preprocessing process of this risk classification model based on cluster analysis was described in detail. Firstly, the data set and data sources used in this study were introduced, the selected drugs and the WHO adverse drug reaction terminology set used for the query were presented in the form of a list, and then the vector space model was established based on the reported data with three signal detection methods, namely, PRR, IC, and binary value, respectively. In order to select the signal detection methods suitable for cluster analysis, realize the drug risk classification, and verify the credibility of the experimental results, this study firstly screened the common signal detection methods and initially determined three signal detection methods, namely, PRR, IC, and binary value; then the best clustering numbers of the three methods were derived based on the elbow rule, and the best clustering numbers of each method were used to conduct the MATLAB simulation tool. In this way, the homogeneity of the elements within the class and the heterogeneity of the elements between the classes are maximized at the same time. An important feature of the data in the era of big data is the huge amount of data. A good clustering model can just solve the data. The specific results of the clustering of these three signal detection methods were

RETRACTED

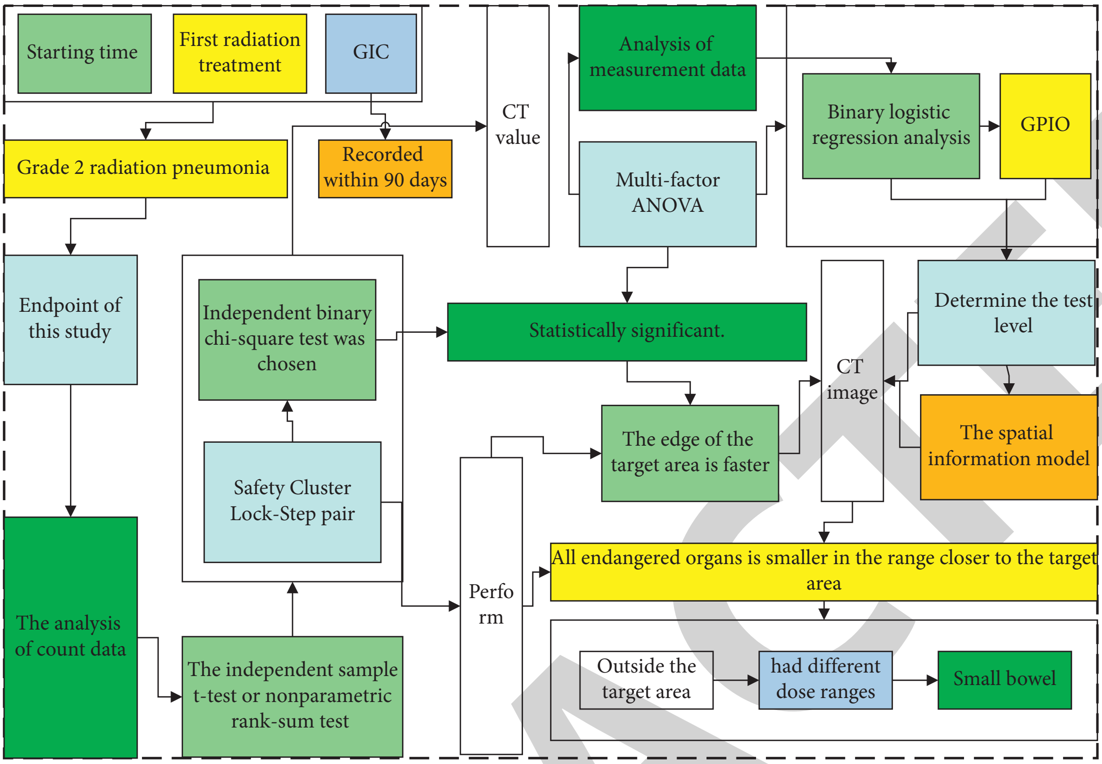

FIGURE 4: Multifactor regression experiment.

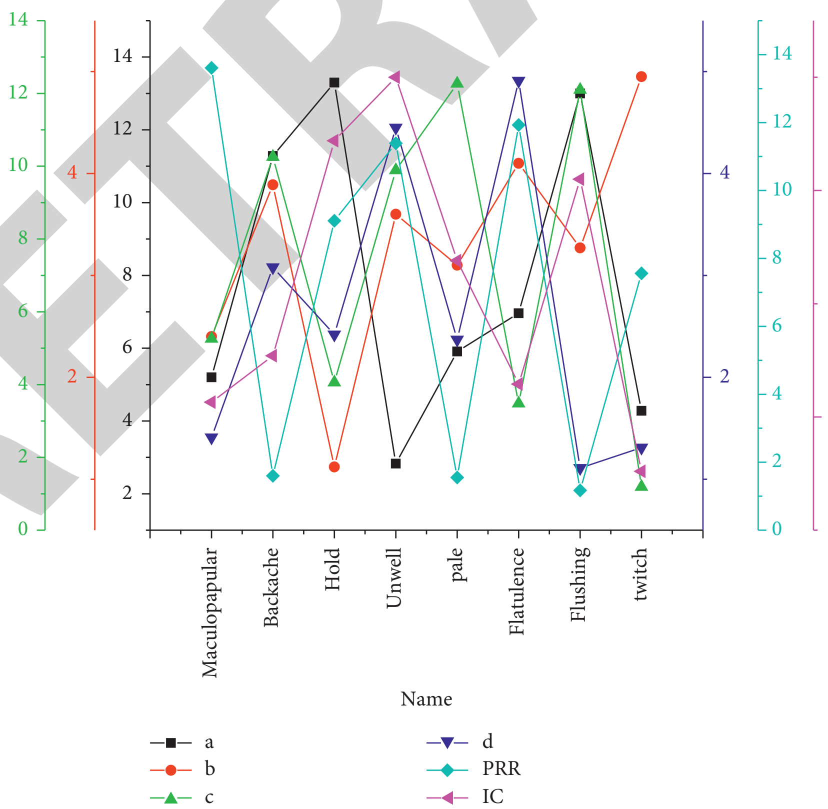

FIGURE 5: Summary of data after signal detection and processing.

RETRACTED

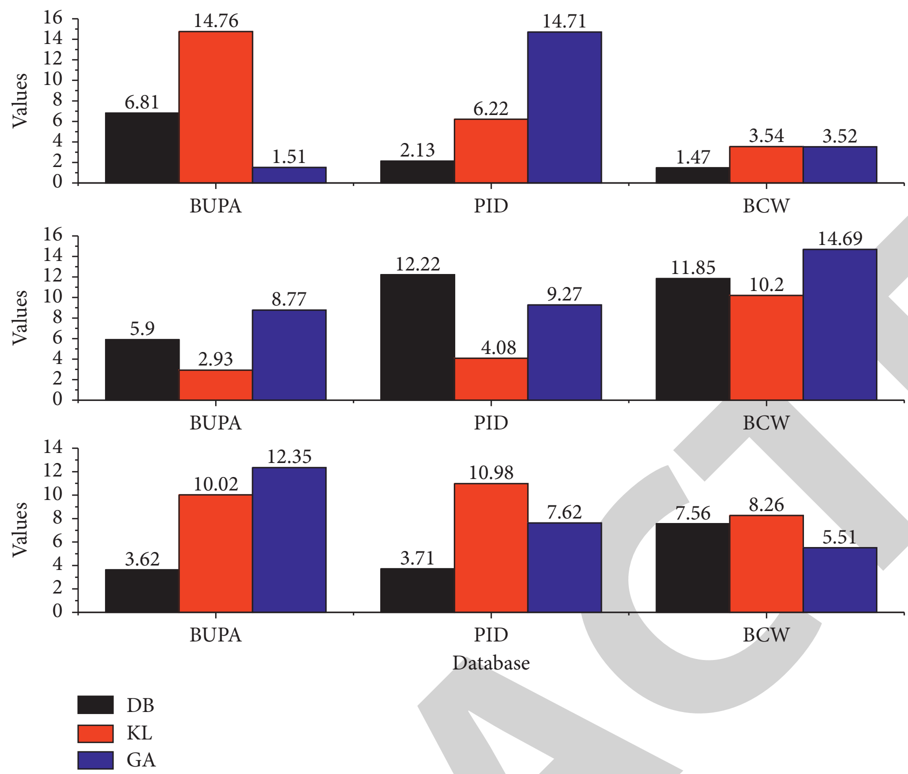

Figure 6: Table of experimental results for comparison of clustering validity indexes.

substituted into the evaluation function for calculation and evaluation to determine the drug risk classification based on the PRR method; subsequently, in order to achieve drug risk classification, this study calculated the damage index values of each type of drugs according to the damage index formula and ranked them to determine the risk level of each clustering result, then the number of each type of prescription drugs and over-the-counter drugs, and the proportion of each type of serious. Then, the reliability of the study was initially verified by the number of prescription drugs and over-the-counter drugs and the proportion of each type of serious adverse reactions, and then the signal proportion of the top 10 key adverse reactions was counted in turn; finally, on the basis of the risk classification results and the signal proportion, the pharmacological correlation of each drug class was analysed and evaluated by searching the data for each risk class of drugs to further verify the rationality and feasibility of this experiment.

The DB indicator, KL indicator, HS indicator, and the GA indicator proposed in this paper were used to evaluate the validity of the clustering results for these three datasets, and the best number of clusters evaluated by each indicator was used as the criterion to measure the merit of each indicator. The experimental results are shown in Figure 6.

The comparison table of cluster validity indicators in Figure 6 shows that the GA indicator can find the best clusters for these three datasets, while the traditional DB indicator cannot get the accurate clusters for each dataset, and the KL indicator can only find the accurate clusters for the BUPA dataset but cannot find the best clusters for the PID and BCW datasets. In this paper, the criterion for evaluating a cluster validity index is whether the index can accurately find the true class number of the dataset, and if it can find the true class number of the dataset, it means that the cluster validity index is reasonable and effective for evaluating the clustering results. Through the experimental results, it can be proved that the GA index proposed in this paper is more effective and stable than the traditional clustering validity index. The main research direction of this paper is how to determine the optimal number of clusters in cluster analysis scientifically and effectively. Cluster analysis is an important multivariate statistical analysis method, which can help people get the distribution pattern of data when facing the cluttered data, to grasp the intrinsic structure and characteristics of the data set. In the field of big data analysis, including machine learning and pattern recognition, cluster analysis often plays an important role in data analysis as one of the means of data mining, so the study of cluster analysis has great significance.

4.2. Multifactor Regression Results. The samples in the same cluster have higher similarity, and the samples of different clusters have higher dissimilarities. Although the cluster analysis has a history of decades, the results are obtained due to different clustering methods. The cluster structure has multiple output modes. A multifactorial unconditional logistic regression analysis of the factors associated with acute radiation pneumonia revealed that lower middle lobe lung cancer, history of chronic lung disease, combined diabetes, FEV1 < 2L before chemotherapy, chemotherapy cycles >2 before radiotherapy, simultaneous application of

RETRACTED

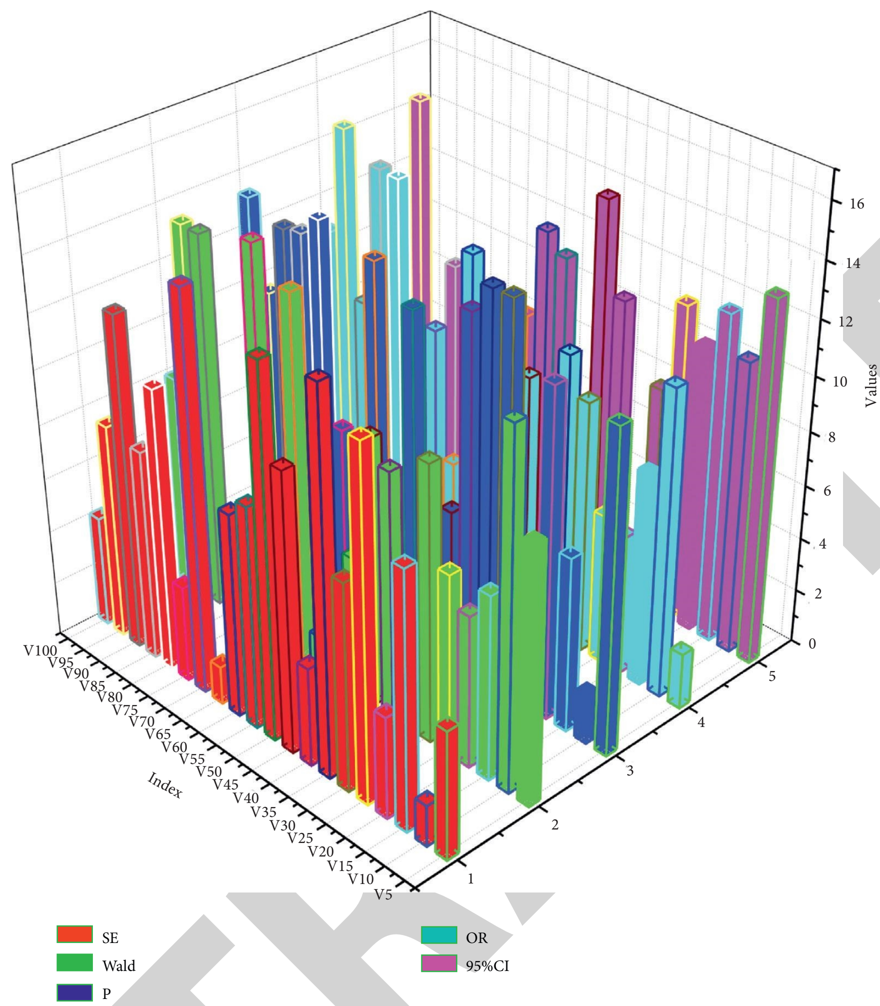

Figure 7: Factorial unconditional logistic regression analysis.

radiotherapy and chemotherapy, total radiotherapy dose >56 Gy, MLD >15 Gy, V5 >40%, V20 > 25%, and V30 > 18% all increased the risk of acute radiation pneumonia, while a history of smoking is a protective factor against the development of acute radiation pneumonia and decreases its risk (all $P < 0.05$, OR < 1), with ORs within the 95% CI interval, as shown in Figure 7.

Smoking is generally considered to be the main risk factor. Smoke is acidic, which tends to make patients form an acidic body, and an acidic body has the risk of inducing lung cancer; environmental pollution also increases the risk of lung cancer; tin, arsenic, and toluene are carcinogenic substances, and air pollution will lead to an increase in these components in the air, thus increasing the risk of lung cancer; chronic lung diseases are also a major risk factor for lung cancer and lung diseases lesions, which can lead to a decrease in lung cell activity and immune capability, increasing the risk of lung cancer; in addition, factors such as occupation and oncogene activation can also increase the risk of lung cancer. The treatment methods of lung cancer include surgery, chemotherapy, and radiotherapy. Surgery is mostly used for the treatment of early-stage tumours, while radiotherapy is the most common treatment method in clinical practice, and according to statistics, more than 60% of lung cancer patients need radiotherapy. Radiotherapy has high clinical value and can effectively improve the local cancer control rate and overall treatment efficiency. The data is preprocessed, and the processed data retains as much information as possible through feature engineering. Select the corresponding clustering algorithm according to the structure of the data; select the appropriate cluster validity index to check the validity of the clustering results. 3D-CRT is the most used radiotherapy treatment for lung cancer in clinical practice. 3D-CRT is based on CT simulation and computer calculation to obtain the real situation of dose distribution, and based on this, the radiotherapy plan is scientifically set to maximize the irradiation of tumour while minimizing the damage to the surrounding tissues and organs. To optimize the clinical effect of radiotherapy implementation, the radiation treatment plan is scientifically set based on the realistic dose distribution based on CT simulation and computer calculation.

Because whole lung V20 is an independent influencing factor for grade ≥2 radiation pneumonia, the value of whole lung V20 was entered into the ROC curve, and the area under the whole lung V20 curve was 0.642, as shown in Figure 8. The area under the ROC curve ranges from 0.5 to

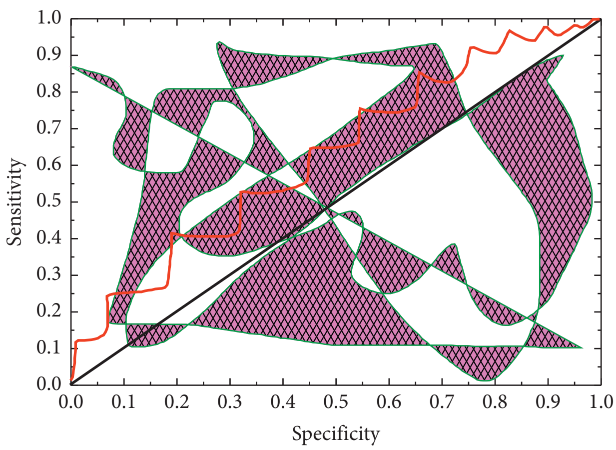

Figure 8: ROC curve of the whole lung V20.

1.0, and an area under the ROC curve of 0.5 to 0.7 indicates a low diagnostic value, between 0.7 and 0.9 indicates a moderate diagnostic value, and greater than 0.9 indicates a high diagnostic value. In general, an area under the ROC curve of 0.5–0.7 indicates low diagnostic value, between 0.7 and 0.9 indicates moderate diagnostic value, and above 0.9 indicates high diagnostic value. In the present study, the area under the V20 curve of the whole lung was calculated to be 0.642, which indicates that it has a diagnostic value.

The sensitivity and false-positive rate of whole lung V20 at each point on the ROC curve were used to calculate the value of all cut-off points, and the diagnostic index corresponding to the maximum cut-off value is the optimal diagnostic threshold of 25.9%. When developing a radiation treatment plan, the dosimetry parameters of whole lung V20 are recommended to be limited to ≤25.9%. If this threshold is exceeded, the risk of grade ≥2 radiation pneumonia will increase.

5. Conclusion

In this study, we first calculated the damage index values of each drug class according to the damage index formula, and based on this, we ranked to determine the risk level of each clustering result; then we initially verified the reliability of the study with the number of each type of prescription drugs and over-the-counter drugs and the proportion of each type of serious adverse reactions and then counted the signal weight of the top 10 key adverse reactions in turn; finally, based on the risk classification results obtained and the signal weight and based on the results of the risk classification and the proportion of the signal, the pharmacological correlation of each drug class was analysed and evaluated to further verify the rationality and feasibility of this experiment. Therefore, the object will be closer to its centre; however, as the number of clusters increases, the average level of distortion continues to decrease. As the number of clusters increases, the place where the level of distortion decreases the most corresponds to the cluster value is the elbow, and cluster analysis can be performed with the cluster value corresponding to the elbow as the best cluster value. No association was found between gender, age, and the occurrence of grade ≥2 radiation pneumonia in this study. There is no evidence-based medical evidence to confirm that gender and age are the main influencing factors for the occurrence of radiation pneumonia, and in the one-way ANOVA, gender and the occurrence of severe acute radiation pneumonia were not related. The present study did not suggest any guiding indexes in terms of clinical factors. Considering the special situation that about 40% of the patients in this group were hospitalized in sister departments such as surgery or chemotherapy during radiotherapy, the occurrence and classification of radiation pneumonia mainly relied on the medication records and course records of the bedside doctors in different departments; there may be interfering factors other than the existing common clinical factors that we have not yet explored. The next study will be a prospective clinical study to further refine and improve the study of clinical factors in radiation pneumonia.

Data Availability

The data used to support the findings of this study are available from the corresponding author upon request.

Conflicts of Interest

The authors declare that there are no conflicts of interest.

Acknowledgments

This work was supported by the project of the National Natural Science Foundation of China (no. 81500071): Study on the effects of chronic intermittent hypoxia on the ER stress in genioglossus and the mechanisms of interventional supplement of adiponectin.

References

[1] K. Bousabarah, O. Blanck, S. Temming et al., “Radiomics for prediction of radiation-induced lung injury and oncologic outcome after robotic stereotactic body radiotherapy of lung cancer: results from two independent institutions,” *Radiation Oncology*, vol. 16, no. 1, pp. 74–14, 2021.

[2] S. Cui, R. K. Ten Haken, and I. El Naqa, “Integrating multiomics information in deep learning architectures for joint actuarial outcome prediction in non-small cell lung cancer patients after radiation therapy,” *International Journal of Radiation Oncology, Biology, Physics*, vol. 110, no. 3, pp. 893–904, 2021.

[3] C. L. Tinkle, C. Singh, S. Lloyd et al., “Stereotactic body radiation therapy for metastatic and recurrent solid tumors in children and young adults,” *International Journal of Radiation Oncology, Biology, Physics*, vol. 109, no. 5, pp. 1396–1405, 2021.

[4] S. Siddique and J. C. L. Chow, “Artificial intelligence in radiotherapy,” *Reports of Practical Oncology and Radiotherapy*, vol. 25, no. 4, pp. 656–666, 2020.

[5] J. Wang, R. Liu, Y. Zhao et al., “A predictive model of radiation-related fibrosis based on the radiomic features of magnetic resonance imaging and computed tomography,” *Translational Cancer Research*, vol. 9, no. 8, pp. 4726–4738, 2020.

RETRACTED

Hindawi
Journal of Healthcare Engineering
Volume 2023, Article ID 9849703, 1 page
https://doi.org/10.1155/2023/9849703

Retraction

Retracted: Analysis of the Mechanism of Breast Metastasis Based on Image Recognition and Ultrasound Diagnosis

Journal of Healthcare Engineering

Received 5 December 2023; Accepted 5 December 2023; Published 6 December 2023

Copyright © 2023 Journal of Healthcare Engineering. This is an open access article distributed under the Creative Commons Attribution License, which permits unrestricted use, distribution, and reproduction in any medium, provided the original work is properly cited.

This article has been retracted by Hindawi, as publisher, following an investigation undertaken by the publisher [1]. This investigation has uncovered evidence of systematic manipulation of the publication and peer-review process. We cannot, therefore, vouch for the reliability or integrity of this article.

Please note that this notice is intended solely to alert readers that the peer-review process of this article has been compromised.

Wiley and Hindawi regret that the usual quality checks did not identify these issues before publication and have since put additional measures in place to safeguard research integrity.

We wish to credit our Research Integrity and Research Publishing teams and anonymous and named external researchers and research integrity experts for contributing to this investigation.

The corresponding author, as the representative of all authors, has been given the opportunity to register their agreement or disagreement to this retraction. We have kept a record of any response received.

References

[1] Y. Huang, S. Zheng, and B. Lai, “Analysis of the Mechanism of Breast Metastasis Based on Image Recognition and Ultrasound Diagnosis,” *Journal of Healthcare Engineering*, vol. 2021, Article ID 4452500, 11 pages, 2021.

Hindawi
Journal of Healthcare Engineering
Volume 2021, Article ID 4452500, 11 pages
https://doi.org/10.1155/2021/4452500

RETRACTED

Research Article

Analysis of the Mechanism of Breast Metastasis Based on Image Recognition and Ultrasound Diagnosis

Yihong Huang,[1] **Shuo Zheng**,[1] **and Baoyong Lai**[2]

[1]*Fuzhou Second Hospital Affiliated to Xiamen University, Fuzhou, Fujian 350007, China*
[2]*Third Affiliated Hospital of Beijing University of Chinese Medicine, Beijing 100029, China*

Correspondence should be addressed to Yihong Huang; likyzhen@163.com and Baoyong Lai; baoyonglai@bucm.edu.cn

Received 10 August 2021; Revised 9 September 2021; Accepted 18 September 2021; Published 11 October 2021

Academic Editor: Gu Xiaoqing

Copyright © 2021 Yihong Huang et al. This is an open access article distributed under the Creative Commons Attribution License, which permits unrestricted use, distribution, and reproduction in any medium, provided the original work is properly cited.

Breast cancer is one of the cancers with the highest incidence among women. In the late stage, cancer cells may metastasize to a distance, causing multiple organ diseases, threatening the lives of patients. The detection of lymph node metastasis based on pathological images is a key indicator for the diagnosis and staging of breast cancer, and correct staging decisions are the prerequisite and basis for targeted treatment. At present, the detection of lymph node metastasis mainly relies on manual screening by pathologists, which is time-consuming and labor-intensive, and the diagnosis results are variable and subjective. The automatic staging method based on the panoramic image calculation of the sentinel lymph node of the breast proposed in this paper can provide a set of standardized, high-accuracy, and repeatable objective diagnosis results. However, it is very difficult to automatically detect and locate cancer metastasis areas in highly complex panoramic images of lymph nodes. This paper proposes a novel deep network training strategy based on the sliding window to train an automatic localization model of cancer metastasis area. The training strategy first trains the initial convolutional network in a small amount of data, extracts false-positive and false-negative image blocks, and uses manual screening combined with automatic network screening to reclassify the false-positive blocks to improve the class of negative categories. Using mammography, ultrasound, MRI, and 18F-FDG PET-CT examinations, the detection rate and diagnostic accuracy of primary cancers in the breast of patients with axillary lymph node metastasis as the first diagnosis were obtained. The detection rate and diagnostic accuracy of breast MRI for primary cancers in the breast are much higher than those of X-ray, ultrasound, and 18F-FDG PET-CT (all P values <0.001). Mammography, ultrasound, and PET-CT examinations showed no difference in the detection rate and diagnostic accuracy of primary cancers in the breast of patients with axillary lymph node metastasis as the first diagnosis. Breast MRI should be used as a routine examination for patients with axillary lymph node metastasis as the first diagnosis. The primary breast cancer in the first diagnosed patients with axillary lymph node metastasis is often presented as localized asymmetric compactness or calcification on X-ray; it often appears as small focal mass lesions and ductal lesions without three-dimensional space-occupying effect on ultrasound.

1. Introduction

Breast cancer is a common malignant tumor that threatens women's lives. Breast-conserving surgery can be performed when detected early, and the prognosis is good, and the five-year survival rate is high. However, radical resection may be necessary after the middle and late stages; not only the quality of life is significantly reduced, but the 5-year disease-free survival rate is also significantly reduced, which increases the economic burden of patients [1, 2]. Early detection of lesions is critical. Commonly used methods of breast cancer diagnosis include mammography, ultrasound, and magnetic resonance imaging [3]. As a classic breast cancer screening method, molybdenum target has a high penetration rate at home and abroad, especially abroad. It is very sensitive to intralesional calcification, and it is highly sensitive to the diagnosis of tumors with calcification, especially for nonmass cancers with calcification, and the detection rate is significantly higher than that of ultrasound [4]. However, for noncalcified masses, the detection rate is affected by the compactness of the breast glands. At the same time, its radioactivity limits the age and frequency of screening. MRI has high definition and high resolution. MRI enhancement has a high sensitivity for the diagnosis of breast cancer. This has been recognized. The sensitivity of the diagnosis of breast cancer reaches 95%–99%. MRI also has many functional imaging methods. For example, diffusion-weighted imaging, magnetic resonance power, magnetic resonance perfusion imaging, etc., can increase the description of the internal biological characteristics of the tumor on the basis of morphology and provide help for the diagnosis of early breast cancer [5]. However, MRI cannot be used as a screening method due to its high scanning cost [6].

In order to increase the accuracy of breast cancer diagnosis and reduce the missed diagnosis rate, it is urgent to combine tumor internal functional imaging on the basis of morphology to assist diagnosis. Malignant tumor cells generate a large number of capillaries in the early stage of formation. Tumor cells are metabolized and consume a large amount of oxygen in the blood, resulting in a state of rich blood supply and hypoxia inside the tumor, resulting in a significant increase in intravascular hemoglobin, especially deoxyhemoglobin [7, 8]. The changes in the internal metabolic function of these malignant tumors are obviously different from those of benign tumors. Ultrasonic Light Scattering Imaging System (DOT) combines ultrasound imaging technology and photon scattering tomography technology. You can use ultrasound to locate the suspicious area, emit near-infrared light through the probe, and use hemoglobin and deoxyhemoglobin as the main absorbers of near-infrared light to measure total hemoglobin, which indirectly reflects the distribution of blood vessels and oxygen and state in the tissue, thereby providing tissue deficiency [9]. Ultrasonic light scattering imaging system realizes the scanning of tumor internal metabolic function on the basis of morphology. At present, there are more researches focusing on injecting the tumor surface or areola skin with ultrasound contrast agent, tracking the movement of lymph vessels to find the sentinel lymph node in the armpit, and then performing the contrast and biopsy of the sentinel lymph node to confirm whether it has metastasis. However, the procedure is complicated and it is a traumatic test. How to predict the metastasis of axillary lymph nodes under the premise of simplicity and non-invasiveness is a challenge [10].

This paper proposes a method based on deep convolutional neural network that can automatically locate and identify the cancer metastasis area in the panoramic image of breast lymph nodes. Specifically, the technical contributions of this article can be summarized as follows:

(1) Through targeted data expansion and training strategies, the cancer metastasis recognition model of the image block is obtained. Then, the model is sent to the preprocessed panoramic image, and the predicted calorific value map about the probability of cancer metastasis is obtained. The model proposed in this paper can better identify cancer metastasis areas and greatly reduce false positive areas, and the model has higher sensitivity.

(2) We retrospectively analyzed axillary tumors in a cancer hospital from January 2018 to November 2020, with axillary tumors as the first diagnosis, and performed breast MRI examination. The axillary tumor was confirmed to be lymph node metastatic adenocarcinoma by biopsy, and the results of immunohistochemical examination supported the original disease. The lesions came from breast tissue, and no obvious malignant lesions were found on clinical palpation of bilateral breasts in 73 patients. Among them, 61 cases underwent mammography at the same time, 69 underwent breast ultrasound at the same time, 19 underwent MRI-guided "second-eye" ultrasound examination, and 22 underwent 18F-FDG PET-CT at the same time.

(3) Two senior breast imaging diagnosticians analyzed the X-ray images, ultrasound images, and MRI images of all cases, and evaluated the composition of breast tissue according to the breast imaging report and data system standards proposed by the American College of Radiology. This topic aims to analyze the mammography, ultrasound, MRI, and 18F-FDG PET-CT manifestations of patients with axillary lymph node metastasis cancer as the first diagnosis (negative breast clinical palpation), and to compare the effects of different imaging methods in the primary breast. The diagnosis efficiency of cancer foci provides a basis for the clinical development of diagnosis and treatment plans.

2. Related Work

Rac1 and Cdc42 are generally believed to promote the invasion and metastasis of breast cancer [11]. However, the relationship between Rho A and breast cancer metastasis remains controversial. The traditional view is that the expression level of Rho A is positively correlated with the pathological stage of breast cancer and the degree of lymph node metastasis, and based on this, it is believed that Rho A can promote the migration and invasion of tumor cells [12]. However, related scholars have constructed a breast cancer cell line that stably interferes with Rho A and found that the invasion ability of this cell is significantly enhanced [13]. It is speculated that Rho A can hinder the invasion of breast cancer cells. These two diametrically opposed views indicate that the relevant mechanisms still need to be studied in depth.

Extracellular signal regulated kinase (ERK) is a key regulatory molecule that transmits signals from cell surface receptors to the nucleus [14]. The RAS/ERK signaling pathway plays an important role in the occurrence and development of breast cancer and other epithelial tumors. Studies have shown that SHP2 participates in the RAS/ERK signaling pathway and plays an important regulatory role [15]. In the study of lung cancer and cartilage tumors, it was found that through the stimulation of EGF, IL-6, and other growth factors or cytokines, the phosphatase domain of SHP2 can activate the RAS signaling pathway and

RETRACTED

phosphorylate SHP2 after autophosphorylation [16]. Phosphorylated SHP2 dephosphorylates and inactivates the inhibitory proteins in the RAS/ERK pathway such as SHPS-1 and palmitoyl phosphoprotein Sprouty, thereby lifting the inhibitory state of the RAS/ERK pathway. They found that SHP2 can continuously activate the RAS/ERK signaling pathway by activating Src Family Kinases (SFKs) [17].

The p LKO.1-puro vector is a lentiviral sh RNA expression vector, which can efficiently and stably infect mammalian cells. Puromycin can be used to screen mutant cell lines. In this experiment, in order to obtain a stable O-Glc NAc expression inhibiting breast cancer cell model, they used the p LKO.1-puro vector to construct an OGT-specific interference vector, which effectively detected the OGT expression in breast cancer cells 4T1 [18].

Studies have shown that PUGNAc can efficiently and specifically inhibit the activity of OGA in vivo and in vitro, thereby increasing the level of O-Glc NAc in cells [19]. In this experiment, a breast cancer cell model with elevated O-Glc NAc was obtained by PUGNAc treatment [20]. In order to ensure the reliability of subsequent experiments, in most experiments, they used both OGT silencing and PUGNAc treatment of two cell models [21]. A large number of studies have shown that the absence or excessive expression of O-Glc NAc can lead to cell cycle inhibition and apoptosis [22]. At the same time, considering the expression of O-Glc NAc in normal breast cells, this article did not completely inhibit the expression of OGT and the activity of OGA in order to study the role of O-Glc NAc in the occurrence and development of breast cancer.

In addition, because tumor metastasis is an overall process, animal experiments should be considered to prove the effect of Gankyrin on tumor metastasis from the overall level. At present, the animal models of breast tumor metastasis are relatively mature. Commonly used are breast fat pad injection model and tail vein injection model. In addition to the observation and counting of metastases by naked eyes, the analysis methods include in vivo imaging analysis and pathological section analysis. The relevant animal experiments of Gankyrin's effect on breast cancer metastasis are being actively prepared [23]. Preliminary preparations are to construct a mouse breast cancer metastasis model through breast fat pad injection and to observe the degree of metastasis through animal in vivo fluorescence imaging technology [24]. Through transfection and screening, breast cancer cells stably expressing luciferase have been obtained.

In another liver cancer study, it was also found that SHP2 can effectively promote the activation of ERK [25]. The activated ERK can significantly inhibit the activity of B lymphocyte tumor-2 protein, thereby inhibiting cell apoptosis and leading to cell cancerization. In the related research of Noonan syndrome, related scholars found through mouse model experiments that inhibiting the protein expression of SHP2 can significantly inhibit the phosphorylation of ERK, and the abnormal activation of SHP2 can overactivate the phosphorylation of ERK1/2 [26]. At present, the role of SHP2 in the RAS/ERK signaling pathway of breast cancer cells remains to be further clarified. Relevant scholars have selected breast cancer cell lines MDA-MB-231 cells and BT549 cells as the research objects, by constructing recombinant plasmids (shSHP2-NC1, shSHP2-NC3) that reduce the expression of SHP2 stably and small interfering RNA fragments that reduce the expression of SHP2 transiently (SiSHP2-1#, siSHP2-2#), analyzing the effect of downregulation of SHP2 protein level on ERK signaling pathway. The experimental results show that in MDA-MB-231 and BT549 cells, the steady decrease or transient decrease of SHP2 protein level will cause the phosphorylation level of ERK to decrease significantly [27]. This indicates that in breast cancer cells, SHP2 participates in the RAS/ERK signaling pathway and plays a positive regulatory role.

3. Research Methods

3.1. Inspection Method. We instruct the patient to take a supine position, hold the head with both hands, and fully expose both breasts and armpits. First, we use a two-dimensional probe to perform routine scans on both breasts and axilla. After the tumor is found, we select the largest section of the lesion and the section with the most abundant blood flow (try to show part of the surrounding glandular tissue as a control) and keep the probe position and patient position unchanged, adjust various machine parameters. During the imaging process, the patient is instructed to maintain the position, avoid deep breathing, and the operator to avoid overpressurization of the probe and maintain the stability of the probe. The storage time is at least 3 minutes. After the contrast is completed, the dynamic images stored in the machine are played back. Two sonographers (mammography work ≥5 years) will analyze the enhanced features. If there is a disagreement, another senior ultrasound is required. The physician participates in the analysis and finally reaches a consistent diagnosis opinion. The specific process of inspection is shown in Figure 1.

3.2. Histological Grade and Immunohistochemical Determination. Experienced pathologists will diagnose the submitted specimens. For the determination of the expression of ER, PR, HER-2, and Ki-67, we used the SP staining method. If the tumor cell nuclear staining is greater than or equal to 10%, it is judged to be positive for ER and PR; if the tumor cell nuclear staining is less than 10%, it is judged to be negative for ER and PR. We judged the nucleus brown staining ≥14% as Ki-67 positive, and the brown-yellow staining nucleus less than 14% as negative. After HER-2 is stained with SP, the cell membrane with brown particles appears as the number of stained positive cells ≥10% as +, the number of stained positive cells ≥20% is considered to be 2+, and the number of stained positive cells ≥30% is considered to be 3+. Among them, "−" or "+" is judged as negative, "+++" is judged as positive, and "++" is judged as positive by HER-2 gene amplification, and if there is gene amplification, it is judged as positive, and if there is no gene amplification, it is judged as negative.

RETRACTED

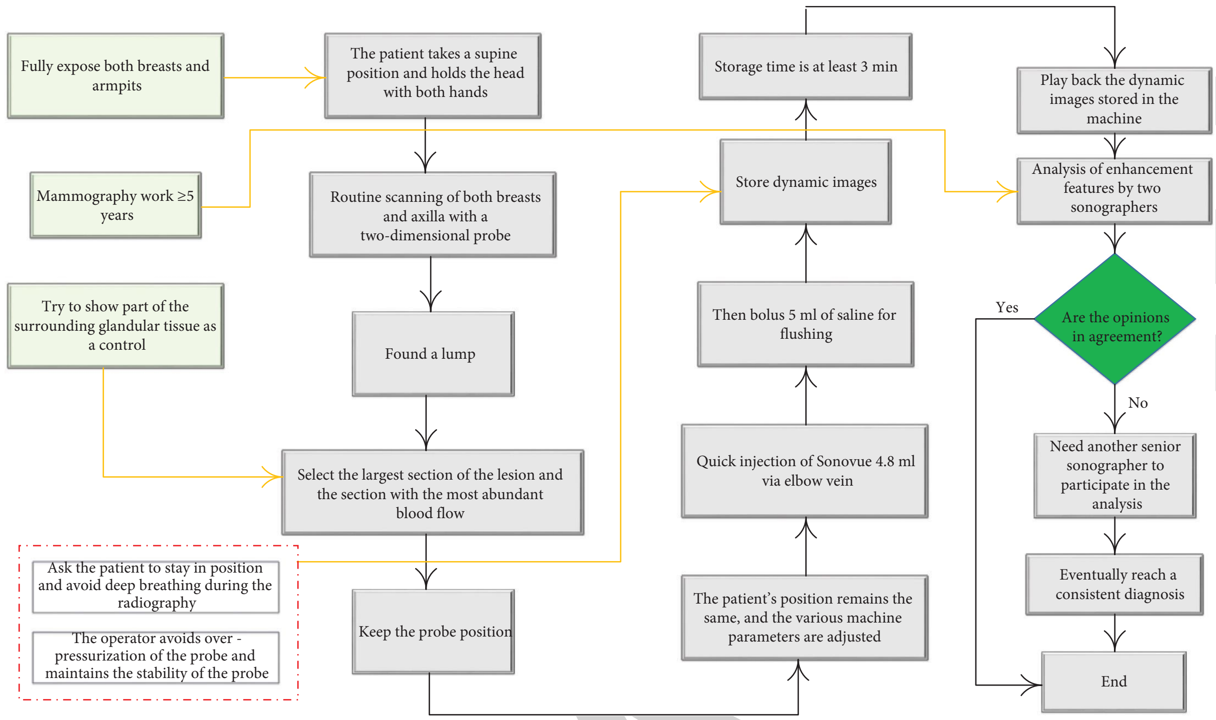

Figure 1: The specific process of breast metastasis examination.

Histopathological grading used Scarff–Bloom–Richardson grading system to divide invasive ductal carcinoma into grade I (highly differentiated), grade II (moderately differentiated), and grade III (poorly differentiated), and axillary lymph node metastasis was recorded.

3.3. Analysis Method. We refer to the relevant content of the breast imaging report data system BI-RADS to understand the patient's menstrual cycle, and compare and observe the bilateral breasts, pay attention to the two-dimensional characteristics of the tumor and the color Doppler data for quantitative analysis. For lesion cases, it is necessary to focus on analyzing the differences in sonograms between the lesions to find out the similarities and differences; whether there are catheters connected between the lesions, if catheter lesions are found, we scan the long and short axis of the catheter to observe whether there is any inside the catheter expansion, echo, and presence or absence of solid nodules; if there are nodules, we observe the morphological boundary and the presence or absence of blood flow; for some solid tumors in the breast, the elastic image can be analyzed to understand its softness and hardness. The ultrasound classification of small breast cancer is divided into 5 types, as shown in Table 1.

We use SPSS 23.0 statistical analysis software. The features of breast cancer enhanced ultrasound imaging include enhancement level, enhancement method, filling defect, range change, and perforating vessels. The correlation analysis of tumor size, axillary lymph node metastasis, histopathological grade, immunohistochemical index ER, PR, HER-2, and Ki-67 expression was analyzed by Pearson's chi-square test and Fisher's exact probability method.

4. Automatic Segmentation Model of the Breast Lymph Node Cancer Metastasis Area

4.1. Image Preprocessing of the Metastatic Area of Breast Lymph Node Cancer. The digitized panoramic image is huge in size and has many white background areas. In order to reduce the calculation time, this article first preprocesses the panoramic image to remove non-histopathological areas to reduce the computational complexity of the digitized pathological image. Panoramic images are usually stored in a multiresolution pyramid structure, containing multiple downsampled samples of the original image, and the image with the largest resolution is called level 0, and the other versions from bottom to top are called level 1 and level 2; the image size of each level differs by approximately 2 times. In order to reduce the amount of calculation in the white unorganized area, this paper uses a multilevel mapping strategy based on the pyramid structure to exclude the unorganized area.

The focus of the pyramid structure multilevel mapping strategy lies in coordinate mapping. Through a specific threshold method, the coordinates of the tissue area are obtained under the low-resolution image, and then the coordinates are mapped to the high-resolution according to the pyramid structure. This paper chooses the image at the 7th level of the pyramid structure as the input image of the coordinate mapping and then obtains the coordinates of the tissue area under the low-resolution image through a specific image algorithm.

The flowchart of removing the background in low-resolution images is shown in Figure 2. First, the image is grayed out, and then two binary images are obtained using

RETRACTED

Table 1: Ultrasound classification of small breast cancer.

Type	Feature
Nodular type	Nodules with the largest diameter of the lesion ≦1 cm
Mass type	The maximum diameter of the lesion >1 cm, ≦2 cm; according to the boundary of the lesion, it can be divided into the following: Type I (clear boundary type): the boundary of the lesion is clear, but there is no obvious envelope; Type II (rough edge type): the edge of the lesion is blurred, showing small burr-like shape, partly with angle sign
Capsule type	The lesion was a mixed nodule with cysts and solids
Catheter type	The catheter is tortuous and dilated, and the lesions are distributed along the inner wall of the dilated catheter
Diffuse type	The lesion showed a hypoechoic area with unclear borders and no obvious nodular echo

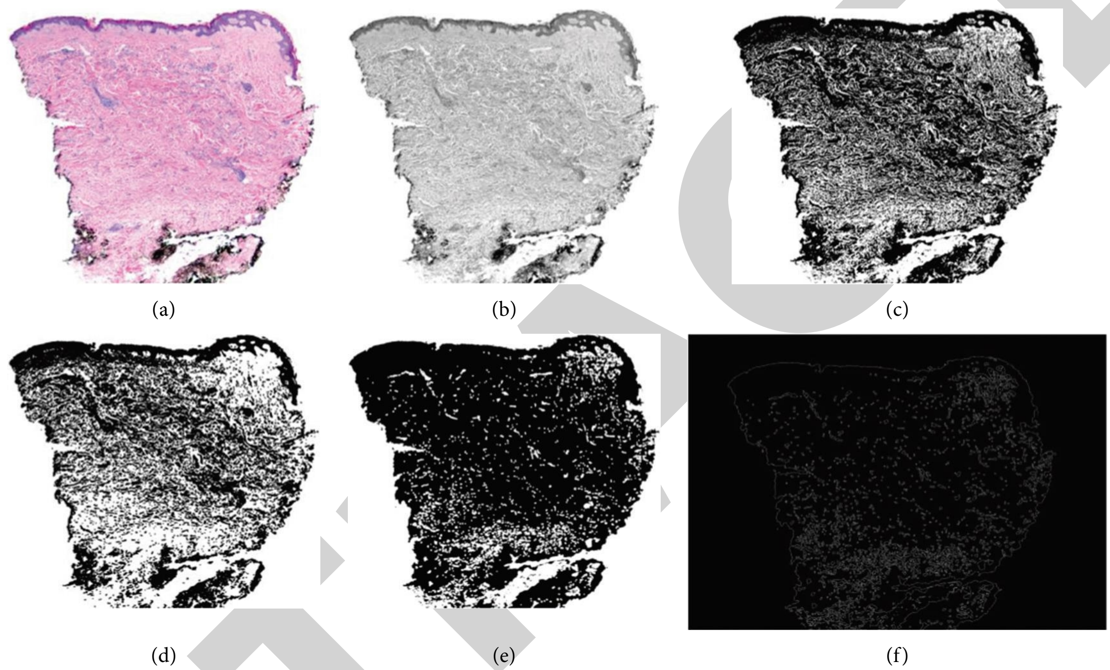

Figure 2: Image removal background flowchart. (a) Top view of the panoramic image. (b) Grayscale. (c) Binary image after special threshold processing. (d) Binary image with closed operation. (e) Binary image with open operation. (f) The nonblack area is the tissue area that needs to be calculated.

the maximum difference between classes method, and then the two binary images are merged according to the AND operation, and the white area obtained is the region of interest containing the tissue area. In this paper, we use a closed operation with a disc structure of 3×3 pixels to reduce the omission of the tissue area, and an open operation with a disc structure of 8×8 pixels to remove small impurity areas, and the final result is an image focusing only on the organized area.

In the pyramid structure of the panoramic image, one pixel at level 4 resolution is equivalent to an image block with a size of 256×256 pixels under level 0 resolution image. Therefore, when the pixels at the level 4 resolution only slide in the organized area, the sliding window with the size of 256×256 pixels at the corresponding position under the level 0 resolution image also slides only in the organized area, as shown in Figure 3.

We establish the image grayscale histogram and normalize the grayscale histogram. Suppose the original gray level N, the number of pixels with gray level i is n_i, and calculate the probability of the appearance of pixels with gray level p_i:

$$p_i = \frac{n_i}{\left|\prod_{i=1}^{L} n_{i-1}\right|}. \quad (1)$$

Assuming that A represents the background (gray level is $0 \sim N$) and B represents the target, for the two types of pixels A and B, the probability of each category is

$$P_A = \prod_{i=1}^{t+1} \left(P_i \cdot P_{i+1}\right),$$
$$P_B = \prod_{i=t+2}^{L} \left(P_i \cdot P_{i+1} \cdot P_{i+2}\right). \quad (2)$$

Finally, we calculate the between-class variance of the two regions, A and B:

RETRACTED

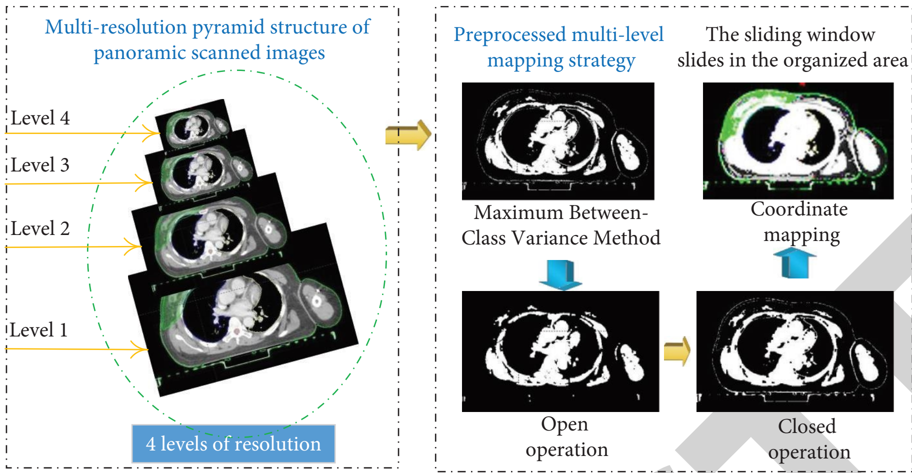

FIGURE 3: Panoramic scan image structure and multilevel mapping strategy.

$$\begin{aligned} w_A &= \prod_{i=1}^{t+1} (iP_A P), \\ w_B &= \prod_{i=1}^{L} (iP_B P_{i+1}), \\ w_0 &= \prod_{i=1}^{L} i(p_A w_A - p_B w_B), \\ \sigma^2 &= 0.5p_A (w_0 - w_A)^2 - 0.5p_B (w_0 - w_B)^2. \end{aligned} \quad (3)$$

Among them, w_A and w_B are the average gray values of the A and B regions, respectively; w_0 is the global gray average of the gray image; and σ^2 is the between-class variance of the A and B regions. The algorithm calculates the optimal threshold to maximize the distinction between the tissue area and the white background area in the pathological image.

4.2. Deep Learning Model Based on the Sliding Window. The construction of training set is the key to network training. This paper first randomly extracts hundreds of thousands of image blocks with a sliding window of 256×256 pixels. If the center of these blocks is within the cancer metastasis area marked by the pathologist, they are positive blocks and marked as 0; otherwise, they are negative blocks. As the AlexNet model converges quickly during training, this article chooses to use AlexNet as the initial network and further extracts the training set based on the initial prediction results. First, an initial binary classification model is trained based on AlexNet and applied to the prediction of the panoramic image of the training sample, so as to obtain an initial segmentation probability map about cancer metastasis.

We extract a large number of image blocks of false positive and false negative regions and recombine them to obtain millions of positive and negative image blocks. Due to the imbalance in the number of samples of positive and negative blocks and the high probability of false positives, this paper reclassifies the negative blocks in the training set to expand the difference between classes and facilitate the model to better identify positive and negative. It is finally classified into 5 categories. Except for the positive category, the other 4 categories are all negative categories, and are marked as negative category 1, category 2, and category 3 according to the characteristics of the block such as more blanks, more cells, and normal black. For negative blocks that are very similar to positives, they are marked as category 4, which is called similar positive category. In addition, in order to reduce the workload of manually selecting data, this article uses a special training strategy to select data and train the model. Considering the calculation cost and calculation time, this article does not use Inception, ResNet, DenseNet, and other networks, but uses VGG-16 with moderate parameters and calculation time as the final five-class network. In order to improve the robustness of the model, in addition to data enhancement such as rotation and mirroring of image blocks, this paper also adds a data enhancement method for H&E dye transformation, which can imitate the color change caused by the proportion of H&E dye reagent. The calculation steps are as follows:

First, we convert the extracted image block from color (RGB) space to optical density (OD) space:

$$\mathrm{OD} = -2 \log_{10} (0.12I). \quad (4)$$

Then, we delete the OD sensitivity of less than 0.12 and create a plane by performing singular-value decomposition on the processed OD value and taking the eigenvectors corresponding to the two largest eigenvalues:

$$\mathrm{OD} \rightleftarrows VS \longrightarrow V^{-1}|\mathrm{OD}|, \quad (5)$$

where I is the color space of the image; OD is the optical density space; and V and S are the corresponding coloring vectors.

5. Results and Analysis

5.1. Pathologically Confirmed Ultrasound Findings of Primary Breast Lesions. Sixty-nine patients underwent breast ultrasound examination, of which 60 underwent radical

RETRACTED

mastectomy and 9 underwent breast-conserving surgery. Pathological examination results showed that 56 cases were breast cancer, and 13 cases were not found to be cancerous. Among the 60 patients who underwent radical mastectomy, 59 underwent radical mastectomy for axillary masses on the ipsilateral side, and 1 case underwent contralateral radical mastectomy for axillary masses on the opposite side of the breast due to MRI findings. Among 56 patients with breast cancer confirmed pathologically, 15 patients (26.8%) had breast cancer lesions detected by ultrasound examination of the breast, of which 10 patients (66.7%) showed hypoechoic masses, and 2 patients (13.3%) showed breast cancers. There were many hypoechoic areas along the catheter, 2 cases (13.3%) showed hypoechoic areas along the catheter, and 1 case (6.7%) had catheter dilation with intra-catheter calcification. The diameter of the mass was 0.5 cm~1.7 cm; 8 cases showed irregular shape, 2 cases were round or oval, 9 cases had unclear borders, and 1 case had clear borders. The blood flow in 6 cases was not abundant, the blood flow in 3 cases was rich, and the blood flow in 1 case was marginal; 5 cases had no rear acoustic shadow, 4 cases had increased rear echo, and 1 case had increased rear echo.

41 cases of primary breast cancer were not detected by ultrasound, of which 39 cases were detected by breast MRI, 23 cases were nonlumps, and 16 cases were tumors, as shown in Figure 4. The diameter of the mass was 0.67 cm~1.56 cm; 10 cases showed irregular shape, 6 cases were oval or round, with irregular edges; after multiphase dynamic enhancement, the inside of the lesion showed uneven enhancement in 12 cases and uniform enhancement in 3 cases. The enhancement distribution of nonmass lesions included 10 cases of linear enhancement, 7 cases of segmental enhancement, 5 cases of focal enhancement, and 1 case of multiple regional enhancement; 16 cases of uneven enhancement, 4 cases of uniform enhancement. There were 3 cases of ring enhancement; 13 cases of type I (increasing type) TIC, 5 cases of type II (platform type), and 5 cases of type III (outflow type).

Among 39 patients, 19 cases underwent MRI-guided "second-eye" ultrasound examination, 10 cases (52.6%) showed hypoechoic masses, and 5 cases (26.3%) showed localized hypoechoic areas. It showed that there were multiple hypoechoic areas distributed along the catheter, and 1 case (5.3%) showed that the catheter was dilated and the interior was hypoechoic. The diameter of the mass was 0.6 cm~2.0 cm, with an average of (1.1 ± 0.4) cm; the masses were all irregular, with unclear borders; 5 cases of masses had inadequate blood flow; and 3 cases of masses had abundant blood flow. There were 2 cases of mass marginal blood flow; 7 cases had no posterior acoustic shadow; 2 cases had posterior acoustic shadow and 1 case had posterior echo enhancement; 2 cases had hypoechoic masses with calcification; and 1 case had ductal dilation. 5 cases of primary breast cancer showed a localized hypoechoic area. The tumors with this appearance did not have a three-dimensional space-occupying effect. Corresponding to their MRI findings, 3 cases showed focal enhancement and 2 cases showed linear enhancement. Three cases of primary breast cancer showed multiple hypoechoic areas along the duct. Corresponding to their MRI findings, 2 cases showed segmental enhancement and 1 case showed linear enhancement.

Among the 60 patients with breast cancer confirmed pathologically, 58 patients had primary breast cancers detected by MRI. The analysis of FGT of 58 cases of breast showed that 36 cases of breast fibroadenoid tissues were unevenly distributed, 16 cases were scattered fibroadenous tissues of breast, and 4 cases were extremely dense. At the same time, after multiphase dynamic enhancement, the mammary fibroglandular background showed slight enhancement in 45 cases, mild enhancement in 11 cases, and moderate enhancement in 2 cases.

The 58 cases of cancer foci detected by MRI included 38 cases of nonmass lesions and 20 cases of mass lesions. The diameter of the mass was 0.7 cm~1.7 cm; 12 cases showed irregular shape, 8 cases were oval or round, with irregular edges; after multiphase dynamic enhancement, the inside of the lesion showed uneven enhancement in 13 cases and uniform enhancement in 4 cases. The distribution of enhancement of nonmass lesions includes 14 cases of linear enhancement, 13 cases of segmental enhancement, 9 cases of focal enhancement, and 2 cases of multiple regional enhancement; there are 25 cases of uneven enhancement, 8 cases of uniform enhancement, and clusters within the lesion. There were 4 cases of shape enhancement and 1 case of clustered small ring enhancement; 16 cases of TIC were type III (outflow type), 15 cases were type I (increasing type), and 7 cases were type II. The MRI appearance of the primary breast lesion is shown in Figure 5.

Two cases of primary cancer in the breast were not detected by MRI. One patient was diagnosed with a left axillary mass as the first patient and underwent radical mastectomy on the left side. DCIS components were found outside the left breast through whole breast specimens and were found in the left breast. Retrospective analysis of the MRI image of this patient showed that the fibroglandular tissues of the affected breast showed uneven distribution. After dynamic enhancement, the fibroglandular background showed moderate enhancement, and there were many spots distributed along the ducts. Another patient was first diagnosed with a left axillary mass and underwent radical mastectomy on the left side. A nonspecial invasive carcinoma with a maximum diameter of 2 mm was found on the upper left side of the left breast through the whole breast. A retrospective analysis of the patient's MRI image showed that the fibroglandular tissues of the affected breast showed uneven distribution. After dynamic enhancement, the fibroglandular background showed moderate enhancement, with multiple patches and enhancements along the duct.

5.2. X-Ray Findings of Primary Breast Lesions Confirmed by Pathology. Sixty-one patients underwent mammography, of which 53 underwent radical mastectomy and 8 underwent breast-conserving surgery. Pathological examination results showed that 51 cases were breast cancer, and 10 cases were not found to be cancerous. Of the 53 patients who underwent radical mastectomy, 51 underwent radical mastectomy

RETRACTED

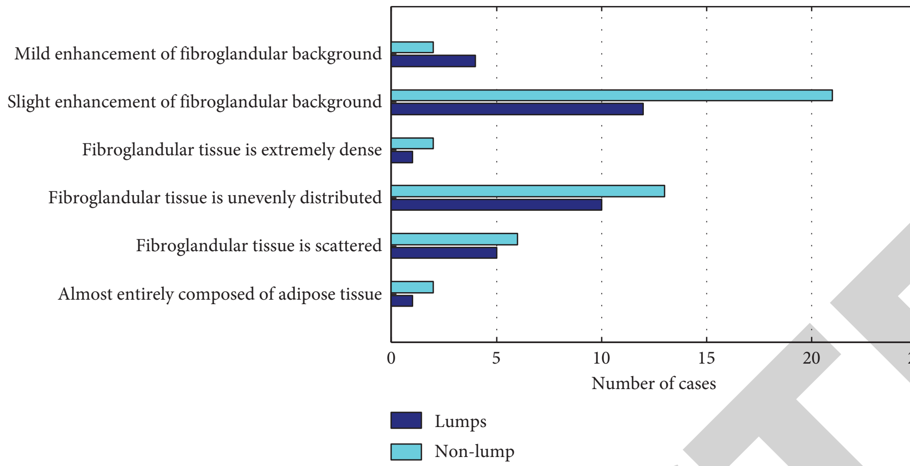

Figure 4: MRI appearance of breast cancer not detected by breast ultrasound. MRI findings of primary breast lesions confirmed by pathology.

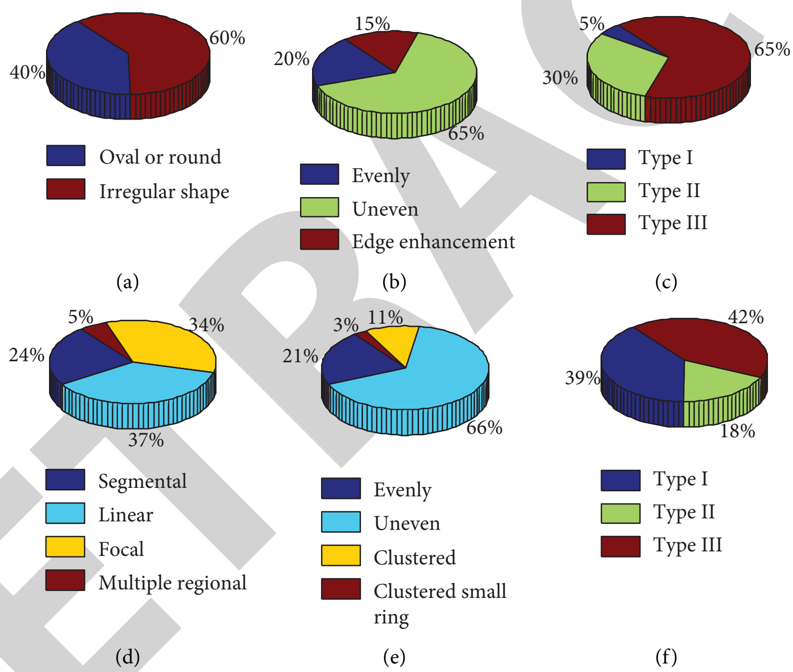

Figure 5: MRI appearances of primary breast lesions. (a) Mass morphology. (b) Internal enhancement characteristics of the tumor. (c) Tumor time-signal intensity curve type. (d) Nonmass distribution. (e) Nonmass internal enhancement features. (f) Nonlump time-signal intensity curve type.

for axillary masses on the ipsilateral side, and 2 cases underwent contralateral radical mastectomy due to suspicious tumors in the contralateral breast of the axillary mass on MRI. Among 51 cases of breast cancer confirmed pathologically, 16 cases of breast cancer were detected by breast X examination. Analysis of the composition of the breast tissues of 16 patients showed that 9 cases of mammary glands were scattered with fibrous glands, and 7 cases of mammary glands were uneven and dense. The primary cancers in the breast detected by X-ray examination showed 8 cases of simple localized asymmetry and compactness, 5 cases of simple calcification, 1 case of simple mass (the mass was irregular, edge burr, and high density), and the mass was accompanied by calcification. From the morphology of calcification, 3 cases showed fine polymorphic calcification, 2 cases showed amorphous calcification, and from the distribution of calcification, 2 cases showed regional distribution, and 2 cases showed calcification. Cases were distributed in segments, and 1 case was distributed in clusters.

X-rays of primary cancers in 35 cases of breast cancer were not detected. Among them, 15 cases showed uneven and dense breasts, 12 cases showed scattered fibrous glands, 5 cases were almost all adipose tissue, and 3 cases were

RETRACTED

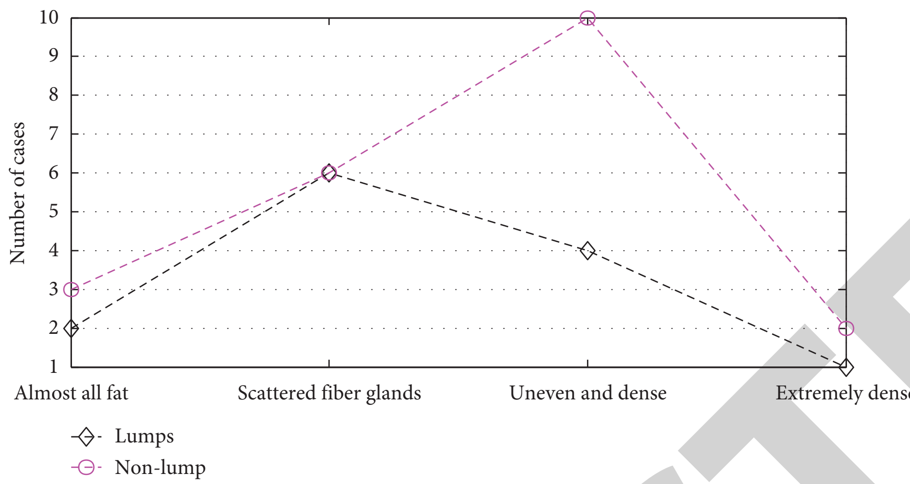

Figure 6: MRI findings of primary cancers in the breast that were not detected by mammography.

Table 2: MRI findings of breast cancers not detected by 18F-FDG PET-CT.

Breast tissue composition on MRI	Nonlumps	Lumps
Fibroglandular tissue is scattered	1	2
Slight enhancement of fibroglandular background	1	12
Almost entirely composed of adipose tissue	1	0
Moderate enhancement of fibroglandular background	0	1
Fibroglandular tissue is unevenly distributed	5	4

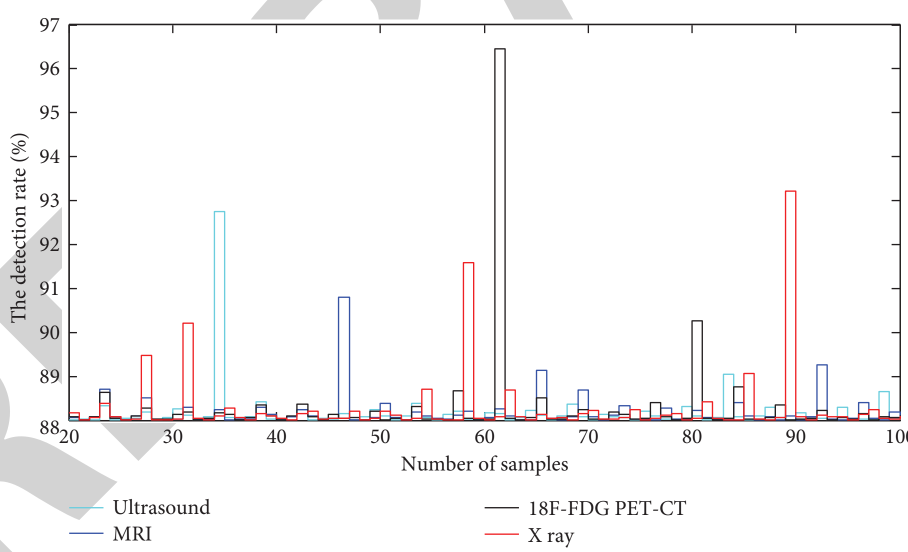

Figure 7: Detection rate of MRI, X-ray, ultrasound, and 18F-FDG PET-CT.

extremely dense. Among these 35 breast cancer patients, 33 cases were examined by breast MRI to detect primary cancers in the breast, of which 22 cases showed no masses and 11 cases showed masses. The diameter of the mass was 0.72 cm~1.61 cm; 8 cases showed irregular shape, 4 cases were oval or round, with irregular edges; after multiphase dynamic enhancement, the inside of the lesion showed uneven enhancement in 8 cases and uniform enhancement in 3 cases. There was 1 case with clusters of small ring enhancement; 7 cases of type II (platform type), 4 cases of type III (outflow type), and 1 case of type I (increasing type) TIC. The enhancement distribution of nonmass lesions included 8 cases of focal enhancement, 7 cases of linear enhancement, and 6 cases of segmental enhancement. There were 11 cases of type I (increasing type), 6 cases of type III (outflow type), and 4 cases of type II (platform type). The MRI findings of primary cancers in the breast that were not detected by mammography are shown in Figure 6.

REDACTED

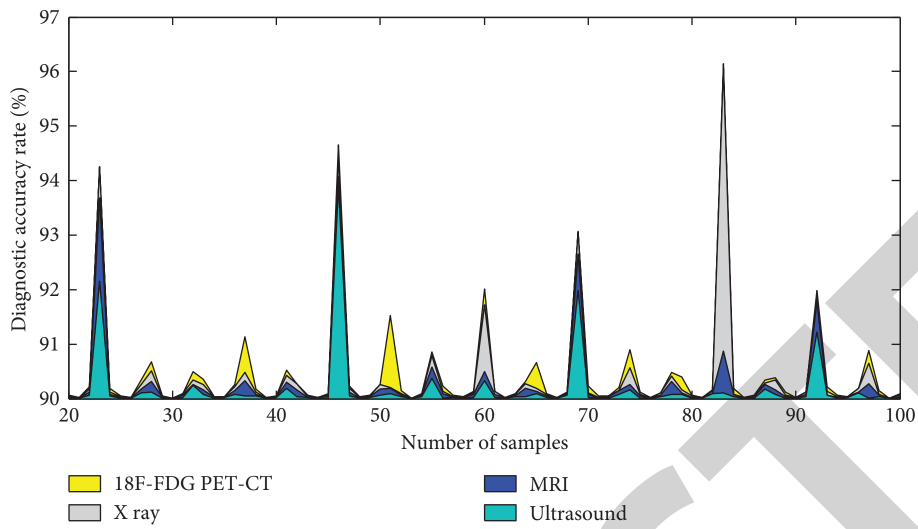

Figure 8: Diagnostic accuracy rate of MRI, X-ray, ultrasound, and 18F-FDG PET-CT.

5.3. 18F-FDG PET-CT Findings of Primary Breast Lesions Confirmed Pathologically. 22 patients underwent 18F-FDG PET-CT examination. 19 cases underwent radical mastectomy for axillary tumors on the ipsilateral side, and 3 cases underwent breast-conserving surgery. Pathological examination results showed that 19 cases were breast cancer, and 3 cases were not found to be cancerous. Among the 19 cases of breast cancer confirmed pathologically, 5 cases of breast cancer were detected by 18F-FDG PET-CT, all of which were mass lesions, and the diameter of the tumor was 1.1 cm~1.6 cm.

14 cases of primary breast cancer were not detected by 18F-FDG PET-CT, 13 cases of which were detected by breast MRI examination, including 8 cases of nonmass lesions and 5 cases of mass lesions. The diameter of 5 cases was 0.8 cm~1.2 cm, of which 3 cases were less than 1.0 cm. The enhancement distribution of nonmass lesions included 6 cases of linear enhancement, 1 case of segmental enhancement, and 1 case of focal enhancement. Table 2 shows the MRI findings of cancers in the breast that were not detected by 18F-FDG PET-CT. Mammography, ultrasound, MRI, and 18F-FDG PET-CT examinations for clinically palpable axillary lymph node metastases in patients with axillary lymph node metastases are shown in Figures 7 and 8, respectively.

6. Conclusion

The degree of lymph node metastasis is one of the important criteria for determining the pathological staging of breast cancer. Early detection and early diagnosis are the key to the treatment of breast cancer. In the image analysis module of the breast cancer lymph node metastasis staging system, the deep learning method is used to automatically locate and identify the cancer metastasis area in the panoramic image of the breast lymph node. And the accuracy of the model has reached a relatively high level, which can support the feature extraction and selection work. Of the 73 patients, 63 underwent radical mastectomy, 9 underwent breast-conserving surgery, and 1 underwent MRI-guided "second-eye" ultrasound-guided puncture. Pathologically confirmed 60 cases of breast cancer, including 41 cases of nonspecific invasive carcinoma, 9 cases of ductal carcinoma in situ, 2 cases of invasive micropapillary carcinoma, and 2 cases of invasive lobular carcinoma. There were 2 cases of microinvasive carcinoma, and 1 case of glycogen-rich clear cell carcinoma. No cancer was found in the specimens of 11 cases of radical breast surgery and 2 cases of breast-conserving surgery. The detection rate and diagnostic accuracy of breast MRI examinations for primary cancers in the breast are significantly higher than those of X-ray, ultrasound, and 18F-FDG PET-CT examinations. There is no difference in the detection rate and diagnostic accuracy of primary cancers. MRI examination of the breast should be used as a routine examination for patients with axillary lymph node metastasis as the first diagnosis. Primary breast cancer in patients with axillary lymph node metastasis as the first diagnosed patient often showed localized asymmetric compactness or calcification on X-ray; it often showed small focal mass lesions and ductal lesions without three-dimensional space-occupying effect on ultrasound. MRI often presents as small focal mass lesions and linear, segmental, or focal nonmassive lesions with enhanced distribution; 18F-FDG PET-CT often presents as a mass lesion with a diameter >1.0 cm.

Data Availability

The data used to support the findings of this study are available from the corresponding author upon request.

Conflicts of Interest

The authors declare that there are no conflicts of interest regarding the publication of this paper.

References

[1] D. O'Loughlin, M. O'Halloran, M. Glavin, E. Jones, M. Moloney, and M. A. Elahi, "Microwave breast imaging: clinical advances and remaining challenges," *IEEE Transactions on Biomedical Engineering*, vol. 65, no. 11, pp. 2580–2590, 2018.

RETRACTED

Hindawi
Journal of Healthcare Engineering
Volume 2023, Article ID 9871531, 1 page
https://doi.org/10.1155/2023/9871531

Retraction

Retracted: Intervention of WeChat Group Guidance in Rapid Rehabilitation after Gynecological Laparoscopic Surgery

Journal of Healthcare Engineering

Received 27 June 2023; Accepted 27 June 2023; Published 28 June 2023

Copyright © 2023 Journal of Healthcare Engineering. This is an open access article distributed under the Creative Commons Attribution License, which permits unrestricted use, distribution, and reproduction in any medium, provided the original work is properly cited.

This article has been retracted by Hindawi following an investigation undertaken by the publisher [1]. This investigation has uncovered evidence of one or more of the following indicators of systematic manipulation of the publication process:

(1) Discrepancies in scope
(2) Discrepancies in the description of the research reported
(3) Discrepancies between the availability of data and the research described
(4) Inappropriate citations
(5) Incoherent, meaningless and/or irrelevant content included in the article
(6) Peer-review manipulation

The presence of these indicators undermines our confidence in the integrity of the article's content and we cannot, therefore, vouch for its reliability. Please note that this notice is intended solely to alert readers that the content of this article is unreliable. We have not investigated whether authors were aware of or involved in the systematic manipulation of the publication process.

In addition, our investigation has also shown that one or more of the following human-subject reporting requirements has not been met in this article: ethical approval by an Institutional Review Board (IRB) committee or equivalent, patient/participant consent to participate, and/or agreement to publish patient/participant details (where relevant).

Wiley and Hindawi regrets that the usual quality checks did not identify these issues before publication and have since put additional measures in place to safeguard research integrity.

We wish to credit our own Research Integrity and Research Publishing teams and anonymous and named external researchers and research integrity experts for contributing to this investigation.

The corresponding author, as the representative of all authors, has been given the opportunity to register their agreement or disagreement to this retraction. We have kept a record of any response received.

References

[1] J. Wang, Y. Lin, Y. Wei et al., "Intervention of WeChat Group Guidance in Rapid Rehabilitation after Gynecological Laparoscopic Surgery," *Journal of Healthcare Engineering*, vol. 2021, Article ID 8914997, 11 pages, 2021.

Hindawi
Journal of Healthcare Engineering
Volume 2021, Article ID 8914997, 11 pages
https://doi.org/10.1155/2021/8914997

Research Article

Intervention of WeChat Group Guidance in Rapid Rehabilitation after Gynecological Laparoscopic Surgery

Jing Wang,[1] Yingying Lin,[2] Ying Wei,[1] Xiuying Chen,[1] Yuping Wang,[1] Longxin Zhang,[1] and Min Zhou[1]

[1]*Department of Anesthesiology, Fujian Maternity and Child Health Hospital, Affiliated Hospital of Fujian Medical University, Fuzhou 350001, China*
[2]*Department of Healthcare, Fujian Maternity and Child Health Hospital, Affiliated Hospital of Fujian Medical University, Fuzhou 350001, China*

Correspondence should be addressed to Min Zhou; zm405@fjmu.edu.cn

Received 23 August 2021; Revised 18 September 2021; Accepted 21 September 2021; Published 29 September 2021

Academic Editor: Gu Xiaoqing

Copyright © 2021 Jing Wang et al. This is an open access article distributed under the Creative Commons Attribution License, which permits unrestricted use, distribution, and reproduction in any medium, provided the original work is properly cited.

Gynecological laparoscopic surgery is the current routine treatment. Although the injury is relatively small, it is still a traumatic operation and also increases the recovery speed of patients. This paper mainly explores the intervention effect of rapid rehabilitation after gynecological laparoscopic surgery by means of WeChat group guidance based on the information adoption model and UTAUT model. Gynecological patients who underwent laparoscopic surgery and met the inclusion and exclusion conditions in a provincial maternal and child health hospital were selected as the research objects. The WeChat intervention group was compared with the nonintervention group, and the oral description score (VRS), comfort score (BCS), and 40-item recovery quality rating scale (QoR-40) were used as the scoring criteria. The results showed that the postoperative VRS and BCS scores in the WeChat intervention group were significantly lower than those in the nonintervention group. The total score of QoR-40 in both groups decreased compared with that before operation, reached the lowest on the first day after operation, and began to rise from the second day. This result is consistent with the patient's postoperative recovery process. After operation, the total score of the WeChat intervention group on days 1 and 2 was higher than that of the non-WeChat intervention group. By comparing the results of the patient's postoperative oral description score (VRS), comfort score (BCS), 40-item recovery quality score scale (QoR-40), etc., it can be shown that the overall recovery quality of the WeChat intervention group was better during these two days. In each section, the oral description score (VRS) and the 40-item recovery quality score scale (QoR-40) indicated that the pain sensation and emotional state scores of patients in the WeChat intervention group were higher than those in the nonintervention group, while the comfort score (BCS) was lower, indicating better comfort in the WeChat intervention group.

RETRACTED

1. Introduction

With the continuous improvement of medical level, the gradual maturity of laparoscopic technology, and the improvement of mutual learning and communication platform, gynecological laparoscopic surgery is more and more widely used in clinic. Laparoscopic surgery is a newly developed minimally invasive method and an inevitable trend in the development of surgical methods in the future [1]. With the rapid development of industrial manufacturing technology, the integration of related disciplines has laid a firm foundation for the development of new technologies and methods. Coupled with the increasingly skilled operation of doctors, many open operations in the past have been replaced by endovascular surgery, greatly increasing the opportunity of operation selection [2]. The traditional method of laparoscopic surgery is to make three 1 cm small incisions at the patient's waist and insert a pipe like working channel called "trocar" respectively. All operations in the future are carried out through these three pipes. Then the special lengthened surgical instrument is used to complete the same steps as open surgery under TV monitoring to achieve the same surgical effect [3].

Laparoscopy is an endoscope used for intraperitoneal examination and treatment. In fact, it is essentially a fiber light source endoscope, including laparoscopy, energy system, light source system, perfusion system, and imaging system. When applied to surgical patients without pain, it can directly and clearly observe the intraperitoneal situation of patients, understand the pathogenic factors, and perform surgical treatment for abnormal conditions at the same time [4]. Laparoscopic surgery is also known as “keyhole” surgery. Using the laparoscopic system technology, the doctor only needs to open several “key holes” around the surgical site of the patient. Without laparotomy, the doctor can visualize the patient’s internal situation in front of the computer screen and perform accurate surgical operation. The operation process takes only a short time, and the treatment technology has reached the international advanced level. The new type of laparoscopic surgery is an operation completed by modern high-tech medical technology with the principle of electronic, optical, and other advanced equipment. It is a cross era progress of traditional laparotomy [5]. It is an operation carried out in a closed abdominal cavity. Under good cold light source illumination, the camera system captures the organs in the abdominal cavity on the monitoring screen through the laparoscopic body connected to the abdominal cavity. Under the monitoring and guidance of high-tech display screen, surgeons operate surgical instruments outside the abdominal cavity for exploration, electrocoagulation, hemostasis, tissue separation, incision, and suturing the diseased tissue [6]. Traditional laparotomy is difficult to operate, with large wound and easy infection. Patients are prone to complications and slow recovery. The new type of laparoscopic surgery is a model of the application of high-tech technologies such as electronics, optics, and photography in clinical surgery [7]. It has the characteristics of less trauma, less complications, safety, and rapid recovery. In recent years, surgical endoscopic surgery has developed rapidly, which can be examined and treated at the same time. It is the most advanced and cutting-edge minimally invasive technology at present.

The concept of rapid postoperative rehabilitation (ERAS) was first proposed by Professor Henrik Kehlet of the University of Copenhagen, Denmark. Its core is to follow the evidence of evidence-based medicine, break the traditional concept, and optimize the clinical treatment and nursing mode during the whole operation period without increasing the readmission rate and reoperation rate [8, 9]. By reducing the traumatic stress response caused by surgery to the human body, this reduces a series of complications that may occur during the whole operation period and finally achieves the purpose of shortening the hospital stay, saving the cost of medical resources, and accelerating the postoperative rehabilitation of patients [10]. After more than 20 years of development, popularization, and application, ERAS concept is more and more widely used in many surgical fields. Its feedback effect is positive, and the results are obvious to all. After ten years of development and application, ERAS has gradually been widely recognized in relevant fields and has formed a series of expert consensuses accepted by most people [11]. However, the concept of ERAS has not been paid enough attention in the field of gynecology, and the available relevant research reports are relatively rare [12]. Since 2014, the application research of ERAS concept in the field of gynecology has gradually increased, involving various surgical methods such as gynecological benign and malignant tumor surgery and uterine prolapse surgery. The application of this concept in the field of gynecology has cross era significance. It shows that people pay more and more attention to gynecological diseases. It also means that we begin to pay more attention to the postoperative recovery effect for the treatment of gynecological diseases, and the postoperative treatment methods of gynecological diseases are more diversified. Nelson et al. summarized and statistically analyzed the literature on the application of ERAS concept in all types of gynecological surgery and ERAS guidelines for abdominal surgery in other disciplines and published a number of guidelines on the use of ERAS concept in the whole operation period in the operation of gynecological benign diseases and gynecological malignant tumors in 2016. The purpose is to provide a unified and standardized standard for the application of ERAS concept in gynecological surgery [13]. ERAS concept guides the nursing mode of postoperative recovery of gynecological diseases, pays more attention to the role of human intervention in nursing, so as to reduce the occurrence of postoperative complications, and advocates standardizing the way of postoperative rapid recovery of gynecological diseases.

Information exchange refers to the communication between individuals with the help of their common symbolic communication system [14]. The “individual” here is generalized and can be an individual, group, or organization. In a broad sense, all activities and processes between information sources and information users belong to the category of “information exchange.” Information exchange is a social phenomenon that has existed since the existence of human society [15]. It is the basic link of information work. With the development of science, technology, and society, the carrier of information, the media, methods, and technology of information exchange are in constant development and change [16]. With the application of modern information technology in the network environment, there are new ways of information exchange, such as e-mail, microblog, WeChat, and so on. Network information exchange is a process in which cognitive subjects exchange and share information with each other by using network technology. Researchers at home and abroad have studied the information exchange behavior of social media from multiple theoretical perspectives, mainly including the network information exchange mode, the conceptual model of the general process of social information exchange, and the integrated technology acceptance theory [17]. This series of theories is suitable for the analysis of the influencing factors of the information exchange behavior of WeChat group users and effectively explains the information exchange behavior of WeChat group users. Chu believes that the application of Wiki is becoming more and more common in different virtual communication. In the research of Wiki, the

RETRACTED

RETRACTED

four elements affecting users' information behavior are community participation, community promotion, community trust, and community identity. Based on the perspective of social network, Liben Nowell studied the prediction of edges in the network and analyzed the structural evolution of the network. Kumar et al. studied the impact of different types of users on the growth environment of social networks [18]. Steinfield and others have studied different social resources in Facebook and found that young users can establish weak contacts outside the circle through their friends. Ellison and others found through the research on SNS website that it can promote users to establish a wider network, and the enthusiasm of users in the network can improve their user capital [19].

This topic aims to explore the intervention role in guiding the rapid rehabilitation after gynecological laparoscopic surgery by means of WeChat.

2. Relevant Theories

2.1. Unified Model of the First Mock Exam Technology Acceptance and Usage. The unified model of the first mock exam technology acceptance and use is developed by Venkatesh et al. The model is composed of eight different theories of technology acceptance and use: ① reasoning behavior theory; ② technology acceptance model; ③ motivation model; ④ planned behavior theory; ⑤ comprehensive theory of planned behavior and technology acceptance model; ⑥ PC utilization model; ⑦ diffusion of innovation theory; ⑧ social cognition theory. Venkatesh believes that the explanatory power of UTAUT model to users' adoption and prediction is as high as 70%, which is much higher than that of other models. According to UTAUT model, performance expectation, effort expectation, social impact, and promotion conditions are the main factors affecting user adoption [20], as shown in Figure 1.

2.2. Information Adoption Model. As for the research on information behavior, most scholars will study a specific link in information behavior, such as user information demand, user information search, and so on [21]. Wilson integrated the specific process of information behavior and proposed a systematic and complete information behavior model. The model completely demonstrated the overall framework from users' information acquisition needs to information utilization for the first time. Since then, most studies on information behavior will refer to this framework for related research [22]. Wilson combined stress coping theory with risk reward theory and social learning theory and proposed a general information behavior model based on the original framework. The new model still takes the user's information needs as the starting point [23]. The difference is that the new model adds five intermediary variables to explore users' information seeking driven by motivation mechanism from the psychological level, demographic level, social level, environmental level, and information source level. The types of information seeking are subdivided into passive attention, passive retrieval, active retrieval, and ongoing retrieval [24]. The model system clearly illustrates the whole process of user information adoption and is suitable for information adoption research. Therefore, this paper selects Wilson's information behavior model as the basic model of WeChat group user information adoption. The establishment of the model makes the adoption process of WeChat official account more clear and convenient for reference, which provides a basis for WeChat to promote the rehabilitation of gynecological laparoscopic surgery.

The specific model diagram is shown in Figure 2:

The specific process of WeChat group user information adoption is as follows: users select health information that meets their own needs by browsing the health information on WeChat group and combining the reliability of health information source and health information content [25]. The specific steps of the information adoption process of health WeChat group users mainly include generating the demand for health information, seeking health information, selection and evaluation of health information, absorption and utilization of health information, etc. Information adoption intention is the premise of information adoption, which will have an impact on the information adoption attitude and behavior of users' health WeChat groups [26]. Based on Wilson's general information behavior model and the characteristics of health WeChat groups, this study proposes the following adoption model, as shown in Figure 3.

Phase I is health information needs. In the trigger stage of information requirements, there are mainly two kinds of information requirements. The first is to clarify the information demand, that is, the unbalanced state formed by the gap between the user's own information state and the user's ideal information state. In order to make up for this unbalanced state, the user will put forward the demand for health information related to the demand. When the user's own health condition has problems, the user tends to know more about the condition. However, in practice, users do not understand it, so an unbalanced state is formed. In this way, when users' emotional cognition is unbalanced (such as the lack of psychological comfort to deal with diseases), they will also seek relevant information. The second is the user's own unconscious health demand, which is the potential health demand; that is, the user browses the health information formed by browsing the circle of friends or being attracted by some forwarded message titles and pictures in the process of reading WeChat group information and browses the health information for adoption. This unconscious health information demand is the potential health information demand. The second stage is health information seeking. Health information seeking includes three steps: information retrieval, information processing, and information integration. The process consists of three parts: information search, information confirmation, and information browsing. In this study, the platform selection section is specifically the health WeChat official account. The third stage is health information selection and evaluation. After searching for information, users will get a large amount of disordered health information. Users must sort out and refine disordered information, so as to quickly screen, identify, and

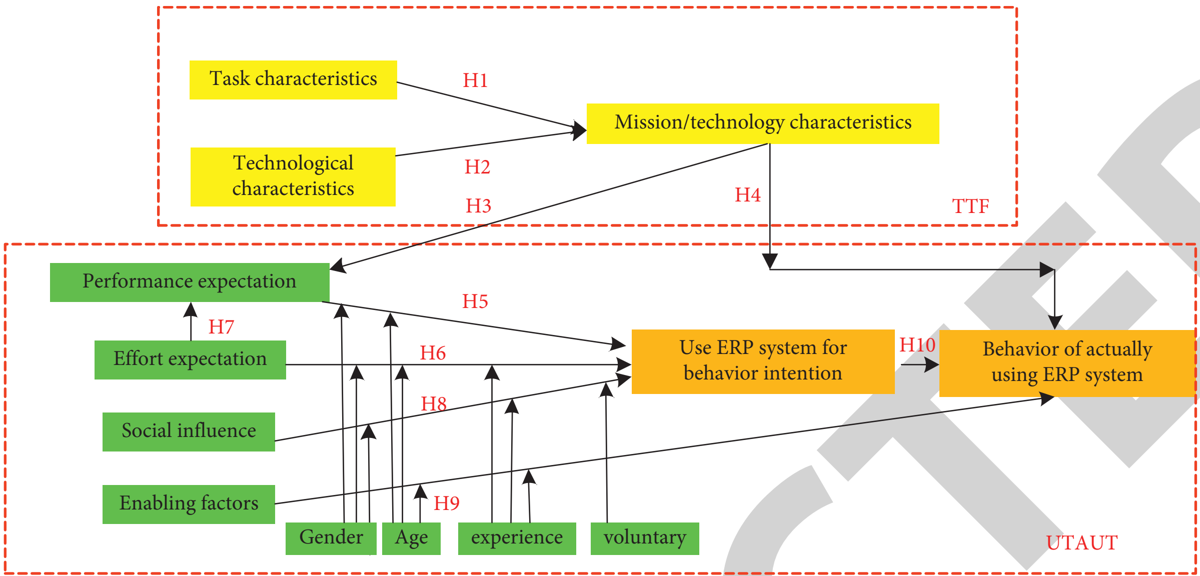

Figure 1: UTAUT model.

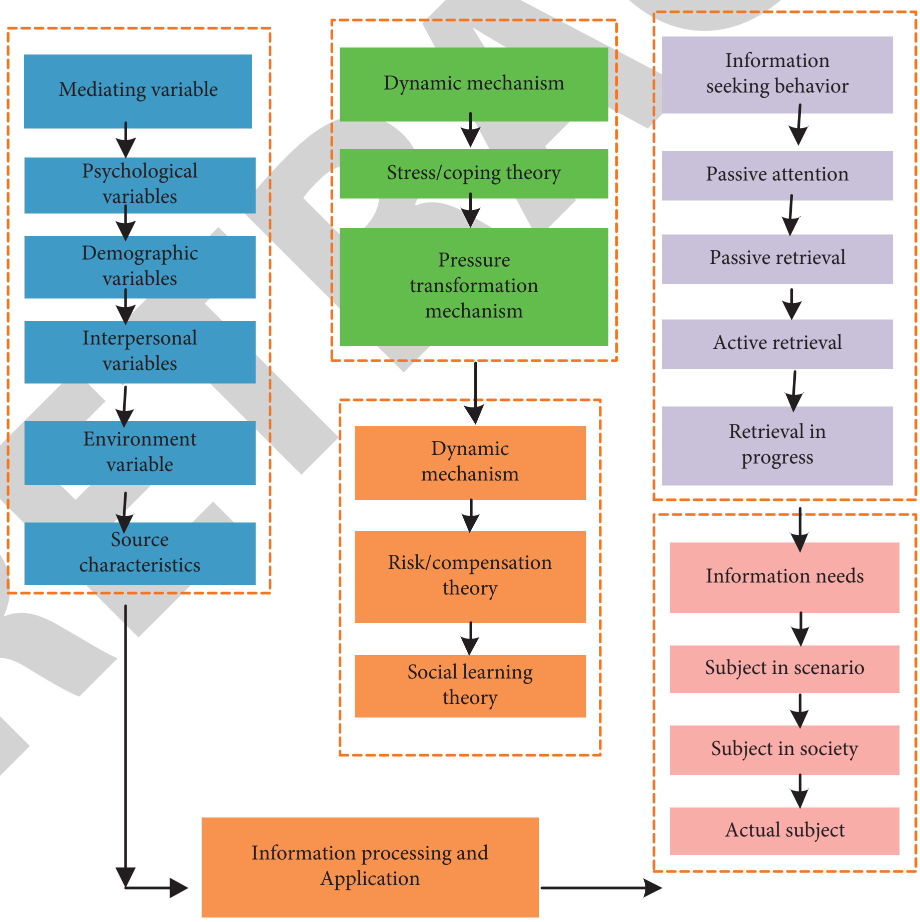

Figure 2: Wilson's information behavior model.

RETRACTED

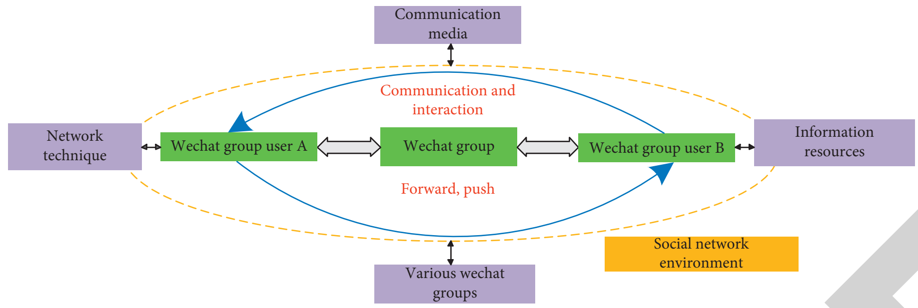

Figure 3: Information behavior model of the WeChat group.

delete the health information that does not meet the demand standards.

3. Materials and Methods

3.1. Source of the Research Object. The subjects were 250 gynecological patients who underwent laparoscopic surgery and met the inclusion and exclusion conditions in a provincial maternal and child health hospital.

3.1.1. Inclusion Criteria. ① Age is <65 years; ② the operative methods were laparoscopic ovarian cyst exfoliation, appendectomy, myomectomy, subtotal hysterectomy, and total hysterectomy; ③ general anesthesia was used; ④ there is no history of intestinal surgery; ⑤ there are no serious internal and surgical diseases; ⑥ there are voluntary collaborators.

3.1.2. Exclusion Criteria. ① Those who could not tolerate chewing gum or chewing gum less than 3 times after operation; ② changing the method of eating halfway; ③ intraoperative bleeding often leading to the decrease of Hb to 8/L or below.

3.1.3. Sample Size Estimation. Calculate the sample size and list the formula according to the experimental results.

$$m = \frac{\int_{i=1}^{k} T_i^2 \times \beta_{u1,u2}^2 \times (i-1)}{\sum_{i=1}^{k}\left(Y^2 - Y_i^2\right)}, \quad (1)$$

where m is the number of samples required by each group, K is the number of treatment groups, and Y and Y_i are the estimated values of the mean and standard deviation of the first i sample, respectively, which can be found in the table.

Due to the difficulty of manual calculation, the sample size of preexperimental results is estimated by using PASS (Power Analysis and Sample Size) software to calculate the sample size required for formal research.

3.2. Intervention Methods

3.2.1. Establishing the WeChat Follow-Up Team. The follow-up personnel are composed of medical staff of hemodialysis center, including 1 deputy chief physician, 1 head nurse, and 5 nurses in charge. All of them have college degree or above, more than 5 years of professional work experience, and good communication, coordination, and expression skills, are proficient in WeChat application, master the operation of various functions, and sign confidentiality agreement. Each of the five nurses in charge is responsible for the WeChat follow-up of 10~20 patients. After the interview with the patients, a WeChat group is established. In order to protect the privacy of the patients, all patients do not appear with their real names but are included in the group with their nicknames and numbers. The deputy chief physician and head nurse are responsible for formulating WeChat scheme and joining the established WeChat group for communication and feedback and quality supervision.

3.2.2. Establishing the Patient Follow-Up File. Before intervention, WeChat follow-up files were established according to the basic information filled in by patients, and each follow-up information and feedback were recorded in WeChat follow-up files. Team members regularly organized discussion and experience exchange and adjusted and improved WeChat follow-up guidance.

3.2.3. Communication Method. The WeChat group uniformly sends the edited content in the WeChat group, which is generally arranged from 19 : 30 to 20 : 30 in the evening, not during lunch break and night, so as not to disturb the patients. At the same time, it also makes a detailed analysis on the patient's illness and feedback problems and sends the required guidance according to the specific situation of each patient. The transmission frequency is 2~4 times a week for 1~3 months and 1~2 times a week for 4~6 months, lasting for 6 months. For patients who do not give WeChat feedback in time or show reluctance to participate, understand the reasons, give telephone supervision, and carry out targeted publicity and education, so that they can receive WeChat follow-up education. Pay attention to humanistic care during WeChat follow-up, send WeChat holiday greetings on holidays, remind or invite patients to review time, remind busy people of medication time, etc.

3.2.4. WeChat Follow-Up Content. According to the education level, acceptance ability, and knowledge of kidney diseases of all patients, teach patients the basic knowledge of

RETRACTED

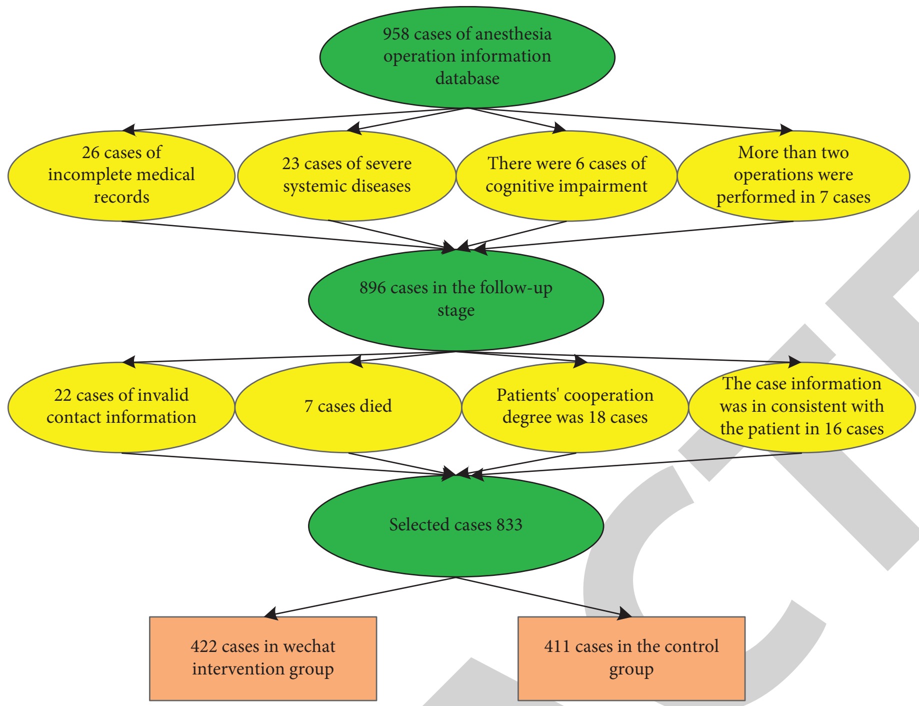

Figure 4: Case collection.

primary diseases, treatment methods, basic principles of hemodialysis, and various matters needing attention during dialysis. Eliminate patients' anxiety and fear caused by lack of disease knowledge, and carry out targeted psychological guidance according to the situation of patients, help patients establish confidence in treating diseases, and actively cooperate with medical staff in treatment and nursing. Reasonable diet has a great impact on whether to obtain good recovery effect. Therefore, patients must formulate a treatment diet plan in line with their condition and follow this plan in their daily life. In this process, patience is extremely important and should be practiced in person.

3.3. Observation Indicators

3.3.1. Verbal Rating Scales (VRS). It was used to measure the postoperative pain level of all patients. 1 point, painless; 2 points, mild pain, pain does not affect the patient's normal life and sleep; 3 points, moderate pain, pain can affect sleep; patients often require the use of painkillers; 4 points, severe pain, severe pain makes the patient's sleep seriously disturbed, and the autonomic nerve function is abnormal. It is often necessary to maintain a passive posture and take analgesic drugs.

3.3.2. Bruggemann Comfort Scale (BCS). It is used to evaluate postoperative patient comfort. 0 point, continuous pain in the wound; 1 point, quiet and painless, severe cough, or deep breathing pain; 2 points, lying flat, quiet, and painless, slight pain in cough or deep breathing; 3-minute deep breathing is also painless; 4 points, cough is also painless.

3.3.3. 40-Item Quality of Recovery Score (QoR-40). QoR-40 scale is an effective measurement tool, which is often used to measure the impact of clinical intervention on postoperative recovery. It has good authenticity, effectiveness, and reactivity. In this study, the scale was mainly used to investigate the early postoperative recovery quality of all patients. The specific methods were as follows: the QoR-40 scores of the two groups before operation and on the 1st, 2^{nd}, and 3rd day after operation were recorded through telephone return visit, and then they were simply sorted out and compared.

3.4. Statistical Analysis. Establish database with Excel, input patient data, and proofread by two people. The data were statistically processed by SPSS 21.0 software, and the mean and standard deviation were described by quantitative data. The comparison at different time points was analyzed by random block analysis of variance; SNK method was used for pairwise comparison at different time points. $P < 0.05$, the difference was considered to be statistically significant.

4. Result Analysis

4.1. Total Number of Cases Collected. A total of 958 patients underwent gynecological laparoscopic surgery. In this experiment, 833 cases were finally selected. Among the excluded cases, there were 16 cases with incomplete medical records or inconsistent information with the patients, 7 cases

RETRACTED

RETRACTED

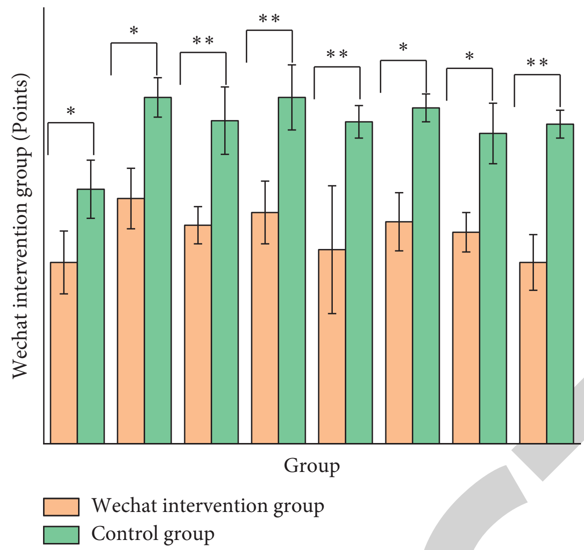

Figure 5: Comparison of VRS scores between different groups of patients.

with two or more operations in the same year, and 6 cases with cognitive impairment or mental diseases. 23 cases were complicated with serious systemic diseases, 22 cases were lost to follow-up, and 7 cases died due to invalid contact information or low patient cooperation and inaccurate index information memory. Among the selected patients, there were 422 cases in the WeChat intervention group (W) and 411 cases in the nonintervention group (D), as shown in Figure 4.

4.2. VRS Score after Operation. Compared with group W (WeChat Guidance Group), the VRS scores of group D (control group) after operation were significantly lower ($P < 0.05$). The specific results are shown in Figure 5.

According to the research results, the postoperative VRS scores of patients in WeChat intervention group were significantly lower than those in non-WeChat intervention group. It shows that there is a significant difference in the degree of pain between the two groups at different times after operation. The overall analgesic status of WeChat intervention group was better than that of nonintervention group.

4.3. Postoperative BCS Score. We also performed BCS scores on 8 groups of patients, and the results are shown in Figure 6. From the figure, we can see that the comfort score of WeChat intervention group is significantly higher than that of the control group. The results show that regular intervention through WeChat group can make patients feel warm, relieve postoperative pain, and accelerate postoperative rehabilitation.

4.4. QoR-40 Score

(1) There was significant difference in QoR-40 total score of W group at different time points ($P < 0.001$). The total score of QoR-40 in group D was also different at different time points, and the difference was statistically significant ($P < 0.001$). The total score of QoR-40 in both groups increased with the passage of time, as shown in Table 1 and Figure 7.

(2) The scores of pain feeling and emotional state in group W were higher than those in group D ($P < 0.05$), and the scores of physical comfort were lower than those in group D ($P < 0.05$). There was no significant difference in the scores of the other parts between the two groups ($P > 0.05$) (Figure 8).

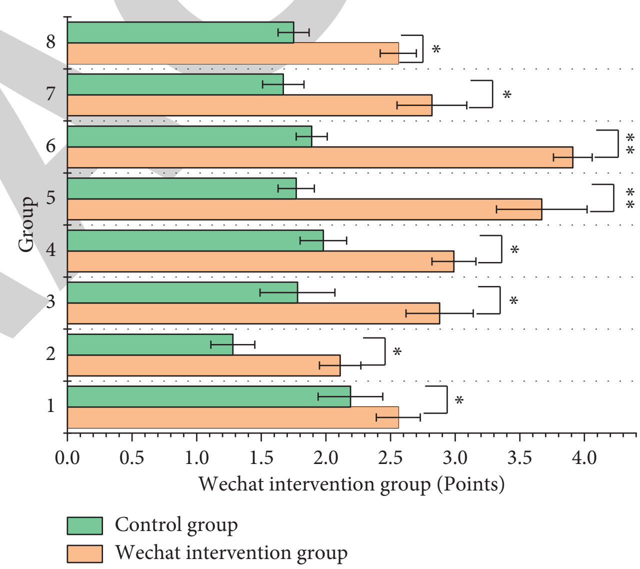

Figure 6: Comparison of BCS scores between different groups of patients.

In this study, we evaluated and compared the postoperative QoR-40 scores of the two groups and found that, in general, the total QoR-40 scores of the two groups increased over time. This result is consistent with the patient's postoperative recovery process. After operation, the total score of

Table 1: Total score of QoR-40.

Group		One month	Two months	Three months	Four months	*P*
First group	W1	176.25 ± 2.71	178.95 ± 4.71	181.33 ± 3.24	187.99 ± 4.23	0.0002
	D1	168.32 ± 5.23	171.29 ± 3.76	174.23 ± 2.87	177.99 ± 6.78	0.0004
Second group	W2	175.36 ± 2.68	179.99 ± 2.23	184.29 ± 5.13	188.49 ± 5.21	0.0008
	D2	165.27 ± 3.44	169.22 ± 4.58	172.44 ± 5.32	176.66 ± 4.18	0.0003
Third group	W3	176.87 ± 4.98	181.22 ± 3.45	188.23 ± 4.48	193.34 ± 5.44	0.0006
	D3	165.25 ± 2.87	168.35 ± 2.55	172.34 ± 3.87	174.22 ± 3.55	0.0009
Fourth group	W4	176.35 ± 3.23	182.55 ± 2355	186.32 ± 4.55	192.35 ± 6.24	0.0001
	D4	168.26 ± 5.68	172.26 ± 4.58	178.46 ± 4.63	182.36 ± 6.56	0.0002

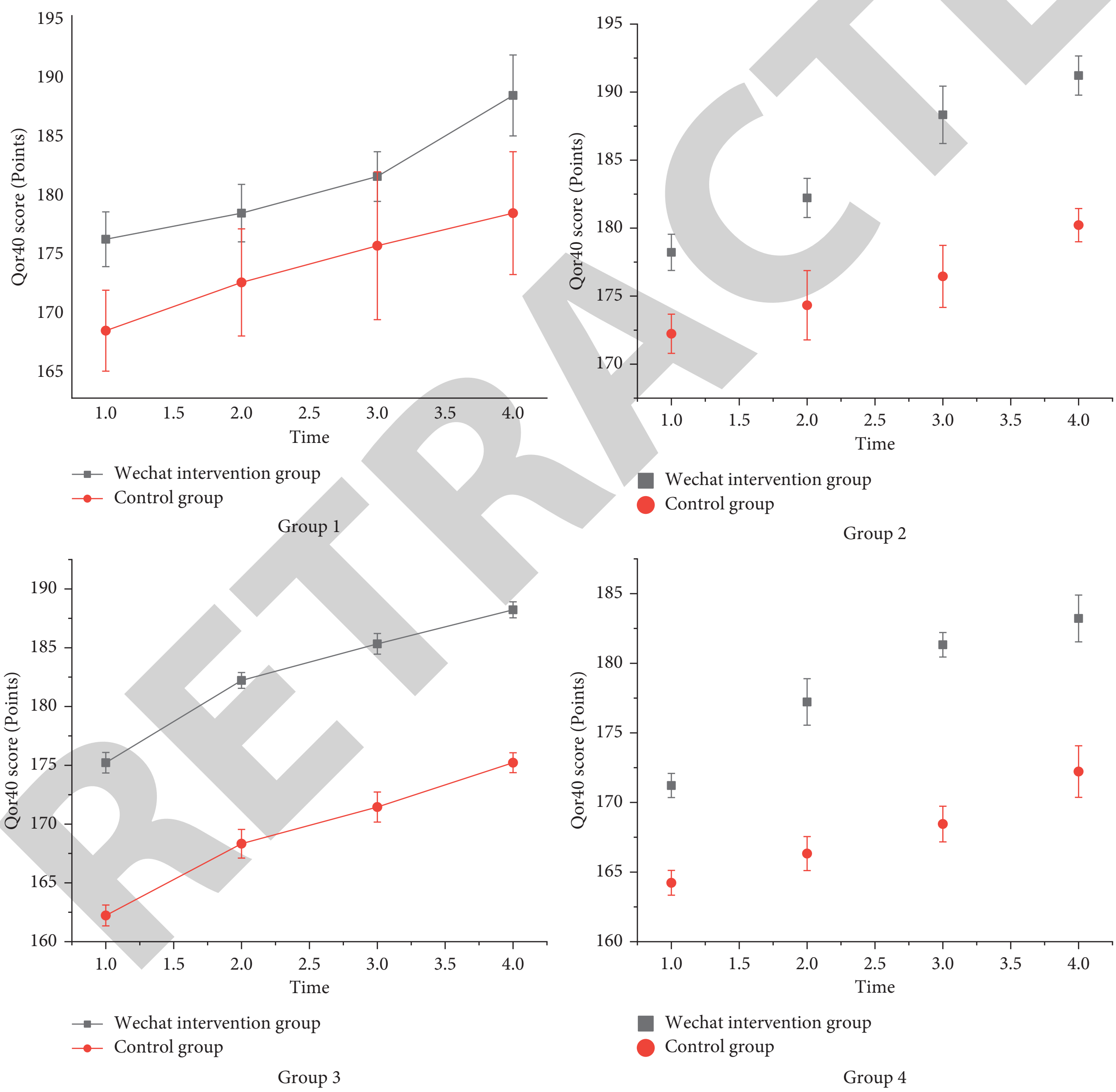

Figure 7: QoR-40 score trend of different groups.

WeChat intervention group was higher than that of non-WeChat intervention group. It shows that, in these two days, the overall recovery quality of patients in the WeChat intervention group is better. In each part of the score, the pain feeling and emotional state scores of patients in the WeChat intervention group were higher than those in the nonintervention group, while the physical comfort score was lower.

RETRACTED

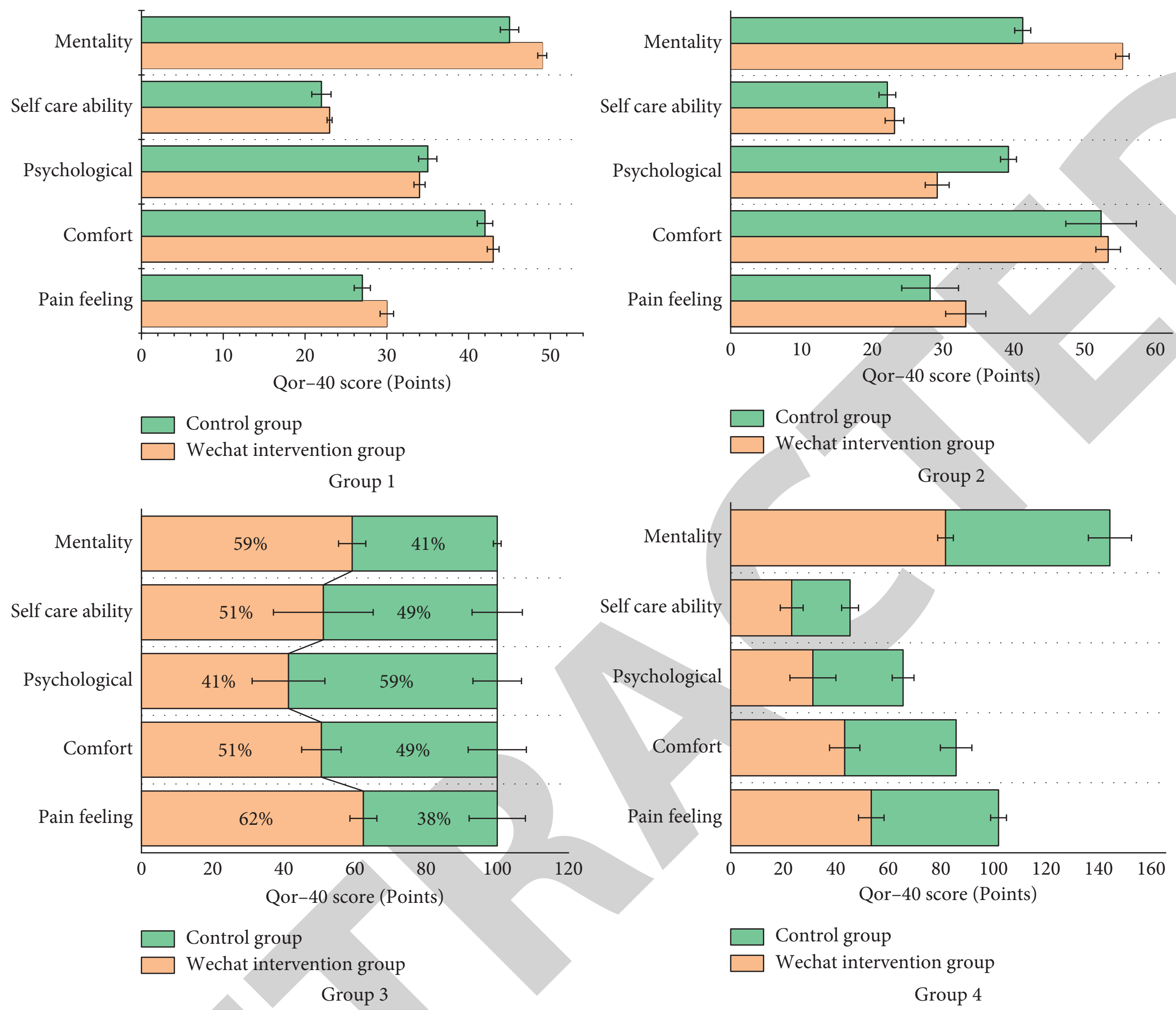

Figure 8: Postoperative QoR-40 scores.

RETRACTED

5. Conclusion

This study is combined with case analysis to study the intervention role of WeChat group in postoperative rehabilitation of gynecological laparoscopy. In the WeChat group, explain relevant health knowledge and methods to deal with relevant problems to patients, give explanations and psychological help in time, maintain the psychological mood of patients, make them optimistic about life, and improve the oral description score and comfort score of patients.

As a new thing in the field of information technology, WeChat has had a significant impact on the society. Because of its low tariff consumption, high compatibility, and rich information transmission modes, it is favored by more and more people. WeChat follow-up breaks the time and space constraints of medical services. Doctors, patients, and nurses can exchange relevant information through smart phones. The dissemination of information is more accurate, flexible, and personalized. Moreover, the data can be saved in WeChat and is not easy to lose, which meets the requirements of patients' repeated access and learning anytime and anywhere. WeChat intervention plays a certain role in improving the rapid recovery of diseases, and WeChat shows the convenience brought by modern network social tools in the experiment. Different from the traditional intervention methods, WeChat intervention can greatly reduce the cost, avoids the cost of printing leaflets in the past, and also has the advantages of greatly saving time and high attention. In the information age, we need to make full use of the convenience brought by high technology. WeChat has become the best way for people to transmit information. We should also make full use of the advantages of large number of WeChat users, instant sending and receiving messages, not limited by time and place, and saving material consumption, so as to make WeChat compatible with powerful learning functions under the entertainment function. At the same time, new forms of use can also promote the continuous updating of WeChat software and bring more convenient and efficient uses to people. As an intervention means, WeChat platform needs to be constantly updated and improved in its infancy. In the WeChat platform intervention, how to monitor the information sent, how to know whether it has viewed the information, and how to deal with the situation that some intervention objects quit the intervention because they are unwilling to accept the message in the intervention process need to be continuously updated and improved in future research, and better methods should be used to implement the intervention to achieve greater intervention effect.

Although the low WeChat tariff is one of the reasons for its popularity, it is also limited by the Internet in the surrounding environment and the aging of vision with the increase of patients' age. And the knowledge of health educators themselves must be richer and more professional and keep pace with the times, which puts forward new challenges and opportunities for medical workers. In view of the above factors, it is recommended to strengthen the professional management of WeChat follow-up, explore and improve better methods and ways of information arrangement and release, provide patients with higher quality continuous nursing, and effectively improve the quality of life of patients.

Data Availability

The data used to support the findings of this study are available from the corresponding author upon request.

Conflicts of Interest

The authors declare that there are no conflicts of interest.

Authors' Contributions

Jing Wang and Yingying Lin contributed equally to this work.

Acknowledgments

The work in this paper was supported by the Affiliated Hospital of Fujian Medical University.

References

[1] T. Wang, "Application effect of WeChat group in extended nursing of the patients with indwelling tube after urological surgery during the COVID-19 epidemic," *Advances in Clinical Medicine*, vol. 10, no. 12, pp. 3176–3180, 2020.

[2] L. Huang, G. An, S. You, S Huang, and J Li, "Application of an education model using the WeChat public platform in the standardized training of anesthesiology residents," *Annals of Palliative Medicine*, vol. 9, no. 4, pp. 1643–1647, 2020.

[3] Y. Xu, L. Xu, W. Zhao et al., "Effectiveness of a WeChat combined continuous flash glucose monitoring system on glycemic control in juvenile type 1 diabetes mellitus management: randomized controlled trial," diabetes, metabolic syndrome and obesity," *Targets and Therapy*, vol. 14, no. 23, pp. 1085–1094, 2020.

[4] X. Chen, D. H. Wu, Z. J. Xu et al., "The effect of WeChat platform in the optimization of emergency treatment for acute ischemic stroke," *Fudan University Journal of Medical Sciences*, vol. 46, no. 1, pp. 84–89, 2019.

[5] Y. Wu and M. Wall, "Prosumers in a digital multiverse: an investigation of how WeChat is affecting Chinese citizen journalism," *Global Media and China*, vol. 4, no. 1, pp. 36–51, 2019.

[6] G. Qi, W. Yi, Y. Huang et al., "The effectiveness of using a WeChat account to improve exclusive breastfeeding in Huzhu County Qinghai Province, China: protocol for a randomized control trial," *BMC Public Health*, vol. 19, no. 1, p. 1603, 2019.

[7] S. W. Phillippi, T. Luo, M. S. Li et al., "Urban and rural disparities in a WeChat-based smoking cessation intervention among Chinese smokers," *International Journal of Environmental Research and Public Health*, vol. 18, no. 13, p. 6731, 2021.

[8] X. Zhen, W. Xi, and L. Zheng, "One-stage posterior debridement and single-segment interbody fusion for treating mono-segmental lumbar and lumbosacral spinal tuberculosis in adults following minimum 5-year follow-up," *Journal of Orthopaedic Surgery and Research*, vol. 15, no. 1, p. 473, 2020.

[9] W. Miao, Z. Zhang, W. Lu et al., "Effect of glucose pretreatment on the effect of rapid rehabilitation surgery in patients undergoing hip replacement," *China Journal of Orthopaedics and Traumatology*, vol. 33, no. 8, pp. 730–735, 2021.

[10] M. S. Vetsheva, O. L. Podkorytova, V. O. Churakov et al., "Evolution of approaches in treatment of acute pain syndrome (review)," *Medical Alphabet*, vol. 4, no. 39, pp. 28–34, 2021.

[11] C. V. Beekum, B. Stoffels, M. V. Websky et al., "Implementierung eines Fast-Track-Programmes," *Chirurg, Der*, vol. 91, no. 2, pp. 143–149, 2021.

[12] N. Garmpis, D. Dimitroulis, A. Garmpi et al., "Enhanced recovery after surgery: is it time to change our strategy regarding laparoscopic colectomy?" *In Vivo*, vol. 33, no. 3, pp. 669–674, 2019.

[13] A. Tang and S. Zhou, "Analysis on the application value of goal-directed fluid therapy in patients undergoing laparoscopy-assisted radical gastrectomy with fast-track anesthesia," *American Journal of Tourism Research*, vol. 13, no. 5, pp. 5174–5182, 2021.

[14] O. Y. Ioffe, O. P. Stetsenko, T. V. Tarasiuk, and M. S. Kryvopustov, "Perioperative nutrition as an important aspect implementing Fast Track surgery principles," *One Health and Nutrition Problems of Ukraine*, vol. 51, no. 2, pp. 21–27, 2019.

[15] L. U. Romano, M. Rigoni, E. Torri et al., "A propensity score-matched analysis to assess the outcomes in pre- and post-fast-track hip and knee elective prosthesis patients," *Journal of Clinical Medicine*, vol. 10, no. 4, p. 741, 2021.

[16] B. Wang, "Therapeutic experience of laparoscopic operation for periappendiceal abscess during the epidemic period of novel coronavirus pneumonia: a case report," *Hans Journal of Surgery*, vol. 9, no. 4, pp. 81–85, 2020.

[17] A. To, B. N. Tanaka, C. A. Oyama et al., "fficacy and safety of low-molecular-weight heparin on prevention of venous thromboembolism after laparoscopic operation for gastrointestinal malignancy in Japanese patients: a multicenter, open-label, prospective, randomized controlled trial – ScienceDire," *Journal of the American College of Surgeons*, vol. 231, no. 5, pp. 501–509, 2020.

[18] X. Feng, J. S Cao, M. Y Chen et al., "Laparoscopic surgery for early gallbladder carcinoma: a systematic review and meta-analysis," *World Journal of Clinical Cases*, vol. 8, no. 6, pp. 1074–1086, 2020.

[19] Hideki, Sakisaka, Yoshiyuki et al., ""[Palliative laparoscopic operation for an extremely elderly patient with cecum cancer]," Gan to kagaku ryoho," *Cancer & chemotherapy*, vol. 46, no. 13, pp. 2158–2160, 2019.

RETRACTED

Hindawi
Journal of Healthcare Engineering
Volume 2021, Article ID 4102183, 11 pages
https://doi.org/10.1155/2021/4102183

Research Article

Estimation of Nuclear Medicine Exposure Measures Based on Intelligent Computer Processing

Junfeng Wang[1], **Fangxiao Wang**[1], **Yue Liu**[1], **Yuanfan Xu**[1], **Jiangtao Liang**[1] **and Ziming Su**[2]

[1]*Hangzhou Universal Medical Imaging Diagnostic Center, Hangzhou,, Zhejiang 31000, China*
[2]*Hangzhou Dianzi University, Hangzhou,, Zhejiang 31000, China*

Correspondence should be addressed to Fangxiao Wang; wfxiao1986@163.com and Ziming Su; 20081321@hdu.edu.cn

Received 11 August 2021; Revised 7 September 2021; Accepted 8 September 2021; Published 27 September 2021

Academic Editor: Kaijian Xia

Copyright © 2021 Junfeng Wang et al. This is an open access article distributed under the Creative Commons Attribution License, which permits unrestricted use, distribution, and reproduction in any medium, provided the original work is properly cited.

This paper provides an in-depth discussion and analysis of the estimation of nuclear medicine exposure measurements using computerized intelligent processing. The focus is on the study of energy extraction algorithms to obtain a high energy resolution with the lowest possible ADC sampling rate and thus reduce the amount of data. This paper focuses on the direct pulse peak extraction algorithm, polynomial curve fitting algorithm, double exponential function curve fitting algorithm, and pulse area calculation algorithm. The detector output waveforms are obtained with an oscilloscope, and the analysis module is designed in MATLAB. Based on these algorithms, the data obtained from six different lower sampling rates are analyzed and compared with the results of the high sampling rate direct pulse peak extraction algorithm and the pulse area calculation algorithm, respectively. The correctness of the compartment model was checked, and the results were found to be realistic and reliable, which can be used for the analysis of internal exposure data in radiation occupational health management, estimation of internal exposure dose for nuclear emergency groups, and estimation of accidental internal exposure dose. The results of the compartment model of the respiratory tract and the compartment model of the digestive tract can be used to calculate the distribution and retention patterns of radionuclides and their compounds in the body, which can be used to assess the damage of radionuclide internal contamination and guide the implementation of medical treatment.

1. Introduction

With the continuous development of nuclear technology, the exposure to ionizing radiation is gradually increasing, and the number of ionizing radiation practitioners is also increasing day by day. Ionizing radiation, also known as nuclear radiation, mainly includes X-rays, α-rays, β-rays, γ-rays, and neutrons. Rays are a high-speed movement of microparticle streams, the process of objects emitting such particle streams is radiation, which can make other atoms, and molecule ionized rays are called ionizing radiation, said to emit ionizing radiation objects for radioactive sources, with radioactive. The main sources of people's exposure to nuclear radiation can be divided into natural radiation and artificial radiation. The Earth is exposed to various types of naturally occurring ionizing radiation every moment; i.e., natural ionizing radiation, generally also known as natural background exposure, is by far the most important source of human exposure to ionizing radiation, with a relatively constant dose rate of irradiation [1]. In recent decades, human exposure to a variety of artificial radiation has been on the rise due to the increase in medical exposures, nuclear power, industrial applications, and the artificial manufacture and use of radionuclides such as nuclear weapons. Among them, the main ones are beta rays, X-rays, and gamma rays [2]. The most widely used in clinical nuclear medicine are single-photon emission computed tomography (SPECT) and positron emission tomography (PET) imaging, which mainly detects gamma rays emitted by radionuclides introduced into the human body and obtains in vivo images, with functional imaging as the main feature, mainly used for metabolic imaging, tumor diagnosis, etc. As our concept of elementary particles continues to change, our understanding of the fundamental forces of nature and the interactions between elementary particles is also evolving [3]. In the process of the gradual deepening of human understanding of the material world, experimental methods and tools have also been gradually improved [4].

While the emergence of clinical nuclear medicine brings great benefits to human health diagnosis and disease treatment, the use of radioisotopes will produce gaseous, liquid, or solid radioactive waste; on the other hand, it is difficult to discharge all radioactive drugs in the body of the patient receiving treatment in a short period. A data processing method that approximates or compares the functional relationship between the coordinates represented by discrete points with a continuous curve. Although the curve obtained by "fitting" cannot guarantee to pass all sample points, it can approximate the true value very well. Therefore, in the practice of clinical nuclear medicine treatment, not only the patients themselves but also the relevant staff and the public may be exposed to additional radiation, potentially posing a certain risk of radiation hazard [5]. For this reason, it is necessary to evaluate the exposure dose and risk assessment of patients and related workers. According to the report, the collective effective dose due to nuclear medicine has tripled in the last decade as the frequency of nuclear medicine diagnostic applications has increased. Reports indicate that nuclear medicine has become the second-largest source of medical exposure after CT scans. In recent years, the world has been developing a study on the trend of dose due to nuclear medicine, but in China, although the frequency of nuclear medicine equipment and treatment has increased significantly in recent years, no study on the collective dose due to nuclear medicine and its trend has been seen, which is not in line with the development of a large country in terms of population and nuclear medicine, so it is necessary to develop a study on the trend of collective dose due to nuclear medicine [6].

During nuclear medicine treatment, radiation exposure to organs or tissues in the patient's body is caused by the presence of radionuclides in the patient's body; therefore, the assessment of internal radiation dose to the patient can be used not only to evaluate the risk of radiation hazards but also to assess the therapeutic effect of certain specific organs or tissues. Internal radiation dosimetry involves not only physics but also radiopharmaceuticals, human-specific biological behavior, and human geometry, which makes the calculation complex and the accuracy of the results poor. Because it is difficult to make in vivo measurements on humans, its dose studies are more of estimation than measurement. There are mainly three different methods for dose estimation, which are the volume element S-value method, the dose point kernel method, and the Monte Carlo calculation method. The dose point kernel method first determines the dose point kernel and then convolutes the source to find the absorbed dose in the corresponding medium. The dose point kernel represents the distribution of the absorbed dose of an isotropic point source in an infinite homogeneous medium, which is essentially a matrix of the absorbed dose rate of a point source of a specific nuclide in a specific medium with the distance from the source, and its physical meaning is the absorbed dose rate at a distance r from the point source of unit activity. The formula for calculating the dose point nucleus is generally based on the experimental data fitting correction but also based on Monte Carlo simulation experimental data after correction. Depending on the particle source, it is divided into electron dose point kernel and photon dose point kernel. Comparing the double exponential function fitting of the original waveform and the original waveform fitting without the baseline part, the baseline information cannot be included in the fitting process if the fitting starts from the starting point of the pulse waveform. The dose point kernel method is suitable for the dose calculation of point sources with a nonuniform distribution of activity inhomogeneous media, and the energy range of particles is also required, so its application conditions limit its wide application. Combining the calculation of common external radiation dose rate calculation models and field experimental measurements, we establish the calculation model of external radiation levels for nuclear medicine treatment patients, combine the calculation model established in this study with the possible exposure scenarios of relevant surrounding personnel, project the exposure doses of relevant personnel, and propose specific methods or measures to strengthen the management of radiation protection in conjunction with the relevant regulations of radiation protection.

2. Related Work

Pyroelectric dosimeter under the action of radiation will produce charge accumulated in it; the number of accumulated charges can characterize the number of electron-hole pairs produced by radiation, that is, the absorbed dose [7]. Using general pyroelectric dosimeter after wearing a period, using a special readout instrument, by heating or irradiation with bright light, and recording the number of photons released, ideally, the number of photons released, and the number of charges accumulated in it, so the total absorbed dose received during this wearing time can be readout [8]. After reading out the dose, all the accumulated charges can be erased and reused [9]. Pyroelectric dosimeters are passive dosimeters (no power supply required) and are currently the most widely used materials based on LiF, which have a very low rate of decay of accumulated charges escaping over time, have an effective atomic number like that of human soft tissue, and have a lower overresponse to low-energy X- and γ-rays than materials with higher atomic numbers [10]. Chemiluminescent dosimeter has the advantages of small size, ease of use, and good tissue equivalence, but it can only record the dose received by personnel, the feedback period of up to several months, cannot indicate the dose accumulation in real time, and cannot promptly remind personnel of the dose being too high to change the work style to reduce the dose received by personnel [11]. Currently, a breakthrough has been made in nuclear radiation monitoring systems built on rapidly developing communication technologies [12]. There is a need to layout a lot of equipment and equipment maintenance personnel; the cost is still too high and is very vulnerable to the weather and geographical environment [13]. Therefore, we still cannot meet the needs of users of the nuclear radiation detection system [14]. Along with the development of wireless communication technology, in the acquisition of nuclear radiation data, environmental radiation detector, and gamma energy spectrometer in the introduction of wireless communication technology, compared to the use of wired communication system, to a certain extent to reduce the cost, but we still cannot overcome the many shortcomings of the nuclear radiation detection system [15].

At present, the commonly used equipment for nuclear medicine imaging diagnosis is γ camera, SPECT, and PET. SPECT is made by adding a tomographic reconstruction function based on the γ camera, so the quality control method of SPECT also includes the quality control method of the γ camera. The number of medical institutions carrying out interventional radiology treatment projects and the number of radiologists engaged in interventional radiology work is increasing year by year [16]. With the continuous expansion of the clinical application of interventional radiology and the complexity of the surgery, the characteristics of bedside close operation, long operation time, high irradiation dose, and protection difficulties of interventional radiologists are becoming increasingly prominent. The radiation protection of interventional radiology staff, especially the operators, has attracted widespread attention. Although interventional radiology has brought tremendous benefits to humankind, scientists have also begun to pay attention to the radiation protection issues that arise from it. Among medical diagnostic X-rays, patients and professionals receive the highest doses, not from CT scans or routine diagnostic X-rays but from radioactive interventional procedures [17]. In this case, the doses can be high enough to cause skin and eye crystal damage. The main causes of high doses are the duration of fluoroscopic exposure, the number of films taken, and the use of lower tube voltages in DSA. Radiation interventions can produce both deterministic damage and random radiation effects. Potentially high doses can cause deterministic effects such as erythema or temporary alopecia [18]. Dose issues are therefore not only a general protection issue for professionals and patients but also an integral part of the treatment plan for interventional techniques. Only a well-controlled radiation dose and good radiation protection of patients and professionals can lead to a significant development of interventional techniques. Therefore, as far as interventional technology itself is concerned, radiation dose control and radiation protection are already an important part of interventional technology, and radiation dose is an essential part of the interventional technology treatment planning system.

Theoretical calculations and experimental validation of the in vitro dose levels of these nuclides in the treatment process were carried out to establish a reasonable calculation model and parameters for the estimation of in vitro dose levels. In addition, the cumulative dose distribution in the rooms of patients treated for thyroid cancer during hospitalization was monitored, and finally, specific protection recommendations for patients and exposed personnel were proposed in the light of relevant radiation protection regulations.

3. Analytical Design of Nuclear Medicine Exposure Measure Estimation with Computer Intelligent Processing

3.1. Intelligent Processing Analysis of Radiometric Computers. In nuclear radiation measurements, processing of the electrical signals generated by and output from the detector is required, including amplification, shaping, screening, analog-to-digital conversion, and analysis of the electrical signals for recording. Front-end electronics are an important part of the detector data readout. However, there are too many summing points, and the longer time to calculate the pulse area may contain too much noise; both will lead to a low signal-to-noise ratio. And the appropriate number of summation points can also reduce the impact of tail accumulation events. According to the characteristics of the detector output signal forming method classification, the preamplifier can be divided into the current-sensitive preamplifier, voltage-sensitive preamplifier, and charge-sensitive preamplifier. The current-sensitive preamplifier is designed as a parallel feedback current amplifier by directly amplifying the current signal from the detector output. The output voltage or current is proportional to the input current [19]. An ideal current-sensitive preamplifier requires a very small input impedance, a very large output impedance, and a good time response and is usually used as a fast amplifier, but the relatively high noise level makes it mainly used in time measurement systems.

Preamplifiers are an important part of signal extraction in both conventional analog and digital energy spectrometry systems. The main challenge in detector electronics is to distinguish small signals from noise. In detector systems, noise is a random signal that is not caused by the physical process to be measured. If the noise only appears at the end of the electronic readout chain, the effect is minimal because the signal is amplified far more than the noise. However, if the noise has appeared in the front part, it may drown out the small signal from the detector output. There are many possible reasons for the appearance of noise, and the noise level can be effectively reduced by careful design of the measurement system, especially the front-end circuitry. The filter not only realizes the low-pass filtering function but also converts the signal from single-ended to differential. To effectively represent the input signal, the amplifier must recover from the load transient and stabilize before the end of the acquisition period. Based on the discussion of preamplifier types, the paper provides design considerations and experimental verification of the front-end circuitry for the strength of the output signal of a γ-ray energy measurement detector.

For the weak signal output from the γ-ray energy measurement detector, the front-end circuit usually uses a charge-sensitive preamplifier or a current-sensitive preamplifier. The weak signal is highly susceptible to interference from external environmental factors and can even be drowned out, and the sensitivity and measurement accuracy of the measurement circuit of the weak signal will be affected to a large extent. The sensitivity of the circuit depends on the size of the feedback resistance, so to measure smaller signals, we need to increase the feedback resistance, as shown in Figure 1.

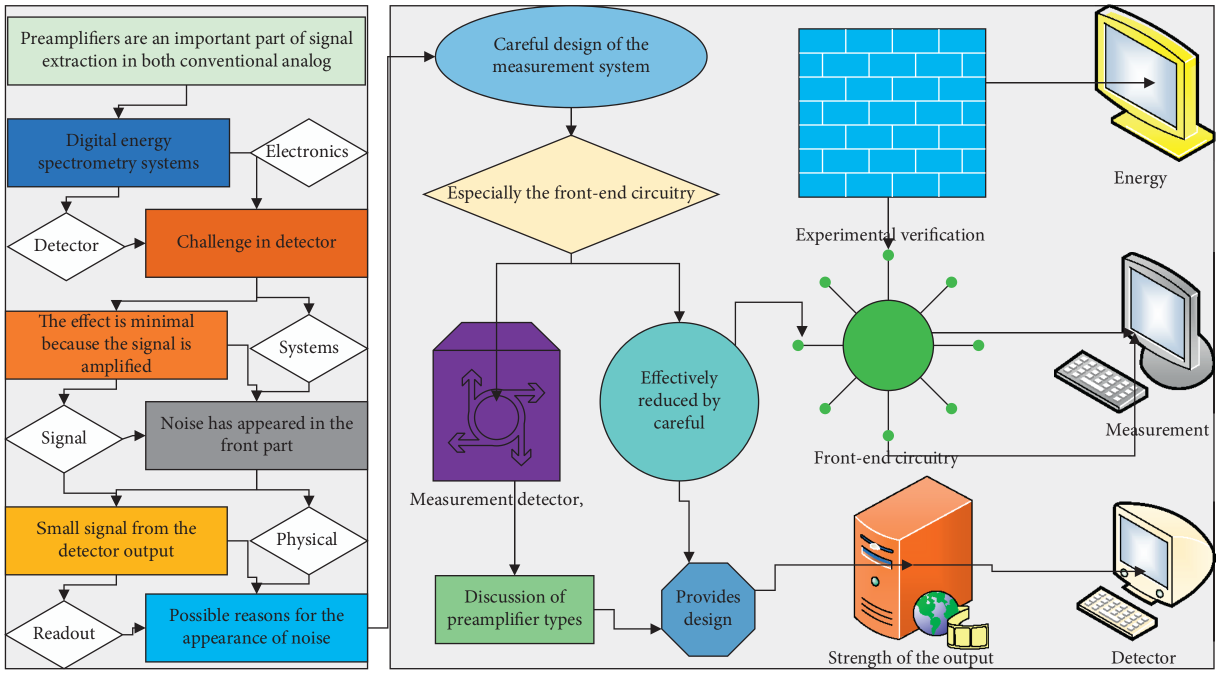

FIGURE 1: Computerized intelligent processing framework for radiometry.

The total capacitance of the amplifier input is

$$C_i = C_A - C_B - C_S. \quad (1)$$

If the input resistance of the amplifier is large, then

$$V_{iM} = \frac{1}{c_i}\int_0^{tW} i_D(t)\mathrm{d}t. \quad (2)$$

This means that the input voltage signal after the input current (t) is integrated over the input capacitor is Vi, and the signal amplitude VoM after passing through the voltage-sensitive preamplifier can be obtained to be proportional to the charge Q, and according to the nature of the detector, it yields that the energy of nuclear radiation is proportional to the charge Q. Then, for the voltage-sensitive preamplifier, the charge carried by the current pulse output from the detector is equal, and then, the amplitude of the voltage signal output from this amplifier $V\ oM$ is also equal, independent of the shape of the detector current pulse. It can be seen from the voltage equation that if Ci is unstable, it will certainly lead to an unstable amplitude value VoM of the output voltage of the voltage-sensitive preamplifier, and the energy resolution of the energy spectrum measurement system will certainly be reduced. As can be seen from the equation of the total capacitance of the amplifier input, instability of its three capacitances is commonly observed, and the stability of the system can be improved if a larger fixed capacitance is connected in parallel at the input.

$$V_{iM} = \frac{1}{c_i}\int_0^{tW} i_D(t)\mathrm{d}t = \frac{Q}{c_i - c_f}. \quad (3)$$

Preamplifiers are an important part of signal extraction in both conventional analog and digital energy spectrometry systems. The main challenge in detector electronics is to distinguish small signals from noise. In detector systems, noise is a random signal that is not caused by the physical process to be measured. If the noise only appears at the end of the electronic readout chain, the effect is minimal because the signal is amplified far more than the noise. However, if the noise has appeared in the front part, it may drown out the small signal from the detector output. There are many possible reasons for the appearance of noise, and the noise level can be effectively reduced by careful design of the measurement system, especially the front-end circuitry. Based on the discussion of preamplifier types, the paper provides design considerations and experimental verification of the front-end circuitry for the strength of the output signal of a γ-ray energy measurement detector.

The short-term stability of the four circuits was tested every 6 hours for a total of 48 hours, and the test data are shown in Figure 2. Compared to the short-term stability test, the gain variation of the circuit under the long-term stability test increased slightly, and the circuit with the protection loop continued to outperform the circuit without the protection loop, where the maximum error of the protection loop single large resistor feedback circuit (LR-R) was -0.464% and the maximum error of the protection loop T-resistor network feedback circuit (TR-R) was -0.178%. The maximum error in the protection loop single large resistor feedback circuit (LR-R) is -0.464%, and the maximum error in the protection loop T-shaped resistor network feedback circuit (TR-R) is -0.178%.

The circuits were tested using a Co source with a radiation intensity of 1.0 Ci, a Cs source at 0.1 Ci, and a Cs source at 20.0 Ci using a gas ionization chamber. An integral nonlinearity of 0.4832% was obtained for a single large resistive feedback circuit with a protection loop and 0.1649% for a T-shaped resistive network feedback circuit with a

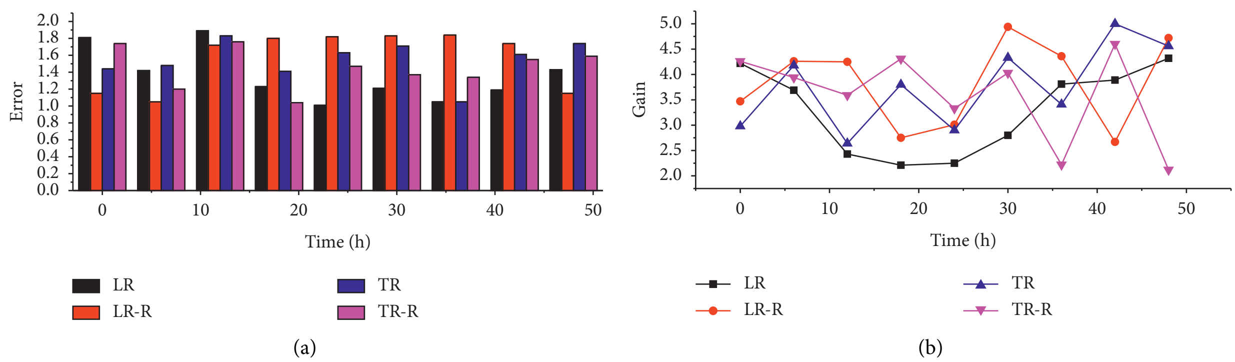

FIGURE 2: Long-term stability of each circuit.

protection loop. Therefore, the EMI simulation and test prove that the protection loop can shield and protect the circuit, especially for the measurement circuit with high input impedance signal to reduce the adverse effects of input leakage current, EMI, and other interference. The above verification results of the front-end circuit design method provide very meaningful reference data for the design of energy spectrum measurement systems.

In the energy spectrum measurement system, the energy resolution can be used to characterize the system to distinguish the different energies of ions, and it is one of the most important indicators of the energy spectrum measurement system, so we are committed to improving the energy resolution of the system as much as possible. When detecting γ-rays, it is desired to have a large detection efficiency for γ-rays, to accurately determine the energy of γ-rays and to improve the ability to identify γ-rays; i.e., the optimal energy spectrum of γ-rays needs to be measured. For charged particles with single energy of $E0$, the energy spectrum measured by the energy spectrum measurement system is not a single straight line. For example, a γ-ray detector consists of a scintillator detector, a photoelectric converter, and a readout system. If all γ-rays deposit all their energy in the scintillator, the readout system will record a pulse height spectrum. We would see peaks at the corresponding locations, a Gaussian curve in the shape of an approximately symmetric bell, and use the full width at half height (FWHM) of the curve as a measure of energy resolution.

$$\eta = \frac{FWHM}{N_{\max}}. \tag{4}$$

The smaller the energy resolution η, the better; it characterizes the competence of the energy measurement system to separate particles of different energies.

$$\begin{aligned}
\frac{dq_{st}(t)}{dt} &= (\lambda_{st} - \lambda_R)q_{st}(t),\\
\frac{dq_{si}(t)}{dt} &= (\lambda_{st} - \lambda_R)q_{st}(t) + \lambda_{si}q_{st}(t), \\
\frac{dq_{ur}(t)}{dt} &= (-\lambda_{st} + \lambda_R q_{st})(t) + (1-f)\lambda_{si}q_{st}(t).
\end{aligned} \tag{5}$$

According to the previous discussion, the energy of gamma photons is proportional to the charge of the detector output pulse signal.

$$E \in Q. \tag{6}$$

That is, the energy of the gamma photon is proportional to the cumulative sum of discrete data after digitizing the pulse waveform. Therefore, a pulse area calculation algorithm can be used to obtain the energy. However, the noise of the pulse waveform, the overshoot of the falling edge of the pulse, the signal stacking, and the sampling rate of the ADC can affect the accuracy of this algorithm.

In the analog energy spectrum measurement system, the pulse peak is directly extracted through a series of processing of the pulse by analog circuit and then sent to the multichannel pulse amplitude analyzer to extract the relevant digital quantity and then classified statistics, where the spreading effect of the peak hold circuit makes it possible to pick up the maximum value of the pulse at a relatively low sampling rate; in the digital energy spectrum measurement system, there is often only a simple preamplifier before the ADC, or a simple amplification and filtering circuit [20]. On the premise that the patient's urination frequency can be changed, we try to arrange for the patient to take the medicine in the morning of the day and then guide the patient to drink more water and consciously control oneself to increase the frequency of urination to increase the patient's urination frequency on the first day after taking the medicine. In digital energy spectrum measurement systems, there is often only a simple preamplifier before the ADC or a simple amplification and filtering circuit, and after the ADC output, the sampled digital quantities are compared by digital devices such as FPGAs, and the pulse peak is obtained online in real time. And if the ADC sampling rate is high enough, several values near the peak can be selected and averaged to obtain the pulse peak. But there are many high-speed ADCs on the system pressure, but also to consider the subsequent digital signal processing process of calculation speed and storage space requirements, the selected ADC sampling rate cannot be as high as possible.

3.2. Nuclear Medicine Exposure Measurement Estimation System Design. The scintillation detector based on silicon photomultiplier Si PM was selected for the detector module, and the system control architecture was determined to be a low-power microcontroller to realize the functions of data processing and system control, etc. Based on the core requirements of high sensitivity, compact structure, and ruggedness, the scintillation detector module was selected. The inherent characteristics of high scintillation crystal density and high atomic number ensure high detection sensitivity; the use of Si PM with higher gain, lower operating voltage, and compact structure replaces the traditional vacuum device photomultiplier, which significantly reduces the size and weight and improves portability with high sensitivity and accuracy; the power supply circuit optimized for Si PM and the choice of low-power microcontroller ensures the overall system. The power supply circuit optimized for the Si PM and the low-power microcontroller ensures the overall low-power consumption of the system and the compact size and easy operation, as shown in Figure 3.

The detector readout circuit converts the current signal from the Si PM output into a voltage signal and connects a spacer circuit to avoid baseline drift that affects the operating state of the subsequent comparison circuit. An ideal current-sensitive preamplifier needs to have a very small input impedance, a large output impedance, and a good time response. The pulse counting circuit uses a comparator to rectify the flicker pulse waveform that exceeds a certain threshold into a logic level pulse that can be easily recognized by the microcontroller and input to the microcontroller for pulse capture [21]. The power supply is a 3.7 V lithium battery, which is supplied to the boost circuit and the regulator circuit to generate the working voltage of the detector, as well as the working voltage and logic high level required for the comparator and the microcontroller to work. Different conversion factors are used for the different energy bands so that the calculated dose contains the effect of energy compensation. When the detector output pulse carries energy information, for example, the amplitude and energy are positively correlated, the energy segmentation can be achieved by amplitude segmentation, which is easier to implement and debug than the above-mentioned scheme of wrapping the compensating material. And because of the large gain of the scintillation detector, the distinction of the signal amplitude corresponding to different energies is greater, which makes it easier to implement the amplitude segmentation method than the silicon semiconductor detector.

The system design requires the use of a material to detect β, X, and γ-rays simultaneously, while β detection is more suitable for materials with low effective atomic number Z to reduce the detection efficiency due to backscattering of β-rays on the surface of the detection material. Therefore, although BGO is more suitable for achieving the detection efficiency and size required in the system design, it is not selected because of its highly effective atomic number, low optical output capability, and poor signal-to-noise ratio due to high refractive index, which affects the detection of low-energy X, β, and other low-amplitude pulses, as well as its long decay time. The Lu element in LSO is radioactive, which increases the background count of the instrument and affects the minimum detectable dose rate and accuracy of the instrument, so it is excluded from the commonly used cerium-doped silicate crystals. Among YSO and GSO, YSO with a relatively small effective atomic number Z is preferred for testing.

In the human respiratory compartment transport model, radionuclides entering the respiratory tract are contoured in two separate ways, partly by particle transport and partly by dissolution and absorption into the blood. In the anterior nasal passage, ET1 compartment, about 1/3 of the deposited material returns to the environment due to the mechanical action of nasal rubbing and breathing, while the remaining 2/3 enters the posterior nasal passage, ET2 compartment, due to swallowing, etc., and then participates in the whole biokinetic process, and due to the lack of blood vessels, it is believed that there is no absorption into the blood in ET1 compartment. A metabolic model with modified parameters applicable to thyroid patients and its computational procedures were used to calculate the activity of the compartments of the stomach, small intestine, blood, thyroid, and the rest of the tissues concerning time. Considering that, for different patients with different thyroidectomies, the thyroid uptake fraction may change, and it was taken to be equal and calculated separately for three cases, as shown in Figure 4.

Looking at equation (6) and its parameter values, it can be found that the formula is divided into two terms, fast and slow exponential terms, in which the share of slow exponential term u2 (0.271) is close to 30% of thyroid uptake fraction in normal subjects, and its corresponding contouring constant ($7.41 \times 10^{\circ}$ min) is also closer to the thyroid contouring rate (6.02×109 min'). Therefore, we modified α to 0.95 to make the model so modified applicable to patients with thyroid cancer. The front-end circuit usually uses a charge-sensitive preamplifier or a current-sensitive preamplifier. Weak signals are extremely susceptible to interference from external environmental factors or even submerged. The sensitivity and measurement accuracy of weak signal measurement circuits will be greatly affected. To verify the rationality of the above changes, we calculated the time-dependent relationship of urinary 1–131 activity using the MIRD normal model, the MIRD model with modified parameters, and the ICRP I-131 metabolic model (three different thyroid uptake fractions) applicable to patients with thyroid cancer, respectively. As can be seen from the figure, the calculated results of the MIRD normal model were significantly lower than those of the ICRP model applied to thyroid cancer patients, but the MIRD model with modified parameters was very close to the calculated results of the ICRP model with a 5% thyroid uptake fraction. This indicates that the changes to the parameters of the MIRD model in this study are reasonable [22] because the signal is amplified much larger than the noise. However, if noise has already appeared in the front end, it may overwhelm the small-signal output by the detector. Curve fitting, also known as function approximation, is a data processing method that seeks to find the best fit curve for experimental data to obtain more accurate data by analyzing the relevant characteristic parameters of the curve, trying to find the

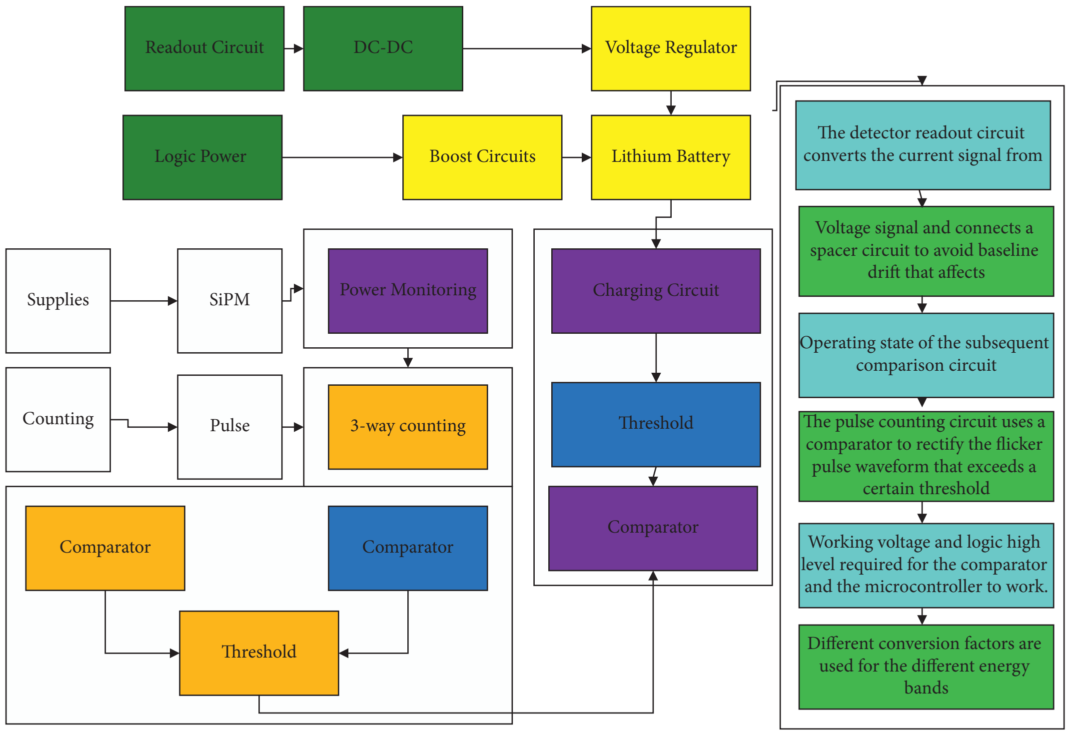

Figure 3: System hardware structure diagram.

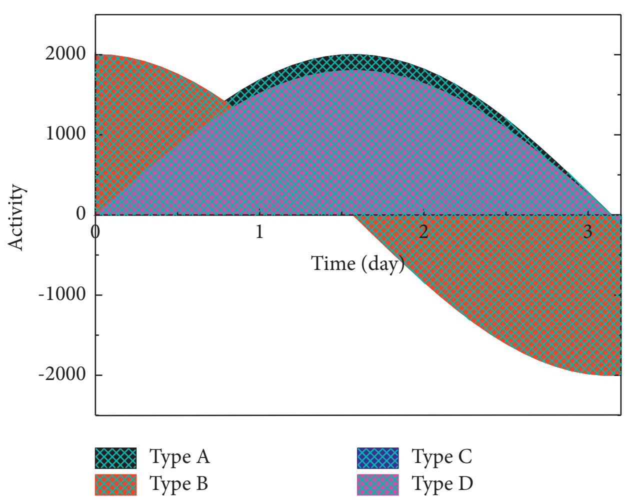

Figure 4: Variation of activity.

inherent pattern of the data, and using continuous curves to approximate or compare the functional relationship between the coordinates represented by discrete points. Although the curve obtained by "fitting" cannot be guaranteed to pass all sample points, it can be a good approximation of the true value, which can fully reflect the intrinsic relationship between known data and bring great convenience to the analysis of data later.

In the simulation process, it was first found that if the sampling points used for polynomial fitting were taken to points with small signal-to-noise ratios, the fitting effect would be significantly reduced, especially for the baseline sampling points that could not be included. The sampling points used for polynomial fitting are fitted with points with larger signal-to-noise ratios near the peak, so the pulse tail stacking has no effect on the fitting, and this algorithm focuses on the information near the peak of the fitted curve, so the polynomial fitting algorithm is only suitable for peak information extraction and not for waveform recovery. During the simulation experiments of this algorithm, it was found that the start time of the waveform has an important influence on the double exponential function fitting. Comparing the double exponential function fitting of the original waveform and the original waveform fitting with the baseline part removed, the baseline information cannot be included in the fitting process, and if the waveform is fitted from the start point of the pulse waveform, it is almost possible to obtain the original waveform.

4. Analysis of Results

4.1. Algorithm Performance Results. The trigger rising edge signal and the trigger mask signal are logically spread, and then Cnt_Flag is generated to start the pulse area calculation logic if they are both valid, and the counter Cnt starts counting. To eliminate the nonzero baseline superimposed in the pulse amplitude, the baseline value is estimated using the averaging method, and the baseline of the pulse signal is recovered by deducting the baseline from the pulse amplitude. The average value of the baseline is calculated in the first 4 sampling clock cycles, which is the baseline valuation baseline for this waveform. When solving for the baseline average value, a right shift of 2 bits is used in the FPGA for convenience and efficiency and speed. As can be seen from the ADC sampling waveform graph, the falling edge of the waveform may produce a down-shoot, so after obtaining the baseline, the next data DATA needs to be compared with the baseline. The experiment uses a Na radiation source to irradiate a detector consisting of a single probe LaBr3 single-crystal strip coupled with XP20D0 PMT to finally obtain the energy resolution. The important effect of the choice of the number of accumulated summation points in the algorithm for calculating the pulse area on the energy resolution of the detector at a fixed sampling rate is analyzed, as shown in Figure 5.

From Figure 5, it can be obtained that the energy resolution fluctuates at different pulse start points, and the best energy resolution can be achieved by starting the summation from the 5th point. We test the short-term stability of the four circuits every 6 hours for a total of 48 hours. By testing the number of summation points in the pulse area calculation algorithm, it can be obtained that fewer summation points result in a shorter calculation time and thus fewer photons are collected, while more summation points result in a longer calculation time and may contain too much noise; both result in a low signal-to-noise ratio. And a proper setting of summing points can also reduce the effect of tail stacking events. Therefore, the choice of the number of summing points is crucial for the energy resolution of the detector.

The energy resolution of various energy extraction algorithms was calculated for different sampling rates. The energy resolution of the algorithm for direct pulse peak extraction from the original waveform is 6.62%, and the energy resolution of the algorithm for calculating the pulse area from the original waveform is 5.59%. The energy resolution of each of the other algorithms is shown in Figure 6, and the trend is consistent with the evaluation results of the above simulation.

To solve the problems posed by high-speed ADCs in digital multichannel energy measurement systems, different algorithms are used to achieve the most accurate energy extraction possible at lower sampling rates. The broadening effect of the peak hold circuit enables the maximum value of the pulse to be collected at a relatively low sampling rate; in digital energy spectrum measurement systems, there is often only a simple preamplifier before the ADC. Several algorithms have been simulated and evaluated on the MATLAB platform, and some preliminary conclusions have been obtained. Calculating the energy resolution of each algorithm better corroborates the simulation results and provides a basis for the design and testing experiments of the heavy-ion cancer treatment in-beam PET digital energy spectrometry system.

The inputs can accept single-ended or differential signals. The rail-to-rail differential output and adjustable output common-mode voltage make it ideal for interfacing with differential input ADCs. These ADCs are typically powered from a single supply down to 3 V (2.7 V minimum) and have an optimal common-mode input range close to the intermediate supply. The sampling process of the ADC generates transients caused by the access of the ADC sampling capacitor. The transient temporarily shorts the output of the amplifier as the charge is transferred between

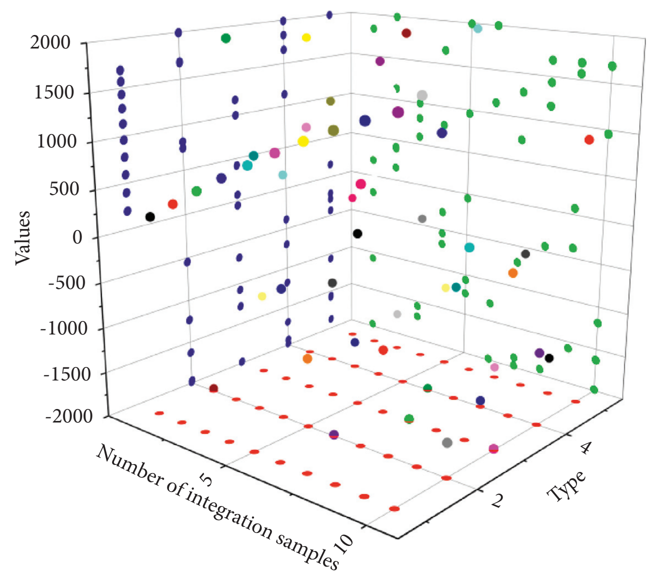

FIGURE 5: Starting point of the scan test 4-channel energy resolution variation graph.

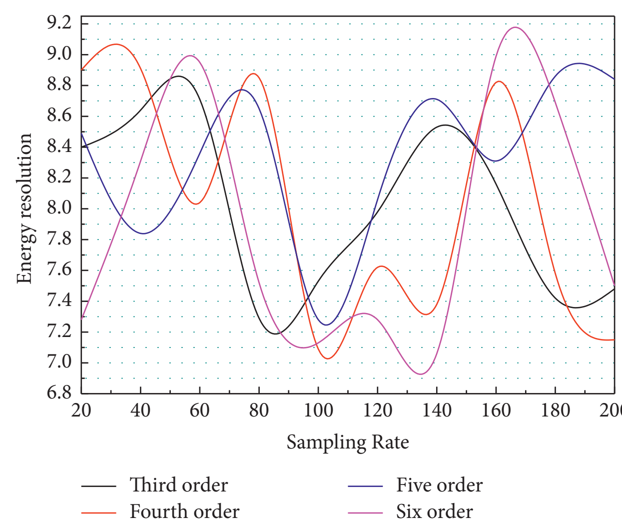

FIGURE 6: Energy resolution of each algorithm.

the amplifier and the sampling capacitor. For a valid representation of the input signal, the amplifier must recover from this load transient and stabilize before the end of the acquisition cycle. The LTC6605-7 is ready to quickly stabilize from these periodic load pulses. The final filter selects a 6.5 MHz filter with a reference voltage generated by the DAC to map the output signal, which allows a single DC offset to be applied to the common-mode pins. The filter not only implements a low-pass filtering function but also allows the signal to be converted from single-ended to differential, making the signal more resistant to noise during propagation.

4.2. Nuclear Medicine Irradiation Measurement Results. The health system has carried out personal dose monitoring since the last century, and the personal dose monitoring rate has been increasing year by year, and the annual effective dose per capita has been decreasing year by year. In particular, the personal dose monitoring rate continues to exceed 90%, and the personal dose monitoring rate has reached 94.5%. There have been 169 personal dose testing institutions reporting data through the system, with data covering 68,342 radiological work-using units and 316,580 monitored people reported by the system. The establishment of the system has played an important role in the improvement of the personal dose monitoring rate and the reduction of annual effective dose per capita. As shown in Figure 7, urine activity in the bladder increases cyclically and then decreases rapidly, with the highest increases in the first two cycles and decreasing amplitude in the subsequent cycles, rapidly decreasing to near 0 within a few days. Cumulative activity in the bladder is mainly contributed by the first day, so it can be expected that the first few cycles are critical in influencing cumulative activity in the bladder and in influencing dose to gonadal organs. In addition to the initial urine volume and bladder urine filling rate, the initial dosing time can be varied in this model.

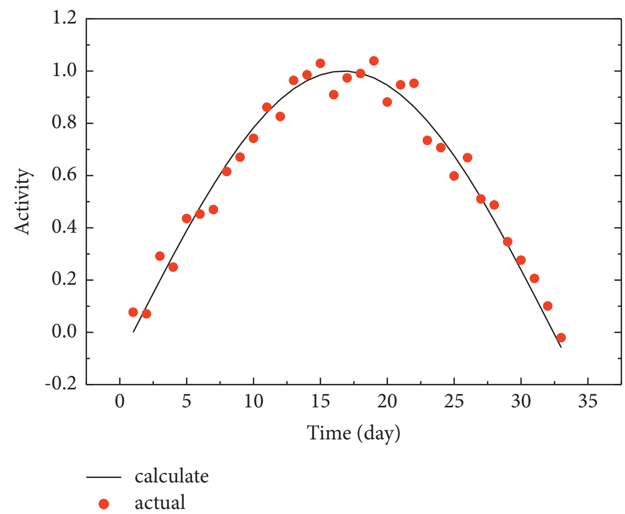

Figure 7: Activity change curve.

As the time of dosing approached the time of first urination, the cumulative bladder urine activity, bladder dose, and gonadal organ dose increased significantly. Please rephrase the part for clarity and correctness. the cumulative bladder urine activity increased nearly, both male and female doses increased nearly, the male gonadal dose increased nearly, and the female gonadal dose increased nearly. This may be because if the first urination is too early, the content within the urine at that time is not high, resulting in a poor effect of the first urination. Therefore, patients are advised to urinate after taking the drug to ensure the effectiveness of the first urination. As the time interval between daytime urination on the first day increased, the cumulative bladder urine activity, bladder dose, and gonadal organ dose increased significantly. As the time interval between daytime urination on the first day increased from 1 h to 6 h, the cumulative bladder urine activity increased by nearly 95%, the bladder dose increased by nearly 80% in both men and women, and the gonadal dose increased by nearly 20% in men and nearly 15% in women. However, this effect will not be so significant if the dosing time is delayed, because the shorter the daytime period after dosing, the smaller the number of cycles to increase the frequency and the smaller the effect. Therefore, it is recommended that patients be scheduled to take the drug in the morning of the day as much as possible, provided that the frequency of urination can be changed and then increase the frequency of urination on the first day after taking the drug by directing patients to drink more water and consciously controlling themselves to increase the frequency of urination.

After the data sending and receiving test of each module of the system is completed, the general tuning of the system is carried out. When the host computer and the remote server establish a connection by TCP/IP, the host computer will identify the nuclear radiation detection terminal hardware module and receive the data sent in a certain format, and the host computer will decode it to view the current real-time data. After the host client sets the threshold value for the radiation intensity and temperature of the whole system, and the received nuclear radiation data and temperature are not within this threshold value, the host client program will light up the nuclear radiation intensity alarm indicator or temperature alarm indicator to detect the temperature and radiation intensity of the whole system in the environment in real time and also display the connection status with the remote server in real-time. In the TCP/IP protocol, each time when establishing a long-term connection, the client needs to send packets to the server at regular intervals to notify the server that it is still online, which is a tedious process. When the detector output pulse carries energy information, such as a positive correlation between amplitude and energy, energy segmentation can be realized by amplitude segmentation, which is easier to implement and debug than the above-mentioned solution of wrapping compensation materials. However, if you use HTTP protocol, HTTP is a short connection mechanism established on TCP protocol, which can only upload data. From the perspective of subsequent development, it is necessary to realize the control of the whole onboard nuclear radiation detection terminal by the upper computer client, to better manage the power consumption of the system. Nuclear radiation data and nuclear radiation data graphical display interface are shown in Figure 8.

In this paper, a Microsoft Access database is taken for the storage of the detection data. Database Connectivity Toolset, a toolkit developed by LABVIEW, is used to connect with the data. The column keywords of the table are measurement time, longitude, latitude, height above ground, temperature, radiation intensity, etc. When users query the historical data, they can choose to query the parameters for a certain period. The GPRS communication of the system is tested by using the serial debugging assistant, the transmission of data acquisition of each module of the system is tested by using the network debugging assistant, the real-time display of the data, and the graphical display of the upper computer client

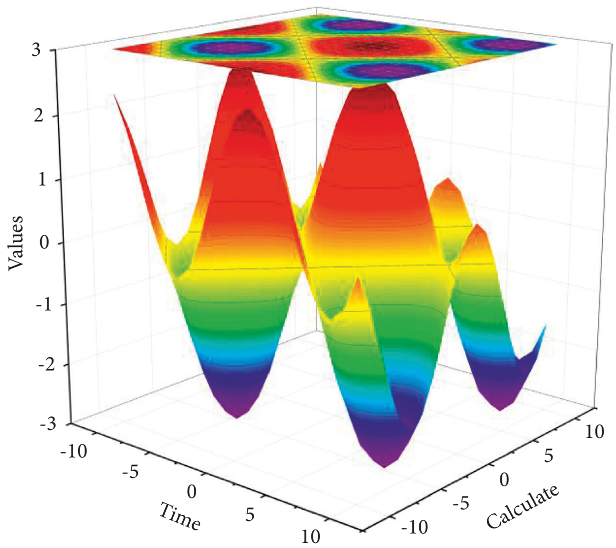

Figure 8: Graphical display of nuclear radiation data.

program of the whole system is tested, and the historical data storage of the system is tested. The comprehensive test effect of the whole system, the accuracy of data acquisition, and the volume, weight, and power consumption of the system have certain advantages, and it is very easy to be installed on small and medium-sized UAVs, which can achieve the expected effect.

5. Conclusion

Based on the contradiction between the need to obtain accurate energy information in the digital measurement system of a heavy-ion cancer treatment device for measuring γ-rays in beam PET and the problems caused by the adoption of high-speed ADC in large-scale systems, this thesis investigates the factors influencing energy resolution and the energy extraction algorithm. From the basic composition of the γ-ray digital energy measurement system, five main factors are affecting the accurate energy extraction of the γ-ray digital energy measurement system. Among them, the selection of ADC of the analog-to-digital converter has a great relationship with it. If many high-speed ADCs are used, there are negative effects on data volume, heat dissipation, system complexity, and cost. It is not practical to use many high sampling rate ADCs in digital energy spectrometry with multiple detector units. The problem of misuse of radiation treatment technology still exists. The awareness of radiation protection among radiation workers in medical institutions is low, especially the health condition of interventional radiology workers is worrying, and the radiation protection of interventional radiology workers needs to be strengthened. We strengthen the personal dose monitoring of internal radiation for nuclear medicine staff; further, we strengthen the supervision and management of radiology treatment institutions, establish a sound system of medical physicists, and improve the radiation health information system.

Data Availability

The data used to support the findings of this study are available from the corresponding author upon request.

Conflicts of Interest

The authors declare that there are no conflicts of interest.

References

[1] F. A. Mettler, M. Mahesh, M. Bhargavan-Chatfield et al., "Patient exposure from radiologic and nuclear medicine procedures in the United States: procedure volume and effective dose for the period 2006–2016," *Radiology*, vol. 295, no. 2, pp. 418–427, 2020.

[2] A. K. Jha, S. Mithun, V. Rangarajan, L. Wee, and A. Dekker, "Emerging role of artificial intelligence in nuclear medicine," *Nuclear Medicine Communications*, vol. 42, no. 6, pp. 592–601, 2021.

[3] J. S. Oh, "Nuclear medicine physics: review of advanced technology," *Progress in Medical Physics*, vol. 31, no. 1, pp. 81–89, 2020.

[4] R. H. J. A. Slart, M. C. Williams, L. E. Juarez-Orozco et al., "Position paper of the EACVI and EANM on artificial intelligence applications in multimodality cardiovascular imaging using SPECT/CT, PET/CT, and cardiac CT," *European Journal of Nuclear Medicine and Molecular Imaging*, vol. 48, no. 5, pp. 1399–1413, 2021.

[5] S. Shahid, K. Masood, and A. W. Khan, "Prediction of impacts on liver enzymes from the exposure of low-dose medical radiations through artificial intelligence algorithms," *Revista da Associação Médica Brasileira*, vol. 67, no. 2, pp. 248–259, 2021.

[6] R. I. Gomaa, "Performance analysis of wireless sensor networks for nuclear medicine applications," *Journal of Radiation Research and Applied Sciences*, vol. 13, no. 1, pp. 714–720, 2020.

[7] Y. Ohno, J. B. Seo, G. Parraga et al., "Pulmonary functional imaging: Part 1-State-of-the-Art technical and physiologic underpinnings," *Radiology*, vol. 299, no. 3, pp. 508–523, 2021.

[8] A. Lin, M. Kolossváry, I. Išgum, P. Maurovich-Horvat, P. J. Slomka, and D. Dey, "Artificial intelligence: improving the efficiency of cardiovascular imaging," *Expert Review of Medical Devices*, vol. 17, no. 6, pp. 565–577, 2020.

[9] Q. Pengjiang, K. Xu, T. Wang et al., "Estimating CT from MR abdominal images using novel generative adversarial networks," *Journal of Grid Computing*, vol. 18, no. 2, pp. 211–226, 2020.

[10] E. Huynh, A. Hosny, C. Guthier et al., "Artificial intelligence in radiation oncology," *Nature Reviews Clinical Oncology*, vol. 17, no. 12, pp. 771–781, 2020.

[11] H. Heryani, C. Anam, H. Sutanto, A. D. Reskianto, and G. Dougherty, "Automated determination of chest characteristics of Indonesians as the basis of chest dosimetrical phantom design," *Polish Journal of Medical Physics and Engineering*, vol. 26, no. 4, pp. 263–268, 2020.

[12] K. Spuhler, M. Serrano-Sosa, R. Cattell, C. DeLorenzo, and C. Huang, "Full-count PET recovery from low-count image using a dilated convolutional neural network," *Medical Physics*, vol. 47, no. 10, pp. 4928–4938, 2020.

[13] M. Bardiès and J. I. Gear, "Scientific developments in imaging and dosimetry for molecular radiotherapy," *Clinical Oncology*, vol. 33, no. 2, pp. 117–124, 2021.

[14] H. Ben Yedder, B. Cardoen, G. Hamarneh, and G. Hamarneh, "Deep learning for biomedical image reconstruction: a survey," *Artificial Intelligence Review*, vol. 54, no. 1, pp. 215–251, 2021.

[15] G. A. Kaissis, M. R. Makowski, D. Rückert, and R. F. Braren, "Secure, privacy-preserving and federated machine learning in medical imaging," *Nature Machine Intelligence*, vol. 2, no. 6, pp. 305–311, 2020.

[16] N. Mahomed, B. van Ginneken, R. H. H. M. Philipsen et al., "Computer-aided diagnosis for World Health Organization-defined chest radiograph primary-endpoint pneumonia in children," *Pediatric Radiology*, vol. 50, no. 4, pp. 482–491, 2020.

[17] R. Armya and A. M. Abdulazeez, "Medical images segmentation based on unsupervised algorithms: a review," *Qubahan Academic Journal*, vol. 1, no. 2, pp. 71–80, 2021.

[18] A. Das, M. S. Nair, and S. D. Peter, "Computer-aided histopathological image analysis techniques for automated nuclear atypia scoring of breast cancer: a review," *Journal of Digital Imaging*, vol. 33, no. 5, pp. 1091–1121, 2020.

[19] R. Jayalekshmy, J. J. Unnithan, A. Mohan Kumar, and S. A. Majid, "Artificial intelligence-finding new frontiers in oral and maxillofacial radiology," *Journal of Dental & Orofacial Research*, vol. 16, no. 1, pp. 32–38, 2020.

[20] D. Ghieh, C. Saade, E. Najem, R. El Zeghondi, M. A. Rawashdeh, and G. Berjawi, "Staying abreast of imaging–current status of breast cancer detection in high density breast," *Radiography*, vol. 27, no. 1, pp. 229–235, 2021.

[21] Q. Zheng, Y. Ding, L. Zhou, C. Fan, and P. Qian, "A novel conversion method from X-ray image to MR image using deep network and auto-encoding technology," *Journal of Medical Imaging and Health Informatics*, vol. 11, no. 5, pp. 1394–1402, 2021.

[22] A. A. Nawaz, M. Urbanska, M. Herbig et al., "Intelligent image-based deformation-assisted cell sorting with molecular specificity," *Nature Methods*, vol. 17, no. 6, pp. 595–599, 2020.

Hindawi
Journal of Healthcare Engineering
Volume 2021, Article ID 2384493, 9 pages
https://doi.org/10.1155/2021/2384493

Research Article

A Method of CT Image Denoising Based on Residual Encoder-Decoder Network

Yali Liu

Faculty of Economics and Management, Shangluo University, Shaanxi, Shangluo 726000, China

Correspondence should be addressed to Yali Liu; 232006@slxy.edu.cn

Received 5 August 2021; Accepted 2 September 2021; Published 23 September 2021

Academic Editor: Kaijian Xia

Copyright © 2021 Yali Liu. This is an open access article distributed under the Creative Commons Attribution License, which permits unrestricted use, distribution, and reproduction in any medium, provided the original work is properly cited.

Low-dose computed tomography (CT) has proved effective in lowering radiation risk for the patients, but the resultant noise and bar artifacts in CT images can be a disturbance for medical diagnosis. The difficulty of modeling statistical features in the image domain makes it impossible for the existing methods that directly process reconstructed images to maintain the detailed texture structure of images while reducing noise, which accounts for the failure in CT diagnostic images in practical application. To overcome this defect, this paper proposes a CT image-denoising method based on an improved residual encoder-decoder network. Firstly, in our approach, the notion of recursion is integrated into the original residual encoder-decoder network to lower the algorithm complexity and boost efficiency in image denoising. The original CT images and the postrecursion result graph output after recursion are used as the input for the next recursion simultaneously, and the shallow encoder-decoder network is recycled. Secondly, the root-mean-square error loss function and perceptual loss function are introduced to ensure the texture of denoised CT images. On this basis, the tissue processing technology based on clustering segmentation is optimized considering that the images after improved RED-CNN training will still have certain artifacts. Finally, the experimental results of the TCGA-COAD clinical data set show that under the same experimental conditions, our method outperforms WGAN in average postdenoising PSNR and SSIM of CT images. Moreover, with a lower algorithm complexity and shorter execution time, our method is a significant improvement on RED-CNN and is applicable for actual scenarios.

1. Introduction

The high radiation technology dose to the human body continues to develop in the computed tomography (CT) scanning process, and CT images have seen ever-wider application in medical diagnosis [1, 2]. By cutting X-ray tube current, low-dose scanning requires less radiation dose and therefore lowers the signal-to-noise ratio in projection data. Noise and artifacts are blended into CT images reconstructed by the filtered back projection (FBP) algorithm, which affects the accuracy of subsequent clinical diagnosis. Therefore, studying how to reconstruct the reconstructed CT image from original noisy projection data is of great significance and practical value [3].

At this stage, the methods of improving the quality of low-dose CT (LDCT) images can be divided into projection domain denoising algorithm [4], image reconstruction algorithm [5], and image domain denoising algorithm [6]. These image-denoising methods, however, prove ineffective in improving CT image quality. Furthermore, it is difficult to describe these methods with a precise model since they have a large number of iterations and take a long time, and the distribution of image noise after processing becomes complicated. And there may be artifacts in images. Thus, the traditional image-denoising methods can hardly attain the desired effects. Thus, it is difficult to achieve the desired effects with traditional image denoising methods. The traditional methods can suppress noise and artifacts, but they are prone to the loss of edge and detailed information. Therefore, the resultant denoised CT images cannot meet the actual clinical diagnosis application [7].

The rapid development of deep neural networks offers new insights into how to address the problem in LDCT image denoising [8, 9]. Because of the powerful feature learning and mapping capabilities of deep neural networks, deep neural networks show better reconstruction quality and faster speed than traditional methods. To date, the deep neural network has achieved good results in LDCT image denoising. However, since these networks use mean square error (MSE) as loss function, minimizing MSE usually incurs detail and loss and excessive edge smoothness. At the same time, the image texture that is important to the human eye perception is ignored [10].

We, therefore, propose RED-CNN, a CT image-denoising algorithm based on residual encoder-decoder (RED) convolutional neural network, namely, RED-CNN. Using sampling operations to learn end-to-end nonlinear mapping in a multiscale space, our method is able to reconstruct the denoised images directly. At the same time, convolution and deconvolution operations are used to better extract features and restore the details of CT images. The main innovations of the paper are as follows:

(1) The proposed CT image-denoising method based on an improved RED network uses the same shallow RED network to recursively construct a new network, thereby reducing network complexity.

(2) In order to improve the visual artifacts of CT images after denoising, a new joint loss is proposed by combining the advantages of MSE loss function and perceptual loss function, which can better reconstruct the details and texture of images.

(3) Residual learning is combined with traditional optimization processing techniques. Introducing distance images into water images can help reduce data inconsistency and better improve the denoising effect of CT images.

2. Related Work

As a noninvasive imaging technique, computed tomography is widely used in industry, medicine, and many other fields. Of all the image reconstruction methods applied in X-ray CT imaging, FEP is the most widely used one. Generally, a good image can be reconstructed when the projection data is complete [11, 12].

The projection domain filtering algorithm filters the original data in the projection domain and then uses FBP to reconstruct CT images. Typical methods include bilateral filtering method [13], adaptive convolution filtering method [14], penalty weighted least square (PWLS) method [15], and so on.

Both the projection domain denoising algorithm and image reconstruction algorithm need to use projection data. In practical applications, however, projection data is usually used as an intermediate result of a CT scanner and is not accessible to ordinary users. As a method not reliant on projection data, the image domain denoising algorithm is able to denoise reconstructed CT images directly. It, therefore, has become a research hotspot in the field of LDCT image denoising [16–18]. In accordance with the theory that image data can be decomposed into information and time uncorrelated noise, reference [19] proposed a CT image-denoising method based on wavelet transformation. It could use the average and weighted wavelet coefficients of input images to reconstruct final denoising images. Reference [20] combined 3D filter with blind source separation (BSS) to extract noise statistics from noise components. A denoising method for CT images based on BSS for multiframe low-dose image sequences was proposed. Reference [21] proposed an improved SNCSR model and used the improved total variation (ITV) model to preprocess images. Aiming at the fringe artifacts in CT images, reference [22] proposed an image denoising algorithm based on discriminative weighted nuclear norm minimization (D-WNNM). The local entropy of images was used to distinguish fringe artifacts and organizational structure, and the weight coefficient of the weighted nuclear norm minimization (WNNM) denoising method was adaptively adjusted.

For its ability to extract features and map, deep learning is now widely used in image processing, and this method has greater advantages over traditional ones in removing complex noise from LDCT images. Reference [23] proposed a CT image denoising method based on generative adversarial network (GAN). By integrating visual perception into image denoising, this method reduces image noise while retaining relevant key information. Reference [24] incorporated structural similarity index into the GAN model and introduced a least square loss function penalty term to constrain CT images and further maintaining the texture detail and sharpness of CT images.

Although the projection domain denoising algorithm can make full use of statistical law for noise distribution in the projection domain, data inconsistencies may occur in the process of noise reduction in the projection domain. It is easy to introduce new noise or artifacts into reconstructed images, and the traditional single image denoising method cannot achieve desired effects [25]. Although the CT image denoising method based on deep learning can greatly remove the stripe artifacts and reduce the noise of CT images, the peak signal-to-noise ratio has been improved. However, the upsampling and downsampling links in network structure and methods based on MSE or weighted MSE are prone to cause loss of image details in the process of image denoising. In addition, the complex network structure model showed greater instability during the training process, and the network is difficult to converge [26, 27]. The RED-CNN is simple in structure, and continuously deepening the network structure can achieve effective denoising of CT images in complex and multinoise scenarios. For example, reference [28] proposed an image denoising method based on RED-CNN. The best denoising effect has been achieved in the objective evaluation index.

Based on easy expansion and strong adaptability of the RED-CNN deep neural network, this paper also proposes a new CT image denoising method combined with the recursive notion of network structure model. This method can better extract and recognize the feature information of images and use the same network structure to recursively construct a new network. By reducing the number of layers and convolution kernels in the RED network, the network complexity is lowered to achieve rapid denoising of CT images. On this basis, the principle of k-means clustering segmentation is integrated. CT images are optimized based on the threshold, which improves the details and texture of denoised images.

The remainder of this paper is arranged as follows. Section 3 introduces CT image denoising model based on the improved RED network and its corresponding network structure model in detail. Section 4 presents the experimental analysis of CT images in the TCGA-COAD clinical data set to verify the effectiveness of the proposed method. This paper is summarized in Section 5.

3. RED Network-Based CT Image Denoising

This section introduces the denoising model, network structure of RED-CNN, overall structure of recursive network, and the image optimization process after the RED-CNN model. Besides, root MSE and perceptual loss function are used as the loss functions of the overall network, which can partially address the problem of detail loss and preserve the image texture as well. Finally, the image optimization process after the RED-CNN model is introduced.

3.1. Noise Reduction Model. Assuming $x \in \mathrm{R}^{N\times N}$ is normal-dose CT (NDCT) image, and $x \in \mathrm{R}^{N\times N}$ is LDCT image. The purpose of CT image denoising is to map z to x by finding a suitable function G, which can be expressed as follows:

$$G: z \longrightarrow x, \tag{1}$$

where $x \in R^{N\times N}$ is the sample of CT image distribution P_r under normal dose and $x \in R^{N\times N}$ is the sample of LDCT image distribution P_L. The function G maps LDCT image distribution P_L to a specific image distribution P_g and make the generated distribution P_g as close as possible to the real sample distribution P_r.

3.2. Network Structure. Figure 1 shows the overall structure of constructed image denoising network based on a shallow RED network. The RED network consists of 8 layers, with 4 of them being convolutional layers and the remainders deconvolutional layers arranged symmetrically. Each of the first 7 hidden layers has 64 convolution kernels, and the last layer is 1 convolution kernel.

In the overall network structure, the shallow encoder-decoder network in Figure 2 is recycled to generate the final denoising image. The specific notion is as follows: in each recursion, the original CT image and the result image output after the s recursion are simultaneously used as the input for the next recursion. It can avoid the loss of original image features in the recursive process, better extract the features of original input images, and retain the detailed information of images.

The recursive process of the network can be expressed as follows:

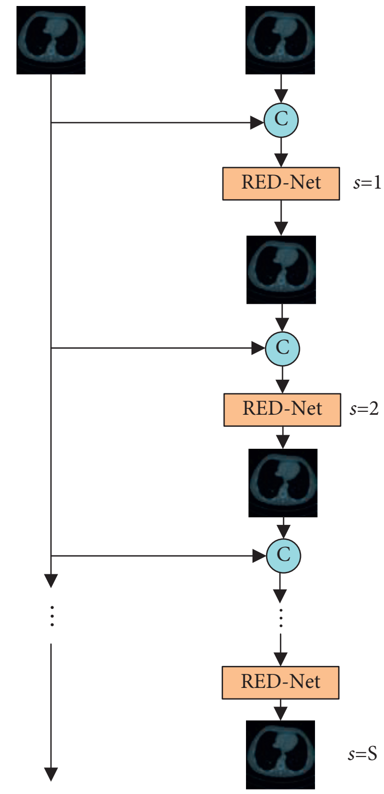

Figure 1: Overall architecture of RED-Net with S stage recursion.

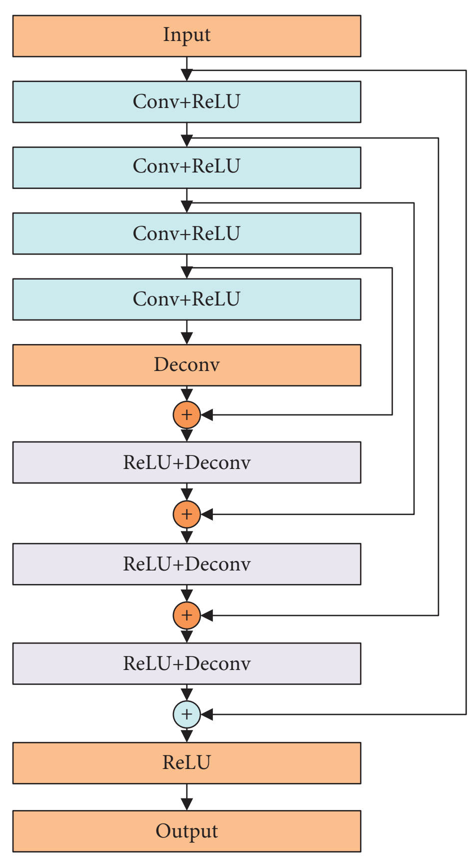

Figure 2: The architecture of shallow RED-Net.

$$\begin{aligned} I_1 &= X, \\ O_s &= F_{\text{RED-Net}}(I_s), \quad 1 \le s < S, \\ I_{s+1} &= f_{\text{in}}(O_s, X), \quad 1 \le s < S, \end{aligned} \tag{2}$$

where S represents the number of recursions, X represents the network input, RED-Net is the shallow RED network, O_s is the denoising CT image obtained from the s recursion, f_{in} represents the cascade operation between output O_s of the s recursion and original LDCT image, and X. I_{s+1} is the input of the $s+1$ recursion.

3.3. Loss Function. In conventional learning-based image reconstruction methods, root MSE is usually used as the objective function. The pixel-by-pixel comparison method can achieve a high signal-to-noise ratio, but the partial loss of detailed information tends to blur the image denoising results. Perceptual loss based on feature comparison is more in line with real visual perception and can help restore clearer images. However, pixel space, when covered evenly, can sometimes generate subtle visual artifacts.

A new joint loss is proposed so as to better reconstruct the details and image texture, a combination of both advantages.

$$L_{\text{Joint}} = L_{\text{MSE}} + L_{\text{Per}}, \tag{3}$$

where L_{MSE} and L_{Per} represent the loss function of pixel-by-pixel comparison and semantic feature comparison, respectively.

(1) MSE loss function. The pixel-by-pixel loss function uses the traditional MSE method to calculate root MSE between denoised CT images and real images through pixel-by-pixel comparing and matching. MSE loss function can be expressed as follows:

$$L_{\text{MSE}} = \frac{1}{W \cdot H} \left\| F(x_{\text{detail}}) - (x - y) \right\|^2, \tag{4}$$

where x is the noise image, y is the real CT image, and W and H are the width and height of input image to $\{x, y\}$, respectively.

(2) Perceptual loss function. The traditional MSE loss pixel-by-pixel comparison method often causes the loss of high-frequency information. A perceptual loss function is introduced to improve the denoising effect of the existing blur, realize edge enhancement, and enhance its texture details. By comparing the differences between image features, the perceptual loss can reconstruct more details and obtain better denoising effects. Experiments prove that the neural network used for image classification and segmentation can learn well the semantic features such as texture edges of images. The pretrained convolutional networks, therefore, can be connected in series to extract the required feature maps.

SegNet model comprising a set of convolutional coding layers and mirrored deconvolutional decoding layers can achieve better effect in semantic segmentation and thus is selected for the loss network. The encoding part uses the visual geometry group (VGG) model with strong generalization ability, and the decoding part uses a symmetrical structure to recover the information lost in pooling. Besides, the pretrained Caffe model is used to ensure the ability of the loss network to extract features.

After determining the loss network, perceptual loss needs to be defined at the semantic feature level. The specific steps are as follows: input the fuzzy denoising result $x - F(x_{\text{detail}})$ and real image y initially generated by the front-end network into SegNet. The feature maps of these two are extracted from the fixed convolutional layer, and then the Euclidean distance represented by these two features is calculated, as shown in the following equation:

$$L_{\text{Per}} = \frac{1}{W_i H_i} \left\| \varphi_i(x - F(x_{\text{detail}})) - \varphi_i(y) \right\|^2, \tag{5}$$

where W_i and H_i represent the width and height of the selected feature map, respectively, and φ_i is the feature map extractor.

The joint perceptual loss consists of two parts, namely MSE and perceptual loss. The structural model is shown in Figure 3. The method is implemented as follows: first, noisy CT image and real CT image y are input into the denoising network. The difference between these two is compared and learned pixel by pixel through the MSE loss function, and the initial denoising result $x - F(x_{\text{detail}})$ that matches pixel y is obtained. At this time, the CT image after initial denoising is blurry. On this basis, y and $x - F(x_{\text{detail}})$ are input into the loss network SegNet, respectively. Then the two feature maps $\varphi(x - F(x_{\text{detail}}))$ and $\varphi(y)$ are extracted from one of the convolutional layers to define the perceptual loss function. The network continues to train by minimizing perceptual loss to learn the difference in semantic features of these two images, reconstruct the edge and detail information, and make the two images more similar in feature perception. Finally, a clearer CT image denoising result is generated.

3.4. Optimization Process. The signal-to-noise ratio of CT images after training on the RED-CNN is significantly improved. To further eliminate the residual artifact noise of CT images, improve its detailed texture, and achieve a better correction effect, CT noise images generated by the RED network are processed by tissue processing technology based on clustering segmentation.

The residual artifact noise is weak. In the process of neural network training, this part of artifact noise is not obvious enough, so it is difficult for the network to accurately identify and remove it. To clear all the residual noise in CT images, there is a need to process the water equivalent tissue. Given that water equivalent tissues are similar in X-ray attenuation and dominate images, a uniform value must be assigned to these pixels so as to clear the residual metal artifacts in flat areas.

Firstly, the k-means clustering segmentation principle is followed, and CT images are automatically segmented into three parts: bone, water (including water equivalent tissue),

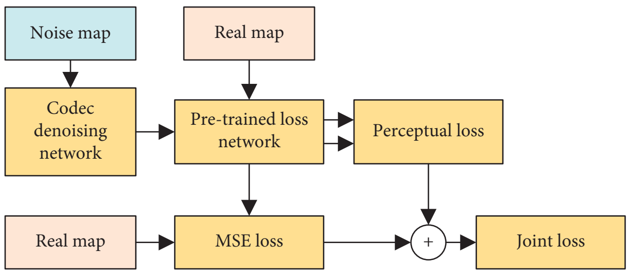

FIGURE 3: Proposed joint loss of cascaded network.

and air based on two thresholds. To avoid clustering errors, the bone-water threshold is set to be no less than 320 HU. On this basis, the image after cluster segmentation is transformed into a binary image. Among them, the water pixel is 1, and the remaining pixels are 0. However, when the water pixel area is a constant value, a false boundary or structure will appear as a result of discontinuity in boundary data. Therefore, based on the calculation of the distance between two pixels, a transition area of $L = 5$ pixels is set in the water pixel area. If the distance between the pixel and its nearest 0 pixel is greater than L, the pixel value is set to L; otherwise, it is set to distance D between the two. The weighted average of water pixels for optimized images of the image trained by the neural network is shown in the following equation:

$$\bar{y}^{\text{Net},w} = \frac{\sum_i D_i y_i^{\text{Net}}}{\sum_i D_i}. \tag{6}$$

Furthermore, the prior image is obtained as shown in the following equation:

$$y_i^{\text{prior}} = \frac{D_i}{L}\bar{y}^{\text{Net},w} + \left(1 - \frac{D_i}{L}\right) y_i^{\text{Net}}. \tag{7}$$

In the algorithm, RED-CNN training and optimization are two mutually beneficial steps. CT images trained by the RED-CNN can eliminate most artifact noise. On this basis, the residual fine artifact noise is further eliminated, and misclassification is avoided combined with optimized processing technology. In this paper, the transition area of water equivalent organization is added to the optimization processing link to eliminate the data discontinuity caused by the same threshold allocation. When a clear and accurate edge structure is restored, the residual artifact noise in the area is cleared, and the generated images attain a higher signal-to-noise ratio.

4. Experiment and Analysis

The hardware environment of the experimental platform is as follows: the operating system is Windows 10, central processing unit (CPU) is Intel Core i7-1065G7, and the graphics card model is Radeon Graphics 8 core. TensorFlow deep learning framework is used to perform denoising tests on CT images from the TCGA-COAD clinical data set. The experiment selects 200 different CT images with a size of 512×512 pixels as training data. LDCT images in the experiment can be simulated by adding noise to the NDCT image projection domain.

4.1. Experimental Parameters and Evaluation Indicators. The experimental parameters of the CT image denoising algorithm based on the RED network are set as follows: the size of the image block is $48 * 48$, the learning rate $\alpha = 10^{-5}$, and the number of cycles $S = 5$. The number of layers in the encoder-decoder network is 8; the number of convolution kernels in the last layer is 1; the number of other layers is 64; and the convolution kernels in all layers have a size of $3 * 3$. The step size of convolution and deconvolution is set to 1 without zero padding. The convolution and deconvolution kernels are initialized with a random Gaussian distribution with a mean value of 0 and a standard deviation of 0.01. The network saves parameter information every 1,000 training, and terminates training after 50,000 iterations.

In order to better evaluate the denoising effect of the algorithm on noisy CT images, quantitative evaluation indexes of peak signal-to-noise ratio (PSNR) and structural similarity (SSIM) are introduced [29, 30]. The two evaluation indicators are defined as follows:

(1) PSNR:

$$\text{PSNR} = 20 \log_{10} \frac{255}{\sqrt{1/mn \sum_{i=0}^{m-1} \sum_{j=1}^{n-1} [I(i,j) - K(i,j)]^2}}, \tag{8}$$

where I is the real CT image of $m \times n$ and K is the CT image after noise removal.

(2) SSIM:

$$\text{SSIM} = \frac{(2\mu_x \mu_{x'} + c_1)(2\sigma_{xx'} + c_2)}{(\mu_x^2 + \mu_{x'}^2 + c_1)(\sigma_x^2 + \sigma_{x'}^2 + c_2)}, \tag{9}$$

where μ_x and $\mu_{x'}$ are the mean values of images x and x', respectively, and σ_x and $\sigma_{x'}$ are the standard deviations of images x and x', respectively. $\sigma_{xx'}$ is the covariance of x and x', and c_1 and c_2 are constants.

4.2. Convergence Analysis. As the network rises in depth, the model's accuracy will reach saturation and then degenerate rapidly, which makes convergence unattainable and cause the training accuracy of the network to decline. The residual network, however, can speed up the convergence of network loss function and solve the problem of gradient disappearance and degradation caused by the increase in the number of network layers. Figure 4 shows the convergence speed of loss function for residual network and nonresidual network with the number of iterations. It can be seen from Figure 4 that compared to the nonresidual network, the residual network converges faster, and the loss value after convergence is smaller. This demonstrates that the residual learning has outstripped direct mapping in the learning effect, which can minimize the difference between input images and target images. The mapping after the introduction of residual is more sensitive to the change of output, which improves the model accuracy while maintaining the depth of the network.

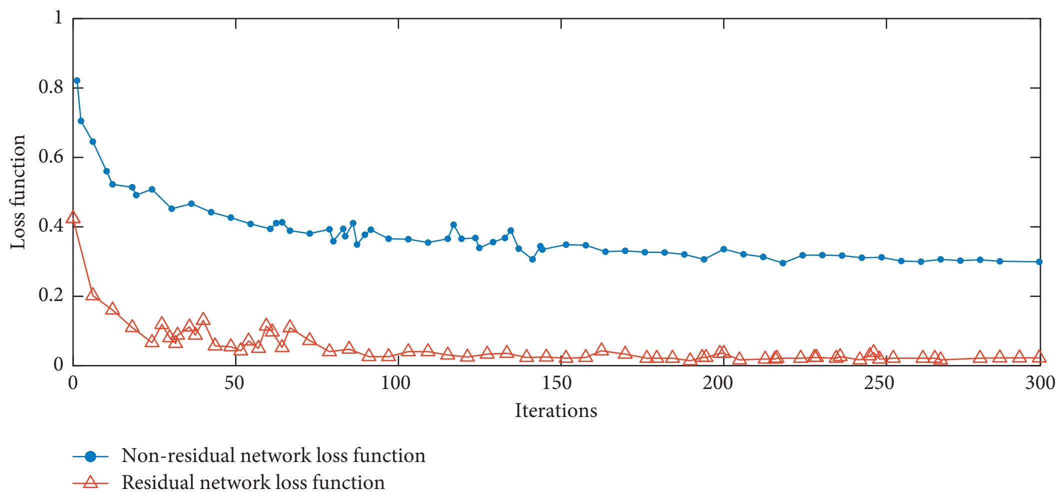

Figure 4: Loss function of residual network and nonresidual network.

The performance of the training model is determined by the number of layers of neural network and residual units. In order to further determine the appropriate number of residual network layers and residual units, this paper has trained and tested the network with the number of layers at 4, 8, and 12 and the number of residual units at 2, 3, and 4, respectively. Table 1 shows the average time required for different network models to iterate once under the same training set. As can be seen from Table 1, the 8-layer RED network iteration takes 247.349 s, which is shorter in time and faster in training speed.

This paper selects hip joint prosthesis as the test set to evaluate the image quality of the network after training with the number of layers at 4, 8, and 12, respectively. Table 2 shows SSIM value, RMSE value, and PSNR value of images after three network training. As can be seen from Table 2, when the number of RED network layers is 8, the output image shows a better evaluation index: a larger SSIM value, a smaller RMSE value, and a larger PSNR value, which indicate that the network has a higher performance in image restoration. In summary, when the network model has 8 layers, it can achieve faster convergence speed, higher image quality after correction, and better performance of metal artifact correction.

Table 1: The average training time for 1 epoch of RED-CNN with the number of layers at 4, 8, and 12.

Network layers	Training time (s)
4	452.287
8	247.349
12	873.374

Table 2: SSIM, RMSE, and PSNR values under RED-CNN with the number of layers at 4, 8, and 12.

Network layers	SSIM	RMSE	PSNR
4	0.9584	0.0065	68.625
8	0.9592	0.0062	68.634
12	0.9576	0.0067	68.612

4.3. Subjective Effects. Nine CT images were randomly selected from the TCGA-COAD clinical data set as test charts. It does not overlap with 200 images used for training, as shown in Figure 5. This paper selects the WGAN algorithm proposed in reference [23] and the basic RED-CNN algorithm proposed in reference [28] as the comparison method. Figure 6 shows the denoising effect by taking the test chart (a) and test chart (c) of Figure 5 as examples.

WGAN and basic RED-CNN are very similar to the proposed improved RED-CNN in subjective visual effects after denoising. However, after careful observation of these pictures, it is found that our proposed network is slightly better than the two in terms of detail retention.

4.4. Objective Indicators. For quantitative analysis, PSNR and SSIM are used to evaluate the denoising effect of LDCT images. Detailed data of the test chart are shown in Table 3. As can be seen from Table 3, our proposed method outperforms WGAN and basic RED-CNN in eight test images in objective indicators. The averaged PSNR is 1.865 dB, higher than that of the WGAN method, and 1.174 dB, higher than that of the RED-CNN method. SSIM is slightly ahead of WGAN in terms of indicators.

4.5. Complexity Comparison. The network complexity E can be defined by the following equation:

$$E = O\left\{\sum_{l} n_{l-1} f_l^2 n_l\right\} n_l, \tag{10}$$

where n_l is the number of feature maps output by the l layer of the network and f_l is the size of the l layer convolution kernel.

By calculating the average time consumption of 30 forward propagation for each test chart, the average CPU time consumption data is obtained. By calling the Caffe interface in python, the average GPU time consumption is obtained, as shown in Table 4.

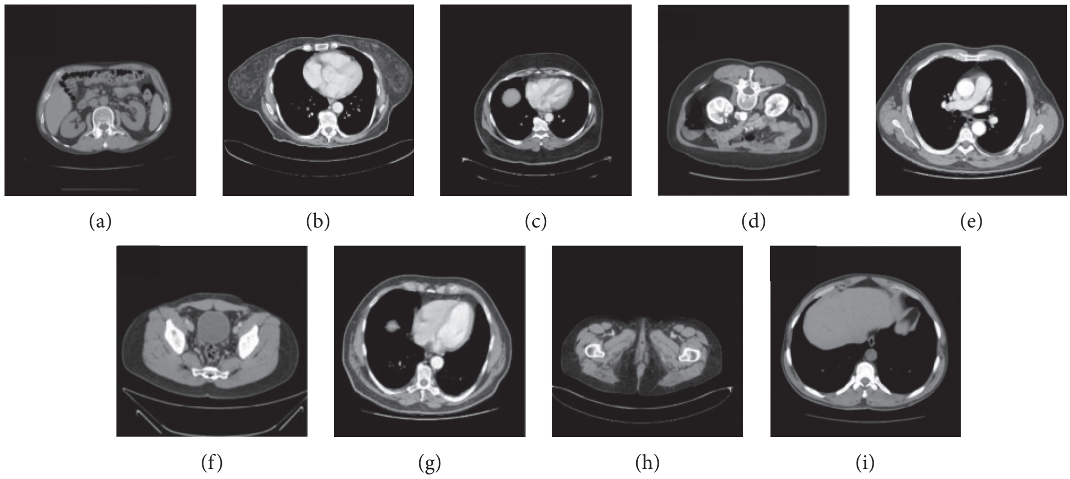

Figure 5: Experimental data.

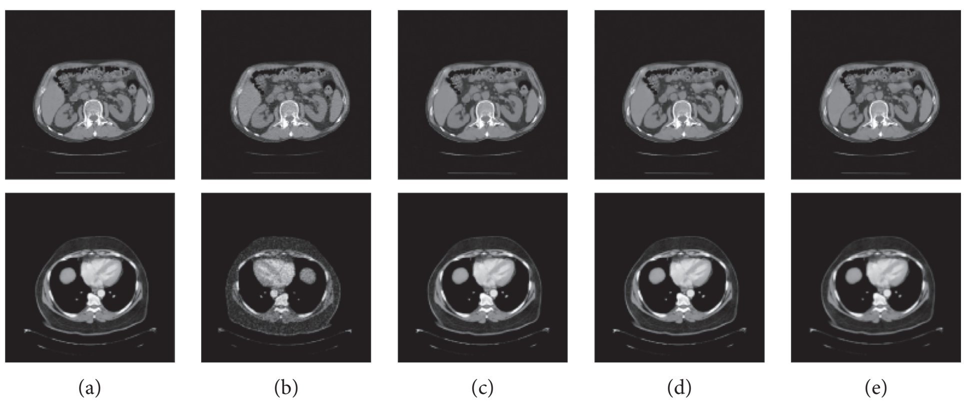

Figure 6: Denoising results comparison images. (a) Original CT image. (b) Low-dose CT image. (c) WGAN. (d) RED-CNN. (e) Proposed algorithm.

Table 3: PSNR and SSIM in experiments.

Number	Index	LDCT image	WGAN [23]	RED-CNN [28]	Proposed algorithm
a	PSNR/dB	25.375	28.346	28.783	30.245
	SSIM	0.768	0.912	0.921	0.942
b	PSNR/dB	24.653	26.398	29.012	29.374
	SSIM	0.731	0.892	0.901	0.911
c	PSNR/dB	24.987	29.321	30.876	31.238
	SSIM	0.763	0.924	0.932	0.953
d	PSNR/dB	23.826	27.873	28.987	30.872
	SSIM	0.711	0.865	0.912	0.934
e	PSNR/dB	30.145	32.146	31.273	31.698
	SSIM	0.863	0.962	0.920	0.925
f	PSNR/dB	27.836	30.124	30.023	30.836
	SSIM	0.792	0.845	0.823	0.912
g	PSNR/dB	26.834	29.834	29.867	31.345
	SSIM	0.723	0.835	0.844	0.902
h	PSNR/dB	26.214	30.013	29.839	31.314
	SSIM	0.719	0.862	0.843	0.909
i	PSNR/dB	22.245	26.215	27.831	30.134
	SSIM	0.712	0.821	0.873	0.901
Average	PSNR/dB	25.791	28.919	29.610	30.784
	SSIM	0.75	0.876	0.885	0.916

Table 4: Computational complexity comparison.

Parameter	WGAN	RED-CNN	Proposed algorithm
Complexity	3,713,000	2,703,000	2,383,000
Time/s(CPU)	15.923	8.344	3.921
Time/s(GPU)	6.213	2.981	0.352

Table 4 demonstrates that RED-CNN can save 40% of the time compared to WGAN. At the same time, the proposed method reduces the complexity of the algorithm through the notion of recursion, speeds up the convergence speed compared with the original RED-CNN, and reduces the time consumption by 75% compared with WGAN. Furthermore, it has better performance on GPU.

5. Conclusion

Due to the difficulty of modeling statistical features in the image domain, the existing methods of directly processing reconstructed images cannot eliminate image noise while maintaining image structure details. Deep learning offers great potential for the research in noise artifact restoration of LDCT images. In an attempt to overcome the problems of poor denoising performance for traditional algorithms, complex network model, and difficulty in training, this paper proposes a CT image denoising method based on an improved RED network. It is mainly divided into three parts: (1) the RED network is used to restore noisy CT images, and the notion of recursion is integrated into the RED network to reduce network complexity and boost operation efficiency; (2) with the advantages of MSE loss function and perceptual loss function combined, a joint loss function is proposed, and the edge and detail information are reconstructed through pixel-by-pixel comparison and minimizing the difference in image semantic features; and (3) the CT noise images generated by the RED network based on clustering segmentation technology are optimized to further suppress the artifacts and restore details. As shown in experimental simulation analysis of the TCGA-COAD clinical data set, the proposed method can generate higher PSNR and SSIM when compared with the WGAN method and original RED-CNN method. Furthermore, our method is low in algorithm complexity and can be well adapted to practical applications.

In the future, our proposed method is applicable to scenarios involving noise suppression, structure preservation, damage detection, and so on.

Data Availability

The data included in this paper are available without any restriction.

Conflicts of Interest

The author declares that there are no conflicts of interest regarding the publication of this paper.

Acknowledgments

This work was supported by the cooperative education project of the Ministry of Education (No. 201702119071) and the Research and Development of Information Visualization of Shangluo Tailings Resources Based on WebGIS (No. SK2014-1-211).

References

[1] M. Li, W. Hsu, X. Xie, J. Cong, and W. Gao, "SACNN: self-attention convolutional neural network for low-dose CT denoising with self-supervised perceptual loss network," *IEEE Transactions on Medical Imaging*, vol. 39, no. 7, pp. 2289–2301, 2020.

[2] Z. Li, J. Huang, L. Yu, Y. Chi, and M. Jin, "Low-dose CT image denoising using cycle-consistent adversarial networks," in *Pro2019 IEEE Nuclear Science Symposium and Medical Imaging Conference (NSS/MIC)*, pp. 1–3, IEEE, Manchester, United Kingdom, October 2019.

[3] S. Wang, Q. Wang, Y. Shao et al., "Iterative label denoising network: segmenting male pelvic organs in CT from 3D bounding box Annotations," *IEEE Transactions on Biomedical Engineering*, vol. 67, no. 10, pp. 2710–2720, 2020.

[4] X. Jia, Z. Bian, J. He et al., "Texture-preserved low-dose CT reconstruction using region recognizable patch-priors from previous normal-dose CT images," in *Pro2016 IEEE Nuclear Science Symposium, Medical Imaging Conference and Room-Temperature Semiconductor Detector Workshop (NSS/MIC/RTSD)*, pp. 1–4, IEEE, Strasbourg, France, October 2016.

[5] X. Zheng, S. Ravishankar, Y. Long, and J. A. Fessler, "PWLS-ULTRA: an efficient clustering and learning-based approach for low-dose 3D CT image reconstruction," *IEEE Transactions on Medical Imaging*, vol. 37, no. 6, pp. 1498–1510, 2018.

[6] Y. Kang, J. Liu, Y. Gu, and Y. Chen, "Sparse tensor constrained for low dose CT reconstruction," in *Pro2019 IEEE 16th International Symposium on Biomedical Imaging (ISBI 2019)*, pp. 1660–1663, IEEE, Venice, Italy, April 2019.

[7] M. A. Gholizadeh, J. Alirezaie, and P. Babyn, "Low-dose CT denoising with dilated residual network," in *Pro2018 40th Annual International Conference of the IEEE Engineering in Medicine and Biology Society (EMBC)*, pp. 5117–5120, IEEE, Honolulu, HI, USA, July 2018.

[8] Q. Yang, P. Yan, Y. Zhang et al., "Low-dose CT image denoising using a generative adversarial network with Wasserstein distance and perceptual loss," *IEEE Transactions on Medical Imaging*, vol. 37, no. 6, pp. 1348–1357, 2018.

[9] H. Yuan, J. Jia, and Z. Zhu, "SIPID: a deep learning framework for sinogram interpolation and image denoising in low-dose CT reconstruction," in *Pro2018 IEEE 15th International Symposium on Biomedical Imaging (ISBI 2018)*, pp. 1521–1524, IEEE, Washington, DC, USA, April 2018.

[10] X. Yin, J. L. Coatrieux, Q. Zhao et al., "Domain progressive 3D residual convolution network to improve low-dose CT imaging," *IEEE Transactions on Medical Imaging*, vol. 38, no. 12, pp. 2903–2913, 2019.

[11] Y. Chen, X. Bao, X. Yin, L. Luo, and W. Chen, "Improving low-dose X-ray CT images by weighted intensity averaging over large-scale neighborhoods," in *Pro2010 3rd International Congress on Image and Signal Processing*, pp. 727–729, IEEE, Yantai, China, October 2010.

[12] Y. Wang, Y. Shao, Q. Zhang et al., "Noise removal of low-dose CT images using modified smooth patch ordering," *IEEE Access*, vol. 5, Article ID 26092, 2017.

[13] K. Thakur, O. Damodare, and A. Sapkal, "Hybrid method for medical image denoising using shearlet transform and bilateral filter," in *Pro2015 International Conference on*

Information Processing (ICIP), pp. 220–224, IEEE, Pune, India, December 2015.

[14] Y. Zhang, H. Lin, Y. Li, and H. Ma, "A patch based denoising method using deep convolutional neural network for seismic image," *IEEE Access*, vol. 7, Article ID 156883, 2019.

[15] W. Liu, J. Rong, P. Gao, Q. Liao, J. Chun, and H. Lu, "Sparse-view reconstruction from restored low-dose CT projections," in *Pro2013 IEEE Nuclear Science Symposium and Medical Imaging Conference (2013 NSS/MIC)*, pp. 1–4, IEEE, Seoul, Korea, October 2013.

[16] Y. Chen, L. Shi, Y. Hu et al., "Confidence Weighted Dictionary Learning algorithm for low-dose CT image processing," in *Pro2013 IEEE Nuclear Science Symposium and Medical Imaging Conference (2013 NSS/MIC)*, pp. 1–4, IEEE, Seoul, Korea, October 2013.

[17] F. Y. Fei, Y. L. Limin, and L. Luo, "CT image denoising based on sparse representation using global dictionary," in *Pro2013 ICME International Conference on Complex Medical Engineering*, pp. 408–411, IEEE, Beijing, China, May 2013.

[18] L. Shi, Y. Chen, H. Shu, L. Luo, C. Toumoulin, and J. L. Coatrieux, "Low-dose CT image processing using artifact suppressed dictionary learning," in *Pro2014 IEEE 11th International Symposium on Biomedical Imaging (ISBI)*, pp. 1127–1130, IEEE, Beijing, China, April 2014.

[19] A. Borsdorf, R. Raupach, T. Flohr, and J. Hornegger, "Wavelet based noise reduction in CT-images using correlation analysis," *IEEE Transactions on Medical Imaging*, vol. 27, no. 12, pp. 1685–1703, 2008.

[20] A. M. Hasan, A. Melli, K. A. Wahid, and P. Babyn, "Denoising low-dose CT images using multiframe Blind Source separation and block matching filter," *IEEE Transactions on Radiation and Plasma Medical Sciences*, vol. 2, no. 4, pp. 279–287, July 2018.

[21] W. Chen, Y. Shao, L. Jia et al., "Low-dose CT image denoising model based on sparse representation by stationarily classified sub-dictionaries," *IEEE Access*, vol. 7, Article ID 116859, 2019.

[22] L. Jia, Q. Zhang, Y. Shang et al., "Denoising for low-dose CT image by discriminative weighted nuclear Norm minimization," *IEEE Access*, vol. 6, Article ID 46179, 2018.

[23] H. S. Park, J. Baek, S. K. You, J. K. Choi, and J. K. Seo, "Unpaired image denoising using a generative adversarial network in X-ray CT," *IEEE Access*, vol. 7, Article ID 110414, 2019.

[24] Y. Ma, B. Wei, P. Feng, P. He, X. Guo, and G. Wang, "Low-dose CT image denoising using a generative adversarial network with a hybrid loss function for noise learning," *IEEE Access*, vol. 8, Article ID 67519, 2020.

[25] D. Ren, J. Li, L. Li, H. Pan, and M. Shu, "Low dose CT image denoising using multi-level feature fusion network and edge constraints," in *Pro2019 IEEE International Conference on Bioinformatics and Biomedicine (BIBM)*, pp. 727–731, IEEE, San Diego, CA, USA, November 2019.

[26] L. L. Chen, S. P. Gou, Y. Yao, J. Bai, L. Jiao, and K. Sheng, "Denoising of low dose CT image with context-based BM3D," in *Pro2016 IEEE Region 10 Conference (TENCON)*, pp. 682–685, IEEE, Singapore, November 2016.

[27] W. Yang, H. Zhang, J. Yang et al., "Improving low-dose CT image using residual convolutional network," *IEEE Access*, vol. 5, Article ID 24698, 2017.

[28] H. Chen, Y. Zhang, M. K. Kalra et al., "Low-dose CT with a residual encoder-decoder convolutional neural network," *IEEE Transactions on Medical Imaging*, vol. 36, no. 12, pp. 2524–2535, 2017.

[29] Q. Xiang and X. Pang, "Improved denoising auto-encoders for image denoising," in *Pro11th International Congress on Image and Signal Processing, BioMedical Engineering and Informatics (CISP-BMEI)*, pp. 1–9, IEEE, Beijing, China, October 2018.

[30] J. M. Parmar and S. A. Patil, "Performance evaluation and comparison of modified denoising method and the local adaptive wavelet image denoising method," in *Pro2013 International Conference on Intelligent Systems and Signal Processing (ISSP)*, pp. 101–105, IEEE, Vallabh Vidyanagar, India, March 2013.

Hindawi
Journal of Healthcare Engineering
Volume 2023, Article ID 9760590, 1 page
https://doi.org/10.1155/2023/9760590

Retraction

Retracted: Detection of 3D Arterial Centerline Extraction in Spiral CT Coronary Angiography

Journal of Healthcare Engineering

Received 10 October 2023; Accepted 10 October 2023; Published 11 October 2023

Copyright © 2023 Journal of Healthcare Engineering. This is an open access article distributed under the Creative Commons Attribution License, which permits unrestricted use, distribution, and reproduction in any medium, provided the original work is properly cited.

This article has been retracted by Hindawi following an investigation undertaken by the publisher [1]. This investigation has uncovered evidence of one or more of the following indicators of systematic manipulation of the publication process:

(1) Discrepancies in scope
(2) Discrepancies in the description of the research reported
(3) Discrepancies between the availability of data and the research described
(4) Inappropriate citations
(5) Incoherent, meaningless and/or irrelevant content included in the article
(6) Peer-review manipulation

The presence of these indicators undermines our confidence in the integrity of the article's content and we cannot, therefore, vouch for its reliability. Please note that this notice is intended solely to alert readers that the content of this article is unreliable. We have not investigated whether authors were aware of or involved in the systematic manipulation of the publication process.

In addition, our investigation has also shown that one or more of the following human-subject reporting requirements has not been met in this article: ethical approval by an Institutional Review Board (IRB) committee or equivalent, patient/participant consent to participate, and/or agreement to publish patient/participant details (where relevant).

Wiley and Hindawi regrets that the usual quality checks did not identify these issues before publication and have since put additional measures in place to safeguard research integrity.

We wish to credit our own Research Integrity and Research Publishing teams and anonymous and named external researchers and research integrity experts for contributing to this investigation.

The corresponding author, as the representative of all authors, has been given the opportunity to register their agreement or disagreement to this retraction. We have kept a record of any response received.

References

[1] W. Cai, Y. Wang, L. Gu, X. Ji, Q. Shen, and X. Ren, "Detection of 3D Arterial Centerline Extraction in Spiral CT Coronary Angiography," *Journal of Healthcare Engineering*, vol. 2021, Article ID 2670793, 16 pages, 2021.

Hindawi
Journal of Healthcare Engineering
Volume 2021, Article ID 2670793, 16 pages
https://doi.org/10.1155/2021/2670793

RETRACTED

Research Article

Detection of 3D Arterial Centerline Extraction in Spiral CT Coronary Angiography

Wenjuan Cai[1] **Yanzhe Wang**[1] **Liya Gu**[1] **Xuefeng Ji**[1] **Qiusheng Shen**[1] **and Xiaogang Ren**[1,2]

[1]*Changshu Hospital of Chinese Medicine, Changshu 215516, Jiangsu, China*
[2]*School of Information and Control Engineering, China University of Mining and Technology, Xuzhou 221116, Jiangsu, China*

Correspondence should be addressed to Qiusheng Shen; csfy027@njucm.edu.cn

Received 18 July 2021; Revised 8 August 2021; Accepted 12 August 2021; Published 23 August 2021

Academic Editor: Gu Xiaoqing

Copyright © 2021 Wenjuan Cai et al. This is an open access article distributed under the Creative Commons Attribution License, which permits unrestricted use, distribution, and reproduction in any medium, provided the original work is properly cited.

This paper presents an in-depth study and analysis of the 3D arterial centerline in spiral CT coronary angiography, and constructs its detection and extraction technique. The first time, the distance transform is used to complete the boundary search of the original figure; the second time, the distance transform is used to calculate the value of the distance transform of all voxels, and according to the value of the distance transform, unnecessary voxels are deleted, to complete the initial contraction of the vascular region and reduce the computational consumption in the next process; then, the nonwitnessed voxels are used to construct the maximum inner joint sphere model and find the skeletal voxels that can reflect the shape of the original figure. Finally, the skeletal lines were optimized on these initially extracted skeletal voxels using a dichotomous-like principle to obtain the final coronary artery centerline. Through the evaluation of the experimental results, the algorithm can extract the coronary centerline more accurately. In this paper, the segmentation method is evaluated on the test set data by two kinds of indexes: one is the index of segmentation result evaluation, including dice coefficient, accuracy, specificity, and sensitivity; the other is the index of clinical diagnosis result evaluation, which is to refine the segmentation result for vessel diameter detection. The results obtained in this paper were compared with the physicians' labeling results. In terms of network performance, the Dice coefficient obtained in this paper was 0.89, the accuracy was 98.36%, the sensitivity was 93.36%, and the specificity was 98.76%, which reflected certain advantages in comparison with the advanced methods proposed by previous authors. In terms of clinical evaluation indexes, by performing skeleton line extraction and diameter calculation on the results obtained by the segmentation method proposed in this paper, the absolute error obtained after comparing with the diameter of the labeled image was 0.382 and the relative error was 0.112, which indicates that the segmentation method in this paper can recover the vessel contour more accurately. Then, the results of coronary artery centerline extraction with and without fine branch elimination were evaluated, which proved that the coronary artery centerline has higher accuracy after fine branch elimination. The algorithm is also used to extract the centerline of the complete coronary artery tree, and the results prove that the algorithm has better results for the centerline extraction of the complete coronary vascular tree.

1. Introduction

The growth of urban economies and the accelerated aging of the population, the prevalence of poor lifestyles, and the continued growth of risk factors that induce cardiovascular disease make it the number one cause of death in humans. According to World Health Organization statistics, in 2018, more than 17.5 million people died of heart-related diseases worldwide, accounting for 31% of the total death population. Among them, more than 7.4 million people suffered from coronary heart disease, which is 42% of all deaths from heart disease. Initial results have been achieved in the treatment of heart-related diseases, but the overall situation remains grim. In recent years, the total number of diseases and deaths from heart-related diseases has continued to increase in our country [1]. It is estimated that presently 290 million people are afflicted with heart-related diseases within our country, close to 21% of the total population. Among these patients, the vast majority suffer from hypertension, amounting to 270 million, and the population suffering from coronary heart disease amounts to 11 million [2]. Heart-related diseases account for 40% of the composition of the population's mortality factors, more than other diseases such as cancer. Experts predict that the population suffering from heart-related diseases will continue to increase in the next 10 years, and the burden of this disease is increasing. Therefore, how to effectively combat heart disease has become a serious issue. If an accurate diagnosis system can be established for heart diseases, targeted treatment can be implemented, and it will be of great importance to reduce the mortality rate due to heart diseases and thereby improve people's quality of life. With the advancement of technology in the field of medical image processing, its role in research and practice is becoming increasingly prominent [3]. Through the combination of computer science, mathematics, and imaging, medical images are analyzed to help locate lesions and improve the speed and accuracy of clinical diagnosis. In the analysis of coronary morphology, the extraction of the vascular tree is a fundamental problem. Accurate segmentation is a prerequisite for describing vascular geometric information and plays a key role in objectively and accurately assessing the extent of vascular lesions [4]. Most coronary vascular segmentation methods are for single-frame (static) images and are a well-established and effective method for helping to identify vascular lesions, but the accuracy of diagnostic results is compromised by temporal limitations that result in a lack of disease information. Therefore, describing the dynamic motion and changes of the vascular tree in the images of contrast sequences has a more important applied research value in medical clinical diagnosis.

Medical images are usually acquired after the completion of a medical imaging examination, and the process of reprocessing such images is often referred to as post-processing of medical images. At present, almost all imaging devices can directly obtain digital medical images, which provides great convenience for postprocessing work. The application of medical image post-processing is mainly for clinicians or imaging technologists, who usually first apply medical image post-processing software to process medical images and then provide clinicians with more advanced diagnostic information. Medical image postprocessing mainly includes medical image enhancement, segmentation, alignment and fusion, visualization techniques, and data compression [5]. Medical image enhancement is mainly to improve the image contrast, make the image clearer, and improve the visual effect of the image. Image alignment and fusion is the correspondence of multiple images in terms of spatial location to combine information from multiple modalities or multiple periods to provide more diagnostic information, such as aligning structural imaging and functional images in MRI [6]. Data compression is used to reduce the amount of data for storage and transmission. Segmentation and visualization are important elements in medical image post-processing, which play a crucial role in modern medical diagnosis and are directly related to the doctor's diagnostic effect [7]. Usually, doctors are interested in an organ or structure, but medical images also contain surrounding tissues, which makes it difficult for doctors to observe the organ of interest directly. For this reason, image segmentation techniques are needed to separate the organ or tissue of interest from the surrounding tissues, which can facilitate observation on the one hand, and allow measurement and quantitative calculation of organ or tissue information such as volume and organ modeling on the other. Medical image visualization technology, on the other hand, is a better way to display the organ or structure of interest in multiple angles and forms, providing doctors with intuitive diagnostic information and thus improving their diagnostic efficiency and accuracy. Medical image segmentation is often considered as the basis of visualization.

Medical image segmentation and visualization techniques are currently widely studied and applied [8]. Cardiac CT angiography (CTA) technology and MRI are widely used in the diagnosis and treatment of cardiac diseases and neurological diseases of the brain [9, 10], respectively, and rely heavily on segmentation and visualization techniques in their diagnosis [11]. In the case of the heart, for example, techniques such as cardiac segmentation, coronary artery segmentation, cardiac body mapping, and coronary surface reconstruction are usually required. The coronary centerline also has an irreplaceable role in the visualization and reconstruction of the coronary arteries. The techniques of decortication and perivascular gap segmentation are mainly studied on brain MRI images and the segmentation of coronary artery lumen and its visualization on cardiac CTA images. Among them, decriminalization is the basic processing step for brain image segmentation, quantification, and other operations, and decriminalization techniques are used in most structural MRI image analyses, while the perivascular gap is associated with a variety of neurological disorders, such as cognitive impairment, brain developmental diseases, and atherosclerosis. Studying the segmentation of the perivascular gap is a prerequisite for quantitative analysis. Currently, several techniques for visual reconstruction based on CTA data have been used in clinical practice for the diagnosis of coronary artery disease, which includes surface reconstruction techniques (CPR), maximum signal projection (MIP), volume mapping techniques (Volume Rendering Techniques), and multiplanar reconstruction techniques (MPR), especially in the reconstruction of CPR and MPR images. The central line of the coronary artery plays a great role in the reconstruction of CPR and MPR images [7]. Also, the central line of coronary arteries can provide preoperative path planning and intraoperative path guidance for coronary surgical treatments, such as Percutaneous Coronary Intervention (PCI) and Coronary Artery Bypass Grafting (CABG). Therefore, obtaining an accurate coronary centerline is of great importance for clinical treatment. In addition, the central line can also be used as a starting point for the segmentation of coronary arteries.

2. Current Status of Research

Since the imaging view of CT completely covers the heart side, the structures presented in the image include a variety of tissues such as bones, muscles, organs, and blood vessels; coupled with the fact that the dose of contrast agent required

RETRACTED

for imaging affects the picture quality, it makes it further difficult to extract the centerline of the coronary arteries [12]. The existing methods of centerline extraction are divided into three categories according to the degree of human intervention: fully automatic extraction, semi-automatic extraction, and manual extraction [13]. Among these three methods, the manual extraction of the centerline is undoubtedly a simple and reliable method, but when a large amount of data is encountered, the manual extraction method will consume a lot of human and material resources, so it is especially important to study the fully automatic and semi-automatic extraction algorithms [14]. The fully automatic method generally refers to the process of extracting the centerline without any human intervention, and the algorithm automatically extracts the centerline of the coronary artery based on the input data information; the more classical methods include the method proposed by Freiman to further extract the centerline based on the extraction of the coronary vascular tree by fitting the cylindrical model; the semi-automatic method refers to the process of vessel extraction [15]. The semi-automatic method refers to the method in which one or several seed points need to be artificially specified as reference points for centerline extraction, and the algorithm extracts the centerline in the image data based on the artificially provided reference points, such as the method proposed by Kojima et al. to extract the centerline of coronary arteries after segmenting the aorta and coronary arteries and performing 3D reconstruction by using the local gray values of the vessels and the orientation of the vessels to select the starting point of the iteration [16]. The various automatic or semi-automatic methods for extracting the centerline can be classified into the following six types according to the extraction ideas they use: topology refinement-based methods, distance transformation-based methods, tracing-based methods, fast marching algorithm-based methods, deep learning-based methods, and other methods [17]. As an important tool for diagnosing cardiovascular diseases, coronary angiography has an irreplaceable position in clinical practice, so the processing technology for coronary angiography images is always a hot spot for research [18]. Traditional coronary angiography segmentation algorithms can be classified into three types based on the similarity of neighborhoods: boundary-based, region-based, and integrated with specific theories [19]. With the development of the artificial intelligence field and the increase of data volume, the breakthrough of convolutional neural networks (CNNs) in the field of image processing is also bringing great changes to the direction of medical image processing [20]. The main method of convolutional neural networks applied to medical image processing is semantic segmentation, which is the pixel-level classification of images by different model classifiers. In the following section, we present representative methods from traditional and deep learning approaches, as well as the problems in research.

With the development in the field of computer vision, convolutional neural networks have brought revolutionary disruptions to large-scale image processing, and related methods have made great progress in the field of medical image processing. The segmentation of medical images belongs to the category of semantic segmentation in deep learning, which essentially classifies each pixel [21]. In recent years, semantic segmentation has made great progress, and Shi et al. proposed the U-Net network, which has a more regular network structure, and compared with FCN, the more significant change is in the upsampling stage; the upsampling layer of U-Net network also includes many layers of features, and then the features obtained from each upsampling layer are added to the decoder to obtain more accurate features [22]. The U-Net network has been widely used in medical image segmentation, such as cell segmentation, retina, and other blood vessel segmentation fields, and has achieved good segmentation results [23]. The second type is the inflated convolution structure, represented by the Deep Lab network and its two improved versions, and the Refine Net network. Until 2016, Tahoces et al. and two enhanced versions were developed. This network employs convolution with voids rather than traditional convolutional computing, employs various scales to improve spatial resolution of segmentation findings [24], and uses conditional random fields as postprocessing to refine the results [25]. Advances in modern medical imaging technology provide higher resolution medical image data for the diagnostic process while analyzing raw data is inefficient. Visualization technology plays an important role in providing doctors with fast and accurate medical images in a noninvasive manner, providing aids to diagnosis, surgical navigation, treatment guidance, and medical teaching. Curvilinear reconstruction, a technique that uses centerlines to visualize tubular structures, has become a must-have feature of medical workstations, with features such as length retention, allowing the entire vessel or even the entire vascular tree to be displayed on a single image [26]. The main ones currently used are projection CPR, extension CPR, and straightening CPR. Traditional single-vessel CPR plays an important role in vascular diagnosis, while multipath CPR can also play a navigational role. In addition, spherical CPR demonstrates multiple vessels while preserving the spatial structure of the vessels well [27]. The application of virtual endoscopy with face-drawing or body-drawing, on the other hand, is a technique that incorporates a variety of techniques implemented in image processing and virtual reality technology to simulate traditional optical endoscopy, overcoming traditional invasive examination methods, and is mainly applied to organs with cavernous structures, such as the trachea, esophagus, colon, andblood vessels, etc. This technique can provide physicians with navigation within tubular structures with a high degree of realism.

Coronary artery structure is complex, individual vascular variation is large, and its grayscale is affected by abnormal tissues such as plaque, stenosis, and stent, and the grayscale range is large, and coronary lumen segmentation is a difficult task. In this study, the coarse segmentation results of coronary arteries and the vascular centerline calculated from this result have been obtained, and this paper mainly uses these data for further segmentation to obtain the accurate segmentation results of the vascular lumen. The main method is to segment the vessel lumen on the vessel cross

RETRACTED

section, so the cross-sectional image needs to be acquired first. Based on the straightening reconstruction algorithm, this paper first constructs the straightened image of the vessel and then segments the vessel lumen layer by layer on the cross section. The traditional CPR method, including extension CPR and straightening CPR, is implemented, and then a spherical CPR method is implemented and improved. Firstly, the conventional extended CPR requires projection of the original centerline at a specified angle, and then the original centerline is sampled at equal intervals using the projected trajectory as the standard, followed by determining the extent of the resulting image and filling it with gray values. Straightening CPR requires sampling the original centerline at equal intervals, establishing a local coordinate system along the centerline, and ensuring that the axes are "parallel" to each other, and using a suitable interpolation algorithm to ensure image quality and efficiency. The spherical CPR can display the whole coronary tree on a single image, and the key issues of the algorithm are the acquisition of the centerline envelope surface and the transformation from globe mode to map mode.

3. Design of Detection and Extraction of the 3D Arterial Centerline in Spiral CT Coronary Angiography

3.1. Spiral CT Coronary Angiogram Preprocessing. Generally, there are two methods for coronary artery centerline extraction: the first one is to directly extract the coronary artery seen in the original image. This has the advantage of not having to segment the coronary artery region. But, the original CT laminar image is affected by noise and there are more irrelevant regions, which often interferes with the extraction results. The other method is to segment the coronary artery first and then use the completed segmented image for centerline extraction. Although this method increases the segmentation step, it has a greater improvement in time and accuracy because there are fewer operations on voxels during centerline extraction [28]. The two proposed algorithms perform centerline extraction in the segmented coronary artery region, so the image needs to be segmented first. Since the imaging principle of CT is X-ray imaging, according to this imaging principle, there is often more noise on the image; in addition, the quality of CTA is influenced by the contrast agent, and there may be blurring in the vascular region, which will often lead to large errors in the segmentation results. So, the necessary denoising and enhancement of the vascular region must be performed before segmentation.

The Anisotropic Diffusion Filter (ADF) is a null domain filter proposed by Gerig et al. Unlike other filters that have only a single filtering effect on the whole image, the anisotropic diffusion filter has different filtering effects in each direction of the image, and these different filtering effects are determined by the diffusion function [29]. The basic theoretical derivation of anisotropic diffusion filtering is presented below, and the process of filtering an image using an anisotropic diffusion filter is

$$u_t = u_{xx}^2. \quad (1)$$

According to the anisotropic diffusion theory, equation (2) can be rewritten as

$$\frac{\partial}{\partial t} u(x,t) = \operatorname{div}(c(x,t)\Delta u(x,t)), \quad (2)$$

where $u(x,t)$ denotes the grayscale of the image, $\Delta u(x,t)$ denotes the gradient image of $u(x,t)$, div denotes the scattering operator, and $c(x,t)$ denotes the diffusion function. For the choice of the diffusion function, Gerig and Kubler give two different functions for reference:

$$c_1(x,t) = exp\left(-\left(\frac{\left|\Delta u(x,t)^2\right|}{k^2}\right)\right), \quad (3)$$

$$c_1(x,t) = \frac{\left(\left|\Delta u(x,t)^2\right|/k^2\right) + 1}{1 - \left(\left|\Delta u(x,t)^2\right|/k^2\right)}, \quad (4)$$

where k is a constant associated with the noise level and the boundary intensity, and here $k = \min|\nabla u|$ is chosen. Solving the partial differential equation of equation (4) with the 4-neighborhood image as an example, the numerical expression required in the iterative process of the algorithm can be obtained:

$$u(t-\Delta t) \approx u(t) - \Delta t \frac{\partial}{\partial t} u(t), \quad (5)$$

where ϕ denotes the diffusion flux, and its expression is

$$\phi = c\Delta u. \quad (6)$$

In 3D images in the medical field, the tissue structure of the human body can be roughly divided into disk-like, tubular, and patchy structures. Therefore, the Hessian matrix of a pixel can be calculated to determine the shape of the tissue structure to which the pixel belongs based on the magnitude, and positive and negative cases of the absolute value of its eigenvalue. N means almost zero, L means small absolute value, H means large absolute value, and "+/−" indicates the positive and negative cases of the eigenvalues, which are indicated by the brightness of the blood vessels: bright blood vessels are negative and darker ones are positive. Therefore, it can be seen from the Figure 1 that the absolute value of $\lambda 1$ should be small and close to 0; the absolute values of $\lambda 2$ and $\lambda 3$ should be much larger than $\lambda 1$, and the positivity and negativity are the same, so the relationship of the eigenvalues of the vascular structure is expressed by mathematical expressions, as shown in Figure 1.

Due to the small amount of coronary angiography image data, data enhancement of sample images is needed to enhance the image quality to improve the generalization ability of the neural network model. In this article, firstly, specular symmetry, image rotation, and contrast stretching methods are used to enhance the quality of the sample images. Subsequently, the full convolutional segmentation

RETRACTED

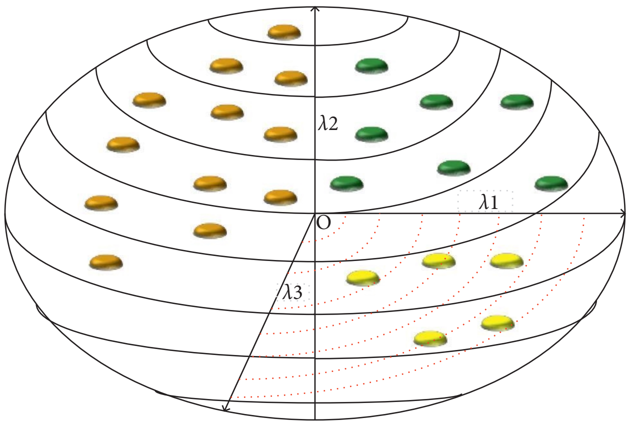

Figure 1: Ellipsoidal model.

network VGG-seg is proposed, which is based on a modification of the VGG-16 network by removing the final fully connected layer and deconvoluting after each pooling layer, and linearly summing the results of the deconvolution of each output layer separately to classify each pixel. In the learning process, the pretraining results on ImageNet were first used as the starting network, and then this initialized model was applied to the fully convolutional segmentation network, and 109 X-ray angiography sequences from the training set were used for training to extract blood vessels; finally, the model was tested using 40 coronary angiography sequences from the test set to achieve real-time vessel segmentation [30]. In deep learning, the number of samples is generally in great demand, and the more the number of samples and the richer the variability, the stronger the generalization ability of the model and the better the effect of the network model obtained by training. Fully convolutional neural network-based coronary angiography image vessel segmentation requires a large amount of real patient data to train the network, and it is very difficult to obtain sufficient sample sets, so image enhancement of existing data is required to lay a good foundation for the subsequent model training.

To increase the difference in gray level between pixels and highlight the blood vessels, enhancement of the image is achieved by using the gray-level change method. The grayscale transformation method alters the contrast of an image by changing the range of grayscale levels and is a histogram change-based method. In theory, the value range of image grayscale is [0, 255], that is, a total of 256 levels, and in the imaging process, due to some factors, such as lighting and equipment quality, the grayscale level of the image is often less than 256, that is, the grayscale range of the image will be compressed to [0, 255] within a certain subinterval, which is the fundamental reason for the low contrast of the image. To increase the contrast, we need to increase the grayscale value range, that is, to map the smaller grayscale range to a larger range by the value range stretching operation. The general case of the grayscale mapping function is defined in equation (7).

$$f = \frac{d + c}{b - a}(g + a) - c. \tag{7}$$

Based on the results of the above preprocessing, the study of the coronary angiography sequence segmentation method will be started in the following. Image segmentation is a prerequisite for image recognition and analysis, to divide the image into multiple parts according to the needs and make it easy to analyze. The essence of image segmentation is to cluster the pixels containing the same characteristics into one class based on their characteristics. A convolutional neural network automatically extracts features by simulating the process of human brain cognition for the ultimate purpose of classification or prediction [31]. The development of convolutional neural networks has revolutionized the field of image segmentation by automatically extracting features of images through multilayer convolutional computation to achieve the pixel-level classification of images, i.e., to achieve image segmentation. Convolutional neural networks have automatic, fast, and accurate characteristics in processing large-scale image data, and have unparalleled advantages over traditional methods, and have achieved wide application in the field of image segmentation.

The human head is protected by the cranium so that its morphological structure is not as susceptible to deformation as the heart and remains largely stable, and therefore can be considered for cranial debridement using an alignment method. Many alignment-based decriminalization methods exist, which are often computationally intensive but have stable results. In this section, the initial mask of the brain parenchyma is first calculated using the alignment method, and then the initial mask is improved using the level set method to generate the final mask.

Image alignment is the process of locating a spatial transformation that maps points in one image to points in another image, connecting points in both images that correspond to the same spatial position, and aligning the two images in a specified space. For medical images, the result of alignment should make the points with diagnostic significance in both images match. Taking the two-dimensional image alignment as an example, as shown in Figure 2, the alignment process can be described as equation (8) by noting the reference image and the image to be aligned as $I_r(x, y)$ and $I_x(x, y)$, respectively.

$$I_x(x, y) = g(I_r(T(x, y))), \tag{8}$$

where $T(x, y)$ denotes the spatial transformation and the function $g(I_r(T(x, y)))$ denotes the grayscale transformation; usually, the grayscale transformation is not necessary and the key is to find the spatial transformation between the two images. The solution of the spatial transformation is usually treated as an optimization problem, which is usually achieved by iteration.

The image alignment process generally consists of two steps: first, extracting the feature information of the image to form a feature space; then, defining a similarity criterion from the feature space and determining a spatial transformation so that the image can achieve the defined similarity

RETRACTED

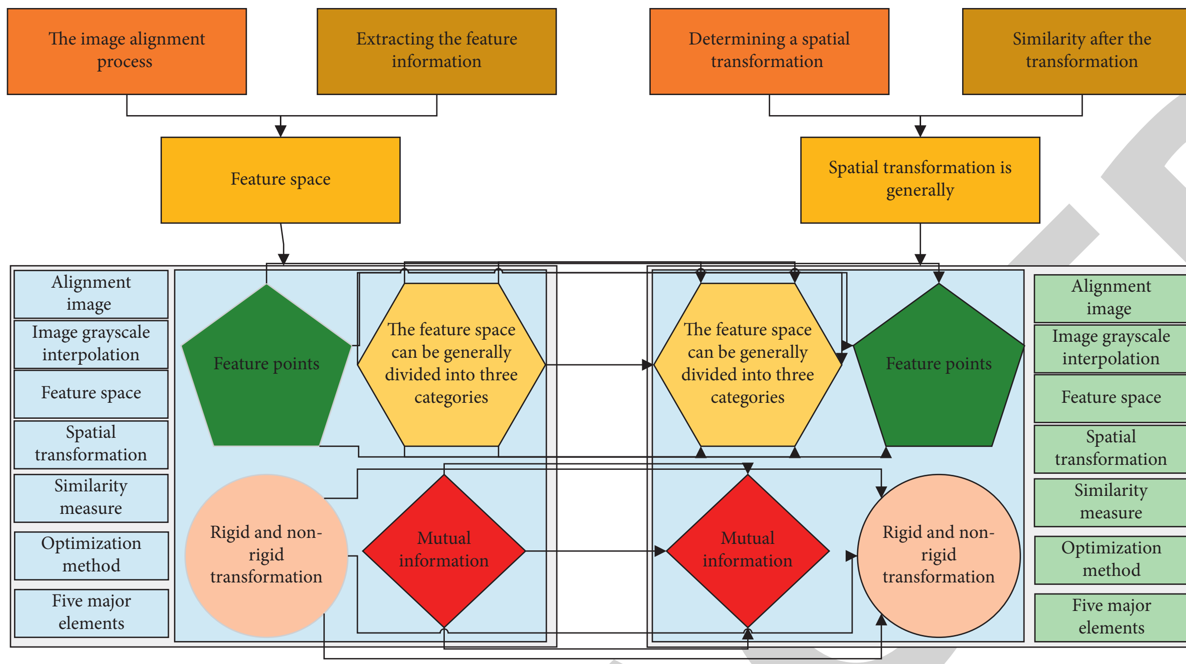

Figure 2: Image alignment principle.

after the transformation. The computation of the spatial transformation is generally done using optimization methods, and the process of generating the alignment image often requires image grayscale interpolation. Therefore, feature space, similarity measure, spatial transformation, optimization method, and interpolation method are the five major elements of image alignment. The feature space can be generally divided into three categories, including feature points, feature curves or feature surfaces, and pixel values. The commonly used similarity measures include meaning square error, correlation, and mutual information. The definition of alignment is based on spatial geometric transformations, which can be divided into rigid and nonrigid transformations according to the different ways of image deformation. Rigid transformations include translation and rotation, which are commonly used in the alignment of human brain images; nonrigid transformations include scaling, affine transformation, projection transformation, and curve transformation. The alignment process is usually transformed into a polar solution problem, using an optimization search algorithm such as the gradient descent method. Commonly used grayscale interpolation methods are linear interpolation, nearest-neighbor interpolation, and spline interpolation. To achieve better computational efficiency and alignment quality, different alignment methods should be selected according to the image deformation mode.

The coronary artery system is composed of three layers of vascular membrane structures, the inner, middle, and outer membranes, in order from the luminal surface (innermost layer) outward, which make up the coronary artery, an elastic, contractable, and expandable system of tubes. The cross section perpendicular to the direction of blood flow in this system can always be considered as a subcircle. Depending on the direction of growth of the coronary arteries, the entire vascular tree can be considered as the root system of the plant. The coronary arteries originate from the root of the ascending aorta, so the ascending aorta can be compared to the main root in the root system. The left and right coronary arteries and the many vessels emanating from them, such as the left circumflex branch, the obtuse marginal branch, the diagonal branch, and the left anterior descending branch, can be compared to the lateral roots in the root system. In the coronary artery system, vessels are usually three-branched or even four-branched, but those with diagnostic value in clinical practice are usually vessels larger than 1.5 mm in diameter, which are often two-branched vessels.

3.2. Contrast Map Centerline Extraction. The extraction of the coronary artery centerline can start from a specified position, and according to the predefined conditions, it is assumed that a small elastic ball is rolled in the direction of blood flow in the coronary artery, and the position of the ball center and the radius size are adjusted in real-time according to the current position until the predefined conditions are met or the largest internal contact ball at that position is found to complete the search at the current position. Then, the ball continues to roll in the direction of blood flow and searches the whole vessel one by one according to the above method until the search is completed. When the sphere encounters a bifurcation point of a coronary artery, the sphere may split into two spheres and then complete the search of the vessel tree in parallel with the above steps [32]. During this process, the positions of the centers of all the maximal internal spheres are recorded, and a curve is formed, which is the centerline of the vessel. However, it has

RETRACTED

been a difficult problem to determine the location of the center of the next internal sphere when searching for the centerline using the maximum internal sphere. One idea to solve this problem is that a point on the sphere of the previous sphere can be selected as the center of the next inner-junction sphere according to the course of the vessel, and the inner-junction sphere at this point must be larger than the inner-junction sphere generated by other voxels on the sphere and cannot be contained by the intersection of other inner-junction spheres. The model of the maximum inner-junction sphere in the vessel is shown in Figure 3.

An object is usually considered to be sampled uniformly in 3D space, where a voxel is the smallest unit, and a voxel contains an Object voxel and a Background voxel. In this method, the target voxel is considered to have 26 neighbors and the background voxel is considered to have only 6 neighbors. In addition, there is a class of Boundary voxels among the target voxels, which are the target voxels with 6 adjacent background voxels, and these boundary voxels form the boundary of the object. For an arbitrary voxel p, it can be defined that its 26 neighbors in space can be split into F-neighbors, Edge-neighbors, and V-neighbors, which are shown in Figure 4. The figure shows that there are 6 F-neighbors of any voxel p (centrally located voxel), which share their 6 surfaces with p; 12 E-neighbors of p, which share their 12 ribs with p; 12 E-neighbors of p, which share their 12 ribs with p; and 12 E-neighbors of p, which share their12 ribs with p. Some voxels share their 8 top angles with p, which make up the V-adjacent voxels of p.

The distance transform can be used to calculate the distance between a pixel point in an image and an area block by using a neighborhood mask, and then the global distance of the image is approximated using the local distance on the way to propagation. To efficiently process 3D data, the target is represented as an octree structure and no background voxels in the image are stored. Since it is not efficient to traverse the octree in array order, the algorithm uses a technique of propagating the distance transform continuously inward from the boundary voxels to increase the efficiency of the traversal, which requires two assignments of the distance transform to the target voxels.

$$L(W) = \sum_i \beta y_j \ln P\left(y_j = 11X\right),$$
$$\sum_i \beta y_j \ln P\left(y_j = 11X\right) = 1 - \beta \sum_i \beta y_j \ln P\left(y_j = 11X\right), \tag{9}$$

The main purpose of the first assignment is to find the boundary voxels in the target region. The 26 adjacent voxels of each target voxel are checked for the presence of background voxels, and if they exist, their distance transform values are assigned according to the following rules and the voxel is classified as a boundary voxel.

In the initialization phase of the algorithm, a list is created for the distance transformation values of each voxel belonging to the target region according to the setup requirements of the algorithm; this list is used to store a pointer to find a node in the octree, and each node in the octree represents the distance transformation value of each voxel, which is found by the values in the list. In the first pass, the circular queue initializes the list with the distance transform values 3, 4, and 5, and the queue starts with 3, assigning the corresponding distance transform value to each voxel belonging to the target region. Starting from the second pass, the boundaries will be shrunk inward as shown in Figure 5.

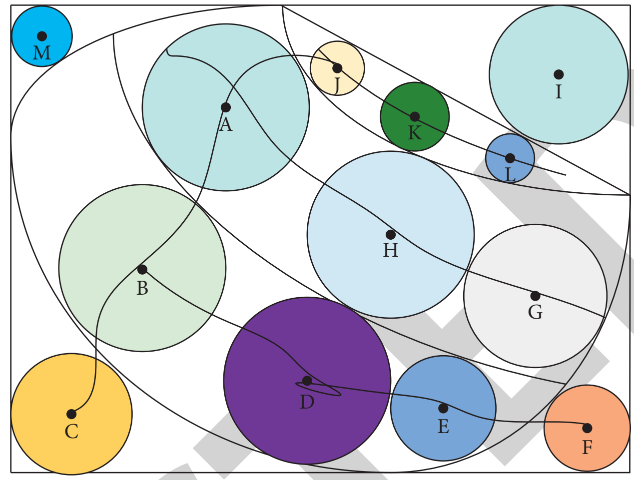

Figure 3: Model of the inner joint ball.

The essential voxels that make up the skeleton lines of the target region can be determined by calculation so that these voxels can be identified using the property that the skeleton lines can reconstruct the original shape. This means that it is possible to reconstruct the approximate shape of the original figure based on the voxels on the skeleton line and their distance transformation values, but it is not enough to have only a rough skeleton line if the precise shape is to be reconstructed; the skeleton line must also contain all the shape features of the original figure [33]. Therefore, it is more important to preserve the skeleton line accurately in the region where the shape changes or the curvature changes suddenly, and the more accurate the skeleton line is, the more accurate the reconstruction can be.

$$\beta = \frac{Y^2}{X}. \tag{10}$$

During this traversal, when the program runs to a certain instant, the point being processed with a distance transformation value of $k\,(k = 3, 4, 5)$ can only have a distance transformation value of $k + 3$, $k + 4$ or $k + 5$ for its neighboring voxels. Iterate through the list at the beginning of the queue and estimate the distance transformation value for all the target voxels adjacent to the boundary voxel. At this point, the distance transformation value is the sum of the list value and the local distance increment, and the size of the increment is 3, 4, or 5 depending on the type of the adjacency. If the new distance transformation value is lower than the value in the current list, the voxel is added to the list corresponding to the new value, and the voxel becomes the new boundary voxel, and the original boundary voxel becomes the background voxel. After processing the list of

RETRACTED

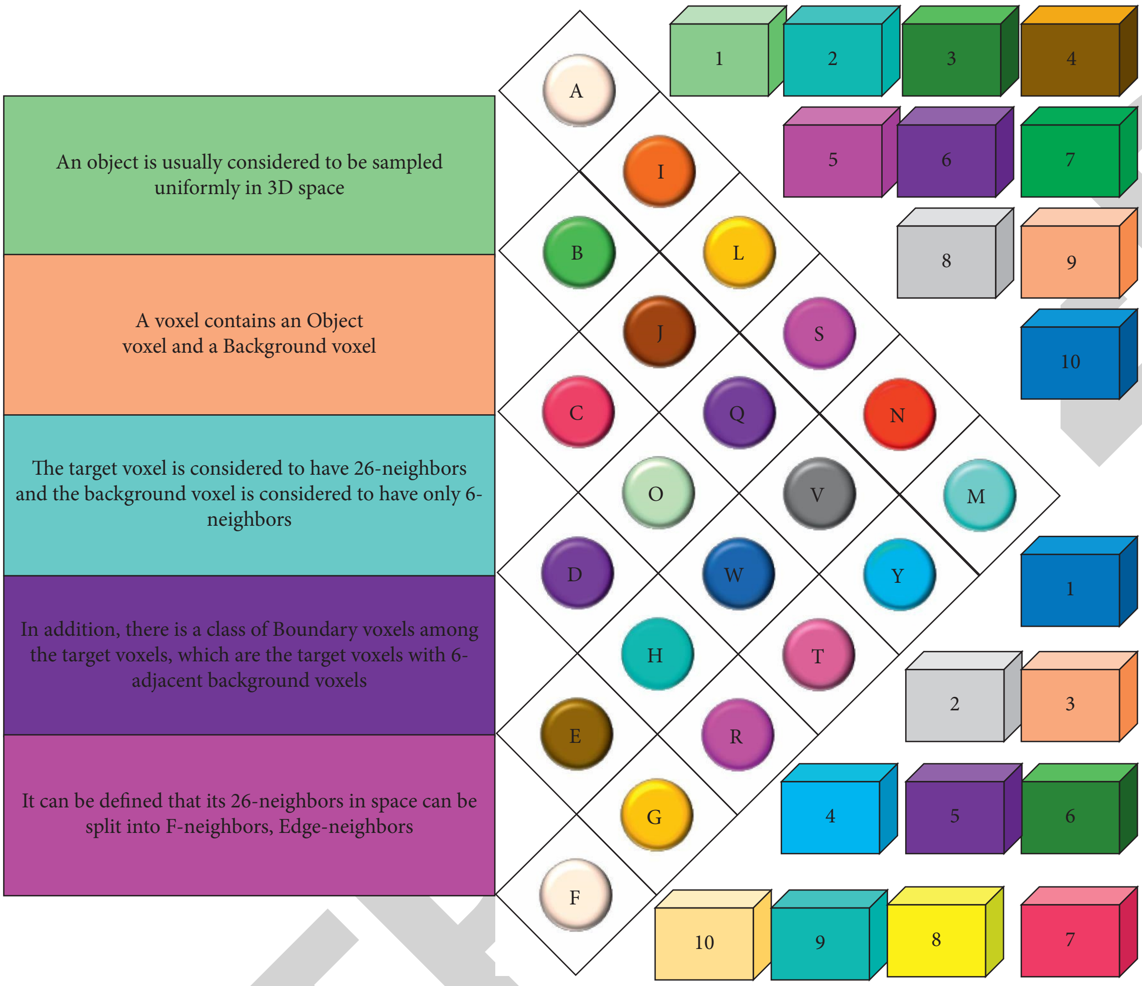

Figure 4: Schematic diagram of the three kinds of adjacencies.

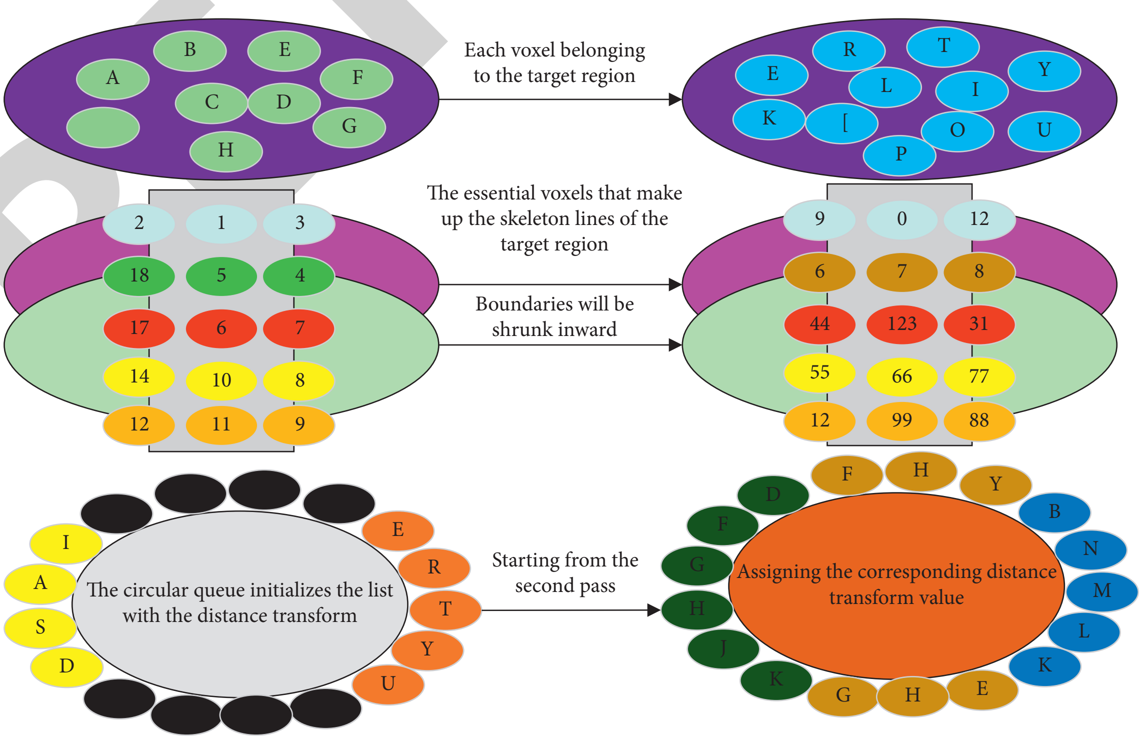

Figure 5: Model of the inner jointed ball of voxel p.

neighboring voxels of the current boundary voxel, the same judgment process is performed for the neighboring voxels of the next boundary voxel until all the boundary voxels of the layer are traversed and the calculation stops, i.e., no more distance transformations of the neighboring voxels of the boundary voxels need to be assigned, as shown in Figure 6.

To find the nonwitness voxels that can complete the graph reconstruction, it is necessary to filter the 26 adjacent voxels of all target voxels. Since all nonwitness voxels have maximal inner-joining spheres, no single maximal inner-joining sphere of a neighboring voxel can completely contain the sphere of nonwitness voxel p. However, according to the above, the maximal inner-joining sphere of a non-witnessing voxel can be contained in the concatenation of the maximal inner-joining spheres of several other voxels. If such voxels exist, their maximal inner-joining spheres must be at least as large as the inner-joining spheres of p, which means that the value of their distance transformation should be greater than or equal to DTp. There is another simpler way to filter for neighboring voxels. The significance of this is that if several of the neighboring voxels of p have higher values of the distance transformations, the inner-joining spheres of p may be contained in the merged set of inner-joining spheres of those voxels.

The core idea of the deep convolutional neural network is to learn about a large amount of data and capture their features by building a model containing three or more hidden layers, to reach the purpose of classification or prediction for new input data. In a deep convolutional neural network, the original image as a whole or its local part is used as the input of the bottom layer, and the information of the original image is passed to different layers at the back through convolutional operations of certain size templates, and each layer extracts the significant features in the image through convolutional operations of different sizes, and finally calculates the classification probability of pixels with certain features through activation functions to achieve classification. According to the above process, CNN mainly contains the input layer, convolutional layer, pooling layer, fully connected layer, activation function, and output structure, as shown in Figure 7.

The input layer is the input to the whole convolutional neural network, which generally represents the pixel matrix of a picture in a convolutional neural network that processes images. As shown in Figure 8, the uppermost part represents a picture (RGB 3D). The length and width of the 3D matrix represent the size of the image, while the depth of the 3D matrix represents the color channel of the image. For example, handwritten characters are recognized as black and white images with a depth of 1. In the RGB color model, the depth of the image is 3. Starting from the input layer, the convolutional neural network transforms the matrix of the previous layer into the matrix of the next layer through different neural network structures until the final fully connected layer.

The pooling layer is a computation that compresses the individual submatrices of the input tensor. It is like the computation of convolution, which is also performed on an image utilizing templates of a specific size, but the difference

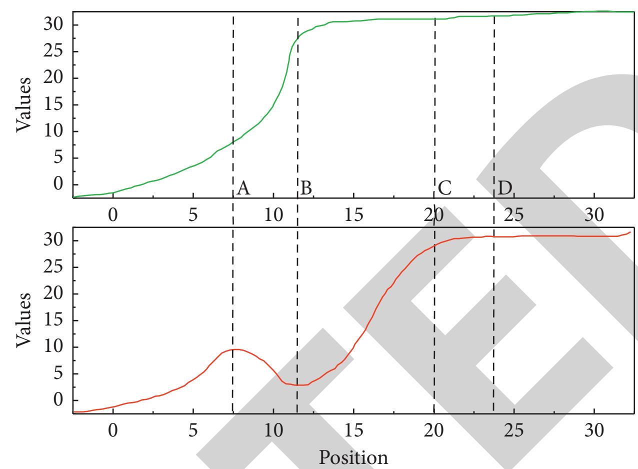

Figure 6: Detection of calcified plaque.

is that the final output of each template has only one value, which is usually the maximum value in the image within the range of the template (at this point called maximum pooling) or the average value (at this point called average pooling). The effect of the pooling layer is to combine similar features within a certain range, which can be very effective in reducing the size of the parameter matrix and thus the number of parameters in the final fully concatenated layer, thus speeding up the computation and having the effect of preventing overfitting.

The power of deep convolutional neural networks lies in their ability to automatically extract features through a combination of multiple convolutions and pooling while being able to learn features at multiple levels. Among them, the front convolutional layer has a small range of receptive fields and can learn features of local regions of the image, while the back convolutional layer has a larger range of receptive fields and can learn more abstract features, which are less sensitive to the position and size of objects. These abstract features are helpful for classification but become difficult for giving object contours and accurately segmenting objects due to the loss of details. When traditional convolutional neural networks perform segmentation, to predict the class of a pixel, they need to be trained and predicted using blocks of images within a certain range of its neighborhood, which requires large storage and is inefficient in terms of computation [34]. To solve this problem, Jonathan Long et al. proposed Fully Convolutional Networks (FCN) for image segmentation. The idea of FCN is to use upsampling of abstract features to predict the class of each pixel of the original image, which is a way to convert the macroscopic (image-level) segmentation problem into a microscopic (pixel-level) classification problem.

FCN is a classification of pixel-level labels, and the segmentation problem of the whole graph is achieved by the classification of all pixels. Unlike CNN, which uses fully connected layers at the end to obtain fixed-length feature vectors for prediction one by one, FCN removes the last fully connected layer and performs deconvolution calculation on the output of the last convolution layer to obtain a feature map of the same size as the original map, which also restores

RETRACTED

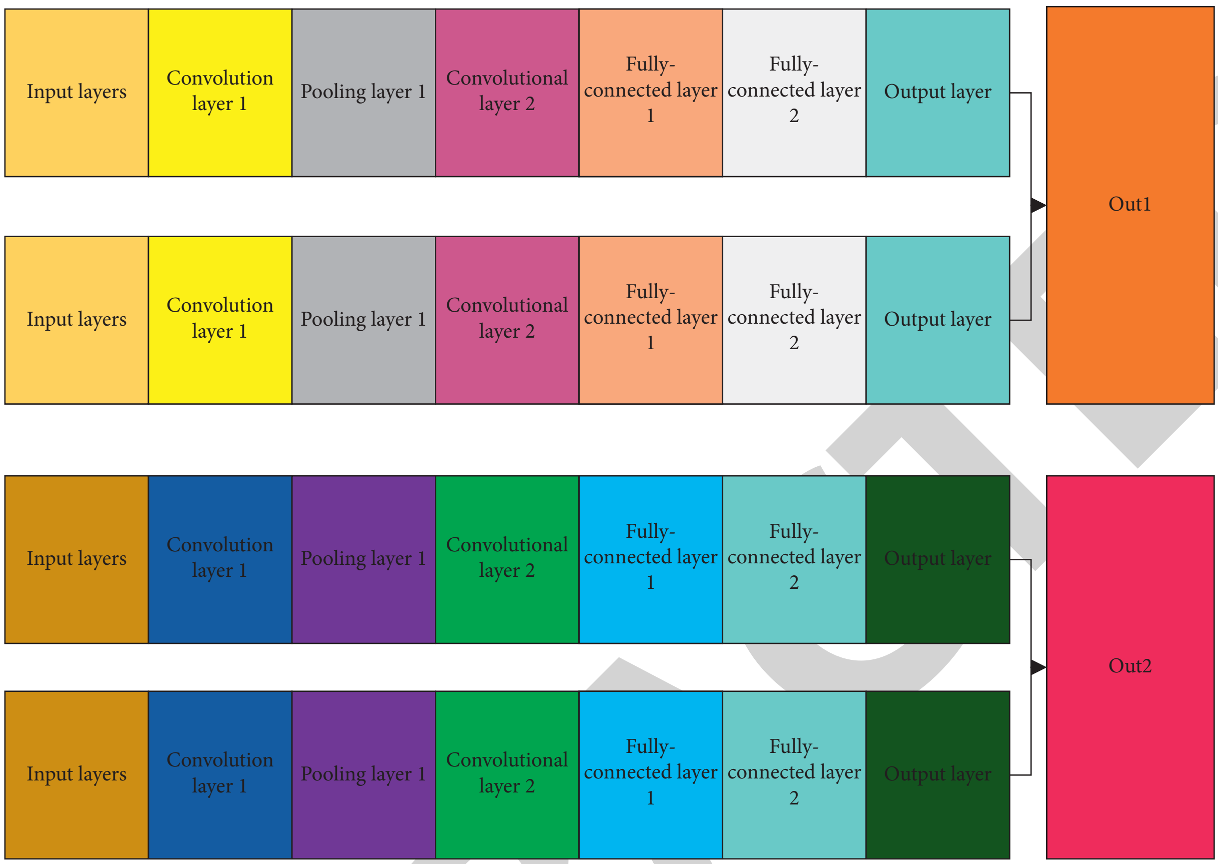

Figure 7: Composition structure of the convolutional neural network.

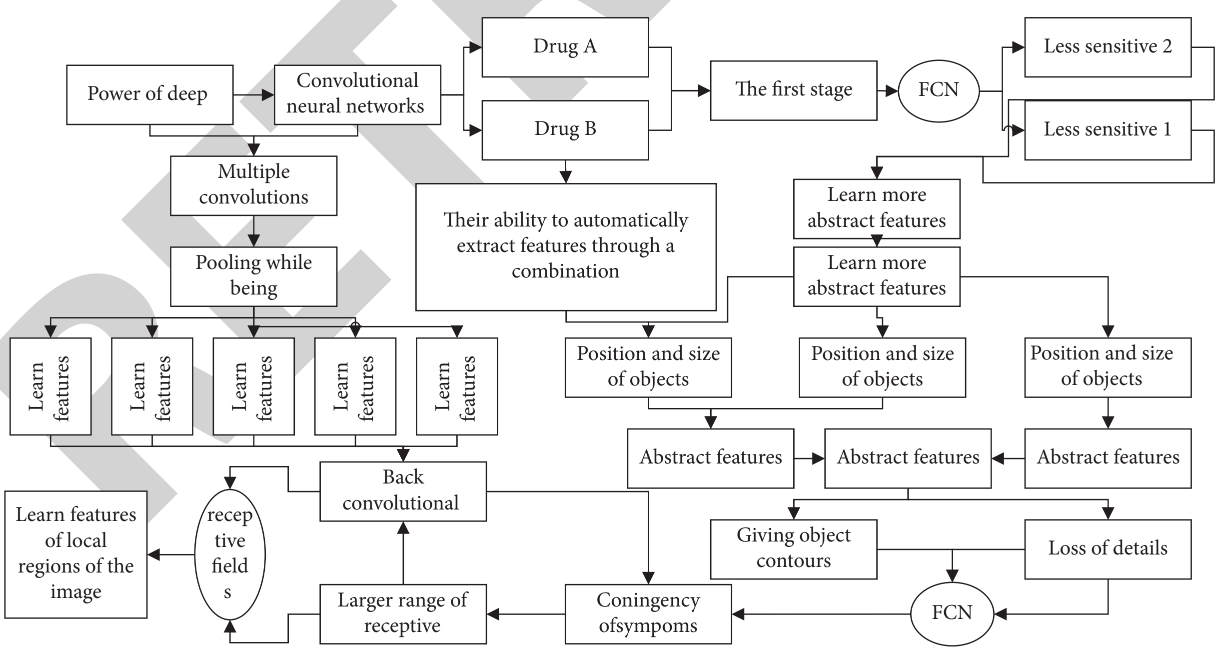

Figure 8: Convolution operation in images.

RETRACTED

the spatial characteristics of the original map, where each pixel in the generated feature map may be used as a sample for training to predict the class of each prediction of the category of each pixel, and so the entire graph can be segmented. The network finally removed the fully connected layer and recovered the image size using deconvolution to predict each pixel category, which resulted in the semantic segmentation of the image.

4. Analysis of Results

4.1. Experimental Results. The topology refinement algorithm described in this chapter is used to extract the centerline of the vessel after 3D reconstruction and to compare the effect of performing the fine branch removal operation on the extraction accuracy. Figure 9 shows the results of centerline extraction using the algorithm in this section in a single vessel, where a right coronary artery is selected in Figures 9(a) and 9(b), and a left anterior descending branch is selected in Figures 9(c) and 9(d). Figures 9(a) and 9(c) show the results of centerline extraction without fine branch removal; Figures 9(b) and 9(d) show the results of extraction with fine branch removal. The gray part of the figure shows the reconstructed coronary artery region, and the blue curve in the middle is the extracted central line. By comparing the four figures, it is easy to find that the Dijkstra algorithm-based fine branch removal method used in this chapter has a good limiting effect on the fine branches generated in the extraction process, greatly reducing the burrs on the centerline, making the extracted centerline smoother and more consistent with the actual shape of the centerline.

To demonstrate that the Dijkstra-based minutiae deletion algorithm can effectively improve the accuracy of the topology refinement algorithm in a single vessel, all vessel data in the dataset were extracted from the centerline separately according to the evaluation criteria proposed in Section 3.2, and then the extraction results were quantified and analyzed, and the results of six vessels were randomly selected for display. Figure 10 shows the results of centerline extraction without fine branch removal, the results of fine branch removal for the extracted skeletal lines after completing the topological refinement in twelve directions. The six vessels include a right coronary artery (RCA3), two left anterior descending branches (LAD1, LAD2), a left gyral branch (LCX2), a sharp-edge branch (MA1), and a posterior descending branch (PDA2).

Also, in this section, CTA data were used to test the effectiveness of the algorithm for centerline extraction in coronary vascular trees. The number of images used varies between 250 and 350 for each case with a single image size of 512×512, a spatial resolution of 0.38 mm, a layer thickness of 0.5 mm, and a minimum reconstructable thickness of 0.6 mm; the bulb voltage used for scanning is 100 VK, and the convolution kernel for 3D reconstruction is Bv36d. The results of the complete coronary vascular tree centerline extraction are shown in Figure 11. The results without fine branch elimination are shown, and the results after fine branch elimination are shown. The gray part of the figure shows the reconstructed vascular region, and the thicker part above is the ascending aorta, from the end of which the coronary arteries diverge into two branches, left and right. Because the centerline of the ascending aorta is not within the scope of this study, its centerline was not extracted. After comparing the two figures, it can be found that the algorithm has a better extraction of the centerline of the coronary vascular tree, and a more complete centerline is also preserved for the end bifurcation part of the left anterior descending branch; after the fine branch elimination, the burr part in the right coronary artery in the figure is effectively restricted, which makes the centerline of the complete vascular tree smoother and more consistent with the actual situation of the centerline. At the same time, this experiment also proves that the algorithm in this chapter has strong robustness and can complete the extraction of centerlines of multiple heeled vessels simultaneously.

Usually, medical images should keep the size and shape of the original structure as much as possible. So, the projection curve is sampled at equal intervals in the process of straightening the collinear, with each sampling point corresponding to one line of the output image. The output image is then sampled in grayscale, usually using trilinear interpolation for grayscale sampling. In extended CPR, the sampled surface defined by the centerline and the direction of interest is essentially a column surface, the line in the direction of interest is the mother line of the column surface, and the curve obtained by projecting the centerline along the direction of interest is the collinear line of the column surface. The collinear dimension of the surface is flattened and then sampled in grayscale from the original body data space to obtain the extended CPR image. As shown in Figure 11, the green arrow is the direction of interest, which is also the centerline projection direction of the extended CPR; the red curve is the vessel or its centerline; and the dashed line on the right side of the plane perpendicular to the green arrow is the projection of the centerline on the plane, which is the collinear line of the column surface; and the final CPR image is obtained by straightening the projection curve.

4.2. Algorithm Results. The main goal of the model training process is to achieve the distinction between foreground and background, i.e., vascular, and nonvascular. One hundred and nine coronary angiography sequences were randomly selected as the training set to train the segmentation model. Each sequence contains 30–50 frames, and the size of each frame is $512 * 512$. Stochastic gradient descent (SGD) is used as the optimization function for the iterations, i.e., only one sample is randomly selected from the total data at a time to update the iteration function with a momentum of 0.9. The initial learning rate is set to 0.001, and then gradually decreases. After training, the generated model is saved as a segmentation model, which enables the segmentation of foreground (vascular) and background (nonvascular). In the training, we found that there is a balance between the time required for prediction and the number of model iterations. Within a certain range, as the number of iterations increases, the segmentation effect is better, while the waiting time is longer. For the balance consideration, the segmentation result of 400 iterations' output is chosen in this paper. The following figure shows the performance curve of the network training process, where loss is the loss function; Dice is the parameter to judge the segmentation effect of the network, the closer to 1 the better the segmentation effect, which will be explained in detail in Chapter 4, as shown in Figure 12.

In the training process, two methods, data enhancement and adding dropout layers, were utilized to prevent

RETRACTED

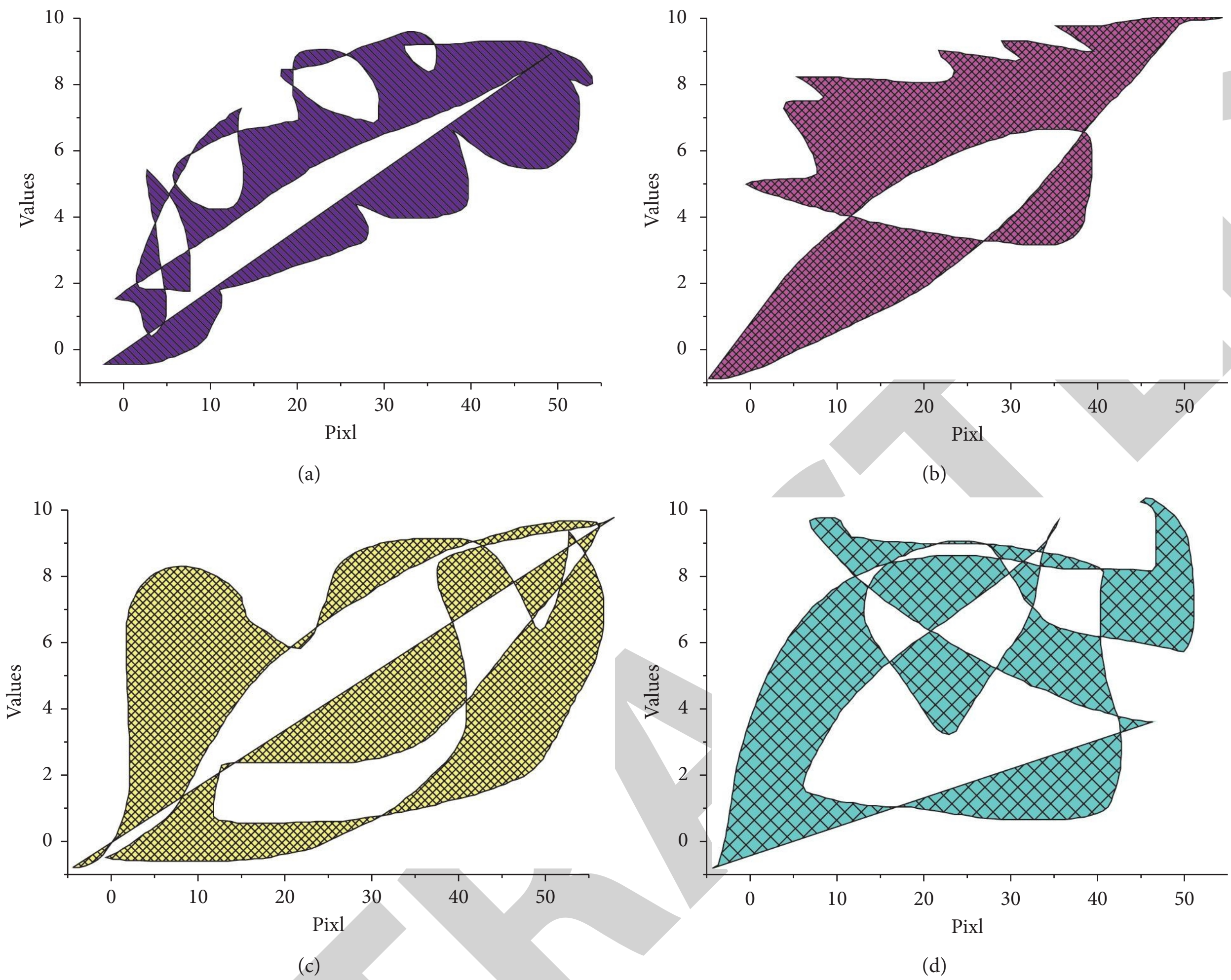

Figure 9: Centerline extraction results.

RETRACTED

overfitting. For data augmentation, we perform random mirror symmetry on the coronary angiography experimental data with 50% probability, followed by random rotation with 50% probability, and finally, the brightness change with 50% probability, and all the data obtained from the augmentation process are input to the network for training. For the dropout layer, the intuitive explanation is to deactivate some nodes in the network randomly, and after several different dropouts, it is equivalent to training several different networks, which is the embodiment of the idea of integrated learning model and realizes the fusion of models in the same network with lower space occupation than the fusion of multiple networks. The random deactivation probability used in this paper is 0.5, and this value is found to minimize the convergence of the loss function in the experiments. Finally, data from 40 patients are used as test set data in this paper to test the performance of the model.

Figure 13 shows the comparison of the results of the two centerline extraction algorithms proposed in this paper with the abovementioned twenty-six directional refinement algorithms. The comparison results used in the table are obtained by taking the average of all the experimental results of the three algorithms after experimenting with all the labeled vessel data. Analyzing the data in the table, we can see that the TDTT algorithm proposed in this paper has improved the overlap rate by 5.4% compared with the MIBTT algorithm; the TDTT algorithm has reduced the average distance to the actual length by about 0.16 mm; the TDTT algorithm has improved the overlap rate before the first error by 63.3% compared with the MIBTT algorithm; the running time of the TDTT algorithm is about 9% of that of the MIBTT algorithm. The average running time of the MIBTT algorithm is 5.217 seconds, which can meet the design requirements of CAD systems in clinical practice.

Comparing the results of centerline extraction based on the twenty-six directional topology refinement algorithm with the TDTT algorithm, we get to see that the overlap rate of the TDTT algorithm is 49.7% higher than that of the algorithm; the average distance is only 20% of that of the algorithm; the overlap rate before the first error is 3.24 times of that of the algorithm; and the extraction time is only 5% of that of the algorithm. After analysis, it is found that the defect of the topology refinement algorithm based on the twenty-six directions is that it does not eliminate the fine branches of the extracted centerline, resulting in a large number of burrs on the extracted centerline, which are

RETRACTED

Figure 10: Results of coronary artery centerline extraction without removing fine branches.

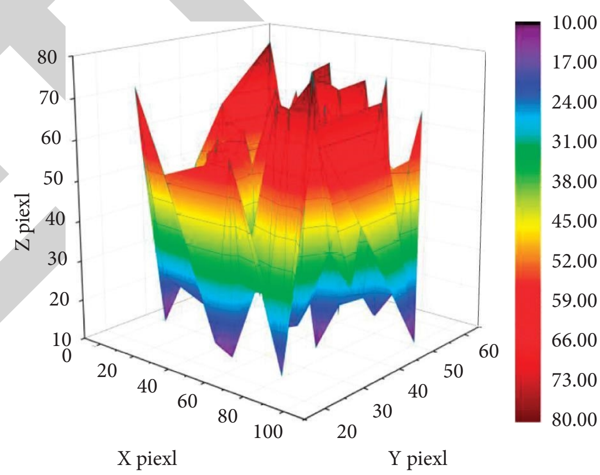

Figure 11: Results of coronary vessel tree centerline extraction.

composed of several or even dozens of voxels, and due to their existence, the overlap rate of the extracted centerline is greatly reduced, and the average distance between the extracted and labeled points appears to increase dramatically. This indicates that the algorithm in this chapter is more suitable than this method for coronary centerline extraction in terms of both running accuracy and running time. By comparing the results of the MIBTT algorithm and the twenty-six direction-based topology refinement algorithm, it is easy to find that the performance of the MIBTT algorithm also has a substantial lead. So, the two coronary centerline extraction algorithms proposed in this paper are more suitable for coronary centerline extraction than the twenty-six direction-based topology refinement algorithm. As the more classical coronary centerline extraction algorithms, the overlap rates of the proposed algorithms are 0.847 and 0.670,

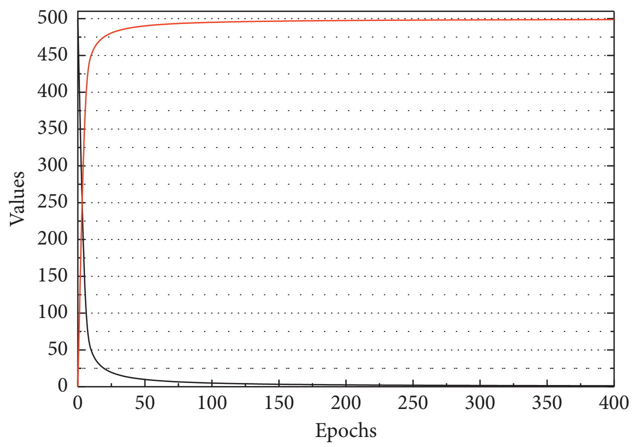

Figure 12: Optimized network after model training.

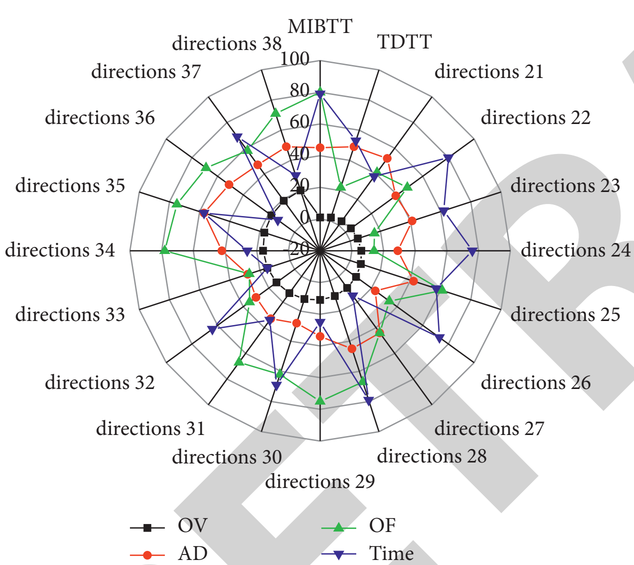

Figure 13: Comparison of algorithm results.

respectively, and compared with this result, the two algorithms proposed in this paper have higher extraction accuracy in coronary centerline extraction.

A method of coronary artery centerline extraction based on a twelve-directional topology refinement algorithm (TDTT) is proposed. The algorithm performs a refinement operation on the reconstructed coronary artery region based on the segmentation of the original image to extract the centerline while maintaining the original topology of the coronary artery as much as possible. At the end of the refinement algorithm, Dijkstra's algorithm is introduced to trim the fine branches in response to the phenomenon of burrs on the centerline during the extraction process, so that it can reflect the actual shape of the coronary artery centerline more realistically. This chapter also evaluates the centerline extraction results of a single vessel in terms of overlap rate, average distance, overlap rate before the first error in the vessel, and running time, and shows the algorithm's extraction results for the centerline of a complete vessel tree. Finally, the two algorithms proposed in this paper are compared, and the results show that the algorithm in this chapter has certain advantages; meanwhile, the algorithm proposed in this chapter is compared with the classical topology refinement algorithm based on twenty-six directions, and it is proved that the algorithm in this chapter is more suitable than this method for extracting the centerlines of coronary arteries.

5. Conclusion

For coronary artery centerline extraction, the basic idea of the study is generally to first segment the original CTA to obtain the coronary artery region, then perform 3D reconstruction, and finally extract the coronary artery centerline in 3D space. The first part of this study follows this idea to segment the CTA. Since the imaging principle of CT is X-ray imaging, the image contains a large amount of scattered noise, and the image is first filtered by an anisotropic diffusion filter, which has the advantage of different smoothing degrees for each direction of the image compared with other filters that only have a single smoothing degree for the image; then, the Frangi vessel enhancement function based on the Hessian matrix is used to filter the image. Enhancement function based on Hessian matrix is then used to enhance the edges of the tubular structure in the image; finally, the coronary artery region in the image is segmented using the region growth method, and the holes generated in the segmentation are filled using the hole filling technique to obtain an accurate segmented image. Based on the completion of segmentation, this paper proposes a method of coronary artery centerline extraction (MIBTT) based on the tubular tissue inner splice ball model. The algorithm first uses two distance transformations to complete the initial contraction of the 3D blood vessels; the first distance transformation is to complete the boundary search of the original figure, and the second traverses the values of the distance transformations of all voxels to contract the original figure to the inside to reduce the computational consumption in the next step of the process; then, the nonwitness voxels are used to construct the maximum internal junction sphere model to find the skeletal voxels that can reflect the shape of the original figure. These initially extracted skeletal voxels are optimized on the skeletal line using a dichotomy-like principle to obtain the final coronary artery centerline. The experimental results show that the algorithm has a good result in extracting the coronary artery centerline, with an overlap rate of 0.934, an average distance of 2.477 pixels from the reference position, an overlap rate of 0.508 before the first error, and an average running time of 5.217 s. However, the algorithm also has shortcomings in that the centerline of the vessel is not well preserved at the two ends of the vessel, and the centerline of the vessel is not well preserved when dealing with a horizontally oriented vessel. However, the algorithm has the disadvantage that the centerline of the vessel is not well preserved at the two ends

RETRACTED

of the vessel, and it is prone to incomplete extraction when dealing with vessels with horizontal orientation.

Data Availability

The labeled dataset used to support the findings of this study is available from the corresponding author upon request.

Conflicts of Interest

The authors declare no conflicts of interest.

Authors' Contributions

Wenjuan Cai and Yanzhe Wang contributed equally to this work.

Acknowledgments

This work was supported by the Health and Family Planning Commission of Changshu under Grant csws201820.

References

[1] M. Zreik, R. W. Van Hamersvelt, and J. M. Wolterink, "A recurrent CNN for automatic detection and classification of coronary artery plaque and stenosis in coronary CT angiography," *IEEE Transactions on Medical Imaging*, vol. 38, no. 7, pp. 1588–1598, 2018, https://pubmed.ncbi.nlm.nih.gov/?term=Leiner+T&cauthor_id=30507498.

[2] H. Cui, Y. Xia, Y. Zhang, and L. Zhong, "Validation of right coronary artery lumen area from cardiac computed tomography against intravascular ultrasound," *Machine Vision and Applications*, vol. 29, no. 8, pp. 1287–1298, 2018.

[3] S. Mabrouk, C. Oueslati, and F. Ghorbel, "Multiscale graph cuts based method for coronary artery segmentation in angiograms," *IRBM*, vol. 38, no. 3, pp. 167–175, 2017.

[4] Y. Kim, J. J. H. Bray, B. Waterhouse et al., "Quantitative evaluation and comparison of coronary artery characteristics by 3D coronary volume reconstruction," *Scientific Reports*, vol. 11, no. 1, pp. 1–8, 2021.

[5] Z. Sedghi Gamechi, L. R. Bons, M. Giordano et al., "Automated 3D segmentation and diameter measurement of the thoracic aorta on non-contrast enhanced CT," *European Radiology*, vol. 29, no. 9, pp. 4613–4623, 2019.

[6] M. Freiman, H. Nickisch, S. Prevrhal et al., "Improving CCTA-based lesions' hemodynamic significance assessment by accounting for partial volume modeling in automatic coronary lumen segmentation," *Medical Physics*, vol. 44, no. 3, pp. 1040–1049, 2017.

[7] V. Tuncay, R. Vliegenthart, M. A. M. Den Dekker et al., "Non-invasive assessment of coronary artery geometry using coronary CTA," *Journal of cardiovascular computed tomography*, vol. 12, no. 3, pp. 257–260, 2018.

[8] Y. Zhang, S. Wang, K. Xia, Y. Jiang, and P. Qian, "Alzheimer's disease multiclass diagnosis via multimodal neuroimaging embedding feature selection and fusion," *Information Fusion*, vol. 66, pp. 170–183, 2021.

[9] Y. Gu and Q. Zheng, "A transfer deep generative adversarial network model to synthetic brain ct generation from MR images," *Wireless Communications and Mobile Computing*, vol. 2021, Article ID 9979606, 2021.

[10] P. Qian, J. Zheng, Q. Zheng et al., "Transforming UTE-mDixon MR abdomen-pelvis images into CT by jointly leveraging prior knowledge and partial supervision," *IEEE/ACM Transactions on Computational Biology and Bioinformatics*, vol. 18, no. 1, pp. 70–82, 2021.

[11] Y. Jiang, Y. Zhang, C. Lin, D. Wu, and C.-T. Lin, "EEG-based driver drowsiness estimation using an online multi-view and transfer TSK fuzzy system," *IEEE Transactions on Intelligent Transportation Systems*, vol. 22, no. 3, pp. 1752–1764, 2021.

[12] J. Von Spiczak, R. Manka, A. Gotschy et al., "Fusion of CT coronary angiography and whole-heart dynamic 3D cardiac MR perfusion: building a framework for comprehensive cardiac imaging," *The International Journal of Cardiovascular Imaging*, vol. 34, no. 4, pp. 649–660, 2018.

[13] S. Y. Guan, T. M. Wang, C. Meng, and J. Wang, "A review of point feature based medical image registration," *Chinese Journal of Mechanical Engineering*, vol. 31, no. 1, pp. 1–16, 2018.

[14] B. Ágg, B. Szilveszter, N. Daradics et al., "Increased visceral arterial tortuosity in Marfan syndrome," *Orphanet Journal of Rare Diseases*, vol. 15, no. 1, pp. 91–10, 2020.

[15] M. Freiman, R. Manjeshwar, and L. Goshen, "Unsupervised abnormality detection through mixed structure regularization (MSR) in deep sparse autoencoders," *Medical Physics*, vol. 46, no. 5, pp. 2223–2231, 2019.

[16] T. Kojima, M. Nagao, H. Yabuuchi et al., "New transluminal attenuation gradient derived from dynamic coronary CT angiography: diagnostic ability of ischemia detected by 13N-ammonia PET," *Heart and Vessels*, vol. 36, no. 4, pp. 433–441, 2021.

[17] K. Fukushima, Y. Matsuo, M. Nagao et al., "Patient based Bull's eye map display of coronary artery and ventricles from coronary computed tomography angiography," *Journal of Computer Assisted Tomography*, vol. 44, no. 1, pp. 26–31, 2020.

[18] L. Hubbard, J. Lipinski, B. Ziemer et al., "Comprehensive assessment of coronary artery disease by using first-pass analysis dynamic CT perfusion: validation in a swine model," *Radiology*, vol. 286, no. 1, pp. 93–102, 2018.

[19] M. Freiman, H. Nickisch, H. Schmitt et al., "A functionally personalized boundary condition model to improve estimates of fractional flow reserve with CT (CT-FFR)," *Medical Physics*, vol. 45, no. 3, pp. 1170–1177, 2018.

[20] P. Rajiah and S. Abbara, "CT coronary imaging-a fast evolving world," *QJM: International Journal of Medicine*, vol. 111, no. 9, pp. 595–604, 2018.

[21] F. Maffessanti, A. R. Patel, M. B. Patel et al., "Non-invasive assessment of the haemodynamic significance of coronary stenosis using fusion of cardiac computed tomography and 3D echocardiography," *European heart journal cardiovascular Imaging*, vol. 18, no. 6, pp. 670–680, 2017.

[22] C. Shi, X. Luo, J. Guo, Z. Najdovski, T. Fukuda, and H. Ren, "Three-dimensional intravascular reconstruction techniques based on intravascular ultrasound: a technical review," *IEEE journal of biomedical and health informatics*, vol. 22, no. 3, pp. 806–817, 2017.

[23] S. Li, C. Chen, L. Qin et al., "The impact of iterative reconstruction algorithms on machine learning-based coronary CT angiography-derived fractional flow reserve (CT-FFRML) values," *The International Journal of Cardiovascular Imaging*, vol. 36, no. 6, pp. 1177–1185, 2020.

[24] P. G. Tahoces, D. Santana-Cedrés, L. Alvarez et al., "Automatic detection of anatomical landmarks of the aorta in CTA images," *Medical, & Biological Engineering & Computing*, vol. 58, no. 5, pp. 903–919, 2020.

RETRACTED